




DAVID PUGH AND
PHILIP WOODWORTH

SEA-LEVEL SCIENCE

Understanding Tides, Surges, Tsunamis and
Mean Sea-Level Changes

The lower half of the cover features a photograph of a powerful ocean wave crashing against a dark, rocky cliff. The water is white with foam, and the sky is overcast with grey clouds. The foreground shows dark, scrubby vegetation.

CAMBRIDGE

Sea-Level Science

Understanding Tides, Surges, Tsunamis and Mean Sea-Level Changes

Sea levels change for many reasons and on many timescales, and extreme sea levels can result in catastrophic coastal flooding, such as the Katrina storm surge in 2005 or the Sumatra tsunami in 2004. As global sea level rises, and coastal populations increase, understanding sea-level processes becomes key to plan future coastal defence effectively.

Ocean tides, storm surges, tsunamis, El Niño and the sea-level rise caused by climate change are among the processes explained in this book. Building on David Pugh's classic graduate-level book *Tides, Surges and Mean Sea-Level*, this substantially updated and expanded full-colour book now incorporates major recent technological advances in the areas of satellite altimetry and other geodetic techniques (particularly GPS), tsunami science, measurement of mean sea level and analyses of extreme sea levels. The authors, both leading international experts, discuss how each surveying and measuring technique complements others in providing an understanding of present-day sea-level change and more reliable forecasts of future changes.

Giving the *how* and the *why* of sea-level change on timescales from hours to centuries, this authoritative and exciting book is ideal for graduate students and researchers working in oceanography, marine engineering, geodesy, marine geology, marine biology and climatology. It will also be of key interest to coastal engineers and governmental policy-makers.

David Pugh is a marine science consultant, also holding positions as Visiting Professor at the University of Liverpool and Visiting Scientist at the National Oceanography Centre (NOC). His research specialises in tides, surges, mean sea level, coastal management and climate change, together with marine economics and the history of sea level. After a career in science and science management with the UK Natural Environment Research Council, Dr Pugh served as President of the Intergovernmental Oceanographic Commission (IOC) of UNESCO, 2003–7. He had previously been Director of the Permanent Service for Mean Sea Level and Founding Chairman of the IOC Global Sea Level network, GLOSS. Dr Pugh has authored two books and recently co-edited *Troubled Waters: Ocean Science and Governance* (Cambridge University Press, 2010) published for the 50th anniversary of the IOC. He has been awarded an OBE for services to marine sciences.

Philip Woodworth is an Individual Merit Scientist in the Natural Environment Research Council based at the NOC in Liverpool, and also a Visiting Professor at the University of Liverpool. He has been Director of the PSMSL and Chairman of GLOSS. Dr Woodworth has published extensively

on tides, sea-level changes and geodesy, including co-editing *Understanding Sea-Level Rise and Variability* (Wiley Blackwell, 2010), and has been involved in each IPCC research assessment. His awards include the Denny Medal of IMAREST, the Vening-Meinesz Medal of the European Geosciences Union, the 50th Anniversary Medal of the IOC, and a minute share in the 2007 Nobel Peace Prize awarded to the IPCC. He was awarded an MBE in 2011 for services to science.

Sea-Level Science

Understanding Tides, Surges, Tsunamis
and Mean Sea Level

David Pugh and Philip Woodworth

University of Liverpool

CAMBRIDGE
UNIVERSITY PRESS

University Printing House, Cambridge CB2 8BS, United Kingdom

Published in the United States of America by Cambridge University Press, New York

Cambridge University Press is part of the University of Cambridge.

It furthers the University's mission by disseminating knowledge in the pursuit of education, learning, and research at the highest international levels of excellence.

www.cambridge.org

Information on this title: www.cambridge.org/9781107028197

© David Pugh and Philip Woodworth 2014

This publication is in copyright. Subject to statutory exception and to the provisions of relevant collective licensing agreements, no reproduction of any part may take place without the written permission of Cambridge University Press.

First edition published as *Tides, Surges and Mean Sea-Level: A Handbook for Engineers and Scientists*, 1987, by David Pugh (Wiley Blackwell, all rights reverted to author)

Second edition published 2014

Printed and bound in the United Kingdom by

A catalogue record for this publication is available from the British Library

Library of Congress Cataloguing in Publication data

ISBN 978-1-107-02819-7 Hardback

Cambridge University Press has no responsibility for the persistence or accuracy of URLs for external or third-party internet websites referred to in this publication, and does not guarantee that any content on such websites is, or will remain, accurate or appropriate.

Contents

Preface page vii

List of acronyms ix

List of symbols xi

-
- 1 Introduction 1**
 - 1.1 Background 1
 - 1.2 Early ideas and observations 1
 - 1.3 Tidal patterns 3
 - 1.4 Meteorological and other non-tidal changes 7
 - 1.5 Some definitions of common terms 8
 - 1.6 Basic statistics of sea levels as time series 11
 - 2 Sea-level measuring systems 17**
 - 2.1 The science of measurement 17
 - 2.2 Datum definitions 20
 - 2.3 Coastal instruments 22
 - 2.4 Open-sea gauges 30
 - 2.5 Data reduction 31
 - 2.6 Data sources 33
 - 3 Tidal forces 36**
 - 3.1 Gravitational attraction 36
 - 3.2 The tidal forces: a fuller development 40
 - 3.3 The Moon–Earth–Sun system 44
 - 3.4 Tidal patterns 49
 - 3.5 Extreme tidal forces 53
 - 4 Tidal analysis and prediction 60**
 - 4.1 Non-harmonic methods 61
 - 4.2 Harmonic analysis 62
 - 4.3 Response analysis 78
 - 4.4 Analysis of currents 82
 - 4.5 Time zone conversion 86
 - 4.6 Stability of tidal parameters 87
 - 4.7 Tidal predictions 89
 - 5 Tidal dynamics 97**
 - 5.1 The real world 97
 - 5.2 Long-wave characteristics 99
 - 5.3 Ocean tides 105
 - 5.4 Shelf tides 111
 - 5.5 Radiational tides 122
 - 5.6 Internal tides 124
 - 5.7 The yielding Earth 126
 - 5.8 Are tides changing? 129
 - 6 Shallow-water and coastal tides 133**
 - 6.1 Introduction: some observations 133
 - 6.2 Hydrodynamic distortions 133
 - 6.3 Representation by higher harmonics 136
 - 6.4 Tidal currents 139
 - 6.5 Tidal asymmetry 142
 - 6.6 Tides in rivers 144
 - 6.7 Energy budgets 149
 - 7 Storm surges, meteotsunamis and other meteorological effects on sea level 155**
 - 7.1 Introduction 155
 - 7.2 The depth-averaged (2-D) equations 155
 - 7.3 Storm surges 156
 - 7.4 Statistics of tidal residuals 164
 - 7.5 Seiches 165
 - 7.6 Meteotsunamis 170
 - 7.7 Wave set-up and surf beat 172
 - 7.8 Air pressure-related changes of sea level in the world ocean 173
 - 8 Tsunamis 189**
 - 8.1 Introduction 189
 - 8.2 Why tsunamis happen 192
 - 8.3 Tsunami propagation across the ocean 199
 - 8.4 Coastal shoaling and runup 203
 - 8.5 Tsunami signals in sea-level and bottom pressure data 206

8.6	Sea-level and related technologies for tsunami monitoring	207	12	Sea-level applications	318
8.7	Tsunami further reading	215	12.1	Design parameters	318
9	Sea-level changes in space	223	12.2	Extreme conditions	319
9.1	Introduction	223	12.3	Coastal defences	327
9.2	The International Terrestrial Reference Frame	223	12.4	Lagoons and channels	329
9.3	The Global Positioning System	224	12.5	Power generation	331
9.4	DORIS	227	12.6	Emersion–submersion probabilities	335
9.5	Satellites and Mean Sea Surface	227	12.7	Flood warning systems	337
9.6	Satellites and the geoid	233	12.8	Economics of coastal defences	341
9.7	Models of the MSS, geoid and MDT	240	13	Sea level and life	345
9.8	A comment on epochs	243	13.1	Introduction	345
9.9	Towards a global vertical datum	243	13.2	The Moon and us	345
10	Mean sea-level changes in time	252	13.3	Intertidal life	346
10.1	Introduction	252	13.4	Human development	351
10.2	Sea-level data	252	13.5	The sea-level present	354
10.3	Mesoscale variability in sea level	254	13.6	The sea-level future	355
10.4	The seasonal cycle of MSL	256			
10.5	Pole tide	259	Appendix A	Basic hydrostatic and hydrodynamic equations	361
10.6	Nodal tide	261	A.1	The hydrostatic equation	361
10.7	Air pressure-related sea-level variability	262	A.2	Conservation of mass	361
10.8	Large-scale patterns of interannual variability	264	A.3	The horizontal momentum equations	361
10.9	Long-term changes in sea level	268	Appendix B	Currents	363
10.10	Understanding sea-level change	276	B.1	Analysis of currents	363
10.11	Future rise in mean and extreme sea levels	280	B.2	Current dynamics	365
11	Sea-level changes in time to do with the solid Earth	296	Appendix C	High and low water times and heights from harmonic constituents	368
11.1	Introduction	296	Appendix D	Theoretical tidal dynamics	370
11.2	Techniques for measuring vertical land movement	296	D.1	Long progressive wave, no rotation	370
11.3	Glacial Isostatic Adjustment	301	D.2	Standing waves	372
11.4	Tectonic sea-level changes	303	D.3	Long waves on a rotating Earth	373
11.5	Man-made crustal movements	307	D.4	Co-tidal and co-amplitude lines	374
11.6	Geophysical fingerprints of sea-level change	308	Appendix E	Legal definitions in the coastal zone	376
11.7	Coastal processes	310	Glossary		380
			Index		389

Preface

We spend much of our time studying sea-level science, a wide-ranging and constantly fascinating subject. We analyse data, read and write papers, and present findings at conferences where there are people in the same sea-level community as us. However, every so often we get to meet other people who have been exposed to this subject in a more personal way: someone who lost relatives in the 1953 North Sea storm surge, another who lost everything more than once in Bangladesh floods, a colleague who survived the 2004 Sumatra tsunami.

We remember at a conference of sea-level experts in the Maldives some years ago a small boy holding a homemade poster declaring ‘Down with sea-level rise’, as he feared for the future of his country. Concern about possible global warming and sea-level rise has rarely been expressed as simply or as effectively. These examples remind us that the results of our work are important, not just for the scientific papers that are produced, but also for many practical reasons, which somehow we find reassuring.

This book is an integrated account of sea level and the physical reasons why it is endlessly changing: tides, weather effects, tsunamis, long-term climate change, and even changes in the solid Earth. The chapters cover many fields: oceanography, geology, geodesy, climate change, coastal engineering, data management and others.

It takes as its starting point David Pugh’s 1987 *Tides, Surges and Mean Sea Level*, which is now long out of print, and significantly out of date. That book was published at a time of renaissance for sea-level science – a rebirth driven by the technology of satellites and ever more powerful computers; and by fundamental public concerns about the effects of climate change and potential increased coastal flooding. These concerns have been reinforced by recent catastrophic tsunami and storm surge events.

This new account has roughly three components. The first component consists of six chapters that follow the 1987 book’s treatment of tides: instruments, forces, analysis and dynamics. In the second component,

spanning [Chapters 7 to 11](#), we review the major new developments in sea-level science: weather effects, tsunamis, satellites and geodesy, and global sea-level changes related to climate change. Our discussion of the latter can be read alongside the recently published *Fifth Assessment Report of the Intergovernmental Panel on Climate Change*, which provides even more facts and figures on sea level and climate.

In the third component, containing the final two chapters, we discuss more generally how humankind has been affected by changes in sea level in the past, and seeks to make practical arrangements for changes in the future. It is undoubtedly the case that changes in sea level affect the way we live our lives today, and they will become increasingly important in the future. Sea-level science matters to us all.

Acknowledgements

We are grateful for the help of many scientific colleagues and friends, who were kind enough to comment on early versions of each chapter and provide valuable advice. Particular thanks go to Trevor Baker, John Hunter, Alexander Rabinovich and Richard Ray, whose expertise on ocean and earth tides, sea-level extremes and tsunamis was so freely made available to us.

Several of our colleagues at the National Oceanography Centre were imposed upon to read draft chapters or advise on others. Special thanks go to Angela Hibbert, Miguel Angel Morales Maqueda, Jo Williams, Simon Williams and Judith Wolf.

We have also appreciated specific guidance and help from Thorkild Aarup, Yasser Abualnaja, Ole Andersen, Isabel Goncalves Araújo, Richard Bingley, David Blackman, David Cotton, Roland Gehrels, Jonathan Gregory, Ivan Haigh, Lee Harris, Kevin Horsburgh, John Howarth, Chris Hughes, Paul Hughes, Antony Joseph, Mark Lawless, David Long, Mark Merrifield, Glenn Milne, Andy Plater, Rui Ponte, Reiner Rummel, Mikis Tsimplis, Javier Valladares, Ian Vassie, Ric Williams and Chris Wilson. We are also

grateful for help and advice from our colleagues in the Permanent Service for Mean Sea Level: Lesley Rickards, Simon Holgate, Svetlana Jevrejeva, Mark Tamisiea, Andy Matthews, Kathy Gordon and Liz Bradshaw.

Other colleagues provided us with top copies of figures from their work or helped us find photographs. In some cases, the figures provided were unpublished

ones, as we have acknowledged appropriately in the captions.

Robert Smith and Kate Davis have advised on and prepared many of the figures. We acknowledge the use of the Generic Mapping Tools package for others.

David Pugh thanks the King Abdullah University of Science and Technology for their hospitality while sections of this book were prepared.

Acronyms

ACC	Antarctic Circumpolar Current	GCN	GLOSS Core Network
ADCP	Acoustic Doppler Current Profiler	GCOS	Global Climate Observing System
AMO	Atlantic Multidecadal Oscillation	GEOSS	Global Earth Observation System of Systems
AMOC	Atlantic Meridional Overturning Circulation	GEV	Generalised Extreme Value
AO	Arctic Oscillation	GFO	GeoSat Follow-on Satellite
AOGCM	Atmosphere Ocean General Circulation Model	GGOS	Global Geodetic Observing System (of the International Association of Geodesy)
AR4	IPCC Fourth Assessment Report	GIA	Glacial Isostatic Adjustment
AR5	IPCC Fifth Assessment Report	GLONASS	Global Orbiting Navigation Satellite System
BM	Bench Mark		
BP	Before Present or Bottom Pressure	GLOSS	Global Sea Level Observing System (of the Intergovernmental Oceanographic Commission)
BPR	Bottom Pressure Recorder		
CGPS	Continuous GPS	GNSS	Global Navigation Satellite System
CM	Centre of Mass	GOCE	Gravity Field and Steady-State Ocean Circulation Explorer Satellite
DART	Deep-ocean Assessment and Reporting of Tsunami	GOOS	Global Ocean Observing System
DD	Double Differencing (GPS data processing method)	GPS	Global Positioning System
DORIS	Doppler Orbitography and Radiopositioning Integrated by Satellite	GRACE	Gravity Recovery and Climate Experiment Satellite
DNA	Deoxyribonucleic acid	GTS	Global Telecommunications System
ECDIS	Electronic Chart Display and Information System	HAT	Highest Astronomical Tide
EGPS	Epochal or Episodic GPS	IAG	International Association of Geodesy
EKE	Eddy Kinetic Energy	IB	Inverse Barometer
ENSO	El Niño–Southern Oscillation	ICESat	Ice, Cloud and Land Elevation Satellite
Envisat	Environmental Satellite of the European Space Agency	IERS	International Earth Rotation Service
EOF	Empirical Orthogonal Function	IGS	International GNSS Service
EOP	Earth Orientation Parameter	InSAR	Interferometric Synthetic Aperture Radar
ERS-1, -2	European Remote Sensing satellite-1 and -2	IOC	Intergovernmental Oceanographic Commission
ESA	European Space Agency		
EUMETSAT	European Organisation for the Exploitation of Meteorological Satellites	IOD	Indian Ocean Dipole
FBM	Fundamental Bench Mark		

List of acronyms

IPCC	Intergovernmental Panel on Climate Change	PSMSL	Permanent Service for Mean Sea Level
ITRF	International Terrestrial Reference Frame	PTWC/S	Pacific Tsunami Warning Center/ System
IWO	Initial Withdrawal of the Ocean	RLR	Revised Local Reference data set of the PSMSL
JCOMM	WMO/IOC Joint Technical Commission for Oceanography and Marine Meteorology	SAM	Southern Annular Mode
LAT	Lowest Astronomical Tide	SLR	Satellite Laser Ranging or Sea Level Rise
LEO	Low Earth Orbit	SSH	Sea Surface Height
LGM	Last Glacial Maximum	SOI	Southern Oscillation Index
LIB	Local Inverse Barometer	SST	Satellite-to-Satellite Tracking or Sea Surface Temperature
LOD	Length Of Day	SWH	Significant Wave Height
MDT	Mean Dynamic Topography	TAR	IPCC Third Assessment Report
MH[L]W	Mean High [or Low] Water	TEC	Total Electron Content
MH[L]WN	Mean High [or Low] Water Neaps	TG	Tide Gauge
MH[L]WS	Mean High [or Low] Water Springs	TGBM	Tide Gauge Bench Mark
MSL	Mean Sea Level	TIGA	Tide GAUge benchmark monitoring project of the IGS
MSS	Mean Sea Surface	TNT	Trinitrotoluene (a ton of TNT being a measure of explosive energy)
MTL	Mean Tide Level	TOPEX/Poseidon	TOPOgraphy EXperiment/ Poseidon radar altimeter satellite
NAM	Northern Annular Mode	UHSLC	University of Hawaii Sea Level Center
NAO	North Atlantic Oscillation	UNESCO	United Nations Educational, Scientific and Cultural Organisation
NLSW	Non-Linear Shallow-Water equations	VLBI	Very Long Baseline Interferometry
NOC	National Oceanography Centre (UK)	WAIS	West Antarctic Ice Sheet
OTL	Ocean Tidal Loading	WMO	World Meteorological Organization
PDO	Pacific Decadal Oscillation		
PGR	Post Glacial Rebound (now usually referred to as GIA)		
POT	Peak Over Threshold		
PPP	Precise Point Positioning (GPS data processing method)		

Symbols

a	Earth radius	p	longitude of lunar perigee
A_b, A_s	right ascensions of the Moon and Sun	p'	longitude of solar perigee
c	wave speed: $c = \sqrt{gD}$ in shallow water	P	general pressure variable
C_b, C_s	hour angles of the Moon and Sun	P_A	atmospheric pressure at the sea surface
C_a	speed of sound in air	P_z	pressure at depth z
C_e	speed of electromagnetic wave	Q_C, Q_{AC}	amplitudes of clockwise and anticlockwise components of currents
D	water depth	q	current speed
d_b, d_s	declinations of the Moon and Sun	r	distance, variously defined
e_b, e_e	eccentricity of lunar and Earth orbits	R_b, R_s	lunar and solar distances from the Earth
f	Coriolis parameter $f = 2\omega_s \sin \phi$	$R(t)$	residual non-tidal component of sea level
F	a form factor that describes the relative importance of diurnal and semidiurnal tides at a particular location	s	geocentric mean ecliptic longitude of the Moon
f_n	nodal amplitude factor for harmonic constituent n	t	time
F_s, F_b	surface and bottom stresses in the X direction	$T(t)$	tidal component of sea level
g	gravitational acceleration	u, v	current components in the X and Y directions
G	universal gravitational constant	u_n	nodal phase factor for harmonic constituent n
g_n	phase lag of harmonic constituent n on the local Equilibrium Tide; relative to the Equilibrium Tide at Greenwich the symbol used is G_n (usually expressed in degrees)	V_n	nodal astronomical phase angle of harmonic constituent n in the Equilibrium Tide, relative to the Greenwich meridian
g_C, g_{AC}	phases of clockwise and anticlockwise components of current	W	wind speed
g_{ux}, g_{vx}	phases of Cartesian current components	x, y, z	coordinates of a point
G_s, G_b	surface and bottom stresses in the Y direction	X, Y, Z	Cartesian coordinate system. Z is positive vertically upwards
h	geocentric mean ecliptic longitude of the Sun	$Z(t)$	mean sea level
H_n	amplitude of harmonic constituent n of tidal levels	α	dimensionless ratio variously defined
H_o	the amplitude of a Kelvin wave at the coast	ϵ_b, ϵ_s	ecliptic latitudes of the Moon and Sun
i, j	general integers	β	a general angular measure
l	length variable	ζ	displacement of water level from the mean
L	length of ocean basin	θ	direction to which current and wind flow, clockwise from north
m_e, m_b, m_s	mass of Earth, Moon, Sun	λ_b, λ_s	true ecliptic longitudes of the Moon and Sun
N	ascending nodal lunar longitude	ρ	seawater density
$O(t)$	observed series of sea levels	ρ_A	air density

List of symbols

σ_n	angular speed of constituent n , usually in degrees per mean solar hour	ω_s	angular speed of the Earth's rotation on its axis relative to a fixed celestial point ($\omega_s = \omega_0 + \omega_3 = \omega_1 + \omega_2$)
τ_s, τ_b	unresolved surface and bottom stresses	Ω	Equilibrium tidal potential
σ	standard deviation of a time series		
Υ	First Point of Aries		
ϕ	latitude of a point on the Earth's surface		Harmonic constituents are shown in heavy type thus: \mathbf{X}_2 , to denote their vector property (H_x, g_x).
ω_n	angular speed of constituent n		Overbars denote time-averaged values.
ω_0 to ω_6	angular speeds of astronomical variables (see Table 3.2)		

Introduction

Prospero: ‘...ye that on the sands with printless foot
Do chase the ebbing Neptune and do fly him
When he comes back’

Shakespeare, The Tempest

Sea levels are always changing, for many reasons. Some changes are rapid while others take place very slowly. The changes can be local, or extend globally. This book is about the science of these changes.

In this first chapter we outline what constitutes sea-level science. A brief account of the development of scientific ideas is followed by an outline of how sea levels are affected by a wide range of physical forces and processes. Finally we give some basic definitions, and discuss the fundamental statistics of sea levels as time series.

1.1 Background

Living by the sea has many benefits. Statistics show that about half the global population lives within 100 km of the sea. Most of the world’s largest cities are on or near the ocean. Ninety per cent of all global trade is carried by sea. The coast offers possibilities of both trade and travel, and increasingly of water-based recreation. Natural geological processes have often conspired to create flat and fertile land near to the present sea level, to which people are drawn or driven to settle.

There are risks. Throughout history, humankind has adjusted and coped with changing sea levels: the ebb and flow of the tides, storm flooding and, for some vulnerable places, the dangers of being inundated by a tsunami. However, as our cities and our patterns of coastal development become more intricate, populated and interdependent, we become more and more vulnerable to disasters. The rural response of driving cattle to higher ground for the duration of a flood is much easier than the urban complexity of rebuilding complete sewage and transport systems. In extreme

cases flooding, with disastrous long-term consequences, may destroy the delicate infrastructure of coastal cities.

Books dealing with the science of sea levels and tidal phenomena are comparatively rare. However, unified treatments of general interest are found in older specialist books [1, 2, 3], and in more recent publications [4, 5, 6]. Accounts are also found in more general books on oceanography, especially the second volume of Defant’s *Physical Oceanography* [7]. Defant and some other experts have also written more popular accounts [8], which are useful introductions, though sometimes hard to find.

1.2 Early ideas and observations

The link between the Moon and tides was known from very early times. Sailors had a very practical need for developing this understanding, particularly for their near-shore navigation in the small ships of those times. A more scientific explanation of the links between tides and the movements of the Moon and Sun evolved much later. Many eminent scientists have been involved in this scientific development.

Even 2000 years ago, historical records show an impressive collection of observed tidal patterns [9]. However, the ideas advanced by the philosophers of that time, and for the following 1600 years, to explain the connection between the Moon and the tides were less valid. Chinese ideas supposed water to be the blood of the Earth, with tides as its beating pulse, with the Earth breathing causing the tides. Arabic explanations supposed the Moon’s rays to be reflected off rocks at the bottom of sea, thus heating and expanding the water, which then rolled in waves

towards the shore. One poetic explanation invoked an angel who was set over the seas: when he placed his foot in the sea the flow of the tide began, but when he raised it, the tidal ebb followed. During this long period there was a decline in critical thought, so that the clear factual statements by the classical writers were gradually replaced by a confusion of supposed facts and ideas. One notable exception was the Venerable Bede, a Northumbrian monk, who described around AD 730 how the rise of the water along one coast of the British Isles coincided with a fall elsewhere. Bede also knew of the progression in the time of high tide from north to south along the Northumbrian coast.

Johannes Kepler (1596–1650), while developing laws to describe the orbits of the planets around the Sun, suggested that the gravitational pull of the Moon on the oceans might be responsible for tides. Isaac Newton (1642–1727) took this idea much further. Almost incidentally to the main insights of his *Principia* published in 1687 (the fundamental laws of motion, and the concept of universal gravitational attraction between bodies), Newton showed why there are two tides a day, and why the relative positions of the Moon and Sun are important. His contemporary, Edmond Halley (1656–1742, [Figure 1.1](#)), made systematic measurements at sea and prepared a map of tidal streams in the English Channel. Halley had encouraged Newton's work, paid for the publication of *Principia* himself, and prepared an account of the tides based on Newton's theories [10]. Many other scientists extended and improved Newton's fundamental understanding, but it remains the basis for all later developments.

Daniel Bernoulli (1700–1782) published ideas about an Equilibrium Tide, which we shall look at in detail in [Chapter 3](#). The Marquis de Laplace (1749–1827) developed theories of a dynamic ocean response to tidal forces on a rotating Earth, and expressed them in periodic mathematical terms. Thomas Young (1773–1829), while developing his theory on the wave characteristics of light, showed how the propagation of tidal waves could be represented on charts as a series of co-tidal lines.

The first operational automatic tide gauge and stilling-well system for measuring sea levels was installed at Sheerness in the Thames Estuary in 1831, to provide continuous sea-level data. These measurements in turn stimulated a new enthusiasm for tidal analysis and the regular publication by British

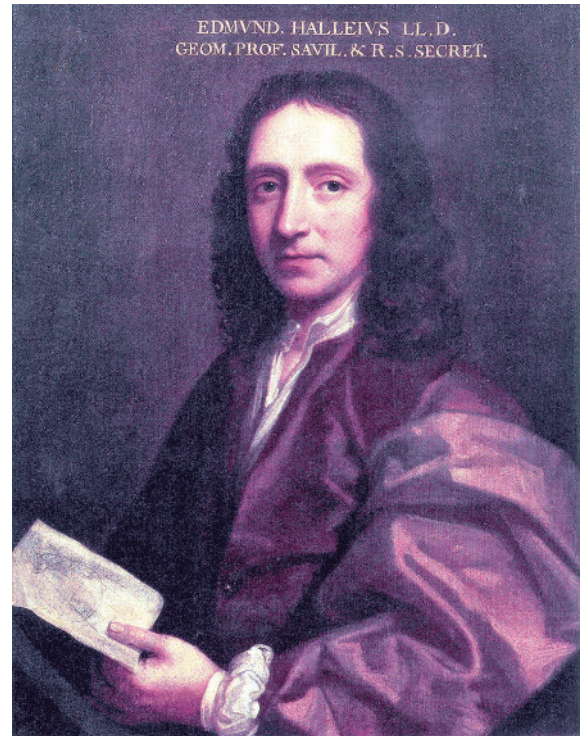


Figure 1.1 Edmond Halley (1656–1742) assisted in the publication of Newton's *Principia*, the basis for tidal science, and also led the first systematic tidal survey, of currents in the English Channel. © The Royal Society.

authorities of annual tidal predictions to assist mariners to plan safer navigation. Even before the official tables, tidal predictions were published commercially, sometimes based on undisclosed formulae, for example those of the Holden family in northwest England [11].

Lord Kelvin (1824–1907) showed in detail how tides could be represented as the sum of periodic mathematical terms, and promoted a machine ([Figure 4.12](#)) that applied this idea for tidal predictions. He also developed mathematical equations for the propagation of tidal waves on a rotating Earth, in a form known as *Kelvin waves*. In 1867 the Coast Survey of the United States took responsibility for the annual production of official national tide tables for the United States. By the beginning of the twentieth century, most major maritime countries around the world began to prepare and publish regular annual official tide tables.

Meanwhile, other factors that influence sea-level changes were being investigated. James Clark Ross

(1800–62) made sea-level measurements when trapped in the ice during the Arctic winter of 1848–9, and confirmed the already-known link between higher atmospheric pressures and lower sea levels. Earlier Ross had helped establish Tide Gauge Bench Marks in Tasmania and the Falkland Islands, as datums for scientific mean sea-level studies during his voyage of exploration in the Southern Ocean. Establishing these fundamental fixed datum levels was done on the advice of the German geophysicist Alexander Von Humboldt (1769–1859).

Harris [9] gives an extensive late-nineteenth-century historical account of early tidal ideas; Wheeler [12] gives a contemporary hydraulic engineering perspective. More recently, Cartwright [13] gives a comprehensive analysis of the scientific history of tides. A more general discussion of sea-level science and its place in the overall development of marine science is given in Deacon [14]; Reidy [15] describes the role of the British Admiralty in tidal science and its application.

1.3 Tidal patterns

Before the development of appropriate instrumentation, sea-level observations were confined to the coast and were not very accurate. Modern measuring systems, many of which will be described in the next chapter, have enabled a systematic collection of sea-level data which shows that regular water movements are a feature on all the shores of the oceans and of their adjacent seas. These regular tidal water movements are seen as both the vertical rise and fall of sea level, and as the horizontal ebb and flow of the water.

The tidal responses of the ocean to the forcing of the Moon and Sun are very complicated and tidal features vary greatly from one site to another. The two main tidal features of any sea-level record are the tidal range, measured as the height between successive high and low levels, and the period, the time between one high (or low) level and the next high (or low) level. [Figure 1.2a](#), which shows the tides for March 2043 at five sites, clearly illustrates this variability. [Figure 1.2b](#) shows the lunar variables for the same month. The details of the relationships between the tides and the movements of the Moon and Sun are developed in [Chapter 3](#). In this section we describe the observed sea-level variations at these five sites and relate them to the astronomy in a more general way.

We can now look in detail at [Figure 1.2a](#). In most of the world's oceans the dominant tidal pattern is similar

to that shown for Bermuda in the North Atlantic, and for Mombasa on the African shore of the Indian Ocean. Each tidal cycle takes an average of 12 hours 25 minutes, so that two tidal cycles occur for each transit of the Moon (every 24 hours 50 minutes). Because each tidal cycle occupies roughly half of a day, this type of tide is called *semidiurnal*. Semidiurnal tides have a range that typically increases and decreases cyclically over a 14-day period. The maximum ranges, called *spring tides*, occur a few days after both new and full Moons (*syzygy*, when the Moon, Earth and Sun are in line), whereas the minimum ranges, called *neap tides*, occur shortly after the times of the first and last quarters (lunar quadrature). The relationship between tidal ranges and the phase of the Moon is due to the additional tide-raising attraction of the Sun, which reinforces the Moon's tides at *syzygy*, but reduces them at quadrature. The astronomical cycles are discussed in detail in [Chapter 3](#), but [Figure 1.2b](#) shows that when the Moon is at its maximum distance from the Earth, known as lunar apogee, semidiurnal tidal ranges are less than when the Moon is at its nearest approach, known as lunar perigee. This cycle in the Moon's motion is repeated every 27.55 solar days. Maximum semidiurnal ranges occur when spring tides (*syzygy*) coincide with lunar perigee [3], whereas minimum semidiurnal ranges occur when neap tides (quadrature) coincide with lunar apogee. Globally, semidiurnal tidal ranges increase and decrease at roughly the same time everywhere, but there are significant local differences. The maximum semidiurnal tidal ranges occur in semi-enclosed seas. In the Minas Basin in the Bay of Fundy (Canada), the semidiurnal North Atlantic tides at Burncoat Head have a mean spring range of 12.9 m. Equally large ranges are found in Ungava Bay, northeast Canada (see [Chapter 5](#)). The mean spring ranges at Avonmouth in the Bristol Channel (United Kingdom) and at Granville in the Gulf of St Malo (France) are 12.3 m and 11.4 m respectively. In Argentina the Puerto Gallegos mean spring tidal range is 10.4 m; at the Indian port of Bhavnagar in the Gulf of Cambay it is 8.8 m; and the Korean port of Inchon has a mean spring range of 8.4 m. More generally, however, in the main oceans the semidiurnal mean spring tidal range is usually less than 2 m.

Close examination of the tidal patterns at Bermuda and Mombasa in [Figure 1.2a](#) shows that at certain times in the lunar month the high water levels are alternately higher and lower than the average. This behaviour is also observed for the low water levels, the differences being most pronounced when

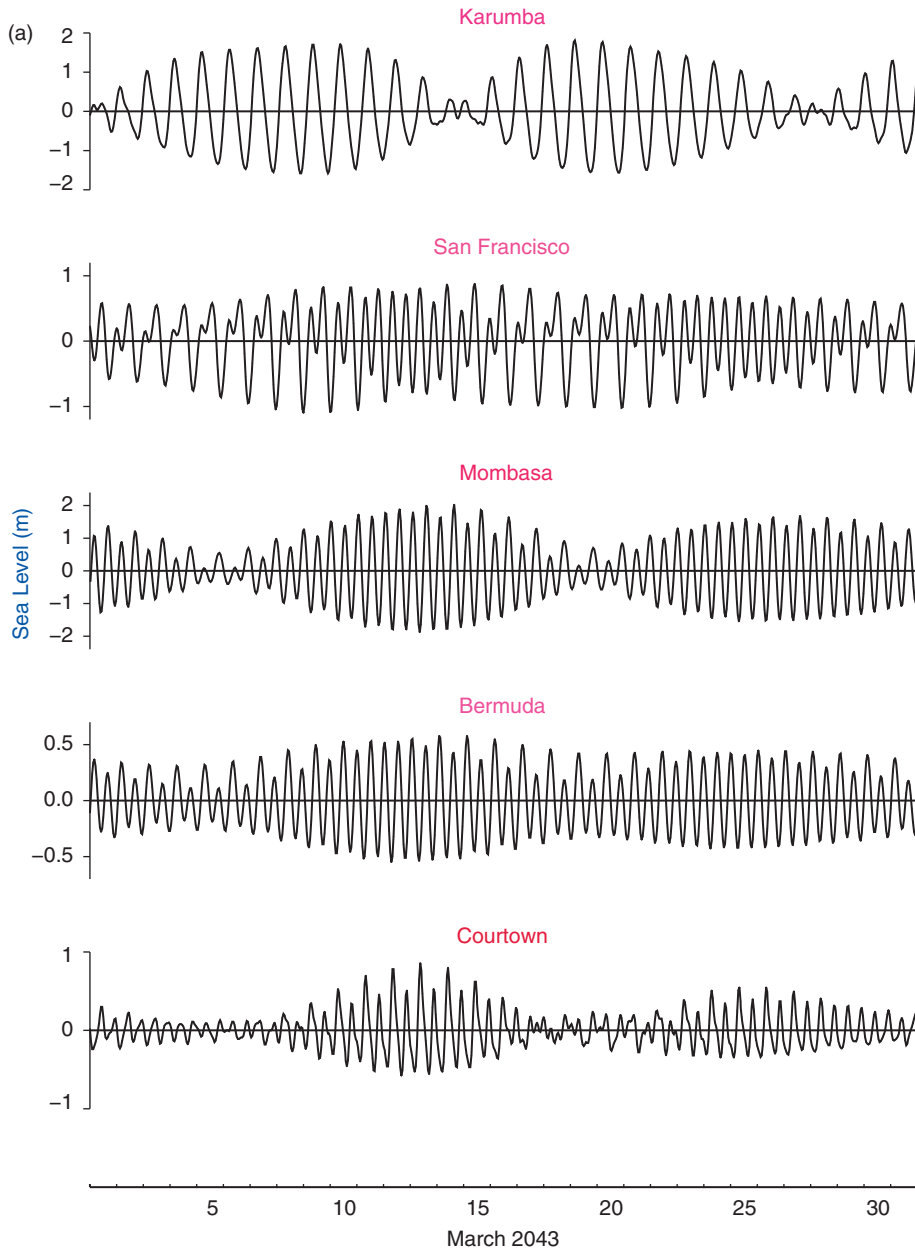


Figure 1.2 (a) Tidal predictions for March 2043 at five sites that have very different tidal regimes. At Karumba, Australia, the tides are diurnal, at San Francisco, United States, they are mixed, whereas at both Mombasa, Kenya, and Bermuda, semidiurnal tides are dominant. The tides at Courtown, Ireland, are strongly distorted by the influence of the shallow waters of the Irish Sea.

(b) The lunar characteristics responsible for these tidal patterns. Solar and lunar tide-producing forces combine at new and full Moon to give large spring tidal ranges every 14.76 days. Lunar declination north and south of the equator varies over a 27.21-day period. Solar declination is zero on 21 March. Lunar distance varies through perigee and apogee over a 27.55-day period. The thumbnail cartoons show the physics of the variations (lunar phase, declination and distance) discussed in detail in [Chapter 3](#).

the Moon's declination north and south of the equator is greatest. The differences can be accounted for by a small additional tide with a period close to one day, which adds to one high water level but subtracts

from the next one. In [Chapters 3 and 4](#) we shall develop the idea of a superposition of several partial tides to produce the observed sea-level variations at any particular location.

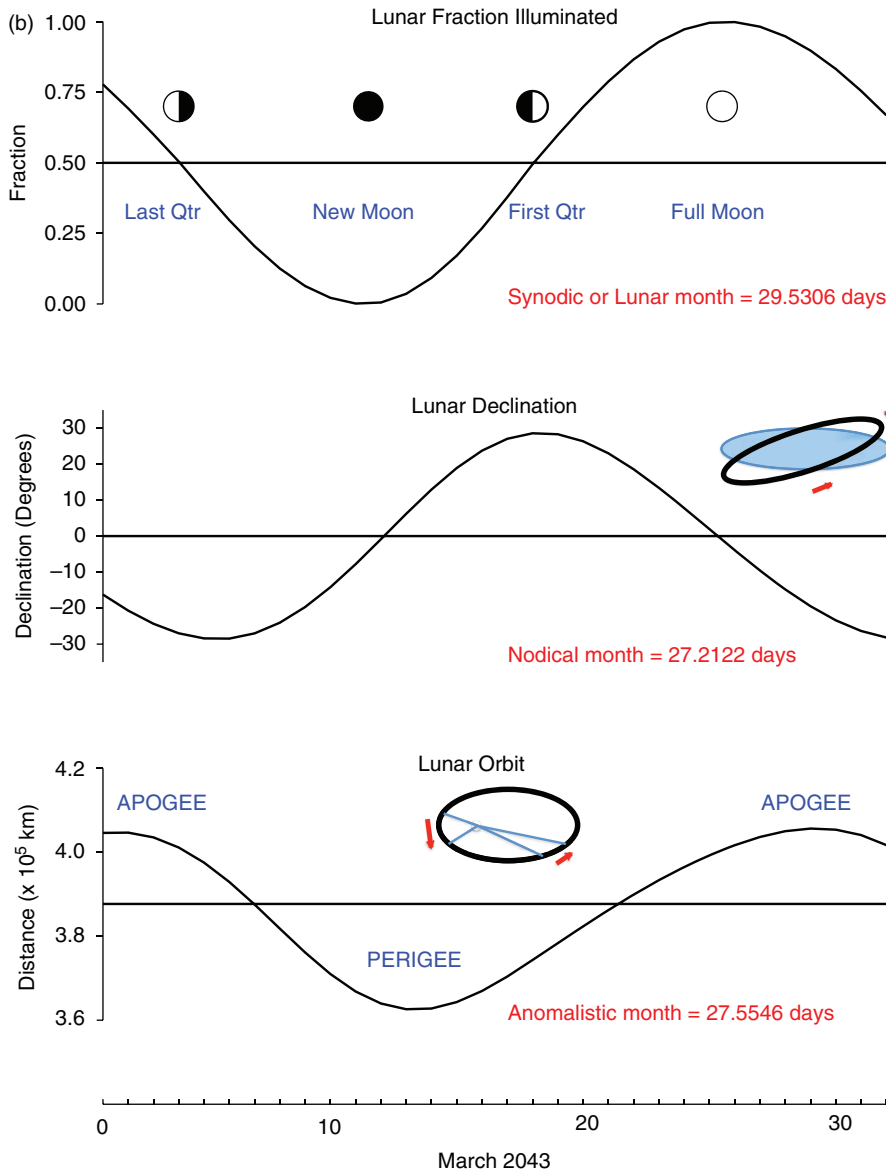


Figure 1.2 (cont.)

In the case of the tide at San Francisco, the tides with a one-day period, which are called *diurnal tides*, are similar in magnitude to the semidiurnal tides. This composite type of tidal regime is called a mixed tide, the relative importance of the semidiurnal and the diurnal components changing throughout the month, as plotted in Figure 1.2a. The diurnal tides are biggest when the Moon's declination is greatest but reduce to zero when the Moon is passing through

the equatorial plane, where it has zero declination. The semidiurnal tides are biggest after new and full Moon; but unlike the diurnal tides, they do not reduce to zero range, being only partly reduced during the period of neap tides.

In a few places the diurnal tides are much larger than the semidiurnal tides. Karumba in the Australian Gulf of Carpentaria is the example shown in Figure 1.2a. Here the tides reduce to zero amplitude

a day or so after the Moon's declination is zero, increasing to their largest values when the Moon is at its greatest declination, either north or south of the equator (Figure 1.2b). Diurnal tides are also found in part of the Persian Gulf, the Gulf of Mexico and part of the South China Seas. The Chinese port of Pei-Hai has the world's largest diurnal tidal range, with a difference of 6.3 m between the highest and lowest predicted tidal levels.

Astronomical forces acting on the major oceans of the world generate and energise the tides. These hydrodynamics are discussed in detail in Chapter 5. From the oceans the tides spread as waves to the surrounding shallower shelf seas.

The tidal ranges on the relatively shallow continental shelves are usually larger than those of the oceans. However, very small tidal ranges are observed in some shallow areas, often accompanied by curious distortions of the normal tidal patterns. Figure 1.2a shows the tides for Courtown on the Irish coast of the Irish Sea, where the range varies from more than a metre at spring tides to only a few centimetres during neap tides. When the range is very small, careful examination shows that four tides a day occur. These effects are due to the distorted tidal propagation in very shallow water. Shallow-water distortions, which are discussed in detail in Chapter 6, are also responsible for the double high water feature of Southampton tides and for the double low waters seen at Portland, both in the English Channel, where semidiurnal tides prevail. Double low waters also occur along the Dutch coast of the North Sea from Haringvlietsluizen to Scheveningen, where they are particularly well developed at the Hook of Holland. Double high waters are also found at Den Helder in the North Sea and at Le Havre in the English Channel.

Tidal currents, often called tidal streams, have similar variations. Semidiurnal, mixed and diurnal currents occur, usually having the same characteristics as the local changes in tidal levels, but this is not always so. For example, the currents in the Singapore Strait are often diurnal in character but the elevations are semidiurnal. The strongest currents are found in shallow water or through narrow channels, which connect two seas, such as the currents through the Straits of Messina between the island of Sicily and the Italian mainland.

Currents in narrow channels are constrained to flow along the channel axis, but in more open waters

all directions of flow are possible. During each tidal period the direction usually rotates through a complete circle while the speeds have two roughly equal maximum and two equal minimum values. Figure 1.3 shows the distribution of tidal currents over one semi-diurnal cycle at the Inner Dowsing light tower in the North Sea. Each line represents the speed and direction at a particular hour. Because each measurement of current is a vector described by two parameters, their variations are more complicated to analyse than changes of sea level.

This book is concerned with movements of the seas and oceans. Two other geophysical phenomena that have tidal characteristics are of interest. In tropical regions there is a small but persistent 12-

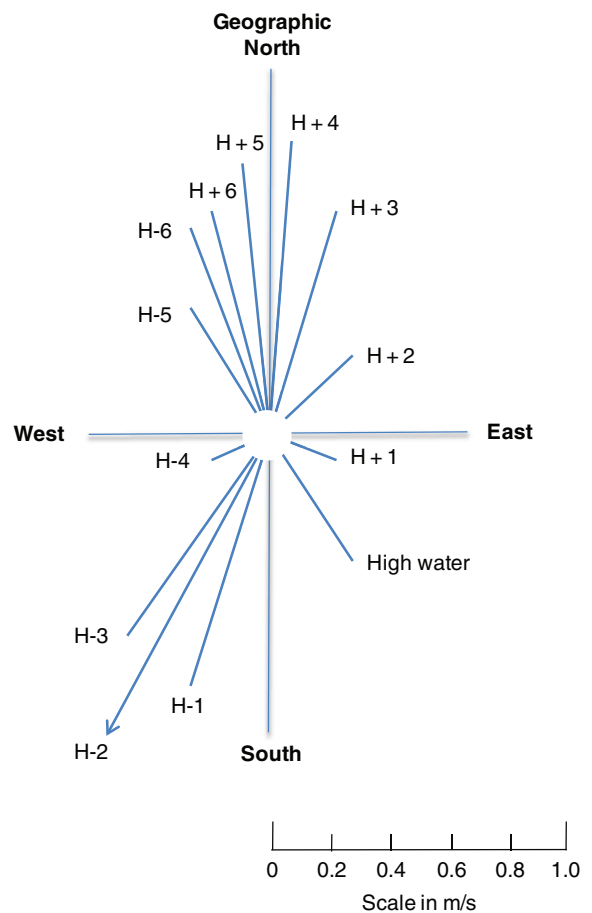


Figure 1.3 Spring tidal current curve, Inner Dowsing light tower, North Sea. Each line represents the velocity of the current at each hour from 6 hours before to 6 hours after local high water (for example, H+2 is the current 2 hours after high water). Semidiurnal tides are strongly dominant. The distance from the centre represents the speed, and the bearing gives the *direction of water flow*. For example, at high water the current is 0.5 m/s to the southeast.

hour oscillation of the atmospheric pressure (Section 5.5) with typical amplitude of 1.2 millibars, which reaches its maximum values near 10:00 hours and 22:00 hours local time. This produces a small tidal variation of sea levels. Also, accurate measurements of the Earth's gravity field and of the tilt of the Earth's crust show vertical movements of the land surface relative to the centre of the Earth that are tidally induced. These Earth tides may have extreme amplitudes of tens of centimetres.¹ For scientific computations of tides on a global scale the Earth tides must be included because of their effects on ocean dynamics. However, for practical purposes only the observed movements relative to the land need be considered.

1.4 Meteorological and other non-tidal changes

The regular and predictable pattern of the tides is modified to a greater or lesser extent by irregular factors, the principal ones being the atmospheric pressure and the wind acting on the sea surface. Figure 1.4a shows how the regular semidiurnal pattern of sea levels at Venice was modified by the weather over a few days in November 2002. These irregular slow changes, known as *storm surges*, are plotted in the same diagram. The coincidence of a spring tide and a large increase in the levels due to the weather caused an exceptionally high total level. Figure 1.4b shows the tide gauge record for Hurricane Katrina flooding in Louisiana in August 2005; the green line is the 1.4 m surge, which persisted for less than a day.

Historically there have been many disastrous coastal floodings caused by the coincidence of large meteorologically induced surges and large or even moderately high tides (see Table 12.5). Thus, in November 1885, New York was inundated by high sea levels generated by a severe storm that also caused flooding at Boston. More than 6000 persons were drowned in September 1900 when the port of Galveston in Texas was overwhelmed by waters that rose more than 4.5 m above the mean high water level, as a result of hurricane winds blowing at more than 50 m/s for several hours. Also in the Gulf of Mexico,

Hurricane Katrina in August 2005 caused severe damage and many lives were lost in Louisiana (Figure 1.4b). Even these disasters were surpassed by the Bangladesh tragedy of 12 November 1970, when winds of 60 m/s raised sea levels by an estimated 9 m. Flooding extended over several low-lying islands, drowning hundreds of thousands of people. Severe storms, floods and loss of life occurred in the same region in both 1876 and 1897, and more recently in 1960, 1961 and 1985. In October 1999, 10,000 people were killed in Orissa, India, by a 7–8 m surge. Along the south coast of Burma, cyclone Nargis caused at least 140,000 deaths in May 2008.

The physics of storm surge generation by air pressures and winds is covered in Chapter 7. The largest surges occur when hurricane winds blow for a long time over large expanses of shallow water. Whilst tropical storms cause the most extreme local flooding, storms at higher latitudes can also produce very large surges over wide areas. In January 1953, catastrophic flooding on both the English and Dutch coasts of the North Sea occurred as a result of a depression tracking into the North Sea across the north of Scotland. This surge, which exceeded 2.6 m at Southend, coincided with slightly less than average spring tides, otherwise even more damage would have occurred. The coastal regions of the North Sea are prone to this type of flooding; there were previous events in 1929, 1938, 1943, 1949, and a particularly severe case in Hamburg in 1962. Similarly, along the Atlantic coast of the United States, the Ash Wednesday storm of 7 March 1962 flooded many low-lying barrier islands, causing millions of dollars of damage. Recently, Hurricane Sandy, the largest Atlantic hurricane on record, in October 2012 caused flooding and major damage along the whole eastern seaboard of the United States, with flooding of streets, tunnels and subway lines and power losses in and around New York.

These dramatic extremes and the resulting coastal flooding are rare events, but there is always a continuous background of sea-level changes due to the weather, which raise or lower the observed levels compared with the levels predicted. At higher latitudes these effects are greater during the stormy winter months. Knowledge of the probability of occurrence of these extreme events is an essential input to the safe design of coastal defences and other marine structures, as discussed in Chapter 12.

The tsunamis generated by submarine earthquakes are another cause of rare but sometimes catastrophic flooding, particularly for coasts around the Pacific Ocean. Tsunamis are sometimes popularly called

¹ Measured coastal sea levels are actually those of the vertical movement of the sea surface relative to the local land level, which may itself be moving relative to the centre of the Earth (Chapter 11).

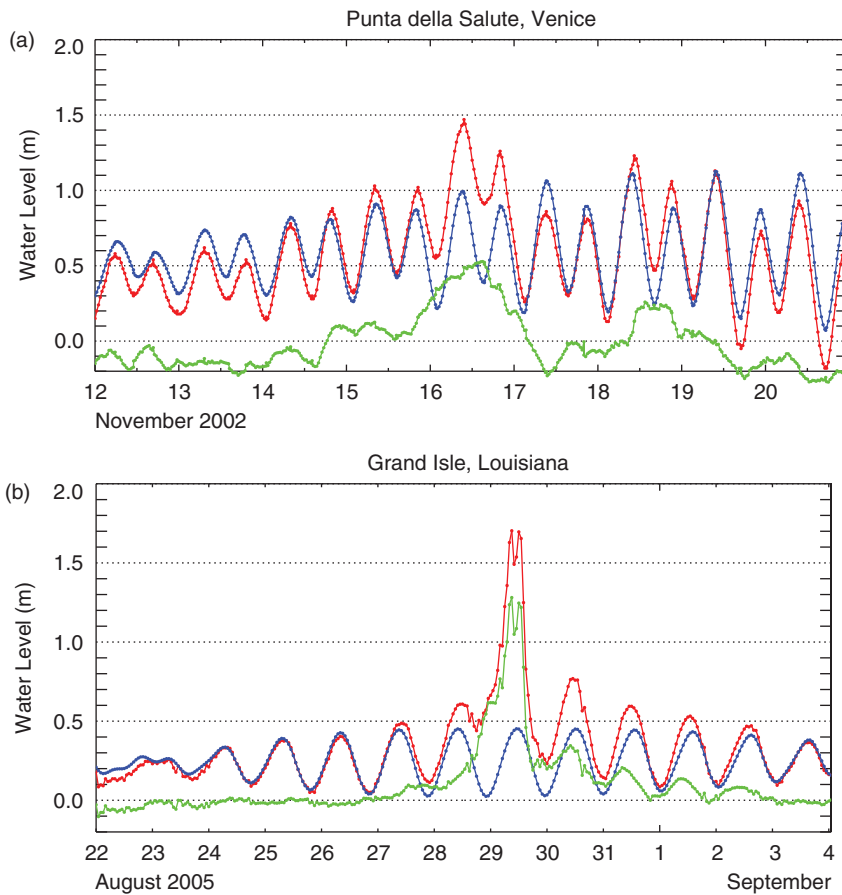


Figure 1.4 Observed (red), tidal (blue) and meteorological (green) variations of sea level: (a) an extratropical surge at Venice, November 1966; (b) a tropical surge, Louisiana (Hurricane Katrina), 29–31, August 2005.

‘tidal waves’ but this is misleading because they are not generated by tidal forces nor do they have the periodic character of tidal movements (see [Chapter 8](#)). Near the earthquake source the tsunami amplitudes are much smaller; the amplification occurs in the shallow coastal waters and is enhanced by the funnelling of the waves in narrowing bays. The coast of Japan is particularly vulnerable to this type of flooding, and the term *tsunami* is of Japanese origin. In March 2011 a major tsunami caused extensive damage to the Fukushima nuclear power plant. Tsunamis can travel long distances across the oceans: the tsunami generated by the major earthquake in the Indian Ocean on 26 December 2004 caused damage thousands of miles from the source, and was detected worldwide. In the Atlantic Ocean tsunamis are comparatively rare, but the flooding after the 1755 Lisbon earthquake is well documented. Tsunamis often set up local oscillations of semi-enclosed sea and basins, called *seiches*, which

are discussed in [Section 7.5](#); more commonly seiches are triggered by winds or internal ocean tides.

1.5 Some definitions of common terms

It is now appropriate to define more exactly some of the common tidal and non-tidal terms, as they will be used throughout this book; the Glossary contains precise summaries.

Throughout this book, we define *sea level* as: the level of the sea after averaging out the short-term variations due to wind waves.²

The first important distinction to make is between the popular use of the word *tide* to signify any change

² This is sometimes called *still water level*.

of sea level, and the more specific scientific use of the word to mean only the regular periodic variations.

Although any definition of tides will be somewhat arbitrary, it must emphasise this periodic and regular nature of the motion, whether it be of the sea surface level, currents, atmospheric pressure or Earth movements. We define tides as periodic movements that are directly related in amplitude and phase to some periodic geophysical force. The dominant geophysical forcing function is the variation of the gravitational field on the surface of the Earth, caused by the regular movements of the Moon–Earth and Earth–Sun systems. Movements due to these forces are termed *gravitational tides*. This is to distinguish them from the smaller movements due to regular meteorological forces, which are called either *meteorological tides* or more usually *radiational tides* because they occur at periods directly linked to the solar day. It can be argued that seasonal changes in the levels and in the circulation of seawater due to the variations of climate over an annual period are also regular and hence tidal.

Any sequence of measurements of sea level or currents will have a tidal component and a non-tidal component. The *non-tidal component*, which remains after analysis has removed the regular tides, is also called the *residual* or *meteorological residual*. Sometimes the term *surge residual* is used, but more commonly the term *surge* or *storm surge* is used for a particular event during which a very large non-tidal component is generated, rather than to describe the whole continuum of non-tidal variability (see [Chapter 7](#)).

Periodic oscillations are described mathematically in terms of amplitude and a period or frequency:

$$X(t) = H_x \cos(\omega_x t - g_x) \quad (1.1)$$

where $X(t)$ is the value of the variable quantity at time t , H_x is the amplitude of the oscillation, ω_x is the angular speed which is related to the period T_x by $T_x = 2\pi/\omega_x$ (ω_x is measured in radians per unit time), and g_x is a phase lag relative to some defined time zero.

For scientific tidal studies H_x may have units of metres (rarely feet) for levels, or metres per second (m/s) for currents. In its simple form [Equation 1.1](#) can only represent the to-and-fro currents along the axis of a channel. If the direction is variable as in [Figure 1.3](#), then [Equation 1.1](#) may define the flow along a defined axis (X). The speed and direction of the total flow is completely specified if the currents along a second axis (Y) at right angles to the first are also defined.

Tidal *high water* is the maximum tidal level reached during a cycle. The observed high water level may be greater or less than the predicted tidal level because of meteorological effects. Similarly *low water* is the lowest level reached during a cycle. The difference between a high water level and the next low water level is called the *range*, which for the simple oscillation defined by [Equation 1.1](#) is $2H_x$, twice the amplitude.

Ocean tides and most shelf sea tides are dominated by semidiurnal oscillations, for which several descriptive terms have been developed through both popular and scientific usage (see [Figure 1.5a](#)). *Spring tides* are semidiurnal tides of increased range, which occur approximately twice a month as a result of the Moon being new or full. The *age of the tide* is an old term for the lag between new or full Moon and the maximum spring tidal ranges. The average spring high water level taken over a long period (maybe a year) is called *Mean High Water Springs* (MHWS) and the correspondingly averaged low water level is called *Mean Low Water Springs* (MLWS). Formulae are available for estimating these useful parameters directly from the results of tidal analyses ([Section 4.2.6](#) and the Appendices). *Neap tides* are the semidiurnal tides of small range that occur near the time of the first and last lunar quarters, between spring tides. *Mean High Water Neaps* and *Mean Low Water Neaps* are the average high and low waters at neap tides. These too may be estimated directly from tidal analyses.

Where the tidal regime is mixed the use of MHWS and other semidiurnal terms becomes less appropriate. *Mean High Water* and *Mean Low Water* are frequently used. *Mean Higher High Water* (MHHW) is the average level over a long period of the higher high water level that occurs in each pair of high waters in a tidal day. Where only one high water occurs in a tidal day, this is taken as the higher high water. *Mean Lower Low Water* (MLLW) is the average of the lower level in each pair of low water levels in a tidal day. Mean Lower High Water and Mean Higher Low Water are corresponding terms that are seldom used.

These terms become increasingly difficult to determine exactly, where the tide is dominated by diurnal oscillations ([Figure 1.5b](#)). Mean High Water (MHW) and Mean Low Water (MLW) averaged for all high and low levels respectively may be computed as datums for survey work, but difficulties arise when considering how to treat the multiple small high and low levels that occur during the time when the diurnal

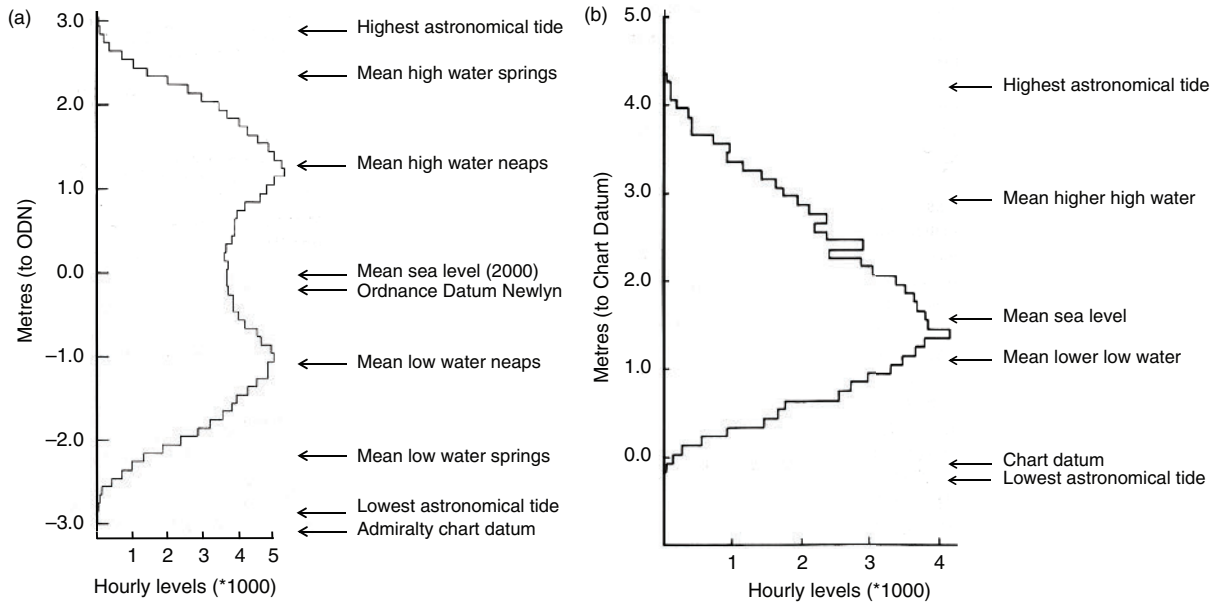


Figure 1.5 Frequency distribution of hourly tidal levels (a) at Newlyn over an 18-year period relative to Ordnance Datum Newlyn and (b) at Karumba over a single year (1982), relative to Chart Datum. For the semidiurnal Newlyn tides there is a distinct but slightly asymmetric double peak in the distribution, but for the diurnal Karumba tides there is a single skewed peak.

range falls to near zero, as for example at Karumba in Figure 1.2a. Diurnal tides show a semi-monthly variation in their range from a maximum to zero and back to a maximum range again because of the monthly cycle in the lunar declination. Some authorities have suggested that these diurnal modulations should be called Diurnal Spring and Diurnal Neap Tides [3], but this usage is uncommon, being usually reserved for the semidiurnal range changes related to the phase of the Moon.

Levels defined by analysis of long periods of sea-level variations are used to define a reference level known as a tidal datum. These datums are often used for map or chart making, or for referring subsequent sea-level measurements. For geodetic surveys the *Mean Sea Level* (MSL) is frequently adopted, being the average value of levels observed each hour over a period of at least a year, and preferably over about 19 years, to average over the cycles of 18.61 years in the tidal amplitudes and phases (see Chapter 3), and to average out weather. Present United Kingdom Mean Sea Levels are now approximately 0.2 m higher than the 1915–21 mean level, adopted as the National Mean Sea Level, land datum. In Section 9.9 we discuss the evolution of the way in which these vertical datums are defined and measured.

The *Mean Tide Level* (MTL), which is the average value of all high and low water heights, is sometimes computed for convenience, where a full set of hourly levels is not available. Before automatic tide gauges, MTL was the only readily calculated mean value. In general, MTL will differ slightly from the MSL because of tidal distortions in shallow water. Chapters 10 and 11 will discuss MSL definition, computations and variations in detail, and show how satellite missions have greatly extended our understanding of global sea levels.

Lowest Astronomical Tide (LAT), the lowest level that can be predicted to occur under any combination of astronomical conditions is recommended a Chart Datum by the International Hydrographic Organization. LAT is adopted for charts prepared by the British Hydrographic Department. The Canadian Hydrographic Department has adopted the level of lowest normal tides. The United States National Ocean Service (NOS) used a Chart Datum that is defined in some areas of mixed tides as the mean of the lower of the two low waters in each day (MLLW); in some semidiurnal tidal areas as mean low water springs (MLWS); and elsewhere as the lowest possible low water. MLLW is now adopted by NOS as the standard datum for all locations (see Appendix E).

Hydrographers prefer to refer levels on their charts to an extreme low water Chart Datum, below which the sea level seldom falls, in order to give navigators the assurance that the depth of water shown on charts is the minimum available whatever the state of the tide. Throughout the world, published predictions of tidal levels are given relative to the local Chart Datum so that by adding them to the water depth shown on the chart, the navigator knows the total depth available for his vessel. Because the Chart Datum is defined in terms of the local tidal characteristics, it is not a horizontal plane. Geodetic datums, however, are theoretically horizontal planes to within the accuracy of the survey that established them. As a result, the amount by which Chart Datum falls below Survey Datum is not constant, being greatest where the tidal range is greatest.

Although for practical navigation requirements tidal predictions are normally published as levels above Chart Datum, for scientific and engineering purposes it is normally more convenient to consider levels relative to a mean sea-level datum. The tidal levels plotted in Figure 1.2a are relative to local mean sea level.

If a long series of hourly tidal predictions are examined for the frequency with which each level occurs, certain values are found to be more probable than others. Highest and Lowest Astronomical Tides occur very seldom whereas, in the case of semidiurnal tides as illustrated by a histogram of 19 years of Newlyn predictions in Figure 1.5a, the most probable levels are near Mean High Water Neaps and Mean Low Water Neaps. Water levels are changing relatively quickly when passing through the mean level and so this appears as a minimum in the frequency histogram, whereas it pauses or 'hangs' at the high water and low water levels. As a general rule, one of the two humps has a maximum that is noticeably greater than the other especially in shallow-water regions. Figure 1.5b shows the corresponding distribution for a year of predicted hourly tides at Karumba where diurnal tides prevail. Note that the double-humped distribution characteristics of semidiurnal tides have been replaced by a continuous and slightly skew distribution. During the single year analysed at Karumba the diurnal tides failed to reach either the Highest or Lowest Astronomical Tide levels. This was because the range of lunar declinations, which has an 18.61-year cycle, was relatively small in 1982. Several of the other tidal terms defined here are also shown relative to the distributions of Figure 1.5. In statistical terms these distributions of levels are called *probability density functions*.

1.6 Basic statistics of sea levels as time series

The full process of tidal analysis will be considered in Chapter 4, but there are certain basic statistical ideas that may be used to describe tidal patterns without applying elaborate analysis procedures. The probability density functions of tidal levels shown in Figure 1.5 are one useful way of representing some aspects of sea-level and tidal ranges. In this section we consider basic ideas: the mean and the standard deviation, and also the variance and spectral analysis of a series of sea-level measurements, made over a chosen period of time.

For most purposes it is useful to regard the observed sea level as the combined result of three main factors:

$$\text{Observed sea level} = \text{mean sea level} + \text{tidal level} \\ + \text{residual level}$$

These factors will be considered in turn in this book.

The general representation of the observed level $X(t)$ that varies with time may be written:

$$X(t) = Z_0(t) + T(t) + R(t) \quad (1.2)$$

where $Z_0(t)$ is the **MSL**, which changes slowly with time,

$T(t)$ is the tidal part of the variation,

$R(t)$ is the residual component.

Measurements of sea levels and currents are traditionally recorded as a series of hourly values; recordings every 15 or every 6 minutes are also common. For satisfactory tidal analysis observations should extend over at least a lunar month, 709 hours, or better over a year of 8766 hours. Suppose that we have M observations of the variable $X(t)$ represented by x_1, x_2, \dots, x_M , then the mean is given by the formula:

$$\bar{x} = \frac{1}{M}(x_1 + x_2 + x_3 + \dots + x_M) \quad (1.3)$$

or, in conventional notation;

$$\bar{x} = \frac{1}{M} \sum_1^M x_m$$

Every value of the variable differs from the mean of the series of observations by an amount that is called its deviation. The deviation of the m th observation is given by:

$$e_m = x_m - \bar{x}$$

Note that the average value of e_m must be zero because of the way in which the mean value \bar{x} is calculated. A better way of describing the extent by which the values of x vary about the mean value \bar{x} is to compute the variance s^2 , the mean of the squares of the individual deviations:

$$s^2 = \frac{1}{M} \sum_1^M (x_m - \bar{x})^2 \quad (1.4)$$

which must always have a positive value. The square root of the variance, s , is called the standard deviation of the distribution of x about \bar{x} .

A further extremely useful technique called Fourier analysis represents a time series in terms of the distribution of its variance at different frequencies. The basic idea of Fourier analysis is that any time series may be represented as the sum of a series of sines and cosines of frequencies that are multiples of the fundamental frequency:

$$\begin{aligned} \sigma &= \frac{2\pi}{M\Delta t} \\ X(t) &= Z_0(t) + \sum_{m=1}^{M/2} A_m \cos m\sigma t + \sum_{m=1}^{M/2} B_m \sin m\sigma t \end{aligned} \quad (1.5)$$

where the coefficients A_m and B_m may be evaluated by analysis of M values of $X(t)$ sampled at constant intervals Δt . Z_0 is the average value of $Z_0(t)$ over the period of observations. An alternative form of Equation 1.5 is:

$$X(t) = Z_0 + \sum_{m=1}^{M/2} H_m \cos(m\sigma t - g_m) \quad (1.6)$$

where

$$\begin{aligned} H_m &= \sqrt{A_m^2 + B_m^2} \\ g_m &= \arctan(B_m/A_m) \end{aligned}$$

H_m and g_m are the amplitude and phase lag of the m th harmonic constituent of the function $X(t)$. Note that the phase lags and angular speeds must be expressed consistently in terms of radian or degree angular measure; see Section 4.2 for a discussion of the usual tidal notations.

The variance of this function about the mean value Z_0 is given by squaring the terms within the summation symbol of Equation 1.6, and averaging over the period of observation. If this long multiplication is

carried through it is found that all of the cross-product terms are zero, except for terms of the form:

$$H_m^2 \cos^2(m\sigma t - g_m)$$

the average value of which, over an integral number of cycles, is $\frac{1}{2}H_m^2$. The total variance in the series is therefore given by:

$$\frac{1}{2} \sum_{m=1}^{M/2} H_m^2$$

We shall see in Chapter 4 that this powerful statistical result, which states that the total variance of the series $X(t)$ is the sum of the variance at each harmonic frequency is very important for tidal analyses.

The methods of tidal analysis to be described in Chapter 4, which enable separation of the tidal and non-tidal components of the series $X(t)$, have a condition that the two components are statistically independent. This means that the sum of their individual variances gives the variance in the total observed series:

$$\sum_{k=1}^M (X(k\Delta t) - Z_0)^2 = \sum_{k=1}^M T^2(k\Delta t) + \sum_{k=1}^M (k\Delta t)$$

Total variance = Tidal variance + Non-tidal variance

Furthermore, the variance of the tides may be computed as the sum of the variance in each frequency element. The important conclusion is that the total tidal variance in a series of observations is the diurnal variance plus the semidiurnal variance plus the variance at other higher and lower frequencies. In shallow water there may be tidal energy at higher frequencies because some semidiurnal tidal energy is shifted, mainly to quarter-diurnal and sixth-diurnal tidal periods. The concentrations of tidal energy in groups of similar period or frequency, which we discuss in detail in Chapter 4, are called tidal *species*. The main species are the daily (diurnal) and twice-daily (semidiurnal) groups.

We now consider how the tidal regime at a particular location may be characterised by the way in which the variance is distributed among the different species. Table 1.1 summarises the distributions of variance for four coastal sites. In Honolulu the total variance is small, and contains nearly equal contributions from the diurnal and semidiurnal species. Tides from higher species due to shallow-water distortions are negligible because Honolulu is adjacent to the deep ocean. At Mombasa the diurnal tides are larger than at Honolulu, but the tidal curves are dominated by the

Table 1.1 Distributions of variance at representative sea-level stations. Long period tidal variations include annual, semi-annual and monthly changes. Units are cm^2 .

		Tidal					Total
		Long period	Diurnal	Semidiurnal	Shallow-water	Non-tidal	
Honolulu	Hawaii	9	154	157	0	35	355
Mombasa	Kenya	5	245	7,555	2	19	7,826
Newlyn	England	17	37	17,055	100	191	17,400
Courtown	Ireland	116	55	284	55	222	732

large semidiurnal tides. There is a narrow continental shelf region adjacent to the Mombasa coast that generates a small variance at higher frequencies. At Newlyn the diurnal tides are very small and the semidiurnal tides are very large. Shallow-water tides are a significant factor, due to the effects of the extensive continental shelf that separates Newlyn from the Atlantic Ocean. Courtown has an exceptional tidal regime: the annual and other long period changes of level are unusually large, but the semidiurnal tides are small for a continental shelf site.

Mombasa and Honolulu have the smallest non-tidal or surge effect in the observed levels. The largest surge residuals are found in the higher latitudes where storms are more severe, and in regions of extensive shallow water.

The frequency distribution of variance shown in Table 1.1 can be taken a stage further. Figure 1.6 shows the results of a frequency distribution of the variance at the whole range of frequencies for a year of hourly sea-level measurements at New York. Theoretically, given a year of 8766 hourly observations, 4383 separate frequency components could be determined, but such a fine resolution gives a spectral plot, which is noisy and irregular. A more satisfactory presentation is obtained by averaging the variance over several adjacent harmonic components. In the case illustrated, the values are averaged over 60 elements, and plotted against a logarithmic vertical scale to accommodate the great range of values obtained. The significance of the semidiurnal and diurnal tides is clear. Most of the non-tidal variance is contained in the low frequencies, equivalent to periods of 50 hours or longer. Although weak, the fourth-diurnal tides stand out clearly above the background noise and there is a spectral peak in the vicinity of the third-diurnal tides near 0.12 cycles per

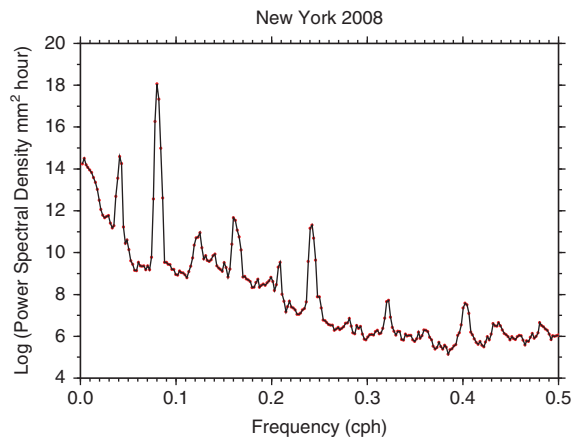


Figure 1.6 Distribution of variance in observed levels over one year (2008) at New York. The biggest peak (0.08 cph) is for the semidiurnal tidal changes of level, but diurnal tidal changes are also apparent. There are smaller peaks of variance in the fourth-diurnal and other tidal species due to distortions of the tide in shallow water.

hour. The averaged values of variance plotted within the diurnal and semidiurnal species conceal a fine structure of variance concentration at a few particular frequencies, which will be considered in more detail in Chapter 3. The increase in spectrum energies at low frequencies is known as *reddening*.

Figure 1.7 is a very schematic time–space map of the main factors affecting sea level. It is drawn in terms of the timescales and the distance scales over which these factors operate. The approximate ranges of the variations associated with each effect are shown; the shapes plotted are only indicative, but note that tidal effects appear as narrow lines at times of one day and half a day. These are the diurnal and semidiurnal tides. Over long geological times, to the right of the diagram, many tectonic processes have changed land and sea

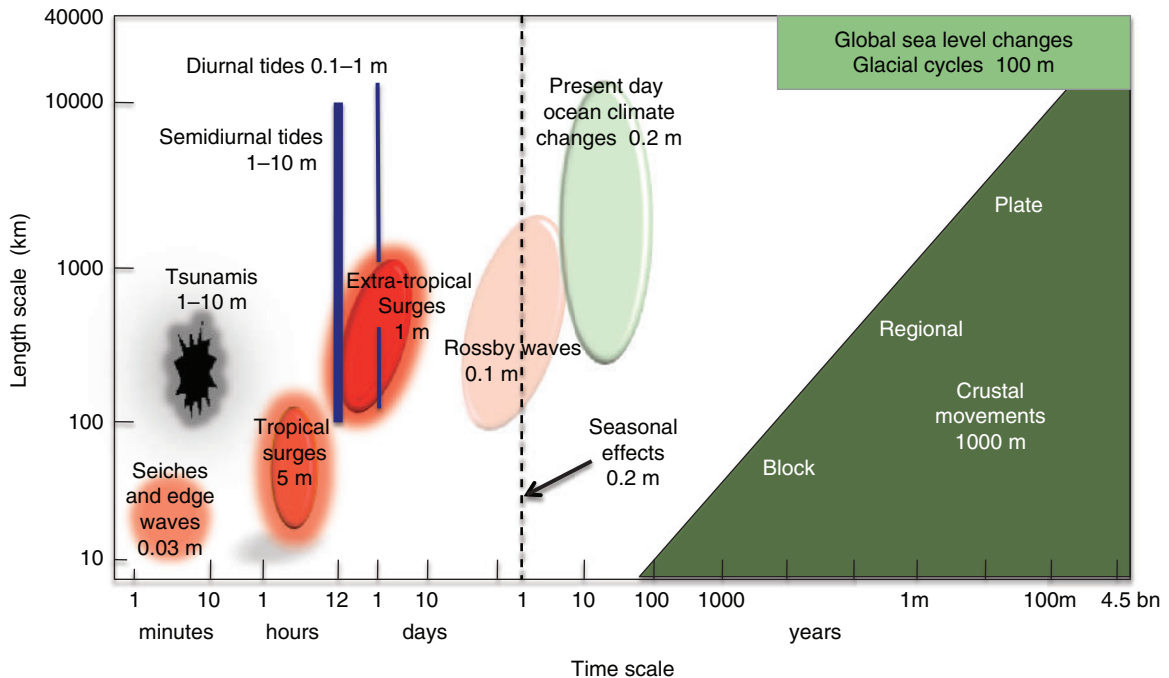


Figure 1.7 A conceptual time–space map of reasons for sea-level changes. The effects vary from wind waves over a few seconds to geological movements over millions of years.

levels; in the left bottom corner, over much shorter periods of seconds, there are local wind waves. The one-year timescale is often taken as the boundary between short- and long-term MSL changes. The maximum values on the X and Y axes are the age and circumference of the Earth, respectively.

Figure 1.8 shows on a global scale the way in which the sea-level variations due to the various factors are spatially distributed. Tidal levels (a) are most variable (red areas) in limited continental shelf areas; air pressure and wind variations are greatest at higher latitudes (b); the seasonal cycle (c) is most notable in tropical areas and in the Gulf Stream and Kuroshio currents; low-frequency changes (d) are also in regions of strong permanent currents; and high-frequency changes are notable at higher latitudes. Figure 1.8e is an important example of a regional sea-level anomaly pattern.

The measurement of variance is conveniently related to the energy contained in a physical system and descriptions of tidal dynamics (see Section 6.7) are often expressed in terms of energy fluxes and energy budgets. The variance of a series of sea levels may be related to the average potential energy of the water mass above and below a regional MSL (see

Chapter 12). In a similar way, for current speeds the variance may be related to the average kinetic energy of the water movements.

The purpose of sea-level analysis is to represent the variations in terms of a few significant parameters. In Chapter 3 and Chapter 4 we discuss the available techniques for separating the regular tides from the other effects in detail. However, our ability to predict future sea-level changes depends first on the collection of high-quality measurements for analysis. In the next chapter we shall consider some of the basic principles on which these measuring systems operate and some of their individual advantages and disadvantages.

Through the twentieth century a series of scientific and technical advances has brought us to the current state of being able to map and to model ocean and shelf tides, and weather effects in great detail, using satellite altimeters and the processing power of modern computers. The results of various Earth-defining satellite altimetry and gravity missions are discussed in Chapter 9. Today, one of the highest priorities is to understand and reliably anticipate changes in mean sea level (Figure 1.8f) and flood risks, particularly those that may be due to global climate change.

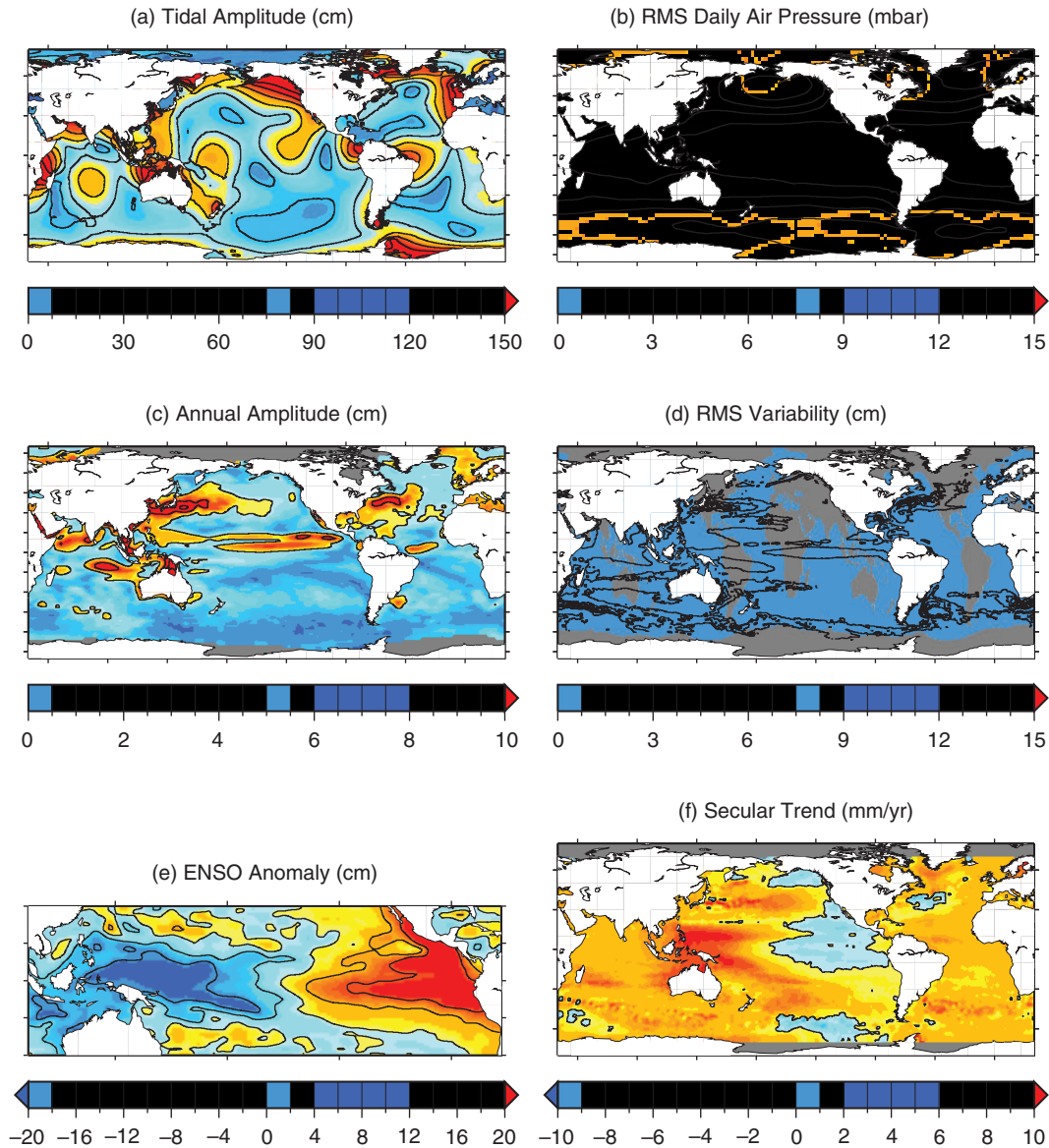


Figure 1.8 Thumbnails of variability in sea level: (a) Amplitude of the tide defined as the sum of the amplitudes of the M_2 , S_2 , O_1 and K_1 constituents.

(b) Rms variability (σ in Equation 1.4) of daily mean values of air pressure (in mbar) which corresponds to rms variability (in cm) of daily sea level due to the inverse barometer effect.

(c) Amplitude of the annual cycle of sea level around the world.

(d) Rms variability of sea level (not including the variability due to the seasonal cycles or long-term trends).

(e) A regional example of the west to east transfer of sea level in the equatorial Pacific due to the El Niño–Southern Oscillation (in this case for January 1998).

(f) Trends in sea level around the world over two decades from 1992.

References

- (1) Darwin, G. H. 1911. *The Tides and Kindred Phenomena in the Solar System* (3rd edition). London: John Murray.
- (2) Marmor, H. A. 1926. *The Tide*. New York: D. Appleton and Company.
- (3) Dronkers, J. J. 1964. *Tidal Computations in Rivers and Coastal Waters*. Amsterdam: North Holland Publishing Company.
- (4) Lisitzin, E. 1974. *Sea Level Changes*. Amsterdam: Elsevier.
- (5) Forrester, W. D. 1983. *Canadian Tidal*

- Manual*. Ottawa: Department of Fisheries and Oceans Canada.
2. Doodson, A. T. and Warburg, H. D. 1941. *Admiralty Manual of Tides*. London: His Majesty's Stationery Office.
 3. Wood, F. J. 2001. *Tidal Dynamics. Volume 1: Theory and Analysis of Tidal Forces*. Palm Beach, FL: The Coastal Education and Research Foundation (CERF).
 4. Pugh, D. T. 2004. *Changing Sea Levels*. Cambridge: Cambridge University Press.
 5. Parker, B. B. 2007. *Tidal Analysis and Prediction*. NOAA Special Publication NOS CO-OPS 3. Washington, D.C.: U.S. Department of Commerce, National Oceanic and Atmospheric Administration, National Ocean Service.
 6. Church, J. A., Woodworth, P. L., Aarup, T. and Wilson, W. S. 2010. *Understanding Sea-Level Rise and Variability*. Chichester: Wiley-Blackwell.
 7. Defant, A. 1961. *Physical Oceanography: Volume II*. Oxford: Pergamon Press.
 8. (1) Defant, A. 1958. *Ebb and Flow*. Ontario: Ambassador Books. (2) Macmillan, D. H. 1966. *Tides*. London: CR Books. (3) Redfield, A. C. 1980. *The Tides of the Waters of New England and New York*. Woods Hole: Woods Hole Oceanographic Institution. (4) Hicks, S. D. 2006. *Understanding Tides*. Washington, D.C.: U.S. Department of Commerce, National Oceanic and Atmospheric Administration, National Ocean Service.
 9. Harris, R. A. 1897–1907. *Manual of Tides: Appendices to Reports of the U.S. Coast and Geodetic Survey*. Washington, D.C.: Government Printing Office.
 10. Cook, A. 1998. *Edmond Halley: Charting the Heavens and the Seas*. Oxford: Oxford University Press.
 11. Woodworth, P. L. 2002. Three Georges and one Richard Holden: the Liverpool tide table makers. *Historic Society of Lancashire and Cheshire*, 151, 19–52.
 12. Wheeler, W. H. 1893. *Tidal Rivers*. London: Longmans, Green and Co.
 13. Cartwright, D. E. 1999. *Tides: A Scientific History*. Cambridge: Cambridge University Press.
 14. Deacon, M. 1997. *Scientists and the Sea, 1650–1900*. Aldershot: Ashgate. (First published 1971, London: Academic Press.)
 15. Reidy, M. S. 2008. *Tides of History*. Chicago: University of Chicago Press.

Sea-level measuring systems

When you can measure what you are speaking about, and express it in numbers, you know something about it.

Lord Kelvin

2.1 The science of measurement

The ocean is its own uncontrollable laboratory and the oceanographer who measures the properties of the sea is an observational rather than an experimental scientist. Sea levels can be measured *in situ*, or by altimetry-satellite remote sensing. Technically the necessity of making *in situ* measurements of sea level presents many challenges in terms of the logistics of travel to the site, for deployment of the equipment, and for its safe and reliable operation in a frequently hostile environment.

This chapter summarises methods of measuring changes of sea levels over tidal and longer periods. The special requirements of tsunami monitoring are further discussed in [Chapter 8](#). Measurements of currents are not included here (but see [Section 4.4](#) on analyses of currents) as they are covered in many general oceanographic textbooks. Measurements of sea level by satellite altimetry, which are closely linked to orbit computations, mean sea level (MSL), and the shape of the Earth, are discussed extensively in [Chapter 9](#).

When we talk about sea-level measuring systems, we mean much more than the sensor that detects the level of the sea surface. A full system includes structures, sensors, recording devices, data transmission, checking procedures, data banking, and arrangements for users to access data on demand. Here we look at all these components of end-to-end systems.

Traditionally gauges that measure sea level have been called ‘tide gauges’ even though the variations they measure include many influences, including tides. The term is so deeply embedded in popular, hydrographic, and even scientific usage, that we use the

terms here synonymously. The term ‘sea-level gauge’ is to be encouraged.

One of the major requirements in the measurement of variations of sea levels is the ability to resolve the longer period variations from shorter period variations due to short period wind-induced waves. These waves often have amplitudes that are much greater than the accuracy demanded for the long period averaged values. It is not unusual to require measurements of tidally changing sea level to an accuracy of 0.01 m in the presence of waves of 1.0 m amplitude. The designer of measuring systems must overcome the problem of averaging these waves in a way that produces no residual distortion.

Measuring systems may be classified as either coastal or offshore measuring devices.

Coastal measurements of sea level have a long history; many countries operate networks of gauges at selected sites, for flood warning, and to monitor MSL changes to assess the long-term risks of flooding from the sea. The British network of more than 40 gauges is an example of a network that transmits the data automatically to a central point for checking and eventual archiving in a special data bank. The National Ocean Service of the United States operates a similar system with more than 250 gauges. Several national systems are linked through the Intergovernmental Oceanographic Commission of UNESCO Global Sea Level Observing System (GLOSS), which consists of 300 key nationally operated gauges, to monitor long period changes in global sea level. GLOSS is part of the Global Ocean Observing System (GOSS). Many series of sea-level observations extend over several decades, and a few of them, which extend over more than a hundred years, are among the longest available series

of ocean measurements. Compared with many other types of ocean measurements, the equipment for measuring sea level is cheap and easy to maintain.

Measurements of sea levels and currents away from the coast are more difficult because there are no obvious fixed reference points. They are also far more expensive because ships are needed to deploy and recover the equipment. Even a modest specially equipped research vessel costs upwards of US\$20,000 per day to operate. As a result of these practical and financial difficulties, few measurements offshore extend over more than a year, and even measurements over a month have become practicable only since the development of automatic digital recording equipment. Tsunami warning systems can include input from offshore sensors.

When planning a measuring programme to monitor sea levels and currents in a particular area, several design factors must be considered. Where should measurements be made? For how long? To what accuracy? Is datum stability and connection to a national levelling datum necessary for the coastal levels? Ultimately, can these requirements be met within acceptable cost limits? The range of equipment now available extends from relatively cheap, imprecise, short-term meters to accurate, long-term, internally

recording, and inevitably expensive, equipment sold in a specialised international market. For a relatively crude local hydrographic survey the former may suffice, but for scientific studies the superior instruments and accuracies are essential. With a little care, target accuracies of 0.01 m in levels and 0.03 m/s in currents are possible. Unfortunately it is easy to make bad measurements, which appear to have this accuracy, but which are later found to contain unidentified systematic or random errors when carefully checked.

When we measure any quantity we are trying to describe it in terms of numbers; we may say that it is big, but by comparison with what other entity? We may say that it has a value of 43, but this is meaningless without properly specified units. We may say that it has a value of 43 metres, but it would be more precise to specify the value as 43.26 metres. It may also be more accurate to give this more precise value, but only if the instruments and procedures used are genuinely capable of achieving that resolution. Oceanographers generally prefer to use SI units; factors for converting among these units are given in [Table 2.1](#).

It is important to realise that all measurements are comparative, and that no measurement is perfectly accurate. The comparative nature of measurements

Table 2.1 Conversion factors to SI units

			Multiply by
Levels			
Conversion to metres			
From	feet		0.3048
	fathoms		1.8288
Pressures			
Conversion to pascals (newtons per square metre)			
From	dynes per square centimetre		0.1000
	bars		100000
	millibars		100
	pounds per square inch		6894.8
Speeds			
Conversion to metres per second			
From	feet per second		0.3048
	knots		0.5144
	kilometres per day		0.0116

implies a system of units and standards established by international agreement and testing. The metre is defined as the length of the path travelled by light in a vacuum in $1/299\,792\,458$ of a second, and the second is defined in terms of radiation from the caesium-133 atom. Secondary standards are adequate for marine physical measurements but it is important that measuring systems are regularly and carefully calibrated against these. An important distinction must be made between the absolute accuracy of a measurement, which is its accuracy compared to an absolute international standard or datum, and the relative accuracy or sensitivity of the measuring system, which is the accuracy with which the difference between individual measurements in a set has been determined. For example, a tide gauge may measure sea-level changes to 0.01 m, but because of inaccurate levelling or poor maintenance, its accuracy relative to a fixed datum may be in error by 0.05 m.

Although the accuracy of a single reading of sea level may be accurate at best to only 0.01 m, the mean of several hourly values is potentially much more accurate, provided that the error in each reading has a random probability distribution. If this distribution is statistically normal the mean of n independent readings is more accurate than a single reading by a factor of the square root of n . On this basis, 100 readings would reduce the error from 0.01 m to 1 mm. It would be unrealistic to claim any greater accuracy than this for mean monthly and annual sea levels (see [Chapter 10](#)), because of unidentifiable systematic errors. The main reason why errors are unlikely to be less than 1 mm is that the original single readings will also contain systematic errors due, for example, to incorrect gauge calibration. Errors can only be reduced by sound observational techniques.

Access to real-time sea-level data is very important for several reasons. One major benefit is that any faults that occur in the tide gauge equipment can be identified and fixed sooner, resulting in better long-term sea-level information. A second benefit is that the data now become available to users who need real-time information for many kinds of operational applications including flood warning and port operations.

Tide gauge data are commonly transmitted to central locations, and are available on-line in near real time through national and international data centres at low cost and with high reliability. Telemetry methods depend on the applications and cost. Mobile telephony is available for local communications, and satellite systems such as Iridium provide worldwide telephone-

based links. Fixed landline and satellite broadband are also affordable options. Many tide gauge agencies will also have access to one or more of the geostationary meteorological satellites, which provide complete longitudinal coverage, but latitude coverage is limited to about 75° north and south. The loggers of a tide gauge can communicate with one of these satellites using a data collection platform within allocated time slots. Tsunami warning systems have been designed to use this form of satellite telemetry. Most data that pass through the geostationary satellites are routed to the Global Telecommunications System (GTS) of the World Meteorological Organization. This system is used for international exchange of all forms of information required by meteorological agencies.

As explained, data from a sea-level station (or ‘platform’) may have several applications, from tsunami warnings to studies of [MSL](#) change. Different sensors are sometimes allocated for different applications. For example, [Chapter 8](#) looks at the special needs of tsunami detection. Nevertheless, there are many cases when an individual sensor can also be ‘multi-use’. The obvious need for major infrastructure improvements, especially in the Indian Ocean following the 2004 tsunami, and several devastating storm surges, led to a recognition that new and refurbished sea-level stations had to be ‘multi-use’ or ‘multi-hazard’. [GLOSS](#) recommendations [1] for these stations now state that they should be equipped with a robust radar gauge to serve as the primary sea-level sensor, recording 3-minute average values, or at higher frequency to serve also as a secondary tsunami sensor. In addition, they should have a differential pressure transducer (one that measures the difference between water pressure and atmospheric pressure) to serve as the primary tsunami sensor, recording 1-minute averages or at higher frequency. Air pressures and other local parameters may be measured; there are also recommendations for backup redundancy in power supply and communications.

Despite their apparent diversity, all measuring systems have some common characteristics ([Table 2.2](#)). Firstly, some physical parameter exists to be measured. For sea level this is the contrast between air and seawater: their density; the velocity with which sound travels within them; or their electromagnetic properties. This physical parameter must be measured by some sensor, which is ideally very sensitive to the parameter itself, but quite insensitive to any other changes. The density contrast between air and water enables the interface to be located by a simple float.

Table 2.2 Summary of the characteristics of commonly used methods for measuring sea level

Category	Type	Wave averaging	Accuracy	Advantages	Disadvantages
Surface following	Tide pole	By eye	0.02–0.10 m	Inexpensive, easy to make and move	Tedious
	Float	Stilling well	0.01–0.05 m	Robust	Needs vertical structure, high maintenance
Fixed sensors	Acoustic reflection	Multiple samples	0.005–0.01 m	Robust, low maintenance Low cost	Needs vertical structure
	Radar reflection Pressure	Hydrodynamics and multiple samples	0.01 m	No vertical structure needed	Density and wave corrections, high maintenance
Remote and mobile	Satellite (see Chapter 9)	Empirical adjustments	0.01 m	Systematic global coverage, high data rate	Expensive, specialist use only, multiple corrections, misses local storms

Table 2.3 Datums used for sea-level measurements

Datum	How fixed	Applications	Advantages	Disadvantages
Tide Gauge Bench Mark	Local levelling	Single tide gauge reference	Long-term stability; an interconnected group covers for accidental damage	Often damaged; includes vertical land movement
Chart Datum	Tidal analysis and levelling	Navigation charts	Level below which sea seldom falls	Varies with tidal range; unsuitable for numerical modelling
Land survey datum (MSL)	Regional levelling and sea-level averaging	Approximate geoid for national mapping	Horizontal surface transferred by levelling	Systematic errors in conventional levelling
Geocentric coordinates	Analysis of satellite orbits (Chapter 9)	Altimetry, GPS	A geometric framework; detects local movements, e.g. of TGBMs	Small changes as mass, e.g. ice, redistributes
Geoid	Satellite orbits and modelling (Chapter 9)	Ocean circulation	True horizontal surface; absolute level for ocean dynamics	Needs special satellite gravity mission

The contrast between the electromagnetic properties of air and water is how the eye detects the level. The signal from the sensor must then be transmitted to a recording system, which will have its own characteristics and limitations. This telemetry may at one extreme be via satellite to a remote data centre, or at the other extreme by human speech to someone who writes the values in a notebook. The choice of sensor, transmitter and recording medium must depend on the applications of the data and the accuracy and speed with which it is required. Flood warning systems need

rapid data transmission, whereas for compilations of statistics of sea-level changes over several years, a delay is of no practical consequence.

2.2 Datum definitions

We must emphasise again the importance of defining and maintaining a clearly defined and stable zero level or datum for sea-level measurements. The datum chosen depends on the application [2]. Those most commonly used are summarised in [Table 2.3](#). The



Figure 2.1 Locating a long-hidden Tide Gauge Bench Mark at Colombo, Sri Lanka. Photograph by David Pugh.

chosen datum may vary from the simple tangible local benchmark at a tide gauge, through to the much more abstract ellipsoid of revolution used for referencing satellite orbits (see [Chapter 9](#)), and the geoid.

The *Tide Gauge Bench Mark (TGBM)* (see [Figure 2.1](#)) is a stable surface or mark near a gauge, to which the gauge zero is referred. The major limitation to the study of sea-level changes over periods of many decades is the stability of the *TGBM* datum. Unfortunately, these marks are often destroyed in the process of harbour development. To enable the recovery of the original datum, and also to check against very local subsidence in the vicinity of the *TGBM*, it is now customary to connect to several auxiliary marks. The levelling between Tide Gauge Zero and the *TGBM*, and onward to the auxiliary marks, should be checked annually to an accuracy of 1 mm for compatibility with the accuracy of the averaged tide gauge levels. The reference level at a site is defined relative to the *TGBM*. The connection between a national geodetic levelling datum and the local *TGBM* is not an essential part of the *MSL* definition (see [Chapter 9](#)). Formerly, many authorities defined their geodetic datum in terms of *MSL*. As a result, after each re-levelling of a country, the local values of the national datum were redefined, introducing discontinuities in the sea-level record, which were not oceanographic in origin. Defining sea levels relative to the *TGBM* has the advantage of clearly separating the oceanographic and the geodetic aspects of the problem of sea-level trends. Although the benchmark itself is usually well above sea level to allow easy access, the levels themselves may be referred to a defined plane

which can be several metres below the benchmark. This has the advantage that all measured sea levels are positive above the datum and values increase as sea level rises. Very rarely, authorities measure sea levels downwards from a tide gauge datum so that the values decrease as sea level rises. A further discussion of datums and their evolution is given in [Section 9.9](#).

Chart Datum is used for nautical charts, as the zero for many gauge sites, and for tidal predictions. The International Hydrographic Organization recommends that Chart Datum approximates to the level of the Lowest Astronomical Tide, the lowest level that can be predicted to occur under average meteorological conditions and under any combination of astronomical conditions. Since 1980, Chart Datum has been implemented to Mean Lower Low Water for all marine waters of the United States. For seafarers this has the important safety factor that the water navigation depths shown on the charts are always the least possible. Predicted tides can always be added to these depths. The height clearance under bridges or cables over tidal rivers is given on charts as above Highest Astronomical Tide, for similar reasons of navigational caution. This definition in terms of the tidal range means that Chart Datum is not a horizontal surface. Spatially, it moves up and down as the tidal range changes along a coast, but it may be considered horizontal over a limited local area. Locally Chart Datums are normally tabulated relative to a land survey datum. In the United States, a National Tidal Datum Epoch [2], over 19 years, is used. This is presently based on 1983–2001; every 25 years or so, the National Ocean Service considers whether a new tidal datum epoch is needed to account for the global sea-level change and long-term vertical adjustment of the local landmass.

Land survey datum is often defined from calculations of *MSL* over a specified period. For example, for the United Kingdom Ordnance Datum Newlyn is the *MSL* at Newlyn measured between 1915 and 1921. Present *MSLs* at Newlyn have risen to about 0.2 m above Ordnance Datum Newlyn. In North America and India an adjustment based on *MSLs* at a grid of coastal stations was used in earlier definitions (see [Chapter 9](#)). In theory the survey datum parallels the geoid (see below, and [Chapter 9](#)), a true horizontal surface, but because of small systematic errors in land levelling techniques, the transfer of the datum from one tide gauge to another can have errors of several centimetres or more. It has never been possible to use

sea-level differences based on land survey connections between gauges as a basis for hydrodynamic modelling, as the land surveys are not accurate enough.

Two geocentric datums, discussed in Chapter 9, are used for satellite orbit calculations. The *reference ellipsoid* reflects the fact that the Earth is not a perfect sphere. It would be nearly spherical if only gravitational forces were involved, but due to its rotation the Earth bulges out slightly at the equator, and is slightly flattened at the poles. The *geoid* datum is a true horizontal surface. It is the theoretical mean sea-level surface, which varies from the ellipsoid of revolution by as much as 100 m due to the uneven distribution of mass within the Earth.

2.3 Coastal instruments

Methods for measuring sea level [1, 3] may be divided into two categories: those appropriate for coastal measurements, and those that can be used offshore. Until quite recently all measurements of any duration were made at the coast, which, although technically easier, can introduce local sea-level distortions, as discussed in Chapter 6. Coastal currents and waves interact with the coastal topography to produce local gradients on the sea surface. Mean sea levels at one site may be higher or lower by several centimetres, compared with the corresponding levels a few kilometres away along the coast, or outside rather than inside a harbour. Differences of 0.03 m would not be exceptional, and so the selection of a suitable site for coastal measurements is important.

A coastal measuring site should ideally be connected by relatively deep water to the area for which the measured levels are intended to be representative. It should experience the full tidal range, if possible, and not dry out at low waters. Sites affected by strong currents or directly exposed to waves should be avoided because of their local effects on sea level. So also should sites near headlands and in harbours with very restricted entrances. Practical requirements include ease of access, proximity to a permanent benchmark for good datum definition, and the availability of electrical power and a suitable building for the recording instruments. Piers and lifeboat stations can be good secure sites but they are not always available.

Intercomparison of gauges is a powerful diagnostic tool, to check accuracy. One particularly useful technique adapted from hydrology is the Van de Casteele test, where differences between a gauge reading and

the true levels, measured by an independent method, are plotted against the true sea levels through a tidal cycle [4].

2.3.1 Tide poles

Levels have been measured using vertically mounted poles for thousands of years. The ancient Egyptians linked their Nilometers to their temples, from where the priests gave warnings of imminent flooding. Tide poles or staffs are cheap, easy to install, and may be used almost anywhere. Many harbours have levels engraved in the walls (Figure 2.2a). Along a broad drying beach a flight of tide poles, all connected to the same datum (Figure 2.2b), may be used. For these, and for all measurements of level, there must be a careful connection of the gauge zero to a permanent benchmark, the TGBM. In calm conditions it should be possible to read a pole to 0.02 m, but the accuracy deteriorates in the presence of waves. Experiments show that experienced observers can achieve a standard deviation for a set of readings of 0.05 m in the presence of waves of 1.5 m amplitude. However, systematic errors may also be present due to operator bias and because of different daytime and night-time illumination. Waves may be averaged out by taking the average between crest and trough levels; but the apparent trough level for an observer viewing at an angle over the sea surface may actually be the crest of an intermediate wave that is obscuring the true trough at the pole. In this case the averaged level will be too high.

Reading accuracy in the presence of waves may be increased by fitting a transparent tube alongside the pole, which connects to the sea through a narrower tube preventing immediate response to external level changes. A transparent tube of internal diameter 0.025 m, with a connecting tube 2.7 m long of internal diameter 0.004 m, gives an averaging time of 30 s, sufficient to still most waves. The level in the transparent tube is easily read against the graduated pole, particularly if some dye is mixed into the tube water [5].

Although notable series of measurements have been made with tide poles, the tedium of reading over several months makes poles unsuitable for long-term measurements; however, they are often the best choice for short-term surveys of only limited accuracy. Commercially available gauges, consisting of a series of spaced electronic water level sensors, which record both waves and tidal changes of level, are available as an alternative to reading by eye.



Figure 2.2 (a) An early example of a tide staff, showing levels above Old Dock Sill datum, engraved on the entrance to Canning Half-Tide Dock, Liverpool. Photograph by Philip Woodworth.

(b) Modern tide staffs are designed for easy reading; this staff is the lowest of a flight of poles at Port Louis, Falkland Islands. Photograph by David Pugh.

2.3.2 Stilling-well gauges

The vast majority of permanent gauges installed from the mid nineteenth century to the 1970s consisted of an automatic chart recorder: the recording pen is driven by a float which moves vertically in a well, connected to the sea through a relatively small hole or narrow pipe. The limited connection damps



(a)



(b)

Figure 2.3 (a) An example of a traditional stilling-well float-operated gauge, at Ilha Fiscal, Rio de Janeiro, operated by the Brazilian Navy.

(b) A tide gauge structure at Aveiro, Portugal. Photographs by David Pugh.

the external short period wave oscillations. The basic idea was described by Moray in 1666 [6]. He proposed that a long narrow float should be mounted vertically in a well, and that the level to which the float top had risen be read at intervals. The first self-recording gauge, designed by Palmer, began operating in 1831 at Sheerness in the Thames estuary [7]. Various mechanisms followed soon after [8]. Chart recording is now obsolete, but the basic stilling well, with all its advantages and limitations, is often a feature of modern installations. [Figure 2.3a](#) shows a tide gauge construction at Rio de Janeiro, in Brazil, and [Figure 2.3b](#) shows a more robust system at Aveiro, Portugal.

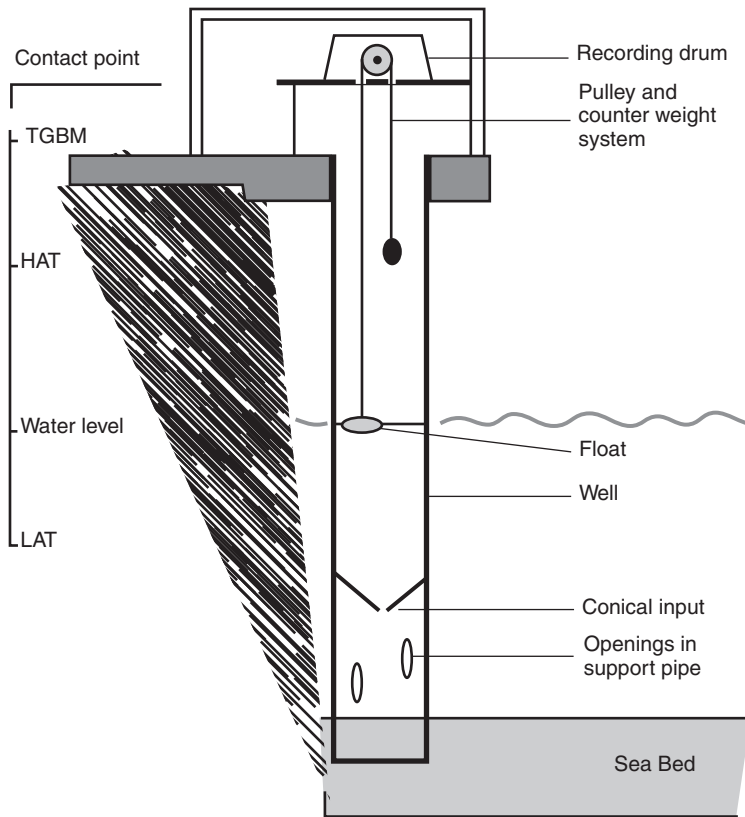


Figure 2.4 A basic stilling-well system used by the U.S. National Ocean Service. The cone orifice diameter is typically 10 per cent of the well diameter, except at very exposed sites. The well diameter is typically 0.3–0.5 m.

Figure 2.4 shows the essential components of such a well system, formerly used by the United States National Ocean Service. Figure 2.5 shows the network of levelling connections that fix the tide gauge datum. The well is attached to a vertical structure, which extends well below the lowest level to be measured. At the bottom of the well is a cone, which inserts into a support pipe; this pipe is fixed in the sea bottom. Six pairs of openings in the support pipe give little resistance to the flow of water, but the narrow cone orifice restricts flow, preventing the rapid fluctuations due to waves from entering the well. However, the slower tidal changes, which it is intended to measure, do percolate. For most tide and wave régimes an orifice to well diameter ratio of 0.1 (an area ratio of 0.01) gives satisfactory results. Where waves are very active the area ratio may be further reduced to perhaps 0.003. Several alternative well arrangements are possible; these include a hole in the side of the well or, where necessary, a straight or syphon pipe connection. Copper is often used to prevent fouling of the narrow connections by marine growth. A layer of kerosene

may be poured over the seawater in the well where icing is a winter problem.

Routine daily and weekly checks are an essential part of a measuring programme. In addition to timing checks, the recorder zero should be checked periodically by using a steel tape to measure the distance from the contact point level to the water surface. The instant the end touches the water may be detected by making the tape and the seawater part of an electrical circuit, which includes a light or meter, which operates on contact. For diagnosing errors in gauge operation, it is useful to plot the difference between the probed and the recorded levels against the true levels as measured by the probe [4]. For a perfect gauge the difference is always zero, but a wrongly calibrated gauge will show a gradual change in the difference. If the gauge mechanism is very stiff, the difference will not be the same for the rising and falling tide.

In addition to regular checks of gauge zero against the contact point, the level of the contact point should be checked against a designated TGBM and a series of auxiliary marks at least once a year, as shown in

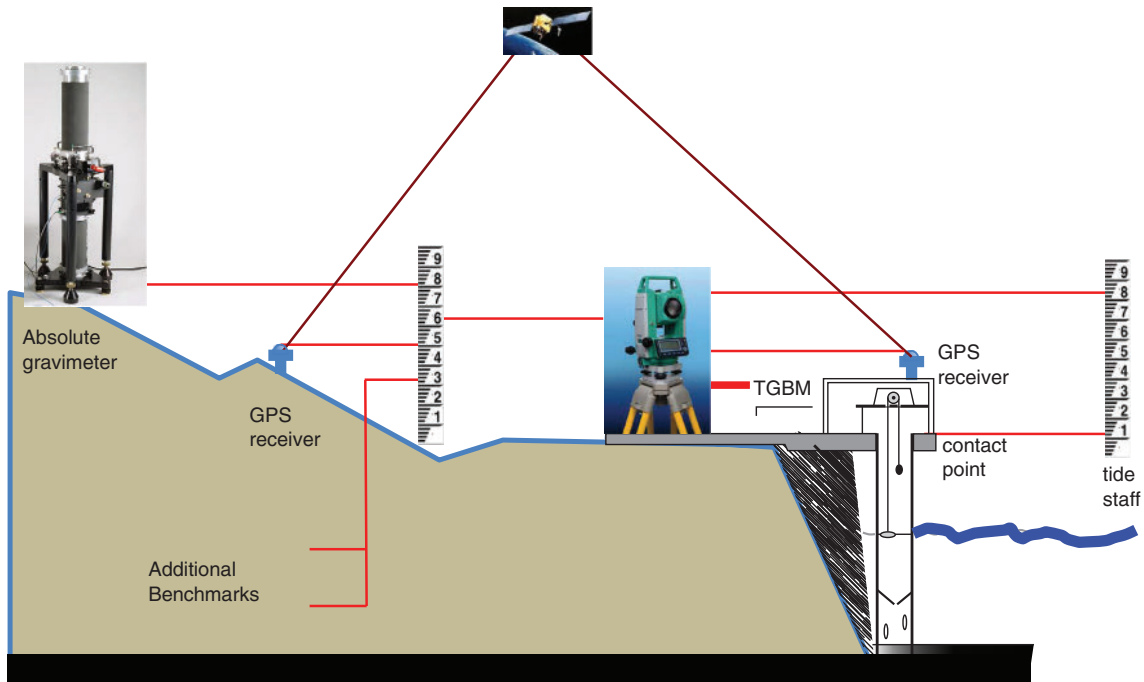


Figure 2.5 The network of datum levelling connections needed to reliably define a tide gauge datum. Geodetic control is provided with the use of GPS equipment: GPS and Absolute Gravity provide data on vertical land movement at the site (Chapter 11).

Figure 2.5. Many gauges also check benchmark movements relative to a GPS benchmark at the site, where either episodic or continuous GPS measurements are made (Chapter 11).

Although stilling-well systems are robust and relatively simple to operate, they have a number of disadvantages: they are expensive and difficult to install, requiring a vertical structure for mounting over deep water. There are also fundamental problems associated with the physical behaviour of the wells. Two such errors are due to water density differences during the tidal cycle, and to drawdown due to flow of water past the well, the Bernoulli effect. In an estuary the water salinity and hence density increases with the rising tide. The water that enters the well at low tide is relatively fresh and light. At high tide the average water density in the well is an average of the open-sea density during the rising tide, while the well was filling. However, the water in the open sea at high tide is denser and so the well level must be higher than the open-sea level for a pressure balance across the underwater connection. As an extreme example, the well level could be 0.12 m higher than the external level on a 10 m tide where the density increases from that of fresh water to that of normal seawater [9].

Seasonal water density changes will also affect measured levels.

Because the well, or the structure to which it is fixed, presents an obstruction to currents, it will distort the underwater pressures. Hence, the pressure at the connection between the well and the sea may not be the true pressure due to the undisturbed water level. The openings in the support pipe of Figure 2.4 are arranged to reduce this pressure distortion. A major limitation for the most accurate measurements is the behaviour of the flow through the orifice in the presence of waves; there can be a systematic difference in the levels inside and outside the well, particularly if the flow due to the waves is less restricted in one direction than another, as with a cone-shaped orifice.

2.3.3 Pressure measuring systems

An alternative approach is to measure the pressure at some fixed point below the sea surface and to convert this pressure to a level by using the basic hydrostatic relationship:

$$P = P_A + \rho g D \quad (2.1)$$

where P is the measured pressure, at the transducer depth, P_A is the atmospheric pressure acting on the water surface, ρ is the mean density of the overlying column of seawater, g is the gravitational acceleration, and D is the water level above the transducer.

The measured pressure increases as the water level increases. Robert Hooke and Edmond Halley first used this relationship to measure water depths in the seventeenth century. At the coast the underwater pressure may be transmitted to a shore-based recorder through a narrow tube. In simple systems the pressure is sensed by connecting the seaward end to a partially inflated bag or an air-filled drum open at the base, in which pressures adjust as water enters and leaves during the tidal cycle.

Better overall performance and datum stability [10] are obtained with the pneumatic system shown in Figure 2.6. Gauges based on this principle are called bubbler gauges or gas-purging pressure gauges. Compressed air (diving cylinder air is good), or nitrogen gas from a cylinder, is reduced in pressure through one or two valves so that there is a small steady flow down a connecting tube to escape through an orifice in

an underwater canister, called a pressure point or bubbler orifice chamber. At this underwater outlet, for low rates of gas escape, the gas pressure is equal to the water pressure P . This is also the pressure transmitted along the tube to the measuring and recording system, apart from a small correction for pressure gradients in the connecting tube.

Historically, several forms of recorder have been used, including temperature-compensated pressure bellows, which move a pen over a strip chart, a mercury manometer with a float arrangement as for a stilling well, and a variety of electronic transducers, which permit a digital signal to be recorded on magnetic tape. Figure 2.6 shows a gas control and pressure recording system. The normal procedure is to measure the pressure using a differential transducer that responds to the difference between the system pressure and the atmospheric pressure ($P - P_A$), so that only the water head pressure $\rho g D$ is recorded. If g and ρ are known, the water level D relative to the pressure point orifice datum may be calculated. For most sites a suitable constant value of ρ may be fixed by observation. However, in estuaries the density may change significantly during a tidal cycle. In this case, allowing

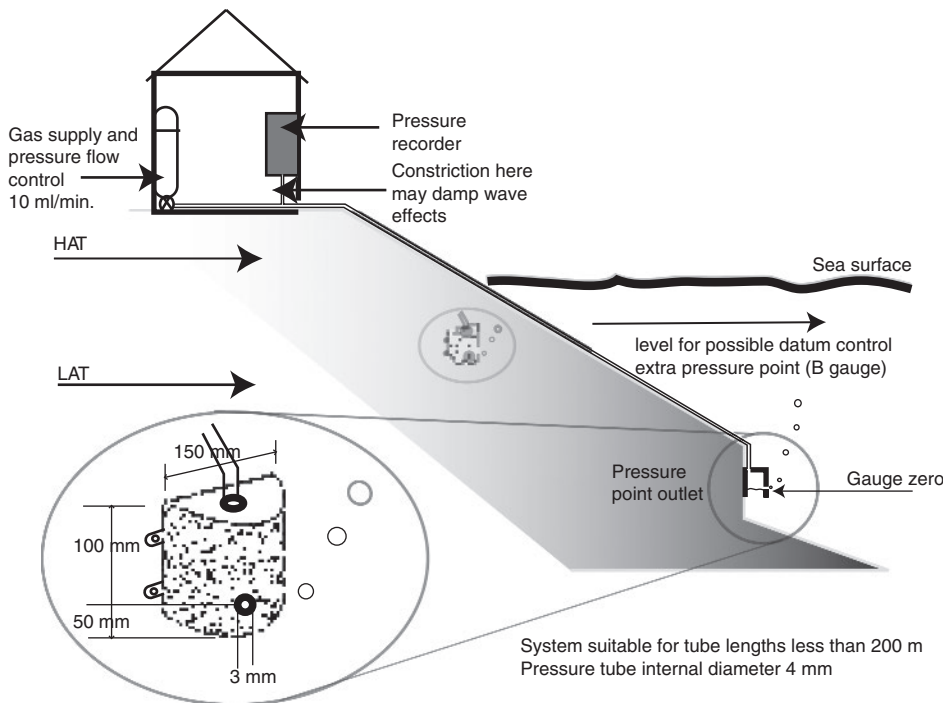


Figure 2.6 A basic pneumatic bubbler system for tube lengths less than 200 m. The pressure at which bubbles escape from the underwater pressure point gives the water head pressure. This is measured on the pressure recorder ashore. Note the possible location of a second, more accessible mid-tide pressure point for regular datum checking.

for a linear increase of density with level is usually an adequate adjustment.

The underwater pressure point is designed to prevent waves forcing water into the connecting tube. If this happened, large errors would result. The critical parameter for wave damping is the ratio between the total volume of air in the pressure point and connecting tube and the area of the pressure point cross-section: this ratio should not exceed 0.20 m; the actual shape of the pressure point cross-section is not important. For tube lengths up to 200 m the pneumatic system shown in Figure 2.6 will be accurate to within 0.01 m water head equivalent. The rate at which air is forced through the tube should be sufficiently large to prevent water backing-up into the pressure point and tube system during the most rapid rate of sea-level rise in a tidal cycle, but too rapid a rate will result in the air bottle having to be replaced more often than necessary. Another constraint is that the pressure drop in the connecting tube, which must be kept small, is proportional to the flow rate. For the system shown in Figure 2.6 and a tidal range of 5 m, a flow of 10 ml per minute will suffice. The error due to pressure drop in the tube depends on both the tube length and the rate of flow, which in turn must increase as greater tube length increases the system volume. The error increases in proportion to $(l_T/a_T)^2$, where l_T is the tube length and a_T is the tube radius. For this reason special care is necessary when designing for connecting tube lengths in excess of 200 m [10].

The datum of a bubbling system is the small bleed hole in the side of the pressure point. This must be rigidly fixed to some structure or to the seabed. Datum control accuracy can be improved by having a parallel system (called a B gauge) with a second and more accessible pressure point fixed near MSL [11]. This serves the same purpose as a fixed datum probe for the stilling-well systems, but in this case comparing the differences between the two bubbling gauges, when both are submerged, checks the datum.

One great advantage of bubbling systems is that they do not need a vertical structure. Other advantages include the stability of a clearly defined datum, the cheap expendable nature of the vulnerable underwater parts, and the possibility of having the underwater pressure point some hundreds of metres from the recorder. Systems with tube lengths of 400 m have been designed for use in special cases; the range enables measurements at virtually all coastal sites provided that the tubing is protected as it passes through

the zone of breaking waves. On beaches, protective outer tubing weighted with scrap chain is very effective for burying the air tube. The pressure point may be fixed to an auger rod twisted into the sand. Levelling to the pressure point datum requires special equipment or the cooperation of a diver to hold the levelling stave. Even if the connecting tube is accidentally cut and flooded it can be repaired, and the system and its datum level re-established by purging water with a high-pressure air flow for a short period.

A differential pressure transducer mounted in the water, with an electric cable connected to a recorder ashore, is an alternative to transmitting the water pressure directly to the surface, provided there is good ventilation to atmospheric pressure. Datum definition is best achieved by checking against a levelled tide pole. The cost of replacing relatively expensive underwater components, possibly using divers, is a small potential disadvantage.

2.3.4 Acoustic reflection gauges

The time taken by a pulse of sound to travel from the source to a reflecting surface and back again is a measure of the distance from the source to the reflector. If a sound source, an acoustic transducer, is mounted inside a vertical sounding tube, the travel time may be used to replace the float and wire assembly. This travel time is given by:

$$t_p = \frac{2l_z}{C_a} \quad (2.2)$$

where l_z is the distance to be measured between transducer and water surface, and C_a is the velocity of sound in air. For dry air (at 10 °C and one atmosphere pressure) $C_a = 337.5$ m/s so that a change in l_z of 0.01 m corresponds to a change in t_p of 0.000059 s. Corrections must be made for the variations of C_a with air temperature, pressure and humidity. For example, if the temperature falls to 0 °C, C_a decreases to 331.5 m/s and it is necessary to reduce the calibration factor of the gauge by 1.8 per cent to compensate. One way of making these adjustments is to record the travel time of a sound pulse over a known standard distance. This method is less accurate without a stilling well or sounding tube, because reflections are directed away from the receiver if they are incident on an irregular or sloping sea surface. Also, it is difficult to have a reliable calibration method that allows for air temperature gradients.

The United States National Oceanic and Atmospheric Administration and other authorities began installing acoustic gauges with sound-transmitting tubes in the early 1990s (Figure 2.7a). The acoustic gauge sends a pulse down a 1.3 cm diameter sounding tube, towards the water surface, and measures the travel time of the reflected signal. The sounding tube has an acoustic discontinuity, sometimes a small hole, at a known distance from the top of the tube, which gives a fixed second reflection point. The elapsed times for the return of the reflected pulses from the water surface and from the fixed point are recorded. The travel time to the fixed reflection point is used as a calibration, automatically allowing for changes in the speed of sound due to air temperature and pressure effects. Accuracy is limited by air temperature gradients, producing variable sound speeds in the tube.

The acoustic sounding tube is mounted inside a 0.15 m diameter protective well that has a symmetrical 0.05 m diameter double-cone orifice at the bottom. The protective well is more open to the local dynamics than the traditional stilling well used for float gauges and only partly filters out the wind waves. Rapid sampling and averaging is used to fully remove the waves. In areas of high-velocity currents and high-energy sea swell and waves, parallel plates are mounted below the orifice to reduce the drawdown effects.

Acoustic systems with data transmitted to a central location are widely used in the United States, Australia and in many other countries. In addition to sea level, other parameters such as water temperature, air pressure and temperature, and wind speed can be logged and transmitted at the same time. In a typical gauge the water levels are measured once per second. Not all of these data are stored and transmitted. The primary water level measurements are averaged typically over a 3-minute period and are stored every 6 minutes. To detect a change in water level of 0.01 m, the timing of the acoustic pulse travel must be accurate to about 60 microseconds.

An alternative method, used in some research work, is to place the transmitter and receiver on the seabed where they operate like an inverted ship's echosounder. The velocity of sound in seawater (10 °C and 35 ppt) is 1490 m/s. To achieve an accuracy of 0.01 m the timing must be accurate to within 0.000013 s. At 0 °C the calibration factor must be reduced by 2.8 per cent; in fresh water a reduction of 3.2 per cent is necessary.

2.3.5 Radar reflection gauges

The principle of timing a reflected signal (Equation 2.2) may also be applied using a pulse of electromagnetic radiation. This travels at 299.792×10^6 m/s in air (at 10 °C and a pressure of one atmosphere) so that timing to an accuracy of 0.6×10^{-10} s is necessary to resolve a level difference of 0.01 m. Careful design avoids reflections from surrounding structures. In one design a pair of copper tubes is used as a waveguide.

Radar tide gauges are now installed at many sea-level stations around the world (Figure 2.7b) owing to their relatively low cost and ease of installation and maintenance. Modern radar gauges draw much less power than earlier devices and can be readily powered by solar panels.

Radar gauges are positioned several metres above the surface of the sea and require neither the extensive fixings to a harbour wall or pier, as would be needed for a stilling well, nor the involvement of divers for underwater fixings, as for pressure gauges. However, a vertical structure is necessary. Some radar systems measure changes in sea level by monitoring the time-of-flight of a radar pulse from a transmitter/receiver unit to the surface and back to the unit, while others use a frequency-modulated continuous-wave system in which transmitted radar waves are mixed with signals reflected from the surface to determine the phase shift between the two waves and thereby the range. Unlike acoustic measurements, radar range gauges are not affected by either temperature or vertical temperature gradients.

Radar gauges can be operated in the open air, without a stilling well, as shown in Figure 2.7b. They have a typical beam-width of 5°. When installed on harbour walls they can be mounted at the end of a cantilevered arm, extending far enough over the water, so that no reflections are obtained from the wall. They can also, in principle, be installed inside a large stilling well, although in this case radar systems that transmit microwave pulses down a waveguide tube are preferable.

The low cost of radar systems stems from their wide use in the monitoring of levels of various solids and liquids in storage tanks, and also the levels of rivers and lakes.¹

¹ If wanted, marine radar gauges can sample rapidly enough to record waves.

(a)



(b)



Figure 2.7 (a) A pair of acoustic tide gauges with satellite transmission on Easter Island. Photograph by David Pugh.

(b) Radar reflection gauge on the island of St Helena with solar panels, recording electronics and satellite transmission equipment. Photograph by Jeff Pugh and Peter Foden, National Oceanography Centre.

Radar gauges provide a cost-effective choice of technology for new or refurbished sea-level stations, but there are some caveats. Experience of them so far has been limited. In particular, there are concerns about wave bias in the radar sea-level measurements (with different bias characteristics, depending on which part of a wave provides a reflection, in different systems), which has not been fully researched by means of comparison of gauges over different sampling periods by different techniques. Other disadvantages include their potential exposure to damage during major storms or tsunamis, including the possibility that the water level in such events may even exceed the height of the radar sensor, and the further possibility that floating debris or boats may pass under the beam resulting in false measurements. Nevertheless, in spite of these limitations, radar gauges are now the first choice for many sea-level agencies.

2.4 Open-sea gauges

Measurements of sea-level variations along the coast define conditions in only a limited area of sea. There are several applications for which the changes in levels at sites well away from the coast, even in the deep ocean, are required. These applications include hydrographic surveys where depths must be adjusted for the changing sea level and where a shore gauge is too distant, navigation of ships through shallow channels, the design and transport of oil rigs, tsunami detection, the operation of flood warning systems, and the scientific study of the hydrodynamic behaviour of oceans and shelf seas.

2.4.1 Bottom pressure gauges

Figure 2.8 shows a robust and relatively inexpensive commercially available pressure recorder, which can be operated on the seabed to depths of 100 m. The instrument is programmed directly by computer to sample at selected intervals from seconds to hours. Waves are averaged digitally by measuring over several seconds before recording a value. These instruments are easy to deploy and ideal for short-term tidal studies. Connection to a datum ashore is possible over small distances by simultaneous readings of a tide pole [12] corrected for air pressure.

Specialised scientific instruments can descend to the ocean bottom to more than 4000 m. After a period of time during which they have made and recorded

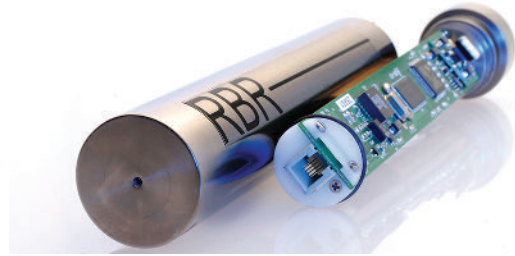


Figure 2.8 Several bottom-mounted sea-level pressure gauges are available commercially. The one shown here was developed by Richard Brancker Research (RBR), for deployment to 100 m depth. These gauges are suitable for measuring seiches and tides, but their zero datum is not stable enough for measuring long-term MSL changes. The instrument is 0.3 m long.

pressure measurements, the instruments are released from their ballast weights and float to the surface where they are recovered by a ship. This seabed pressure, which is related to water level by the hydrostatic Equation 2.1, includes atmospheric pressure. Operation of these bottom pressure recorders (BPRs) requires a high level of technical skill for deployment and recovery of the equipment and to ensure reliability and precise calibration [6].

Although the study of ocean tides in bottom pressures remains of interest, bottom pressure recorders are now mainly used by oceanographers to study the non-tidal signals in bottom pressure due to changes in the ocean circulation. The UK National Oceanography Centre has used them across the Drake Passage since the 1980s in order to monitor changes in the Antarctic Circumpolar Current [13] (Figure 2.9). Over very long recording periods, data can be relayed to the surface either by acoustic links to passing ships or with the use of releasable ‘podules’ that communicate with satellites once they reach the surface. Studies of ocean circulation related to sea level generally use data from satellite altimetry (Chapter 9), as it gives global coverage and is readily available. However, ocean bottom pressure recorders still have a use at high latitudes not reached by altimetric satellites, and where long-term fixed measurements and better temporal resolution are needed. Bottom pressure is also a closely related parameter to ocean mass as measured by GRACE (see Section 9.6).

Open-sea bottom pressure data can also be obtained by linking sensors to cables, which extend across several ocean sections [14]. Tsunami warning systems use DART (Deep-ocean Assessment and



Figure 2.9 The National Oceanography Centre (NOC) deep-sea pressure gauge MYRTLE (Multi-Year Return Tide Level Equipment), ready for deployment. Photograph from NOC.

Reporting of Tsunami) buoys and sensors stationed far out to sea. Offshore sea-level buoys as part of tsunami warning systems are discussed in [Chapter 8](#).

2.4.2 Surface buoys and GPS

A less common approach for measuring sea surface levels offshore is to install GPS receivers and transmitters on moored buoys offshore and even in the deep ocean. Technically this is reasonably straightforward, and water-level heights are related to the reference ellipsoid, after some intermediate computing. Although in theory offshore sea surfaces could be mapped in a specific location, to a geocentric datum, over long periods, the method is not yet sufficiently understood to allow its use for [MSL](#) studies. Uncertainties include the response of the antenna's mean level to [MSL](#) in the presence of waves, and possibilities of biological fouling affecting the settling of the buoy in the water over long periods.

2.5 Data reduction

Before the raw data recorded by the instrumental system are ready for scientific analysis, they must go through a process of checking and preparation known as data reduction. A good source of information is the series of [GLOSS](#) Manuals, which is regularly updated [[01](#), [15](#)]. Often, but not invariably, sea-level changes with a strong tidal component are presented for analysis in the form of hourly, 10- or 6-minute values, either in local time or in Universal Time. Most tide gauges now use internal quartz crystal or satellite timing control, accurate to a few seconds a month, and so timing is not a problem, though with historical chart records corrections of a few minutes may be needed. However, when a value is logged after taking several high-frequency readings to average out waves, the correct time must be shifted back to the middle of the averaging period.

Current meter data should be converted to speeds and directions. As above, if a meter has counted rotor turns over a 10-minute period, the calculated speed applies to a time 5 minutes before the recording time. The instantaneous 10-minute readings of current direction at the start and end of each 10 minutes may be averaged to give a direction for this central time. The recorded values, which will usually be relative to magnetic north, must be adjusted to geographic north by adding the magnetic variation. For further processing and analysis it is usual to convert these to current components in the north–south and east–west directions, with the flow to the north and to the east being defined as positive. Note that this is the opposite of the convention for winds where, for example, a north wind comes from the north. An alternative is to resolve the currents into two components aligned and at right angles to the main direction of tidal flow. A current speed in a direction measured clockwise from geographic north ([Figure 2.10](#)) resolves into:

$$\text{An eastward component: } u = q \sin \theta$$

$$\text{An northward component: } v = q \cos \theta$$

The process of checking both levels and current components for recording errors depends on some preconceptions about the parameter being recorded. Clearly an isolated sea level 10 m higher than anything previously observed is an error, but smaller less obvious errors should be considered with care and only rejected if there is independent evidence of

malfunction. Otherwise there is a danger of disregarding real but unexpected events. The first check is to identify values that lie outside the expected range, or that appear as isolated spikes in the data. Computer files may be checked against values on either side by ensuring that the difference between a value at one hour does not differ by more than a specified tolerance (τ) from a function fitted through the surrounding values. For example, a seven-point Lagrangian fit requires each x_t value to satisfy the condition:

$$\begin{aligned} & -0.0049x_{t-7} + 0.0410x_{t-5} - 0.1709x_{t-3} \\ & + 0.6836x_{t-1} + 0.35127x_{t+1} - 0.0684x_{t+3} \\ & + 0.0068x_{t+5} - x_t < \tau \end{aligned} \quad (2.3)$$

Where tides are dominant a simpler method is to check against values at similar states of the tide on previous and subsequent days:

$$\frac{1}{6} |-x_{t-50}| + 4x_{t-25} + 4x_{t+25} - x_{t+50} - x_t < \tau \quad (2.4)$$

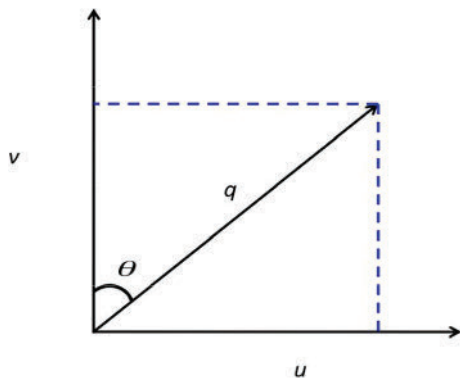


Figure 2.10 The simple Cartesian convention for resolving current components.

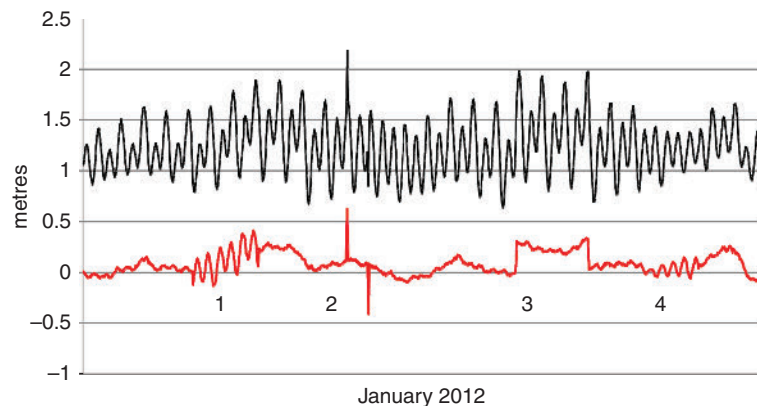


Figure 2.11 An example of non-tidal residuals plotted (red) to show characteristic errors due to: (1) a missed 1-hour value; (2) 0.5m positive and negative spikes; (3) a datum shift of 0.3m; and (4) a slow reduction in gauge sensitivity due to blockage. The record, for Spring Bay, Tasmania, includes the low-frequency natural variations due to weather effects. The black curve is the 'observed' sea level. The errors are artificially introduced.

Any value that fails this test should be marked for further scrutiny. However, because any isolated wrong value will also be used to fit smooth curves to check other values, it may automatically cause surrounding values to be incorrectly flagged as errors.

A more sensitive check for records dominated by tides is to remove the tidal part by subtracting predicted tidal values (see [Chapter 4](#)) from observed values and to plot these residual values against time. Some common errors in tide gauge operation have well-defined characteristics in these plots. [Figure 2.11](#) shows a residual plot with a two successive days' curves on the chart interchanged (1), isolated errors of 1 metre (2), a datum shift (3), and a timing error (4) [01].

A more detailed technique is 'buddy checking', which involves the comparison of sea-level records from nearby stations using either the original (e.g. hourly) data or daily, monthly or annual MSL values. Inspection of the differences between their time series, or of the non-tidal residuals, provides a powerful means for spotting data errors.

A separate problem relates to the filling of gaps in records. Gaps may extend from a few hours to several days, usually due to instrument failure. There will also be small gaps between successive records that need to be filled to obtain a complete series. Fitting a function through the observed values on either side, if the gap is not too large, can fill small gaps. The 25-hour function of [Equation 2.4](#) can be used for gaps up to a day. Gaps should only be interpolated if there is a special need, such as the application of a numerical filter with a broad window, if treating the original observations as two separate series would lose too much data. A more elaborate interpolation method is to add predicted

tides to an interpolation of the observed low-frequency non-tidal residuals.

Filters for tidal time series

The theory of designing and applying numerical filters to separate tidal and non-tidal effects is beyond the scope of this account [16]; packages are available in standard scientific software. Generally, the longer the width of the filter window, the sharper the frequency cut-off, but the more the record is truncated. When processing sea-level and current data a symmetrical filter should be used to avoid introducing time shifts.

Two filters that have only a short sampling window, specifically designed for separating tidal variations from other sea-level changes, have been developed, originally when computations were much more labour intensive. The Doodson filter extends from $(t - 19\text{ h})$ to $(t + 19\text{ h})$, so loses very few data in its application. The Demerliac filter is longer than Doodson's, extending from $(t - 35\text{ h})$ to $(t + 35\text{ h})$, but it has a sharper cut-off [17].

2.6 Data sources

The final stage of data reduction is to deposit the data in an oceanographic data bank, together with the metadata: details of the methods used for measurement; datum controls; the steps taken in the processing; clear indications of the data that have been interpolated or that are unreliable in some way; and GPS location coordinates, maps and images. Although this may seem a tedious additional requirement for a single researcher or project, the high cost of making oceanographic measurements means that data should be available for use in as many investigations as possible, and in the long-term.

Different applications require different qualities and availability of sea-level data. Three streams can be identified:

- *Real or near real-time* information required for operational oceanography, including navigation, storm and tsunami flood warnings. In this case very limited automated quality control is possible; users have to be aware of the possibility of data errors.
- *Fast* data for which some form of quality control may be possible, such as the correction of obvious spikes in the record. Fast data are required in some applications such as the forecasting of ocean circulation variability, gauge performance monitoring, and for checks on the stability of the

sea-level information obtained from space by satellite radar altimetry (Chapter 9).

- *Delayed mode* data for which full quality control is possible, as discussed above. Such data will be accompanied by complete documentation.

Delayed mode data, consisting of hourly (or 6-, 10- or 15-minute) levels, can be filtered to provide daily *MSL* values, and subsequently monthly and annual *MSL* values, for use in climate change research, geology and geophysics. These data are frequently submitted to the Permanent Service for Mean Sea Level (*PSMSL*), and the University of Hawaii Sea Level Center (*UHSLC*).

Governments have set up a Global Sea Level Observing System (*GLOSS*), to which more than 80 countries contribute measurements from their sea-level gauges. *GLOSS* has a core of some 300 gauges, which provide an approximately geographically evenly distributed sampling of coastal sea levels (see Figure 2.12). *GLOSS* incorporates a set of gauges for identifying long-term trends in global sea levels. Wherever possible these gauges are linked to *TGBMs*, maintained in geocentric coordinates, for example by GPS monitoring of these benchmarks, in terms of geocentric height analysed in conjunction with the tide gauge data. This allows separation between local vertical land movement and *MSL* changes (see Section 10.2).

The *UHSLC* collects data from a subset of the *GLOSS* network in real time so they are available almost immediately for a range of operational purposes: the Fast Delivery *GLOSS* Sea Level Center [18]. The *UHSLC* collects, processes, analyses and distributes tide gauge data from around the world in support of climate and oceanographic research. Tide gauge observations from nearly 500 stations and 70 international agencies are reviewed and archived regularly. The Center also produces a Research Quality Data Set of delayed-mode hourly sea level data.

The *PSMSL* [19], on Merseyside, United Kingdom, has collected and analysed monthly and annual data since 1933 for the science of sea-level changes. It holds more than 50,000 station-years of data from over 1800 tide gauges worldwide, and from almost 200 national authorities. The data can be accessed through the Internet. If the datum history can be clearly established so that a homogeneous series of levels can be prepared, these levels are adjusted to a Revised Local Reference datum (*RLR*), which is defined relative to the *TGBM* so that the mean level in a specified year is approximately 7.0 m. This arbitrary value of 7.0 m has been chosen to avoid troublesome negative quantities

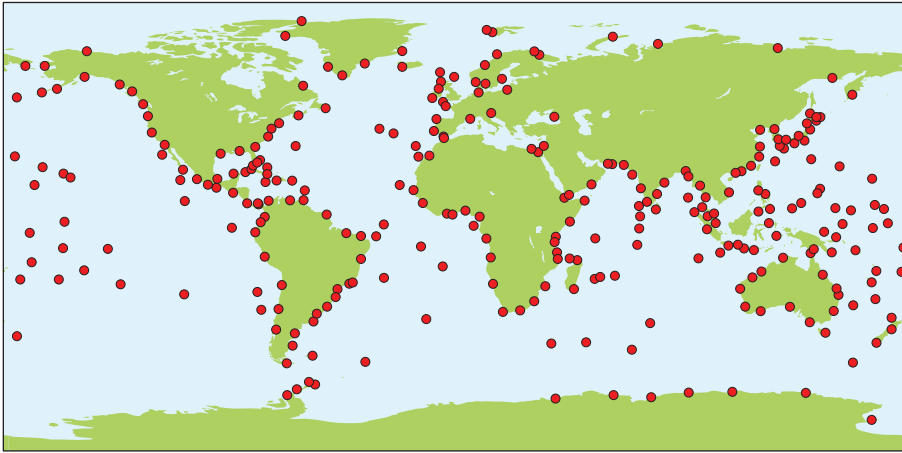
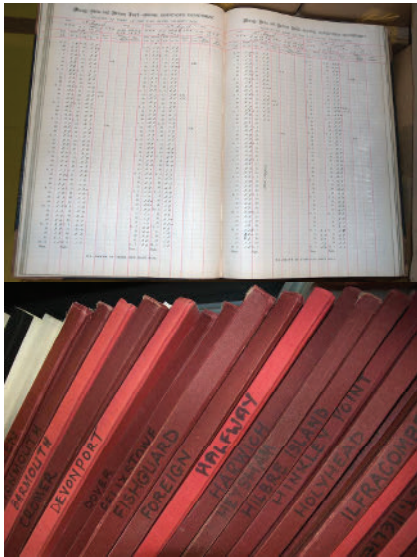


Figure 2.12 The Global Sea Level System, GLOSS, of the Intergovernmental Oceanographic Commission of UNESCO.



Old sea level records are difficult to access

Figure 2.13 Data archaeology of old records can provide important information for research. Photographs by David Pugh.

and to emphasise its difference from any other system of datum definition. The PSMSL holds benchmark-related data from over 1000 stations; of these stations, 112 have recorded data from before 1900.²

Most national data centres now provide displays of near real-time sea levels from their networks of gauges and may also offer delayed-mode data and other sea-level products (tidal constants, extreme sea-level estimates etc.). Some centres will charge for such data and information while others will provide data freely. A

list of national centres can be found on the [PSMSL](#) website [19].

An interesting and productive approach to documenting long-term sea-level trends involves locating and digitising old records of sea level, data archaeology, for comparison with recent measurements, especially where old benchmarks can be located [12, 20]. Old data of this kind are fairly common in many national hydrographic archives, data centre depositories, and even within individual ports (see [Figure 2.13](#)). Invariably, digitising these old records is a slow process, but valuable evidence for long-term MSL changes can be built up in this way [12].

² The longest record held, which is from Brest, France, begins in 1806.

References

1. IOC, 2006. *Manual on Sea-Level Measurement and Interpretation. Volume 4: An Update to 2006.* (eds. T. Aarup, M. Merrifield, B. Perez, I. Vassie and P. Woodworth). Intergovernmental Oceanographic Commission Manuals and Guides No. 14. Paris: UNESCO/Intergovernmental Oceanographic Commission. Note that Volumes I–III (Vol. 1, 1985; Vol. 2, 1994; Vol. 3, 2001) are still useful and provide extensive information for people intending to install and operate tide gauges. All are available from www.psmsl.org.
2. U.S. Department of Commerce. 2001. *Tidal Datums and Their Applications*. NOAA Special Publication NOS CO-OPS 1. Washington, D.C.: U.S. Department of Commerce, National Oceanic and Atmospheric Administration, National Ocean Service. Available from http://tidesandcurrents.noaa.gov/publications/tidal_datums_and_their_applications.pdf.
3. (1) Joseph, A. 2011. *Tsunamis: Detection, Monitoring and Early-Warning Technologies*. Burlington, MA: Academic Press. (2) Forrester, W. D. 1983. *Canadian Tidal Manual*. Ottawa: Department of Fisheries and Oceans Canada. Available from www.psmsl.org/train_and_info/.
4. Miguez, B., Testut, L. and Wöppelmann, G. 2008. The Van de Casteele test revisited: an efficient approach to tide gauge error characterization. *Journal of Atmospheric and Oceanic Technology*, **25**, 1238–1244, doi:10.1175/2007JTECHO554.1.
5. Herschel, J. F. W. (ed.) 1849. *A Manual of Scientific Enquiry; Prepared For the Use of Her Majesty's Navy; And Travellers in General*. London: John Murray.
6. Cartwright, D. E. 1999. *Tides: A Scientific History*. Cambridge: Cambridge University Press.
7. Palmer, H. R. 1831. Description of graphical register of tides and winds. *Philosophical Transactions of the Royal Society of London*, **121**, 209–213, doi:10.1098/rstl.1831.0013.
8. Bunt, T. G. 1838. Description of a new tide-gauge, constructed by Mr. T.G. Bunt, and erected on the eastern bank of the River Avon, in front of the Hotwell House, Bristol, 1837. *Philosophical Transactions of the Royal Society of London*, **128**, 249–251, doi:10.1098/rstl.1838.0012.
9. Lennon, G. W. 1971. Sea level instrumentation, its limitations and the optimisation of the performance of conventional gauges in Great Britain. *International Hydrographic Review*, **48**, 129–147.
10. Pugh, D. T. 1972. The physics of pneumatic tide gauges. *International Hydrographic Review*, **49**, 71–97.
11. Woodworth, P. L., Vassie, J. M., Spencer, R. and Smith, D. E. 1996. Precise datum control for pressure tide gauges. *Marine Geodesy*, **19**, 1–20.
12. Woodworth, P. L., Pugh, D. T. and Bingley, R. M. 2010. Long term and recent changes in sea level in the Falkland Islands. *Journal of Geophysical Research*, **115**, C09025, doi:10.1029/2010JC006113.
13. Spencer, R., Foden, P. R., McGarry, C. *et al.* 1993. The ACCLAIM programme in the South Atlantic and Southern Oceans. *International Hydrographic Review*, **70**, 7–21.
14. Thomson, R., Fine, I., Rabinovich, A. *et al.* 2011. Observation of the 2009 Samoa tsunami by the NEPTUNE-Canada cabled observatory: Test data for an operational regional tsunami forecast model. *Geophysical Research Letters*, **38**, L11701, doi:10.1029/2011GL046728.
15. <http://www.psmsl.org/manuals/>.
16. <http://www.sonel.org/Les-filtres-pour-le-calcul-des.html>.
17. Pugh, D. T. 1987. *Tides, Surges and Mean Sea Level*. Chichester: Wiley. **18**. <http://uhslc.soest.hawaii.edu/>.
19. (1) Woodworth, P. L. and Player, R. 2003. The Permanent Service for Mean Sea Level: an update to the 21st century. *Journal of Coastal Research*, **19**, 287–295. (2) www.psmsl.org. (3) Holgate, S. J., Matthews, A., Woodworth, P. L. *et al.* 2013. New data systems and products at the Permanent Service for Mean Sea Level. *Journal of Coastal Research*, **29**, 493–504, doi:10.2112/JCOASTRES-D-12-00175.1.
20. Hunter, J., Coleman, R. and Pugh, D. T. 2003. The sea level at Port Arthur, Tasmania from 1841 to the present. *Geophysical Research Letters*, **30**, 1401, doi:10.1029/2002GL016813.

Tidal forces

Nature is relentless and unchangeable, and it is indifferent as to whether its hidden reasons and actions are understandable to man or not.

Galileo Galilei

The essential elements of a physical understanding of tide and surge dynamics are contained in Newton's laws of motion and in the need to conserve mass. Newton's first law asserts that a body, which for our purposes can be an element of seawater, continues at a uniform speed in a straight line unless acted upon by a force. The second law relates the rate of change of motion, or momentum, to the magnitude of the imposed force:

$$\text{Acceleration} = \frac{\text{Force}}{\text{Mass}}$$

with the acceleration taking place in the direction of the force.

For this law to be valid, motion, for example in a straight line, must be observed in an external system of space coordinates, not on a rotating Earth. It therefore follows that motion which appears to be in a straight line to an observer on a rotating Earth but which follows a curved path when observed from space can only be produced by an additional terrestrial force, though this force may not be immediately apparent.

In the [first chapter](#) we distinguished different types of physical forces ([Figure 1.7](#)), and the different movements of the seas that they produce. The tidal forces, due to the gravitational attraction of the Moon and Sun, are the most regular and most precisely defined in the whole field of geophysics (but see the box later in this chapter on geological period changes). Like the tidal motions that they produce, they are coherent on a global scale. In contrast, the meteorological forces due to atmospheric pressures and to winds are no more predictable than the weather itself, and their influence during any particular storm is limited to a more local area.

This chapter develops the basic equations for tidal forces. [Appendix A](#) summarises how all the forces acting on the sea can be incorporated into hydrodynamic equations derived from Newton's second law; together with what can be called the principle of conservation of mass, these provide a physical and mathematical basis for the analyses in the chapters that follow.

Readers who do not require a more elaborate mathematical development should read [Section 3.1](#) which outlines the basic principles of tidal forces, [Section 3.4](#) which discusses the astronomical reasons for observed tidal patterns, and perhaps scan [Section 3.3](#) on the more detailed movements of the Moon–Earth–Sun system; they may omit [Section 3.2](#) which deals with potential theory. General descriptions are given in earlier texts [1, 2].

3.1 Gravitational attraction

Newton's law of gravitation states that any particle of mass m_1 attracts another particle of mass m_2 with a force that depends on the product of the two masses and the inverse of the square of their distance apart, r :

$$\text{Force} = G \frac{m_2 m_1}{r^2} \quad (3.1)$$

where G is the universal gravitational constant whose value depends only on the chosen units of mass, length and force. Although this law does not hold strictly for very accurate work where relativistic effects become important, it is more than adequate for all tidal computations. G has units $\text{M}^{-1}\text{L}^3\text{T}^{-2}$, and a numerical value of $6.67 \times 10^{-11} \text{ N m}^2 \text{ kg}^{-2}$ in MKS units.

Table 3.1 The basic astronomical constants of the Moon–Earth–Sun system, which control the tidal forces and amplitudes. For tidal analyses, accuracy to three decimal places is sufficient.

	Value	Units	Symbol
Moon			
Mass	7.35×10^{22}	kg	m_l
Mean radius	1737.5	km	
Mean distance from Earth	$384,400 = 60.3$	km Earth radii	\bar{R}_l
Orbital eccentricity	0.0549		e_l
Earth			
Mass	$5.9722 \times 10^{24} = 81.3$	kg lunar masses	m_e
Equatorial radius	6378.137	km	a
Mean distance from the Sun	$149,600,000 = 23,460$	km Earth radii	\bar{R}_s
Mean distance from Earth's centre to Earth–Moon mass centre	4671	km	
Orbital eccentricity	0.0167		e_e
Sun			
Mass	$1.9884 \times 10^{30} = 332,964$	kg Earth masses	m_s
Radius	695,500	km	

The total gravitational attraction between two large masses such as the Earth and the Moon is the vector sum of forces between the innumerable pairs of particles that constitute the two bodies. Fortunately, the total forces can be calculated by assuming that for each body the total mass is concentrated at a single point, which for a sphere is at its centre (Gauss's law of gravitation). The net force of attraction between the Earth and Moon:

$$\text{Force} = G \frac{m_e m_l}{R_l^2}$$

where R_l is the distance between the two mass centres and m_e and m_l are the total masses of the Earth and Moon. Table 3.1 summarises the several physical constants of the Moon–Earth–Sun system (updated to 2009 [3]). The scales and distances are hard to appreciate. In relative terms, if the Moon is represented by a table-tennis ball, the Earth may be represented by a sphere with the same radius as a table-tennis bat 4 m distant, and the Sun may be represented by a sphere of 15 m diameter some 2 km away.

Consider for the moment only the Moon–Earth system. The two bodies will revolve about their common *centre of mass*, as shown for two point masses in

Figure 3.1, with a period called the *sidereal period*. The centre of mass of the Moon–Earth system actually lies within the Earth, because the Earth is 81 times more massive than the Moon. However, to make things clearer, the relative scales in the diagrams that follow have been distorted. Both masses continue to move about their common centre of mass, the necessary acceleration of each body towards this centre of revolution being produced by their mutual attraction. The

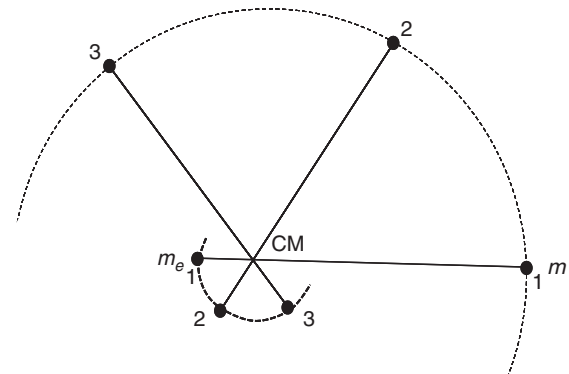


Figure 3.1 Part of the orbits of the Earth and Moon about their common centre of mass.

sidereal period for the Moon–Earth system is 27.32 days, defined as one sidereal month.

As the two bodies rotate in the system, each individual element of each body moves in a circle, which has the same radius as the circle described by its centre of mass. The motion is illustrated in Figure 3.2, where the different parts of the hand travel in sequence 1 to 4 around the centre of mass in circles that have the same radius. It is necessary to remember that in this argument we are not considering, at the moment, the rotations of the bodies about their own axes; the important influence of this rotation on the generation of tides will be introduced later. The fact that all particles describe circles of the same radius is not trivial, nor is it immediately obvious.

As already indicated, for the Earth, Figure 3.1 is slightly misleading because the revolution is shown about a point outside the Earth, whereas the actual motion is about an axis that passes through the sphere at a distance of 4671 km from the centre; however, the principle of equal circles of revolution for all the particles still applies. The force necessary to give each particle of the Earth the acceleration to perform this

revolution is the same as for the particle at the centre of the Earth: for such a particle the gravitational force provides this necessary acceleration. For those particles nearer the Moon than the centre particle, the gravitational attraction is greater than that necessary to maintain the orbit. For those further away the forces are weaker. The differences between the forces necessary for the orbit and the forces actually experienced generate the tides on the surface of the Earth.

We can now look at what this means in more detail. Consider a particle of mass m located at P_1 on the Earth's surface, as shown in Figure 3.3. From Equation 3.1 the force towards the Moon is:

$$G \frac{mm_1}{(R_l - a)^2}$$

where, as the force necessary for its rotation is the same as for a particle at O:

$$G \frac{mm_1}{R_l^2}$$

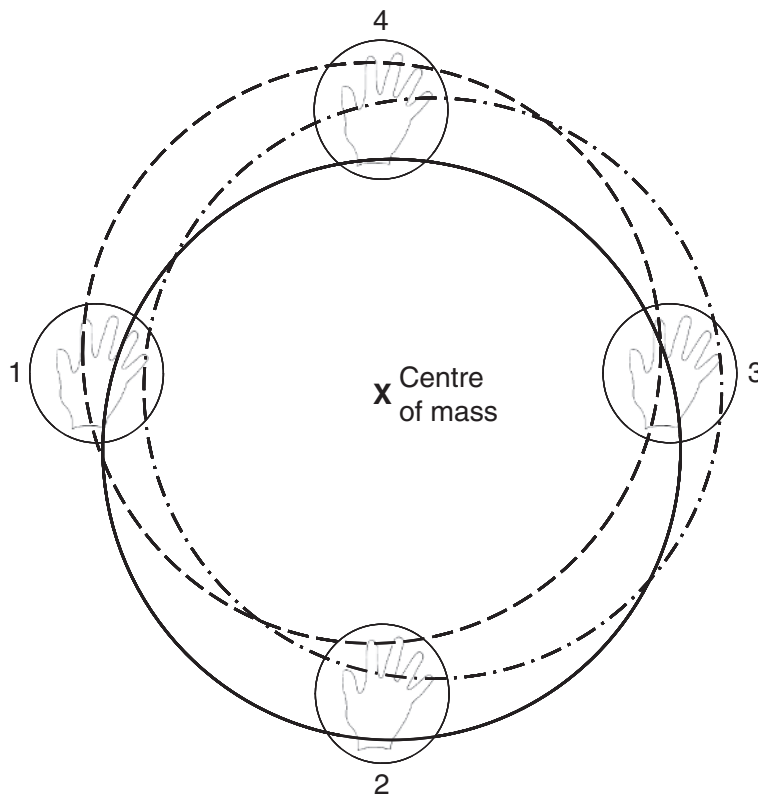


Figure 3.2 The Earth circles about the centre of mass of the Earth–Moon system, without any rotation in absolute space. Each element of the Earth travels around in circles that have the same radius.

The difference between these is the tide-producing force at P_1 :

$$G \frac{mm_1}{R_l^2} \left[\frac{1}{\left(1 - \frac{a}{R_l}\right)^2} - 1 \right]$$

The term within the brackets can be expanded, making use of the approximations:

$$\left[\frac{a}{R_l}\right]^2 \ll 1 \quad \text{since} \quad \frac{a}{R_l} \approx \frac{1}{60}$$

and expanding the expression $[1/(1-\alpha)^2] \approx (1+2\alpha)$ for small α to give a net force towards the Moon of:

$$\text{Tidal force at } P_1 \quad \frac{2Gmm_1a}{R_l^3} \quad (3.2)$$

Similar calculations for a particle at P_2 show that gravitational attraction there is too weak to supply the necessary acceleration for the orbit. There is a net force away from the Moon:

$$\text{Tidal force at } P_2 \quad -\frac{2Gmm_1a}{R_l^3}$$

The net force at P_3 is directed towards the Earth centre.

By making use of the approximation $\sin(\theta) = \frac{a}{R_l}$, the force along P_3M is:

$$\frac{Gmm_1}{R_l^2}$$

and the component of this force towards O is:

$$\frac{Gmm_1a}{R_l^3} \quad (3.3)$$

The net effect is for particles at both P_1 and P_2 to be displaced away from the centre of the Earth, whereas particles at P_3 are displaced towards the centre. This results in an equilibrium shape (assuming static conditions) for a fluid Earth that has opposing bulges,

lined up on a line between the centres of the Moon and the Earth.

If we consider [Figure 3.3](#) to show an equatorial section of the Earth (looking down on the North Pole), and now introduce the rotation of the Earth on its own axis (rotation about O), each point on the circumference will pass through two maximum and two minimum levels for each daily rotation. This results in two tides a day, the semidiurnal tides.

The diurnal tides are generated because, except for the special case of the Moon in the equatorial plane shown in [Figure 3.3](#), the maxima and minima in each daily rotation are unequal in amplitude. This asymmetry is illustrated later in discussion of [Figure 3.12](#).

These simple arguments have shown that the tide-producing forces depend on the finite radius of the Earth a , the mass of the Moon m_1 , and on the inverse cube of the distance R_l .

We can simplify [Equation 3.2](#) by substituting for G , the universal gravitational constant. The gravitational force on a particle of mass m on the Earth's surface is given by [Equation 3.1](#):

$$mg = \frac{Gmm_e}{a^2} \quad (3.4)$$

so the tidal force at P_1 may be written:

$$2mg \left(\frac{m_1}{m_e}\right) \left(\frac{a}{R_l}\right)^3 \quad (3.5)$$

From the values in [Table 3.1](#), the acceleration is approximately:

$$2g \left(\frac{1}{81.3}\right) \left(\frac{1}{60.3}\right)^3 = 11.2 \times 10^{-8}g$$

so that the value of g is very slightly reduced at P_1 and P_2 . A person weighing 100 kg would weigh 11.2 mg less when passing through P_1 than P_2 .

In the same way that we have calculated the tidal forces due to the Moon, the tidal forces due to the Sun

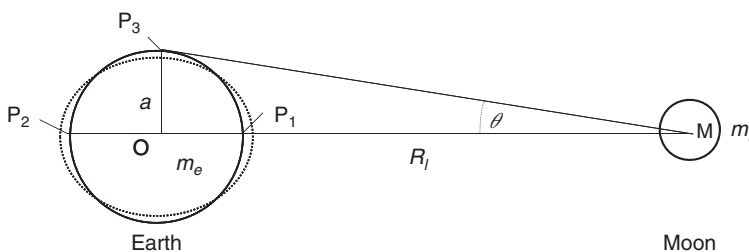


Figure 3.3 Diagram to show positions in the Earth–Moon system that are used to derive the tidal forces. The separation is distorted but the relative diameters of the Earth and Moon are to scale.

are calculated by replacing m_l and R_l by m_s and R_s in Equation 3.5. The acceleration is:

$$2g(332946)\left(\frac{1}{23460}\right)^3 = 5.2 \times 10^{-8}g$$

The solar tidal forces are a factor of 0.46 weaker than the lunar tidal forces on the Earth. The much greater solar mass is more than offset by its greater distance from the Earth.

The other planets in the Solar System produce negligible tidal forces. Venus has a mass $0.82m_e$ and a nearest approach to the Earth (called *opposition*) of approximately 38 million km; this is approximately 6000 Earth radii, which gives a maximum tidal acceleration of:

$$2g(0.82)\left(\frac{1}{6000}\right)^3 = 7.5 \times 10^{-12}g$$

which is only 0.000 067 of the Moon's tidal acceleration. Jupiter, whose mass is $318m_e$ has maximum accelerations that are an order of magnitude less than those of Venus (0.000 006) because of Jupiter's greater distance from the Earth. Mars (0.000 001), Mercury (0.000 0003) and Saturn (0.000 0002) have even smaller effects.

Of course tides are not only a terrestrial phenomenon. They are experienced on other celestial bodies. The role of tides in the development of the dynamics of the Moon–Earth system is discussed later in this chapter.

Box 3.1 Planetary tides

The tidal effects of the Earth on the Moon produce a small elongation along the Earth–Moon axis, but because the Moon always presents the same face to the Earth, there are no tides on the Moon equivalent to the diurnal and semidiurnal tides on Earth. Some flexing of the solid Moon occurs as the Earth–Moon distance changes in its elliptical orbit. There are also small changes due to a slight rocking motion in longitude in the lunar orbit, called lunar librations.

The satellites of Jupiter suffer much more dramatic tidal effects. Io has a similar mass to our Moon and its orbital distance from Jupiter is almost the same as our Moon is from the Earth. However, because Jupiter has such an enormous mass, the Equilibrium Tides on the solid surface of Io can be up to 100 m high. The regular flexing, every 42 hours, heats the interior of Io, energising several active

volcanoes. Europa, also a satellite of Jupiter, has weaker tides and a thick covering of ice. Cracks as long as 1500 km in the ice surface may be due to tidal stresses and the orbits of the other satellites. If, as many scientists suspect, there is a thick layer of melted water below its ice cover, then the tides on Europa may be the nearest equivalent in the Solar System to our own ocean tides.

3.2 The tidal forces: a fuller development

3.2.1 Potential fields

A more general development of the tidal forces than that outlined in Section 3.1 makes use of the concept of the gravitational potential of a body: gravitational potential is the work that must be done against the force of attraction to remove a particle of unit mass to an infinite distance from the body. The potential at P on the Earth's surface in Figure 3.4 due to the Moon is:

$$\Omega_p = -\frac{Gm_l}{\text{distance}(MP)} \quad (3.6)$$

The angle between the sub-lunar point and P is called the lunar angle, ϕ .

Our definition of gravitational potential, involving a negative sign, is the one normally adopted in physics, but there is an alternative convention often used in geodesy, which treats the potential in Equation 3.6 as positive. The advantage of the geodetic convention is that an increase in potential on the surface of the Earth will result in an increase of the level of a free water surface. Potential has units of $L^2 T^{-2}$. The advantage of working with gravitational potential is that it is a scalar property, which allows simpler mathematical manipulation. In particular, the gravitational force on a particle of unit mass is given by $\nabla\Omega_p$, the gradient operator acting on Ω_p .

Conceptually it is possible to consider by analogy the potential energy of a ball on a mountain slope. The potential energy depends on the height of the ball up the mountain, but the accelerating force on the ball forcing it down the slope depends on the steepness of the slope, and is zero if the ball is sitting on a level plateau.

Applying the cosine law to the triangle defined by OPM in Figure 3.4:

$$MP^2 = a^2 + R_l^2 - 2aR_l \cos \phi$$

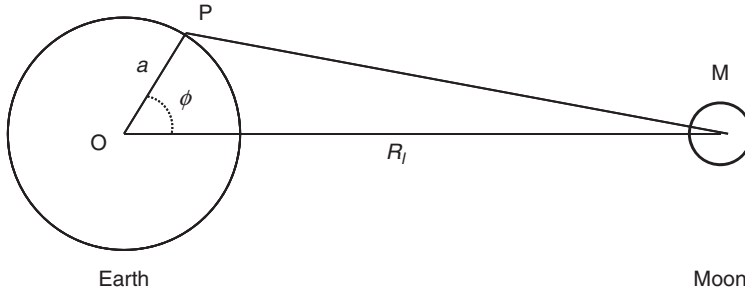


Figure 3.4 Diagram to show the location of the point P on the Earth's surface.

we have:

$$\Omega_p = -\frac{Gm_l}{R_l} \left[1 - 2\frac{a}{R_l} \cos \phi + \frac{a^2}{R_l^2} \right]^{-\frac{1}{2}}$$

which may be expanded as a series of Legendre polynomials:

$$\left[1 + \frac{a}{R_l} P_1(\cos \phi) + \frac{a^2}{R_l^2} P_2(\cos \phi) + \frac{a^3}{R_l^3} P_3(\cos \phi) + \dots \right] \quad (3.7)$$

The terms $P_1(\cos \phi)$ etc. are Legendre polynomials:

$$P_1(\cos \phi) = \cos \phi$$

$$P_2(\cos \phi) = \frac{1}{2}(3 \cos^2 \phi - 1)$$

$$P_3(\cos \phi) = \frac{1}{2}(5 \cos^3 \phi - 3 \cos \phi)$$

The tidal forces represented by the terms in this potential are calculated from their spatial gradients $-\nabla(P_n)$. The first term in Equation 3.7 is constant (except for variations in R_l) and so produces no force. The second term produces a uniform force parallel to OM because differentiating with respect to $(a \cos \phi)$, the projected vector along OM, yields a gradient of potential:

$$-\frac{\partial \Omega_p}{\partial (a \cos \phi)} = -\frac{Gm_l}{R_l^2}$$

This is the force necessary to produce the acceleration in the Earth's orbit towards the centre of mass of the Moon–Earth system. **The third term is the major tide-producing term.** For most purposes the fourth term may be neglected because $\frac{a}{R_l} \approx \frac{1}{60}$. So too may all the higher terms. The effective tide-generating potential is therefore written as:

$$\Omega_p = -\frac{1}{2} Gm_l \frac{a^2}{R_l^3} (3 \cos^2 \phi - 1) \quad (3.8)$$

The force on the unit mass at P corresponding to the potential may be resolved with two components:

$$\text{Vertically upwards: } -\frac{\partial \Omega_p}{\partial a} = -2g\Lambda_l \left(\cos^2 \phi - \frac{1}{3} \right) \quad (3.9)$$

Horizontally in the direction of increasing

$$\phi: -\frac{\partial \Omega_p}{a \partial \phi} = -g\Lambda_l \sin 2\phi$$

$$\text{where } \Lambda_l = \frac{3}{2} \frac{m_l}{m_e} \left(\frac{a}{R_l} \right)^3$$

and Equation 3.4 is used to substitute for G after evaluating the gradients of potential. Λ_l is very small (8.4×10^{-8}) so that compared with the forces due to the Earth's gravity, these tidal forces are also very small. They vary slowly as R_l varies. The vertical forces, shown in Figure 3.5a, produce small changes in the weight of a body, as previously discussed, but it is the small horizontal forces that produce the tidal accelerations necessary to produce the water movements. Figure 3.5b shows the distribution of these horizontal tractive forces on the surface of the Earth.

The tractive forces over the Earth's surface vary as the Earth rotates and as the Moon moves in its orbit. It is possible to regard these variations as due to small periodic rotary tilting of the Earth's horizontal plane at each point on the surface.

The lunar angle ϕ must be expressed in suitable astronomical variables. These are chosen to be the declination of the Moon north of the equator d_l , the north latitude of P, ϕ_p , and the hour angle of the Moon, which is the difference in longitude between the meridian of P and the meridian of the sub-lunar point V, as shown in Figure 3.6 (see also Section 3.3.4).

The angle ϕ is related to the other angles shown in Figure 3.6 by a standard formula in spherical trigonometry [4]:

$$\cos \phi = \sin \phi_p \sin d_l + \cos \phi_p \cos d_l \cos C_p$$

(a)

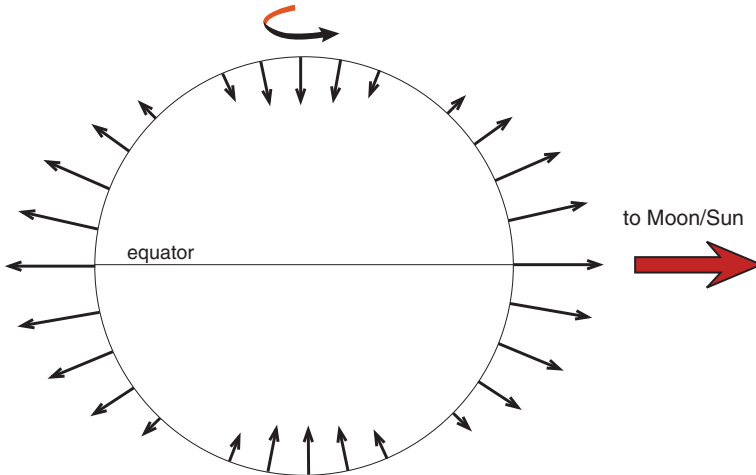


Figure 3.5 The distribution of the horizontal tidal tractive forces on the Earth's surface.

(b)

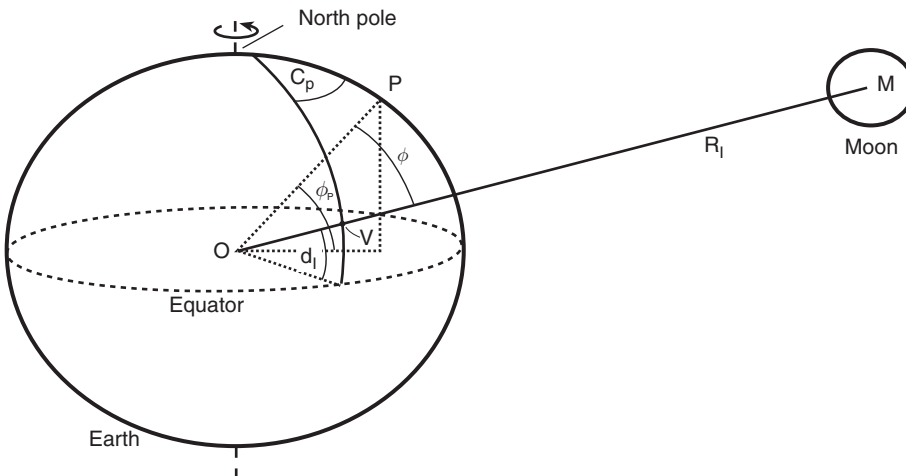
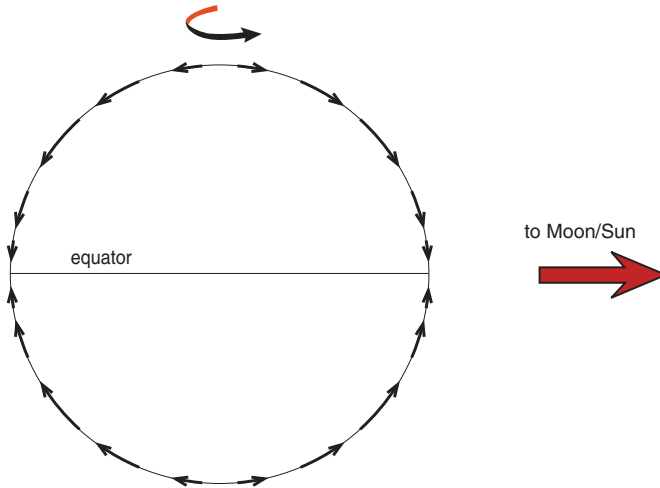


Figure 3.6 The three-dimensional location of a point P on the Earth's surface relative to the sub-lunar position. The angle is ϕ . This is a difficult diagram to convert into three dimensions, but it helps to recall that V is on the surface of the Earth and on the line O to M.

Substituting for $\cos \phi$ in Equation 3.8, with some further rearrangement, eventually yields:

$$-\Omega = \frac{3}{2} ag \frac{m_l}{m_e} \left(\frac{a}{R_l}\right)^3 \left[\begin{aligned} &\frac{3}{2} \left(\sin^2 d_l - \frac{1}{3}\right) \left(\sin^2 \phi_p - \frac{1}{3}\right) \\ &+ \frac{1}{2} \sin 2d_l \sin 2\phi_p \cos C_p \\ &+ \frac{1}{2} \cos^2 d_l \cos^2 \phi_p \cos 2C_p \end{aligned} \right] \quad (3.10)$$

As before, d_l is the lunar declination, ϕ_p is the latitude of P, and C_p is the hour angle of P.

From this formula, it is usual to compute an expression for the *Equilibrium Tide*. The Equilibrium Tide is defined as the elevation of the sea surface that would be in equilibrium with the tidal forces if the Earth were covered with water to such a depth that the response of the water is instantaneous. The Equilibrium Tide bears no spatial resemblance to the real observed ocean tide, but its development is an essential part of these discussions because it serves as an important reference system for tidal analysis.

3.2.2 The Equilibrium Tide

In the Equilibrium theory of tides, the free surface, here denoted by $\bar{\zeta}$, is assumed to be a level surface under the combined action of the Earth's gravity and the tidal disturbing force. Strictly, we should adjust the Earth's gravity for the centrifugal effects of its rotation, and consider apparent gravity, but the difference is not important here.

The tractive tide-generating forces may be regarded as causing a deflection of the vertical, as shown in Figure 3.7. Over a tidal cycle this tilting performs a rotation about the vertical. This is the same as a slight rotational tilting of the horizontal plane. This force is $-\left(\frac{\partial \Omega}{\partial x}\right)$ where x is a direction at right angles to the direction of undisturbed gravity.

Considering the magnitude of the forces, with α as defined in Figure 3.7:

$$\tan \alpha = -\left(\frac{\partial \Omega_p}{\partial x}\right)/g$$

and also:

$$\tan \alpha = \left(\frac{\partial \bar{\zeta}}{\partial x}\right)$$

so that:

$$g \left(\frac{\partial \bar{\zeta}}{\partial x}\right) + \left(\frac{\partial \Omega_p}{\partial x}\right) = 0 \text{ or } \frac{\partial}{\partial x} (g\bar{\zeta} + \Omega_p) = 0$$

and similarly:

$$\frac{\partial}{\partial x} (g\bar{\zeta} + \Omega_p) = 0$$

Integrating over a finite area gives:

$$g\bar{\zeta} + \Omega_p = \text{constant} \quad (3.11)$$

If the integral is taken over the whole area of the ocean surface so that the total volume of water is conserved,

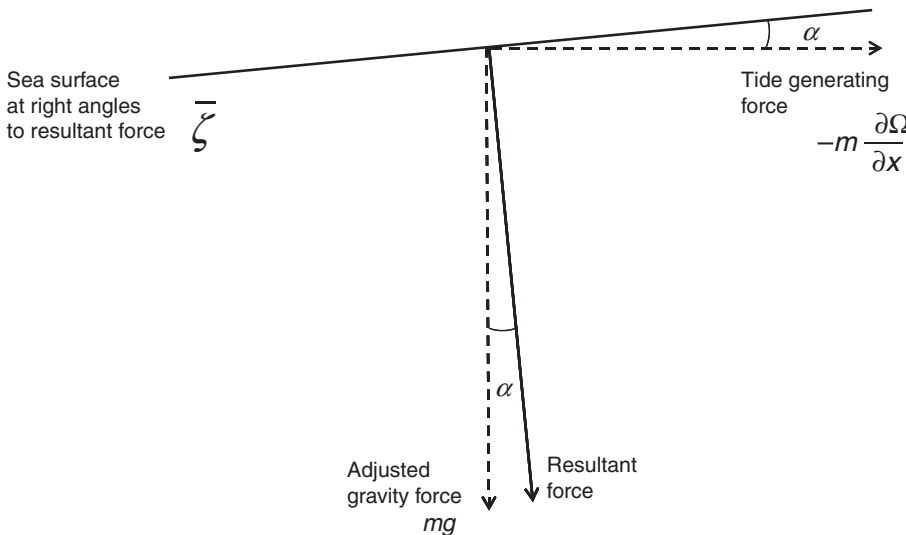


Figure 3.7 The relationship between the Equilibrium water surface, the tide-generating force, and the normal Earth's gravity force.

then the constant is zero. Applying this condition to Equation 3.10 the Equilibrium Tide becomes:

$$\bar{\zeta} = a \frac{m_l}{m_e} \left[C_0(t) \left(\frac{3}{2} \sin^2 \phi_p - \frac{1}{2} \right) + C_1(t) \sin 2\phi_p + C_2(t) \cos^2 \phi_p \right]$$

where the time dependent coefficients are:

$$\begin{aligned} C_0(t) &= \left(\frac{a}{R_l} \right)^3 \left(\frac{3}{2} \sin^2 d_l - \frac{1}{2} \right) \\ C_1(t) &= \left(\frac{a}{R_l} \right)^3 \left(\frac{3}{4} \cos^2 d_l \cos C_p \right) \\ C_2(t) &= \left(\frac{a}{R_l} \right)^3 \left(\frac{3}{4} \sin 2d_l \cos 2C_p \right) \end{aligned} \quad (3.12)$$

These three coefficients characterise the three main species of tides:

- the long period species,
- the diurnal species at a frequency of one cycle per day ($\cos C_p$) and
- the semidiurnal species at two cycles per day ($\cos 2C_p$).

The magnitudes of all three species are modulated by a common term, which varies inversely as the cube of the lunar distance R_l .

- The long-period tidal species is also produced because of the monthly variations in lunar declination d_l . It has maximum amplitude at the poles and zero amplitude at latitudes $35^\circ 16'$, north and south of the equator (see Chapter 10).
- The diurnal species is modulated at twice the frequency with which the lunar declination varies and it has a maximum amplitude when the declination is a maximum. Spatially it has maximum amplitude at 45° latitude and zero amplitude at the equator and the poles. The variations north and south of the equator are in opposite phase.
- The semidiurnal species is also modulated at twice the frequency of the lunar declination, but is a maximum when the declination is zero. It has maximum amplitude at the equator and zero amplitude at the poles.

The amplitudes of the Equilibrium Tides are small. For the semidiurnal tide at the equator when the declination is zero the amplitude calculated using the values in Table 3.1 is 0.27 m. However, the observed ocean tides are normally much larger than the Equilibrium Tide because of the dynamic response of the ocean to the tidal forces, as discussed in Chapter 5,

but the observed tides have their energy at the same frequencies as the Equilibrium Tide. The importance of the Equilibrium Tide is in its use as a reference to which the observed ocean phases and amplitudes of harmonic tidal constituents can be related, when preparing models for tidal prediction as described in Chapter 4. It also gives an indication of the important harmonic constituents to be included in a correct tidal analysis model.

The Equilibrium Tide due to the Sun is expressed in a form analogous to Equation 3.12 with m_l , R_l and d_l replaced by m_s , R_s and d_s . The resulting amplitudes are smaller by a factor of 0.46 than those of the lunar tides, but the essential details are the same.

3.3 The Moon–Earth–Sun system

In order to calculate the total Equilibrium Tide on the Earth as a reference for tidal analysis it is necessary to define the change with time of the coordinates of the Moon and Sun, which are used as a reference for tidal analyses. The full relative movements of the three bodies in three dimensions are very complicated and their elaboration is beyond the scope of this account [5]. However, there are several obvious features that we may consider. We begin by recognising that there are two alternative reference systems that may be used to define the astronomical coordinates.

The most natural reference system for a terrestrial observer is the equatorial system, in which declinations are measured north and south of a plane that cuts the Earth's equator. Angular distances around the plane are measured relative to a point on this celestial equator, which is fixed with respect to the stellar background. The point chosen is for this system is the vernal equinox, also called the 'First Point of Aries', which is represented by the symbol Υ . The angle, measured eastwards, between Υ and the equatorial intersection of the meridian through a celestial object is called the Right Ascension of the object. The declination and the Right Ascension together define the position of the object on the celestial background. In fact, the vernal equinox is not absolutely fixed with respect to the stars, but moves slowly against the stellar background with a period of 26,000 years, a movement called the precession of the equinoxes.

The second system uses the plane of the Earth's revolution around the Sun as a reference. The celestial extension of this plane, which is traced by the Sun's annual apparent movement, is called the ecliptic. Conveniently, the point on this plane that is chosen

for a zero reference is also the vernal equinox Υ , at which the Sun crosses the equatorial plane from south to north, near 21 March each year. Celestial objects are located by their ecliptic latitude and ecliptic longitude. The angle between the two planes, of $23^\circ 27'$, is called the obliquity of the ecliptic, and is usually represented as ϵ . Figure 3.8 shows the relationship between these two coordinate systems.

3.3.1 Elliptical motion, satellites

In Section 3.1, for simplicity, we considered bodies moving in circular orbits, but more generally Newton showed from his law of gravitation that two masses orbiting in space under the sole influence of their mutual attraction travel in ellipses. Each mass moves in its own ellipse, and each ellipse has the centre of mass of the two bodies as a focus. This is Kepler's first law of planetary motion, which he derived from observations.

In Figure 3.9 the mass at C is travelling in orbit around a mass at A in an ellipse, which has foci at A and B. The geometry of an ellipse is defined by $AC + CB = \text{constant}$. The distance of the mass from the focus at A is a maximum when the mass is at C_A and a minimum when the mass is at C_P . These positions are called the apogee and perigee of the orbit. The ratio OA/OC_A is called the eccentricity, e , of the ellipse. For a circular orbit A and B coincide at O, and the eccentricity is zero. Orbits that are very narrow and

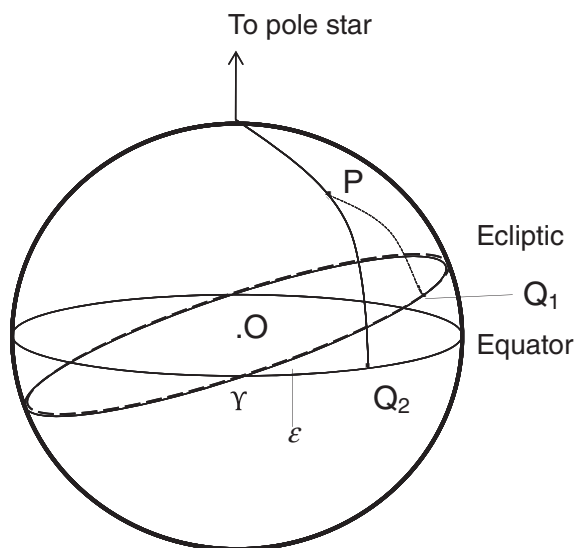


Figure 3.8 The relationship between equatorial and ecliptic coordinates. Υ is the Vernal Equinox, the 'First Point of Aries'; ϵ is the obliquity of the ecliptic.

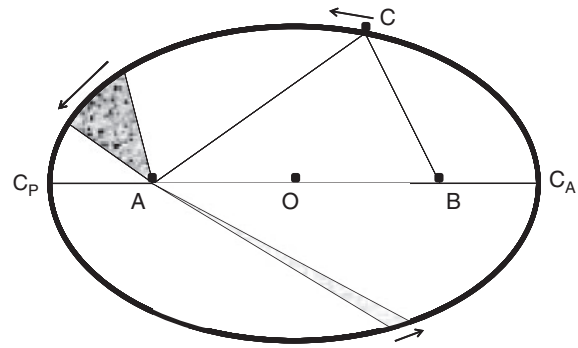


Figure 3.9 The properties of ellipses and elliptical orbits.

elongated have an eccentricity close to unity. The ratio between the separation of the masses at the apogee and perigee is:

$$\frac{AC_A}{AC_P} = \frac{OC_A(1+e)}{OC_P(1-e)} = \frac{(1+e)}{(1-e)} \quad (3.13)$$

The distance $OC_A = OC_P$ is called the semi-major axis.

Kepler's second law states that the radius vector AC sweeps out equal areas in equal times. This is shown in Figure 3.9 where the two shaded segments have equal areas. This means that for an observer at A the planet will have its maximum angular speed at the point of nearest approach, C_A , and its minimum angular speed at apogee, C_P .

Kepler's third law relates the period of a complete orbit to the semi-major axis of the ellipse. From the law of gravitation, this period for a revolution may be derived theoretically:

$$(\text{period})^2 = 4\pi^2 \frac{r^3}{G(m_1 + m_2)} \quad (3.14)$$

where r is the semi-major axis, and m_1 and m_2 are the masses of the two bodies. The periods for Earth satellite orbits discussed in Chapter 9 may be checked against this formula. In astronomy the orbit described by a body and the position of the body in the orbit can be completely described by six parameters, called orbital elements. The size and shape of the orbit are described by the semi-major axis and the eccentricity. Three parameters are necessary to define the orientation of the orbit with respect to a coordinate system. For example, the plane of the ecliptic in Figure 3.8 is defined relative to the equatorial plane by the orientation of their line of intersection OY and by the obliquity ϵ . Obliquity is the angle between the orbital plane and the equatorial plane of the Earth. For an ellipse it is

also necessary to define the direction of perigee in the plane of the orbit. The sixth element of the motion in an ellipse is the time of passage of the orbiting body through perigee.

3.3.2 The Earth–Sun system

The Equilibrium Tide in Equation 3.12 is expressed in terms of the distance, declination and hour angle of the tide-producing body. We need values for R_s , d_s and C_s . These three parameters are easier to define for the Earth–Sun system than for the Moon–Earth system because the solar motions are always in the plane of the ecliptic, which means that the declination in ecliptic coordinates is always zero. The eccentricity of the Earth’s orbit about the Sun is 0.0168.

From orbital theory the solar distance, R_s , may be shown to be given approximately by:

$$\frac{\bar{R}_s}{R_s} = (1 + e \cos(h - p')) \quad (3.15)$$

where \bar{R}_s is the mean solar distance, h is the Sun’s geocentric mean ecliptic longitude (which increases by $\sigma = 0.0411^\circ$ per mean solar hour), and p' is the longitude of solar perigee, called perihelion, which completes a full cycle in 21,000 years.

The true ecliptic longitude of the Sun increases at a slightly irregular rate through the orbit in accord with Kepler’s second law (Equation 3.13). The true longitude λ_s is given to a first approximation by:

$$\lambda_s = h + 2e \sin(h - p') \quad (3.16)$$

Here, the value of λ_s is expressed in radians to facilitate the development of harmonic expansions discussed in Chapter 4.

The Right Ascension is calculated from the ecliptic longitude and ecliptic latitude. Both the ecliptic longitude and the Right Ascension are zero when the Sun is in the First Point of Aries (Υ) at the vernal equinox, and also at the autumnal equinox. They both have values of $\pi/2$ when the Sun has its maximum declination north of the equator in June, and both have values of $3\pi/2$ when the Sun has its maximum declination south of the equator in December. Between these times there are small regular differences due to the obliquity of the orbit. The effect can be shown [4] to be represented to a first approximation by:

$$A_s = \lambda_s - \tan^2\left(\frac{\varepsilon_s}{2}\right) \sin 2\lambda_s \quad (3.17)$$

where ε_s is the solar ecliptic latitude.

The difference between the Right Ascension of the mean Sun and the Right Ascension of the true Sun (sundial time) at any time is called the Equation of Time. It may be calculated by combining the elliptical and obliquity effects, from Equations 3.16 and 3.17, to give the annual variation plotted in Figure 3.10. During the annual cycle, differences of more than 15 minutes occur between clock time and solar time. The biggest difference is on 3 November when the solar position, shown on a sundial, is 16 minutes, 25 seconds ahead of the clock. Noon coincides with twelve o’clock on four days in the year: 15 April, 13 June, 1 September and 25 December. The cyclical nature of these differences is accounted for in tidal analysis by a series of harmonic terms, as discussed in Chapter 4.

The solar declination in equatorial coordinates is given in terms of the ecliptic longitude of the Sun:

$$\sin d_s = \sin \lambda_s \sin \varepsilon_s$$

This is greatest when $\lambda_s = \pi/2$ and the maximum declination is $\varepsilon_s = 23^\circ 27'$, the angle that defines the Tropic of Cancer. When $\lambda_s = -\pi/2$ the Sun is overhead on the Tropic of Capricorn at the time of its maximum declination $23^\circ 27'$ south of the equator.

3.3.3 The Moon–Earth system

The motions of the Moon are more difficult to define in ecliptic or equatorial coordinates than those of the Sun, because the plane of the motion is inclined at a mean angle of $5^\circ 9'$ to the plane of the ecliptic. Moreover, this plane rotates slowly over a period of 18.61 years. The ascending node, at which the Moon crosses the ecliptic from south to north, moves backwards along the ecliptic at a nearly uniform rate of 0.053° per mean solar day. This regression completes a revolution in 18.61 years. Viewed in equatorial coordinates when the ascending node corresponds to the First Point of Aries (Υ), the Moon’s maximum declination north and south of the equator during the next month will be $(23^\circ 27' + 5^\circ 9') = 28^\circ 36'$; 9.3 years later, when the descending node is at the vernal equinox, the maximum lunar declination is only $(23^\circ 27' - 5^\circ 9') = 18^\circ 18'$. Clearly those terms in the Equilibrium Tide that depend on the lunar declination will have a pronounced 18.61-year modulation.

The eccentricity of the Moon’s orbit has a mean value of 0.0549, more than three times greater than the eccentricity of the Earth–Sun orbit. However, because of the effects of the Sun’s gravitational attraction the lunar obliquity or inclination varies between $4^\circ 58'$ and $5^\circ 19'$,

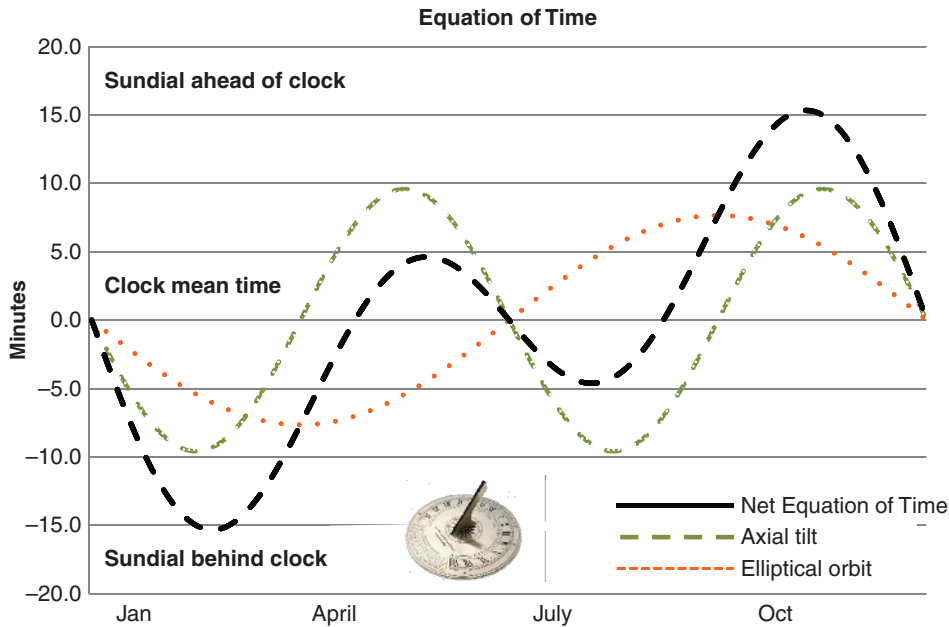


Figure 3.10 The *equation of time*, showing the difference between clock time and solar time, due to the solar Right Ascension being affected by the ellipticity and obliquity (axial tilt) of the Earth's orbit.

and the lunar eccentricity varies from 0.044 to 0.067. The lunar distance R_b , to a first approximation [6] is:

$$\frac{\bar{R}_l}{R_l} = 1 + e \cos(s - p) + \text{solar perturbations} \quad (3.18)$$

where \bar{R} is the mean lunar distance, s is the Moon's geocentric mean ecliptic longitude, which increases by $\sigma_2 = 0.5490^\circ$ per mean solar hour, and p is the longitude of lunar perigee, which rotates with an 8.85 year period. The true ecliptic longitude of the Moon also increases at a slightly irregular rate through the orbit, as does the solar longitude:

$$\lambda_1 = s + 2e \sin(s - p) + \text{solar perturbations} \quad (3.19)$$

where λ_1 is in radians.

The Right Ascension of the Moon is calculated from its ecliptic longitude and ecliptic latitude:

$$A_l = \lambda_l - \tan^2\left(\frac{\epsilon_l}{2}\right) \sin 2\lambda_l$$

Relative to the ecliptic the Moon's latitude is given by:

$$\sin(\text{ecliptic latitude}) = \sin(\lambda_l - N) \sin(5^\circ 9')$$

where λ_l is the ecliptic longitude and N is the mean longitude of the ascending node, which regresses over

an 18.61-year cycle. The lunar declination can be calculated from this ecliptic latitude using similar formulae.

The declination and Right Ascension of the Moon and of the Sun may all be represented as series of harmonics with different amplitudes and angular speeds. The Equilibrium Tide may also represent these astronomical terms as the sum of several harmonics by entering these values into Equation 3.12, as we shall see in Chapter 4.

Box 3.2 Palaeo-tides

There is strong scientific interest in palaeo-tides and understanding how energy losses due to tides might have changed and influenced the evolution of the Earth–Moon system (Section 3.3.3). If the present rate of increase in the Earth–Moon separation of 38 mm/yr were extrapolated backwards, the separation would have been 3800 km smaller 100 million years ago. From Equation 3.10 this reduced separation means an increase in the tidal forces and amplitudes of about 3 per cent. Further extrapolation suggests that the Moon was within a few Earth radii of the Earth between 1000 and 2000 million years ago. The close proximity indicated by these gross extrapolations, called the Gerstenkorn Event, implies enormous

tides and energy losses [7]. The Earth is believed to be at least 4500 million years old.

The geological record gives no indication of such an extreme event at any time in the past. Ancient tides are found in sedimentary rocks: indications include sand waves, longitudinal sandbanks, interleaved sand and mud sheets, and scoured surfaces. These features can be seen in recent sediments and have also been tentatively identified by geologists in sedimentary rocks from as early as 1500 million years; spring-neap modulations are sometimes clearly visible. An alternative palaeo-tidal clock is found in the growth rate of animals, particularly corals, bivalves and stromatolites. These generally show that the number of days in a month and in a year was higher hundreds of millions of years ago when the Earth was rotating more rapidly.

The absence of an extreme Gerstenkorn Event means that the near-resonance semidiurnal responses in the present ocean are not typical of previous ocean and continent configurations [8, 9]. Computer models of previous configurations of continental blocks and mid-ocean ridges suggest that during epochs when the drifting continents are in consolidated masses the semidiurnal tides are reduced relative to the longer-wavelength diurnal tides. Fragmentation of continents tends to favour the semidiurnal oscillations.

From the Late Carboniferous through to the end of the Jurassic period diurnal tides may have been dominant. Thus, over a period from roughly 350 to 100 million years ago losses due to tidal friction opposing the slower diurnal currents may have been significantly less than those in today's predominately semidiurnal regime. Tidal conditions in older continental shelf seas, particularly related to MSL increases since the Last Glacial Maximum, have been speculatively constructed using estimated water depth and basin. A major uncertainty is the way in which the sediments and the tidal basins adjust to different tidal ranges and currents. One interesting area of interaction between geological processes and tidal dynamics is the relationship between basin development and tidal resonance.

3.3.4 Basic astronomical frequencies

The hour angle C_p for the lunar or solar Equilibrium Tide used in Equation 3.10 needs further clarification. Table 3.2 summarises the basic astronomical frequencies involved in the motions of the Moon–Earth–Sun system. The time taken for one complete cycle of the lunar hour angle C_l is called the mean lunar day.

For the Sun, one cycle of C_s is the mean solar day that we use for normal civil activities. Because of the movement of the Moon and Sun, these days are slightly longer than the sidereal day:

$$\text{Mean solar day} \quad \frac{2\pi}{(\omega_s - \omega_3)} \equiv \frac{2\pi}{\omega_0}$$

$$\text{Mean lunar day} \quad \frac{2\pi}{(\omega_s - \omega_2)} \equiv \frac{2\pi}{\omega_1}$$

with the symbols as defined in Table 3.2. Hence we have:

$$\omega_s = \omega_0 + \omega_3$$

$$\omega_s = \omega_1 + \omega_2$$

for the frequency of sidereal Earth rotation. By convention the ω speeds are in units of radians per unit time.

C_p is the angular difference between the terrestrial longitude of the point P and the longitude of the sub-lunar point V. Figure 3.11 shows a projection of the celestial sphere onto the plane of the equator, with the positions P and V as defined in Figure 3.6. All angles are related to the fixed direction of the First Point of Aries, Υ . The lunar hour angle C_l is:

$$C_l = E_1 \hat{O} \Upsilon - E_2 \hat{O} \Upsilon$$

$E_1 \hat{O} \Upsilon$ increases as the Earth rotates on its axis, completing a revolution in absolute space in one sidereal day, 23 hours 56 minutes, with an angular speed ω_s . It is conveniently expressed as:

$$\lambda_p + \beta = \lambda_p + \omega_s t$$

where λ_p is positive east longitude of P, and β is Right Ascension of the Greenwich meridian = $\omega_s t$; here t is

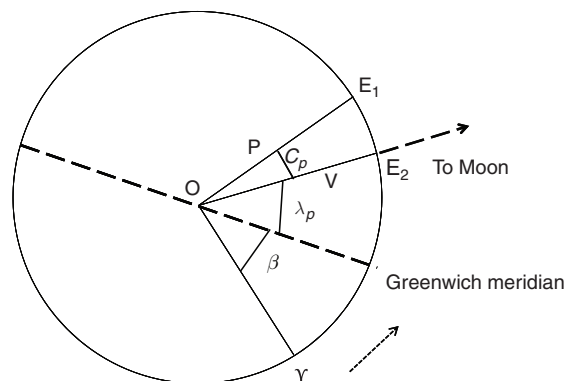


Figure 3.11 Projection of the celestial sphere on the plane of the equator to show the relationship between the hour angle C_p , the movement of the sub-lunar point, and the Earth's rotation.

the sidereal time at the Greenwich meridian, measured from Υ . Mean solar time at the Greenwich meridian is the familiar Greenwich Mean Time, measured from the lower transit of the mean Sun:

$$\omega_0 t + h - \pi = (\omega_0 + \omega_3)t - \pi$$

where $(2\pi/\omega_0)$ is the mean solar day, and $(2\pi/\omega_3)$ is the tropical year.

The angle $E_2\hat{O}\Upsilon$ is the lunar Right Ascension A_l , which increases more slowly as the Moon orbits through a period of one sidereal month with a mean angular speed we call ω_2 .

Combining these factors we have:

$$C_l = \lambda_p + (\omega_0 + \omega_3)t - \pi - A_l \quad (3.20a)$$

Similarly, the solar hour angle may be expressed as:

$$C_s = \lambda_p + (\omega_0 + \omega_3)t - \pi - A_s \quad (3.20b)$$

The angular speeds ω_2 , ω_3 , ω_4 , ω_5 and ω_6 in Table 3.2 are the mean rates of change with time of the astronomical coordinates s , h , p , N and p' respectively. In

addition to defining three types of day, the basic astronomical frequencies in Table 3.2 may also be used to define several different kinds of months and years, as listed in Table 3.3. These definitions in terms of simple sums and differences of basic astronomical frequencies illustrate the basic ideas for the harmonic expansion of the tidal potential that will be developed in Section 4.2. Although it is usual to define the astronomical speeds numerically in terms of radians per unit time, for which we use the symbol ω , tidal applications usually work in terms of degrees per unit time, for which we use the symbol σ (see Section 4.2).

3.4 Tidal patterns

The detailed descriptions of the Equilibrium Tide and of the lunar and solar motions developed in Sections 3.3.2 and 3.3.3 are necessary for a rigorous tidal development, but several features of the observed tides, many plotted in Figure 1.2a, can be

Table 3.2 Basic astronomical periods and frequencies

			Frequency		Angular speed	
			f cycles per mean solar year	σ degrees per mean solar hour	Symbol in rate of radians	Rate of change of
Mean solar day	1.00	mean solar days	1.00	15.0000	ω_0	C_s
Mean lunar day	1.0351	mean solar days	0.9661369	14.4921	ω_1	C_l
Sidereal month	27.3217	mean solar days	0.0366009	0.5490	ω_2	S
Tropical year	365.2422	mean solar days	0.0027379	0.0411	ω_3	h
Moon's perigee	8.85	Julian years	0.0003093	0.0046	ω_4	p
Regression of Moon's nodes	18.61	Julian years	0.0001471	0.0022	ω_5	N
Perihelion	20,942	Julian years	–		ω_6	p'

Table 3.3 Different days, months and years

Type			Frequency	Period (msd)
Days				
	Sidereal	Fixed celestial point	$\omega_5 = \omega_0 + \omega_3$ $\omega_5 = \omega_1 + \omega_2$	0.9973
	Mean solar	Solar transit	Ω_0	1.0000
	Mean lunar	Lunar transit	Ω_1	1.0350
Months				
	Nodical	Lunar ascending node	$\omega_2 + \omega_5$	27.2122
	Sidereal	Fixed celestial point	ω_2	27.3217
	Anomalistic	Lunar perigee	$\omega_2 - \omega_4$	27.5546
	Synodic	Lunar phases	$\omega_2 - \omega_3, \omega_0 - \omega_1$	29.5307
Years				
	Tropical		ω_3	365.2422
	Sidereal	Fixed celestial point γ		365.2564
	Anomalistic	Perihelion	$\omega_3 - \omega_5$	365.2596

explained in more general terms. These features include:

- the relationship between lunar and solar declination and diurnal tides,
- the spring–neap cycle of semidiurnal amplitudes,
- varying intervals between successive high semidiurnal tides in a spring–neap cycle,
- varying spring tidal amplitudes from month to month,
- larger diurnal tides in June and December,
- an approximate 18.6-year cycle in diurnal and semidiurnal amplitudes.

3.4.1 Diurnal tides

Comparing the tidal changes of sea level plotted in [Figure 1.2a](#) for Karumba with the lunar changes plotted in [Figure 1.2b](#), we observed that maximum diurnal tidal ranges occur when the lunar declination is greatest, and that the ranges become very small when the declination is zero. This is because the effect of declination is to produce an asymmetry between the two high and the two low water levels observed as a point P rotates on the Earth within the two tidal bulges. In [Figure 3.12](#), where

these tidal bulges have been exaggerated, the point at P_1 is experiencing a much higher Equilibrium tidal level than it will experience half a day later when the Earth's rotation has brought it to P_2 . The two high water levels would be equal if P were located on the equator. However, as we shall discuss in [Chapter 5](#), the ocean responses to tidal forcing are too complicated and not sufficiently localised for there to be zero diurnal tidal amplitudes at the equator, nor may the latitude variations of the observed tides be described in terms of [Figure 3.12](#). When the Moon is above the latitude of the Tropics of Cancer and Capricorn, the strong diurnal effects produce so-called tropic tides. The weak diurnal effects when the Moon is overhead at the equator are sometimes called equatorial tides.

The solar declination varies seasonally from 23.5° in June to -23.5° in December. In [Figure 1.2a](#) the diurnal tides at Karumba approach zero amplitude when the lunar declination is zero because during the month of March the solar declination is also zero. Similarly, the total amplitude of the diurnal forcing becomes very small in September. In other months the solar diurnal forces are significant and so the total diurnal tides will not completely disappear. The largest diurnal tides occur in June and December when the

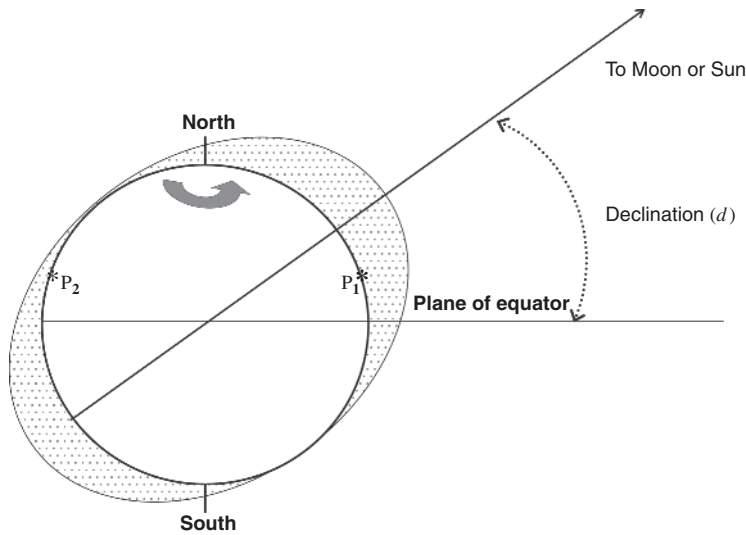


Figure 3.12 Showing how the unequal semidiurnal tides are produced when the Moon or Sun are north or south of the equator (diurnal tide generation).

solar contribution is greatest; these are sometimes called *solstitial tides*.

At times and places where the solar diurnal tides are important, if the diurnal high water levels occur between midnight and noon during the summer, they will occur between noon and midnight during the winter because of the phase reversal of the Equilibrium solar bulges and hence the diurnal tidal forces. This effect is also noticeable where semidiurnal tides dominate, as it affects the phasing of the maximum of the diurnal inequality, night or day.

3.4.2 Spring–neap tides

The fortnightly increase and decrease in semidiurnal tidal amplitudes is due to the various combinations of lunar and solar semidiurnal tides. At Mombasa, Bermuda and Courtown in [Figure 1.2a](#), maximum ranges are seen shortly after the times of new Moon and of full Moon. The minimum ranges occur at first quarter and last quarter. This is because at times of spring tides the lunar and solar forces combine together, but at neap tides the lunar and solar forces are out of phase and tend to cancel. [Figure 3.13](#) shows how the phases of the Moon and the ranges of the semidiurnal tides are related. In practice the observed spring and neap tides lag the maximum and minimum of the tidal forces, usually by one or two days.

The synodic period from new Moon to the next new Moon is 29.5 days, $\frac{2\pi}{(\omega_2 - \omega_3)}$ or $\frac{2\pi}{(\omega_0 - \omega_1)}$, from the angular speeds defined in [Section 3.3.4](#) and [Tables 3.2](#)

and [3.3](#). The time from one group of spring tides to the next is 14.8 days. Note that the spring–neap cycle is not an exact number of cycles of the semidiurnal lunar tides.

The average interval between successive lunar high tides is 12 hours and 25 minutes; this is the average over a spring–neap cycle. However the solar tides would occur every 12 hours, and so there are times over a spring–neap cycle when the Sun has the effect of speeding up the tidal interval, and then later in the cycle of slowing it down. [Figure 3.14](#) shows the effect on the interval between high (or low) tides over a spring–neap cycle for the Equilibrium tidal ratio (0.46) of solar and lunar amplitudes. Semidiurnal tidal intervals are close to 12 hours and 25 minutes at new and full Moon (spring tides), and also at the first and last lunar quarter (neap tides). However, between the new Moon and the first quarter (see [Figure 1.2b](#)), the high tides occur early, that is before the expected lunar high tide. The same effect happens between full Moon and last quarter. This phenomenon is called *tidal priming*, or sometimes *tidal leading*. Conversely, between first quarter and the full Moon and between last quarter and a new Moon, the tidal interval is longer and the tides are later. This is called *tidal lagging*.

Where the ratios between solar and lunar tides differ from the Equilibrium ratio, the priming and lagging effects are reduced or enhanced. These priming and lagging effects are readily reproduced by harmonic representation, as we shall see in [Chapter 4](#).

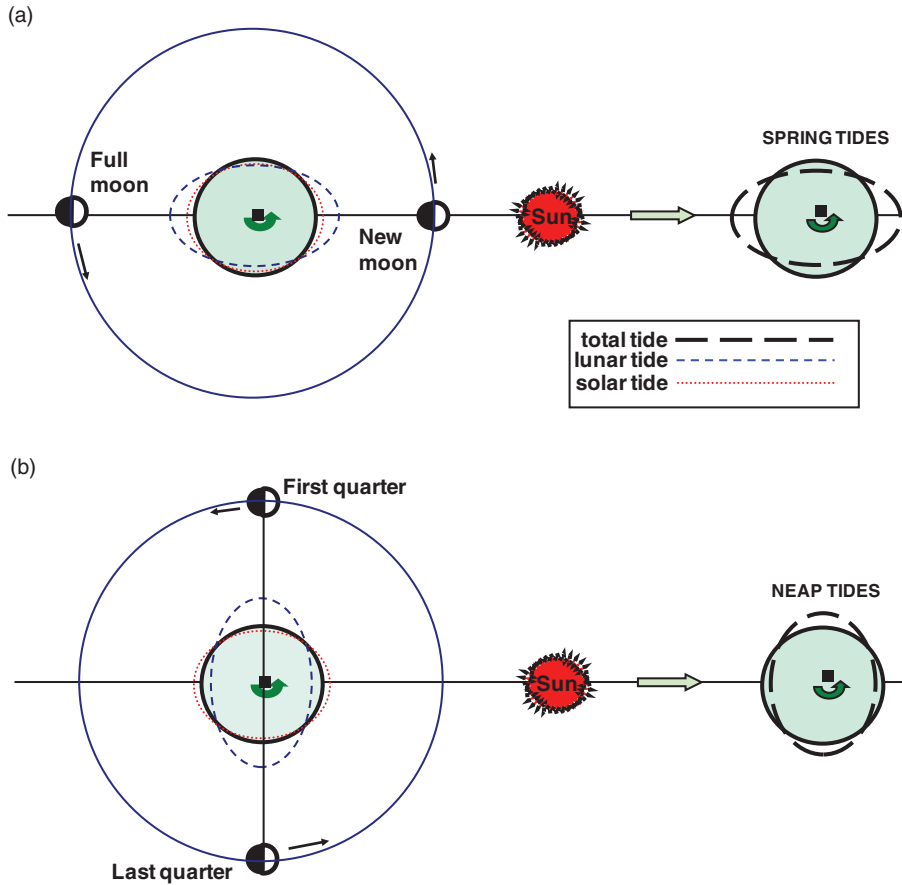


Figure 3.13 Spring–neap tidal cycles are produced by the relative motions of the Moon and Sun, at 14.8-day intervals. The lunar and solar Equilibrium tides combine to produce (a) spring tides at new and full Moon and (b) neap tides at the Moon’s first and last quarter.

3.4.3 Perigean spring tides

Within a lunar synodic period the two sets of spring tides are usually of different amplitudes. For example, in [Figure 1.2a](#) the Mombasa record shows that the ranges of the first set are larger than those in the second set. This difference is due to the varying lunar distance; lunar perigee (the nearest approach of the Moon to the Earth) occurs on this occasion just after the new Moon that accompanies the first set of spring tides ([Figure 1.2b](#)) so that the Moon is near apogee (furthest from the Earth) for the second set of spring tides. One complete cycle from perigee to perigee takes an anomalistic month of 27.6 days. At perigee, the $(1/R_l^3)$ term of [Equation 3.12](#) gives tidal forces that are 15 per cent larger than the forces when R_l has its mean value. At apogee, when the Moon is at its furthest distance from the Earth, the lunar forces are 15 per cent less than those for the mean value of R_l . These

modulations due to distance variations are much smaller than the 46 per cent modulations in the total semidiurnal forces produced by spring–neap variations, but their effects are nevertheless significant.

Because of local Atlantic Ocean responses to the tidal forces, these perigean effects are particularly evident in the tidal regimes of the east coast of North America.

3.4.4 Declinational tidal modulations

A different modulation of the semidiurnal forces is produced by the varying declination of the Moon and of the Sun according to the $\cos^2 d$ relationship ([Equation 3.12](#)) that produces maximum forces when they are in the equatorial plane. For example, the semidiurnal lunar forces are reduced by 23 per cent when the Moon has its maximum declination of $28^\circ 36'$. The solar semidiurnal forces are reduced by a

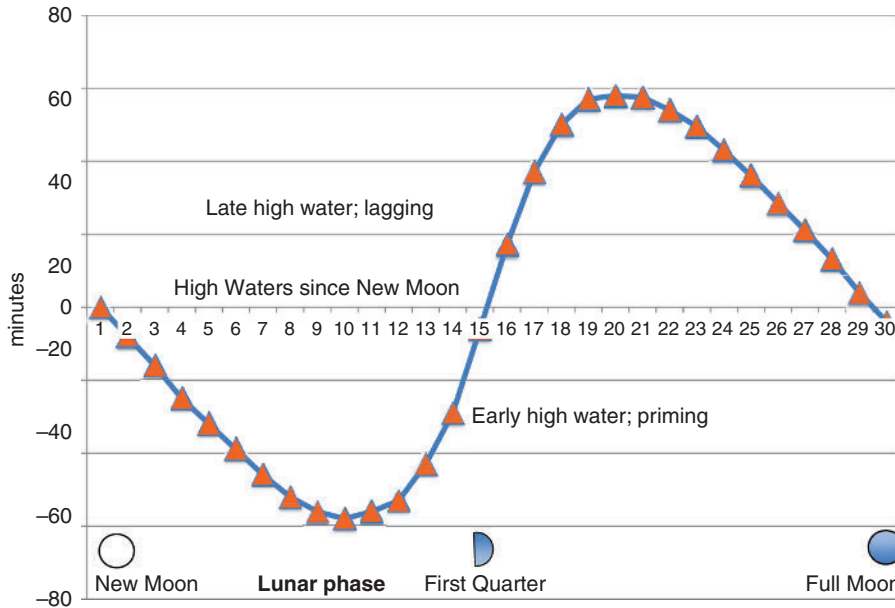


Figure 3.14 The lagging and leading of tidal high waters compared with the Local Establishment, over a spring–neap cycle. The curve is for the Equilibrium M_2/S_2 amplitude ratio. The curves are similar, but the maximum excursion is 40 minutes for a ratio of 0.32, and 76 minutes for a ratio of 0.60.

factor of 16 per cent in June and December when the declination reaches its maximum value of $23^\circ 27'$. In March and September near the equinoxes $\cos^2 d_s = 1$ and so the solar semidiurnal forces are maximised with the result that spring tides near the equinoxes are usually significantly larger than usual; these tides are called equinoctial spring tides.

3.4.5 Nodal tidal changes

As discussed, the Earth's equatorial plane is inclined at $23^\circ 27'$ to the plane in which the Earth orbits the Sun (the ecliptic). This inclination causes the seasonal changes in our climate, and the regular seasonal movements of the Sun north and south of the equator. The plane in which the Moon orbits the Earth is inclined at $5^\circ 09'$ to the plane of the ecliptic; this plane rotates slowly over a period of 18.61 years. As a result, over this 18.61-year nodal period the amplitude of the lunar declination increases and decreases slowly. The maximum lunar monthly declination north and south of the equator varies between $18^\circ 18'$ and $28^\circ 36'$. There are maximum values of the lunar declination in 1969, 1987, 2006, 2025 and 2043, and minimum values in 1978, 1997, 2015, 2034 and 2053.

Increases in the range of the lunar declination over 18.61 years increase the amplitude of the diurnal lunar

tides, but as explained above, there is a corresponding decrease in the amplitude of the semidiurnal lunar tides. These nodal modulations decrease the average lunar semidiurnal Equilibrium Tide by 3.7 per cent when the declination amplitudes are greatest, with a corresponding 3.7 per cent increase 9.3 years later. In [Chapter 4](#) these effects are represented by f and u nodal factors.

3.5 Extreme tidal forces

Extreme tidal forces are important because the times of greatest risk of coastal flooding are those of extreme tides. By simple arguments it is evident that extreme tidal forces will occur when the Moon and Sun are in line with the Earth (syzygy) and at their closest respective distances. However, as we shall discuss in [Chapter 5](#), the ocean response to tidal forces is much greater for semidiurnal tides than it is for diurnal tides. For maximum semidiurnal tidal forces, the Moon and Sun must also be in the plane of the equator, that is they both have zero declination.

Identifying times of extreme tides from discussion of orbits and angular speeds (the six speeds, ω_1 to ω_6 in [Table 3.3](#)) had some limited success [[10](#), [11](#)], but eventually became overwhelmed by very detailed arguments [[12](#), [13](#)]. The more direct approach of

Table 3.4 Times and heights of the largest (positive) values of the Equilibrium Tide between 1980 and 2050 for the degree-2 semidiurnal component of the tide only. These maximum values necessarily occur on the equator. Normalisation of the heights in this table is that used for the Cartwright–Tayler–Edden tables [20]. Times of other maximum values that have occurred during the years 1–3000 CE are available [21].

Year	Day	Month	Day	Hour GMT	Eq cm	Sun				Moon			
						Declination	Distance (AU)	cos d	$1/d$	cos d	R_{MEAN}/R		
<i>Vernal equinox</i>													
1980	76	3	16	20.8	45.94	-1.306454	0.99512081	0.9997	1.0049	-3.116174	356927.257	0.9985	1.0770
1984	77	3	17	11.2	45.57	-1.083701	0.99522646	0.9998	1.0048	5.269381	357477.752	0.9958	1.0753
1985	95	4	5	7.7	45.58	6.179189	1.00052874	0.9942	0.9995	-2.595622	357161.794	0.9990	1.0762
1989	67	3	8	1.1	45.77	-4.903124	0.9926801	0.9963	1.0074	-1.973103	357620.229	0.9994	1.0749
1993	67	3	8	11.8	46.17	-4.734221	0.99273141	0.9966	1.0073	-0.38239	356549.09	1.0000	1.0781
1997	68	3	9	1.5	45.60	2.58975	1.00530621	0.9990	0.9947	-3.709426	358189.006	0.9979	1.0732
1998	87	3	28	2.1	45.90	2.867731	0.99806097	0.9987	1.0019	0.664196	357053.701	0.9999	1.0766
2002	87	3	28	15.6	45.80	3.083725	0.99820128	0.9986	1.0018	1.933957	357128.955	0.9994	1.0763
2007	78	3	19	5.3	45.70	-0.748887	0.99548529	0.9999	1.0045	0.913559	358126.693	0.9999	1.0733
2010	59	2	28	19.2	45.40	-7.84197	0.9906605	0.9906	1.0094	3.603502	358591.751	0.9980	1.0720
2011	78	3	19	16.6	45.95	-0.561841	0.99552972	1.0000	1.0045	-3.742917	356583.047	0.9979	1.0780
2015	79	3	20	7.0	45.79	-0.342297	0.99576323	1.0000	1.0043	0.071656	357802.407	1.0000	1.0743
2020	98	4	7	20.2	45.60	7.130517	1.00121098	0.9923	0.9988	-1.08948	356912.523	0.9998	1.0770
2024	70	3	10	13.8	45.79	-3.899029	0.9933095	0.9977	1.0067	-4.557709	356978.832	0.9968	1.0768
2028	70	3	10	23.8	45.75	-3.761397	0.99334415	0.9978	1.0067	0.724764	357959.51	0.9999	1.0738
2033	60	3	1	15.0	45.84	-7.484851	0.99093052	0.9915	1.0092	-3.135532	357200.201	0.9985	1.0761
2038	80	3	21	6.2	45.64	0.076648	0.99598774	1.0000	1.0040	3.495925	357599.704	0.9981	1.0749
2042	80	3	21	18.0	45.98	0.263962	0.99619888	1.0000	1.0038	-1.654243	356942.531	0.9996	1.0769
2046	81	3	22	4.1	45.66	0.418703	0.99619056	1.0000	1.0038	-2.510607	357535.747	0.9990	1.0751
2050	52	2	21	20.7	45.63	-10.531615	0.98905192	0.9832	1.0111	-4.658362	357171.882	0.9967	1.0762

Autumnal equinox

1980	268	9	24	15.3	45.48	-0.79004	1.00282182	0.9999	0.9972	-1.819724	357665.031	0.9995	1.0747
1984	269	9	25	4.5	45.66	-1.005362	1.00277103	0.9998	0.9972	2.415523	356970.955	0.9991	1.0768
1988	269	9	25	14.6	45.43	-1.159857	1.00260159	0.9998	0.9974	1.544004	357901.115	0.9996	1.0740
1993	259	9	16	5.9	45.43	2.58975	1.00530621	0.9990	0.9947	-2.441711	357534.73	0.9991	1.0751
1997	259	9	16	20.3	45.58	2.375828	1.00513147	0.9991	0.9949	-2.526075	357002.799	0.9990	1.0767
1998	278	10	5	20.3	45.43	-4.899772	0.99987271	0.9963	1.0001	1.702497	358120.006	0.9996	1.0734
2002	279	10	6	8.7	45.78	3.083725	0.99820128	0.9986	1.0018	-0.561621	356949.706	1.0000	1.0769
2015	271	9	28	1.4	45.78	-1.741947	1.00218702	0.9995	0.9978	1.091459	356877.769	0.9998	1.0771
2020	290	10	16	13.5	45.48	-9.082081	0.99675326	0.9875	1.0033	-1.608587	357459.125	0.9996	1.0753
2024	262	9	18	6.9	45.50	1.780512	1.00474498	0.9995	0.9953	-1.431668	357355.112	0.9997	1.0757
2028	262	9	18	17.0	45.57	1.628667	1.00464951	0.9996	0.9954	-2.22573	357058.092	0.9992	1.0766
2033	281	10	8	6.8	45.51	-5.850804	0.99918209	0.9948	1.0008	4.873586	356873.12	0.9964	1.0771
2037	281	10	8	20.5	45.57	-6.047343	0.99908132	0.9944	1.0009	-0.2724	357618.926	1.0000	1.0749
2042	272	9	29	10.6	45.52	-2.32378	1.00179142	0.9992	0.9982	1.475787	357703.609	0.9997	1.0746

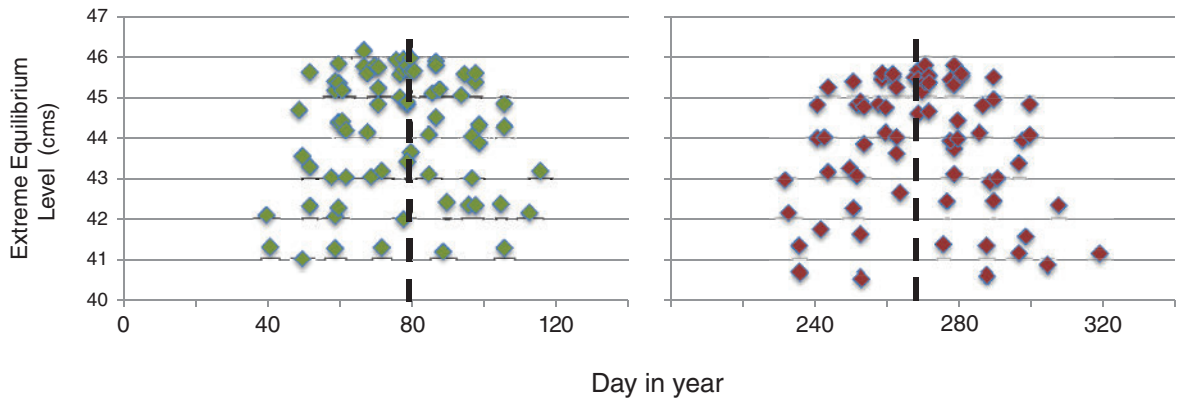


Figure 3.15 The maximum Equilibrium semidiurnal tide at the spring and the autumnal equinoxes for each year from 1980 to 2050, plotted to show the clustering around each equinox, denoted by dashes lines. Values were calculated by summing potentials from an expansion of the Equilibrium Tide [20].

computing and looking at maximum values of the actual tidal potential was initially limited by available computing power: for example, computing extremes of a semidiurnal tide every hour will inevitably underestimate by not sampling at the actual extreme [14]. Modern computing power makes it possible to calculate the Equilibrium Tide every minute over millennia: this more complete picture shows that several extremes were missed in earlier computations [15].

A useful distinction can be made between two different types of extremes [16]. The first type, which occurs at a near coincidence of syzygy and lunar and solar perigee (and for semidiurnal tides, zero declinations of the Moon and Sun), is called ‘repeat coincidence’. The second type arises from the slow beating of physical effects, for example the 18.61-year nodal modulations in the lunar tides; these modulations are termed ‘harmonic beats’. ‘Repeat coincidence’ tidal extremes are transient, of short duration, and have only slightly greater amplitudes than ordinary high tides. ‘Harmonic beat’ extremes are sustained over longer periods.

At present the Earth’s closest annual approach to the Sun, perihelion, is near 4 January, advancing slowly over a cycle of 21,000 years (ω_6); this slowly increasing enhancement is an example of ‘harmonic beating’. The coincidence of simultaneous perihelion and zero solar declination, near 21 March, will not occur for another 4400 years. However, there are many near-extreme values, ‘repeat coincidence’ events, at times when lunar perigee occurs almost simultaneously with zero lunar declination, and with the zero solar declination of either the spring or autumnal

equinox. Extreme semidiurnal tides cluster around the equinoxes for this reason. Figure 3.15 shows the spreading of semidiurnal extremes around the equinoxes for the period 1980–2050: the spring equinox values are slightly greater, consistent with perihelion in early January. The differences are small: spring and autumn levels would have been equal around 1247 [15], when perihelion coincided with the winter solstice.

More information on amplitudes and times of extreme semidiurnal tidal forcing are given for vernal and autumnal equinoxes in Table 3.4, also for the period 1980–2050, together with the corresponding values of the orbital parameters for distance and for declination. These extremes have been identified by predicting the hourly values of the Equilibrium semidiurnal tide at the Greenwich meridian, for each half-year, and then computing every minute for 3 hours either side to find the time and value of the full extreme. The highest value in each period was then tabulated, provided that it was more than $0.4540 m$. For comparison, the Equilibrium lunar twice-daily tidal amplitude, H_{M_2} (in the symbols to be developed in Chapter 4), is $0.2440 m$.

The highest value in Table 3.4 ($0.4617 m$; 8 March 1993) is $1.89 H_{M_2}$. For these ‘repeat coincidence’ events, exact coincidence of other conditions with the solar equinox is not essential, as is illustrated by the spread of days in Figure 3.15, and in particular by the values in early March in 1993 and 1997, and in October 2002.

Figure 3.16 shows a cycle of approximately 4.5 years in the 1980–2050 semidiurnal extremes. These

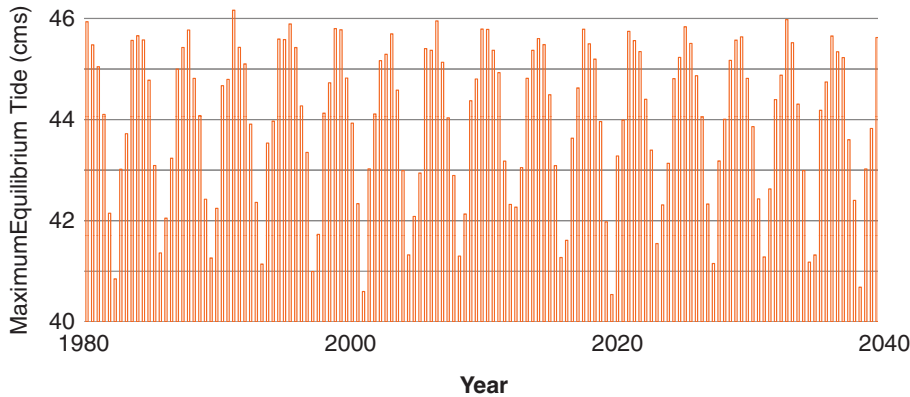


Figure 3.16 The maximum Equilibrium semidiurnal tide at the spring and the autumnal equinoxes for each year from 1980 to 2050, plotted to show the 4.5-year cycle in the extremes due to the perigean cycle beating with lunar declination and equinox cycles. Values calculated as for Figure 3.15.

include 2015, 2020, and at typically 4.5-year intervals thereafter. These maximum 4.5-year ranges occur when there is a repeat coincidence in the time of lunar perigee (a maximum in the $(\bar{R}_l/R_l)^3$ term) and lunar declination is also near zero ($\cos^2 d_l = 1$), which also corresponds with spring tides, and either the March or September equinox ($\cos^2 d_s = 1$) when the Sun is overhead at the equator during its 8.85-year cycle. In practical terms, hydrographic authorities often evaluate Highest and Lowest Astronomical Tides (used as Chart Datum) by scrutiny of 5 years of tidal predictions.

The 18.61-year nodal cycle is not evident in Figure 3.16, although H_{M_2} , the amplitude of the M_2 tidal constituent, has a very clear modulation over this period, as shown in Figure 4.3. This is because the M_2 amplitude is the *average* over the long period of data analysed, whereas the extreme values are transient, repeat coincidences of several factors. These extreme semidiurnal tides depend on the Moon being near the plane of the equator, and so the magnitude of the declination excursions north and south are not important; however, there is a secondary effect, reducing the probability of repeat coincidences, and hence extreme semidiurnal tides, when the nodal declinations are a maximum, as the Moon's declination will then be changing more rapidly as it transits through the equatorial plane.

Maximum diurnal tides need a different set of conditions: coincidence of solar and lunar maximum declinations at the summer and winter solstice, with lunar perigee. For diurnal tidal extremes, and in contrast with semidiurnal tides, the nodal variations of lunar declination over an 18.61-year cycle are very important.

Detailed computations over very long periods also show that extreme repeat coincidence events always occur near the times of full Moon rather than new Moon, due to the complex way the Sun's gravity slightly increases the eccentricity of the Moon's orbit [12, 15]; this is a well-known astronomical process termed *lunar evection*.

Other periodic 'repeat coincidences' in the recurrence of extreme tides can be expected as different factors in the orbits coincide. These include:

- lunar perigee and zero lunar declination coincide every 6 years,
- the Saros period of Earth–Moon–Sun alignment of 18.03 years, noted for the pattern it produces in repeat eclipses,
- the Metonic cycle of 19 tropical years, which is very close to 254 tropical lunar months,
- a 93-year coincidence of five nodal cycles and 10.5 lunar perigee cycles (noting that half cycles are valid for lunar perigee effects),
- Milankovich orbital effects of eccentricity, obliquity and precession, all of tens of thousands of years.

Although they have similar periods, the Saros, Nodal and Metonic cycles are not directly related. The Metonic cycle is interesting because it means that tide predictions are very similar at 19-year intervals.

Tidal maxima due to a combination of the anomalistic year ($\omega_3 - \omega_6$), together with six times the speed of both the nodal and lunar perigee speeds:

$$\omega_3 + 6\omega_4 + 6\omega_5 - \omega_6 = 1/1795 \text{ years}$$

have been identified by several authors [10, 11, 16]. Some climate scientists [17] have linked this to cycles in ice-core and deep-sea sediment-core records through enhanced tidal energetics and vertical ocean mixing. However, the link is very improbable [16, 18] given the transient nature of these tidal extremes, and the reality that tidal ‘extremes’ are in fact only fractionally more extreme than typical spring tides near perigee, as Table 3.4 shows.

It should be realised that, although maximum predicted tidal ranges usually result from extremes in the Equilibrium tidal forcing, local ocean responses to these forces may produce local extreme tides at times other than those tabulated. Pragmatically, the effects of the 18.61-year and 8.85-year nodal and perigean cycles on real ocean tides have been modelled [19], and confirm that nodal 18.61-year modulations are most evident in places where diurnal tides predominate; for the more widespread ocean and shelf regions of semidiurnal tidal dominance, the 4.5-year perigean cycle is important.

Of course, the small differences between these predictions of extreme tides are of mainly academic interest: the observed extremes, and resulting serious flooding, will also depend on the prevailing weather conditions, whose influences, discussed in Chapter 7, are normally much bigger than these small distinctions in tidal extremes. The calculation of probabilities of combined tidal and weather effects on extreme levels is discussed in Chapter 12.

References

- (1) Godin, G. 1972. *The Analysis of Tides*. Liverpool: Liverpool University Press. (2) Schureman, P. 1976. *Manual of Harmonic Analysis and Prediction of Tides*. Special Publication 98, Coastal and Geodetic Survey. Washington, D.C.: U.S. Department of Commerce (1st edition, 1924; latest reprint 1976). (3) Foreman, M. G. G. 1977. *Manual for Tidal Heights Analysis and Prediction*. Canadian Pacific Marine Science Report No. 77-10, <ftp://canuck.seos.uvic.ca/docs/MFTides/heights.pdf>. (4) Doodson, A. T. and Warburg, H. D. 1980. *Admiralty Manual of Tides*. London: Her Majesty's Stationery Office (1st edition, 1941; latest reprint 1980). (5) Parker, B. B. 2007. *Tidal Analysis and Prediction*. NOAA Special Publication NOS CO-OPS 3. Washington, D.C.: U.S. Department of Commerce, National Oceanic and Atmospheric Administration, National Ocean Service.
- Earlier accounts are (1) Doodson, A. T. 1921. Harmonic development of the tide-generating potential. *Proceedings of the Royal Society of London, A*, **100**, 305–329, doi:10.1098/rspa.1921.0088. (2) Lamb, H. 1932. *Hydrodynamics* (6th edition). Cambridge: Cambridge University Press.
- Luzum, B., Capitaine, N., Fienga, A. *et al.* 2011. The IAU 2009 system of astronomical constants: the report of the IAU Working Group on Numerical Standards for Fundamental Astronomy. *Celestial Mechanics and Dynamical Astronomy*, **110**, 293–304, doi:10.1007/s10569-011-9352-4.
- Textbooks on spherical astronomy are rare. Smart, W. M. 1940. *Spherical Astronomy* (Cambridge University Press) was a notable one since updated as: Smart, W. M. (revised by R. M. Green) 1977. *Textbook on Spherical Astronomy* (6th edition). Cambridge: Cambridge University Press.
- Murray, C. D. and Dermott, S. F. 1999. *Solar System Dynamics*. Cambridge: Cambridge University Press.
- Roy, A. E. 1978. *Orbital Motion*. Bristol: Adam Hilger.
- Gerstenkorn, H. 1955. Über gezeitenreibung beim zweikörperproblem. *Zeitschrift für Astrophysik*, **36**, 245–274.
- Webb, D. J. 1982. Tides and the evolution of the Earth-Moon system. *Geophysical Journal of the Royal Astronomical Society*, **70**, 261–271, doi:10.1111/j.1365-246X.1982.tb06404.x.
- Bills, B. D. and Ray, R. D. 1999. Lunar orbital evolution: a synthesis of recent results. *Geophysical Research Letters*, **26**, 3045–3048, doi:10.1029/1999GL008348.
- Pettersson, H. 1913. *Long Periodical Variations of the Tide-Generating Force*. Conseil Permanent International pour L'Exploration de la Mer, Publications de Circonstance No 65. Copenhagen: Høst & fils.
- Amin, M. 1979. A note on extreme tidal levels. *International Hydrographic Review*, **56**, 133–141.
- Wood, F. J. 1986. *Tidal Dynamics. Coastal Flooding and Cycles of Gravitational Force*. Dordrecht: D. Reidel.
- Wood, F. J. 2001. *Tidal Dynamics. Volume 1: Theory and Analysis of Tidal Forces*. Florida: The Coastal Education and Research Foundation (CERF).
- Cartwright, D. E. 1974. Years of peak astronomical tides. *Nature*, **248**, 656–657, doi:10.1038/248656a0.
- Ray, R. D. and Cartwright, D. E. 2007. Times of peak astronomical tides. *Geophysical Journal International*, **168**, 999–1004, doi:10.1111/j.1365-246X.2006.03293.x.
- Munk, W., Dzieciuch, M. and Jayne, S. 2002. Millennial climate variability: is there a tidal connection? *Journal of Climate*, **15**, 370–385, doi:10.1175/1520-0442(2002)015<0370:MCVITA>2.0.CO;2.

17. Keeling, C. D. and Whorf, T. P. 2000. The 1800-year oceanic tidal cycle: a possible cause of rapid climate change. *Proceedings of the National Academy of Sciences*, **97**, 3814–3819, doi:10.1073/pnas.070047197.
18. Ray, R. D. 2007. Decadal climate variability: is there a tidal connection? *Journal of Climate*, **20**, 3542–3560, doi:10.1175/JCLI4193.1.
19. Haigh, I. D., Eliot, M. and Pattiaratchi, C. 2011. Global influences of the 18.61-year nodal cycle and the 8.85-year cycle of lunar perigee on high tide levels. *Journal of Geophysical Research*, **116**, C06025, doi:10.1029/2010JC006645.
20. Cartwright, D. E. and Edden, A. C., 1973. Corrected tables of tidal harmonics, *Geophysical Journal of the Royal Astronomical Society*, **33**, 253–264.
21. Ray, R. D. and Cartwright, D. E. 2007. Times of peak astronomical tides. *Geophysical Journal International*, **168**, 999–1004, doi:10.1111/j.1365-246X.2006.03293.x.

Tidal analysis and prediction

By what astrology of fear or hope
Dare I to cast thy horoscope!
By the new Moon thy life appears;
Longfellow, To a child

Tidal analysis of data collected by observations of sea levels and currents has two purposes. Firstly, a good analysis provides the basis for predicting tides at future times, a valuable aid for shipping and other operations. Secondly, the results of an analysis can be interpreted scientifically in terms of the hydrodynamics of the seas and their responses to tidal forcing. An analysis provides parameters that can be mapped to describe the tidal characteristics of a region. Preliminary tidal analyses can also be used to check tide gauge performance, as discussed in [Chapter 2](#).

The process of analysis reduces many thousands of numbers, for example a year of hourly sea levels consists of 8760 values, to a few significant stable numbers that contain the soul or quintessence of the record [1]. An example of statistical tidal analysis is given in the description of sea levels in [Section 1.6](#). In tidal analysis the aim is to produce significant time-stable parameters that describe the tidal régime at the place of observation. These parameters should be in a form suitable for prediction, should be related physically to the process of tide generation, and should have some regional stability.

The parameters are often termed *tidal constants* on the implicit assumption that the responses of the oceans and seas to tidal forcing do not change with time. Also implicit in the use of this term is the assumption that if a sufficiently long series of levels or currents is available at a site, then a true value for each constant is obtained by analysis. In practice measurements extend over finite periods, often a year, a month or even a few days, and so the results from analysing these finite lengths of data can only

approximate the true constants. The longer the period of data available for analysis, the better will be the approach to these true values. Of course there is ultimately no absolute true value, as tidal characteristics change over time, but the assumption is still implied.

A good system of analysis represents the data by a few significant, stable numbers, but a bad analysis represents the data by a large number of parameters that cannot be related to a physical reality, and for which the values obtained depend on the time at which the observations were made. If possible, an analysis should also give some idea of the confidence that should be attributed to each tidal parameter determined. Details of analysis procedures are given in separate publications [2, 3, 4, 5]. The reader of the older texts is warned that many of the techniques designed to reduce labour of calculation, in the days before digital computers, are fortunately no longer necessary.

The close relationship between the movements of the Moon and Sun and the observed tides makes the lunar and solar coordinates a natural starting point for any analysis scheme. The Equilibrium Tide developed in [Chapter 3](#) defines a tidal level at each point on the Earth's surface as a function of time and latitude. The observed tides differ very markedly from the Equilibrium Tide because the oceans have complicated responses that are limited and controlled by their real depths and boundaries. In shallow water the tides are further distorted from the Equilibrium form by the loss of energy through bottom friction and by the preservation of the continuity of water flow. Tidal behaviour in shallow water will be considered in detail in [Chapter 6](#), but in this chapter we need to remember

that any good analysis scheme must be capable of resolving these complications.

Three basic methods of tidal analysis have been developed. The first, which is now generally of only historical interest, termed the *non-harmonic method*, consists of relating high and low water times and heights directly to the phases of the Moon and other astronomical parameters. The second method, which is generally used for predictions and scientific work, called *harmonic analysis*, treats the observed tides as the sum of a finite number of harmonic constituents whose angular speeds and phases are determined from knowledge of the astronomical forcing. The third method, the *response method*, develops the concepts, widely used in electronic engineering, of a frequency-dependent system response to a driving mechanism. For tides the driving mechanism is the Equilibrium potential. The latter two methods are special applications of the general formalisms of time series analysis. We shall discuss their relative advantages and disadvantages in [Section 4.3.4](#).

Analyses of changing sea levels, which are scalar quantities, are obviously easier to perform than those of currents, which are vectors. The development of the different techniques is first discussed in terms of sea levels; their application to currents is treated in a subsequent section. More elaborate details of the procedures are given in [Appendix B](#).

4.1 Non-harmonic methods

The simplest and oldest technique of tidal analysis is to relate the time of local semidiurnal high water to the time of lunar transit. The time interval between lunar transit at new or full Moon and the next high tide used to be known as the local establishment. Small adjustments may be made to allow for variations in the time interval through a spring–neap cycle, including the priming and lagging discussed in [Section 3.4.2](#). The *age of the tide* is an old but still scientifically useful term applied to the interval between the times of maximum tidal forces at new or full Moon, and the time of maximum spring range; this delay is usually about two days. See [Appendix C](#) on some harmonic equivalence terms.

The harmonic method of tidal analysis and prediction is now so standard in oceanography that it is possible to forget that non-harmonic methods existed before, and have been developed since, the late nineteenth century when Kelvin, Darwin and others

proposed the harmonic approach [6]. For example, the first accurate, publicly accessible tide tables in the United Kingdom were produced for Liverpool by Richard and George Holden starting in 1770 [7]. Their method estimates how the lunar semidiurnal tide (in effect what we shall call M_2 , later in this chapter) varies due to changes in lunar distance (parallax) and declination. These parameters were by then readily available since the publication of the first edition of *The Nautical Almanac* in 1767. The lunar tide is then combined with the smaller solar semidiurnal tide (in effect S_2) using the method proposed by Bernoulli in 1740. To replicate the real tide the Holdens needed only four parameters: the relative importance of the solar tide to the lunar one (roughly 0.4), a lag in hours of the real tide compared to the combined one from the Bernoulli method, a lag compared to that predicted in the magnitude of the tide (i.e. the age of the tide, approximately 2 days at Liverpool), and an overall scale factor. All of these concepts were well understood at the time and could be estimated from real tidal observations. Fortunately, for analysis, the Holdens had 4 years of heights and times of high water that the Liverpool dock master William Hutchinson had collected starting in 1764.

Hutchinson went on to record the tides at Liverpool until 1793. In the 1830s, John Lubbock used his data in his ‘synthetic method’ of tidal analysis. In this enormous computational task for the period, undertaken primarily by his assistant Joseph Dessiou, the 13,000 pairs of height and time of high water were compiled against tables of lunar parameters (lunar transit time, parallax, declination) in order to understand the functional dependence of the tide on each one. The resulting computed dependencies could then be used as the basis for tidal prediction using known future lunar and solar ephemerides. This method was claimed to be more accurate than previous ones and was adopted for general use by the Admiralty, although for a further half a century, Liverpool preferred predictions using the Holden method.

Several other non-harmonic tidal parameters determined from simple analysis of the data have been defined in [Chapter 1](#). The advantage of these non-harmonic parameters is their ease of determination and of application. Their limitations for predictions include lower accuracy, the difficulty of using them in scientific work, and the fact that they contain insufficient information for a full tidal description and prediction scheme. See also [Appendix C](#) and the Glossary.

4.2 Harmonic analysis

4.2.1 Expansion of the Equilibrium Tide

Even though the individual tidal curves at the coastal sites are very different, [Figure 1.2a](#) shows that all locations have tides that appear as periodic oscillations. It is natural for a detailed analysis system to take this regular waveform as a starting point. Mathematically, periodic oscillations are described in terms of an amplitude, and a period or frequency.

The basis of harmonic analysis is the assumption that the tidal variations can be represented by a finite number, N , of harmonic terms of the form:

$$H_n \cos(\sigma_n t - g_n)$$

where H_n is an amplitude, and g_n is a phase lag on the Equilibrium Tide. The time zero for g_n may be in local time, but it is often taken as the phase lag on the Equilibrium Tide phase at the Greenwich meridian, in which case it may be called G_n . This use of the Equilibrium Tide as a reference for tidal analysis is one of its important functions (see [Sections 4.2.2](#) and [4.2.4](#)). σ_n is an angular speed.

For a correct mathematical development the angular speeds and phase lags should be expressed in radians. However, in tidal notation the phase lags g_n are usually expressed in degrees. We use the notation ω_n for speeds in radians per mean solar hour through most of this chapter. The angular speed in degrees per mean solar hour is denoted by $\sigma_n = \frac{360\omega_n}{2\pi}$. A further useful extension of the convention is to express angular speeds in cycles per unit time as f_n : $f_n = \frac{\sigma_n}{360}$ cycles per mean solar hour or $f_n = \frac{\sigma_n}{15}$ cycles per mean solar day.

The angular speeds ω_n are determined by an expansion of the Equilibrium Tide into similar harmonic terms; the speeds of these terms are found to have the general form:

$$\omega_n = i_a\omega_1 + i_b\omega_2 + i_c\omega_3 + i_d\omega_4 + i_e\omega_5 + i_f\omega_6 \quad (4.1)$$

where the values of ω_1 to ω_6 are the angular speeds already defined in [Table 3.2](#) (i.e. the rates of change of C_b , s , h , p , N and p'), and the coefficients i_a to i_f are small integers. The amplitudes and phases are the parameters determined by analysis that define the tidal conditions at the place of observation. The phase lags g_n are defined relative to the phase of the term in the harmonic expansion of the Equilibrium Tide that has

the same angular speed, σ_n (ω_n in radian measure). As discussed, by convention these phases of the Equilibrium Tide are expressed relative to the Greenwich meridian.

This abstract representation of the tides can seem a little remote from the observed movements of the Moon and Sun, but it is possible to relate individual tidal harmonics to real astronomical behaviour. Firstly, we can look at the simplest possible orbit of the Moon and see how the tides this produces can be represented by a single harmonic term. Suppose the Moon were to circle continuously in an equatorial plane around the Earth at a constant distance, with the Earth rotating underneath it every 24 hours. The tides on the Earth would have two maximum values (high waters), for each rotation period. However, because the Moon will have moved on slightly in its monthly orbit (both Earth and Moon rotation are in the same sense), the two tides take 24 hours and 50 minutes. Each individual tide will follow the previous one at intervals of 12 hours 25 minutes and each high water will have the same amplitude.

The single harmonic that represents these tides is called M_2 . The naming convention is that the M represents the Moon, and the suffix '2' shows that it is in the twice-daily semidiurnal tidal species. In this book we print tidal constituents in bold, to show that as vectors they have two numbers associated with them, amplitude (H_n) and phase lag (g_n).

If the Sun's orbit were to be also in the plane of the equator, the same arguments would apply to give a semidiurnal tide. This has a period of exactly 12 hours, because we base our clocks on the solar time. These two solar tides a day are represented by the symbol S_2 using the same convention. We now have two tidal constituents.

The combination of these, M_2 and S_2 , will produce the spring-neap tidal cycle, which would be completely represented by four parameters, the times of lunar and solar high waters and the amplitudes of the two tides. These two terms are the only ones that can be considered to have a physical reality.

The real movements of the Moon and Sun through varying distances and angular speeds in their orbits, and north and south of the equator, can be represented as the combined effects of a series of phantom satellites. These phantom satellites are of various masses and they move in various planes and at various speeds, each one moves either in an orbit parallel to the equator or stands in a fixed position amongst the stars.

Each satellite therefore represents a simple tide with an amplitude and a time of high water, or phase. These concepts of phantom satellites formed the basis for the early development of harmonic analysis by Laplace, Lord Kelvin and George Darwin [8]. The additional frequencies are also analogous to the side-bands of a modulated radio communication carrier frequency, as discussed below.

The first necessary step in the development of harmonic analysis is an expansion of the Equilibrium Tide into a series of harmonic terms from the expressions of Equation 3.12 and the full formulae for distance, declination and hour angle, which are given in attenuated form in Section 3.3. The most complete algebraic expansions were completed by Doodson (1921) [9]. The standard values used today are from Fourier analysis of an extended time series of the Equilibrium Tide computed from parameters describing the lunar and solar orbits, called the ephemerides, the lunar and solar coordinates [10].

Consider first the expansion of a term of the form:

$$\gamma(1 + \alpha \cos \omega_x t) \cos \omega_y t$$

which, by the basic rules of trigonometry for combining sine and cosine terms becomes:

$$\gamma \left[\cos \omega_y t + \frac{\alpha}{2} \cos (\omega_y + \omega_x) t + \frac{\alpha}{2} \cos (\omega_y - \omega_x) t \right] \quad (4.2)$$

Hence, the harmonic modulation in the amplitude of a constituent of speed ω_y is represented by two additional harmonic terms with speeds at the sum and difference frequencies $(\omega_y + \omega_x)$ and $(\omega_y - \omega_x)$.

Consider as an example the effects of the variation over a period of 27.55 days of the lunar distance, R_b , and the lunar longitude. Substituting for R_l from Equation 3.18 in the semidiurnal part of the Equilibrium Tide in Equation 3.12:

$$C_2(t) = \left[\left(\frac{a}{R_l} \right)^3 \frac{3}{4} \cos^2 d_l \right] [1 + e \cos (s-p)]^3 \cos 2C_1$$

For convenience and further simplification we write:

$$\psi = \left[\left(\frac{a}{R_l} \right)^3 \frac{3}{4} \cos^2 d_l \right]$$

We make the approximation:

$$[1 + e \cos (s-p)]^3 \approx 1 + 3e \cos (s-p)$$

where terms in e^2 and above are omitted.

For the lunar longitude, from Equation 3.20a we have:

$$\cos 2C_1 = \cos 2[\omega_0 t + h - s - \pi - 2e \sin (s-p)]$$

with the approximations that $A_l = \lambda_b$, and λ is given by Equation 3.19. We adopt the convention of expanding the potential for the Greenwich meridian, so $\lambda_p = 0$.

We can also write:

$$\delta \equiv \omega_0 t + h - s - \pi$$

and approximate:

$$\cos 2C_1 = \cos 2\delta \cos [2e \sin (s-p)] + \sin 2\delta \sin [2e \sin (s-p)]$$

to

$$\cos 2C_1 \approx \cos 2\delta + 2e \sin (s-p) \sin 2\delta$$

Hence by multiplying out and neglecting the terms in e^2 we have:

$$\begin{aligned} C_2(t) &= \psi [\cos 2\delta + 4e \sin (s-p) \sin 2\delta \\ &\quad + 3e \cos (s-p) \cos 2\delta] \\ &= \psi \left[\begin{array}{l} \cos 2\delta \\ + \frac{4}{2}e \cos (2\delta - s + p) - \frac{4}{2}e \cos (2\delta + s - p) \\ + \frac{3}{2}e \cos (2\delta + s - p) - \frac{3}{2}e \cos (2\delta - s + p) \end{array} \right] \\ &= \psi \left[\begin{array}{l} \cos 2\delta \\ + \frac{7}{2}e \cos (2\delta - s + p) - \frac{1}{2}e \cos (2\delta + s - p) \end{array} \right] \end{aligned} \quad (4.3)$$

Replacing the full definition of δ and writing $-\cos \beta = \cos (\beta + 180^\circ)$:

$$C_2(t) = \psi \left[\begin{array}{l} \cos (2\omega_0 t + 2h - 2s) \\ + \frac{7}{2}e \cos (2\omega_0 t + 2h - 3s + p) \\ + \frac{1}{2}e \cos (2\omega_0 t + 2h - s - p + 180^\circ) \end{array} \right]$$

The first term in $\cos (2\omega_0 t + 2h - 2s)$ is the main semidiurnal lunar tide M_2 due to the mean motion of the Moon. The lunar and solar mean longitudes s and h increase at rates of ω_2 and ω_3 , respectively, which gives $2(\omega_0 - \omega_2 + \omega_3)$ as the total speed of M_2 . The values in Table 3.2 give speeds of 1.9323 cycles per mean solar day or 28.9842° per mean solar hour. Of course, this speed is the same as $2\omega_1$, twice

the speed of the mean Moon, as shown in Section 3.3.3.

The second and third terms have total angular speeds:

$$2\omega_1 - \omega_2 + \omega_4; f = 1.8960 \text{ cpd}; \sigma = 28.4397^\circ \text{h}^{-1}$$

$$2\omega_1 - \omega_2 - \omega_4; f = 1.9686 \text{ cpd}; \sigma = 29.5285^\circ \text{h}^{-1}$$

They represent the two extra terms in Equation 4.2, with the important difference that in this case the amplitudes of the terms are not equal. This is because our analysis included both the amplitude variation, which would have produced terms of equal amplitude, and the effects of the varying angular speed on the right ascension, which increases the amplitude of the term at the lower speed and decreases the amplitude of the term at the higher speed. To emphasise their speed symmetry about the speed of M_2 , these are called N_2 and L_2 . According to the expansion in Equation 4.3 the relative amplitudes are (for the lunar orbit, $e_1 = 0.0549$):

$$N_2 : M_2 : L_2 = 0.196 : 1.000 : 0.027$$

and these compare favourably with the relative amplitudes given in Table 4.1c. The full expansion of $C_2(t)$ must also include the effects of the obliquity on the right ascension, and the effects of the declination, $\cos^2 d_1$ as discussed in Chapter 3. The approximation for the orbit parameters given in Section 3.3.3 must also be expanded to further terms. When this is done for both the Moon and Sun the list of harmonic constituents is very long. Nevertheless, examination of their relative amplitudes shows that in practice a limited number of harmonics are dominant. Similar expansions for the long period and diurnal terms show that these too are dominated by a few major harmonic terms.

Table 4.1 lists the most important of these constituents, and gives the appropriate values of s , h , p , N and p' and the corresponding periods and angular speeds. The amplitudes are all given relative to $M_2 = 1.0000$. If the coefficient ψ is evaluated separately, the M_2 amplitude is 0.9081 and the principal solar semi-diurnal harmonic amplitude is 0.4229. Because only the relative coefficients are of further interest, the normalisation to $H_{M_2} = 1.000$ is more convenient. The different latitude variations for the three species are given in Equation 3.12. The spectrum of tidal harmonics may be plotted for each species, as shown in Figure 4.1, to illustrate the importance of

a few major tidal harmonics and their distribution into groups.

At this stage it is useful to reassure ourselves that further development of the Equilibrium Tide will be relevant for subsequent tidal analysis. Figure 4.2 shows the relationships between the Equilibrium Tide amplitudes and phases, in the diurnal and semidiurnal species, and those obtained by harmonic analysis of observations at for the principal constituents of the two main tidal species. The values are for Brooklyn Bridge, New York; San Francisco; and Honolulu, Hawaii. It confirms that the relationships are generally similar for the phases and amplitudes of constituents of similar angular speed. The fitted lines are either straight or first-degree polynomials. We shall return to this similarity of tidal characteristics for close frequencies in Section 4.3.1.

The values of s , h , p , N and p' at any time are given in Table 4.2. Times are calculated from noon on 1 January 2000. The speeds are given as a linear approximation. Small secular changes [11] in the rates of increase of these angular speeds, involving terms in T^2 , are not given. The 0.5 arises because the constants in the five equations refer to midday on 1 January, midday being the start of the astronomical day. These equations, which are linear in time, will be adequate for most tidal work during the twenty-first century. The rates of increase of these arguments are the angular speeds ω_2 , ω_3 , ω_4 , ω_5 and ω_6 given in Table 3.2. In Table 4.1 the angular speed of each constituent is calculated using Equation 4.1, where $i_a = 0, 1, 2$, for the long period, diurnal and semidiurnal tides. The values of i_a are said to define the tidal *species*.

The basic astronomical movements that each constituent represents are also given in Table 4.1. The elliptical terms and the declinational terms have already been discussed in a general way in Chapter 3. Variational terms are due to the changes in the Sun's perturbing force on the Moon's motion during a synodic month. Evection is the change in the eccentricity of the Moon's orbit caused by the Sun's gravitational pull.

The energy in these species is modulated by harmonic terms involving ω_2 , ω_3 , ω_4 , ω_5 and ω_6 . Here we use 'energy' rather loosely for the magnitude of the effect; later we can relate it to the square of harmonic amplitude. In the complete expansion i_b varies from -5 to $+5$ and defines the *group* within each *species*. Within each *group* the value of i_c , which also varies from -5 to $+5$ is said to define the *constituent*. In

Table 4.1 The major tidal harmonic constituents (based on Doodson, 1921; Schureman, 1976; and Cartwright and Edden, 1973). The latitude variations are given in Equation 3.12. EDN is the seventh, Extended Doodson Number, the angle in degrees used to adjust sine and cosine terms in the expansions, so they are all positive cosines.

Table 4.1a

	Argument						Period	Speed	Relative coefficient	Origin		
	i_a	i_b	i_c	i_d	i_e	i_f	EDN	σ (°per hour)				
	s	h		p	N	p'	(msd)	f (cpd)		$M_2 = 1.0000$		
S_a	0	0	1	0	0	-1	0	364.96	0.0027	0.0411	0.0127	Solar annual
S_{sa}	0	0	2	0	0	0	0	182.70	0.0055	0.0821	0.0802	Solar semi-annual
M_m	0	1	0	-1	0	0	0	27.55	0.0363	0.5444	0.0909	Lunar monthly
M_f	0	2	0	0	0	0	0	13.66	0.0732	1.0980	0.1723	Lunar semi-monthly

*Strongly enhanced by seasonal climate variations. For this reason the p' argument is ignored in modern tidal analysis (see text and Section 10.4).

Table 4.1b

	Argument						Period	Speed	Relative coefficient	Origin		
	i_a	i_b	i_c	i_d	i_e	i_f	EDN					
	s	h	p		N	p'	(msd)	f (cpd)		$M_2 = 1.0000$		
2Q₁	1	-3	0	2	0	0	270	1.167	0.8570	12.8543	0.0105	Second-order elliptical lunar
σ₁	1	-3	2	0	0	0	270	1.160	0.8618	12.9271	0.0127	Lunar variation
Q₁	1	-2	0	1	0	0	270	1.120	0.8932	13.3987	0.0794	Larger elliptical lunar
ρ₁	1	-2	2	-1	0	0	270	1.113	0.8981	13.4715	0.0151	Larger evectional
O₁	1	-1	0	0	0	0	270	1.076	0.9295	13.9430	0.4151	Principal lunar
	1	0	0	-1	0	0		1.035	0.9658	14.4874	0.0117	Smaller elliptical lunar
M₁	1	0	0	0	0	0	180	1.035	0.9661	14.4920	0.0073	Lunar parallax
	1	0	0	-1	0	0		1.035	0.9664	14.4967	0.0326	Smaller elliptical lunar
χ₁	1	0	2	-1	0	0	0	1.030	0.9713	14.5695	0.0062	Smaller evectional
π₁	1	1	-3	0	0	1	270	1.006	0.9945	14.9179	0.0113	Larger elliptical solar
P₁	1	1	-2	0	0	0	270	1.003	0.9973	14.9589	0.1932	Principal solar

Table 4.1b (cont.)

	Argument						Period	Speed	Relative coefficient	Origin		
S_1	1	1	-1	0	0	0	90	1.000	1.0000	15.0000	0	Radiational
K_1	1	0	0	0	0	0	90	0.997	1.0027	15.0411	0.399	Principal lunar
	1	0	0	0	0	0		0.997	1.0027	15.0411	0.1852	Principal solar
Ψ_1	1	1	1	0	0	-1	270	0.995	1.0055	15.0821	0.0046	Smaller elliptical solar
ϕ_1	1	1	2	0	0	0	270	0.992	1.0082	15.1232	0.0083	Second-order solar
θ_1	1	2	-2	1	0	0	0	0.967	1.0342	15.5126	0.0062	Evectional
J_1	1	2	0	-1	0	0	270	0.962	1.0390	15.5854	0.0326	Elliptic lunar
OO_1	1	3	0	0	0	0	90	0.929	1.0759	16.1391	0.0179	Second-order lunar

All the terms apart from the parallax part of M_1 and the radiational S_1 (see Section 5.5) arise from the effects of lunar and solar declinations. The relative amplitude of the vector combination of the lunar and solar parts of K_1 is 0.5838.

Table 4.1c

	Argument							Period	Speed	Relative coefficient	Origin	
	i_a	i_b	i_c	i_d	i_e	i_f	EDN					
		s	h	p	N	p'		(msd)	f (cpd)		$M_2 = 1.0000$	
$2N_2$	2	-2	0	2	0	0	0	0.538	1.8597	27.8954	0.0253	Second-order elliptical lunar
μ_2	2	-2	2	0	0	0	0	0.536	1.8445	27.9682	0.0306	Variational
N_2	2	-1	0	1	0	0	0	0.527	1.8960	28.4397	0.1915	Larger elliptical lunar
ν_2	2	-1	2	-1	0	0	0	0.526	1.9008	28.5126	0.0364	Larger evectional
M_2	2	0	0	0	0	0	0	0.518	1.9322	28.9841	1	Principal lunar
λ_2	2	1	-2	1	0	0	180	0.509	1.9637	29.4556	0.0074	Smaller evectional
L^2	2	1	0	-1	0	0	180	0.508	1.9686	29.5285	0.0283	Smaller elliptical lunar
	2	1	0	1	0	0		0.508	1.9692	29.5378	0.0071	Smaller elliptical lunar
T_2	2	2	-3	0	0	1	0	0.501	1.9973	29.9589	0.0273	Larger elliptical solar
S_2	2	2	-2	0	0	0	0	0.500	2.0000	30.0000	0.4652	Principal solar
R_2	2	2	-1	0	0	-1	180	0.499	2.0027	30.0411	0.0039	Smaller elliptical solar

Table 4.1c (cont.)

	Argument						Period		Speed	Relative coefficient	Origin	
K_2	2	2	0	0	0	0	0	0.499	2.0055	30.0821	0.0865	Declinational lunar
	2	2	0	0	0	0	0.499	2.0055	30.0821	0.0402	Declinational solar	
M_3	3	0	0	0	0	0	180	0.345	2.8984	43.4761	0.0131	Lunar parallax

The relative amplitude of the vector combination of the lunar and solar parts of K_2 is 0.1266.

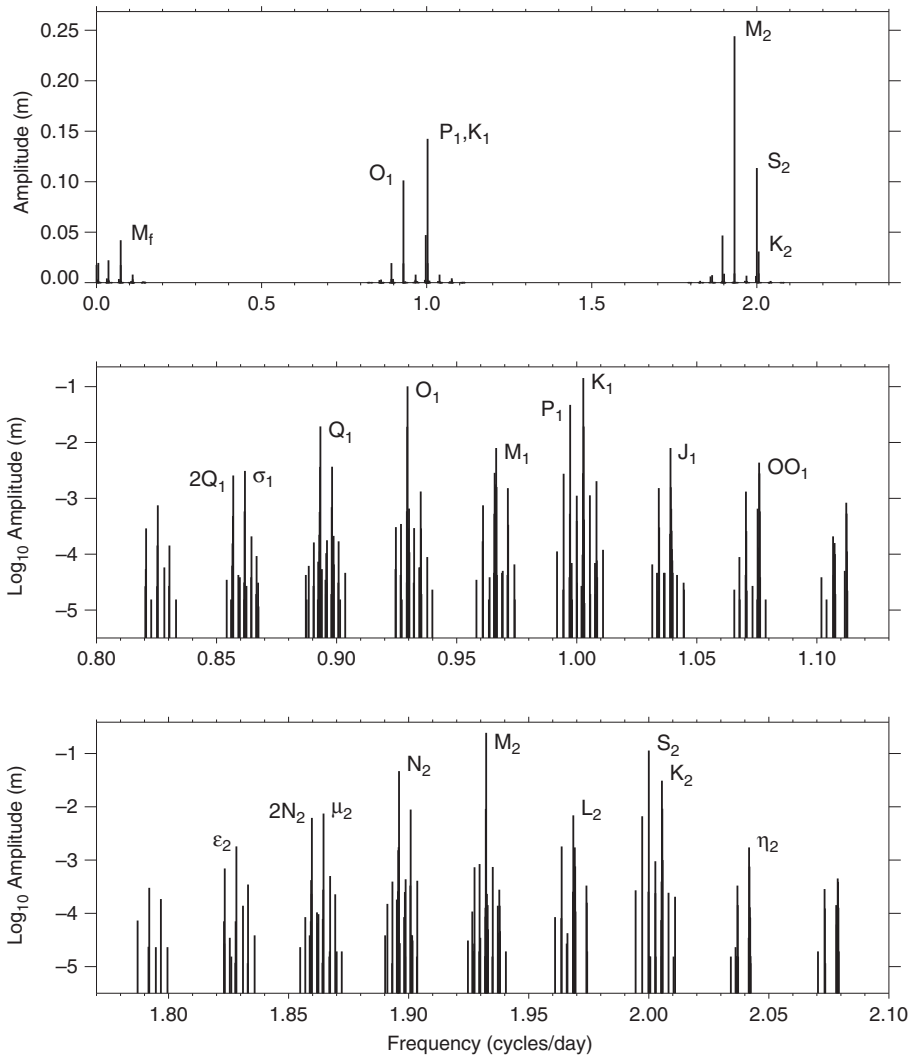


Figure 4.1 The Equilibrium Tide consists of a series of partial tides at discrete periods or frequencies. This shows the pattern of the periods found in the diurnal and semidiurnal tidal species, based on the expansion of Cartwright and Edden. Each individual line represents a tidal constituent. Note the clustering of constituents into groups within each species. The height of the lines indicates the relative amplitude of the constituents, but the scales, on a logarithmic axis for the bottom two plots, are compressed.

general, analysis of a month of data can only determine independently those terms that are separated by at least one unit of ω_2 (that is $\partial s/\partial t$); $\Delta\sigma = 0.5490^\circ/\text{h}$. Similarly, analysis of a year of data can determine harmonic constituents that differ by one unit in ω_3 ($\partial h/\partial t$); $\Delta\sigma = 0.0411^\circ/\text{h}$. The full set of integers i_a to i_f is sometimes said to define a *harmonic*, but this word is also more generally used to describe any term determined by a harmonic analysis.

Table 4.2 The orbital elements used for harmonic expressions of the Equilibrium Tide

Mean longitude of the Moon	$s = 218.32 + 481267.88^\circ \times T$
Mean longitude of the Sun	$h = 280.47 + 36000.77^\circ \times T$
Longitude of lunar perigee	$p = 83.35 + 4069.01^\circ \times T$
Longitude of lunar ascending node	$N = 125.04 - 1934.14^\circ \times T$
Longitude of perihelion	$p' = 282.94 + 1.72^\circ \times T$
$T = \frac{(\text{Time}-0.5)}{36525}$	

T is in units of a Julian century (36,525 mean solar days). Time is measured in days from 0 hours UT on 0/1 January 2000. The 0.5 arises because the constants in the five equations refer to midday on 1 January.

Note that our Equation 4.1 defines species in terms of ω_1 lunar speeds, rather than in terms of ω_0 , the time in solar days. Times in lunar days are favoured by many writers [5, 9, 10]; the Doodson coding for M_2 is then (2 0 0 0 0). The alternative [3], with time in solar days, has (2 -2 2 0 0 0) for M_2 because Schureman uses ω_0 instead of ω_1 . Conversion between the two systems is straightforward by using the relationship $\omega_1 = \omega_0 - \omega_2 + \omega_3$: it shows that Schureman's values of i_b will be one unit less than ours for the diurnal species, and two units less for the semidiurnal species. Also, his values of i_c are one unit more than ours for the diurnal species and two units more for the semidiurnal species. The conversion to the system in solar days is an essential step in the preparation of predictions in solar time (see Table 4.10). In Doodson's tabulations he avoided negative values of i by adding five units to each so that his M_2 became (2 5 5 5 5).

There is an extra, seventh number, sometimes called the Extended Doodson Number (EDN in Table 4.1 [12]), that takes account of the fact that the full expansion of the Equilibrium Tide includes some negative cosine terms and some sine terms. Equation 4.3 shows this for the third term, involving an additional 180° in the phase. This number adjusts the phases by zero, 90° , 180° or 270° , so that the cosine terms in Equation 4.5 are all positive. Specifically, in the expansions of the Equilibrium Tide, the time-dependent expression is described by a cosine or sine depending on whether the sum

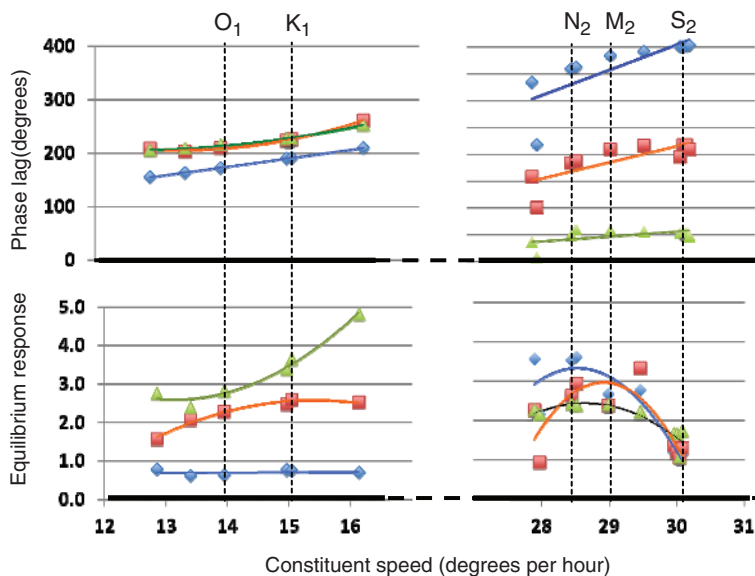


Figure 4.2 The ratios $\left(\frac{\text{Constituent amplitude}}{\text{Equilibrium amplitude}}\right)$, and the phase lags on the Equilibrium Tide at the Greenwich meridian for the principal constituents of the two main tidal species. The values are for Brooklyn Bridge, New York (blue); San Francisco (orange); and Honolulu (green). The sequence of diurnal constituents is: $2Q_1; Q_1; O_1; P_1; K_1; OO_1$. For the semidiurnal constituents: $2N_2; Mu_2; N_2; Nu_2; M_2; Lam_2; T_2; S_2; R_2; K_2$. Note the smooth curves across frequencies for each species, at the individual sites.

$(m + n)$ is even or odd respectively, m being 0, 1, 2 for the long period, diurnal and semidiurnal bands and n being the spherical harmonic degree in the expansion of the potential that the particular term occurs (n being 2 or 3 for the lunar potential and 2 only for the solar potential). For example, to describe the total tide as a harmonic expansion of cosines only (Equation 4.5), the sines of Cartwright and Tayler [10] are expressed as cosines but with an additional phase angle (90° or 270°).

The traditional alphameric labelling for the individual larger harmonics has been developed to include all the terms in our tables, but the full expansion contains hundreds of smaller unnamed terms. Strictly, these labels apply only for terms defined by the full six integers i_a to i_f , but they are also applied to the constituents determined by a finite length of data such as a year (i_a to i_c). The use of a suffix to denote the species is standard for all except the long period tides, where the zero is usually omitted.

In addition to the harmonics derived by expansion of the astronomical forces, there are a few non-astronomical harmonic constituents that are primarily due to periodic meteorological forcing, notably the annual and semi-annual tides and the S_1 diurnal tide. These are have been called the *radiational* tides because of their relationship to the cycles in direct solar radiation.

The largest term in the long period species is usually S_a , the annual variation in mean sea level, which has an angular speed of $(\omega_3 - \omega_6)$; this term exists, but is very small in the gravitational forcing. The large observed annual variations of level are due to seasonal climatological effects. These seasonal effects have a speed of ω_3 and are of course indistinguishable from the gravitational tide in a harmonic analysis. It is standard practice to analyse for the radiational S_a term of speed ω_3 ; although the frequency difference is insignificant, it is vital to define the phase reference consistently. The gravitational semi-annual tide S_{sa} ($2\omega_3$) is larger than the annual gravitational tide; the S_a observed tide also includes seasonal effects. These long period tides are discussed in detail in Chapter 10. The terms M_m ($\omega_2 - \omega_4$) and M_f ($2\omega_2$), the lunar monthly and fortnightly tides, are the lunar equivalent to S_a and S_{sa} , but there are no extra radiational effects at these periods.

In the diurnal species all but two small terms arise directly from the effects of lunar and solar declination. These diurnal terms have a tendency to occur in pairs

that balance each other when the lunar or solar declination and hence the diurnal component amplitude is zero, as shown in Figure 1.2a for March 2043. The lunar declination is represented by the two terms O_1 ($\omega_1 - \omega_2$) and K_1 ($\omega_1 + \omega_2$), which are in phase every 13.66 days. The K_1 ($\omega_1 + \omega_2 = \omega_0 + \omega_3$) term also contains a part due to the solar declination, which balances the P_1 solar term ($\omega_0 - \omega_3$) at intervals of 182.55 days, the times of spring and autumn equinoxes when the solar declination d_s is zero. The constituents Q_1 ($\omega_1 - 2\omega_2 + \omega_4$), J_1 ($\omega_1 + 2\omega_2 - \omega_4$) and parts of the M_1 ($\omega_1 \pm \omega_4$) constituent are due to the changing lunar distance R_l ($\omega_1 \pm \omega_4$).

The small M_1 term is complicated because it contains three factors: two related to the lunar declination and varying lunar distance, and a third part that is an exact sub-harmonic of the principal semidiurnal lunar tide. Separation of these terms theoretically requires 8.85 years of data according to the Rayleigh criteria discussed in Section 4.2.5. The exact sub-harmonic M_1 (ω_1), is derived by expanding the $P_3(\cos \phi)$ term in Equation 3.7.¹ If the orbit of the Moon were permanently in the plane of the equator none of the declinational diurnal tides would occur, but this small lunar diurnal tide would remain. For practical purposes it is too small to be important, but its determination is of some analytical interest [13].

Turning to another small but interesting constituent, the gravitational tide-producing force at S_1 is negligible, but the observed tides contain significant energy at this frequency because of the diurnal meteorological forcing, and this radiational S_1 tide may have amplitudes of a few centimetres in extreme cases (see Section 5.5). Temperature-sensitive sea-level recorders have also been known to introduce a spurious S_1 term into the data. In older records, an incorrectly mounted chart drum that rotates once every 24 hours may also introduce a spurious S_1 value.

The semidiurnal species is dominated by the principal semidiurnal lunar tide M_2 ($2\omega_0$) and the principal semidiurnal solar tide S_2 ($2\omega_1$), which are in phase at spring tides, every 14.76 days. Of the two main terms that represent the movement of the Moon in its elliptical orbit, N_2 ($2\omega_1 - \omega_2 + \omega_4$), is much bigger than L_2 ($2\omega_1 + \omega_2 - \omega_4$) as already discussed. The two terms

¹ Physically it represents the fact that the diameter of the Earth is not negligible compared with the lunar distance, so that the double bulge is not quite symmetrical.

that similarly represent the effects of the varying solar distance show the same asymmetry (the calculations above can be repeated to show this) with the T_2 term ($2\omega_0 - \omega_3 + \omega_6$) being much larger than the term at the higher frequency, R_2 ($2\omega_0 + \omega_3 - \omega_6$). The K_2 term [$2(\omega_0 + \omega_2) = 2(\omega_0 + \omega_3)$], represents the lunar and the solar declination effects. Also shown in Table 4.1c is the small third-diurnal harmonic M_3 ($3\omega_1$) which, like the (ω_1) part of the M_1 term, arises from the asymmetry of the semidiurnal tidal bulges; this term is also obtained by expanding the $P_3(\cos \phi)$ term in Equation 3.7.

4.2.2 Nodal factors

Certain lunar constituents, notably L_2 , are affected by the 8.85-year cycle. The L_2 constituent is interesting because it contains two terms whose angular speeds differ by ($2\omega_4$). These two terms cannot be separated from analysis of only a year of data; because of this special methods must be used to represent the slowly changing amplitude of the total L_2 constituent.

All the lunar constituents are affected by the 18.61-year nodal cycle. Figure 4.3 shows the 18.61-year cycle in the semidiurnal tides at Newlyn, with standard deviations changing by a small percentage.

These modulations, which cannot be separately determined from a year of data, must be represented in an analysis in some way. In the full harmonic expansion they appear as terms separated from the main term by angular speeds:

$$i_d\omega_4; i_e\omega_5$$

The terms that are separated by $i_f\omega_6$, which change over 21,000 years, may be considered constant for all practical purposes. The modulations are represented in harmonic expansion by small adjustment factors f and u . Each constituent is written:

$$H_n f_n \cos [\sigma_n t - g_n + (V_n + u_n)] \quad (4.4)$$

where V_n is the phase angle at the time zero, shown in Table 4.2. The nodal terms are:

f the nodal amplitude factor

u the nodal angle

both of which are functions of N and sometimes of p . The nodal factor and the nodal angle are 1.0 and 0.0 for solar constituents.

The application of nodal terms can be illustrated by the variation of M_2 . If yearly analyses are made throughout a nodal period of 18.61 years, without

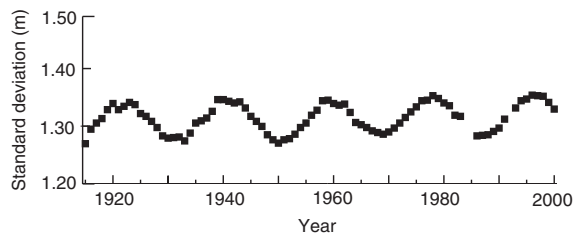


Figure 4.3 The amplitude of the semidiurnal tides varies over an 18.61-year period due to changes in the amplitude of the lunar declination. This figure shows the standard deviation in the observed sea-level variations at Newlyn: the 18.61-year modulations are evident. The semidiurnal tides are greatest when the declination range is least.

adjustment, the value of the M_2 amplitude will increase and decrease from the mean value by about 3.7 per cent. The full harmonic expansion of the tidal potential confirms that in addition to the main M_2 term ($2\omega_1$) there are several other nearby terms; the only significant one has angular speed ($2\omega_1 + \omega_5$) and a relative amplitude of -0.0373 , the negative coefficient signifying that in the full expansion this term appears as $-\cos(2\omega_1 + \omega_5)t$.

Writing the total constituent as:

$$H_{M_2} \cos(2\omega_1)t - \alpha H_{M_2} \cos(2\omega_1 + \omega_5)t$$

we have:

$$\begin{aligned} H_{M_2} [(1 - \alpha \cos \omega_5 t) \cos 2\omega_1 t + \alpha \sin \omega_5 t \sin 2\omega_1 t] \\ = H_{M_2} [f \cos u \cos 2\omega_1 t - f \sin u \sin 2\omega_1 t] \\ = H_{M_2} [f \cos(2\omega_1 t + u)] \end{aligned}$$

where:

$$f \cos u = (1 - \alpha \cos \omega_5 t)$$

$$f \sin u = (-\alpha \sin \omega_5 t)$$

and hence for small values of α we can ignore α^2 :

$$f^2 = 1 - 2\alpha \cos \omega_5 t + \alpha^2$$

and so $f \approx 1 - \alpha \cos \omega_5 t = 1 - 0.0373 \cos \omega_5 t$ and

$$\tan u = \frac{-\alpha \sin \omega_5 t}{1 - \alpha \cos \omega_5 t}$$

(where α is in radians)

$$u \approx -\alpha \sin \omega_5 t = -2.1^\circ \sin \omega_5 t$$

The phase of the nodal angle $\omega_5 t$ is measured from the time when the ascending lunar node, at which the Moon crosses the ecliptic from south to north, is at

Table 4.3 Basic nodal modulation terms for the major lunar tidal constituents

	f	u
M_m	$1.000-0.130 \cos(N)$	0.0°
M_f	$1.043-0.414 \cos(N)$	$-23.7^\circ \sin(N)$
Q_1, O_1	$1.009-0.187 \cos(N)$	$10.8^\circ \sin(N)$
K_1	$1.006-0.115 \cos(N)$	$-8.9^\circ \sin(N)$
$2N_2, \mu_2,$ ν_2, N_n, M_2	$1.000-0.037 \cos(N)$	$-2.1^\circ \sin(N)$
K_2	$1.024-0.286 \cos(N)$	$-17.7^\circ \sin(N)$

$N = 0$ March 1969, November 1987, June 2006, April 2025, September 2043, . . . , at which times the diurnal terms have maximum amplitudes, whereas M_2 is a minimum. M_2 has maximum Equilibrium amplitudes in July 1978, March 1997, October 2015, March 2034, March 2053, . . .

the First Point of Aries (Y) (see Figure 3.9). Around this time the excursions of the Moon north and south of the equator reach maximum declinations of $28^\circ 36'$, and the f value for M_2 has a minimum value of 0.963. After an interval of 9.3 years, when the Moon has minimum declination excursions of $18^\circ 18'$, the M_2 value reaches its maximum, 1.037. If the nodal adjustments were not made, analyses of a year of data made at the time of maximum declinations would give values of H_{M_2} that were 7.5 per cent lower than those that would be obtained 9.3 years later.

The factors that determine f and u for the major lunar constituents are given in Table 4.3. For the constituents K_1 and K_2 only the lunar part has a nodal modulation and this has been allowed for in the development. The terms that represent the changes in declination have the largest nodal variations. The O_1 amplitude varies by 18.7 per cent, the K_1 amplitude by 11.5 per cent and the K_2 amplitude by 28.6 per cent. Small terms in these expansions, involving arguments of $2N$ and $3N$, have been omitted.

For the constituents M_1 and L_2 , the arguments also involve the longitude of lunar perigee, p , which has an 8.85-year cycle. Some authorities make more elaborate expansions of the long-term modulations and include the effects of p in the factors for other constituents; these are called j and ν to distinguish them from the f and u factors that are usually used. Older publications used to include tables of f and u for each constituent and for each year, but modern computing procedures make this practice obsolete.

4.2.3 Shallow-water terms

In shallow water the progression of a tidal wave is modified by bottom friction and other physical processes that depend on the square or higher powers of the tidal amplitude itself. Figure 1.2a shows the presence of strong higher harmonics at Courtown, on the east coast of Ireland; the double high and double low waters are due to non-linear shallow-water effects. These distortions can also be expressed as simple harmonic constituents with angular speeds that are multiples, sums or differences of the speeds of the astronomical constituents listed in Table 4.1. To illustrate this, consider that shallow-water effects are proportional to the square of the tidal water level through a spring–neap cycle:

$$\begin{aligned} & \kappa_2 [H_{M_2} \cos 2\omega_1 t + H_{S_2} \cos 2\omega_0 t]^2 \\ &= \kappa_2 \left[\frac{1}{2} H_{M_2}^2 + \frac{1}{2} H_{S_2}^2 + \frac{1}{2} H_{M_2}^2 \cos 4\omega_1 t + \frac{1}{2} H_{S_2}^2 \cos 4\omega_0 t \right. \\ & \quad \left. + H_{M_2} H_{S_2} \cos 2(\omega_1 + \omega_0)t + H_{M_2} H_{S_2} \cos 2(\omega_0 - \omega_1)t \right]^2 \end{aligned}$$

where κ_2 is a small constant of proportionality for square-law interaction.

The relationship involving the square of the amplitude has produced additional harmonics at $4\omega_1 t$ and $4\omega_0 t$, which are called M_4 and S_4 because their frequencies appear in the fourth-diurnal species. The term at speed $2(\omega_1 + \omega_0)t$, also in the fourth-diurnal species, is called MS_4 to show that it originates from a combination of M_2 and S_2 . The interaction has also produced a change in the mean sea level, represented by the terms in $H_{M_2}^2$ and $H_{S_2}^2$, and a long period harmonic variation with a speed equal to the difference in the speeds of the interacting constituents, $2(\omega_0 - \omega_1)$, called MS_6 , which has a period of 14.77 days, exactly the same as the period of the spring–neap modulations on the tidal amplitudes. For the Equilibrium Tide, the additional terms MS_6 , M_4 , MS_4 , and S_4 are in the ratios: 38:41:38:09.

This development may be continued to include interactions between other tidal harmonic constituents, and may also be extended to higher powers of interaction. Suppose, for example, that the interactive effects are related to the cube of the elevations, and that only the M_2 constituent is present:

$$\begin{aligned} & \kappa_3 [H_{M_2} \cos 2\omega_1 t]^3 \\ &= \frac{1}{4} \kappa_3 [H_{M_2}^3 (3 \cos 2\omega_1 t + \cos 6\omega_1 t)] \end{aligned}$$

Table 4.4 Some of the more important shallow-water harmonic tidal constituents

	Generated by	Angular speed	°per hour	Nodal factor (f)	Nodal factor (u)	
Long period						
	* MS_f	M_2, S_2	$S_2 - M_2$	1.0159	$f(M_2)$	$u(M_2)$
Diurnal						
	MP_1	M_2, P_1	$M_2 - P_1$	14.0252	$f(M_2)$	$u(M_2)$
	SO_1	S_2, O_1	$S_2 - O_1$	16.0570	$f(O_1)$	$u(O_2)$
Semidiurnal						
	MNS_2	M_2, S_2, N_2	$M_2 + S_2 - N_2$	27.4238	$\hat{P}(M_2)$	$2u(M_2)$
	* $2MS_2$	M_2, S_2	$2M_2 - S_2$	27.9682	$f(M_2)$	$u(M_2)$
	MSN_2	M_2, S_2, N_2	$M_2 + S_2 - N_2$	30.5444	$\hat{P}(M_2)$	$2u(M_2)$
	$2SM_2$	M_2, S_2		31.0159	$f(M_2)$	$u(M_2)$
Third-diurnal						
	MO_3	MO_3	$M_2 + O_1$	42.9271	$f(M_2) \times f(O_1)$	$u(M_2) + u(O_1)$
	MK_3	M_2, K_1	$M_2 + K_1$	44.0252	$f(M_2) \times f(K_1)$	$u(M_2) + u(K_1)$
Fourth-diurnal						
	MN_4	M_2, N_2	$M_2 + N_2$	57.4238	$\hat{P}(M_2)$	$2u(M_2)$
	M_4	M_2	$M_2 + M_2$	57.9682	$\hat{P}(M_2)$	$2u(M_2)$
	MS_4	M_2, S_2	$M_2 + S_2$	58.9841	$f(M_2)$	$u(M_2)$
	MK_4	M_2, K_2	$M_2 + K_2$	59.0662	$f(M_2) \times f(K_2)$	$u(M_2) + u(K_2)$
	S_4	S_2	$S_2 + S_2$	60.0000	1.0	0
Sixth-diurnal						
	M_6	M_2	$M_2 + M_2 + M_2$	86.9523	$\hat{P}(M_2)$	$3u(M_2)$
	$2MS_6$	M_2, S_2	$2M_2 + S_2$	87.9682	$\hat{P}(M_2)$	$2u(M_2)$
Eighth-diurnal						
	M_8	M_2	$4M_2$	115.9364	$\hat{P}^A(M_2)$	$4u(M_2)$

where κ_3 is a small constant of proportionality for triple interaction.

Two non-linear terms are present. The first is at exactly the M_2 constituent speed $2\omega_1$, and the second is in the sixth-diurnal species. This term, which has a speed $6\omega_1$, three times the speed of M_2 , is called M_6 .

In practice a whole range of extra constituents is necessary to represent distortions in shallow water. Some of the more important of these are given in Table 4.4.

The nodal factors for shallow-water constituents, f and u , are assumed to follow the factors for the constituents involved in their generation. For example:

$$f(M_4) = f(M_2) \times f(M_2)$$

$$u(M_4) = 2u(M_2)$$

Clearly the shallow-water part of M_2 , generated by cubic interactions, will have a greater nodal variation than that of the dominant astronomical part. In Table 4.4, the terms marked with asterisks are at the same speeds as pure astronomical constituents; $2MS_6$ is at the same speed as μ_2 , and there is a weak astronomical harmonic constituent that coincides with MS_f .

Two terms that have not been included in Table 4.4 are sometimes necessary to represent a seasonal modulation in the M_2 constituent. This modulation, which is characteristic of M_2 tides in shallow-water regions, may be thought of as an interaction between M_2 and S_a , but its physical origin is more likely to be due to seasonal changes in the weather and surges (Chapter 7), and river discharge, and their effects on the tides. These two terms are:

$$\begin{aligned} \text{MA}_2 \quad 2\omega_1 - \omega_3 \quad \sigma &= 28.9430^\circ \text{ per hour} \\ \text{MB}_2 \quad 2\omega_1 + \omega_3 \quad \sigma &= 29.0252^\circ \text{ per hour} \end{aligned}$$

Harmonic analyses of observed tidal levels show that shallow-water terms in the fourth, sixth and higher even-order bands are usually more important than the terms in the odd-order bands (third, fifth, etc.). However, the relative importance of the shallow-water terms and the number required to represent the observed tidal variations varies considerably from region to region, depending on the physics, and on the severity of the interaction, as we discuss in [Chapter 6](#).

4.2.4 Least-squares fitting procedures

In the harmonic method of analysis we fit a tidal function:

$$T(t) = Z_0 + \sum_N H_n f_n \cos [\sigma_n t - g_n + (V_n + u_n)] \quad (4.5)$$

where the unknown parameters are Z_0 and the series (H_n, g_n). The fitting is adjusted so that $\sum R^2(t)$, the square of the difference between the observed and computed tidal levels:

$$R(t) = O(t) - T(t)$$

when summed over all the observed values, has its minimum value. The f_n and u_n are the nodal adjustments and the terms $\sigma_n t$ and V_n together determine the phase angle of the Equilibrium constituent. V_n is the Equilibrium phase angle, sometimes called the astronomical argument, for the constituent at the arbitrary time origin. The accepted convention is to take V_n as for the Greenwich meridian, and to take the time, t , in the standard time zone of the station concerned (see [Section 4.5](#) for conversion procedures).

It is necessary to emphasise again that to represent the tide as a sum of only positive cosines, as in [Equation 4.4](#), the parameters V_n may involve the additional 270° or 90° angles discussed above. If these are ignored in any empirical analysis of tide gauge data, then incorrect phase lags g_n will be obtained. Software packages use various different conventions for defining astronomical arguments. As discussed, the arguments for the seasonal terms S_a and S_{sa} are defined in some tidal software packages as they appear in the tidal potential, whereas in other packages their phases are defined to be consistent with their climatological forcing. Amplitudes and phase lags derived from one package should never be employed in a different package for tidal prediction.

An older method, now obsolete for analysis and prediction, calculated the phase lags of the harmonic constituents relative to the Equilibrium constituent transit at the station longitude; these phases were termed the ‘kappa’ phases and were denoted by κ . The main disadvantage of working in terms of local time was that for an ocean as a whole, which spans several time zones, the harmonic constants were difficult to interpret physically. The kappa notation is still widely used for analyses of Earth tides.

The least-squares fitting procedure involves matrix algebra, which is outside the scope of this account (standard subroutines are available in mathematical software packages), but schematically the equations may be written here specifically for each constituent frequency:

$$\begin{aligned} &[\text{observed level}] \\ &\quad \textit{known} \\ &= [\text{Equilibrium tide}] \times [\text{complex scaling factors}] \\ &\quad \textit{known} \qquad \qquad \qquad \textit{calculated} \end{aligned} \quad (4.6)$$

The tidal variation is represented by a finite number of N harmonic constituents, depending on the length and quality of the observed data. Typically, for a year of data sixty constituents, $N = 60$, will suffice, but in shallow water more than a hundred constituents may be necessary. The choice of which constituents to include depends on the relative amplitudes in the expansion of the astronomical forcing ([Table 4.1](#) and [Figure 4.1](#)). However, the Equilibrium amplitudes are not themselves involved in the computations.

The least-squares fitting is now performed rapidly by computer matrix inversion. Earlier versions of the harmonic method used tabulated filters to facilitate manual calculations of the constituents. In these older filtering techniques, gaps in the data were likely to cause difficulties, and interpolation was necessary. To overcome some of these difficulties, graphical analysis techniques were developed, which allowed the determination of many harmonic constituents, and had the virtue of allowing the analyst to understand the limitations of the data.

Least-squares fitting has several advantages over the older methods:

- Gaps in the data are permissible. The fitting is confined to the times when observations were taken. Analyses are possible where only daylight readings are available, or where the bottom of the range is missing [14]. However, care is necessary to

avoid energy leaking from one harmonic to another.

- Any length of data may be treated. Usually complete months or years are analysed.
- No assumptions are made about data outside the interval to which the fit is made.
- Transient phenomena are eliminated – only variations with a coherent phase are picked out.
- Fitting can be applied to any suitable observing interval (usually an hour, or 10 or 6 minutes).
- With care, where the tidal signal is dominant, resolving constituents closer than their synodic period can be attempted.

4.2.5 Choice of constituents: related constituents

The selection of the values of σ_n whose harmonic amplitudes and phases are to be determined in an analysis is sometimes thought of as a black art. However, certain basic rules exist. In general, the longer the period of data to be included in the analysis, the greater the number of constituents that may be independently determined.

One criterion often used is due to Rayleigh, which requires that only constituents that are separated by at least a complete period from their neighbouring constituents over the length of data available should be included. Thus, to determine M_2 and S_2 independently in an analysis requires:

$$\begin{aligned} & 360 / (30.00 - 28.98) \text{ hours} \\ & = 14.77 \text{ days, a complete spring-neap cycle} \end{aligned}$$

To separate S_2 from K_2 requires 182.6 days. This minimum length of data necessary to separate a pair of constituents is called their *synodic period*. It has been argued that the Rayleigh criterion is unnecessarily restrictive where instrumental noise and the background meteorological noise are low. In practice, the Rayleigh criterion is a good guide for tidal analyses of continental shelf data from middle and high latitudes, but finer resolution is feasible in ideal conditions such as tropical oceanic sites. Hence, periods shorter than the theoretical requirement for the Raleigh criteria for separating different tidal constituents can give useable results if background noise levels are low, but should not normally be relied on.

When choosing which values of σ_n to include, scrutiny of tidal analyses from a nearby Reference Station is helpful. Where the data length is too short

to separate two important constituents (separation of K_2 and S_2 is an obvious example), it is usual to relate the amplitude ratio and phase lag of the weaker term to the amplitude and phase of the stronger term. If a local Reference Station is not available for specifying these relationships, then their relationships in the astronomical forcing function, the Equilibrium Tide, may be used:

$$\begin{aligned} \alpha_E &= \frac{\text{related constituent amplitude}}{\text{reference constituent amplitude}} \\ \beta_E &= \text{related constituent phase} \\ &\quad - \text{reference constituent phase} \end{aligned} \quad (4.7)$$

Both these terms are included in the tidal analysis constraints. The validity of this approach is confirmed by the relatively smooth curves in Figure 4.2. In the case of S_2 and the weaker K_2 , the Equilibrium Tide suggests $\alpha_E = 0.27$, and there is no difference in the phase lags. Table 4.5 gives a set of eight related constituents and the Equilibrium relationship that are effective for analyses of 29 days of data around the northwest European shelf, when included with the independently determined constituents listed alongside. As explained, for analyses of a year of data, sets of 60 or even 100 constituents are normally used. Analyses of 19 years of data may legitimately require more than 300 independent constituents.

Any use of related constituents from a nearby station assumes that these relationships have some regional stability. The use of an Equilibrium relationship assumes that the ocean response to forcing at the different frequencies is the same, which is generally valid for ω_4, ω_5 , the fine nodal frequency differences. For *constituents* whose speeds are separated by the annual factor ω_3 or for *groups* separated by the monthly factor ω_2 the assumption needs more careful justification, particularly where there are extensive shallow-water distortions (see Section 4.2.3). The ocean responses to the astronomical forcing from different species are quite different, as shown in Figure 4.2, and as we shall discuss in Section 4.3.

In the process of least-squares harmonic analysis, it is also possible to remove a constituent whose regional characteristics are widespread, and known, before fitting for the independent constituents. The most probable constituents for removal are the long period harmonics S_a and S_{sa} , and possibly monthly harmonics. This input can improve the reliability of the final analysis.

It is also necessary to observe another basic rule of time series analysis, related to the frequency at which

Table 4.5 A basic set of 27 independent and 8 related tidal constituents for the analysis of data, for a mainly semidiurnal tidal regime

Independent constituents				
	Mean sea level	Z_0		
	Long period	M_m, MS_f		
	Diurnal	$Q_1, O_1, M_1, K_1, J_1, OO_1$		
	Semidiurnal	$u_2, N_2, M_2, L_2, S_2, 2SM_2$		
	Third-diurnal	MO_3, M_3, MK_3		
	Fourth-diurnal	MN_4, M_4, SN_4, MS_4		
	Sixth-diurnal	$2MN_6, M_6, MSN_6, 2QMS_6, 2SM_6$		
Related constituents				
		Related to	Equilibrium relationships	
			α_E	β_E
	π_1	K_1	0.019	0.0
	P_1	K_1	0.331	0.0
	ψ_1	K_1	0.008	0.0
	ϕ_1	K_1	0.014	0.0
	$2N_2$	N_2	0.133	0.0
	v_2	N_2	0.194	0.0
	T_2	S_2	0.059	0.0
	K_2	S_2	0.272	0.0

observations are made. The Nyquist criterion states that only terms having a period longer than twice the sampling interval can be resolved. In the case of hourly data sampling, this shortest period is 2 hours, so that resolution of M_{12} would just be possible (but in theory S_{12} would not). Obviously, more frequent sampling can resolve much higher frequencies. In practice this is not a severe restriction except in very shallow water, where sampling more often than once an hour, say every 10 or 6 minutes, is necessary to represent the full tidal curves. This is especially so at low water where the tidal levels turn rapidly (Figure 6.13).

4.2.6 Harmonic equivalents of some non-harmonic terms

The harmonic constituents can be related to some of the common non-harmonic terms used to describe the tides, as defined in Section 1.4. Very detailed relationships are developed in some seldom-accessed older publications [2, 15]. Appendix C gives more details,

but here we develop some basic relationships. The most useful of these non-harmonic terms describes the spring–neap modulations of the tidal range which, in the absence of shallow-water distortions are given by the combination of the principal lunar and principal solar semidiurnal harmonics:

$$Z_0 + H_{M_2} \cos(2\sigma_1 t - g_{M_2}) + H_{S_2} \cos(2\sigma_0 t - g_{S_2})$$

where the time is now taken for convenience as zero at syzygy, when the Moon, Earth and Sun are in line at new or full Moon. This is when the gravitational forcing reaches its maximum value. We also note that $H_{M_2} > H_{S_2}$ and $\sigma_0 > \sigma_1$. If we develop similar trigonometrical arguments to those used for the nodal effects in Section 4.2.2, and rewrite:

$$2\sigma_1 t - g_{S_2} = 2\sigma_1 t - g_{M_2} - \theta$$

where:

$$\theta = 2(\sigma_1 - \sigma_0)t + (g_{S_2} - g_{M_2})$$

the combined level becomes:

$$\begin{aligned} Z_0 + (H_{M_2} + H_{S_2} \cos \theta) \cos(2\sigma_1 t - g_{M_2}) \\ + H_{S_2} \sin \theta \sin(2\sigma_1 t - g_{M_2}) \\ = Z_0 + \alpha' \cos(2\sigma_1 t - g_{M_2} - \beta') \end{aligned} \quad (4.8)$$

where:

$$\begin{aligned} \alpha' &= (H_{M_2}^2 + 2H_{M_2}H_{S_2} \cos \theta + H_{S_2}^2)^{\frac{1}{2}} \\ \tan \beta' &= \frac{H_{S_2} \sin \theta}{(H_{M_2} + H_{S_2} \cos \theta)} \end{aligned}$$

The maximum values of the combined amplitudes are:

$$\begin{aligned} \text{Mean High Water Springs} &= Z_0 + (H_{M_2} + H_{S_2}) \\ \text{Mean Low Water Springs} &= Z_0 - (H_{M_2} + H_{S_2}) \end{aligned}$$

when $\cos \theta = 1$.

The minimum values are:

$$\begin{aligned} \text{Mean High Water Neaps} &= Z_0 + (H_{M_2} - H_{S_2}) \\ \text{Mean Low Water Neaps} &= Z_0 - (H_{M_2} - H_{S_2}) \end{aligned}$$

when $\cos \theta = -1$.

Clearly, from this it follows that the Mean Spring Range is $2(H_{M_2} + H_{S_2})$, and Mean Neap Range is $2(H_{M_2} - H_{S_2})$.

However, and perhaps counterintuitively, over a spring-neap cycle of just M_2 and S_2 , the mean of the high waters and of the low waters is in excess of $\pm H_{M_2}$ by about 6 per cent. This result is explained theoretically in [Appendix C](#).

In [Equation 4.8](#), the lagging and leading of semi-diurnal high waters on a regular 12 hours 25 minutes interval, as discussed in [Section 3.4.2](#), is represented by the variable phase, β' . Substituting Equilibrium Tide values in the $\tan \beta'$ term gives a maximum excursion leading or lagging of 25° , equivalent to 51 minutes, which agrees with [Figure 3.14](#).

The time of maximum tidal ranges after new or full Moon is given when:

$$\theta = 2(\sigma_1 - \sigma_0)t + (g_{S_2} - g_{M_2})$$

that is:

$$t_{\max} = \frac{(g_{S_2} - g_{M_2})}{2(\sigma_1 - \sigma_0)} \quad (4.9)$$

This lag usually has a positive value of several hours. It is the previously defined age of the tide. From the data used in [Figure 4.2](#), the semi-diurnal age of the tide at Brooklyn Bridge, New York, is 18 hours, and 8 hours at San Francisco. On average globally this age is about

2 days. An age for the diurnal tides can be similarly defined:

$$t_{\max} = \frac{(g_{K_1} - g_{O_1})}{2\sigma_2}$$

which gives diurnal ages of 17 and 15 hours for Brooklyn Bridge and San Francisco, respectively.

In shallow water there will be other constituents that modify these range expressions, notably M_4 and MS_4 , and so the basic formulae are only accurate where shallow-water distortions can be neglected. See [Section 10.2.1](#) for a discussion of the differences between mean sea level and mean tide level.

The Mean High Water Interval between lunar transit and the next high tide in the usual case of a predominantly lunar semi-diurnal tide is given by:

$$\frac{g_{M_2}}{2\sigma_1}$$

where the phase lag is calculated on local time (see [Section 4.5](#)).

Highest and Lowest Astronomical Tides ([HAT](#) and [LAT](#)) are not easily defined in terms of harmonic constituents [16]. Merely to add together all the amplitudes of the harmonic constituents would give values that were too extreme, because the constituents are not physically independent. For example, the semi-diurnal tides are slightly reduced when the diurnal tides are greatest ($\cos^2 d$ and $\sin^2 d$ dependence).² Values of [HAT](#) and [LAT](#) are usually determined by examination of at least 5 years of predictions, or by making predictions for years of known astronomical extremes.

Chart Datum is defined locally to be close to the [LAT](#) level (see [Appendix E](#)). One early definition, used for Chart Datum where diurnal and semi-diurnal tides are both important, as they are in parts the Indian Ocean, was Indian Spring Low Water:

$$Z_0 - (H_{M_2} + H_{S_2} + H_{K_1} + H_{O_1})$$

Based on harmonic tidal terms, the relative importance of the diurnal and semi-diurnal tidal constituents is sometimes expressed in terms of a form factor:

$$F = \frac{(H_{M_2} + H_{S_2})}{(H_{K_1} + H_{O_1})}$$

² Also, the shallow-water constituents conspire to reduce the extreme ranges: they represent the tendency for non-linear processes in nature to reduce extremes (see [Chapter 6](#)) by enhancing energy dissipation.

The tides may be roughly classified as follows:

$F = 0$ to 0.25	semidiurnal form
$F = 0.25$ to 1.50	mixed, mainly semidiurnal
$F = 1.50$ to 3.00	mixed, mainly diurnal
$F =$ greater than 3.0	diurnal form

The tidal variations plotted in Figure 1.2a have form factors of 7.5 (Karumba), 1.2 (San Francisco), 0.25 (Bermuda) and 0.20 (Mombasa). The variations at Courtown, which has strong shallow-water distortions, are not sensibly represented by a form factor.

Tides have been classified in various other general ways that can be related to the tidal constituent amplitudes. Some coastal scientists still use a very crude classification, calling tides with a range greater than 4 m *macrotidal*; those between 2 m and 4 m are called *mesotidal*; those less than 2 m are called *microtidal*.

A more exact definition of the tidal régime in terms of the relative importance of the diurnal and semidiurnal components must involve the ratios of the total variance in each species, but at best this type of description is only an approximate representation of the full tidal characteristics.

The standard methods, described in this chapter, of analysing regularly sequenced site-specific values of sea level observed over a month, or a year, are not applicable to the spatial data produced by the altimetry instruments.

4.2.7 Analysis of altimeter data

Chapter 9 gives a detailed description of the technique of satellite radar altimetry. One of the main achievements of this technique has been to provide accurate maps of the ocean tide for most of the world ocean. Orbital parameters can be chosen such that the sea surface height at points along the ground tracks can be sampled every orbit ‘repeat period’. The result is that the tides measured at each point do not have the familiar periods seen by a tide gauge, but are aliased into longer periods as shown in Table 4.6. There is a time series of sea-level values at every point, for every repeat period. This repeat period is 9.9156 days for TOPEX/Poseidon, which has M_2 and S_2 aliased periods of about 60 days (6 cycles), analogous to the 12 hours; they decouple in 1,072 days (107 cycles), analogous to a fortnight in tide gauge data.

Over two decades of precise altimetry are now available so that, although the aliased periods appear to be long, they are in general much shorter than the

Table 4.6 Periods of the four main semidiurnal and diurnal tidal constituents, their aliased periods when sampled by the 9.9156-day TOPEX/Poseidon repeat period, and their aliased periods when sampled by the 35-day ERS/Envisat repeat period

Constituent	Period (hr)	TOPEX/Poseidon (days)	ERS/Envisat
K_1	23.93447	173.2	1 year
O_1	25.819342	45.7	75.1 days
P_1	24.06589	88.9	1 year
Q_1	26.868357	69.4	132.8 days
M_2	12.420601	62.1	94.5 days
S_2	12	58.7	infinite
N_2	12.65834	49.5	97.4 days
K_2	11.967235	86.6	0.5 year

available altimetric time series. Therefore, the amplitudes and phase lags of tidal constituents at each point in the ocean can be determined by harmonic analysis in a similar manner to the usual analysis of a tide gauge time series. This is a major advance on the earlier necessity to use response techniques when altimeter data sets were shorter and less accurate [17]. The only major difficulty in the harmonic approach concerns the computation of solar tidal constituents using data from sun-synchronous missions. In these cases, the solar tides (S_1 and S_2) have infinite alias period while other constituents (K_2 , K_1 , P_1) are aliased to periods of half or one year.

The repeat period of the TOPEX/Poseidon mission orbits was chosen so that the aliased periods of the major tidal constituents would be sufficiently different, enabling the separation of constituents in a harmonic analysis from data obtained from the first years of the mission [18]. Subsequently, TOPEX/Poseidon, and the following Jason series of missions, have provided accurate tidal parameters at each point along the ground track and have enabled the production of near-global tidal models (or ‘atlases’) by different techniques, some involving sophisticated data assimilation methods. Examples include the TPXO series of models of Oregon State University [19], the GOT series of the Goddard Space Flight Center [20], the FES series of the Observatoire Midi-Pyrénées, Toulouse [21], and the EOT series of the Deutsches Geodätisches Forschungsinstitut, Munich [22].

Many of these models are based on the analysis of data from multiple missions. In particular, although the ERS/Envisat missions were sun-synchronous, the use of their data in combination with TOPEX/Poseidon has enabled altimetric tidal information to be obtained from higher fixed latitudes [23]. They also make use of response type methods to infer the smaller constituents when they have the big ones from harmonic methods.

Global models of the main tidal constituents are now considered accurate at the centimetre level in most parts of the ocean, although uncertainties are much larger in coastal areas [24]. From time to time, comparisons of the different models are undertaken by expert groups and recommendations made as to which performs best in particular applications. In practice, the main application is as a routine correction to altimeter measurements of sea surface height within ocean circulation studies.

It is important to note that the tidal signals measured by a satellite are geocentric (Earth-centred) quantities that differ from the ocean tide measured by a coastal tide gauge or bottom pressure recorder:

$$\text{Geocentric tide} = \text{Ocean tide} + \text{Body tide} \\ + \text{Load tide}$$

where this relationship applies for all constituents individually. The body and load tides are collectively called the Earth tides and represent the movement of the surface of the solid Earth relative to its centre. The body tide for each constituent can be calculated readily as the product of the corresponding constituent in the Equilibrium Tide times the h Love number (Section 9.5), while the load tide can be computed by an iterative Green's function technique if one has a global (or near global) map of either the geocentric or ocean tide (Section 5.7).

As a result, a global map of a constituent of the ocean tide can be computed if one has a (near-) global map of the corresponding geocentric tide [25]. Hence, altimetric tidal information can be validated by comparison with conventional tide gauge information [26].

4.3 Response analysis

The basic ideas involved in response analysis are common to many activities and areas of science. A system, sometimes called a 'black box' is subjected to an external stimulus or input. The output from the system

depends both on the input and on the system's response to that input. The response of the system may be evaluated by comparing the input and output functions. The ratio of the output and input functions defines an 'admittance' for the system.

Mathematical techniques for describing system responses have been developed and applied extensively in the fields of electrical and communication engineering. In our own field, we have already considered the response of a stilling well, as measured by the levels in the well, to external variations (tides and wind waves) of different amplitudes and periods (Section 2.3.2). The response depends on the period of the forcing. For oscillations of long period (tides) the internal variations are not attenuated. In practice there may be a small phase lag. For short period oscillations the stilling-well system is designed to have a very small response (the amplitude response approaches zero).

In tidal analysis we have as the input the Equilibrium tidal potential. The tidal variations measured at a particular site may be considered as the output from the system. The system itself is the ocean. In response analysis we seek to describe its response to the gravitational forces. This treatment has the conceptual advantage of clearly separating the astronomy, the input, from the oceanography, which is the 'black box'. Although primarily intended to describe linear systems, where the output is proportional to the input, the techniques of response analysis can be extended to deal with moderately non-linear situations, such as the propagation of tides in shallow water. The ideas can also be extended to include other inputs such as the weather, in addition to the gravitational tidal forcing.

The response method of tidal analysis is relatively recent, dating from the 1960s [27]. It describes how one observational tidal record could be compared to a second 'reference tide', which is often taken to be the Equilibrium Tide. But as a powerful alternative, the reference could be a record from an existing and long-term neighbouring station. The observational and reference records constitute the 'output' and 'input' of our system. The response is dependent on the frequency of the forcing. This is the same concept as for Equation 4.6, but applied for all the frequencies.

4.3.1 The credo of smoothness

The fundamental assumption of the response method is the 'credo of smoothness' whereby the admittance, the ratio of output to input, is not allowed to vary dramatically as a function of frequency for any one

frequency band. For example, consider neighbouring tidal frequencies in each band, such as P_1 and K_1 in the diurnal band or N_2 and M_2 in the semidiurnal band. These frequencies are very similar so why should the ocean behave very differently in response to only a small frequency change?

This turns out to be a valid assumption. If the ratio between the observed amplitudes, determined by harmonic analysis, and the Equilibrium Tide amplitudes is plotted as a function of the angular speed of the constituents, as in Figure 4.2, it is clear that a pattern exists within the harmonic data. For the diurnal harmonic constituents the values generally fit well to polynomial curves for Brooklyn Bridge, New York; San Francisco; and Honolulu, Hawaii. For the semidiurnal constituents, the phases vary smoothly, increasing with frequency, but the amplitude responses on this scale are a little more complicated. There are some frequencies where the responses deviate from the smooth curves a little, for reasons we shall discuss later.

We have already made this smoothness assumption, that responses to gravitational forcing at adjacent frequencies will be the same or very similar, in our development of formulae for the nodal adjustments of harmonic constituents (Section 4.2.2). The use of Equilibrium relationships in the harmonic analysis of short periods of data also makes this implicit assumption.

4.3.2 Analysis procedures

The full details of the methods of response analysis [27] are too complicated for this discussion. Here we simply outline a method of deriving response curves as a function of frequency for a particular tide gauge record. There are different ways of doing this, many derived from general signal processing analysis, but a simplified version is as follows. Consider the observed tide to be parameterised as:

$$T(t) = \sum w(s)V(t-s\tau)$$

where $T(t)$ is the tidal elevation at time t expressed as a weighted sum of past and future values of the relevant components of the Equilibrium Tide V with the summation over a number of lags $s = -S$ to $+S$, where the lag increment is denoted by τ . In the analysis, the values of T and V used will be filtered values of their total values so as to focus on the frequency bands corresponding to each species separately.

For physical systems, it is reasonable to expect $w(s)$ to become small as $s\tau$ becomes large. From experience

of analyzing many tidal records it has been found that $S = 2$ and $\tau = 2$ days gives satisfactory results. Thus:

$$T(t) = w(2)V(t-2\tau) + w(1)V(t-\tau) + w(0)V(t) + w(-1)V(t+\tau) + w(-2)V(t+2\tau) \quad (4.10)$$

The response weights for positive lags in the first two terms have a physical meaning, representing the remaining effects of the system response from a previous impulse. However, although future weights are physically difficult to justify, there are mathematical advantages in using both past and future values of the potential, so the fourth and fifth terms ($+\tau$ and $+2\tau$) are also used.

The complex admittance of the ocean, with respect to the Equilibrium Tide, is given as a function of frequency by the Fourier transform of the weights:

$$Z(\omega) = \int_{-\infty}^{\infty} w(\tau)\exp(-i\omega\tau)d\tau$$

or in discrete terms:

$$Z(\omega) = w(2)\exp(-i\omega 2\tau) + w(1)\exp(-i\omega\tau) + w(0) + w(-1)\exp(i\omega\tau) + w(-2)\exp(i\omega 2\tau)$$

The choice of $\tau = 2$ days results in a conversion from the time to the frequency domain that gives smooth curves across the band, which is what we want. Exactly why 2 days works so suitably, rather than other possible choices of lag, is rather complicated, but in practice it works well.

In the absence of lags, $w(0)$ would give a uniform admittance across the band. However, if more weights and lags are included (i.e. as S increases), then more detailed variations occur in the admittance curve. The amplitude and phase of the admittance are then derived from its real and imaginary parts:

$$|Z(\omega)| \quad \text{and} \quad \arg(Z(\omega))$$

Once the admittances for each band are known for a site, the response method can be used for tidal prediction by using these admittances, and future values of the Equilibrium Tide.

4.3.3 Non-gravitational inputs

The normal response analysis procedure deals with the linear response of the ocean to the gravitational tidal forces. However, the amplitudes and phases

determined by harmonic analyses do not always fit exactly on the response curves: notable differences occur for μ_2 , L_2 and even for M_2 and S_2 . The diurnal species S_1 , which has a very weak gravitational input, has an anomalously large amplitude response. The strength of the response analysis technique is that it not only identifies these anomalies, but it also allows us to investigate them in terms of additional input forcing functions. It is not possible to go into mathematical detail here, but the basic ideas behind the possible additional inputs may be outlined to emphasise the flexibility of the response approach.

Radiational inputs

Periodic influences on the oceans due to approximately regular cycles in the weather are recognisable in tidal observations as contributions to the annual term S_a and the diurnal term S_1 , both of which are relatively large compared with their gravitational input. The semidiurnal term S_2 also has slightly anomalous phases and amplitudes in the data from all parts of the world; response analysis separates the gravitational part from the radiational part of S_2 . Physically, the regular variations of tropical atmospheric pressure with a period of 12 hours and maximum values near 10:00 and 22:00 local time, the atmospheric tides, are the driving force. These pressure variations have amplitudes that vary approximately as $1.25 \cos^3 \phi$ millibars, (where ϕ is the latitude); a fuller discussion is given in Section 5.5. The physics of the annual and the diurnal constituents is related more directly to the solar radiation. Response analysis avoids the details of the physics by defining an input radiation potential that is calculated from the Sun's coordinates [10].

Shallow-water inputs

Non-linear effects are negligible at ocean stations, but become increasingly important on the continental shelf and in regions of shallow water (Section 4.2.3). Harmonic analysis represents the distortions explicitly by introducing many additional constituents, and implicitly by absorbing them into the estimates of constituents already included.

Response analysis allows us to manufacture additional inputs to represent the shallow-water interaction [28]. These inputs are taken as the products of the local first-order linearly computed long period, diurnal and semidiurnal changes of sea level $\hat{\zeta}_0(t)$, $\hat{\zeta}_1(t)$ and $\hat{\zeta}_2(t)$ Because non-linear effects

Table 4.7 Interactive terms in response analyses

Species	Products	Notation
0	$\hat{\zeta}_2(t)\hat{\zeta}_2(t)$	$\hat{\rho}^2 - 2$
1	$\hat{\zeta}_2(t)\hat{\zeta}_1(t)$	$\hat{\rho}^2 - 1$
2	$\hat{\zeta}_2(t)\hat{\zeta}_2(t)\hat{\zeta}_2(t)$	$\hat{\rho}^2 + 2 - 2$
3	$\hat{\zeta}_2(t)\hat{\zeta}_1(t)$	$\hat{\rho}^2 + 1$
4	$\hat{\zeta}_2(t)\hat{\zeta}_2(t)$	$\hat{\rho}^2 + 2$
6	$\hat{\zeta}_2(t)\hat{\zeta}_2(t)\hat{\zeta}_2(t)$	$\hat{\rho}^2 + 2 + 2$

are locally generated, local values of the tide are used for computing these non-linear inputs. The relative importance of the paired and the triple products depends on the type of local tidal regime. The $\hat{\zeta}(t)$ terms are actually mathematically complex quantities, which have complex conjugates $\hat{\zeta}^*(t)$ and these are also included in the inputs.

Table 4.7 gives some interactions that may be important where semidiurnal tides are dominant. These interactions are neatly summarised in the I notation in column three. It is not generally necessary to compute lagged weights for these inputs, but the I^{2+2} term produces a much better fit if a lag term is introduced.

Standard Station levels

For analysing short periods of data of a month or even a few days, direct reference to the gravitational potential is not always satisfactory.

In harmonic analysis, several constituents are linked according to their Equilibrium Tide relationship or according to their relationships in a full analysis for a nearby Standard Station (Section 4.2.5). The response analysis equivalent is to apply the observed or predicted tides at the Standard Station as an input, and to compute the response of the Secondary Station to this input, equivalent to the procedure in Section 4.3.2.

Only four weights need be computed for this local response. The full structure of the local response curve is then inferred by using the characteristics of the Standard Station responses. This reference to a permanent local station is particularly useful for analysis of short periods of bottom pressure records, because it allows the mapping of a pattern of regional tidal behaviour, without separate direct reference to the astronomical forcing.

4.3.4 Comparisons between response and other analysis procedures

Basically, the non-harmonic, harmonic and response methods of tidal analysis and prediction are very similar, put simply as in Equation 4.6, but expressed through different mathematical approaches and language. In all cases, the astronomy is being linked to the ocean observations, and vice versa. Inevitably, the different parameters from each method can be related.

For example, the nineteenth-century methods (see Section 4.1) are conceptually similar to the response method, although the technical details of the latter are much more complicated. The estimated lunar and solar tides in the eighteenth century Bernoulli/Holden method are scaled to the Equilibrium Tide, which is often used as the gravitational reference tide in the response method. The overall scale factor is analogous to the magnitude of the ‘admittance’: the 0.4 (where it differs from the equivalent ratio between the amplitude of the observed and the reference tide in the response method) defines the dependence of admittance on frequency; while the Holden lag in hours corresponds to the phase of the admittance.

The response equivalence to the harmonic method is emphasised in Figure 4.2. When the amplitude and phase responses at a station have been computed it is a simple matter to calculate the equivalent harmonic constituents from the harmonic equivalents in the gravitational and radiational tidal potentials. The calculations are less straightforward for the responses to the shallow-water inputs, because the individual harmonic terms have to be multiplied first. The equivalence of the two methods also enables approximate response functions to be computed from the factors H_n/A_n (A_n is the Equilibrium amplitude) and κ_n as in the plots of Figure 4.2.

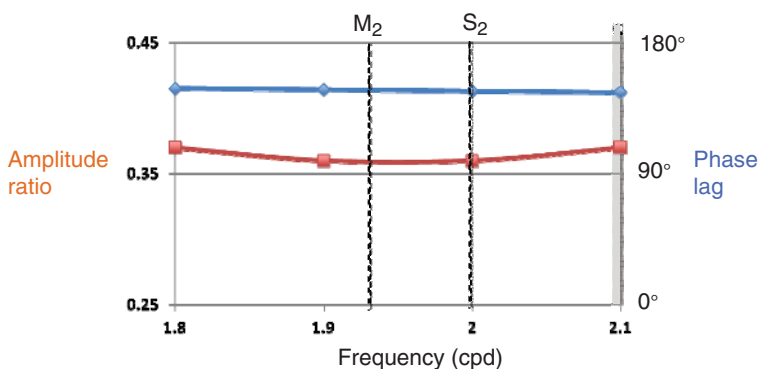


Figure 4.4 Response functions for currents (output) on elevations (input) for semidiurnal tides at an offshore site in the North Sea. This shows the versatility of the response method of tidal analysis, as the variation of progressive and standing wave dynamics with frequency can be plotted. For a true progressive wave the phase lag would be 180°.

According to our criterion of a good analysis being one that represents the data with the smallest possible number of parameters, the response procedure is superior to the harmonic approach: typically the response technique can account for slightly more of the total variance than the harmonic method can accommodate, using fewer than half the number of parameters. Its advantages as a research tool include the identification of additional forcing inputs, and the opportunity of making subtle choices of factors for inclusion as inputs. A typical response analysis will have the gravitational input, the solar radiation input and a series of shallow-water interactive inputs.

By comparison, the harmonic analysis approach offers few alternatives, apart from the addition of extra constituents, and little scope for development. The laborious adjustments for nodal variations illustrate this restriction. These variations are automatically taken care of in response analysis. In harmonic analyses the shallow-water effects and the radiation effects are automatically absorbed together into the estimates of the constituents, but with no direct physical interpretation. The penalty for the more flexible response approach is that more elaborate computations are required; for example, the shallow-water treatment requires a preliminary response analysis to calculate the linear inputs $\hat{\zeta}_1(t)$, $\hat{\zeta}_2(t)$ for input to the final analysis.

The response concept of the oceans as a ‘black box’ whose physical characteristics are isolated for further study is very appealing to the research physical oceanographer, and offers scope for further developments in terms of identifying inputs (see Figure 4.4 for an example), which, perhaps surprisingly, has not yet been fully exploited.

Because harmonic methods are so generally accepted, today the response method is most widely applied

in the analysis of short records from temporary tide gauges or current meters. As discussed, such short records are not analysed well using harmonic analysis, even with the use of related constituents in the set of constituents to be solved for. It is more practical and analytically robust to use a nearby, more complete tide gauge record as the reference (or the Equilibrium Tide again if necessary), conduct a response analysis and use the resulting admittances to scale the harmonic constants of the reference into those appropriate for the shorter record. The response method was used for the tidal analysis of satellite altimeter data when records were short [29], although as the records have lengthened harmonic analyses have taken over.

The response admittances, or more specifically their amplitude and phase responses at a particular frequency, are 'stable' in the same way as the amplitudes and phases of the harmonic constituents are stable. Nevertheless, it is still usual to present maps of tides in terms of the harmonic amplitudes and phase lags for individual constituents. They have clearly identified units of length and of time that

are useful for practical applications. Also, charts of harmonic constituents can be interpreted scientifically in terms of wave propagation, as discussed in Chapter 5.

4.4 Analysis of currents

Currents are intrinsically more difficult to analyse than elevations because, as vector quantities, they require more parameters for a proper description [1, 5, 30]. More detailed formulae for currents are developed in Appendix C, but here we look at some of the basic processes. Also, on continental shelves and near-shore, measurements of currents usually show a larger proportion of non-tidal energy than do elevations, which makes the errors in the estimated tidal components larger (Section 4.6). In the open ocean, tidal currents are usually only a small component of total water movements. A third restriction, despite new, efficient systems such as acoustic current Doppler profiling and Doppler radar reflection technology (see Figure 4.5), is difficulty and expense in making current measurements offshore, often involving

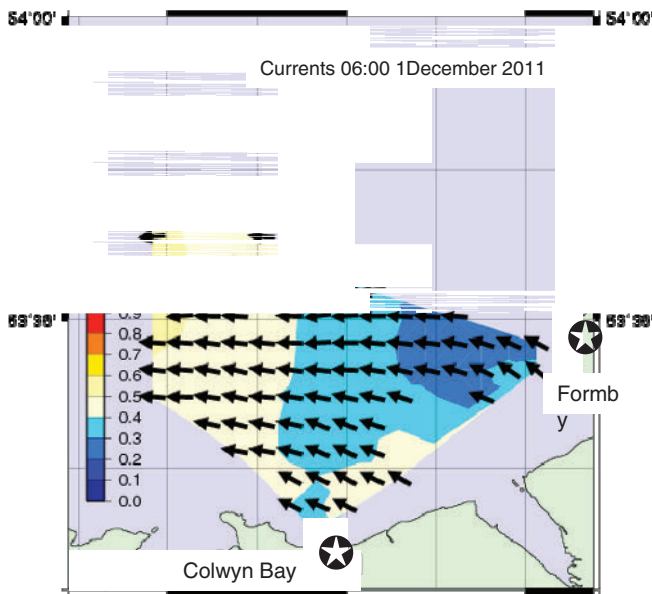


Figure 4.5 Surface currents measured by high-frequency radar over an offshore grid, by reflected Doppler shift analysis. Regional coverage of the approach to the port of Liverpool is obtained at lower cost than deploying *in situ* meters, as there are no moving parts or offshore installations. The image shows the aerial network of the radar site at Formby, UK, operated by the National Oceanography Centre. Photographs from John Howarth, NOC.

special moorings and deployment of ships. Vector techniques are available for analysing currents, which are not applicable to levels.

Currents are traditionally measured as a speed, q , and a direction of flow, θ , clockwise from the north. Mathematically it is usual to work with Cartesian coordinates and current components in a positive north and positive east direction, v and u . The relationships are straightforward (see Section 2.5):

$$v = q \cos \theta$$

$$u = q \sin \theta$$

The convention is to define the direction towards which the current is flowing; this is the opposite of the convention that defines the wind direction as that from which the wind blows. The wind convention was established on land where the local weather is strongly influenced by that of the region from which the wind blows, whereas the currents convention was established by navigators, who were concerned where the current was taking their ship. Mariners call the direction of current flow the set; the speed of the water due to currents (tidal and non-tidal) is called the *drift* [31].³

4.4.1 Non-harmonic methods for currents

Currents traditionally measured from an anchored ship consisted of hourly or half hourly speeds and directions over a period of 13 or 25 hours. Doppler radar can measure currents over a grid (Figure 4.5), but the principles of analysis are still the same. When plotted these would form a series of vectors as in Figure 1.3, called a central vector diagram. The vector lines may be replaced by a single dot at the outer end, marking the vector point. When several hundreds of these vector points are plotted to represent observations of currents made over some weeks, by a recording current meter (usually these meters sample every 10 or 15 minutes rather than every hour) a clear pattern emerges. An example of one of these dot plots is given in Figure 4.6 for 54 days of 10-minute samples of current at the Inner Dowsing light tower. The axes shown are for the components of speed in a positive north-going and positive east-going convention. At strong south-going spring currents, the flows are deflected more towards the west than is the case for neap currents, because of the local coastal topography.

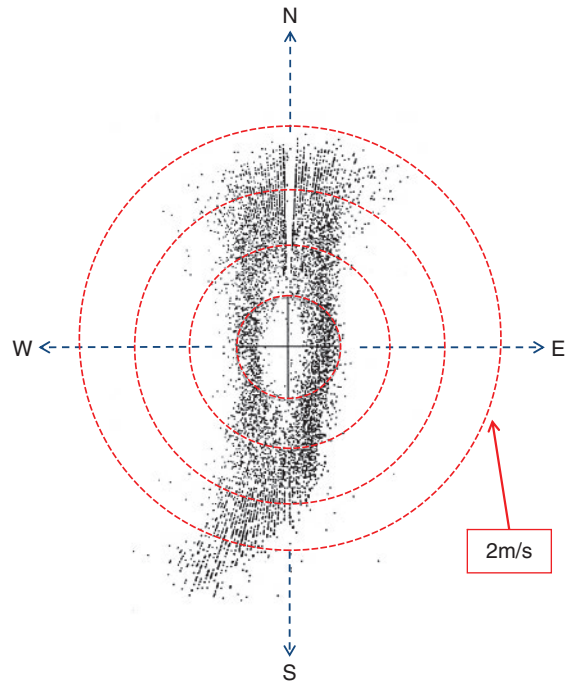


Figure 4.6 Vector dot plot of hourly currents over 54 days at a site in the North Sea. The red circles are at 0.5 m/s intervals. Dots away from the regular pattern show the influence of the weather on the measured currents. The strong extreme currents to the southwest are towards an area that only floods at spring tides. The central area, which is nearly blank, shows that zero current speeds are very rare; the missing segment at the top is a dead area of the direction-sensing potentiometer.

The narrow blank segment at the top of the pattern is due to a dead space in the potentiometer used in the current meter to sense the direction of the flow.

A series of 25 hourly measurements of current speed and direction may be analysed by comparison with the times of high water at a nearby Standard Port as described in Table 4.8. The spring and neap ranges and the mean range of the tide for the period of the observations are also needed for scaling the current speeds. As an example of preparing a tidal vector table, we analyse 25 hours of currents at the Inner Dowsing light tower. Current speeds and directions are plotted separately against time in Figure 4.7. Note again, that for this analysis it is usual to measure directions in the geographical sense, clockwise from north.

The observations are then joined by a series of smooth lines and the times of high water at the chosen Standard Port, in this case Immingham, are marked on the time axis. The next step is to list the Inner Dowsing current speeds and directions for the hourly times relative to the time of Immingham high water;

³ The distance a craft is moved by currents and winds is sometimes also called the *drift*.

Table 4.8 Calculations of tidal current parameters for an offshore North Sea site, where the 24-hours of data are linked to high water levels at a nearby Standard Port, Immingham

Time relative to Immingham high water	Direction from north			Speed (m/s)				
	First cycle	Second cycle	Mean	First cycle	Second cycle	Mean	Springs**	Neaps*
High water	130	163	147	0.48	0.50	0.49	0.51	0.25
+1 hours	94	107	101	0.21	0.20	0.21	0.22	0.11
+2 hours	43	47	45	0.32	0.32	0.32	0.34	0.17
+3 hours	16	18	17	0.70	0.71	0.71	0.74	0.37
+4 hours	7	3	5	0.93	0.91	0.92	0.97	0.48
+5 hours	355	353	354	0.91	0.79	0.85	0.89	0.44
+6 hours	343	342	343	0.83	0.68	0.76	0.79	0.39
-6 hours	338	341	340	0.82	0.68	0.75	0.79	0.39
-5 hours	324	322	323	0.58	0.42	0.50	0.53	0.26
-4 hours	257	233	245	0.21	0.20	0.21	0.22	0.11
-3 hours	214	213	214	0.76	0.84	0.80	0.84	0.42
-2 hours	209	210	210	1.10	1.06	1.08	1.13	0.56
-1 hours	201	200	201	0.90	0.89	0.90	0.94	0.47

** Spring conversion factor = $\frac{\text{Mean spring range at Immingham}}{\text{Mean range on observation day}} = \frac{6.4\text{m}}{6.1\text{m}} = 1.05$

* Neap conversion factor = $\frac{\text{Mean spring range at Immingham}}{\text{Mean range on observation day}} = \frac{3.2\text{m}}{6.1\text{m}} = 0.52$

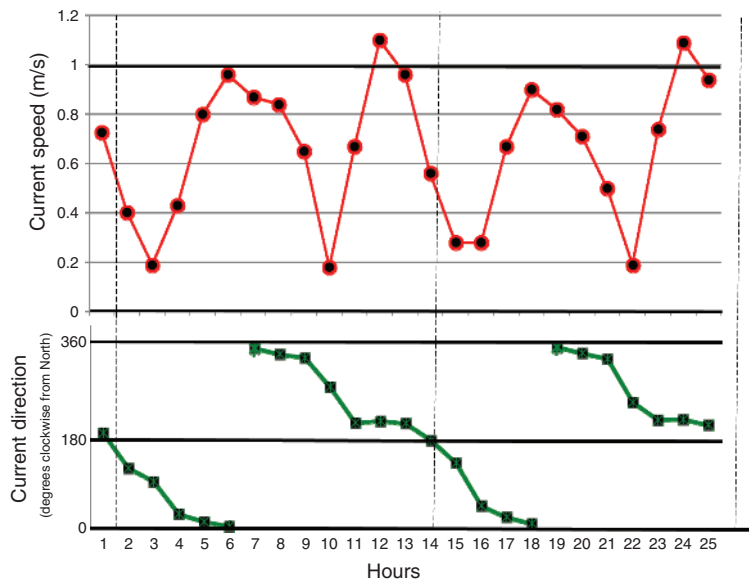


Figure 4.7 Observed hourly current speeds and directions over 25 hours at an offshore North Sea station. This is the starting point for computing tidal current diamonds, shown on many nautical charts.

these are read off the curves for each of the two cycles. The observed values will not be identical for each cycle because of diurnal tidal changes, measuring errors and weather effects. The mean values are then calculated for the two sets. Finally, the current speeds for mean springs and mean neaps are calculated by using the adjustment factors. If residual flows are significant these should be removed before preparing Figure 4.7. The correct procedure for removing the residual flows is to resolve each measured speed and direction into two components; then take the mean over 25 hours for each component and remove it from each measured value prior to re-computing the hourly tidal speeds and directions from the adjusted components. In many cases, including the one discussed here, the residual currents are too weak to be significant, but in other cases they must be allowed for and stated in the final analysis. A response analysis would similarly treat the north–south and east–west components separately.

4.4.2 Harmonic methods

If the currents are resolved into east-going and north-going components, u and v , the speeds and angles are:

$$q = \sqrt{(u^2 + v^2)}$$

$$\theta = \arctan \left(\frac{v}{u} \right) \text{ anticlockwise from the east}$$

$$\theta = \arctan \left(\frac{u}{v} \right) \text{ clockwise from the north}$$

The two components u and v can be subjected to separate harmonic analyses by least-squares fitting:

$$u(t) = U_0 + \sum_N U_n f_n \cos [\sigma_n t - g_{u_n} + (V_n + u_n)]$$

$$v(t) = V_0 + \sum_N V_n f_n \cos [\sigma_n t - g_{v_n} + (V_n + u_n)]$$

$$(4.11)$$

as for elevations (Equation 4.5).⁴ The unknown parameters to be determined by the analysis are the mean current components, U_0 and V_0 , and two sets of harmonic constituent amplitudes and phases, $(U_n, g_{u_n}), (V_n, g_{v_n})$. Each harmonic tidal constituent is represented by four parameters: two amplitudes and two phases.

In Appendix B these four parameters are shown to define an ellipse, the *current ellipse*, which is traced by the tip of the current vector during one complete cycle. Several valuable properties of the constituent ellipses can be derived from the component parameters:

$$\text{current direction} = \arctan \left(\frac{V \cos(\sigma t - g_v)}{U \cos(\sigma t - g_u)} \right)$$

$$\text{current speed} = [U^2 \cos^2(\sigma t - g_u) + V^2 \cos^2(\sigma t - g_v)]^{\frac{1}{2}}$$

$$\text{for anticlockwise rotation: } 0 < (g_v - g_u) < \pi$$

$$\text{for clockwise rotation: } \pi < (g_v - g_u) < 2\pi$$

$$\text{for rectilinear flow: } (g_v - g_u) = 0, \pi, 2\pi \dots$$

Major and minor axes of the ellipse are calculated using Equation B.5a and B.5b. The direction of the major axis is given by Equation B.8.

Although the analyses define a separate ellipse for each harmonic constituent, experience shows that those constituents that have similar angular speeds have ellipses of similar shape and orientation, although of course, different amplitudes. This is dynamically reasonable, and corresponds to the uniform elevation responses plotted in Figure 4.2. Figure 4.8 shows the ellipses for the principal constituents in each species at the Inner Dowsing light tower. There is a steady clockwise rotation of the major axis of the ellipses as we move from diurnal currents through to the sixth-diurnal currents. Another interesting feature at this location is the sense of rotation, which is anticlockwise for all the harmonic constituents from the astronomical forces, but clockwise for those generated by shallow-water dynamics. The changes in amplitudes of the ellipses are also consistent with their different amplitudes in the astronomical forcing.

When choosing the constituents to be included in an analysis of a month of current observations, the terms most likely to be important are the same as the major terms for elevations at a nearby coastal station, and in the Equilibrium Tide. Non-resolvable constituents may be related to neighbouring constituents using the local elevation relationship, but care should be exercised when doing this for currents and elevations near an amphidrome (see Chapter 5). Although it is common practice to resolve the current components into north and east directions, it is sometimes preferable to resolve along the major and minor axes of the dominant flow; the major axis of flow is usually the major axis of the semidiurnal species (in Figure 4.6, by chance, the north–south axis nearly

⁴ Here the u_n terms are, as usual, the nodal variations in the astronomical phase arguments, not to be confused with the east-going currents, $u(t)$.

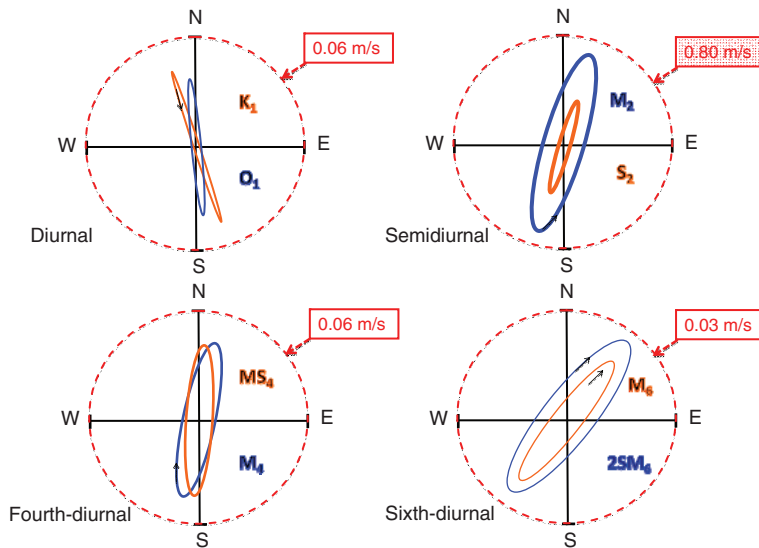


Figure 4.8 Current ellipses for the principal constituents in tidal species at the Inner Dowsing light tower in the North Sea. Note the very different scales for each species. The arrows show the sense of rotation of the current vector.

coincides with the major axis of the ellipse). Resolution along the major axis would be particularly appropriate if the currents are in a narrow channel, and are nearly rectilinear. Of course, all the properties of the ellipses themselves are independent of the axes chosen.

Analyses of currents at the same site but at different depths will have similar but not identical ellipses, because of the effects of bottom friction.

4.4.3 Rotary current components

An alternative way of representing each tidal constituent ellipse, and the ellipse characteristics, is to replace the amplitudes and phases of two components $(U, g_u), (V, g_v)$ by the amplitudes and phases of two vectors each of which has a constant amplitude, which rotate at the angular speed of the constituent, but in opposite directions. When the vectors are aligned there are maximum currents, but when they are opposed the current speeds are a minimum. Further details of the calculations of the amplitudes and phases of the clockwise and anticlockwise amplitudes and phases $(Q_c, g_c), (Q_{ac}, g_{ac})$ are given in [Appendix B](#).

The technique of analysing currents into rotary components is particularly valuable when studying inertial currents. This class of currents has a non-tidal origin, being generated by rotary winds and maintained by a balance between Coriolis and centrifugal accelerations. Their period is given by $2\omega_s \sin \phi$ where

ϕ is the latitude. They appear as a peak in the residual spectrum of currents, after removing the tides from the rotary components, but only in the clockwise component in the northern hemisphere and in the anticlockwise component in the southern hemisphere.

4.5 Time zone conversion

Omitting the nodal factor, the cyclic, harmonic part of a tidal constituent is:

$$\cos(\sigma_n t - G_n + V_n)$$

where σ_n is the angular speed of the n th constituent in degrees per unit time, and V_n is its phase, called the astronomical argument, in the Equilibrium Tide at the Greenwich meridian at the zero time. G_n is the phase lag of the constituent in the observed tide on the Equilibrium Tide at the Greenwich longitude. Traditionally this was called Greenwich Mean Time. However, the world now uses Coordinated Universal Time (UTC), which is periodically adjusted against a network of atomic clocks. For tidal work, Universal Time (strictly UTC) is needed for analyses and predictions [32].

If we wish to express the time in some other zone instead of Greenwich, we may do this, while still relating our phases to the same astronomical time zero, by rewriting:

$$t' = t - j$$

where j is the number of hours difference between the UTC value t and the zone time t' . By convention j is measured positive for zones west of the Greenwich (zero) Meridian. The constituent argument is then:

$$\begin{aligned} &\cos[\sigma_n t' - (G_n - j\sigma_n) + V_n] \\ &\text{or } \cos[\sigma_n t' - g_n + V_n] \end{aligned}$$

where g_n is the phase lag in the new time zone:

$$g_n = G_n - j\sigma_n$$

The phase adjustment is slightly different for each constituent, even within a species. Note that where observations are supplied and predictions are required for the same time zone j , the values of g_n may be calculated in the analyses and used for prediction without any adjustment. For many purposes, such as preparing co-tidal maps of oceans, the phases must all be adjusted to the same time zero, usually to the 'big G' notation. In this case the adjustment is:

$$G_n = g_n + j\sigma_n \quad (4.12)$$

Greenwich phase = Local time zone phase
+ [Zone shift in hours, west positive]
× [Constituent speed in degrees per hour]

Two examples show this applied in practice:

Suppose measurements of sea levels in time zone (GMT +5), as for longitude 75° W, produce an M_2 phase of g_{M_2} . Any predictions based on this phase will be correct for the same time zone. To convert g_{M_2} for predictions in the Greenwich time zone:

$$G_{M_2} = g_{M_2} + 5 \times 28.98 = g_{M_2} + 145^\circ$$

Suppose the local phase for O_1 at 150° E (time zone GMT - 10) needs to be converted to GMT. The conversion is

$$G_{O_1} = g_{O_1} - 10 \times 13.94 = g_{O_1} + 139.4^\circ$$

The old convention of referring phases to local Equilibrium arguments involved redefining the astronomical zero time and hence V_n for each longitude: the λ_p factor in Equation 3.20 was not kept at zero. Because of the difficulty of comparing tides at different longitudes the system is now obsolete, and these phases (called κ , the 'kappa notation') are no longer used for marine tides. However, Earth tide analyses still favour this notation.

4.6 Stability of tidal parameters

It is usual to refer to harmonic tidal constituents rather than tidal constants when presenting the results of an analysis. Nevertheless, we expect these constituents to have only slight changes if a different period of data for the same place is analysed. However, analyses of individual months of tidal data from the same location invariably show small variations in the tidal parameters about some mean value.

Figure 4.9 shows the amplitudes and phases of sea levels M_2 at Newlyn over an 85-year period. Reasons for the variability of the tidal parameters include analysis limitations due to non-tidal energy at tidal frequencies, inconsistencies in the measuring instruments and changes and real oceanographic modulations of the tidal behaviour. For example, the reduction in phase at Newlyn after 1980 is due to replacing an old stilling well with a narrow connecting

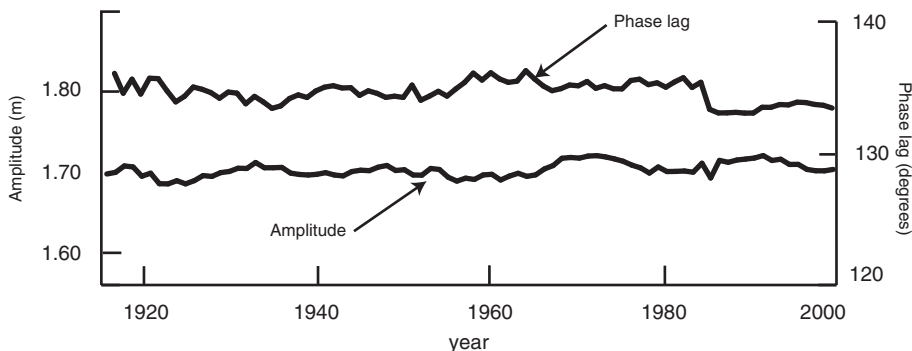


Figure 4.9 The amplitudes and phase lag of the principal semidiurnal lunar tide (M_2) at Newlyn are plotted each year. The Equilibrium nodal effects are allowed for in this analysis.

Table 4.9 Stability of Newlyn sea-level tidal constituents from annual analyses over the period 1916–2005

	Phase (degrees)				Amplitude (mm)			
	mean	sd	max	min	mean	sd	max	min
S_A	231.1	33.8	321.3	121.4	64.2	24.2	124.6	2.1
O₁	342.9	2.2	350.4	338.6	53.2	2.0	59.3	48.0
K₁	109.1	1.7	113.4	105.7	62.4	1.9	65.9	56.9
M₂	134.5	0.9	136.3	132.9	1706.9	9.0	1724.5	1688.6
S₂	178.2	0.9	179.9	176.4	571.2	6.4	583.8	558.8
M₄	168.2	1.8	171.4	164.7	110.5	3.0	115.6	103.0

Table 4.10 Stability of the amplitudes and phases of the Inner Dowsing offshore tower current and level tidal constituents, over a year of 29-day analyses. The elevations are generally much less variable than the currents.

			Amplitude		Phase	
			mean	sd	mean	sd
O₁	H	mm	0.177	0.012	114.0	7.3
	U	m/s	0.006	0.002	153.1	75.2
	V	m/s	0.045	0.008	232.2	13.3
M₂	H	mm	1.969	0.029	162.2	1.0
	U	m/s	0.200	0.028	231.1	10.6
	V	m/s	0.693	0.056	304.0	11.3
M₄	H	mm	0.035	0.004	242.3	8.9
	U	m/s	0.033	0.021	107.3	65.3
	V	m/s	0.065	0.012	30.1	20.0

pipe, with an external sensor. Table 4.9 summarises the variability and range of six important constituents at Newlyn [33].

Tidal constituents for currents vary more than for sea levels, changing vertically with depth due to bottom friction, and locally over small distances due to seabed and coastal topography. Table 4.10 summarises the variability of the O₁, M₂ and M₄ harmonic constituents of elevation and current components at the Inner Dowsing light tower. In general, elevations are less variable than currents; the greatest percentage variability is found in the weaker constituents of the current components. For M₂ the standard deviations of the monthly values of elevations, the V-component and the weaker U-component of current are, 1.5 per cent, 8.1 per cent and 14 per cent of the mean values of

constituent amplitude in each case. Variability of the constituents from year to year is much less, but still not negligible.

In the case of a harmonic tidal analysis we may estimate the confidence limits by comparison with the random background noise at the frequency and adjacent frequencies [5]. We make use of the fact that the standard error due to a random background noise of variance S^2 in the bands around a constituent frequency is:

$$\begin{aligned} \text{Standard error in amplitude (H):} & \quad S/\sqrt{2} \\ \text{Standard error in phase (in radians):} & \quad S/(H\sqrt{2}) \end{aligned}$$

For a time series of length T , the elemental band has a frequency span $1/T$. However, better stability is

achieved by averaging the noise level over a series of elemental bands; for example, the whole of the diurnal or of the semidiurnal frequency band might be included. If the non-tidal residual variance in the averaging band, of width $\Delta\omega$, $S_{\Delta\omega}^2$ is, then the noise density is $S_{\Delta\omega}^2/\Delta\omega$. The value of S^2 to be used to calculate standard errors is given by:

$$S^2 = \frac{S_{\Delta\omega}^2}{T\Delta\omega}$$

Averaging over a whole tidal species for $S_{\Delta\omega}^2$ will tend to underestimate background noise and errors, because it assumes a uniform noise density across the band, whereas in some sea-level records, the noise background rises around the major tidal lines, a phenomena called tidal cusping [27]. Recent Newlyn data do not show cusping, but the record at Honolulu does have energy increased in adjacent bands. This is attributed to the effects of internal tides propagating at variable speeds from a distant source [34]. For this reason, some workers choose a narrower band centred on the individual constituents to compute the residual variance. In either case, a spectral analysis of the residual variance is required to determine its frequency distribution. When the above procedures are applied to shelf tides, the standard errors computed are significantly less than the observed variations of constituent amplitudes and phases from month to month.

In older data, some of the variability is undoubtedly instrumental – for example, a chart recorder cannot normally be read to better than 2 minutes, equivalent to a phase error of 1° in the semidiurnal constituents, and operating errors may easily be greater than this.

Nevertheless, particularly for monthly analyses, there remains a small real oceanographic variability, which is not due to variations in the astronomic forcing functions, as these variations persist, no matter how fully the forces are represented. In any particular region, the amplitudes and phases at several simultaneous measuring stations are similarly influenced during a particular month. These regional modulations present a problem when seeking undistorted ‘true’ harmonic constants from 29 days or less of data at a site. One possible palliative to reduce the error is to compare the results with a 29-day analysis of simultaneous data from a nearby Standard Port, for which a reliable long-term mean value of the constituent has been determined from analysis of a long period of

data. The 29-day constituents at the site may then be adjusted according to the ratio and phase differences of the short- and long-term constituents at the Standard Port.

4.7 Tidal predictions

Tidal levels and current predictions take many forms [35], depending on the accuracy and validity required. At one extreme, national authorities prepare and publish predictions annually, both on the Internet and in printed form. At the other extreme, bespoke local current predictions can be delivered free, or for a small charge, to a mobile phone. The standard practice is to publish high and low water times and heights in official tables, for a selected list of Standard or Reference Stations. (The normal Gregorian calendar is used, though in the Muslim calendar, where months always begin with a new Moon, spring and neap tides are always on the same days!) Times are in hours and minutes, and heights are in metres; by convention a midnight turning point is given as 00:01 hours. The tables also include sets of constants for adjusting the times and heights for intermediate places, called Secondary or Subordinate Stations. Tables refer predicted levels to the local Chart Datum of soundings.⁵ There is no bar to independent preparation and publication of predictions; these are often favoured by yachtsmen and coastal anglers.

4.7.1 Reference or Standard Stations

Predictions for the Standard or Reference Stations are prepared directly from the astronomical arguments, using sets of harmonic constituents previously determined by analysis. The procedure, which reverses the methods of harmonic analysis, begins with the astronomical coordinates of the Moon and Sun, and then computes the levels for each harmonic constituent from the known amplitude and phase relationships. The left-hand side of Equation 4.6 is now the unknown factor. Table 4.11 shows how this is done for the M_2 constituent at Newlyn for a particular time in 2043. Figure 4.9 shows that it is reasonable to

⁵ To avoid any confusion due to publication of two slightly different sets of tidal predictions for a port, based on different methods, agreements exist between the national publishing authorities for exchange of predictions, each authority being responsible for ports in their own country.

Table 4.11 Steps in the procedure for calculating the M_2 tidal constituent at Newlyn on 13 July 2043, by entering the appropriate values from various tables in this book, and Equation 4.5. The total sea levels are obtained by adding similar computations for a full set of tidal constituents.

From analysis:	$H_{M_2} = 1.701 \text{ m}$	$g_{M_2} = 134.5^\circ$	Table 4.9
	$Z_0 = 3.125 \text{ m above Admiralty Chart Datum}$		
From Table 4.2:	$s = 183.3^\circ$		
	$h = 110.8^\circ$		
	$p = 54.6^\circ$		00.00 13 July 2043
	$N = 3.2^\circ$		Day 194
	$p' = 283.7^\circ$		
From Table 4.1(c) and Section 4.2.1:	$V_{M_2} = -2s + 2h = -145.0^\circ$ (in solar time $M_2 = (2 \ -2 \ 2 \ 0 \ 0 \ 0)$)		
and from Table 4.3:	$f_{M_2} = 1.000 - 0.037 \cos(N) = 0.963 \dots u_{M_2} = -2.1 \cos(N) = -2.1^\circ$		
The M_2 harmonic is:	$H_{M_2} f_{M_2} \cos [\omega_{M_2} t - g_{M_2} + (V_{M_2} + u_{M_2})]$ $= 1.72 \times 0.963 \times \cos [28.98^\circ t - 135.2^\circ + (-145.0^\circ - 2.1^\circ)]$		
t is measured in hours from midnight:	$= 1.66 \cos [28.98^\circ t - 282.3^\circ]$		
Some calculated values are:			
00:00	$Z_0 + 0.33 = 3.46 \text{ m}$		ACD
06:00	$Z_0 - 0.50 = 2.62 \text{ m}$		
12:00	$Z_0 + 0.66 = 3.79 \text{ m}$		
18:00	$Z_0 - 0.82 = 2.26 \text{ m}$		
24:00	$Z_0 + 0.95 = 4.08 \text{ m}$		

Figure 4.10 shows the curve through the hourly values of the M_2 constituent predictions, and through the full predictions for 13 July 2043, based on the sum of 100 constituents.

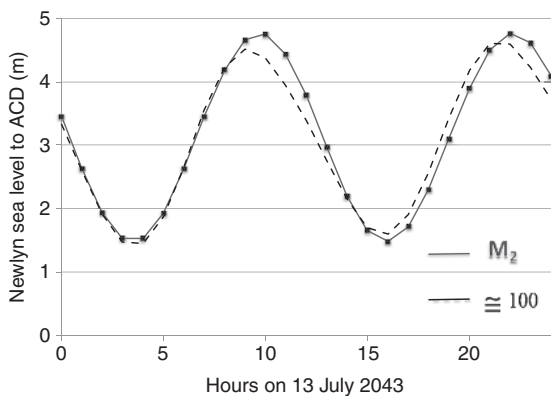


Figure 4.10 Newlyn predictions of M_2 for 13 July 2043 (blue line) and using a full set of 100 constituents (dashed line). Here the agreement is very good, but see Figure 4.11 for the effects of adding all constituents over a long period.

assume the tidal constituents will not change much by then. The method may be repeated for all the other constituents previously determined by analysis, and the full set of harmonics added together to give the prediction of levels. Figure 4.10 compares the levels predicted by M_2 alone, and by summing the set of 110 constituents.

Usually, the greater the number of constituents included in this process, the more reliable are the predictions. Figure 4.11 compares the levels predicted at Newlyn for March 2002 by M_2 alone, and by adding first S_2 , and then $(N_2 + L_2)$. The spring–neap changes are introduced by S_2 , and the effects of lunar distance changes by $(N_2 + L_2)$. The final curve shows the contribution to a full tidal prediction if a further 58 terms, including diurnal and shallow-water species

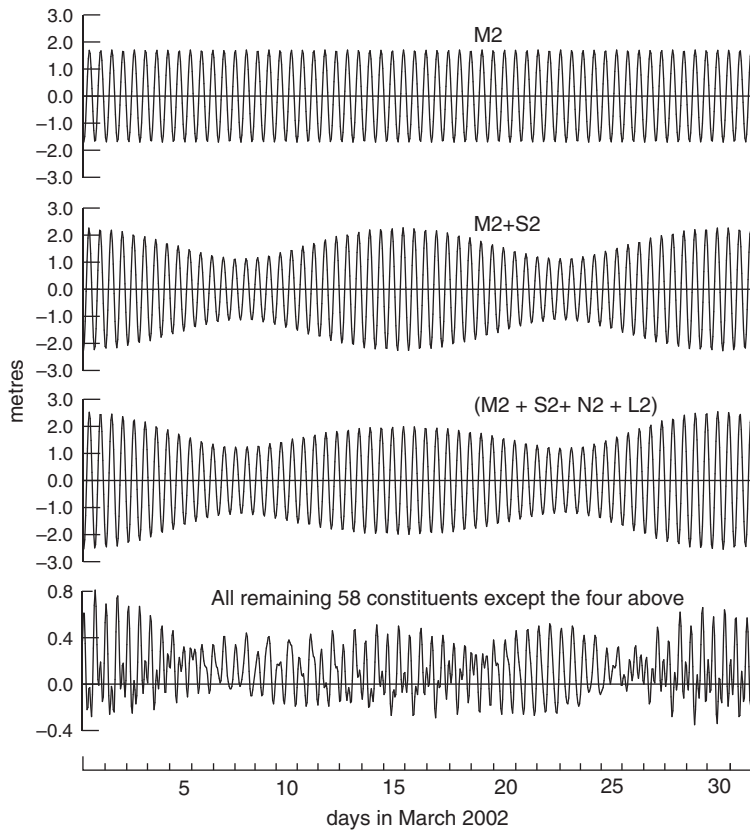


Figure 4.11 The effects of predicting tides with M_2 , $(M_2 + S_2)$ and $(M_2 + S_2 + N_2 + L_2)$ at Newlyn for March 2002. $(M_2 + S_2)$ gives the spring–neap modulation. Adding $(N_2 + L_2)$ allows for the varying distance of the Moon from the Earth during a lunar month. The bottom line shows the additional contribution to a full prediction, by a further 58 constituents, including diurnal and shallow water terms.

constituents are included. Typically, published predictions for Reference Stations are based on 60 or more constituents.

The times of high and low water are difficult to determine from the curves of total levels. An alternative method makes use of the turning point relationship:

$$\frac{\partial T(t)}{\partial t} = 0$$

and since, in simplest terms:

$$T = \sum_N H_n \cos(\sigma_n t - g_n)$$

$$\frac{\partial T(t)}{\partial t} = \sum_N H_n \sigma_n \sin(\sigma_n t - g_n) \quad (4.13)$$

Times of zero rate of change of water level, the high and low water times, can be found by summing Equation 4.13 for all the constituents, and finding the times of zero values. One approach is to compute

values every minute and identify turning points. Some of the more elaborate old mechanical tide predictors (see Figure 4.12) had the facility for simultaneously computing both the $\sin(\sigma_n t - g_n)$ terms and the $\cos(\sigma_n t - g_n)$ terms to get the best estimates of the times and the heights of the turning points.

In estuaries and regions of shallow water the harmonic method may fail to represent completely the sharp turning points, especially those of low water (see Figure 6.13). Although the number of constituents in the higher species can be increased to improve the predictions, eventually, more elaborate adjustments are necessary. Often these adjustments take the form of empirical corrections that are particular to each location.

Although high and low waters are the traditional method of presenting tidal predictions, for some operations it is better to have levels or currents predicted at hourly or even more frequent intervals. Again, there are problems when predicting the full curve of a severely distorted shallow-water tide. Tidal streams are also included in tables but usually only for

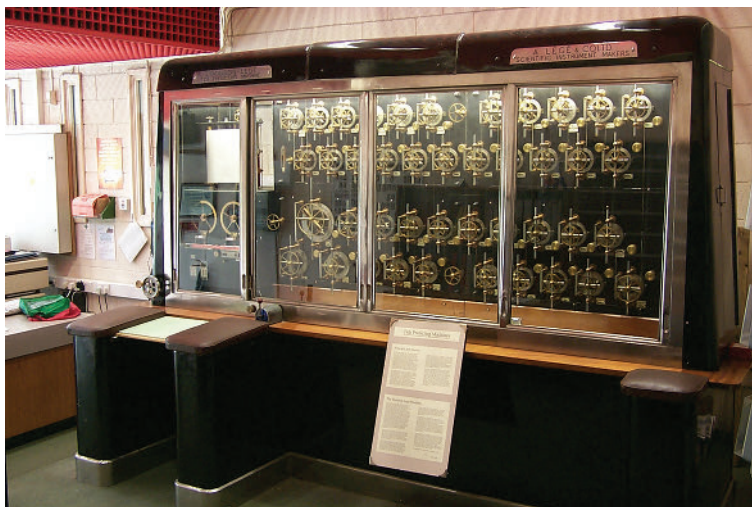


Figure 4.12 A mechanical tide-predicting 'Kelvin' machine, one of the first operational analogue computers. Each pulley wheel simulates the amplitude phase and period of a harmonic constituent. This particular machine is called a Doodson–Légé predictor and simulates 42 constituents. These machines remained in use for tidal predictions until around 1965. Photograph from the UK National Oceanography Centre.

rectilinear streams in straits where they are critical for planning shipping movement. Examples include the Torres Strait north of Australia, the approaches to Singapore Harbour, and the San Francisco Bay Entrance. The more common method for predicting tidal streams is to use a tabulation of current speeds and directions, sometimes called *tidal diamonds*, which are related to local high water levels, as in Table 4.8. Some important navigation areas have hourly maps of tidal streams through a tidal cycle (see Figure 5.18). Ideally real-time computer displays aboard ships, of local currents, would be available to a ship's navigator.

Although predictions for hard-copy publication could be prepared several years ahead, this is not usually done until about two years before, because the latest datum or time zone changes need to be incorporated. Normally the tidal constituents change very little over several tens of years, as discussed in Section 4.6. If there are major port developments, it is advisable to identify any changes that may have been inflicted on the tidal regime, by making a new analysis of a year of data. Because of the Metonic cycle of 19 tropical years, which is very close to 254 tropical lunar months, tidal predictions have a notable repeat pattern every 19 years, though not close enough for practical purposes.

4.7.2 Secondary or Subordinate Stations

Although the published annual tide tables contain daily high and low water information for several hundred stations, worldwide, these represent only a

fraction of the places for which tidal parameters, and hence predictions, are available. It would be impractical to prepare daily predictions from the astronomical arguments for all of these places. Instead, local time and height differences are published that allow adjustment to the published values to give predictions to Chart Datum for the Secondary or Subordinate Stations. The predictions published by the United States National Oceanic and Atmospheric Administration contain data for more than 3000 Subsidiary Stations. The British Admiralty also publishes data for several thousand Secondary Ports, worldwide.

Secondary Port time and height adjustment parameters may be based on analyses of long periods of data, but a month of observations is more usual, and normally adequate. In some remote locations observations may extend over only a few days.

The term Secondary Port does not imply secondary importance as a port and the same port may be a Standard Port in one publication but a Secondary Port in another. The Standard Port chosen may not be the nearest – the most suitable standard will be a port that has similar tidal characteristics. For this reason the Admiralty Tide Tables choose to refer some Japanese ports, where semidiurnal tides are dominant, to the Australian port of Darwin, which has similar tides, rather than the nearer Japanese Standard Ports, which have mixed tides.

In cases of extreme distortion, such as at Swanage or Selsey on the south coast of England (Chapter 6), special curves must be prepared for each individual port. British Admiralty tables also allow more

Table 4.12a Computations of Secondary Port times and heights at Monterey based on San Francisco as a Standard Port and NOAA conversion factors; and for Burncoat Head, Minas Basin, from the Canadian Tables, based on Saint John as a Standard or Reference Port.

30 Mar 02							
		Standard Port San Francisco		Secondary adjustment for Monterey		Computed tides for Monterey	
	time	height (ft)	time	height (ft)	time	height (ft)	
hw	00:19 am	6.2	-1:08	-0.5	11:11 pm	5.7	previous day
lw	06:23 am	-0.3	-0:47	-0.0	05:36 am	-0.3	
hw	12:59 pm	5.4	-1:08	-0.5	11:51 am	4.9	
lw	06:28 pm	1.0	-0:47	-0.0	05:41 pm	1.0	

Monterey tides are earlier and slightly smaller than those in San Francisco. Note that the United States publish tide tables in feet.

Table 4.12b

30 Mar 02							
		Standard Port Saint John		Secondary adjustment for Burncoat Head		Computed tides for Burncoat Head	
	time	height (m)	time	height (m)	time	height (m)	
hw	00:25	8.7	+1:07	6.8	01:32	15.5	
lw	06:40	-0.1	+1:11	-0.2	07:51	-0.3	
hw	12:50	8.6	+1:07	6.8	13:57	15.4	
lw	19:05	0.2	+1:11	-0.2	20:16	0	

Burncoat Head tides are later and much bigger than at Saint John. The secondary adjustments are those given for large tides. The Canadian tables give slightly different adjustments for medium tides.

elaborate calculations based on the harmonic constituents O_1 , K_1 , M_2 and S_2 , and allow adjustments for shallow-water fourth- and sixth-diurnal amplitudes and phases f_4 , F_4 ; f_6 , F_6 , but these are unnecessarily complicated. Other national authorities have slightly different methods of making the adjustments: full details of the procedures are given in the individual publications. Table 4.12 shows how Monterey high and low water parameters for a particular day can be calculated from San Francisco Reference Port values; and values for Burncoat Head are derived from Canadian predictions for Saint John.

Another practical and flexible method of presenting the tidal level characteristics of a Secondary Station is shown in the reduction curves of Figure 4.13. These are prepared from a series of tabulations of observations over at least one spring-neap cycle. Better results are obtained if several cycles are included. Here the

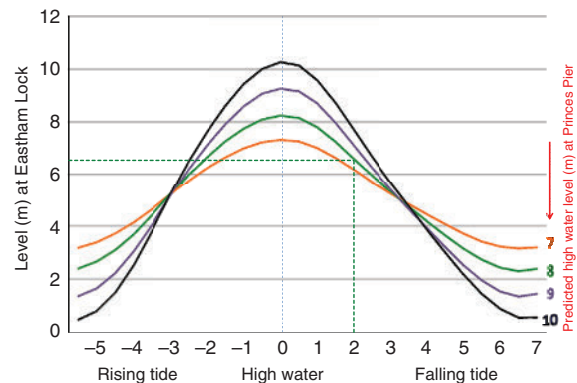


Figure 4.13 Levels at Eastham Lock, River Mersey, relative to high water times and ranges at Princes Pier, Liverpool. Liverpool is close to the open Irish Sea, whereas Eastham Lock (the Secondary Station in this case) is 15 km up-river. For example, if the predicted high water level at Princes Pier is 8 m, then the level at Eastham Lock two hours after this time will be 6.4 m above the datum level. Some tide tables show curves for spring and neap tides.

Box 4.1 Development of tidal predictions

An ability to predict future events, particularly those of practical importance, must inevitably have attracted some veneration to those who practiced the art. The ability to predict tides could also be a source of income for those who knew the secret. The priests of the early Egyptian temples could predict the onset of the flooding of the River Nile with their Nilometers. The English cleric the Venerable Bede (AD 673–735), familiar with the tides along the coast of his native Northumbria, discussed the phases of the Moon and how the tides could be calculated by the 19-year lunar cycle. Chinese methods of predicting the Qiantang river bore were carved in stone in the tenth or eleventh century [6]. By the early ninth century, tide tables and diagrams, showing how neap and spring tides alternated during the month, were appearing in several European countries. A later example of these is the St Albans Abbey tide table (c. 1250), which gives times of high water at London Bridge in terms of the age of the Moon. By the seventeenth century, annual tide tables of times for London Bridge were produced regularly; Flamsteed, the UK Astronomer Royal, commented that his 1683 predictions were the first to give the times of two high waters each day.

The first accurate, publicly accessible tide tables in the United Kingdom were produced for Liverpool by Richard and George Holden starting in 1770 [7]. Their method estimates how the lunar semidiurnal tide (in effect M_2) varies due to changes in lunar distance (parallax) and declination, and this is then combined with the solar semidiurnal tide (in effect S_2). These astronomical parameters were by then readily available since the publication of the first edition of *The Nautical Almanac* in 1767.

The first United States printed tide tables were privately published in 1830 [6]. In 1833, the British Admiralty published its first official annual tidal predictions (of high water times only), for four ports: Plymouth, Portsmouth, Sheerness and London Bridge. Today the harmonic method is easily applied by computers, but in earlier times they would have been difficult to apply for routine predictions without the ingenious tide-predicting machines developed by Lord Kelvin and Edward Roberts in 1872. These machines, which were an early form of mechanical computer, consisted of a set of pulleys, one for each constituent, which rotated at different speeds scaled according to the speed of the constituent they represented (Figure 4.12). The rotations were converted into harmonic motions and summed by means of a wire that passed over each pulley in turn. Phases and amplitudes for each constituent were set by adjusting the pulley settings for each port before running the

machine. To compute high and low water times and heights for a single port for one year took about two days of work. These machines were the basis for tidal predictions until around 1965, when they were replaced by electronic computers. A year of tidal predictions can now be calculated in a fraction of a second. Predictions for thousands of coastal locations worldwide are now instantly available on the Internet.

New data processing and position-fixing systems such as GPS have changed the traditional ways in which ship navigators make use of sea-level data. Paper charts and calculations from published tide tables will be around for many years to come, but it is common for port authorities to provide real-time chart, water level and tidal current information to ships entering harbour. Electronic Chart Displays (ECDIS), which can incorporate predicted or measured sea levels and currents, are available to assist mariners, according to regulations approved by the International Maritime Organization. It will be mandatory for vessels engaged on international voyages to be fitted with an ECDIS using Electronic Navigation Charts from 2018.

One small conceptual problem with ECDIS is that the shape and location of specific depth contours will change as sea levels rise and fall. However, the original contour lines and shapes can be retained if the depth that they represent is allowed to change with time. Smaller boat operators will probably find paper charts and mobile phone predictions cheaper and more convenient, and for the time being electronic charts must be backed up with traditional navigation methods.

curves are plotted for different tidal ranges at the same station. Alternatively curves could be drawn for several stations in an estuary for a specified fixed range at the reference port (MHWs and MHWN, for example). Increasingly, shipping movement in coastal areas benefits from real-time observations of currents and sea levels, transmitted to the bridge, and incorporated into Electronic Chart Display and Information Systems (ECDIS); (see Box 4.1). However, planning for shipping movements a day or so ahead must rely on tidal prediction, ideally adjusted for weather forecasts.

Many people continue to regard tidal analysis and prediction as a black art, as did people in earlier times. However, tidal analysis is neither as difficult nor as mysterious as they imagine. It is important to decide which level of complexity is appropriate for a particular application. Provided that certain basic rules relating to the data length and to the number of independent

parameters demanded in an analysis are followed, satisfactory results are obtainable. Inexperienced analysts often go wrong when they ask for too much from too few data. Nevertheless, to extract the maximum tidal information from a record, for example by exploiting the complementary aspects of different analysis techniques, and especially the flexibility of using various inputs to response analyses, further experience and informed judgement are necessary.

References

- Godin, G. 1972. *The Analysis of Tides*. Liverpool: Liverpool University Press.
- Doodson, A. T. and Warburg H. D. 1980. *Admiralty Manual of Tides*. London: Her Majesty's Stationery Office. (1st edition, 1941; latest reprint, 1980).
- Schureman, P. 1976. *Manual of Harmonic Analysis and Prediction of Tides*. Special Publication 98, Coastal and Geodetic Survey. Washington, D.C.: U.S. Department of Commerce (1st edition, 1924; latest reprint, 1976).
- (1) Foreman, M. G. G. 1977. *Manual for Tidal Heights Analysis and Prediction*. Canadian Pacific Marine Science Report No. 77–10. See <ftp://canuck.seos.uvic.ca/docs/MFTides/heights.pdf>. (2) Parker, B.B. 2007. *Tidal Analysis and Prediction*. NOAA Special Publication NOS CO-OPS 3. Washington, D.C.: U.S. Department of Commerce, National Oceanic and Atmospheric Administration, National Ocean Service. (3) Simon, B. 2007. *La Marée Océanique Côtière*. Paris: Institut Océanographique.
- Pawlowicz, R., Beardsley, B. and Lentz, S. 2002. Classical tidal harmonic analysis including error estimates in MATLAB using T_TIDE. *Computers and Geosciences*, **28**, 929–937, doi:10.1016/S0098–3004(02)00013–4.
- Cartwright, D. E. 1999. *Tides: A Scientific History*. Cambridge: Cambridge University Press.
- Woodworth, P. L. 2002. Three Georges and one Richard Holden: the Liverpool tide table makers. *Transactions of the Historic Society of Lancashire and Cheshire*, **151**, 19–51.
- Darwin, G. H. 1911. *The Tides and Kindred Phenomena in the Solar System* (3rd edition). London: John Murray.
- Doodson, A. T. 1921. Harmonic development of the tide-generating potential. *Proceedings of the Royal Society of London, A*, **100**, 305–329, doi:10.1098/rspa.1921.0088.
- (1) Cartwright, D. E. and Tayler, R. J. 1971. New computations of the tide-generating potential. *Geophysical Journal of the Royal Astronomical Society*, **23**, 45–74, doi:10.1111/j.1365–246X.1971.tb01803.x.
- (2) Cartwright, D. E. and Edden, A. C. 1973. Corrected tables of tidal harmonics. *Geophysical Journal of the Royal Astronomical Society*, **33**, 253–264, doi:10.1111/j.1365–246X.1973.tb03420.x. (3) For a general review of subsequent more precise expansions of the tidal potential, see Wihelm, H., Zurn, W. and Wenzel, H. G. 1997. *Tidal Phenomena*. New York: Springer-Verlag.
- Meeus, J. 1998. *Astronomical Algorithms* (2nd edition). Richmond, VA: Willmann-Bell.
- Amin, M. 1976. The fine resolution of tidal harmonics. *Geophysical Journal of the Royal Astronomical Society*, **44**, 293–310, doi:10.1111/j.1365–246X.1976.tb03658.x.
- Cartwright, D. E. 1975. A subharmonic lunar tide in the seas off Western Europe. *Nature*, **257**, 277–280, doi:10.1038/257277a0.
- Evans, J. J. and Pugh, D. T. 1982. Analysing clipped sea-level records for harmonic tidal constituents. *International Hydrographic Review*, **59**, 115–122.
- U.S. Coast and Geodetic Survey. 1952. *Manual of Harmonic Constant Reductions*, NOAA Special Publication 260. Washington, D.C.: U.S. Department of Commerce. Available at docs.lib.noaa.gov/rescue/cgs_specpubs/QB275U35no2601952.pdf.
- Amin, M. 1979. A note on extreme tidal levels. *International Hydrographic Review*, **56**, 133–141.
- Woodworth, P. L. and Cartwright, D. E. 1986. Extraction of the M2 ocean tide from SEASAT altimeter data. *Geophysical Journal of the Royal Astronomical Society*, **84**, 227–255, doi:10.1111/j.1365–246X.1986.tb04355.x.
- Parke, M. E., Stewart, R. H., Farless, D. L. and Cartwright, D. E. 1987. On the choice of orbits for an altimetric satellite to study ocean circulation and tides. *Journal of Geophysical Research*, **92**, C11, doi:10.1029/JC092iC11p11693.
- Derived from Egbert, G. D. and Erofeeva, S. Y. 2002. Efficient inverse modeling of barotropic ocean tides. *Journal of Atmospheric and Oceanic Technology*, **19**, 183–204, doi:10.1175/1520–0426(2002)019<0183:EIMOBO>2.0.CO;2.
- Developments of Ray, R. D. 1999. *A global ocean tide model from TOPEX/Poseidon altimetry: GOT99*, NASA Technical Memorandum 209478. Maryland: Goddard Space Flight Center.
- Developed from Lyard, F., Lefevre, F., Letellier, T. and Francis, O. 2006. Modelling the global ocean tides: modern insights from FES2004. *Ocean Dynamics*, **56**, 394–415, doi:10.1007/s10236–006–0086-x.
- Savcenko, R. and Bosch, W. 2012. EOT11a: Empirical Ocean Tide Model from Multi-Mission Satellite Altimetry. Deutsches Geodätisches Forschungsinstitut (DGFI), Munich, Report No. 89.

23. Cheng, Y. and Andersen, O. B. 2011. Multimission empirical ocean tide modeling for shallow waters and polar seas. *Journal of Geophysical Research*, **116**, C11001, doi:10.1029/2011JC007172.
24. Ray, R. D., Egbert, G. D. and Erofeeva, S. Y. 2011. Tide predictions in shelf and coastal waters: status and prospects. In *Coastal Altimetry* (eds. S. Vignudelli, A. Kostianoy, P. Cipollini and J. Benveniste), pp. 191–216, Berlin: Springer-Verlag, doi:10.1007/978-3-642-12796-0_8.
25. Francis, O. and Mazzega, P. 1990. Global charts of ocean tide loading effects. *Journal of Geophysical Research*, **95**, 11411–11424, doi:10.1029/JC095iC07p11411.
26. Shum, C. K., Woodworth, P. L., Andersen, O. B. et al. 1997. Accuracy assessment of recent ocean tide models. *Journal of Geophysical Research*, **102**, 25173–25194, doi:10.1029/97JC00445.
27. Munk, W. H. and Cartwright, D. E. 1966. Tidal spectroscopy and prediction. *Philosophical Transactions of the Royal Society of London, A*, **259**, 533–581, doi:10.1098/rsta.1966.0024.
28. Cartwright, D. E. 1968. A unified analysis of tides and surges round north and east Britain. *Philosophical Transactions of the Royal Society of London, A*, **263**, 1–55, doi:10.1098/rsta.1968.0005.
29. Cartwright, D. E. and Ray, R. D. 1991. Energetics of global ocean tides from Geosat altimetry. *Journal of Geophysical Research*, **96**, 16897–16912, doi:10.1029/91JC01059.
30. Foreman, M. G. G. 1977. *Manual for Tidal Heights Analysis and Prediction*. Canadian Pacific Marine Science Report No. 77–10. See <ftp://canuck.seos.uvic.ca/docs/MFTides/heights.pdf>.
31. International Hydrographic Organization. 1994. *Hydrographic Dictionary*. Special Publication No. 32, 5th edition. Monaco: International Hydrographic Organization.
32. Cartwright, D. E. 1985. Tidal prediction and modern time scales. *International Hydrographic Review*, **62**, 127–138.
33. Araújo, I. B. and Pugh, D. T. 2008. Sea levels at Newlyn 1915–2005: analysis of trends for future flooding risks. *Journal of Coastal Research*, **24**, 203–212, doi:10.2112/06-0785.1.
34. Colosi, J. A. and Munk, W. 2006. Tales of the venerable Honolulu tide gauge. *Journal of Physical Oceanography*, **36**, 967–996, doi:10.1175/jpo2876.1.
35. The many countries that make tidal predictions available include: United States <http://tidesandcurrents.noaa.gov/> France <http://www.shom.fr/les-services-en-ligne/predictions-de-maree/predictions-en-ligne> United Kingdom Admiralty <http://easytide.ukho.gov.uk/EasyTide/EasyTide/index.aspx> UK NOC <http://www.ntlslf.org> Canada <http://www.charts.gc.ca/publications/ctct-tmcc-eng.asp> Australia <http://www.bom.gov.au/oceanography/tides/>

Tidal dynamics

Who can say of a particular sea that it is old? Distilled by the sun,
kneaded by the moon, it is renewed in a year, in a day, or in an hour.
Thomas Hardy, The Return of the Native

5.1 The real world

The Equilibrium Tide developed from Newton's theory of gravitation consists of two symmetrical tidal bulges, directly under and directly opposite the Moon or Sun. Semidiurnal tidal ranges would reach their maximum value of about 0.5 m at the equator. The individual high water bulges would track around the Earth, moving from east to west in steady progression. These characteristics are clearly not those of the observed tides.

The observed tides in the main oceans have mean ranges of about 0–1 m (amplitudes 0–0.5 m), but there are considerable variations. The times of tidal high water vary in a geographical pattern, for the daily solar and semidiurnal lunar tides, which bears no relationship to the simple ideas of a double bulge. The different tidal patterns generated by the global and local ocean responses to the tidal forcing are clear in [Figure 5.1](#). The tides spread from the oceans onto the surrounding continental shelves, where much larger ranges are observed. In some shelf seas the spring tidal ranges may exceed 10 m: the Bay of Fundy, the Bristol Channel, the Baie de Mont Saint Michel and the Argentine Shelf are well-known examples of big tides. In the case of the northwest European shelf, tides approach from the Atlantic Ocean in a progression to the north and to the east, which is quite different from the Equilibrium hypothesis.

The reasons for these complicated ocean responses may be summarised as follows.

- (1) Movements of water on the surface of the Earth must obey the physical laws represented by the hydrodynamic equations of continuity and momentum balance: we shall see that this means they must propagate as long waves. Any propagation of a wave from east to west around the Earth would be impeded by the north–south continental boundaries. The only latitudes for unimpeded circumpolar movement are around the Antarctic continent and in the Arctic basin. Even around Antarctica the connection is very restricted through the Drake Passage between Cape Horn and Graham Land.
- (2) Long waves travel at a speed given by $c^2 = (\text{water depth} \times \text{gravitational acceleration})$. Even in the absence of barriers it would be impossible for an Equilibrium Tide to keep up with the Moon's tracking, because the oceans are too shallow, and the long-wave speed is too slow. Taking an average depth of 4000 m the wave speed is 198 m/s, whereas at the equator the sub-lunar point travels westwards at an average speed of 450 m/s. Around Antarctica, however, at 60° S the speeds are nearly equal. At one time it was thought that the tides were generated in Antarctic latitudes, from where they spread northwards to other areas. This spreading was supposed to explain the age of the tide, the time between new or full Moon, and the maximum observed tides in northern latitudes. However, we now know that the responses are more complicated than these simple ideas suggest.
- (3) The various ocean basins have their individual natural modes of oscillation which influence their responses to the tide-generating forces. There are many local resonant frequencies, but the whole global ocean system seems to be near to resonance at semidiurnal tidal frequencies, so the observed tides are substantially larger than the Equilibrium Tide. The ocean responses to forcing at diurnal tidal frequencies are much weaker. However, the

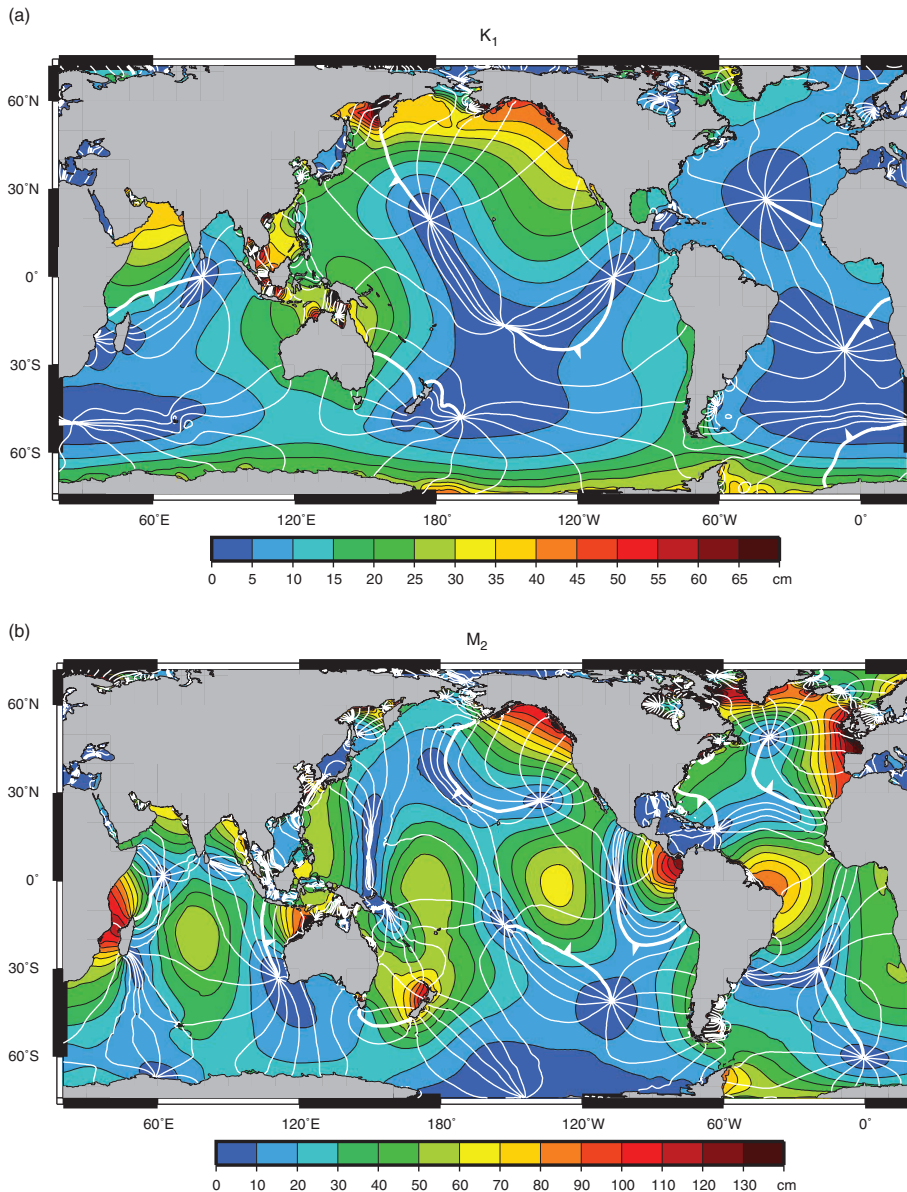


Figure 5.1 Co-tidal charts: global map of lines joining places where high tides for (a) K_1 and (b) M_2 occur simultaneously, and places with equal tidal range. The direct and loading tides have been removed. The lines indicate Greenwich phase lag every 30° , a lag of zero degrees being shown by the bold line, and the arrows showing the direction of propagation. Images supplied by Dr Richard Ray, Goddard Space Flight Center.

local responses of each area of the continental shelf to the driving by the ocean tides allows different sets of local resonances to apply. In some cases such a local resonance selectively amplifies diurnal tides; so there is a local amplification of the diurnal tides, as in the Gulf of Tonkin and the Gulf of Carpentaria (see Karumba in Figure 1.2a).

(4) Water movements are affected by the rotation of the Earth. The tendency for water movement to maintain a uniform direction in absolute space means that it performs a curved path in the rotating frame of reference within which we make observations. Alternatively, motion in a straight line on a rotating Earth is curved in absolute space and must be sustained by forces at right angles to

the motion. These effects are represented by the Coriolis accelerations in the hydrodynamic equations. The solutions to the equations show that certain modified forms of wave motion are possible, the most important of which have a form described as Kelvin waves.

- (5) The solid Earth responds elastically to the imposed tidal forces, as discussed in [Section 5.7](#). The extent of this response is described in terms of Love numbers. Although the response of the solid Earth to the direct tidal forcing is well described in these terms, there are additional local and far-field effects due to the depression caused by the tidal loading. The tide measured at a coastal station, or by a pressure sensor on the seabed, is the difference between the change in the geocentric position of the sea surface, and the geocentric position of the land surface reference point. Altimetry measurements give the strictly geocentric displacements of the sea surface ([Chapter 9](#)).

In this chapter we discuss the generation of ocean tides, their propagation onto the surrounding continental shelves, and the characteristics of shelf tides. The development of our understanding of tides in the oceans and in continental shelf seas has been through a synthesis of theoretical ideas of wave propagation on a rotating Earth and direct observations. In the first part of the chapter we concentrate on the basic physical ideas. In the second part we show how they are applied to describe the observed tidal patterns in selected areas. These regional accounts are presented in some detail because the information is not readily available in a single text; the best-integrated detailed account remains Defant's classic two-volume treatise [1]. Fuller mathematical treatment of the more important ideas is given in [Appendix D](#) for those who require a more theoretical approach.

5.2 Long-wave characteristics

Waves are commonly observed in nature. The most familiar form is probably the progression and breaking of waves on the beach. These waves, which are generated by winds acting on the sea surface, have periods from a few seconds to perhaps 15 seconds. Tidal waves have similar characteristics of propagation and individual wave crests can be followed and charted. Historically, the Venerable Bede (673–735) knew of the progression of the time of high water from north to south along the east coast of Britain

[2]. However, the tidal waves have periods of about 24 hours and 12 hours, corresponding to diurnal and semidiurnal tides, and so their wavelengths are increased to many hundreds of kilometres. Waves with wavelengths much longer than the water depth are called long waves and they have some special properties. When presenting information on tides in a region it is usual to draw maps for each individual harmonic constituent. These maps have contours joining places where high waters occur simultaneously, which are called co-tidal lines; for a harmonic constituent this also means that low water and all other phases of the tide also occur simultaneously at all places joined by a co-tidal line. The maps may also have contours joining places that have harmonic constituents of equal amplitude (also, of course, equal range) called co-amplitude lines (or co-range lines).

5.2.1 Wave propagation in a non-rotating system

We begin by summarising some basic properties of wave motion on the surface of water in the absence of rotation. [Figure 5.2](#) shows a disturbance travelling in the positive X direction without change of shape, in water of depth D below the undisturbed sea level. As the wave moves past some fixed point, A , a succession of high and low sea levels will be observed. If the wave travels at a speed c and has a period T , the wavelength λ is:

$$\lambda = cT$$

It can be shown [[3](#), [4](#), [5](#)] ([Appendix D](#)) that provided the wave amplitudes are small compared with the water depth, and the depth is small compared with the wavelength, then the speed is:

$$c = \sqrt{gD} \quad (5.1)$$

where g is gravitational acceleration. Similarly, the currents u are related to the instantaneous level at A :

$$u = \zeta \sqrt{g/D} \quad (5.2)$$

At local high water there is a maximum current in the direction of wave propagation, but at low water there is a current in the opposite direction. These results are not dependent on the exact shape of the travelling disturbance.

To derive these expressions from the continuity and horizontal momentum equations (see [Appendix](#)

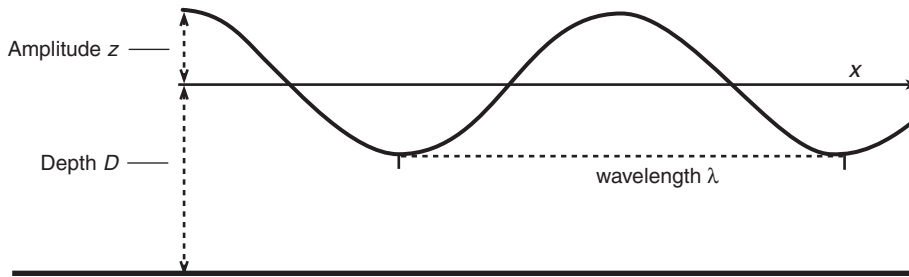


Figure 5.2 Characteristics of the one-dimensional progressive wave. The wave period is the time it takes to travel one wavelength.

A), the equations are reduced to a very simple form for small disturbances propagating in a deep channel:

$$\begin{aligned} \frac{\partial \zeta}{\partial t} + D \frac{\partial u}{\partial x} &= 0 \\ \frac{\partial u}{\partial t} + g \frac{\partial \zeta}{\partial x} &= 0 \end{aligned} \quad (5.3)$$

and these have a solution in ζ and u :

$$\begin{aligned} \zeta &= H_0 \cos(kx - \omega t) \\ u &= H_0 \sqrt{\frac{g}{D}} \cos(kx - \omega t) \end{aligned} \quad (5.4)$$

which represent a free progressive harmonic wave travelling in the positive X direction, where:

ω is the harmonic angular speed = $2\pi/T$
 k is the wave number = $2\pi/\lambda$

This can be considered as an individual tidal constituent of amplitude H_0 , travelling at a speed:

$$c = (\omega/k) = (\lambda/T) = \sqrt{gD}$$

Long waves have the special property that the speed c is independent of the angular speed ω , and depends only on the value of g and the water depth. Any disturbance that consists of a number of separate harmonic constituents will not change its shape as it propagates. This is called non-dispersive propagation. Waves at tidal periods are long waves, even in the deep ocean, as shown in Table 5.1, and their propagation is non-dispersive. Wind waves, which have much shorter periods and wavelengths, usually undergo dispersive propagation, with swell from distant storms travelling more rapidly ahead of the shorter period waves. Details of the behaviour of progressive waves when they encounter a step change in water depth and of their energy fluxes are given in Appendix D.

Table 5.1 Speeds and wavelengths of the tidal waves in water of different depth

Depth (m)	Speed		Wavelength (km)
	m/s	km/hr	diurnal
4000	198	715	17,720
200	44	160	3,960
50	22	80	1,980
20	14	50	1,250

5.2.2 Standing waves, resonance

In the real oceans, tides cannot propagate endlessly as progressive waves. They undergo reflection at sudden changes of depth, and at the coastal boundaries. The reflected and incident waves combine together to give the observed total wave [1]. Consider the simplest case of a wave travelling in a long channel being reflected without loss of amplitude at a closed end. The interference between the two waves produces a fixed pattern of standing waves which have alternate nodes, positions where the amplitude is zero, and antinodes, positions where the amplitude is a maximum, each separated by a distance $\lambda/4$ where λ is the wavelength of the original progressive wave as illustrated in Figure 5.3. The first node is located at a distance $\lambda/4$ from the reflecting barrier and at this point there is no net change of water level, but the currents have their maximum amplitude. At a distance $\lambda/2$ from the barrier there is an antinode where the changes in level have the same range as at the reflecting barrier, but there are no currents. The absence of horizontal water movements at this antinode means that a solid impermeable boundary could be inserted into the channel at this point without affecting the oscillations once they had become established.

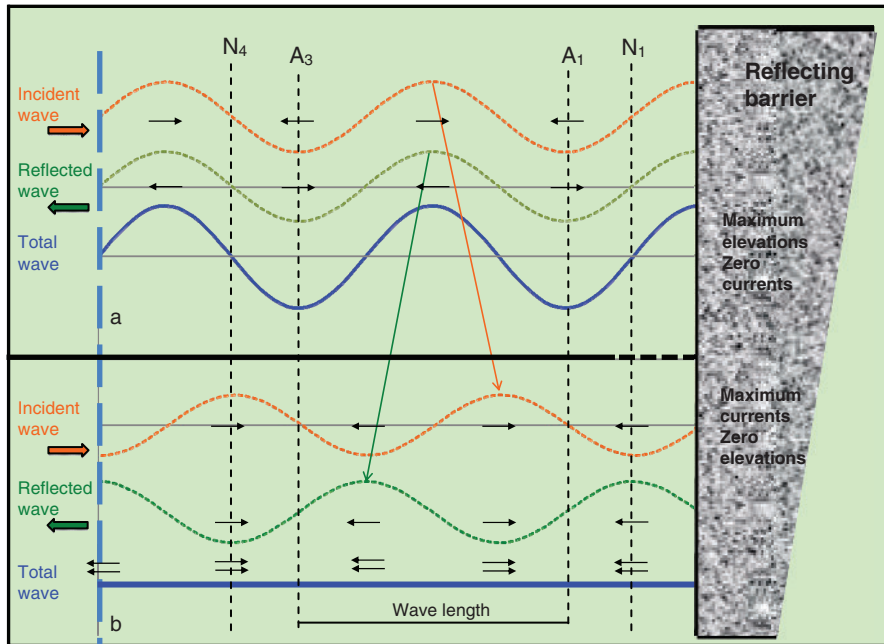


Figure 5.3 Showing how incident and reflected waves of equal amplitude produce a standing wave pattern with nodes and antinodes (arrows are currents). (a) High water at the reflecting barrier. (b) A quarter of a cycle later, the incident wave has moved a quarter wavelength towards the barrier, and the reflected wave has moved a quarter wavelength in the opposite direction, away from the barrier. After half a cycle the elevations and currents are the reverse of (a); after three-quarters of a period they are the reverse of (b).

Consider the movement of water in a rectangular box of length L , as shown in [Figure 5.4](#). This box may represent a domestic bath, a swimming pool, or a long narrow lake or sea. The water movements can be compared with those of a pendulum, with the least horizontal motion at high and low water [(1) and (3)] and the maximum horizontal motion at the middle of the oscillation [(2) and (4)]. There is a continuous transfer from maximum potential energy (1) through a position of zero potential energy but maximum kinetic energy (2) to a second position of maximum potential energy (3). The sequence continues through a second condition of maximum kinetic energy (4) as it returns to its initial state of maximum potential energy (1).

This regular water movement can be considered as two progressive waves travelling in opposite directions with perfect reflections at both ends. The natural period of oscillation of the water is the time taken for a wave to travel from one boundary and to return after reflection at the second boundary. From [Equation 5.1](#) this time is:

$$\frac{2 \times \text{box length}}{\sqrt{g \times \text{water depth}}} = \frac{2L}{\sqrt{gD}} \quad (5.5)$$

[Equation 5.5](#) is known as ‘Merian’s Formula’ after its originator [4]. Examples of some natural periods for this half-wave oscillation are given in [Table 5.2](#). Natural periods of long lakes may be estimated using this formula, but the observed periods will vary slightly because the depths are not uniform. For the fundamental mode of oscillation there is one node, and the term uninodal seiche is often applied. The next highest mode has two nodes, and so on. The irregular shapes of real lakes result in several natural periods of oscillation including lateral as well as longitudinal modes.¹

Standing waves may also occur in a box that is closed at one end but driven by oscillatory in-and-out currents at the other open end ([Figure 5.5](#)). The simplest case is a box whose length is a quarter wavelength of the oscillation, so that the open end is at the first node (case 2 in [Figure 5.5](#)), equivalent to half the box in [Figure 5.4](#). The current at the entrance produces large changes of level at the head of the box or basin. The natural period for this type of forced oscillation is:

¹ Harbour basins also have natural oscillation periods that give rise to seiches as discussed in [Chapter 7](#).

$$\frac{4 \times \text{box length}}{\sqrt{g \times \text{water depth}}} = \frac{4L}{\sqrt{gD}} \quad (5.6)$$

Although this model of an open box approximates to the tidal behaviour of many shelf sea basins, an exact quarter-wave dimension would be very unlikely. In reality, although the open boundary may lie within the node (3) or outside the node (1), as shown in Figure 5.5, the probability of tidal amplification still exists. However, if the length of the basin is only a small fraction of the tidal wavelength (4), then the amplification will be small. The semidiurnal tide in Long Island Sound, on the east coast of the United States, is an example of quarter-wave resonance.

This type of oscillation will only continue for as long as the currents and elevations drive it from the

Table 5.2 Examples of the natural periods of oscillation of water bodies in the first gravitational mode from Merian's formula (Equation 5.5)

Basin type	Length	Depth (m)	Period
Bath	1.5m	0.2	2.1 s
Swimming pool	10 m	2.0	4.5 s
Loch Ness, Scotland	38 km	130	35 min

open end. This forced motion is different from the natural free seiche oscillations of a body of water, which can be initiated by an impulse such as a sudden squall, and which will continue until damped by frictional energy losses and imperfect reflections. Table 5.3 gives the lengths and corresponding depths of basins that would have quarter wavelengths appropriate for the semidiurnal M_2 tide. Systems that are forced by oscillations close to their natural period have large amplitude responses. This resonant behaviour is familiar in many physical systems including electrical circuits and badly designed acoustic speakers. As we shall discuss later, the responses of oceans and many seas are close to resonance.

In nature the forced resonant oscillations cannot grow indefinitely because energy losses due to friction increase more rapidly than the amplitudes of the oscillations themselves. Because of energy losses, tidal waves are not perfectly reflected at the head of a basin, which means that the reflected wave is smaller than the ingoing wave. It is easy to show that this is equivalent to a progressive wave superimposed on a standing wave (Appendix D), with the progressive wave carrying energy to the head of the basin. Standing waves cannot transmit energy because they consist of two progressive waves of equal amplitude travelling in opposite directions.

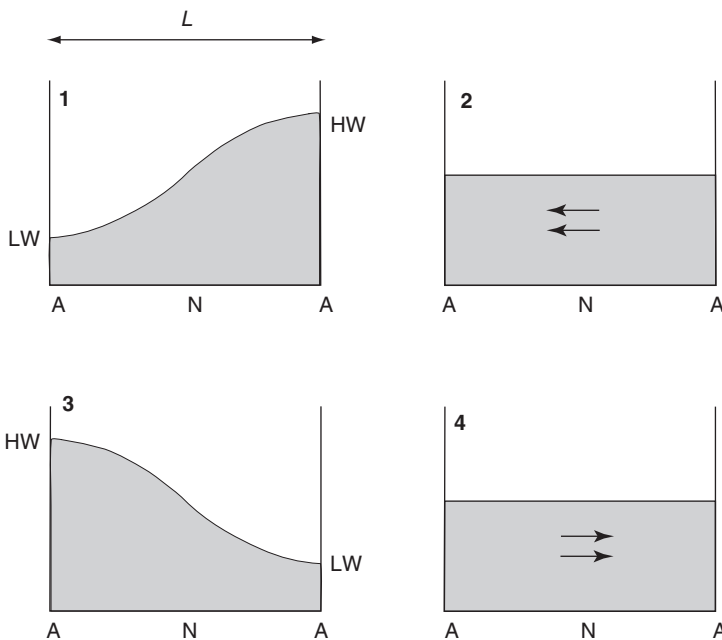


Figure 5.4 A simple standing wave oscillation in a closed rectangular box, showing nodes and antinodes, for levels and currents. The sequence moves from 1 to 4, and then back to 1, in quarter-period steps.

5.2.3 Waves on a rotating Earth

A long progressive wave travelling in a channel on a rotating Earth behaves differently from a wave travelling along a non-rotating channel. The forces that describe the motion of ocean currents in a rotating-Earth system cause a deflection of the currents towards the right of the

Table 5.3 Some lengths and depths of basins that would have quarter-wave resonance if driven by a semidiurnal M_2 tide

Water depth (m)	Basin length (km)
4000	2200
1000	1100
200	500
100	350
50	250

direction of motion in the northern hemisphere and conversely in the southern hemisphere. This sideways component of the flow continues until impeded by the right-hand boundary of the wave channel. The build-up of water on the right of the channel gives rise to a pressure gradient across the channel, and this slope develops until at equilibrium it balances the Earth-rotation (geostrophic) force. The mathematical description of the resulting waves is given in [Appendix D](#). These waves were originally described by Lord Kelvin and are now named after him. Rotation influences the way in which the wave amplitude H_y decreases across the channel away from the value H_0 at the right-hand boundary, as shown in [Figure 5.6a](#) (in the northern hemisphere):

$$\begin{aligned}\zeta(y) &= H_0 \exp(-fy/c) \\ u(y) &= \sqrt{gD} \zeta(y)\end{aligned}\quad (\text{D.15})$$

where H_0 is the amplitude at $y = 0$.

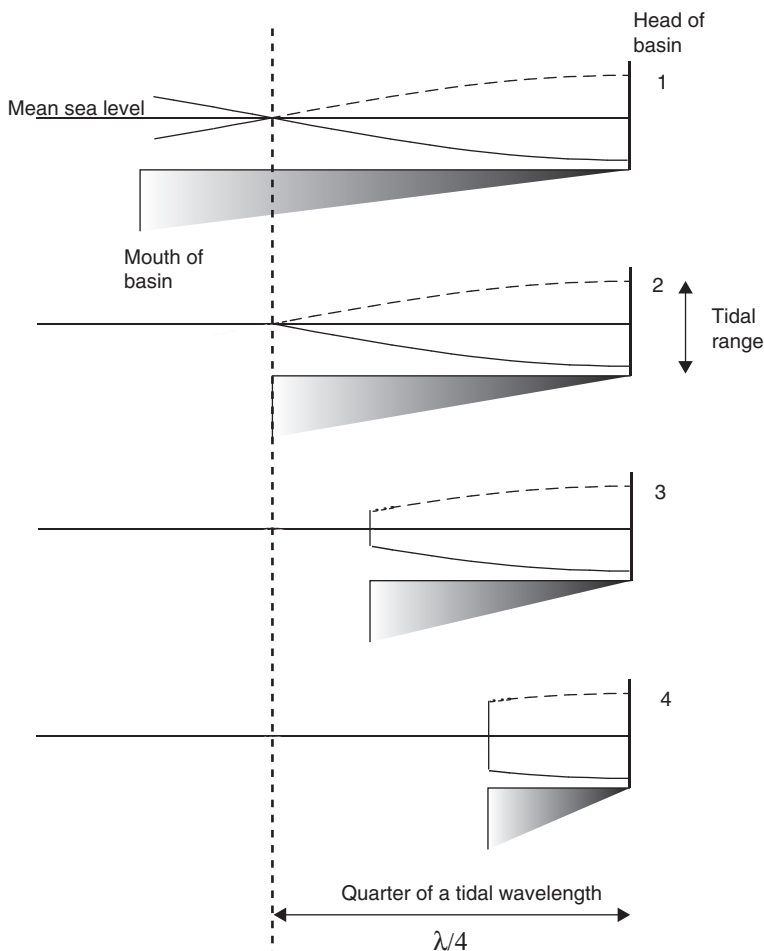


Figure 5.5 Responses of four sea basins of reducing lengths, driven by tidal level changes at the open end, near to quarter-wave resonance. There is maximum amplification (measured as the ratio between the range at the mouth and at the head of the basin) when the basin length corresponds to a quarter of a tidal wave length (case 2).

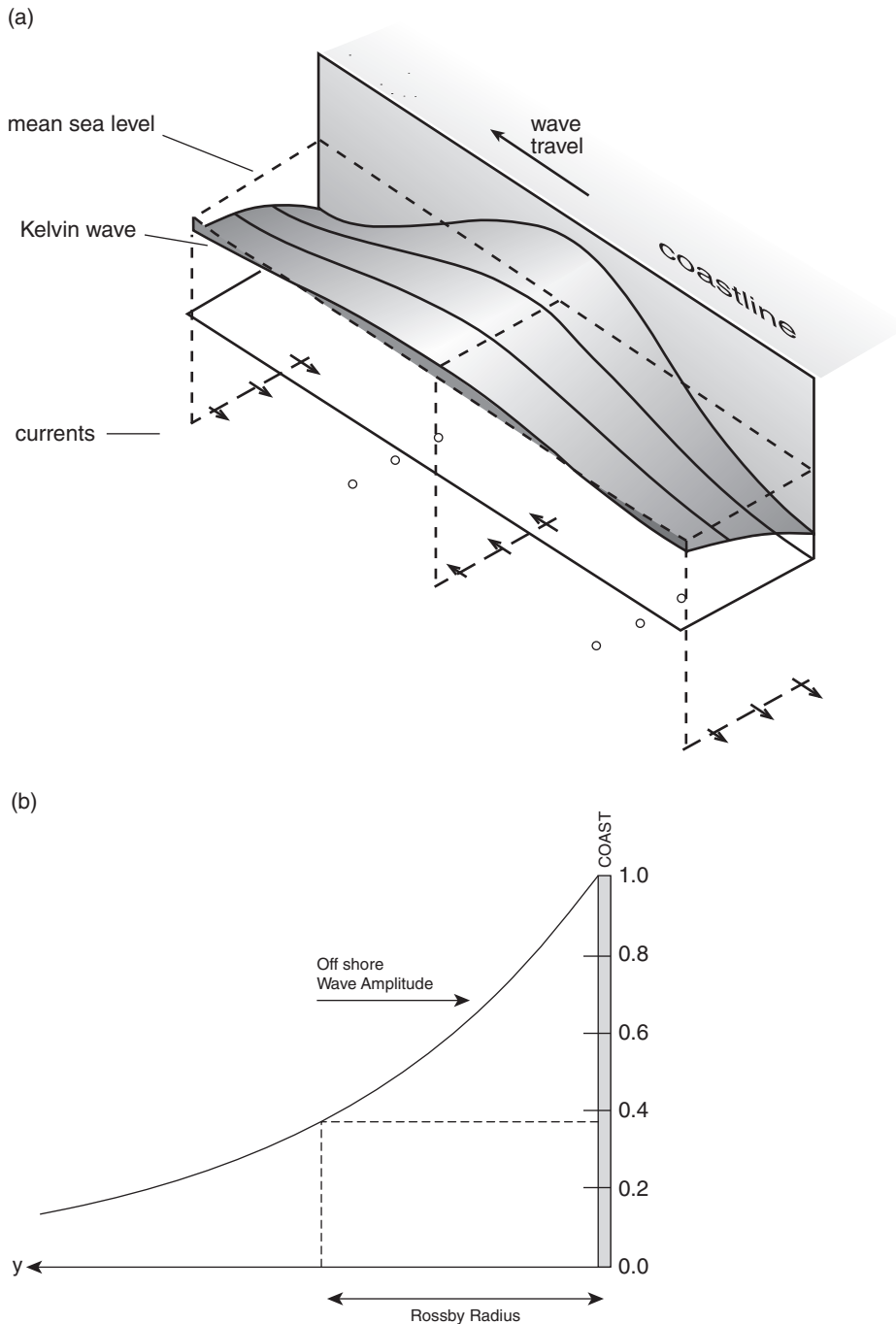


Figure 5.6 Kelvin wave dynamics: (a) a three-dimensional illustration of the elevations and currents for a Kelvin wave running parallel to a coast on its right-hand side (northern hemisphere). The normal dynamics of wave propagation are altered by the effects of the Earth's rotation which act at right angles to the direction of wave travel. (b) A two-dimensional section across the Kelvin wave at high tide, showing how the tidal amplitude falls away exponentially from the coast; at one Rossby radius the amplitude has fallen to 0.37 of the coastal amplitude. The wave is travelling into the paper.

Amplification falls off according to an exponential decay law with a scale length cf , which is called the Rossby radius of deformation, where c is the wave speed \sqrt{gD} , and f is the Coriolis parameter. At a distance $y = cf$ from the boundary the amplitude has fallen to $0.37H_0$. In this type of wave motion, the speed is the same as for a non-rotating case, and the currents are always parallel to the direction of wave propagation. Figure 5.6b shows the profile across a Kelvin wave. Note that Kelvin waves can only move along a coast in one direction. In the southern hemisphere the coast is on the left of the direction of propagation.

The case of a standing wave oscillation on a rotating Earth is of special interest in tidal studies. At the head of a basin, where reflection takes place, the currents and elevations have waveforms that can only be described by complicated mathematics, but away from the boundary the tidal waves can be represented by two Kelvin waves travelling in opposite directions. Instead of oscillating about a nodal line, the wave can now be seen to rotate about a nodal point, which is called an amphidrome. Figure 5.7 shows the co-tidal and co-amplitude lines for a Kelvin wave reflected without energy loss at the head of a rectangular channel [6]. The sense of rotation of the wave around the amphidrome is anticlockwise in the northern hemisphere and clockwise in the southern

hemisphere. The co-tidal lines all radiate outwards from the amphidrome and the co-amplitude lines form a set of nearly concentric circles with the centre at the amphidrome, at which the amplitude is zero. The amplitude is greatest around the boundary of the basin.

If the reflected Kelvin wave is weaker than the incoming Kelvin wave, then the amphidrome is displaced from the centre of the channel to the left of the direction of the in-going wave (northern hemisphere). Figure 5.8 shows this displacement increasing as the reflected Kelvin wave is made weaker [7]. In a narrow channel the amphidromic point may move outside the left-hand boundary, and in this case (not illustrated), although the full amphidromic system shown in Figure 5.7 is not present, the co-tidal lines will still focus on an inland point, which is called a virtual or degenerate amphidrome (see Section 6.6.2). We are now able to apply these theoretical ideas of progressive and standing waves, resonance, Kelvin waves and amphidromic systems to describe the dynamics of the observed tides in the oceans and shelf seas.

5.3 Ocean tides

Dynamically there are two essentially different types of tidal régime [1]. In the wide and relatively deep ocean

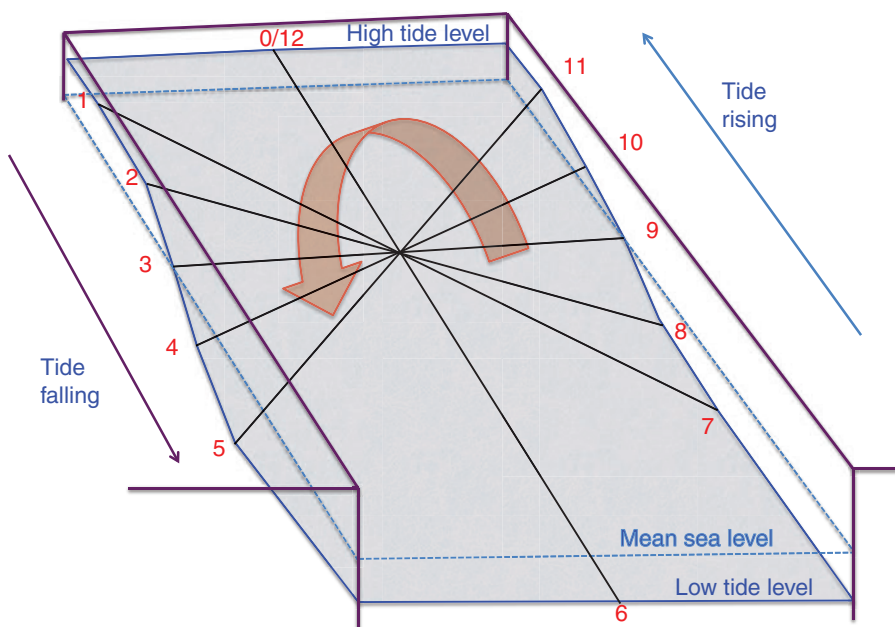


Figure 5.7 Amphidrome dynamics: a three-dimensional drawing exaggerated to illustrate how a tidal wave progresses around an amphidrome in a basin in the northern hemisphere. The red numbers are hours in the semidiurnal cycle.

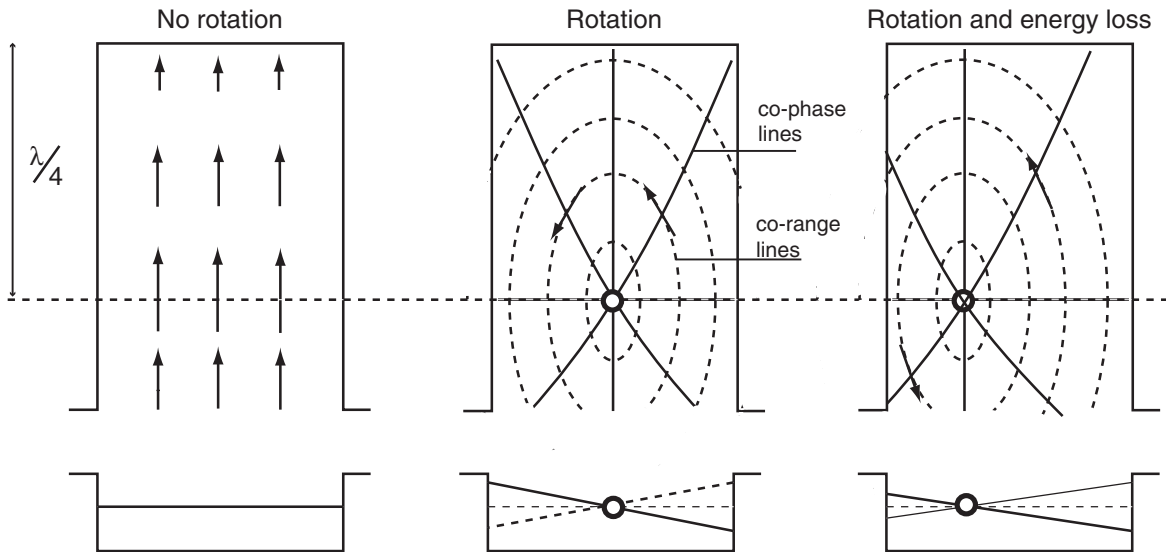


Figure 5.8 Amphidrome dynamics: the effects of the Earth's rotation on a standing wave in a basin that is slightly longer than a quarter wavelength. With no rotation there is a line of zero tidal amplitude. Because of the Earth's rotation, the tidal wave rotates around a point of zero amplitude, called an amphidromic point. In the third case, because the reflected wave has lost energy through tidal friction, the amphidrome is displaced from the centre line.

basins the observed tides are generated directly by the external gravitational forces. In the shelf seas the tides are driven by co-oscillation with the oceanic tides. The ocean response to the gravitational forcing may be described in terms of a forced linear oscillator. Tides propagate as waves from the deep oceans on to the shelf. Tidal energy is dissipated in the deep ocean through generation and decay of internal tides, and on the shelf by bottom friction opposing the tidal currents. This sense of tidal progression from the oceans to the shelf is also followed in our discussions.

5.3.1 Towards tidal charts

Originally, the most direct way of preparing co-tidal and co-amplitude charts of ocean tides was simply to interpolate the coastal and island tidal parameters across oceans and later to supplement these where possible with data from bottom-pressure observations. With so few observations available it was advisable to constrain the charts by the known theoretical properties of long waves propagating on a rotating Earth. As explained, these include the previously developed ideas of progressive and standing waves, resonance, Kelvin waves, and amphidromic systems. It is useful to extend [Section 1.2](#), the development of scientific understanding, and to place modern ideas in a historical context [8]. Following

Newton's development of the Law of Gravitation, and Bernoulli's concept of an Equilibrium Tide, Laplace established in 1775 the hydrodynamic equations of continuity and momentum for a fluid on a rotating Earth similar to those given in Appendix A, including the rotation term later credited to Coriolis. Laplace assumed a spherical Earth with a geocentric gravitational field uniform both horizontally and with time, a rigid ocean bottom and a shallow ocean, which allowed Coriolis accelerations associated with vertical movements and with the horizontal component of the Earth's rotation to be neglected. The consequences of neglecting vertical accelerations have been carefully considered by subsequent theoretical work, which shows that for the vertically stratified ocean the approximation is justified. Using these equations Laplace considered the types of wave motion possible on a thin sheet of fluid of uniform depth on a rotating sphere and showed that the response to the tide-generating forces was critically dependent on the depth. For depths that exceed a critical value the driven tide is in phase with the gravitational forcing and is said to be direct; but for depths less than the critical value the driven tide has the opposite sign to the forcing and is said to be inverted. The dynamics of propagation in zonal canals, which had previously been considered in 1740 by Bernoulli, was further investigated in 1845

by Airy, who introduced energy losses through a linear frictional term and considered the resulting distortions to the progressive wave.

A completely different approach was taken by Harris (1897–1907) [9], who pictured the global tides as a mosaic of standing wave systems, each with natural period equal to that of the tides. Although severely criticised for its lack of mathematical rigour and its neglect of the Earth's rotation, Harris's techniques produced charts that were generally compatible with the available observations and a considerable improvement on those previously drawn. His emphasis on the influence of resonance was an important contribution to modern ideas of near-resonant ocean response to semidiurnal forcing. Attempts to solve Laplace's tidal equations for ocean basins of different geometrical shapes and depths have served to demonstrate the types of motion that may occur and to investigate the sensitivity of the ocean tides to parameters such as basin width and depth, but the real oceans are too complex for detailed realistic analytical solutions.

Numerical solutions of the equations by powerful computers can give better realistic fits to all of the observations. The principle is straightforward: the oceans are divided into a network of elementary areas sufficiently small to define their shape and depth variations. Some compromise is necessary between a very detailed resolution and the computing power available. Three general approaches have been used: models based on the analysis of altimetric data to extract various tidal signals; hydrodynamic models computed directly from gravitational tidal forcing; and dynamic models adjusted to assimilate observed tidal data (altimeter, and coastal and pelagic tide gauges). Energy dissipation can be introduced by radiating energy through the boundaries, by bottom friction or by a form of eddy viscosity; three-dimensional models can also allow. As a general rule these conform to internal tides. Two-dimensional (depth-averaged) global tidal models have tended to produce unreasonably large tidal amplitudes that cannot be reduced by varying the generally accepted friction parameters and require additional damping with the use of unfeasibly large horizontal eddy viscosity (see Section 5.6 and Section 6.7.3). Both the solid Earth tides and the ocean loading effects can be included, as can the gravitational self-attraction of the tidal bulges. Figure 5.1 is an example of K_1 and M_2 charts produced by analysis of altimeter data.

5.3.2 General features

In detail, the principal lunar semidiurnal tidal constituent M_2 in Figure 5.1b shows a large number of amphidromes. As a general rule these conform to the expected behaviour for Kelvin wave propagation, with anticlockwise rotation in the northern hemisphere, and clockwise rotation in the southern hemisphere. Some caution is necessary: for example, the M_2 system west of Africa in the South Atlantic Ocean rotates anticlockwise, showing that other types of wave dynamics are also involved. Similar charts have been prepared for all the other major tidal constituents, and each of these contains many amphidromes. The amplitudes of the semidiurnal tides are significantly greater than the amplitudes of the diurnal tides because the oceans have a near-resonant response to forcing at semidiurnal frequencies. The possibility of a near-resonant response for semidiurnal tides is confirmed by rough estimates using Merian's formula (Equation 5.5). In 4000 m depth the progressive wave speed of 198 m/s and a typical ocean length scale of 10,000 km gives a period of 14 hours. Examples of the relative importance of the diurnal and semidiurnal tides are given in Table 1.1, in the form factors of Section 4.2.6, and in Figure 4.2.

For progressive tidal waves to develop fully as Kelvin waves, the channel in which they propagate must be wide compared with the Rossby radius (c/f) (see Equation D.15). At 45° latitude, the Rossby radius in 4000 m depth is 1900 km, but this increases as the latitude decreases (Table 5.4). The Pacific is clearly wide enough for full development, but the Atlantic may be too narrow. Ocean tidal currents are very weak. For a progressive wave of 0.5 m in amplitude in 4000 m depth, Equation 5.2 gives a speed of 0.025 m/s, which is small compared with currents generated by other forces. Internal tides (Section 5.6) give currents at tidal periods with greater speeds, but these currents are irregular and lack the coherence of shelf tidal currents.

In the Pacific, as elsewhere, semidiurnal tides are dominant, but in the north diurnal tides are also well developed. The semidiurnal amphidrome at 25° N, 135° W has been firmly established by observations, as has the amphidrome near 25° S, 150° W. This amphidrome gives very small M_2 tides in the vicinity of the Society Isles. Because the S_2 amphidrome is not identically placed, the S_2 tides are dominant at some sites. Where this occurs the semidiurnal tides have their high and their low water at the same times every day. This is a very local phenomenon, but something similar is found along the coast of southern Australia from western

Tasmania to Cape Leeuwin, where the M_2 and the S_2 constituents have similar amplitudes. At Thevenard, for example, for part of the spring–neap cycle the times of high water are similar for several successive days.² The semidiurnal ocean tides progress around New Zealand as around an amphidrome, but in an anticlockwise sense, which is not as expected in the southern hemisphere, and the dynamics cannot be those of cancelling Kelvin waves because the amplitudes are greatest at the coast. The reason for this behaviour is probably the trapping of the tidal waves by the topography of the surrounding continental slope. Changes in bottom topography have a strong influence on the tidal propagation. As the tide approaches the Hawaiian Islands the wave is diffracted by the submarine ridge, which extends over 500 km, rather than by the individual islands; this gives a focussing of co-tidal lines from a more extensive region, as illustrated for a coastal headland in Figure D.4. The semidiurnal tides at Honolulu have a negative age, with maximum amplitudes 14 hours ahead of maximum M_2 gravitational forcing, which is unusual as the age of the tide generally has a lag of one or two days.

The semidiurnal tides in the northern **Indian Ocean** have two distinct regimes. The Arabian Sea is broad enough for the standing wave system to develop an amphidrome; however, this amphidrome, which is situated close to the equator, cannot be described simply in terms of Kelvin waves. The entrance to the Bay of Bengal is too narrow for an amphidromic system to develop. The wave propagates to the north along the west coast of Sumatra and Thailand and also along the east coast of Sri Lanka, where the range is low and there is a tendency towards a degenerate amphidrome. In the south central Indian Ocean there is an extensive region of large semidiurnal tides over which the phases change only slowly. Dynamically this phenomenon, which corresponds to an antinode in Figure 5.3, is called an *anti-amphidrome*. A similar semidiurnal system is shown in the south central Pacific Ocean. Large tidal ranges are also observed between the island of Madagascar and the African mainland, in the Mozambique Channel, because of a similar double standing wave system.

In the **Southern Ocean**, there is a circumpolar zonal channel around 60° S. Early scientific ideas supposed that this would allow a resonant response to the tidal forces: for a circumference of 20,000 km and a

wave travelling in 4000 m water depth, simple theory gives a complete cycle in 28 hours, and allows resonances at harmonics of this. Whewell argued in 1833 that the directly driven tides of the Southern Ocean were the source of Atlantic tides, which were ‘derivative’ tides. The observed and computed tides of the Southern Ocean do show a general westward propagation, particularly for the diurnal tides, but the amplitudes are not particularly large. The narrowness of the Drake Passage between South America and Graham Land has a strong restricting influence on the pattern of wave propagation. Whewell argued further that the one to two day age of the semidiurnal tide in the North Atlantic was a consequence of the time taken for the wave to propagate from the Southern Ocean. Measurements were made in June 1835 on both sides of Atlantic for a fortnight at 28 places, the results from which caused Whewell to review his earlier ideas [10]. The observed diurnal tides were particularly difficult to reconcile with their generation in the distant Southern Ocean because the maximum inequality in successive semidiurnal high water levels occurred two or three days later on the European side than on the American side. Further, simultaneous observations at the Cape of Good Hope near the supposed tidal source showed maximum inequalities simultaneous with those at Spain and Portugal. With no prospect of the necessary mid-ocean observations, Whewell abandoned his plan to draw co-tidal lines for the oceans, and prepared a chart only for the northwest European continental shelf.

The **Atlantic** tides show a systematic northward progression of the semidiurnal phases along the coast of Brazil and West Africa, as shown in Figure 5.1, with an amphidrome in the central South Atlantic around 35° S. The ranges are relatively large near the equator and the phases nearly constant over an extensive area, high waters occurring along the whole coast of northern Brazil from 35° W to 60° W within an hour, behaviour consistent with standing wave dynamics. Further north, around 20° N, smaller amplitudes and a rapid northward increase of phase show a tendency for an amphidrome to develop. The most fully developed semidiurnal amphidrome is located near 50° N, 39° W. The tidal waves appear to travel around the position in a form that approximates to a Kelvin wave, from Portugal along the edge of the northwest European continental shelf towards Iceland, and thence west and south past Greenland to Newfoundland. There is a considerable leakage of energy to the surrounding

² This type of behaviour can be analysed in terms of the equations developed in Section 4.2.6 for the combination of two harmonic constituents.

continental shelves and to the Arctic Ocean, so the Kelvin wave, which is reflected in a southerly direction, along the coast of eastern North America, is much weaker than the wave travelling northward along the European coast. Subsidiary anticlockwise amphidromic systems are formed between the Faeroe Islands and Iceland and between Iceland and Greenland. This results in a complete circulation of the semidiurnal phase around Iceland in a clockwise sense, similar to that observed around New Zealand, but for reasons that involve the dynamics of Arctic tides rather than local topographic trapping alone.

As in other oceans, for constituents in the same tidal species the tidal charts show broad similarities, but in the Atlantic Ocean there are also significant differences. The ratio between the M_2 and S_2 amplitudes, 0.46 in the Equilibrium Tide, falls in the North Atlantic to 0.22 at Bermuda. This relative suppression of the principal solar semidiurnal tide S_2 extends over a very large area of the North Atlantic and is observed on both the American and European coasts. This relative suppression of S_2 means that along much of the eastern coast of the United States, N_2 is the second largest tidal constituent. As a result, for tidal amplitudes, the lunar orbital perigee–apogee cycle is often as important as the spring–neap cycle. Along this Atlantic coast of North America from Nova Scotia to Florida the ocean tides are nearly in phase, consistent with standing wave dynamics along the northwest to southeast axis; superimposed on this is a slow progression of phase towards the south.

The semidiurnal tides of the Gulf of Mexico and the Caribbean have small amplitudes. An anticlockwise amphidromic system is apparently developed in the Gulf of Mexico for the semidiurnal tides. The diurnal tides of the Gulf of Mexico are larger than the semidiurnal tides (see [Figure 1.4b](#)) because of a local resonant response, but the diurnal tides for the Atlantic Ocean as a whole are generally weaker than in the other oceans. They can be described in terms of amphidromic systems, a clockwise system in the south Atlantic and an anticlockwise system in the north Atlantic, consistent with Kelvin wave dynamics, as shown in [Figure 5.7](#).

Although the link with Antarctic tides is important for tides in the Atlantic (but not in the simple way originally proposed by Whewell), it is clear that the role of direct gravitational forcing within the Atlantic is also important.

Even for longer period tides, the Equilibrium values are not present. Significant departures from Equilibrium occur for the fortnightly and monthly long period tides. For M_f modeling even a schematic ocean can reproduce plausible amplitudes and phases for M_f that depart from Equilibrium [11]. Although the departures from Equilibrium are less for the monthly than the fortnightly tides, the question remains as to how much of a departure occurs at the lower frequencies of the semi-annual, annual and nodal astronomical tides [12] (see [Chapter 10](#)).

5.3.3 Tides in enclosed seas

Basins of oceanic depths such as the **Mediterranean Sea** and the **Red Sea**, which connect to the oceans through narrow entrances, have small tidal ranges. The dimensions of the basins are too restricting for the direct tidal forces to have much effect, and the areas of the entrances are too small for sufficient oceanic tidal energy to enter (Section D.1) to compensate for the energy losses that would be associated with large tidal amplitudes. The semidiurnal tides of the Red Sea are of interest because they are closely represented by a standing wave having a single central node ([Figure 5.9](#)). Careful analysis shows that there is a progression of the wave in the expected anticlockwise sense around a central amphidrome. From Merian's formula ([Equation 5.5](#)) the period of oscillation of the Red Sea would be approximately 12.8 hours, for a depth of 500 m and a length of 1600 km, the distance between the northwest and southeast antinodes of the main oscillation. Because of its long narrow shape and steep sides, the Red Sea has been used to test dynamical theories of tides, including early numerical solutions of the equations of motion [1].

The tides of the Mediterranean are also weak [13]. Essentially there are two basins, separated by the Sicilian Channel and the Straits of Messina. The tides of the western basin are strongly influenced by the Atlantic tides, which penetrate through the Straits of Gibraltar, and a semidiurnal amphidrome is developed near the line of zero longitude. There is a second amphidromic region near the boundary between the two basins, and a third in the eastern basin south of Greece. Because the connection with the Atlantic Ocean through the Straits of Gibraltar is so restricted, the influence of direct gravitational forcing within the Mediterranean is probably of comparable importance

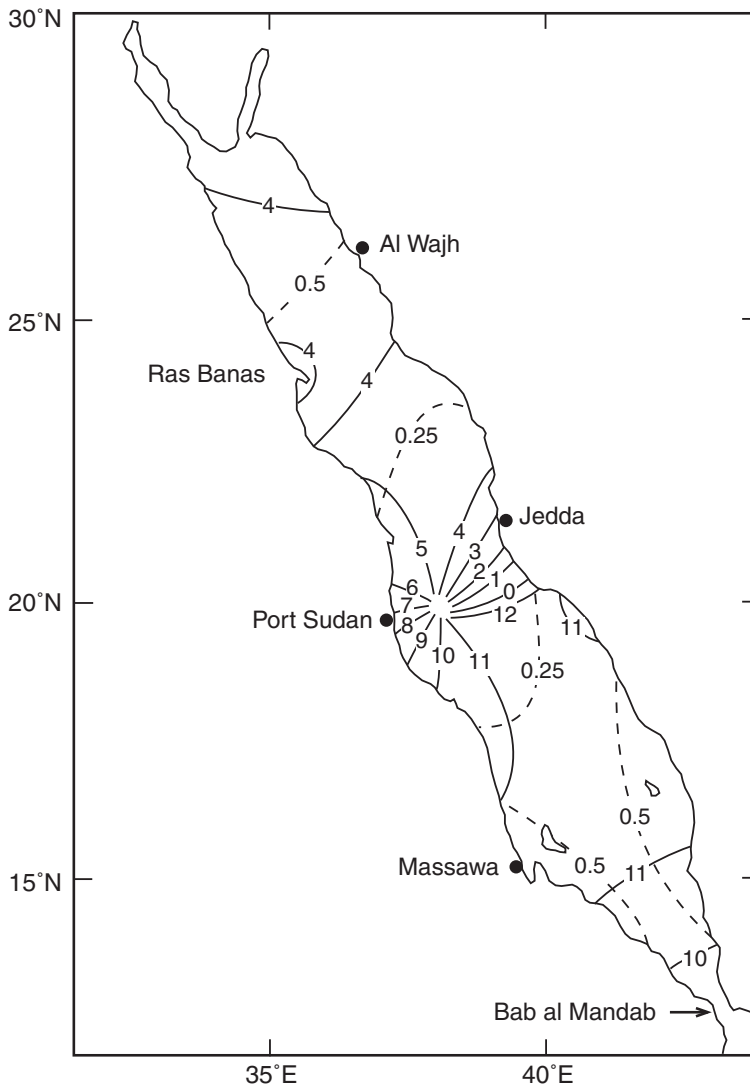


Figure 5.9 A chart of the M_2 tide in the Red Sea. The ranges are small because of the narrow connection to the Indian Ocean at Bab al Mandab. The pattern is very close to that for a half-wave oscillation with an amphidrome between Port Sudan and Jeddah.

to the external forcing. The diurnal tides of the Adriatic are relatively large because a natural oscillation is excited by the Mediterranean tides at the southern entrance. A simple amphidromic system similar to that in the Red Sea is developed. The effect of the standing oscillation is to produce large tides at the northern end, in the vicinity of Venice. Tides are also relatively large, up to 2.1 m at spring tides, in the Gulf of Gabès, Libya. The tides of the Black Sea [1], although dynamically connected to the Mediterranean, are substantially generated by the direct gravitational forcing: M_2 has amplitudes of a few centimetres, with co-tidal lines rotating around a single central amphidrome.

Although the tidal amplitudes are generally small in the Mediterranean, strong tidal currents occur where separate basins having different tidal regimes are connected by a narrow channel. The currents in the Straits of Messina may exceed 2 m/s because of the strong gradients on the sea surface. Even stronger currents are observed through the Euripus between mainland Greece and the island of Euboea [14]; tidal currents under the bridge at Khalkis can exceed 3 m/s at spring tides.

The **Arctic Ocean** has depths in excess of 5000 m, but also contains the world's most extensive shelf region. Its tides are driven by the Atlantic tides, through the connection between Scandinavia and

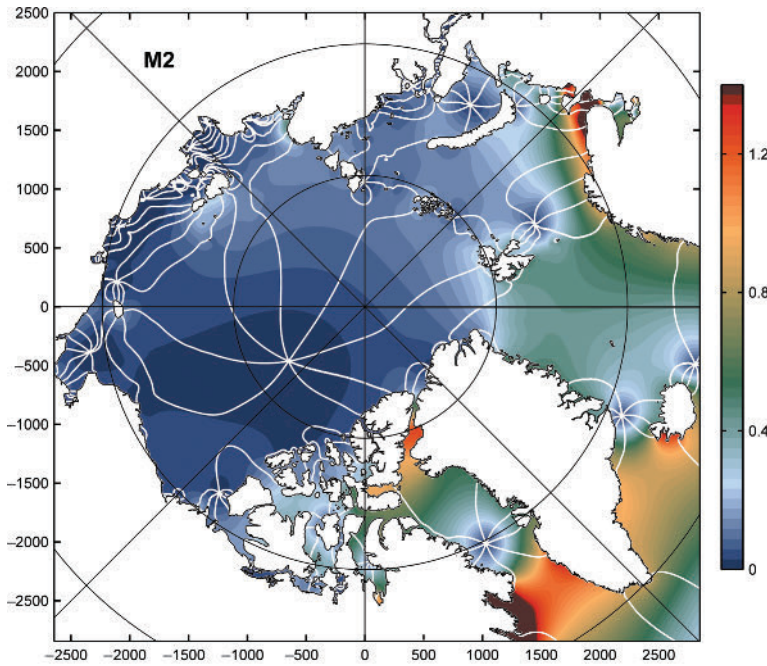


Figure 5.10 A co-tidal chart of the M_2 tide in the Arctic Ocean. Image supplied by Dr Laurence Padman, Earth & Space Research.

Greenland, which is small compared with the ocean area [15]. Figure 5.10 shows the complicated co-tidal and co-range lines for the M_2 tide. The wave enters primarily through the Greenland Sea to the west of Spitzbergen. As it propagates northwards it decreases in amplitude as it circles an anticlockwise amphidrome located near $81^\circ 30' N$, $133^\circ W$ in the deep waters of the Canadian Basin. Part of the wave propagates onto the broad shallow shelf of the East Siberian Sea where its energy is dissipated. Tides on the extensive North Siberian Shelf have been described [16] in terms of a particular type of non-coastal Poincaré wave (also here called a Sverdrup wave; see Appendix D). A secondary branch of the M_2 tide enters the Arctic between Spitzbergen and Norway; this produces high tides in the southern Barents Sea and around Novaya Zemlya. Satellite altimetry is of limited use in the Arctic because of sea ice cover, and because some satellite orbits are inclined at angles that preclude high latitudes (see Chapter 9). The gravity satellite GRACE has been used for testing Arctic tidal models [17]. The permanent ice covering is thought to have little influence on the observed tides, but where tidal currents diverge on the shallow shelf seas, they can cause a periodic opening and closing of the cracks in the ice cover, a process called *tidal straining*.

5.4 Shelf tides

5.4.1 Transition from the ocean to the shelf

The process of transition of the oceanic tidal wave (depth around 4000 m) onto the relatively shallow continental shelves (with depths about 200 m) is dynamically the same as for any other kind of long wave. As the depth decreases, so does the wave speed c , as a result of which the wave is bathymetry contours. Suppose that the boundary is represented by a step discontinuity in depth from 4000 m to 200 m. For a plane wave approaching an infinitely long ocean shelf boundary at an angle, Snell's law of wave refraction applies, the angles of incidence and refraction being related by:

$$\frac{\sin(\text{incident angle})}{\sin(\text{refracted angle})} = \frac{\text{ocean wave speed}}{\text{shelf wave speed}} = \sqrt{\frac{4000}{200}} \approx 4.5$$

In the absence of other effects such as the Earth's rotation, a wave approaching nearly parallel to the shelf edge (incident angle 90°) would have a refracted angle of 13° ; the direction of wave propagation is turned through 77° .

Table 5.4 Rossby radius in km for different water depths and latitudes. A Kelvin wave amplitude is reduced by e^{-1} (0.37) in a distance of one Rossby radius.

Rossby radius = \sqrt{gD}/f					
	Latitude (degrees)				
	10	30	50	70	90
$f \times 10^{-5}$	2.53	7.29	11.2	13.7	14.6
Water depth (m)					
4000	7820	2720	1770	1450	1360
200	1750	610	395	325	305
50	875	305	200	160	150
20	550	190	125	102	96

A normally incident long wave will be partly reflected back to the ocean and partly transmitted onto the shelf. Of course, a real, sloping and indented, continental margin will have a different response to that of the theoretical sharp step, but considering the relative theoretical amplitudes is instructive. For an incident wave of amplitude 1.0 m the reflected wave has a theoretical amplitude of 0.64 m and the transmitted wave has an amplitude of 1.64 m (Appendix D.1). The reason for this can be argued by energy flux considerations. In Appendix D.1 the energy transmitted in unit time by a progressive wave is shown to be:

$$\frac{1}{2} \rho g H_0^2 \sqrt{gD}$$

per unit distance along the wave front. As the wave moves into shallower water, and in the absence of both reflection and energy losses due to bottom friction, the quantity:

$$(\text{wave amplitude})^2 \times \sqrt{\text{water depth}}$$

must remain constant. If the depth is reduced by a factor of 20 (4000 m/200 m) and there is total energy transmission, the wave amplitude increases by a factor of:

$$\sqrt[4]{20} = 2.1$$

For the step model of the boundary between the ocean and the shelf, 60 per cent of the incident energy is transmitted and 40 per cent is reflected, but the transmitted energy is still enough to give larger amplitudes in the shallower water by a factor of 1.64.

The tidal currents on the shelf are also enhanced. Applying Equation 5.2, which relates currents to wave amplitude and water depth, the ocean wave of amplitude 1.0 m in 4000 m depth has current speeds of 0.05 m/s, whereas the transmitted wave of amplitude 1.64 m in 200 m depth has current speeds of 0.36 m/s. The current speeds are increased by a greater factor than the increase in the elevation amplitudes.

Waves incident at an angle to the actual sloping topography of the continental margins will undergo continuous refraction. Reflected waves may also be refracted back again from the ocean, giving rise to a succession of topographically trapped edge waves travelling along the ocean-shelf interface. For waves travelling with the shallow water to their right (northern hemisphere) trapping is also possible because of the Earth's rotation. The tides around New Zealand have also been explained in terms of weakly trapped semidiurnal waves [18].

The relative importance of the different kinds of hydrodynamic waves that may exist at the continental margin will depend on the particular circumstances. One well-studied example is the northward progression of the semidiurnal tidal phases (140 m/s) along the Californian coast of the western United States, where the continental shelf is narrow [19]. This progression can be described as the superposition of a Kelvin-like edge wave, a free Poincaré wave (see Appendix D) and a directly forced wave, with amplitudes at the coast of 0.54, 0.16 and 0.04 m respectively. Phase progression is consistent with the semidiurnal amphidrome located at 25° N, 135° W. Diurnal tides may also be explained in terms of these three wave types. They have a faster (214 m/s) speed and a

southern progression; their component wave amplitudes are 0.21, 0.24 and 0.09 m respectively at the coast.

The importance of the Earth's rotation in the generation and propagation of different types of waves, and the different responses to the diurnal and semidiurnal tides is illustrated by the behaviour of sea levels and currents off the west coast of Scotland [20]. The observed semidiurnal levels and currents are scaled according to expected Kelvin wave dynamics, but the diurnal waves have very large currents compared with the small amplitudes of sea surface vertical diurnal tides. The diurnal tides include a continental shelf wave, constrained to travel parallel to the shelf edge with shallow water to the right in the northern hemisphere; because these waves are only possible for waves whose period exceeds the inertial period due to the Earth's rotation (14.3 hours at 57° N), they are impossible for the semidiurnal tides at that latitude. Similarly enhanced diurnal currents due to non-divergent shelf waves are observed on the continental shelf off Vancouver Island, British Columbia [21, 22], and on the shelf between Nova Scotia and Cape Hatteras [23].

5.4.2 Some examples of shelf tides

The patterns of tidal waves on the continental shelf are scaled down as the wave speeds are reduced. Table 5.1 gives the wavelengths for typical depths. The Rossby 4 radius, which is also reduced in the same proportion, varies as shown in Table 5.4. Tidal parameters vary over relatively short distances. In the very shallow water depths (typically less than 20 m) there will be strong tidal currents and substantial energy losses due to bottom friction; these severe non-linear distortions are discussed in Chapter 6. For average shelf depths the waves are strongly influenced by linear Kelvin wave dynamics and by basin resonances. Energy is propagated to the shallow regions where it is dissipated. In this discussion it will be possible to describe only a few representative cases of shelf tidal behaviour.

The tides of the **northwest European continental shelf** have been mapped in detail as shown in Figure 5.11. The Atlantic semidiurnal Kelvin wave travels from south to north. Energy is transmitted across the shelf edge into the Celtic Sea between Brittany and southern Ireland [24]; this wave then propagates into the English Channel where some energy leaks into the southern North Sea, and into the Irish Sea and the Bristol Channel. The Atlantic wave progresses

northwards, taking 5 hours to travel from the Celtic Sea to the Shetlands. The diurnal tidal progression is not so simple because the phase increases and decreases several times rather than increasing regularly. The semidiurnal wave is partly diffracted around the north of Scotland where it turns to the east, then to the south into the North Sea.

The semidiurnal tides of the **North Sea** (which is broad compared with the Rossby radius) consist of two complete amphidromic systems and a third, probably degenerate, system that has its centre in southern Norway. The largest amplitudes occur where the Kelvin south-travelling wave moves along the British coast. Co-amplitude lines are parallel to the coast, whereas co-tidal lines are orthogonal. The amphidromic system shown in Figure 5.11 may be compared with Taylor's theoretical amphidrome in Figure 5.7. However, although the southern amphidrome is located near the centre of the sea, progressive weakening of the reflected north-going Kelvin-type wave places the second and third amphidromes further and further to the east of the central axis. Indeed, even the central position of the southern amphidrome is probably partly due to an enhancement of the reflected wave by a north-going wave entering through the Dover Straits.

The **English Channel** and the **Irish Sea** are relatively narrow in terms of the Rossby radius. They respond similarly to the incoming wave from the Celtic Sea. The wave takes about 7 hours to travel from the shelf edge to the head of the Irish Sea, and a similar time to reach the Dover Straits. The wave that travels along the English Channel reaches the Dover Straits one complete cycle earlier than the wave that has travelled the greater distance around Scotland and through the North Sea. The large tidal amplitudes in the Dover Straits (greater than 2.0 m) are due to these two meeting waves combining to give an anti-amphidrome. The English Channel has a response similar to that of a half-wave resonator (Equation 5.5) with a nodal line between the Isle of Wight and Cherbourg. Tidal levels at the Straits of Dover have the opposite phase to those at the shelf edge. The large amplitudes on the French coast (3.69 m at St Malo near La Rance tidal power station, for the M_2 constituent) are due to Kelvin wave dynamics and local standing wave resonance. Because of frictional dissipation and leakage of energy into the southern North Sea, the reflected tidal wave is much weaker than the ingoing wave. A full amphidromic system cannot develop because the Channel is too narrow;

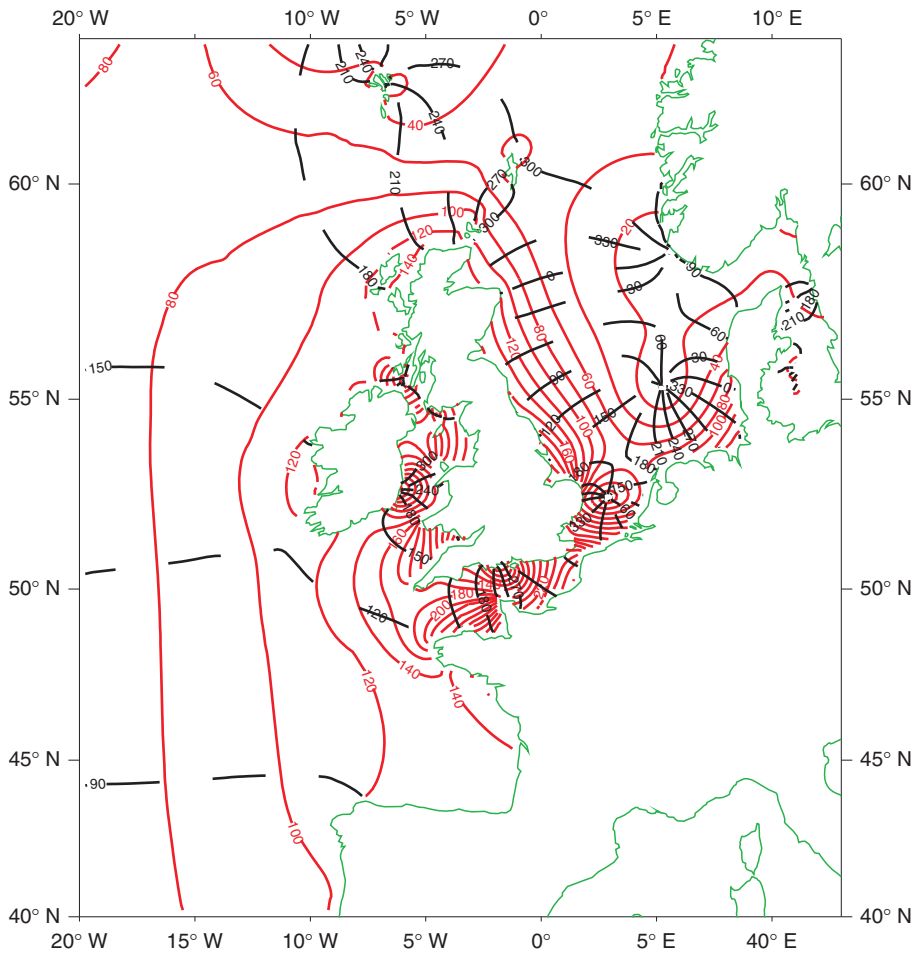


Figure 5.11 The M_2 tides of the northwest European continental shelf. Broken lines (black) are phases in degrees (G); continuous lines (red) show amplitudes in centimetres. Note the displacement of the amphidromes in the North Sea away from the centre line because the reflected wave has been weakened by bottom friction. Compare this with Figure 5.12, inverted. Image supplied by Jane Williams, National Oceanography Centre, UK.

instead, there is a clustering of co-tidal lines towards a degenerate amphidrome located some 25 km inland of the English coast.

The large tidal amplitudes in the upper reaches of the **Bristol Channel** ($H_{M_2} = 4.25$ m at Avonmouth) appear to be due to quarter-wave resonance (Equation 5.6); the quarter-wave resonant period of the Celtic Sea and Bristol Channel together has been estimated at slightly greater than 12 hours, close to but less than the period of M_2 .

The standing wave response of the **Irish Sea** is similar to that of the English Channel. In this case the nodal line is located between Wales and Ireland, with a degenerate amphidrome located some 10 km inland from the Irish coast [7, 25, 26]. Energy is transmitted

through this nodal region into the northern part of the Irish Sea. Over this northern part the tidal times are nearly simultaneous, characteristic of a standing wave. The strength of the reflected wave returning through St George's Channel varies throughout the spring–neap cycle because of the varying frictional energy losses, as we discuss in Chapter 6.

The semidiurnal tides of the **Yellow Sea**, shown in Figure 5.12, may be compared with those of the North Sea: the main basin has three amphidromes, progressively displaced from the central axis. The wave that enters from the East China Sea travels in an anticlockwise sense as a Kelvin wave. The largest amplitudes are found along the coast of Korea. The returning Kelvin wave, which travels south along the

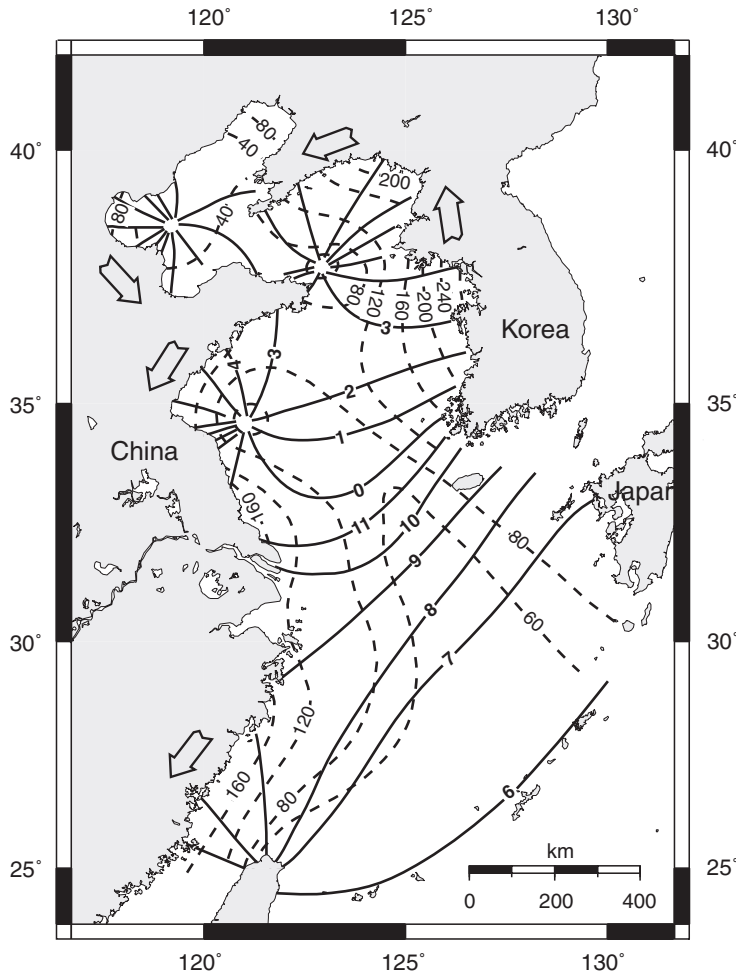


Figure 5.12 The M_2 tides in the Yellow Sea, which show many similarities in amphidrome distribution with the M_2 chart of the North Sea in Figure 5.11. The white arrows indicate the direction of propagation.

coast of China, is much weakened by energy losses to Po Hai basin and to Korea Bay. As a result, the amphidromes are progressively nearer the Chinese coast and the third amphidrome near Shanghai may be degenerate.

The nearly simultaneous semidiurnal tides observed over more than 1000 km along the **east coast of the United States** between Long Island and Florida have been explained in terms of an Atlantic Ocean tide that is nearly simultaneous along the shelf edge [27]. Standing waves develop across the shelf, with the coastal amplitude being greatest where the shelf is widest, as shown in Figure 5.13. The smallest ranges occur near Cape Hatteras where the shelf is narrowest. Extrapolating the values in Figure 5.13 to zero shelf width suggests an oceanic M_2 amplitude of about 0.4 m. The shelf is too narrow for any resonant responses to develop. The reflected wave was slightly weaker than the incident

wave because of energy dissipation at the coast. As a result there is a small progressive wave component, with coastal tides occurring up to an hour later than those at the shelf edge where the shelf is wide, off Charleston.

The semidiurnal tides of **Long Island Sound** are dominated by a standing wave oscillation with an approach to a quarter-wave resonance, driven from its eastern entrance. Amplitudes increase from the entrance to the western head of the Sound (Figure 5.14a), and the phases or times are almost simultaneous (Figure 5.14b). Long Island Sound is a body of water having a length of about 150 km and a depth of about 20 m. There is also a smaller tidal flow that enters through the East River from New York. The effect of this flow from the west into Long Island Sound is to shift the antinode where maximum tidal amplitudes occur slightly to the east of the head of the Sound. Near to Glencoe the spring tidal range exceeds 2.6 m. The strong

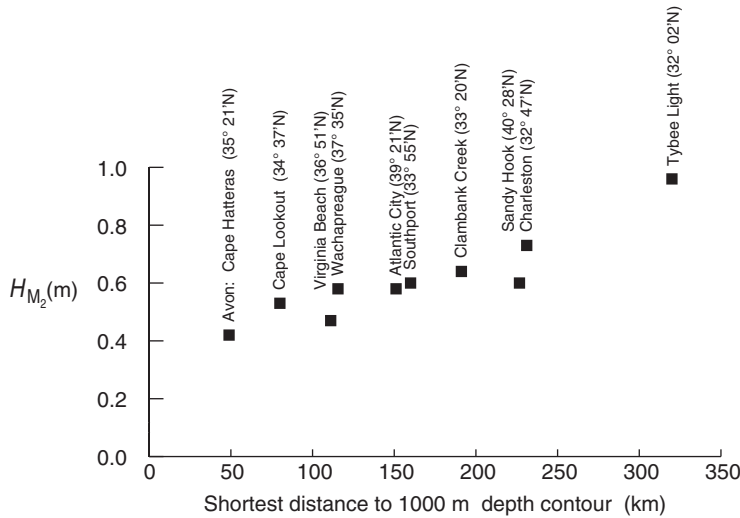


Figure 5.13 The relationship between the width of the continental shelf and the coastal tidal amplitude. Here the M_2 amplitudes for various sites along the coast of the northeast United States are plotted against the shortest distance to the 1000-metre depth contour.

tidal currents of New York's East River are driven by the level differences between the Long Island Sound tides at one end, and the quite different Atlantic/New York Harbour tides at the other end.

The tidal system that develops in the Gulf of Maine and the Bay of Fundy consists of near-resonant oscillations, which produce one of the world's greatest tidal amplitudes (see [Box 5.1](#)), in the Minas Basin. [Figure 5.15a](#) shows how the amplitudes increase from less than 0.5 m at the shelf edge to more than 5.64 m at Burncoat Head. It has been estimated that the natural quarter-wave period of this system is close to 13.3 hours, which explains the large near-resonant response to semidiurnal tides. Further north, the semidiurnal tidal wave enters the Gulf of St Lawrence [[28](#)] through the Cabot Strait, and a full semidiurnal amphidromic system is developed near the Magdalen Islands, and north of Prince Edward Island ([Figure 5.15b](#)); a further small system appears in Northumberland Strait between Prince Edward Island and New Brunswick. North and west of Prince Edward Island, the tides are mainly diurnal, because the semidiurnal tides are small. The tidal range increases as it progresses up the St Lawrence River.

The many islands and connecting straits complicate the tides of the **Canadian Arctic**. A local resonance produces very large semidiurnal amplitudes in Ungava Bay, up to 4.36 m for M_2 at Leaf Basin (see [Box 5.1](#)). In Baffin Bay a full anticlockwise semidiurnal amphidrome has been mapped; the diurnal tides appear to behave as a standing wave with amplitudes of 0.3 m at the northern end. The semidiurnal tides of

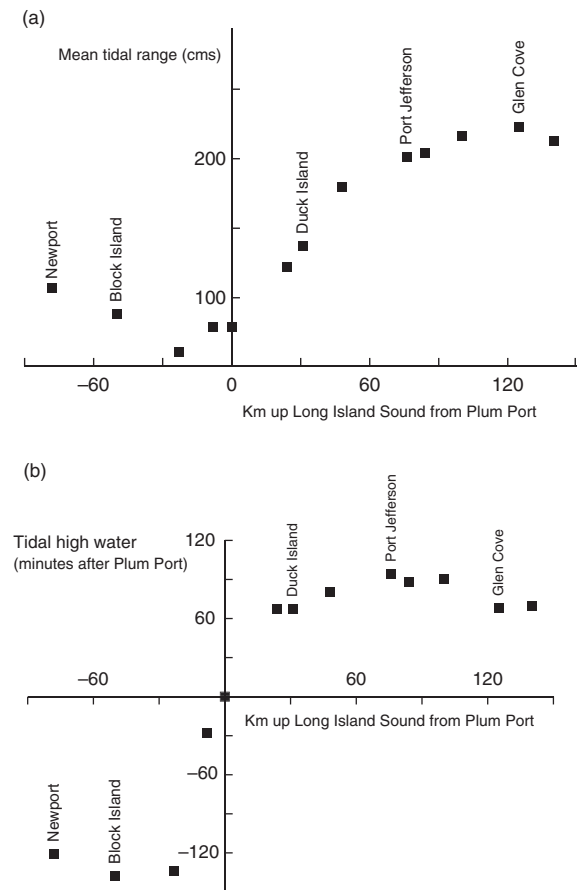


Figure 5.14 The M_2 tidal amplitudes (a) and phases (b) along Long Island Sound, on the east coast of the United States. This can be compared with the standing wave behaviour in [Figure 5.5](#), with maximum amplitudes at the head of the Sound.

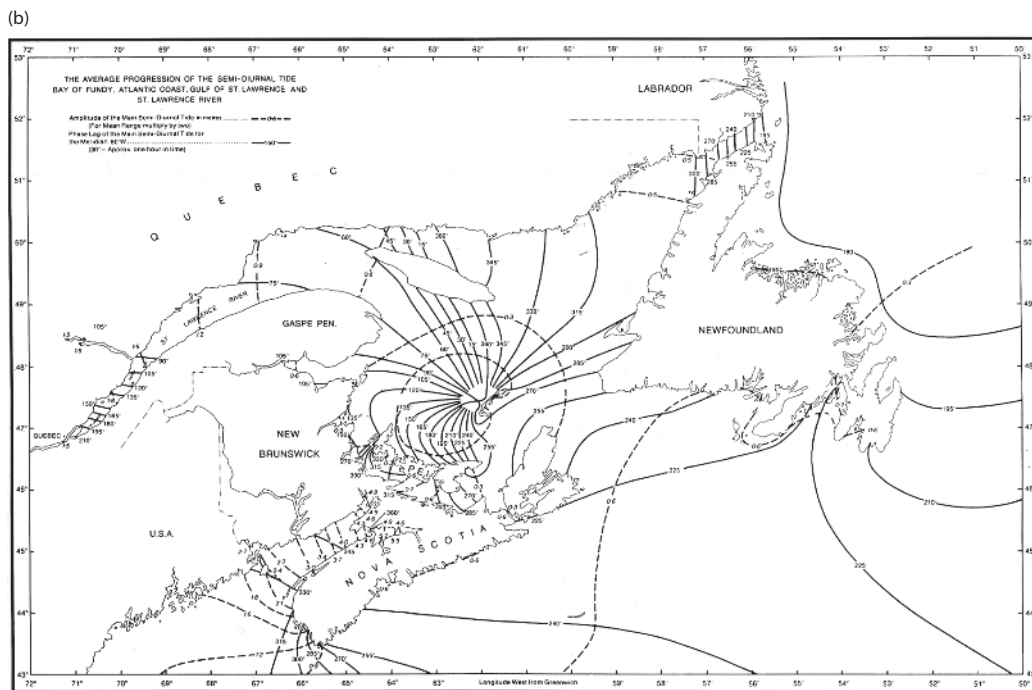
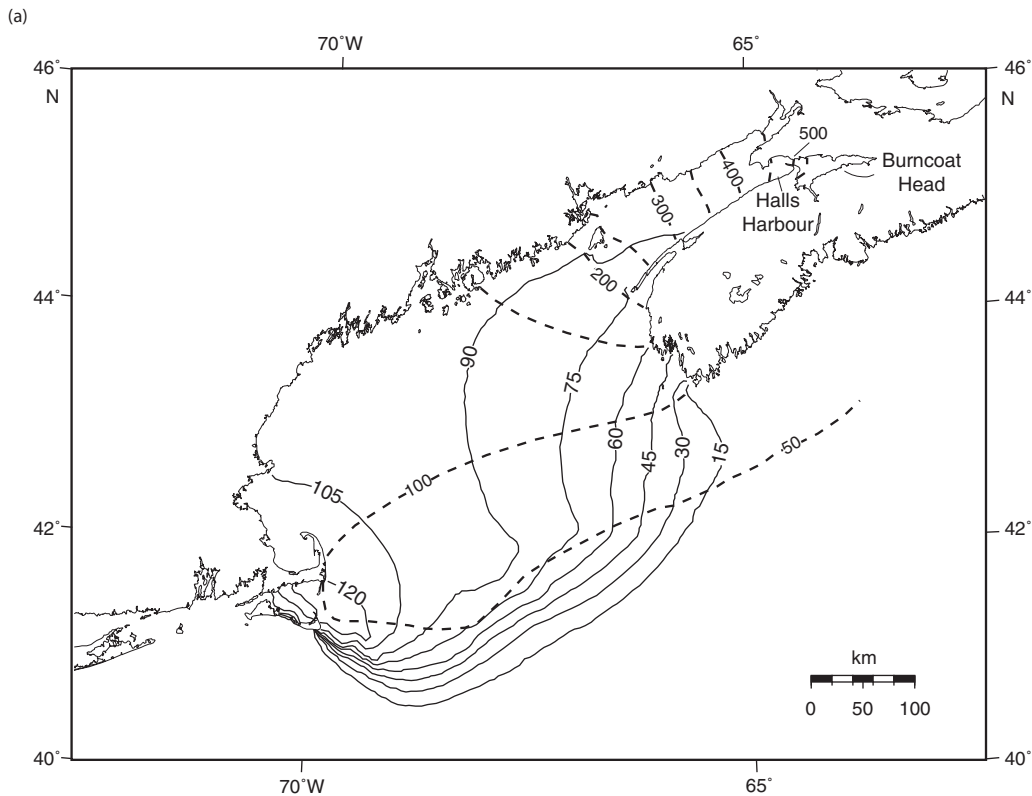


Figure 5.15 (a) A tidal chart of the Gulf of Maine showing amplitude (solid lines, in cm) and phase lag (dashed lines, in degrees) for M_2 , showing progression to the north and east with maximum ranges in the upper reaches of the Bay of Fundy. Based on information provided by Dr David Greenberg, Bedford Institute of Oceanography. (b) Tidal chart of the average semidiurnal tide (in practice M_2) of the Gulf of St. Lawrence. Amplitudes are shown by the dashed lines (in metres) and phase lags by the solid lines (based on the 60° W meridian rather than Greenwich) [69].

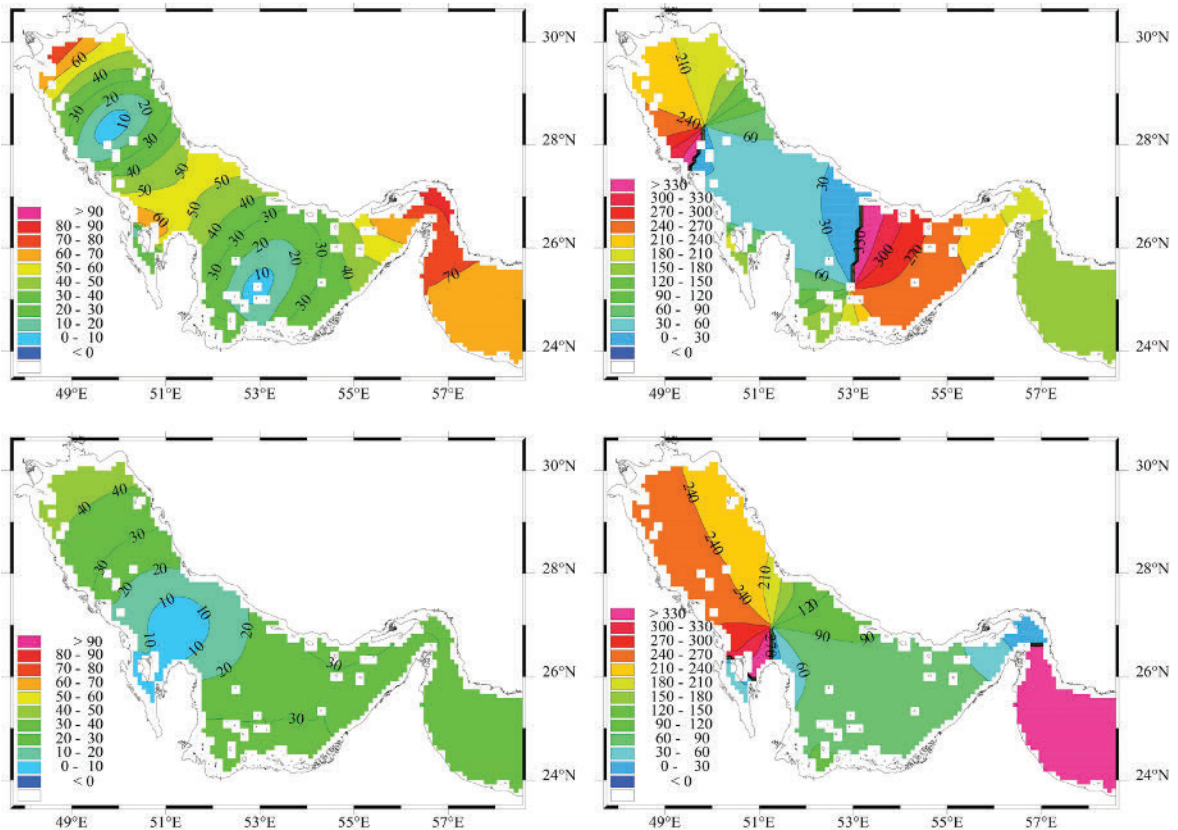


Figure 5.16 Maps of equal amplitude (left, in cm) and Greenwich phase lag (right, in degrees) for the M_2 (top) and O_1 (bottom) constituents in the Persian Gulf. From [29].

Hudson Bay, which are driven through Hudson Strait, show a complex of several amphidromes, with amplitudes generally less than 0.3 m. However, for the small diurnal tides, the pattern, which consists of a single anticlockwise amphidromic system, is particularly simple [28].

The Persian Gulf, Figure 5.16, is a shallow sea with mixed diurnal and semidiurnal tides [29]. It is a largely enclosed basin with only a limited connection to the Indian Ocean through the Strait of Hormuz. Along the major northwest to southeast axis it has a length of about 850 km. The average depth is approximately 50 m, giving a resonant period near 21 hours, according to Equation 5.5. The Rossby radius at 27° N (c/f) is 335 km, comparable with the basin width. As a result the response to the diurnal forcing through the Strait of Hormuz is a single half-wave basin oscillation with an anticlockwise amphidrome. The semidiurnal tides develop two anticlockwise amphidromic systems, with

a node or anti-amphidrome in the middle of the basin. Near the centre of the basin the changes in tidal level are predominately semidiurnal, whereas near the semidiurnal amphidromes they are mainly diurnal. At the northwest and southeast ends of the basin the tidal levels have mixed diurnal and semidiurnal characteristics. Direct gravitational forcing is probably significant.

The tides of the Indonesian Seas are shown in Figure 5.17 [30]. The complexities are due to narrow straits, islands, wide shelves and shallow water all contributing to the interaction of ocean tides from both the Indian and Pacific Oceans. Diurnal tides are unusually strong. Large tides from the Indian Ocean dominate the semidiurnal response; the diurnal tides progress southwards through the Makassar Strait and Molucca Sea, meeting the tide from the Indian Ocean in the Banda and Flores Seas. To the southeast the large diurnal tides of the Gulf of Carpentaria are formed (see Karumba

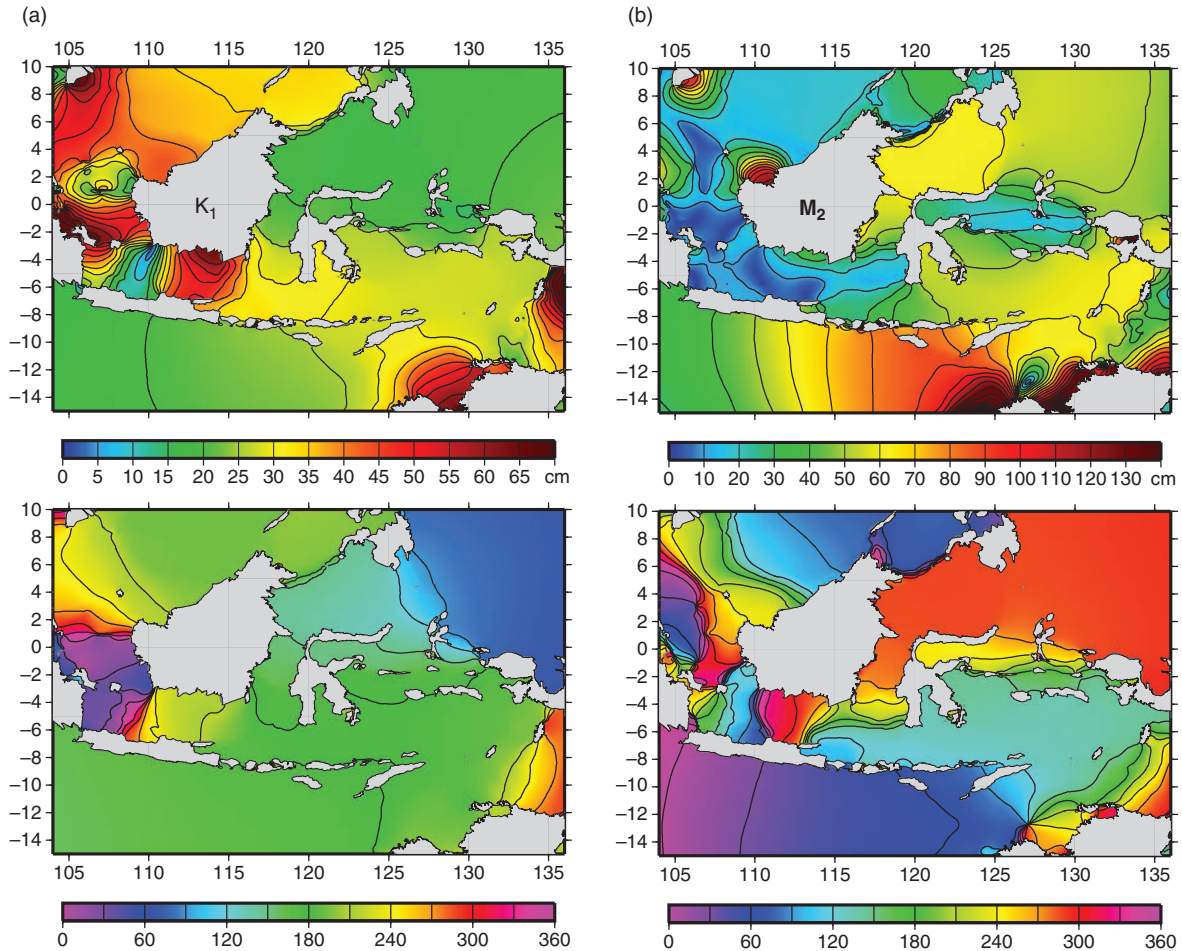


Figure 5.17 Maps of amplitudes and phase lags of the (a) diurnal K_1 and (b) semidiurnal M_2 tides in the Indonesian Seas. Images from Dr Richard Ray, Goddard Space Flight Center.

in Figure 1.2a). Very strong currents flow between islands where the tides have different amplitudes and phases on either side.

Figure 5.1 shows these and other locations of large shelf tides. Apart from those already discussed, there are also large tides along the Argentinian coast of Patagonia [31], associated with the very broad continental shelf and standing waves, as for the east coast of North America (Figure 5.13). The broad continental shelf and the near-resonant period of Cook Inlet from the Gulf of Alaska also lead to very high tides at Anchorage in the northwest Pacific Ocean.

These discussions of observed tides have concentrated on the dominant semidiurnal and the lesser diurnal responses. Although, by comparison, the third-diurnal forcing in the Equilibrium Tide is

weak, a local resonance on the shelf off Brazil gives M_3 amplitudes in excess of 0.10 m at Paranagua [32], and there is similar M_3 quarter-wave resonant amplification along the southern coast of Australia, with a 0.11 m amplitude at Thevenard [33].

5.4.3 Shelf tidal currents

Tidal currents are often termed tidal streams by hydrographic authorities. These tidal currents are more variable from place to place than changes of tidal levels because they are sensitive to changes of depth, and to the influences of coastal embayments and headlands. However, at any particular location, the tidal currents may be measured, analysed and predicted in the same way as levels. Total currents

may be analysed and plotted as detailed in Section 4.4. More elaborately, they may be broken down into their harmonic constituent ellipses or rotary components as described in Sections 4.4.2 and 4.4.3, Appendix B, and Figure 4.7. Tidal currents show little vertical structure, except near the seabed (see Section 6.4.1) or in stratified estuaries, and so the concept of a depth mean current is valid, except in very shallow water.

For a progressive wave, the currents, which are a maximum in the direction of wave propagation at local high water, are related to the wave amplitude by Equation 5.2. The excursion of a water particle over half a tidal cycle is given by Equation D.3. For a simple progressive harmonic wave in 20 m depth and 1 m amplitude, the particle excursion is 10 km; in 200 m depth it is 3.15 km; and in the deep ocean of 4000 m depth, 0.7 km. The displacements will be twice this amount between extremes. A theoretical progressive Kelvin wave has rectilinear currents. In reality rectilinear currents are only found near to steep coasts or in narrow channels. In the North Sea, for example, in addition to the Kelvin wave that propagates southward along the British coast there is a standing wave with a current component at right angles to the coast, whose amplitude is typically 15 per cent of the amplitude of the parallel component. The phase relationships between currents for a station in this area are shown in Figure 4.4. For a south-going progressive wave the currents (positive to the north) should lag the elevations by 180° rather than 150° observed in the semi-diurnal band. In this case maximum currents in the direction of wave propagation occur one hour before local high water.

In a pure standing wave system, currents are again rectilinear with maximum amplitudes near the nodes or amphidromes. Strong currents are observed near amphidromes such as in the southern North Sea, and the southern entrance to the Irish Sea. Along the Atlantic coast of the United States the standing wave has maximum tidal currents at the shelf edge, directed towards and away from the coast.

On the northwest European shelf, the strongest currents are observed in the English Channel and Dover Straits, in the Irish Sea and north of Ireland. Currents in excess of 1.0 m/s are also observed in the channels between Scotland and the Orkney and Shetland Islands as the Atlantic tide enters the North Sea. In the Pentland Firth the spring currents exceed 4.0 m/s. Currents in narrow straits such as these, between two tidal regimes, are controlled by

the balance between pressure head and friction, according to the laws of open channel hydraulics; these are discussed in Chapter 6. Figure 5.18 shows the current system that develops between a complex of islands in the Gulf of Saint Lawrence; the power of the numerical modelling technique for producing these complicated charts is evident. Elsewhere, very strong currents flow between some Indonesian Islands.

The ratios between the amplitudes of different current constituents are usually fairly stable over large regions; for example, the S_2/M_2 current amplitude ratio over the northwest European shelf is close to 0.35 except near amphidromes. The ratio between diurnal and semidiurnal currents is usually stable, and close to the ratio in the elevations. However, there are places where these ratios become anomalous because of the wave dynamics. In the centre of the Persian Gulf (Figure 5.16) the proximity of a diurnal amphidrome and a semidiurnal anti-amphidrome means that the currents are predominately diurnal, whereas the elevation changes are predominantly semidiurnal. A similar juxtaposition of a diurnal amphidrome and a semidiurnal anti-amphidrome gives diurnal currents and semidiurnal elevation changes for Singapore at the southern end of the Malacca Strait.

The sense of rotation, clockwise or anticlockwise, of a current ellipse is controlled by many factors and there are no simple rules to decide which effects will be most important. In some cases the rotation sense may be different at the top and bottom of the water column. In the oceans, well away from the influences of the coast, the direct tidal forcing and the Coriolis accelerations both act to induce circulation of the semidiurnal current ellipses in a clockwise sense in the northern hemisphere and in an anticlockwise sense in the southern hemisphere. On the continental shelf the sense of rotation is usually controlled by the bathymetry and by coastal wave reflections. The theoretical amphidromic system shown in Figure 5.7 has anticlockwise circulation of current ellipses near the reflecting boundary in the northern hemisphere and anticlockwise circulation in the southern hemisphere.

Another important influence on the sense of ellipse rotation near a coastline is the presence of a shelving beach or an embayment, as illustrated in Figure 5.19. Consider a progressive wave travelling with the coast on its right. At high water (1) the flow

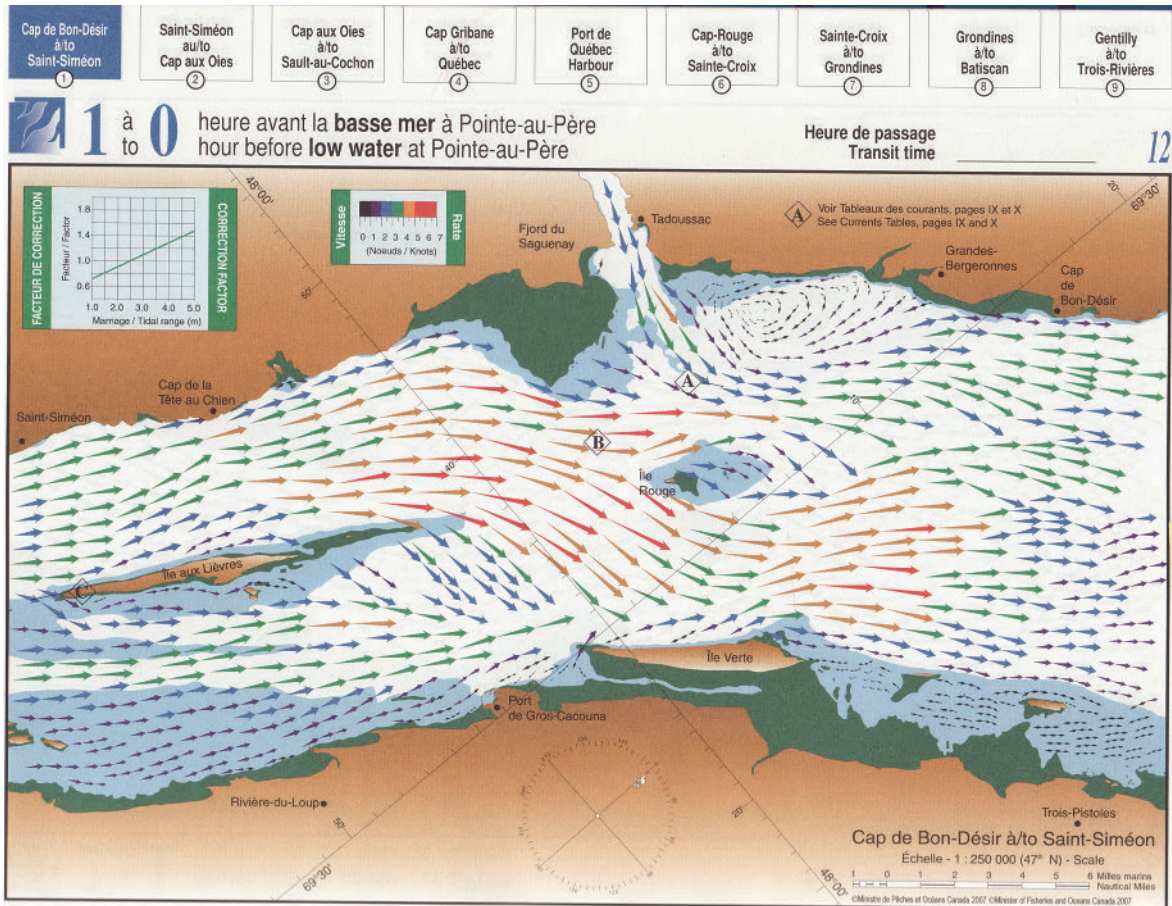


Figure 5.18 A complex map of tidal currents in the St Lawrence Estuary, 1 hour before low water. Red arrows are greater than 5 knots (2.5 m/s) [70].

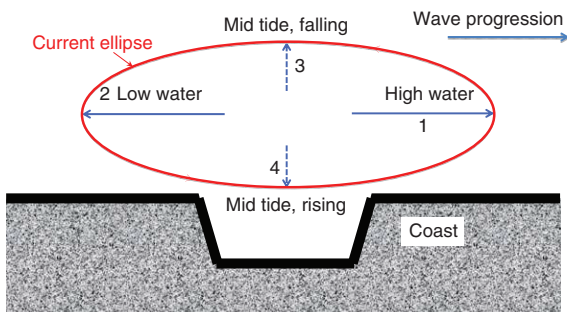


Figure 5.19 Development of an anticlockwise current vector rotation for a progressive wave with an embayment or a shelving coast to the right.

is directed parallel to the coast as shown. At mid-water level on the falling tide there is no contribution to the flow from the wave progression, but the fall of water level in the embayment produces an

offshore flow. At low water (3) the progressive wave gives a flow as shown, parallel to the coast, but as levels in the embayment are not changing, there is no component towards the coast. At mid water on the rising tide (4) the progressive wave has no current, but the rapid increase of level in the embayment is fed by an onshore flow. The net result of this cycle is an anticlockwise sense of rotation for the current ellipse. Of course, this applies in both hemispheres, as it has nothing to do with the Earth's rotation. However, progressive waves with a coast to the right are more probable in the northern hemisphere. In a basin or channel that is too narrow for a full amphidromic system to develop, a progressive wave will also have a coast to the left of its direction of propagation and the embayments in this coast will influence the currents to rotate in a clockwise sense.

Box 5.1 The world's biggest tides

Where are the world's biggest tides? This is a simple, often asked question [34], but there is no simple answer. It depends on what is meant by 'biggest tide'. If we want the largest M_2 tides, these are found in the Minas Basin at the upper end of the Bay of Fundy. Near Burncoat Head (Figure 5.20) the M_2 amplitude is 5.64 m. Large values of M_2 are also found at Hansport and other places in the Minas Basin. This means that averaged over many tides the tidal range is greatest in the Minas Basin. A different measure of 'biggest tides' is the highest high water sea levels above the mean sea level, generated by the tides; these are probably found at the head of the Minas Basin, around Truro, but here the total range is smaller because the shore dries out as the tides recede and the extreme low waters are not observed.

Interestingly, in the Minas Basin the semidiurnal solar tide S_2 is suppressed at only about 15 per cent of M_2 , and so the spring–neap modulations are not as large as in the Equilibrium Tide (see Section 4.2). This means that there are sometimes larger tidal ranges at other places where S_2 is larger. Lac aux Feuilles in Ungava Bay, in the Hudson Strait of northeast Canada, also has exceptionally high tides ($M_2 = 4.36$ m), due to a local resonance period of about 12.7 hours [35]; but here S_2 is bigger than in the Bay of Fundy, so there are larger spring–neap modulations. For 30 March 2002, for example (see Table 4.12b), the tidal range in Lac aux Feuilles, calculated from the Canadian tide tables, was 16.0 m, slightly larger than the range for Burncoat Head.

Measurements at both places led the Canadian Hydrographic Service to state that the contest 'was concluded to be a draw', within experimental limits [33].



Figure 5.20 Burncoat Head, Nova Scotia, Canada, at low tide. Photograph by David Pugh.

5.5 Radiational tides

In addition to the ocean responses to gravitational forcing, there is another type of forcing related to the solar heating variations, generally called radiational forcing. Here we continue the discussion of Section 4.3.3.

Detailed harmonic tidal analyses, usually of a year of data, show a constituent of 24-hour period S_1 (speed ω_0) which is much larger than in the Equilibrium Tide (the true S_1 does not exist in the Equilibrium Tide, but there is a small term with a speed of $(\omega_0 + \omega_6)$ that cannot be separated in analysis). In addition, the amplitudes and phases of the S_2 constituent are anomalous compared with the responses to the gravitational forcing at other adjacent frequencies, for example M_2 and N_2 . These apparent anomalies are due to additional, regular forcing by the weather; so too are parts of the large seasonal variations of mean sea level discussed in Chapter 10. The S_1 constituent is driven by diurnal air pressure changes, and in some places additionally by the local diurnal land/sea winds [36]; the radiational S_2 constituent is driven by the 12-hour oscillation of air pressure in the tropics.

The largest S_1 tides are found in the Arabian Sea, the Labrador Sea, the Sea of Okhotsk, and the Gulf of Alaska, a very similar pattern to that shown for the K_1 diurnal gravitational tide in Figure 5.1a, except that there is no Antarctic enhancement [36]. As an example of local forcing, at Mombasa on the east coast of Africa, the S_1 amplitude is 0.027 m; the land/sea diurnal winds have an S_1 amplitude of 2.0 m/s, with maximum onshore winds at 15:30 hours local time. Maximum S_1 levels occur 6 hours later, just after the wind reverses and begins to blow offshore, which suggests a piling-up of the water rather than an immediate response to an imposed wind stress. Instrument errors, especially in old chart recorders on a cylinder that rotates daily, or even from altimeter corrections, may also produce an apparent S_1 constituent in a harmonic analysis.

Figure 5.21a shows the variations of air pressure at Ascension Island in the central Atlantic Ocean; it is clear that these are dominated by a 12-hour variation, but there is also a diurnal inequality. Figure 5.21b shows the co-amplitude and co-phase lines for semidiurnal atmospheric pressure variations [37], making clear the east–west progression and the maximum amplitudes near the equator. In the upper atmosphere the diurnal heating cycle gives rise to diurnal pressure waves, but the

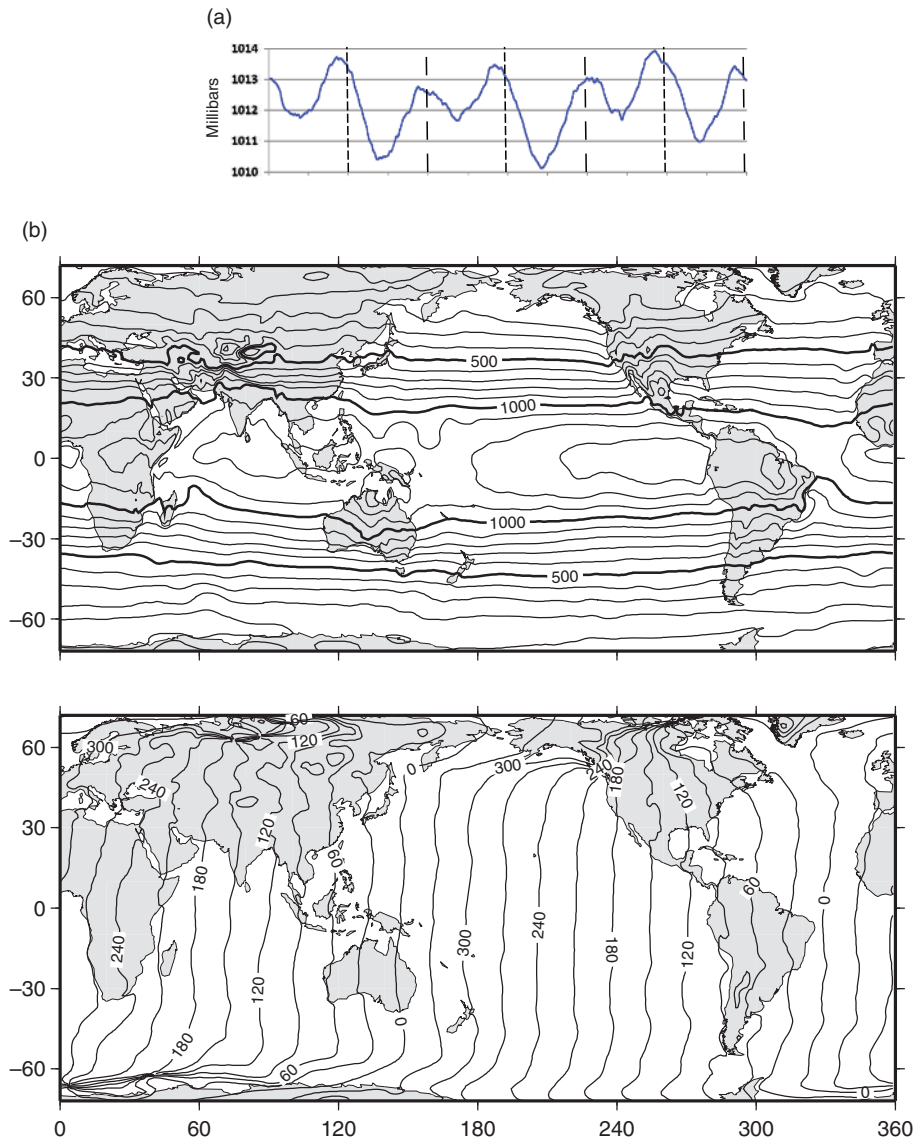


Figure 5.21 (a) An example of air pressure variations in the tropics showing S_2 variations at Ascension Island, south central Atlantic Ocean, over 3 days. The vertical lines indicate noon (dots) and midnight (dashes).

(b) Amplitudes (top, in microbars) and Greenwich phase lags (bottom, in degrees) of the S_2 air pressure tide. The phase contour interval of 30° corresponds to 1 hour in time [71].

dynamic structure of the atmosphere causes the semi-diurnal harmonic to dominate at sea level. The equatorial amplitude is about 1.25 mb. The gravitational Equilibrium Tide decreases as $\cos^2\phi$ where ϕ is the latitude [38], but the atmospheric pressure tide is observed to decrease as $\cos^3\phi$.

By the usual inverted barometer arguments (see Chapter 7), the low atmospheric pressures at approximately 04:00 and 16:00 local time are equivalent to a maximum sea-level increase of 0.0125 m at the

equator. By comparison, the Equilibrium *gravitational* forcing at S_2 has a maximum of 0.164 m, at 00:00 and 12:00, local time. If the ocean response to the two forcing systems is the same, the radiational S_2 should have an amplitude 0.076 that of the gravitational S_2 , and should lag it by 4 hours, or 120° . Models of the ocean response to the atmospheric pressure S_2 suggest atmospherically driven ocean tides with average values of 14.7 per cent of the gravitational amplitudes, and a 109° phase lag [39].

At Bermuda the ratio is 0.10, but on both the east and west coasts of the United States, the average ratio is 0.16. In the Celtic Sea and English Channel the mean ratio is 0.15. These higher ratios away from the equator have caused some scientists to propose, using local spectroscopic analyses, that local frictional and non-linear processes are the cause of at least part of the observed radiational tide [40, 41].

5.6 Internal tides

Our main interest in this book is in changes in the surface level of the sea, and the most important influence is the astronomical tide. However, there are also tidal movements within the interior of the oceans that have small surface signals [42], and which are of increasing interest to oceanographers [43]. Internal tides (also called baroclinic tides) have been known for a long time, but are difficult to measure. Long-term current meter and temperature measurements often show internal currents and temperatures at tidal periods, though, unlike surface tides, they are generally not coherent with the movements of the Moon and Sun.

Internal tides occur where the different density water layers are forced by the overall, depth-averaged, tidal currents to move up and down topographic features of the ocean bottom, such as at the continental shelf edge, deep ocean ridges or ocean islands. As the tidal currents move up over a rise they move the denser lower water up with them; on the other side the denser water falls back to its normal level, generating internal tidal waves. There is significant dissipation of tidal energy by internal processes over rough topography, in the open ocean (see Section 6.7) [44].

In a simple way we can explain the existence of internal tides by analogy with surface tidal waves. The propagation of waves on the sea surface depends on the density difference between air and water, and on the gravitational acceleration; the air density is small enough to be ignored in the usual theoretical development. Waves may also propagate along density gradients within the ocean, at speeds that depend on the density differences. For internal waves at the interface between two ocean layers we must consider the density of both layers.

The speed of propagation C of a long wave in a sea at the interface between two layers of density ρ_1 and ρ_2 , the upper layer having a thickness D_1 , and the lower layer having a thickness D_2 , is given by:

$$C = \left[\left(\frac{\rho_2 - \rho_1}{\rho_2} \right) g \left(\frac{D_1 D_2}{D_1 + D_2} \right) \right]^{\frac{1}{2}}$$

If the thickness of the bottom layer is much greater than that of the surface layer, this reduces to:

$$C = \left[\left(\frac{\rho_2 - \rho_1}{\rho_2} \right) g D_1 \right]^{\frac{1}{2}}$$

which is similar to the speed of a long surface wave, but with the gravitational acceleration reduced by $\left(\frac{\rho_2 - \rho_1}{\rho_2} \right)$ as the reduced density difference supplies a much weaker restoring force.

Typical speeds for internal waves are around 1.0 m/s, much smaller than for surface waves, because of these smaller restoring forces. However, because they can have large amplitudes (up to 50 m), the currents associated with internal tides (greater than 2 m/s) can be large [45].

Internal tides can vary in size through the year as the density composition of the water varies with the seasons. As is the case with the surface tides, internal tides are generated most strongly around the spring tides of new and full Moon; but they can take many days to propagate across an ocean basin to where they may break on a distant continental shelf. The slow speed means that irregular currents, eddies and density field variations can change the phase of the tidal currents in unpredictable ways, which explains why the internal tides are not usually coherent with the astronomical forcing [45].

An internal tidal wave can be detected as a small change in sea surface levels: assuming pressure balance at depth, above the peak of a 10 m internal tidal wave at a density surface where $(\rho_2 - \rho_1)$ is 1 kg/m^3 , the surface level will be reduced by 0.01 m. These surface level changes, though small, can be detected in analyses of long records of altimeter data, but only for those internal waves that are regular and astronomically coherent. The method is to analyse repeat tracks over many cycles to remove other effects by averaging, and then to fit amplitudes and phases at successive points along the track for individual constituents. At the sea surface the effects of the currents can sometimes also be detected in satellite images, where they are seen in bands moving away from the areas of internal tide generation (Figure 5.22).

These analyses have shown that energy in the internal tides is radiated from localised areas of marked sudden depth changes and rough topography such as

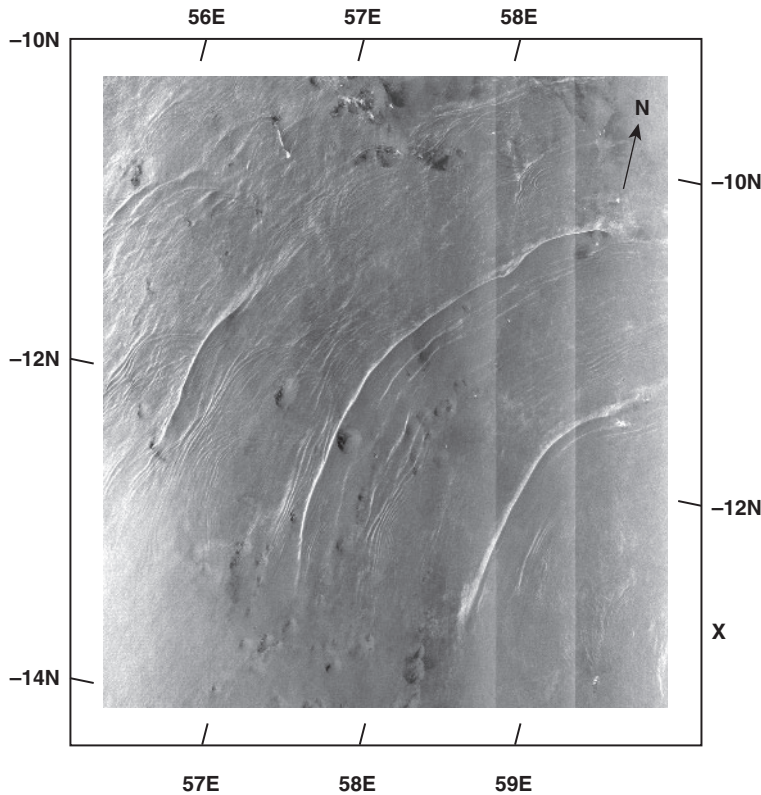


Figure 5.22 A synthetic aperture radar (SAR) image, showing 300 km features propagating to the west of the Mascarene Plateau in the Indian Ocean. They are from individual internal solitary waves that occur in tidally generated packets and coincide with the troughs of internal tidal depressions of the thermocline. The X shows a probable generation area from which the waves propagate. Image provided by Professor Adrian New, National Oceanography Centre, based on data from the European Space Agency.

the Hawaiian Ridge in the Pacific Ocean. Other areas include the Mascarene Plateau in the Indian Ocean [46], the Tuamotu Archipelago in the South Pacific, and near seamounts (Figure 5.23). There is also evidence for strong generation at straits that separate two areas of deep stratified seas; examples include the Straits of Gibraltar and the Straits of Messina in the Mediterranean Sea. The waves can propagate and can be identified over very long distances [47]. Small changes in internal tides can slightly alter the phases of the main tide, moving energy to adjacent tidal bands in an analysis, the cusping discussed in Section 4.6 [48].

In some cases, for example the Australian north-west shelf, the response of shelf tides to ocean tidal forcing (surface *and* internal) may be different from the response to surface tides alone [45, 49]. The process of internal tidal mixing is enhanced in submarine canyons (well-studied examples include the Monterey Bay Canyon off California and the Hudson Canyon off the eastern United States). In these canyons the waves are funnelled and concentrated to give strong flows along the axis of a canyon,

converging at the upper end where they meet the continental shelf.³

Currents associated with internal tides may be responsible for much of the sediment exchange between the shelf and the ocean, but as with many aspects of the dynamics of internal tides, much remains unknown. One sea-level variation that can be clearly related to internal tide propagation is the generation of harbour seiches, as we shall see in Chapter 7; the strongest seiche activity in Sri Lanka occurs at neap tides, the internal tides having taken a week to cross the Bay of Bengal from the Andaman Sea, where they are generated on the preceding spring tide [50].

Theoretical studies of internal waves show that for a flat-bottomed ocean, away from coastal boundaries, there are free wave solutions with speeds related to $\sqrt{(\omega^2 - f^2)}$, where here ω is the wave frequency,

³ The vertical internal movements can be important for bringing deep-water nutrient to the surface layers, both along continental margins and on the coasts of ocean islands, to nourish plankton, coral reefs and seaweeds.

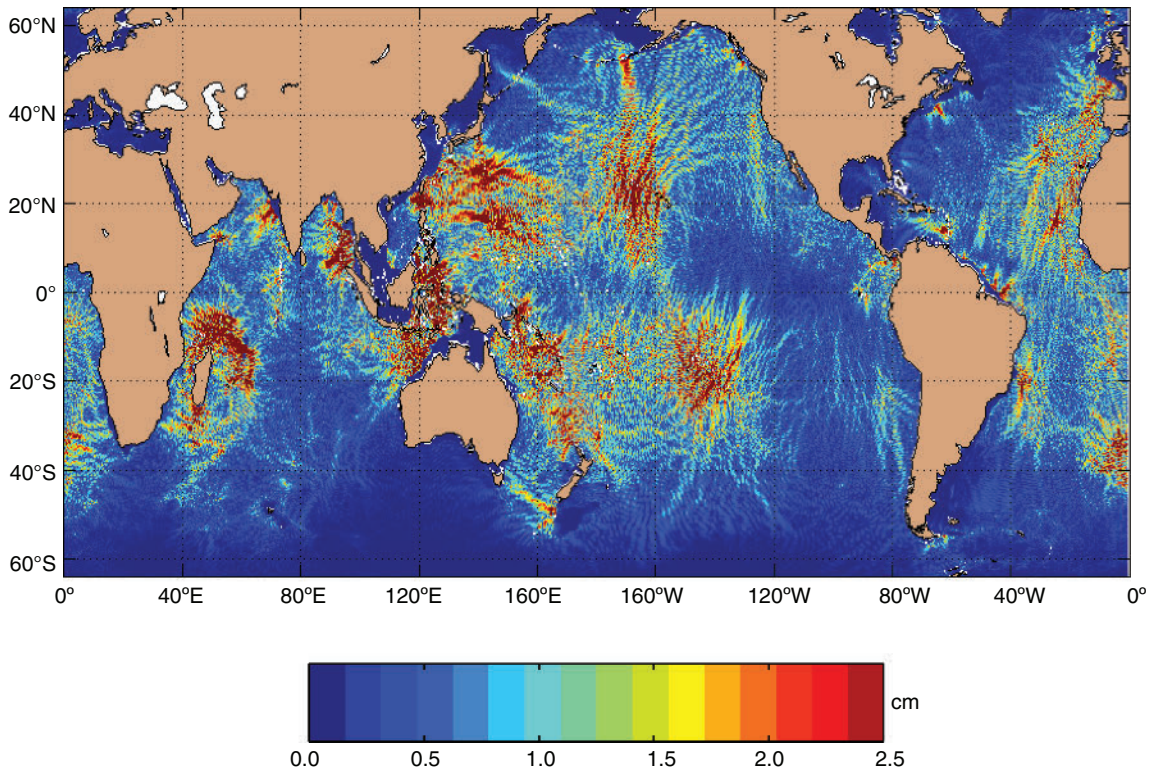


Figure 5.23 Map of areas of internal tide generation. Values are the amplitude (cm) of the M_2 internal tide signature in steric sea surface height. Figure provided by Dr Jay Shriver, Naval Research Laboratory and Dr Brian Arbic, University of Michigan.

and f is the usual Earth rotation factor, $f = 2\omega_s \sin(\text{latitude})$; nearer the poles than certain *critical latitudes*, where $(\omega^2 < f^2)$ progressive internal waves are not theoretically possible [47, 51]. For internal tides the critical latitudes are 30° for K_1 and 74° for M_2 . However, internal semidiurnal tides are observed poleward of 74° latitude, associated with topographic influences [52].

5.7 The yielding Earth

The solid Earth responds elastically to the imposed tidal forces. Although the ocean tides are the obvious terrestrial manifestation of the effects of tidal forces, sensitive instruments can also observe tidal effects in movements of the solid Earth [53, 54]. These solid Earth tidal movements have two contributing effects: the direct response of the Earth to tidal gravitational forces (the direct or body tide), and the indirect effects of the tidal loading and mass redistribution of the water in the oceans due to the tides. This redistribution causes a change of weight on the surface of the Earth,

which deforms the Earth and is called ocean tide loading (OTL). The direct effect is typically 20 cm in the amplitude of vertical displacement of the Earth's surface and varies with latitude. The ocean tide loading vertical displacement is over 5 cm in amplitude under some ocean basins, but the amplitude decreases relatively slowly with distance from the coast and is sometimes over 1 cm in amplitude at distances of 1000 km from the ocean.

For sea levels, Earth tides are important because:

- they affect the generation of ocean tides;
- satellites measure sea levels relative to the centre of the Earth; the marine tide at a coastal station, or measured by a pressure sensor on the seabed, is the *difference* between the tide in geocentric position of the sea surface observed by the altimeter, and the geocentric position of the land on which the gauge is located.

Precise geodetic studies of Earth dynamics require tidal corrections to observations. Also, the response of the Earth to regular tidal forcing can be used to investigate its elastic and inelastic properties.

The hydrodynamic equations of motion given in Appendix A have to be modified to include the effects of the direct Earth tide and ocean tide loading when modelling the global ocean tide [55].

Consider first the directly forced Earth tides, also called the *body tide*. If the Earth were totally fluid the free surface would respond by adapting to the shape of the Equilibrium Tide. Conversely, if the Earth were totally rigid, there would be no surface deformation. In fact the Earth is not totally rigid, but responds mainly elastically to the imposed forces. Moreover, because the natural modes of oscillation of the solid Earth have periods of about 54 minutes or less, the response of the solid Earth to the tidal forces can, to a good approximation, be regarded as in static equilibrium. In contrast, the natural periods of the oceans are much longer than this and similar to the period of the tidal forcing, which is one of the reasons why the ocean response is much more complicated.

The Equilibrium Tide amplitude Ω_p/g (from Equation 3.11) is a second-order spherical harmonic, and for this case the elastic response of the Earth is a surface distortion of amplitude $h\Omega_p/g$ where h is a known elastic constant. In addition, the redistribution of mass in the tidal cycle further increases the gravitational potential by an amount that alters the Equilibrium level by $(1 + k - h) = 0.69$, where k is another known elastic constant. The combined effect is a change in the height of the Equilibrium level above the solid Earth of:

$$(1 + k - h) \frac{\Omega_p}{g}$$

A tide gauge mounted on the seabed would therefore sense a static Equilibrium ocean response that is lower than the true Equilibrium Tide by a factor:

$$(1 + k - h) \frac{\Omega_p}{g} = 0.69$$

Of course, this is a hypothetical case because the fluid oceans do not respond tidally in this static way. The factors k and h are called Love numbers; the 0.69 term is called the diminishing factor.

A fixed land-based gravimeter measuring tidal changes on an undeformable (i.e. totally rigid) Earth would measure the vertical component of the tide-generating force. On a deformable Earth, the gravimeter would record an amplitude of $(1 + h - \frac{3}{2}k)$ [this is, 1.1542 (O_1); 1.1617 (M_2)] times greater than this [56]. Note that there is a difference for the tidal species. The

Love numbers, h and k , are measures of the total elastic behaviour of the solid Earth, and in the latest models, the effects of the mantle's inelasticity and the ellipsoidal shape of the Earth are included. The latter gives a small latitude dependence for the Love numbers [56]. Global tidal gravity observations have been used to verify this model at the 0.1 per cent level [57].

The frequency dependence of the Love numbers can be related to Earth geophysics. For seismic waves, and substantially for tides, they are not frequency dependent, but at increasingly longer time periods there is a transition between an elastic Earth response and a viscous Earth response because the Earth cannot resist the slow imposed stresses. From the long period monthly tides up to the 18.61-year nodal tide, the Earth's response is still mainly elastic, but with an increasingly important inelastic component [58]. The Earth becomes viscous on a 10,000-year timescale, for example for Glacial Isostatic Adjustment (GIA, see Section 11.3). Note that there is an important frequency dependence of the Love numbers for tidal harmonics immediately adjacent to K_1 , caused by a tidal resonance in the fluid core [52, 54, 56]. The effect of the resonance at K_1 is large, i.e. 14 per cent in h [54]. This has to be included correctly when modelling the K_1 ocean tide.

The effects of the loads, the *load tide*, can be computed in two ways from maps of ocean tides: using a sum of spherical harmonics [53], or as a convolution of the tide height with a Green's function [59]. To

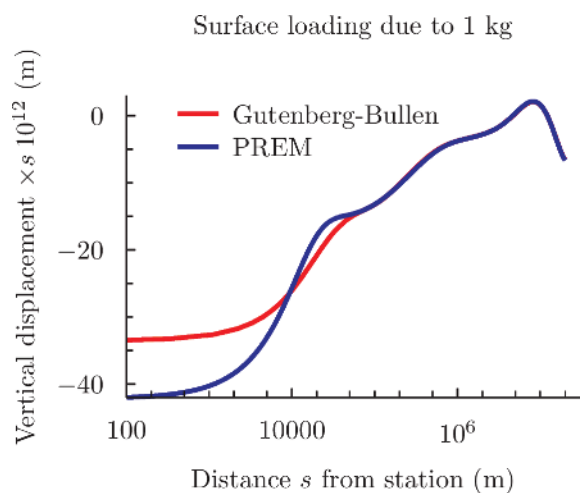


Figure 5.24 Plot of Green's functions based on alternative models of Earth structure (the Gutenberg-Bullen and the Preliminary Earth Reference Models), showing the vertical displacements that would occur a distance s away from a load of 1 kg on the solid Earth. Figure supplied by Dr Machiel Bos, University of Porto.

compute the tidal loading effect at a specific location, Green's functions have an advantage because they can resolve very local marine tidal loading. The Green's function gives the response of the Earth to a 1 kg point load as a function of distance from the point load. The integration is taken over the global ocean, as far-field loads are important for vertical displacements.

The computations of the loading effects at a point are done numerically by summing the tides over the ocean surface of the globe:

$$\text{Loading vertical displacement} = \int_A \rho T(r') G |r - r'| dA \quad (5.8)$$

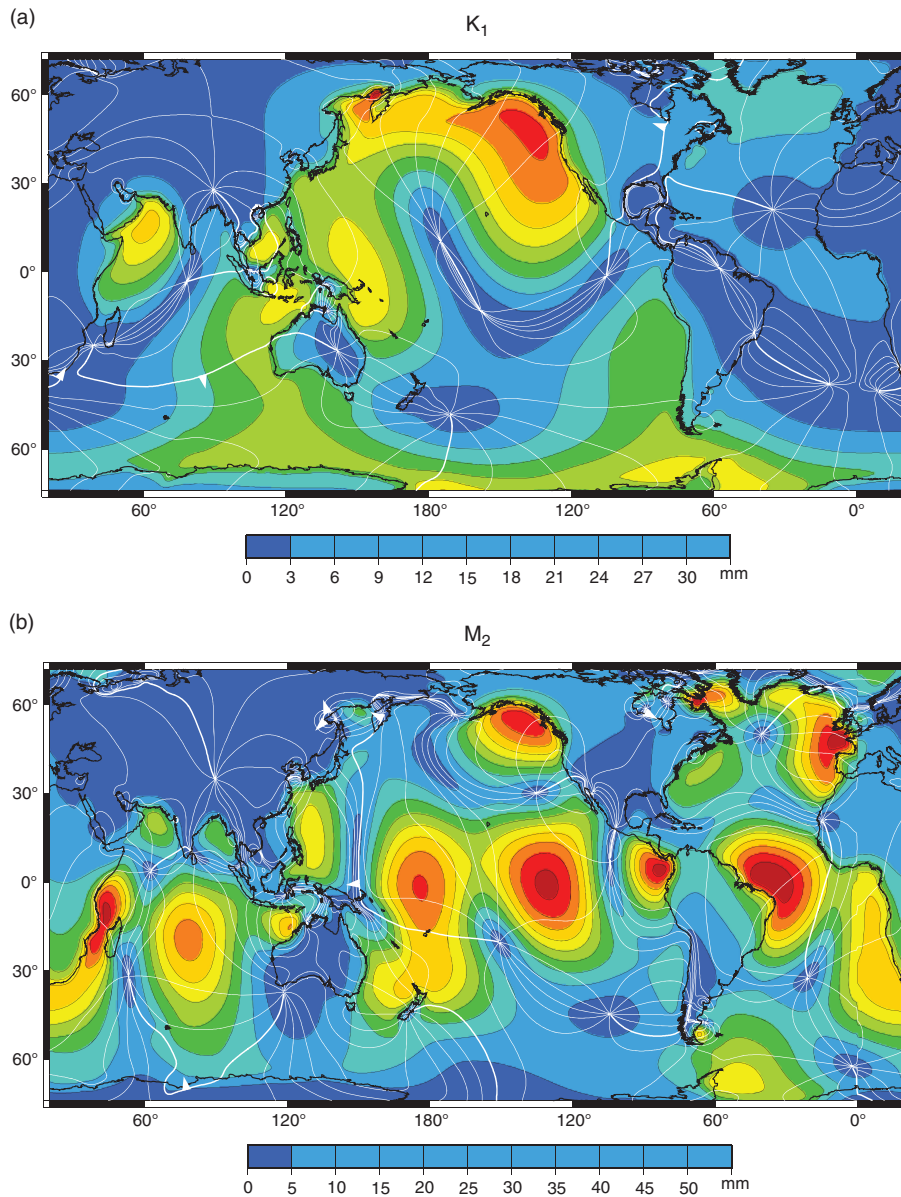


Figure 5.25 Global loading maps for vertical crustal movement due to the (a) K_1 and (b) M_2 ocean tides. The lines indicate Greenwich phase lag every 30° , a lag of zero degrees being shown by the bold line, and the arrows showing the direction of propagation. Note that the loading is expressed as positive upwards, so in many parts of the ocean the loading maps have an approximately 180° different phase lag to the ocean tide maps of Figure 5.1. Images supplied by Dr Richard Ray, Goddard Space Flight Center.

where ρ is the seawater density, $T(r')$ is the ocean tide at a radial distance r' from the point, and $G(r)$ is the vertical displacement Green's function for radial distance r . The vertical displacement Green's function is computed, taking into account the Earth's vertical internal density structure [60, 61]. Figure 5.24 shows computed Greens functions for two models of the Earth's structure, with the vertical displacement as a function of distance r . Beyond 10 km the two curves are very similar. $T(r')$ is taken from tidal models, and has both amplitude and phase. In the numerical computations grid sizes become increasingly small as r decreases. This Green's function approach also applies for other loading effects including horizontal displacement and gravity potential. There are dedicated websites that provide on-line facilities to compute tidal loading at specific points on the Earth's surface [62]. Figure 5.25 shows the actual loading displacements for the K_1 and M_2 ocean tides.

An example of the crustal tilts caused by Earth tides, direct (body) and loading, is shown in Figure 5.26 [63]. Here in vector form the lake tilt tides, a compound of the body tide and tidal loading, measured to better than 10^{-8} , are shown, within experimental error, to be in good agreement with the theoretical computed direct tides, and the loading tides.

5.8 Are tides changing?

The tides are driven by the gravitational forces of the Moon and Sun, whose movements are extremely regular and stable. Ocean tidal amplitudes depend on the response of the oceans to the tidal forces, which in turn change as the depth and shape of the ocean basins change. These will change only slowly over geological time. Direct comparisons of old and recent tidal observations are rare, but between 1761 and 1961 the oceanic semidiurnal tides at St Helena in the South Atlantic were constant in amplitude to within 2 per cent [64]. For the French port of Brest, which is well connected to the Atlantic Ocean, there was similar stability in the tidal amplitude between 1711 and 1936 [65].

Both natural processes and engineering works can affect local tides. Siltation, changes in dredging practices for navigation, and canalisation of rivers are all relevant factors. Locally there have been significant changes in tidal amplitudes. In London, more than 80 km up the River Thames from the North Sea, high water levels have increased by around 0.8 m per century whereas low water increases were only around

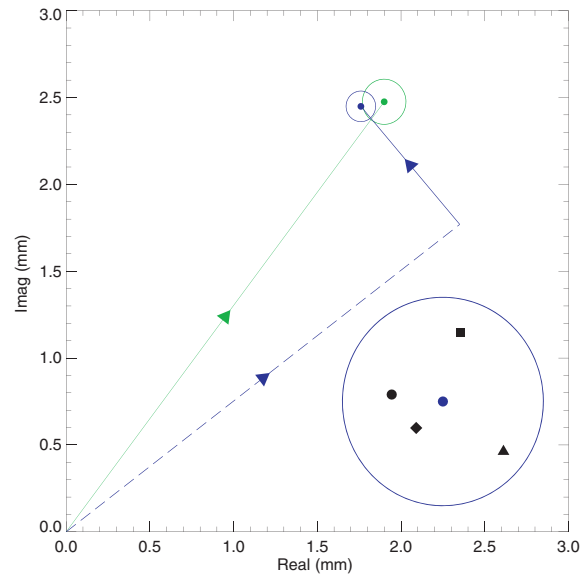


Figure 5.26 A vector plot describing the difference in the M_2 tide observed at the two ends of Loch Ness, Scotland. The Real/Imag axes correspond to $H \cos/\sin G$ in the M_2 tidal difference. Observations shown by the green line can be accounted for by the loading of the land under the loch by the M_2 ocean tide (blue dashed line) together with the direct gravitational effect on the solid Earth due the Moon (blue solid line). The green circle indicates one standard error in the measurements, the blue circle indicates the modelling uncertainty. The blue dashed vector is an average of the loading computed from four recent ocean tide models: on the bottom right, the blue circle has been expanded to show more clearly the combined tidal differences estimated using each individual mode [63].

0.1 m per century. Similar increases have been found in northern Germany. The increase in range is found to be due to an increase in high water levels, while the low water levels have remained roughly the same. The standard deviation of sea levels about the annual MSL, shown in Figure 4.3, includes this small trend against the normal 18.61-year nodal variations. Along the Netherlands and Belgian coasts the tidal range has also increased locally: at Flushing the increase in mean tidal range over the period 1900–80 was 0.14 m per century, or approximately 4 per cent. These increased ranges are due to changes in the coastal configurations.

Systems that are near resonance are more likely to be sensitive to small changes. For Saint John Harbour in the Bay of Fundy, an amplification of M_2 of around 0.10–0.15 m per century is reported, but it appeared that S_2 is decreasing [66]. It is suggested that in future flooding risks will probably increase [67] as a consequence. For tidal systems near resonance, as in the Bay of Fundy, there will be greater sensitivity to

changes in depth and local frictional losses of energy through bottom friction.

It appears that the localised resonances and large tides as shown in Figure 5.1 are, on a geological time-scale, mobile and ephemeral. A global survey of tidal changes suggests that there were some local variations of the ocean tide during the twentieth century [68]. However, it has not always been clear whether the observed changes have been local or regional in scale. Little evidence has been found in Europe or the Far East (including Australasia and Asia) for the extensive regional changes to the main tidal constituents reported recently for North America. However, evidence for change more locally, in smaller regions, can be identified wherever the density of tide gauge information allows. Therefore, it seems that tidal changes may be commonplace around the world, although not necessarily with large spatial scales.

References

- Defant, A. 1961. *Physical Oceanography: Volume II*. Oxford: Pergamon Press.
- Jones, C. W. 1943. *Bedae Opera de Temporibus*. Cambridge, MA: The Medieval Academy of America.
- Lamb, H. 1932. *Hydrodynamics* (6th edition). Cambridge: Cambridge University Press.
- Proudman, J. 1953. *Dynamical Oceanography*. London: Methuen and Co.
- Gill, A. E. 1982. *Atmosphere–Ocean Dynamics*. London: Academic Press.
- Taylor, G. I. 1922. Tidal oscillations in gulfs and rectangular basins. *Proceedings of the London Mathematical Society*, **S20**, 148–181, doi:10.1112/plms/s2-20.1.148.
- Pugh, D. T. 1981. Tidal amphidrome movement and energy dissipation in the Irish Sea. *Geophysical Journal of the Royal Astronomical Society*, **67**, 515–527, doi:10.1111/j.1365-246X.1981.tb02763.x.
- Cartwright, D. E. 1999. *Tides: A Scientific History*. Cambridge: Cambridge University Press.
- Harris, R. A. 1897–1907. *Manual of Tides: Appendices to Reports of the U.S. Coast and Geodetic Survey*. Washington, D.C.: Government Printing Office.
- Whewell, W. 1836. On the results of an extensive system of tide observations made on the coasts of Europe and America in June 1835. *Philosophical Transactions of the Royal Society of London*, **126**, 289–341, doi:10.1098/rstl.1836.0019.
- Egbert, G. D. and Ray, R. D. 2003. Deviation of long-period tides from equilibrium: kinematics and geostrophy. *Journal of Physical Oceanography*, **33**, 822–839, doi:10.1175/1520-0485(2003)33<822:DOLTFE>2.0.CO;2.
- Woodworth, P. L. 2012. A note on the nodal tide in sea level records. *Journal of Coastal Research*, **28**, 316–323, doi:10.2112/JCOASTRES-D-11A-00023.1.
- Tsimplis, M. N., Proctor, R. and Flather, R. A. 1995. A two-dimensional tidal model for the Mediterranean Sea. *Journal of Geophysical Research*, **100**, 16223–16239, doi:10.1029/95JC01671.
- Tsimplis, M. N. 1997. Tides and sea level variability at the strait of Euripus. *Estuarine Coastal and Shelf Science*, **44**, 91–101, doi:10.1006/ecss.1996.0128.
- Padman, L. and Erofeeva, S. 2004. A barotropic inverse tidal model for the Arctic Ocean. *Geophysical Research Letters*, **31**, L02303, doi:10.1029/2003GL019003.
- Sverdrup, H. U. 1927. Dynamic of tides on the north Siberian shelf: results from the Maud expedition. *Geofysiske Publikasjoner*, **4**(5).
- Killett, B., Wahr, J., Desai, S., Yuan, D. and Watkins, M. 2011. Arctic Ocean tides from GRACE satellite accelerations. *Journal of Geophysical Research*, **116**, C11005, doi:10.1029/2011JC007111.
- Bye, J. A. T. and Heath, R. A. 1975. The New Zealand semi-diurnal tide. *Journal of Marine Research*, **33**, 423–442.
- Munk, W., Snodgrass, F. and Wimbush, M. 1970. Tides off-shore: transition from California coast to deep-sea waters. *Geophysical Fluid Dynamics*, **1**, 161–235.
- Cartwright, D. E. 1969. Extraordinary tidal currents near St. Kilda. *Nature*, **223**, 928–932, doi:10.1038/223928a0.
- Flather, R. A. 1988. A numerical model investigation of tides and diurnal-period continental shelf waves along Vancouver Island. *Journal of Physical Oceanography*, **18**, 115–139, doi:10.1175/1520-0485(1988)018<0115:ANMIOT>2.0.CO;2.
- Crawford, W. R. and Thomson, R. E. 1991. Physical oceanography of the western Canadian continental shelf. *Continental Shelf Research*, **11**, 669–683, doi:10.1016/0278-4343(91)90073-F.
- Smith, P. C. 1989. Inertial oscillations near the coast of Nova Scotia during CASP. *Atmosphere–Ocean*, **27**, 181–209, doi:10.1080/07055900.1989.9649333.
- Robinson, I. S. 1979. The tidal dynamics of the Irish and Celtic Seas. *Geophysical Journal of the Royal Astronomical Society*, **56**, 159–197, doi:10.1111/j.1365-246X.1979.tb04774.x.
- Robinson, I. S. 1979. The tidal dynamics of the Irish and Celtic Seas. *Geophysical Journal of the Royal Astronomical Society*, **56**, 159–197, doi:10.1111/j.1365-246X.1979.tb04774.x.

26. Taylor, G. I. 1920. Tidal friction in the Irish Sea. *Philosophical Transactions of the Royal Society of London*, **A**, **220**, 1–33, doi:10.1098/rsta.1920.0001.
27. Redfield, A. C. 1958. The influence of the continental shelf on the tides of the Atlantic coast of the United States. *Journal of Marine Research*, **17**, 432–458.
28. Forrester, W. D. 1983. *Canadian Tidal Manual*. Ottawa: Department of Fisheries and Oceans Canada.
29. Pous, S., Carton, X. and Lazure, P. 2012. A process study of the tidal circulation in the Persian Gulf. *Open Journal of Marine Science*, **2**, 131–140, doi:10.4236/ojms.2012.24016.
30. Ray, R. D., Egbert, G. D. and Erofeeva, S.Y. 2005. A brief overview of tides in the Indonesian Seas. *Oceanography*, **18**, 74–79, doi:10.5670/oceanog.2005.07.
31. Glorioso, D. G. and Flather, R. A. 1997. The Patagonian Shelf tides. *Progress in Oceanography*, **40**, 263–283, doi:10.1016/S0079-6611(98)00004-4.
32. Huthnance, J. M. 1980. On shelf-sea resonance with application to Brazilian M_3 tides. *Deep-Sea Research*, **27A**, 347–366, doi:10.1016/0198-0149(80)90031-X.
33. Richard Ray, personal communication.
34. O'Reilly, C. T., Solvason, R. and Solomon, C. 2005. Where are the world's largest tides? In *Bedford Institute of Oceanography 2004 in Review* (ed. J. Ryan), pp. 44–46, Dartford, Nova Scotia: Bedford Institute of Oceanography.
35. Arbic, B. K., St.-Laurent, P., Sutherland, G. and Garrett, C. 2007. On the resonance and influence of the tides in Ungava Bay and Hudson Strait. *Geophysical Research Letters*, **34**, L17606, doi:10.1029/2007GL030845.2007.
36. Ray, R. and Egbert, D. E. 2004. The global S_1 tide. *Journal of Physical Oceanography*, **34**, 1922–1935, doi:10.1175/1520-0485(2004)034<1922:TGST>2.0.CO;2.
37. Ray, R. D. and Ponte, R. M. 2003. Barometric tides from ECMWF operational analyses. *Annales Geophysicae*, **21**, 1897–1910, doi:10.5194/angeo-21-1897-2003.
38. Chapman, S. and Lindzen, R. S. 1970. *Atmospheric Tides, Thermal and Gravitational*. Dordrecht: Reidel.
39. Arbic, B. K. 2005. Atmospheric forcing of the oceanic semidiurnal tide. *Geophysical Research Letters*, **32**, L02610, doi:10.1029/2004GL021668.
40. Godin, G. 1986. Is the abnormal response of the tide at the frequency of S_2 really due to radiational effects? *Continental Shelf Research*, **6**, 615–625, doi:10.1016/0278-4343(86)90026-9.
41. Marone, E. 1996. “Radiational tides” as nonlinear effects: bispectral interpretation. *Continental Shelf Research*, **16**, 1117–1126, doi:10.1016/0278-4343(95)00025-9.
42. Ray, R. and Mitchum, G. T. 1996. Surface manifestation of internal tides generated near Hawaii. *Geophysical Research Letters*, **23**, 2101–2104, doi:10.1029/96GL02050.
43. St. Laurent, L., Alford, M. H. and Paluszkiwicz, T. (eds.) 2012. An introduction to the special issue on internal waves. *Oceanography*, **25**, 5–19, doi:10.5670/oceanog.2012.37.
44. Garrett, C. and Kunze, E. 2007. Internal tide generation in the deep ocean. *Annual Review of Fluid Mechanics*, **39**, 57–87, doi:10.1146/annurev.fluid.39.050905.110227.
45. Arbic, B. K., Richman, J. G., Shriver, J. F. *et al.* 2012. Global modeling of internal tides within an eddying ocean general circulation model. *Oceanography*, **25**, 20–29, doi:10.5670/oceanog.2012.38.
46. da Silva, J. C. B., New, A. L. and Magalhaes, J. M. 2011. On the structure and propagation of internal solitary waves generated at the Mascarene Plateau in the Indian Ocean. *Deep-Sea Research*, **58**, 229–240, doi:10.1016/j.dsr.2010.12.003.
47. Zhao, Z., Alford, M. H. and Girtton, J. B. 2012. Mapping low-mode internal tides from multisatellite altimetry. *Oceanography*, **25**, 42–51, doi:10.5670/oceanog.2012.40.
48. Colosi, J. A. and Munk, W. 2006. Tales of the venerable Honolulu tide gauge. *Journal of Physical Oceanography*, **36**, 967–996, doi:10.1175/jpo2876.1.
49. Kelly, S. M. and Nash, J. D. 2010. Internal tide generation and destruction by shoaling internal tides. *Geophysical Research Letters*, **37**, L23611, doi:10.1029/2010GL045598.
50. Wijeratne, E. M. S., Woodworth, P. L. and Pugh, D. T. 2009. Meteorological and internal wave forcing of seiches along the Sri Lanka coast. *Journal of Geophysical Research*, **115**, C03014, doi:10.1029/2009JC005673.
51. Rainville, L. and Pinkel, R. 2006. Propagation of low-mode internal waves through the ocean. *Journal of Physical Oceanography*, **36**, 1220–1236, doi:10.1175/JPO2889.1.
52. Albrecht, N., Vennell, R., Williams, M. *et al.* 2006. Observation of sub-inertial internal tides in McMurdo Sound, Antarctica. *Geophysical Research Letters*, **33**, 1–5, doi:10.1029/2006GL027377.
53. Agnew, D. C. 2007. Earth tides. In *Treatise on Geophysics: Geodesy* (ed. T. A. Herring), pp. 163–195, New York: Elsevier.
54. Baker, T. F. 1984. Tidal deformations of the Earth. *Science Progress*, **69**, 197–233.
55. Hendershott, M. C. 1972. The effects of solid Earth deformation on global ocean tides. *Geophysical Journal*

- of the *Royal Astronomical Society*, **29**, 389–402, doi:10.1111/j.1365-246X.1972.tb06167.x.
56. Dehant, V., Defraigne, P. and Wahr, J. M. 1999. Tides for a convective Earth. *Journal of Geophysical Research*, **104**, 1035–1058, doi:10.1029/1998JB900051.
 57. Baker, T. F. and Bos, M. S. 2003. Validating Earth and ocean tide models using tidal gravity measurements. *Geophysical Journal International*, **152**, 468–485, doi:10.1046/j.1365-246X.2003.01863.x.
 58. Benjamin, D., Wahr, J., Ray, R. D., Egbert, G. D. and Desai, S. D. 2006. Constraints on mantle anelasticity from geodetic observations, and implications for the J2 anomaly. *Geophysical Journal International*, **165**, 3–16, doi:10.1111/j.1365-246X.2006.02915.x.
 59. Farrell, W. E. 1972. Deformation of the Earth by surface loads. *Reviews of Geophysics*, **10**, 3, doi:10.1029/RG010i003p00761.
 60. Sung-Ho, N. and Jeongho, B. 2011. Computation of the Load Love Number and the Load Green's Function for an elastic and spherically symmetric Earth. *Journal of the Korean Physical Society*, **58**, 1195–1205, doi:10.3938/jkps.58.1195.
 61. Bos, M. S. and Scherneck, H.-G. 2013. Computation of Green's functions for tidal loading. In *Sciences of Geodesy: II, Innovations and Future Developments* (ed. Guochang Xu), Berlin, Heidelberg: Springer-Verlag, doi:10.1007/978-3-642-28000-9-1.
 62. <http://geodac.fc.up.pt/loading/loadingprimer.html>
 63. Pugh, D. T., Woodworth, P. L. and Bos, M. S. 2011. Lunar tides in Loch Ness, Scotland. *Journal of Geophysical Research*, **116**, C11040, doi:10.1029/2011JC007411.
 64. Cartwright, D. E. 1971. Tides and waves in the vicinity of Saint Helena. *Philosophical Transactions of the Royal Society, A*, **270**, 603–646, doi:10.1098/rsta.1971.0091.
 65. Cartwright, D. E. 1972. Secular changes in the oceanic tides at Brest, 1711–1936. *Geophysical Journal of the Royal Astronomical Society*, **30**, 433–449, doi:10.1111/j.1365-246X.1972.tb05826.x.
 66. Godin, G. 1995. Rapid evolution of the tide in the Bay of Fundy. *Continental Shelf Research*, **15**, 369–372, doi:10.1016/0278-4343(93)E0005-S.
 67. Greenberg, D. A., Blanchard, W., Smith, B. and Barrow, E. 2012. Climate change, mean sea level and high tides in the Bay of Fundy. *Atmosphere-Ocean*, **50**, 261–276, doi:10.1080/07055900.2012.668670.
 68. Woodworth, P. L. 2010. A survey of recent changes in the main components of the ocean tide. *Continental Shelf Research*, **30**, 1680–1691, doi:10.1016/j.csr.2010.07.002.
 69. Forrester, W. D. 1983. *Canadian Tidal Manual*. Department of Fisheries and Oceans. Reproduced with the permission of the Canadian Hydrographic Service.
 70. Fisheries and Oceans Canada 2008. *Atlas of Tidal Currents, St. Lawrence Estuary*. Reproduced with the permission of the Canadian Hydrographic Service.
 71. Ray, R. D. and Ponte, R. M. 2003. Barometric tides from ECMWF operational analyses. *Annales Geophysicae*, **21**, 1897–1910, doi:10.5194/angeo-21-1897-2003. Images redrawn by Richard Ray.

Shallow-water and coastal tides

‘... I don’t see the good of the tides. What’s the good of a sea if it’s going to be mud in a few hours.’ ‘It’s like breathing,’ said Titty. ‘Up and down. Up and down. It makes everything alive.’
Arthur Ransome, Secret Water

In the [previous chapter](#) we showed how the amplitudes of the tidal waves generated in the deep oceans increase when they spread onto the shallow surrounding continental shelves. In this chapter we consider the further and more extreme distortions that occur as the tidal waves propagate into the even shallower coastal waters and rivers. The behaviour of these distorted tides is very important for near-shore human activities such as recreational pursuits and coastal navigation. The distortions are also important for geological and biological processes in the coastal zone.

6.1 Introduction: some observations

Sea-level records from shallow-water locations normally show that the interval from low to high water is shorter than the interval from high to low water: the rise time is more rapid than the fall. Offshore the flood currents are stronger than the ebb currents. High waters occur earlier than simple predictions, and low waters are later.

The extreme distortion takes the form of a double high water or a double low water. [Figure 6.1](#) shows the tidal variations at Southampton on the south coast of England. During spring tides (31 March 2002 in this case), following low water, the water level rises, but there is then a slackening of the tidal stream and a water level stand for a further two hours before the final rapid rise to high water, over the next three hours. The slackening effect is known locally as the ‘young flood stand’. The flood and the double high water last approximately 9 hours, leaving only 3 hours for the tidal ebb, which is therefore associated with very strong ebb currents. Observations at other places along the coast of the English Channel show that the effects are not limited to Southampton; at Portland, 90

km to the west, there are sometimes double low water levels at spring tides. Elsewhere, double high waters are also observed at Falmouth in Buzzards Bay, Massachusetts [1], and at the Hoek van Holland and Den Helder on the Dutch coast.

6.2 Hydrodynamic distortions

In this section we consider three separate physical factors, each of which may contribute to tidal distortions. Firstly, the stronger currents that develop in the shallow waters are resisted by the drag due to bottom friction, a process that eventually removes much of the propagating tidal energy, and reduces the wave amplitudes. Secondly, the amplitude of the tidal waves becomes a significant fraction of the total water depth and this restricts the wave’s travel. A third distorting factor is the influence of topography: irregular coastlines and varying depths impose complicated tidal current patterns. All three effects may apply to varying extent, in any real coastal location.

Nevertheless, it is useful to examine some simple solutions of the hydrodynamic equations ([Appendix A](#)) for each separate process. In the case of one-dimensional dynamics, such as might approximate to the situation for a narrow channel, or estuary, [Equations \(A.2\)](#) and [\(A.4\)](#) become:

$$\frac{\partial \zeta}{\partial t} + \frac{\partial [(D + \zeta)]u}{\partial x} = 0 \quad (6.1)$$

$$\frac{\partial u}{\partial t} + u \frac{\partial u}{\partial x} = -g \frac{\partial \zeta}{\partial x} + \frac{1}{\rho} \frac{F_b}{(D + \zeta)} \quad (6.2)$$

where direct tidal forcing is considered negligible for the local dynamics, and F_b is the force on the water due to bottom friction. On the basis of these simplified

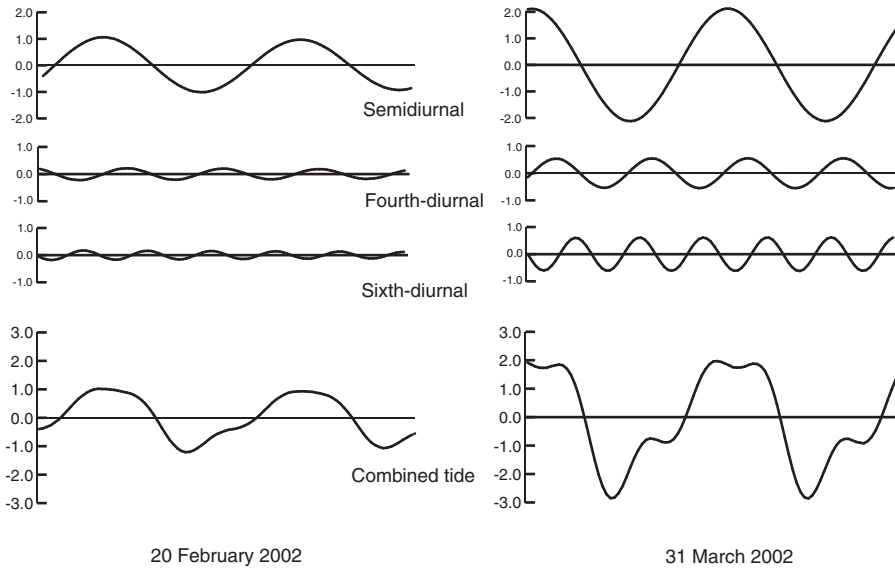


Figure 6.1 Typical tidal curves at Southampton at neap (20 February 2002) and spring (31 March 2002) tides. The latter shows the double high waters and the increased distortion due to M_4 and M_6 at spring tide.

equations we may consider the three shallow-water effects in turn.

6.2.1 Bottom friction

The effects of bottom friction are to oppose the flow and to remove energy from the motion. Experiments and theoretical dimensional analysis arguments support a relationship between the drag and the current speed of the form:

$$\tau_b = -C_D \rho \mathbf{q} |\mathbf{q}| \quad (6.3)$$

where τ_b is the bottom stress, C_D is a dimensionless drag coefficient, ρ is the water density, and q is the total current vector. In a similar way to the relationship between wind speed and the stress on the sea surface, the value of C_D depends on the level above the seabed at which the current is measured; usually this level is taken as 1 m, and for this case the value of C_D may lie between 0.0015 and 0.0025. The two components of bottom stress are:

$$\begin{aligned} F_b &= -C_D \rho \mathbf{q} |\mathbf{q}| \cos \theta - C_D \rho q u \\ G_b &= -C_D \rho \mathbf{q} |\mathbf{q}| \sin \theta = -C_D \rho q v \end{aligned}$$

in the usual Cartesian system (see Section 2.5). In the case of flow in a channel this reduces to:

$$F_b = -C_D \rho u |u|$$

Suppose that the currents vary harmonically as $u = U \cos \sigma t$. The $u|u|$ term may then be expanded mathematically as a cosine Fourier series [2] that contains only odd harmonics:

$$u|u| = U_0^2 (a_1 \cos \sigma t + a_3 \cos 3\sigma t + a_5 \cos 5\sigma t + \dots)$$

where $a_1 = \frac{8}{3\pi}$, $a_3 = \frac{8}{15\pi}$ etc.

This shows that tidal currents in a channel that vary as $u = U_{M_2} \cos 2\omega_1 t$ will result in frictional forces that include terms in $\cos 6\omega_1 t$, $\cos 10\omega_1 t$ etc. In the more general case of two-dimensional flow, both even and odd harmonics of the basic tidal frequencies are present in the frictional resistance terms.

6.2.2 Finite water depth

Most people are familiar with the behaviour of wind waves as they approach the shore. Gradually the wave front steepens until eventually the wave breaks. Similar behaviour occurs with tidal waves, but the effect is not obvious because the wavelengths and periods are so much greater. Figure 6.2 shows an exaggerated profile of a wave moving in the direction of increasing X . At any particular location the rise and fall of the water as the wave passes will not take equal times. The rate of rise of the water level is more rapid than the rate of fall. This difference becomes greater as the wave progresses (X increases).

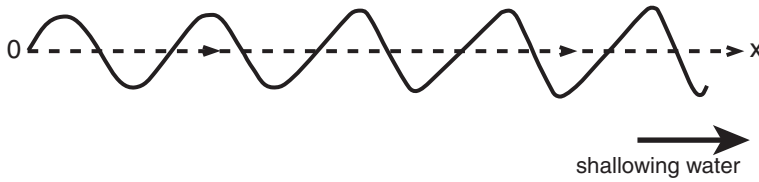


Figure 6.2 Distortion of a progressive wave travelling in shallow water up a channel in the positive X direction. Note the shorter rise time as the wave passes a fixed observer, as distortion increases.

The wave speed decreases as the water depth decreases, so the troughs of the waves will tend to be overtaken by the crests, giving rise to the asymmetry. Previously we have shown (Equation 5.1) that the wave speed c , where the depth is large compared with the amplitude and the wavelength is long compared with the depth, is given by $c = \sqrt{gD}$. Where the wave amplitude is comparable with the total depth, a more exact relationship is given by $c = [g(D + \frac{3}{2}\zeta)]^{\frac{1}{2}}$ as will be shown in Section 6.5.2, Equation 6.15; the differences between wave crest and wave trough speeds given by these formulae enhance the development of asymmetry. However, a more elaborate theoretical analysis of the dynamics proceeds from Equations 6.1 and 6.2; omitting the effects of friction and making the partial differentiation in Equation 6.1:

$$\begin{aligned} \frac{\partial \zeta}{\partial t} + (D + \zeta) \frac{\partial u}{\partial x} + u \frac{\partial \zeta}{\partial x} &= 0 \\ \frac{\partial u}{\partial t} + u \frac{\partial u}{\partial x} &= -g \frac{\partial \zeta}{\partial x} \end{aligned} \quad (6.4)$$

If these two equations are compared with Equations 5.3, we see that a first-order solution, ignoring for the moment the additional non-linear term, is given by Equations 5.4 [3]:

$$\begin{aligned} \zeta &= H_0 \cos(kx - \omega t) \\ u &= H_0 \sqrt{\frac{g}{D}} \cos(kx - \omega t) \end{aligned}$$

Substituting these first-order solutions into the non-linear extensions of Equation 6.4 and retaining terms up to H_0^2 , a more exact solution is obtained. For sea levels this gives:

$$\zeta = H_0 \cos(kx - \sigma t) - \frac{3}{4} \frac{kx H_0^2}{D} \sin 2(kx - \sigma t) + \dots \quad (6.5)$$

The second term is a harmonic of the original wave. Its amplitude increases as the inverse of the depth, linearly as the distance increases along the channel, and as the square of the amplitude of the original wave.

Further refinement would lead to solutions containing higher harmonics. Relating this basic example to an input M_2 tidal wave shows that an M_4 component will be generated as the wave progresses into shallow water.

6.2.3 Flow curvature

The effects of variations of bottom topography and of coastal configurations on tidal currents have been discussed briefly in Section 5.4.3 for the cases of shelving beaches and embayments. The tidal currents tend to follow the contours of the coast. The forces that change the directions of current flow along the coast are the pressure gradients across the directions of the streamlines. In Figure 6.3 the arrows on the broken lines show the downward slope of the sea surface to give this gradient. Assuming that the sea surface well away from the coast is level, then the sea levels at the headland will be slightly lower and the levels in the bays will be slightly higher than those offshore. When the tidal flows reverse during the second half of the cycle, the same gradients are again generated to maintain the curvature along the coast.

Because these gradients are in the same sense for both the flood and the ebb flows, the result is a relative

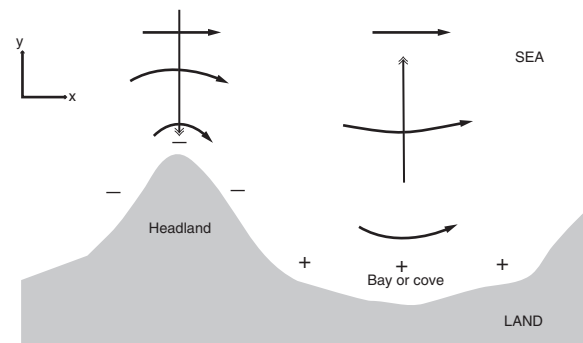


Figure 6.3 Curvature of streamlines for tidal flows near a coast (solid arrows). The surface gradients, which produce the curvature, are represented by the dashed arrows, which point down the slope. The currents are reversed half a tidal cycle later, but the gradients are the same.

depression of sea level at the headlands twice in a tidal cycle. This would appear as an enhanced M_4 constituent in a harmonic analysis of the headland sea levels.

The gradient necessary to produce the flow curvature can be calculated in terms of the current speed u and the radius of curvature of the flow (there is a direct analogue with the forces that keep a satellite in orbit):

$$g \frac{\partial \zeta}{\partial y} = \frac{u^2}{r} \quad (6.6)$$

where r is the radius of curvature of the flow. For a radius of curvature of 1 km and a current speed of 1 m/s, the gradient is 0.1 m in 1 km. The effects on sea level at the coast will depend on the distance over which this curvature of flow and the corresponding gradient are maintained. Around Portland Bill, which protrudes into the English Channel, this curvature effect is responsible for an M_4 amplitude of 0.10 m, in addition to the normal M_4 amplitude in the region [4]. Because headlands are sharper coastal features than bays, the flow curvature and associated surface gradients are more severe. As a result, gauges located in broad bays will measure levels that are more representative of open-sea conditions than those located near headlands.

Curvature of streamlines near the coast also affects the coastal mean levels over a spring-neap cycle, with lower headland levels at springs. In harmonic terms this 14.8-day variation will be represented by an enhanced local MS_f constituent. The overall mean sea level at the end of Portland Bill is estimated to be 0.06 m lower than the general level along the coast and offshore.

6.3 Representation by higher harmonics

We have shown in a general way how the progression of a tidal wave in shallow water is modified by bottom friction and other physical processes that depend on the square or higher powers of the tidal amplitude itself. Figure 6.1 shows the double high and double low water extreme distortions at Southampton on the south coast of England due to non-linear shallow-water effects. The distortions of the normal harmonic variations of tidal levels and currents can be represented by the addition of higher harmonics, as was discussed in Chapter 4. These new constituents have angular speeds that are multiples, sums or differences of the speeds of the astronomical constituents listed in Table 3.2. Section 4.2.3 shows how the combination of M_2 and S_2 leads to terms in M_4 , MS_4 etc.

Consider the simplest case of M_2 and its first harmonic, M_4 . The phase of the higher harmonic relative to the basic wave controls the shape of the total curve, as is shown in Figure 6.4. Rapid rise followed by a slow fall of level (Figure 6.4(1)) corresponds to the case of the M_4 phase leading the M_2 phase by $\phi = 90^\circ$, at $t = 0$. The case of the slow rise and rapid fall (Figure 6.4(3)) corresponds to the M_4 phase lagging the M_2 phase by $\phi = 90^\circ$ at $t = 0$. Double high water may occur (Figure 6.4(2)) when the M_4 phase is $\phi = 180^\circ$ different from the M_2 phase at $t = 0$, and the corresponding case of double low water (Figure 6.4(4)) occurs when $\phi = 0$, the phases of M_2 and M_4 are the same at $t = 0$. In the cases plotted the M_4 amplitude is set at 0.3 times the M_2 amplitude. Table 6.1 summarises these effects.

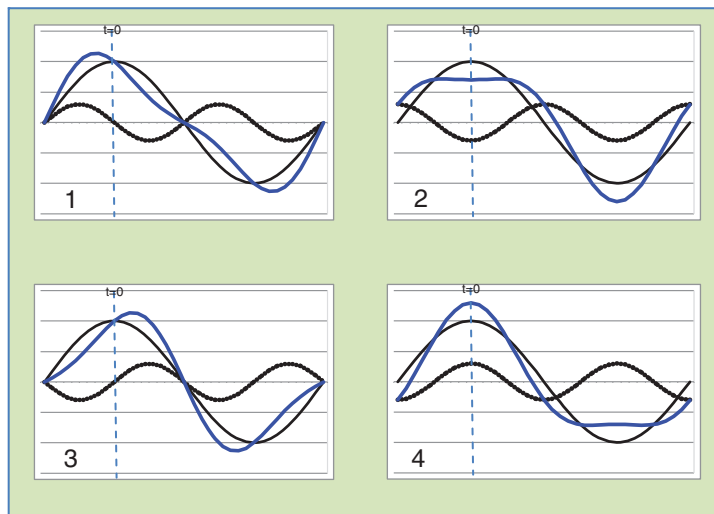
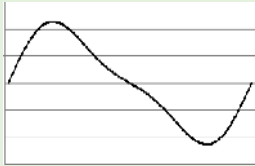
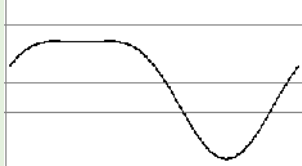

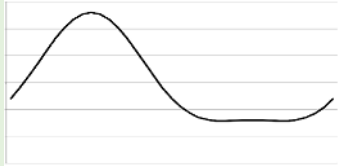


Figure 6.4 Showing how the shape of the composite sea-level curve is controlled by the relationship between the M_2 and M_4 phases. Here $H_{M_4} = 0.3 H_{M_2}$, which is an extreme case, for illustration.

Table 6.1 The characteristics of the composite tides in Figure 6.2. *Increased* low water heights means lower sea levels than for M_2 alone. *Normal* means as for M_2 .

		1	2	3	4
					
		1	2	3	4
	$(2g_{M_2} - g_{M_4})$	-90°	180°	90°	0°
Rise		fast	normal	slow	normal
Fall		slow	normal	fast	normal
High water	time	early	normal	late	normal
	height	increased	reduced	increased	increased
Low water	time	late	normal	early	normal
	height	increased	increased	increased	decreased

For a double high water or a double low water, there is a minimum M_4 amplitude that can produce the effect. Consider the total water level at $t = 0$ in Figure 6.4(2):

$$H_{M_2} \cos 2\omega_1 t - H_{M_4} \cos 4\omega_1 t = H_{M_2} - H_{M_4}$$

If this is a minimum value between two maxima, then the amplitude at time Δt , later or earlier, must be greater. Using the trigonometric expansion $\cos \beta = 1 - \beta^2$ for small β , this new level is:

$$H_{M_2}(1 - 4\omega_1^2 \Delta t^2) - H_{M_4}(1 - 16\omega_1^2 \Delta t^2)$$

which only exceeds the previous value if:

$$4H_{M_4} > H_{M_2} \quad (6.7)$$

Similar arguments may be used to show that a double high water involving only M_6 requires:

$$9H_{M_4} > H_{M_2} \quad (6.8)$$

At Southampton neither M_4 nor M_6 is large enough, alone, to produce the double high waters: a combination of several shallow-water harmonic terms represents the observed distortions. Figure 6.1 shows how harmonic terms in the fourth-diurnal and sixth-diurnal species can fit and reproduce the effects, for both neap tides (20 February 2002) and spring tides (31 March).

A valuable alternative to the analysis of long periods of data for several harmonics, which are separated from each other by frequency increments equivalent to a month (groups) or a year (constituents), is to analyse *single days of data* for the harmonics present in each *species*. These daily harmonics may be called D_1 , D_2 , $D_4 \dots$, by analogy with the usual notation for the naming of harmonic constituents. Modulations of

these D_n terms will take place over the spring–neap cycle, over a month and over a year, in the same way as the many lunar constituents in more detailed analyses vary over 18.6 years. Although not suitable for prediction purposes, daily analysis can give some insight into the physics of non-linear dynamics not possible by other means. Figure 6.5 shows the variation of the D_4 and D_6 amplitudes at Southampton, as a function of the D_2 amplitude. D_4 increases fourfold between 1 m and 2 m values of D_2 ; the increase for D_6 is even more rapid.

Double high and low waters are more likely where the M_2 amplitude is low. In Figure 1.2a there are several additional turning points during neap tides when the semidiurnal amplitude at Courtown becomes very small.

In many cases it is possible to draw co-tidal and co-amplitude charts for the shallow-water constituents. For the northwest European shelf, the M_4 amplitude is comparable with the amplitude of the diurnal constituents, in the range 0.05–0.15 m. The amplitude of M_6 is smaller, rarely exceeding 0.10 m except in the vicinity of Southampton Water where it reaches 0.20 m. Higher harmonics than M_4 are only significant in estuaries and restricted local areas. Figure 6.6 shows a co-tidal chart for the M_4 constituent. The direction of phase propagation, which is consistent along the coast, is shown by arrows. Note a well-developed pattern of double amphidromes in the English Channel. There is also an anti-amphidrome with M_4 amplitudes in excess of 0.3 m in the vicinity of the Dover Straits. In the semidiurnal tidal regime the odd shallow-water harmonics (M_3 , M_5 , M_7 etc.) are usually very small, but where mixed tides occur, diurnal and semidiurnal tides can interact, and the fifth-diurnal tides may be appreciable. Anchorage in Alaska is a good example.

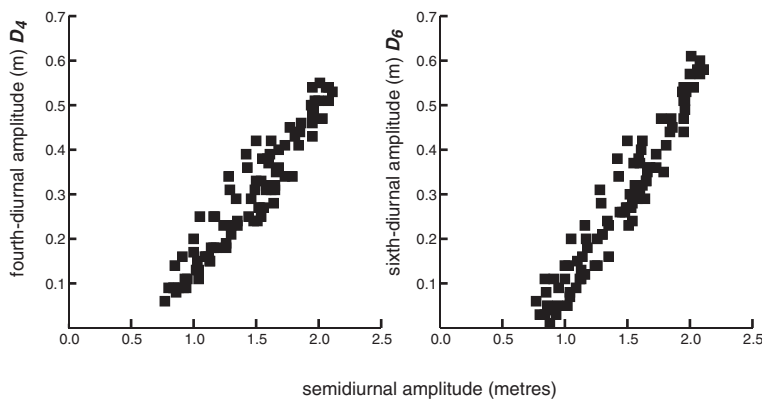


Figure 6.5 The amplitude of the *daily* non-linear tides, D_4 and D_6 , as a function of the amplitude of the composite semidiurnal tide D_2 , also determined each day, at Southampton, February–April 2002.

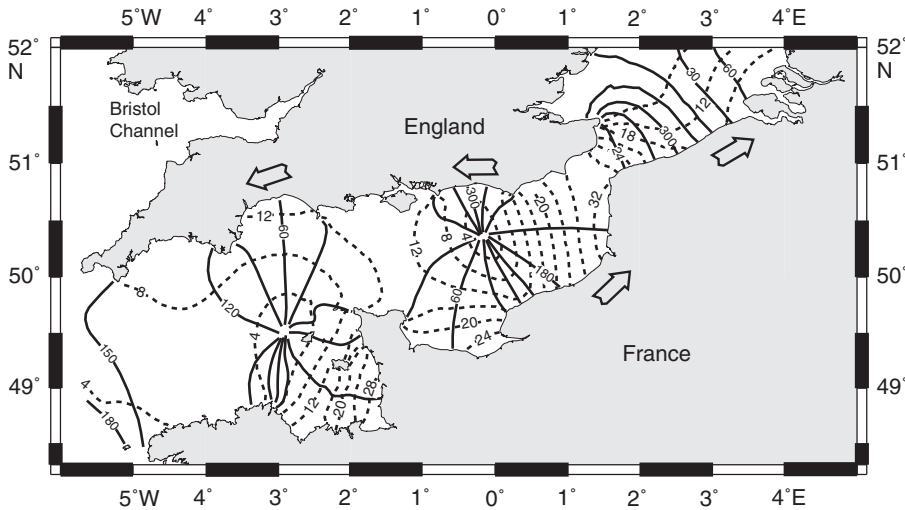


Figure 6.6 A tidal chart of the M_4 shallow water harmonic in the English Channel. Note the coherent pattern around amphidromes in mid Channel. The white arrows indicate the direction of propagation. Based on information supplied by Dr Roger Flather, National Oceanography Centre.

Harmonic analysis of the observed tides gives amplitudes that are usually slightly smaller and lag by a few minutes compared with the linear gravitational tides computed by the response technique. For example, at Newlyn, a 1-year *harmonic analysis* of the actual M_2 tide gave an amplitude and a phase of 1.700 m and 135.5° , compared with the linear gravitational *response analysis* tide of 1.872 m and 131.3° . Physically the difference results from the effects of the finite M_2 amplitude on its own propagation characteristics in shallow water – in a sense M_2 is self-limiting; wave amplitudes are reduced and the arrival time is delayed. In terms of triple interaction, this is represented by the notation of Chapter 4 as I^{2+2-2} , and may be considered as a shallow-water harmonic component of the total M_2 constituent. At Newlyn this M_2 non-linear tide has an amplitude of 0.179 m and a phase of 276° . By comparing results from the two different types of analysis, the compound nature of the observed M_2 constituent is apparent.

6.4 Tidal currents

Near the shore and in shallow water, tidal currents become much stronger and important. This section looks at three non-linear processes that control currents in these regions: bottom friction, restricted channel flow, and the generation of residual long-term flow due to periodic tides.

6.4.1 Bottom friction effects on current profiles

Tidal currents are driven locally by the pressure gradients of sea surface slopes; these pressure-generated forces act uniformly through the water depth. However, at the seabed the opposing forces due to bottom friction act to reduce currents. The flow at the seabed is important for many reasons, including the movement of sediment and the installation of cables and pipelines. An understanding of the influence of bottom friction on the currents at higher levels, called the *tidal current profile*, is necessary for studies of mass transport and dispersion.

The water layer that is affected by the physical effects of the seabed is called the *benthic boundary layer*. Usually, tidal currents near the seabed have phases that are in advance of those in the main body of water. This may be explained in general terms: as the sea-level gradients reverse at low water, the existing flow continues until its momentum has been overcome by the reversed tidal pressure gradient, and by the drag of bottom friction. At the bottom where the friction overcomes the momentum very shortly after the pressure gradient reverses, flow in the reverse direction begins with only a short delay. At higher levels in the water column the reversal takes longer because the effects of bottom friction are weaker and are not felt immediately. Typically, changes of

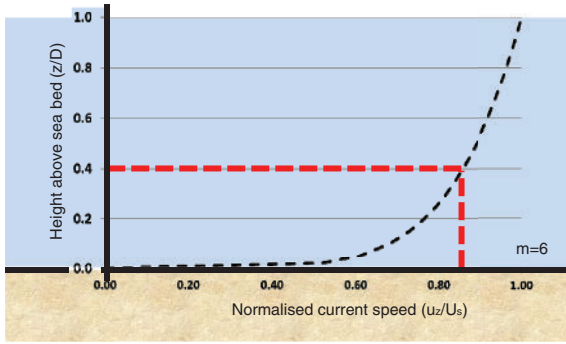


Figure 6.7 The variation with depth of a tidal current affected by bottom friction. Here $m = 6$ (see text). A depth mean current would be measured by a meter at 40 per cent of the total depth above the seabed.

bottom currents lead those in the upper layers by 20–40 minutes.

In the main body of water above the seabed, the gradual increase of current towards the surface may be represented by a power law of the form:

$$u_z = u_s \left(\frac{z}{D} \right)^{\frac{1}{m}} \quad (6.9)$$

D is the total depth of water and z is the level above the seabed. Observations suggest values of m between 5 and 7. u_s is the undistorted surface flow; see Figure 6.7.

Typically, the thickness of the benthic boundary layer lies between 50 m and 100 m, so the effects of the bottom friction extend to the surface over many parts of the continental shelf. Integration of Equation 6.9 from the bottom to the surface gives an estimate of the relationship between the surface current and the depth-averaged current:

$$\bar{u} = \frac{m}{m+1} u_s = \alpha_m u_s \quad (6.10)$$

For the experimentally determined range of values of m , 5 to 7, the corresponding range for α_m is 0.83 to 0.88. Further algebra shows that the value of z at which $u_z = \bar{u}$ is close to $0.4D$. This suggests that if a single current meter is to estimate the mean tidal water transport, it should be deployed at a level 40 per cent of the total depth above the seabed.

Within the upper layers, the effects of the Earth's rotation must also be considered, though there is insufficient time for full Ekman dynamics to develop in oscillating tidal flows. One consequence of the Earth's rotation is an enhancement of the anticlockwise component of current rotation (northern hemisphere) relative to the clockwise component. In some cases the

normal sense of ellipse rotation (see Section 5.4.3) may be reversed from a clockwise sense at the surface to an anticlockwise sense at the seabed. As a general rule there is little change of current direction with depth for tidal currents in water less than 50 m deep, but as the above discussion has shown, this is not invariably the case.

6.4.2 Currents in channels

Strong tidal currents are often found in straits where different tidal ranges and phase lags prevail at the two ends. Spectacular examples of channel currents include flows through the Strait of Messina between Italy and Sicily, flow between the Indonesian islands, Singapore Strait, the Cape Cod Canal, and the reversing falls in the Saint John River, New Brunswick. These strong currents are driven by the pressure head generated by the differences in levels acting across a short distance. This distinguishes them from the currents due to tidal wave propagation discussed in Chapter 5. These channels are often important for ship passage, and so an understanding of their currents is essential.

For tidal hydraulic flow in straits to be important, the volume of water exchanged between the two sides must be too small to change the independent tidal wave dynamics of the separate sea-level regimes at either end. Slack water with zero currents in the channel may occur at times other than those of high or low water at either end (see also Section 5.4.3).

For these channels, which are short compared with a tidal wavelength, the hydraulic currents are essentially a balance between the driving pressure head and the bottom friction that opposes the flow. Retaining only these terms in Equation 6.2 and using the quadratic friction law developed in Section 6.2.1 we have for the condition of dynamic equilibrium:

$$g \frac{\partial \zeta}{\partial x} = \frac{C_D}{D} \mathbf{u} |\mathbf{u}|$$

and integrating along the channel of length L :

$$u = \left[\frac{Dg}{C_D L} (\zeta_1 - \zeta_2) \right]^{\frac{1}{2}} \quad (6.11)$$

Of course, the values of ζ_1 and ζ_2 , the levels at the ends, may be calculated separately from harmonic constituents. The most direct approach for using this relationship to predict tidal currents in a particular channel is to calibrate it by measuring flows over a

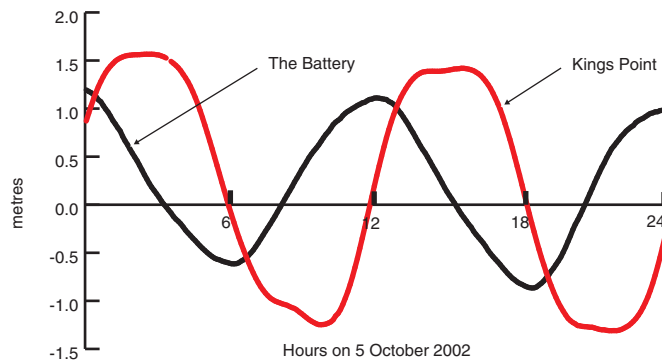
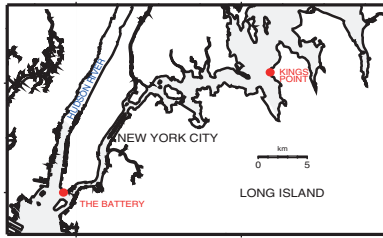


Figure 6.8 Sea levels observed by NOAA on 5 October 2002 at either end of the East River, New York (see insert), showing the strong surface slopes that drive the tidal currents in the channel.

few tidal cycles and plotting them as a function of the square root of the water level differences across it.¹

As an example, [Figure 6.8](#) shows the water levels observed by NOAA at two places near New York on 5 October 2002. Kings Point at the top of the channel of Long Island Sound has larger tides due to the quarter-wave resonance discussed in [Chapter 5](#). The timing of the tidal phases there is very different from those of the smaller tides at The Battery at the southern end of Manhattan Island, which are driven directly from the Atlantic Ocean. The level differences, which may reach 2 m between these places that are only 15 miles apart, gives the hydraulic gradient to drive the currents in the East River; the phases of these gradients are quite different from the phases of the levels. Elsewhere in New York Harbour, complicated tidal currents and phases are found in the Hudson and Harlem Rivers.

The very strong currents associated with channel flows sometimes give rise to strong eddies or vortices, which occur at fixed times in the tidal cycle. Some, such as the Maelstrom in the channel between Moskenesoy and Mosken in northern Norway, and the Charybdis

and Scilla whirlpools associated with the flow through the Strait of Messina, are more celebrated in literature than they are in oceanography. For the Norwegian whirlpool, the Admiralty Sailing Directions report, ‘rumour has greatly exaggerated the importance of the Maelstrom’, and add, ‘The current attains its greatest velocity, which may be estimated at about 6 knots, during westerly gales in winter. Contrary to popular legend, the eddy and the strait in which it develops are not bottomless: detailed surveys show a relatively shallow maximum depth of 36 m.

6.4.3 Residual tidal currents

If the currents measured at an offshore station are averaged over several tidal cycles, a residual water movement is usually apparent. This mean flow past a fixed point is called the Eulerian residual circulation to distinguish it from the long-term movement in space of a particle of water or of a drifting buoy, the Lagrangian residual circulation. Residual circulation may be driven by density gradients, by wind stress or by tidal movements. Here we confine ourselves to a description of some of the main features of the tidally driven residual flows.

Averaged over several tidal cycles, tidally driven residual currents (typically a few centimetres per

¹ This automatically allows for the many complicated physical processes such as boundary turbulence, channel meanderings and effects at the open ends of the channel.

second) are usually one or two orders of magnitude less than the tidal currents themselves, but they are important because their persistence may allow them to dominate the overall distribution and transport of characteristic water properties such as temperature and salinity; radioactive isotopes have been used to trace these residual currents [5]. Essentially they are generated by interaction of the tidal currents with coastal features and with bottom topography.

In the simplest case of a progressive tidal wave that has an associated current that is a simple harmonic, $U_0 \cos \omega t$, the transport at $t = 0$ in the direction of wave propagation is $U_0(D + H_0)$ per metre of section, where H_0 is the wave amplitude. At low water the reduced return flow is weaker, $U_0(D - H_0)$. Over a tidal cycle there is a net transport of water in the direction of wave propagation.

Tidal residuals associated with coastal features and bottom topography can be described in terms of the vorticity or rotational qualities of a body of water. Like momentum and energy, vorticity is a physical quantity, which is conserved for any water mass in the absence of external forces. To illustrate the significance of vorticity, consider a uniform current flowing parallel to the coast (Figure 6.9) and encountering a headland. The currents near the end of the headland will be much stronger than those further offshore, and will be opposed by a much stronger frictional resistance as a consequence, particularly if the water shallows near shore. This increased friction imparts an anticlockwise vorticity to the current and this vorticity is then advected with the water to the bay behind the headland. In the bay an anticlockwise eddy will persist for a large part of the tidal cycle. Similarly, when the tide turns a clockwise eddy will be established by the reversed currents in the bay on the other side of the headland because of the clockwise vorticity imparted to the water as it again passes the headland. Averaged over a tidal cycle there is a net clockwise flow in the bay to the west of the headland, and a net anticlockwise flow in the bay to the east. Observations of currents around the previously discussed Portland Bill in the English Channel [6] show this pattern of residual flows along the coast towards the tip of the promontory on both sides. This kind of persistent coastal residual has important implications for the design and location of sewage discharge systems, radioactive or other waste disposal.

In the case of the flow past islands it is possible for four eddies to form, as shown in Figure 6.10.

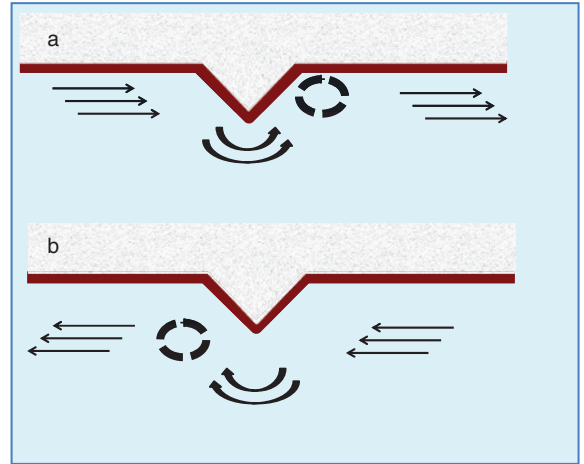


Figure 6.9 Eddies produced by headlands that impede tidal currents: (a) residual eddy generated by a headland; (b) the corresponding eddy generated when the stream reverses.

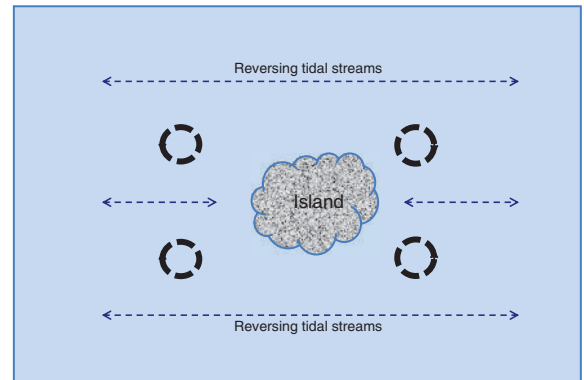


Figure 6.10 The pattern of four eddies generated by an island in a tidal stream.

6.5 Tidal asymmetry

Tidal asymmetry can take many forms: the different times of rise and fall of sea levels (Figure 6.2); the different speeds of currents into (flow) and out of (ebb) an estuary or lagoon, and the different probabilities of sea levels as shown in probability density functions (Figure 1.5). The causes may be coastal morphology, frictional effects, or even, in the absence of local shallow-water distortions, ocean tides and the interaction of semidiurnal and diurnal constituents. Asymmetry can be important for sediment movements, and maybe for other, biological, processes.

6.5.1 Ebb and flow

The classic asymmetry is where a tidal wave steepens as it approaches shallow water. This case is shown in Figure 6.4(1). The rise time is shortened and the currents are strongest in this phase; the system is said to be flood dominant. The slower fall time of the sea levels as the water drains away has lower currents. However, in some lagoons, the reverse is true Figure 6.4(3) as the local morphology causes the ebb currents to dominate.

Asymmetry in the ebb and flow of tidal currents affects the net transport of bottom sediment. Transport is related to the cube, or higher powers, of the current speed [7], but only once the speed reaches a threshold that starts the sediment movement. The effect of this is shown in Figure 6.11. If the current is written as the sum of a small residual mean flow, a dominant M_2 , and a smaller M_4 :

$$u = \bar{u} + U_{M_2} \cos(2\omega_1 - g_{u_{M_2}}) + U_{M_4} \cos(4\omega_1 - g_{u_{M_4}})$$

the integral for transport over several complete tidal cycles of M_2 is given by evaluating u^3 over a complete cycle. Ignoring the threshold factor for simplicity [8, 9]:

$$\langle u^3 \rangle = U_{M_2}^2 \left(\frac{3}{2} \bar{u} + \frac{3}{4} U_{M_4} \cos(2g_{u_{M_2}} - g_{u_{M_4}}) \right)$$

For the same amplitudes of residual flow and of the higher harmonics, the effects are comparable, but the residual flow is the more important.

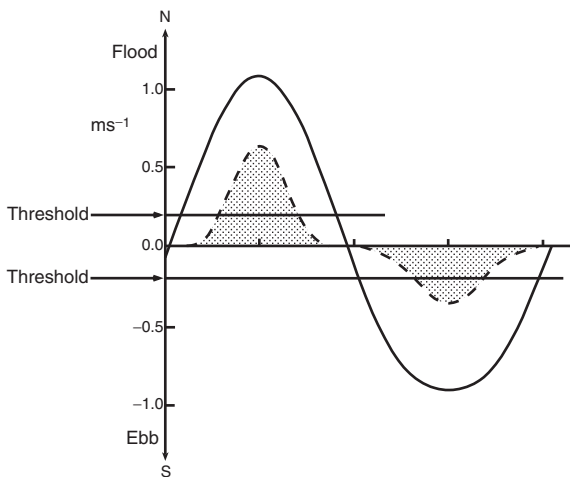


Figure 6.11 The simplified relationship between the net bed-load transport and the asymmetry in the strength of flood and ebb flows, assuming a threshold speed of 0.2 m/s for sediment movement, and a cubic law of transport related to current speed.

Formulae developed for steady channel flow conditions in the laboratory may require modification when applied to oscillating tidal flows in the sea. For example, sediments raised into suspension at times of maximum currents will be transported by the flow at later times, as they settle back to the seabed. Also, turbulence and the associated bottom drag, which moves the sediments, are greater on the decelerating phase of a tidal cycle and less when the currents are increasing. There is an increasing delay for tidal current reversals at higher levels above the seabed (Section 6.4.1), which has important implications for suspended sediment transport. This lag can significantly alter the directions and volumes of sediment transport.

Tidal current speed asymmetry has been generally supposed to be due to formation of higher harmonics, in mixed tidal regimes. However, where the diurnal tidal currents, O_1 and K_1 , are significant, asymmetry can be generated by a combination of these two constituents acting on M_2 [10, 11], even in the absence of higher harmonics. Other combinations of diurnal and semidiurnal tidal constituents can produce asymmetry; for example, K_1 and S_2 produce 6-monthly modulations of the duration of ebb and flood tidal currents of the Murray Mouth, southeastern Australia [12].

If the law of sediment transport is cubic, the theoretical transport can be shown [14] to be the independent sum of the diurnal interaction with M_2 of O_1 and K_1 , and the interaction of M_2 with M_4 :

$$\langle u^3 \rangle_{\infty} = U_{M_2} \left(\frac{3}{2} U_{K_1} U_{O_1} \cos(g_{u_{K_1}} + g_{u_{O_1}} - g_{u_{M_2}}) + \frac{3}{2} U_{M_2} U_{M_4} \cos(2g_{u_{M_2}} - g_{u_{M_4}}) \right)$$

but this independence does not hold for laws of higher powers.

6.5.2 Level probabilities (PDFs)

The observed asymmetry in the two-peaked probability distribution of sea levels in a semidiurnal tidal regime (Figure 1.5a), has also generally been attributed to higher harmonics, but observations in the Falkland Islands showed a marked asymmetry even though there is no shallow-water influence, due to the O_1 and K_1 interaction with M_2 [13, 14]. Figure 6.12 shows the probability density functions (PDFs) at four representative sites. Newlyn is nearly symmetrical, but at nearby Fishguard the shallow-water effects introduce asymmetry. At Port Stanley the asymmetry is due to

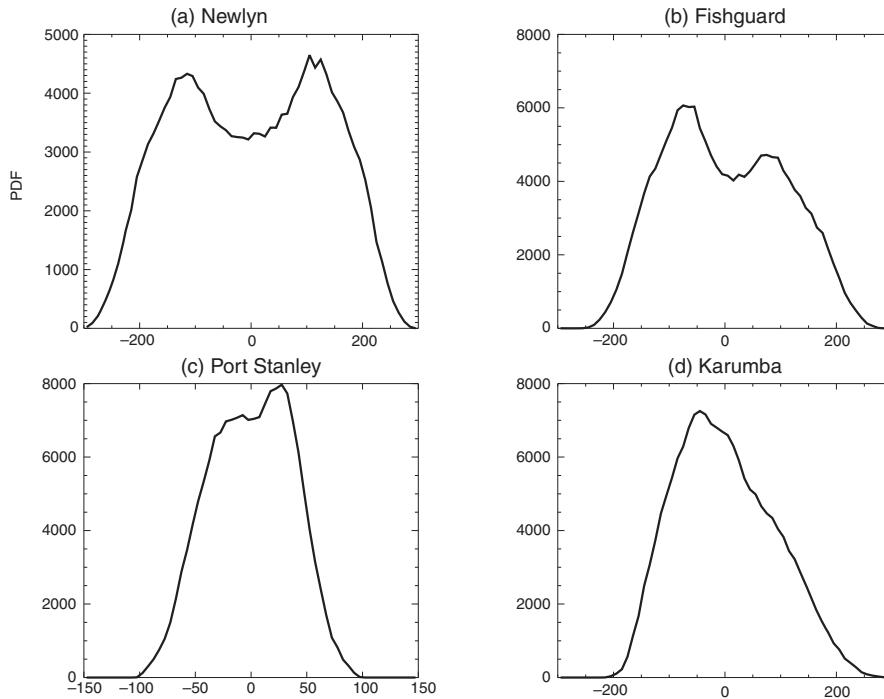


Figure 6.12 Probability distribution functions of sea level at four representative locations: Newlyn on the south coast of England, Fishguard in southwest Wales, Port Stanley in the Falkland Islands and Karumba on the Gulf of Carpentaria coast of Australia [37].

diurnal astronomical tides, as there are no significant shallow-water harmonics.

The single-humped diurnal PDF for Karumba (Figure 1.5b) is attributed to the beating of the O_1 and K_1 constituents. These have roughly equal amplitudes, beat together such that their combination represents a modulated carrier wave, with a frequency half of M_2 , and a beating period of 13.66 days. Thus, the effective M_1 constituent causes a variation of the asymmetry over this 13.66-day period. The fortnightly MS_f constituent also affects the PDF asymmetry.

Conversion between ebb/flow current asymmetry and asymmetry in the PDFs is analytically challenging. For a single harmonic the PDF is given by $1/\sqrt{H^2 - h^2}$, where H is the amplitude, and h is the observed height. However, extension to more harmonics has not been possible. Instead, PDFs are generated from long time series of observations, or tidal predictions based on many constituents.

More systematic mathematical analyses have suggested basing asymmetry characterisation on the statistical skewness of the time series [15, 16]. This is a subject of on-going research, important for

understanding the dynamics of sediment movement and the development of coastal geomorphology.

6.6 Tides in rivers

Many important coastal towns are situated on estuaries or towards the highest navigable point of major rivers. Interaction between tides and sediments can control the geomorphology of alluvial estuaries [17]. The unusual and extreme distortions of the tides in these narrowing and shallowing regions, which are often densely populated and economically important, are of considerable practical interest. The ultimate and most spectacular distortion of the tide is a tidal bore. However, there are other important distortions and constraints that apply before these extremes are reached.

The gradual narrowing of an estuary tends to increase the tidal amplitudes, and initially as the tide enters the estuary it may still be considered in terms of wave dynamics. A progressive wave conveys energy at a rate proportional to the square of the amplitude (Equation D.5b) and proportional to the width of the wave front. If energy is being transmitted at a constant rate to an area of dissipation, as in the upper reaches of

an estuary, then a reduction of the width of the wave front must result in an increase in the wave amplitude; and a reduction in the depth also increases the amplitude (see also Section 5.4.1):

$$H_0 \propto \sqrt{\text{width}} \times \sqrt[4]{\text{depth}}$$

The relationship, which assumes no energy dissipation, is sometimes called Green's formula, the same Green associated with potential theory and tidal loading [18, 19]. In practice, energy loss occurs along the whole length of an estuary, and the propagation of tides into estuaries and rivers is a highly non-linear physical process.

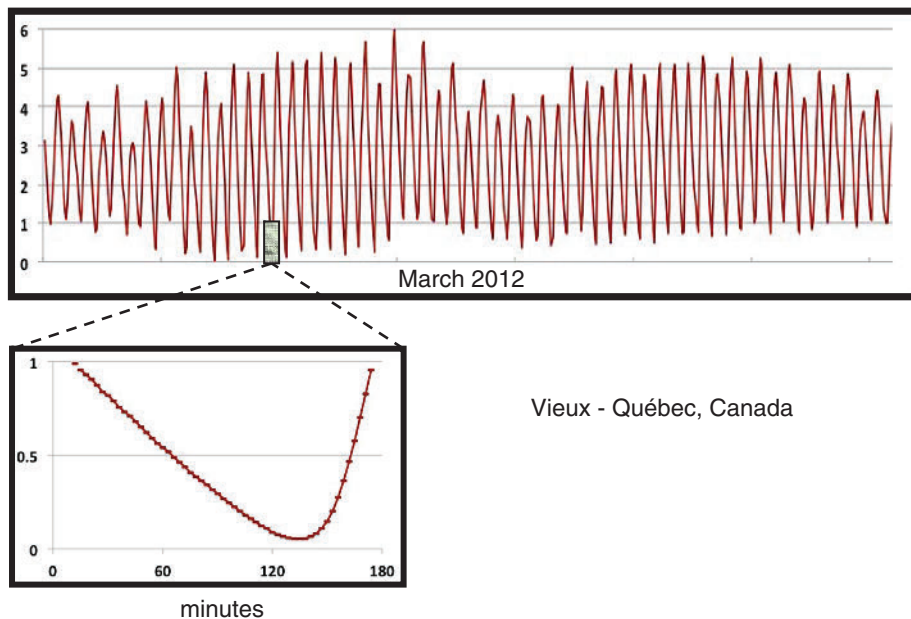
6.6.1 Spring–neap effects

As an example of effects in tidal rivers, Figure 6.13 shows a month of typical tidal levels at Vieux-Québec, in the upper reaches of the St Lawrence River in eastern Canada. The tides propagate up the St Lawrence River for more than 600 km, as far as Lake St Peter, over a period of 10 hours from Seven Islands. In the upper reaches of the river the high waters at different places have roughly the same

level, but the low waters have a considerable slope downstream. The inset to Figure 6.13 shows detailed levels at one low water, with the strong asymmetry in the reversal. Above Quebec City, low water level is higher on spring tides than at neaps because there is not enough time for the water to drain away against the frictional forces before the arrival of the next high water of the tidal wave. Tidal influences are sometimes elusive at the upper limits, as water levels are also very sensitive to the amount of water flowing down the river at any particular time.

The shallow-water tides in several of the world's major estuaries and rivers have many common features:

- Increasing asymmetry between rise and fall times, represented by an enhanced M_4 tidal amplitude;
- Moving inland, levels at low water increase rapidly, but maximum water levels increase more gradually [20]; often the low water levels change very little over the spring–neap tidal cycle, compared with the much larger changes in high water levels;



Vieux - Québec, Canada

Figure 6.13 Water levels at Vieux-Québec, St Lawrence River, Canada, for March 2012. The lowest levels are not coincident with spring tides. The inset shows a 3-hour period at low water and the rapid initial water level rise. Reproduced with the permission of the Canadian Hydrographic Service.

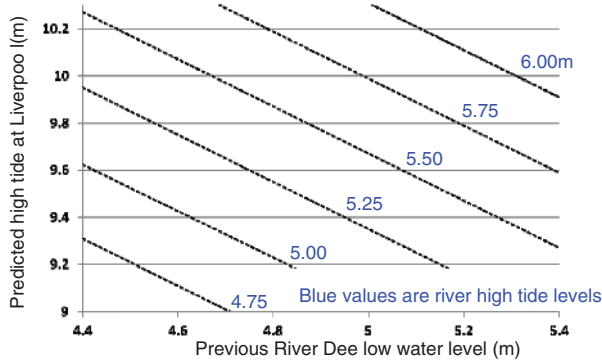


Figure 6.14 A simple way of forecasting tidal high water levels in the River Dee, UK, which depend on external tides (high water predicted for Liverpool) and local river conditions.

- Velocity amplitudes remain largely constant along the channels, as the energy losses by friction are compensated for by channel narrowing and convergence [17];
- Higher up the river, spring–neap change in mean water level (MS_f) results in neap low water levels, lower than spring low water levels [20, 21, 22];
- This MS_f cycle sometimes penetrates up-river, further than the normal semidiurnal tidal variations;
- The above characteristics are strongly dependent on downstream river flows.

Moving up-river, the tide propagation becomes less wave-like, and the water-level gradient is balanced directly by the frictional resistance to the flow [23]:

$$g \frac{\partial \zeta}{\partial x} = \frac{1}{\rho} \frac{F_b}{(D + \zeta)}$$

Any analytical solution must account for the non-linear friction term F_b , which varies as the square of the velocity, the depth variations, and the river flow downstream. These expansions can become very complicated [21], though they do give additional physical insight. However, for prediction purposes a numerical model, iterating these equations, and driven by tidal and river inputs at the sea and upstream ends, gives good results, showing that the essential physics is captured in the equations.

The spring–neap MS_f variations in the higher river levels can be considered in terms of the normal down-river surface gradient, and the effective bottom friction that opposes the flow. Well upstream, river flows are driven by surface gradients of 0.024 to 0.034 m per km (St. Lawrence [21]) and 0.02 m per km

(Amazon [22]).² In the tidally affected area the effective friction is much increased because the tidal speeds are much greater than the river discharge flows, and especially so at spring tides. To transport the same volume of river water through this tidal region requires a greater downward mean surface gradient to overcome the friction. This is even more apparent at springs than at neaps: this greater surface slope manifests as an extra increase in upstream water levels, and as an MS_f term in analyses [20].

Even in the case of low or zero river flow, there is an MS_f effect. For normal river discharges in the upper Amazon, MS_f amplitudes are in the range 0.1 m to 0.2 m, but modelling for zero river discharges gives amplitudes reduced by about 50 per cent. In general terms, the shallow-water frictional resistance becomes the dominant physical process over most of the tidal cycle with slower drainage at low water when the depth D is small, as shown by Equation 6.11. The time taken for the water to drain away after high water under gravity becomes longer than the tidal periods themselves, with the result that long-term pumping-up (priming) of mean water levels occurs over the period of spring tides. Electronic engineers will recognise this MS_f spring–neap effect as equivalent to demodulation of amplitude-modulated radio transmission through a capacitance–resistance circuit.

One of the simplest ways of forecasting tidal high water levels in rivers is shown in Figure 6.14 for the river Dee at Chester, United Kingdom. Curves based on observations relate levels to the predicted open sea tidal predictions at Liverpool, and to the river flow, represented by the initial level.

² River levels are often used as a proxy for flow rates, and are termed *stands*.

6.6.2 Tidal bores

The most spectacular form of tidal distortion, the tidal bore (from the old Norse ‘bara’, meaning a wave), is seen in only a few rivers. The basic requirement for its appearance is a large tidal range, but this alone is not sufficient as the estuary geomorphology has a strong influence. The main characteristic of a bore is the very rapid rise in level as its front advances past an observer; from the riverbank it often appears as a breaking wall of water a metre or so high which advances upstream at speeds up to 20 km/h or more.

Bores are known by many other names in the regions where they occur. The bore in the Amazon is called the *pororoca*, in the French Seine, *mascaret* or *la barre*, and in the English River Trent, *aegir* or *eagre*. The famous bore on the Qiantang river in China (Figure 6.15a) is reported to have a height in excess

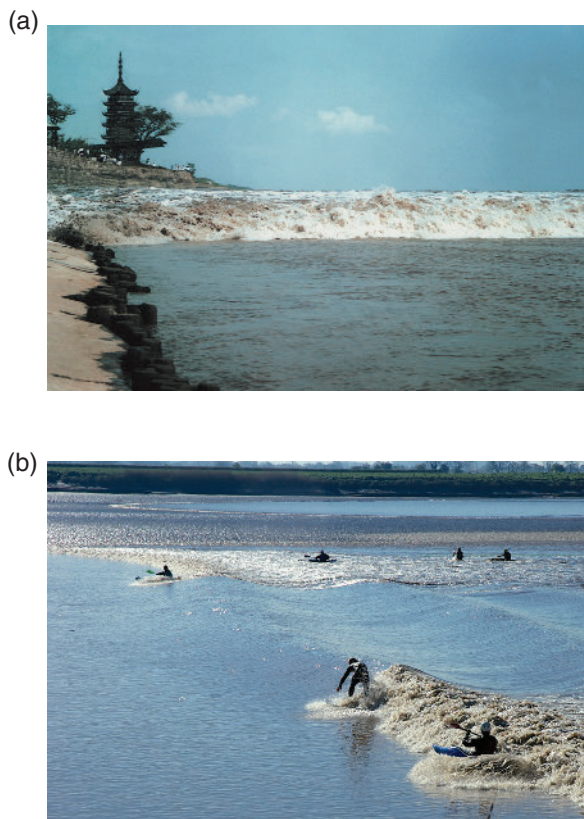


Figure 6.15 (a) The spectacular tidal bore on the Qiantang river, China, which can exceed 2 m in height and travel at speeds greater than 6 m/s. Photograph provided by Professor Lin Bingyao, Zhejiang Institute of Hydraulics and Estuaries. (b) Recreational surfing on the Severn Bore, England, as it forms first at the edges of the river channel. Photograph by David Pugh.

of 3 m and to advance at speeds in excess of 25 km/h. Other bores are found in the Orinoco, Venezuela; the Petitcodiac and the Salmon rivers, which flow into the Bay of Fundy; in the Hooghly river in India; the River Indus in Pakistan; the Colorado river in Mexico; the Turnagain Arm, Cook Inlet, Alaska; and the Victoria river, Australia.

The largest bores are found around the times of high equinoctial spring tides; large bores occur at Easter, because Easter Day is defined in the western Christian calendar as the first Sunday after the full Moon that happens upon or next after 21 March. A low barometric pressure and a positive surge on top of a spring tide are most effective for producing big bores. The volume of river discharge is also critical: high rates of river flow tend to reduce the size of the bore, while increasing its speed, because of the greater river depth. Careful analysis sometimes shows that a bore is slightly bigger for the tides immediately before the maximum spring tide, presumably because there is still some component of residual tidal flow in the subsequent river discharge, corresponding to the pumping and MS_f enhancement described above. Bores often emit a low-frequency rumble, which can be heard well in advance of the arrival. Benefits of bores can include recycling of nutrients in the sediments, by the intense turbulence, and recreational surfing [24], as shown in Figure 6.15b.

The speed of advance of the wave front of a bore may be calculated using the following approximate theory [19, 25]. Suppose that the bore is travelling upstream in the positive X direction with a speed u_b (Figure 6.16). Before the arrival of the bore, the water in the river has negligible speed and the total depth is D_2 . Behind the bore the water speed is u_1 upstream, and the total depth is D_1 . In order to apply the conditions of continuity of flow and of conservation of particle energy on either side of the bore, we ‘freeze’ the motion by imposing an opposite velocity of $-u_b$ on the process. For continuity, the rate of flow of water through sections across the channel ahead of and behind the bore must be equal:

$$(u_b - u_1)D_1 = u_b D_2 \quad (6.12)$$

Similarly, equating the kinetic energy of a particle ahead of the bore with the sum of the kinetic energy and potential energy behind the bore:

$$\frac{1}{2}(u_b - u_1)^2 + g(D_1 - D_2) = \frac{1}{2}u_b^2 \quad (6.13)$$

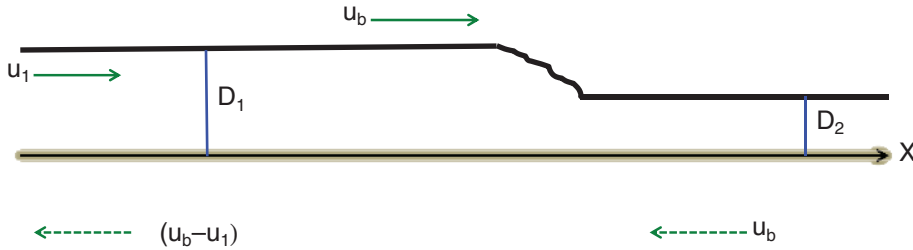


Figure 6.16 The basic configuration for calculating the approximate speed of a bore. The bore is travelling upstream in the positive X direction.

Expanding (6.13) and substituting from (6.12) for u_1 :

$$g(D_1 - D_2) = u_b^2 \left(\frac{D_1 - D_2}{D_1} \right) - \frac{1}{2} u_b^2 \left(\frac{(D_1 - D_2)}{D_1} \right)^2$$

which yields, after some rearranging:

$$u_b^2 = \frac{2gD_1^2}{(D_1 + D_2)} \quad (6.14)$$

Replacing D_1 by $D_2 + h_b$ where h_b is the height of the bore:

$$u_b^2 = \frac{2g(D_2 + h_b)^2}{(2D_2 + h_b)}$$

In the case of $h_b \ll D_2$ the bore speed is $\sqrt{gD_2}$

If $h_b \ll D_2$ the theoretical speed is $\sqrt{2gh_b}$

If h_b is less than, but not negligible compared with D_2 the speed is:

$$\left[g \left(D_2 + \frac{3}{2} h_b \right) \right]^{\frac{1}{2}} \quad (6.15)$$

(eliminating terms in $(h_b/D_2)^2$)

For a bore of height 1 m travelling into water 3m deep, the formula gives a speed of 6.6 m/s or 24 km/h. If the river depth is reduced to 2 m the speed reduces to 21 km/h.

Studies of bore-type movement along open channels for irrigation and other applications have shown that a bore travels as a solitary wave, analogous to a sonic boom where an air pressure disturbance is forced to travel faster than the speed of sound (see Chapter 8). The character of a bore may be described in terms of the hydraulic dimensionless Froude

number, the ratio of the speed of a body of water to the speed of a free wave travelling through the water. The Froude number is related to the water depths in front of and behind the bore:

$$F_R^2 = \frac{1}{2} \frac{D_1}{D_2} \left(\frac{D_1}{D_2} + 1 \right)$$

The larger the ratio D_1/D_2 , the larger the Froude number and the stronger the hydraulic jump of the bore, and the more spectacular its behaviour. If $F_R > 1$ the flow is supercritical but where $F_R < 1.7$ the energy difference is too small for a proper bore to develop: instead there is a train of standing waves, called an undular bore or whelps, with some backward wave energy radiation. In this régime the roughness of the river bed is an important factor, with a breaking wave more likely to occur when the bottom is too smooth to absorb energy by friction losses. For the range $1.7 < F_R < 2.5$ the front breaks, but is relatively quiet. Within the range $2.5 < F_R < 4.5$ the upstream flow penetrates the turbulent front as a jet oscillating between the river bed and the surface; surface waves of large amplitude, which persist for a considerable distance downstream are also generated. Between $F_R = 4.5$ and $F_R = 9.0$ the jump is strong, and free from waves because of the effective dissipation of energy; the bore moves in a jerky way with high-speed jets shooting ahead of the main turbulent front.

Equation 6.15 for the bore speed up a river is only approximate because it makes several assumptions, including the assumption that there is no energy loss within the bore; an alternative theoretical approach considers momentum conservation. In fact there must be significant energy losses due to the turbulence

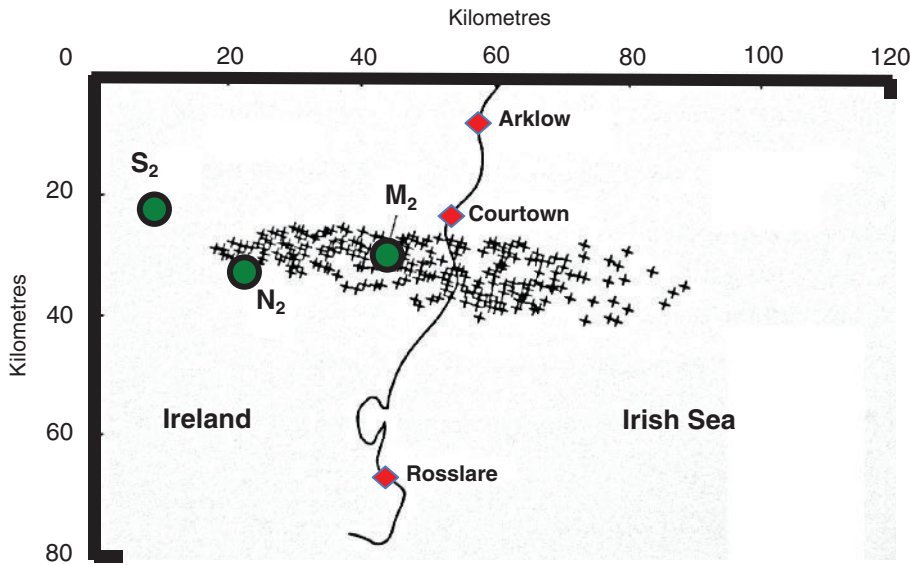


Figure 6.17 Scheme of energy flux from the astronomical forcing of the oceans, to the continental shelves, and eventual dissipation by bottom friction in shallow water, and internal tides in the deep ocean. The figures are based on References 18 and 19.

and to the bottom friction. This energy loss increases approximately as $(D_1 - D_2)^3$. As energy is dissipated the speed of the bore is reduced until at an advanced stage of decay it may eventually be stopped and even carried back downstream by the river flow.

Because bores are due to instabilities in the hydraulics of tidal flow, they are very sensitive to changes in river morphology. Increasing the river depth by dredging, and speeding the river flow by building embankments, both reduce the chances of a bore developing. While there are reasons for supposing that the bore in the Qiantang, China, has become more spectacular over the centuries, in other rivers there have been deliberate attempts to reduce bores, because of the damage they can cause to river banks. The pattern of silting and dredging at the entrance to the River Seine has reduced the size of the Mascaret. Similarly, the *burro*, the bore in the Colorado river, has been progressively reduced by siltation and land drainage schemes.

6.7 Energy budgets

The energy lost by the tides through bottom friction in shallow water is converted to turbulence, and eventually generates a small amount of heat. The original source of this energy is the dynamics of the Earth–Moon system and, over geological time, gradual but

fundamental changes have occurred in the system because of these steady losses of energy.

In Chapter 5 we discussed the development of tidal oscillations in the major ocean basins and their propagation into the surrounding shallow shelf regions. The tidal energy also propagates in the same sense, from the astronomical forcing of the oceans, through the ocean-shelf margin and shelf seas, to the shallow-water dissipation. Figure 6.17 shows a basic scheme for the energy flux.

6.7.1 Local dissipation

First we consider the nature of the tidal energy processes at each stage, beginning with E_3 , the processes of local dissipation (Figure 6.17). In Equation 6.3 the stress per unit area due to bottom friction is related to the square of the current speed; since the work done is equal to the product of force and the distance moved by the force:

$$\text{rate of doing work} = \tau_b q = C_D \rho q^2 |q|$$

For a harmonically varying tidal current $U_0 \cos \omega t$:

$$\text{energy dissipation} = \text{rate of doing work} = C_D \rho U_0^3 \cos^2 \omega t |\cos \omega t|$$

which averages over a tidal cycle to:

$$\frac{4}{3\pi} C_D \rho U_0^3 \text{ per unit area} \quad (6.16)$$

The cubic law of energy dissipation implies that tidal energy loss due to friction is a strictly localised phenomenon; estimates of dissipation, E_3 , demand high-resolution tidal models.

The average energy losses through a spring–neap tidal cycle exceed the losses for M_2 alone. Equation 4.8 gives the combined M_2 and S_2 currents:

$$u = \alpha' \cos(2\sigma_1 t - g_{M_2} - \beta')$$

Here we replace the sea-level amplitudes and phases by the corresponding values for the M_2 and S_2 currents, assuming rectilinear currents as previously. We seek the average value of the dissipation:

$$\langle (\alpha')^3 \rangle = (U^2_{M_2} + 2U_{M_2}U_{S_2} + U^2_{S_2})^{\frac{3}{2}}$$

over a spring–neap cycle of θ . Expanding as a binomial in powers of the ratio $U_{S_2}/U_{M_2} \equiv \gamma$, and neglecting terms in γ^6 and higher powers, this average value [26] is:

$$U^3_{M_2} \left(1 + \frac{9}{4}\gamma^2 + \frac{9}{64}\gamma^4 \right)$$

For the Equilibrium Tide the ratio $\gamma = 0.46$, which implies that the average energy dissipated over a spring–neap cycle is 1.48 times that dissipated by M_2 alone. Around the northwest European shelf where $\gamma = 0.33$, the average dissipation over a spring–neap cycle is 1.25 times the M_2 dissipation. In the Equilibrium case, the rate of tidal energy dissipation at springs is 20 times the rate of dissipation at neaps; in the case of the European shelf, the spring dissipation exceeds the neap dissipation by a factor of eight.

The turbulence generated by bottom friction can destroy stratification of the water column in shallower water and near the coast [27]. Tidal mixing fronts are formed between stratified and un-stratified seas; because of the enhanced nitrate levels, tidal fronts are areas of high primary production, and are also important for many commercially exploited fish stocks.

6.7.2 Regional energy losses

The energy transmitted across the boundary of a shallow sea, E_2 , may be calculated by integrating the energy fluxes given by Equation D.8 either using observed or modelled currents and elevations, or currents and elevations computed by numerical models [28]. Clearly, if numerical models represent the currents and elevations over an area correctly, they must include the correct distribution of the areas of frictional energy dissipation.

For a unit width of section over a tidal cycle:

$$\text{average energy flux} = \frac{1}{2} \rho g D H_0 U_0 \cos(g_{\zeta_0} - g_{U_0}) \quad (\text{D.8})$$

where ρ is the water density, g is gravitational acceleration, D is the water depth, and (H_0, g_{ζ_0}) and (U_0, g_{U_0}) are the amplitudes and phases of the elevations and currents. For a progressive wave the currents and elevations are in phase and the currents are a maximum in the positive direction at the same time as high water. As a result there is maximum energy flux in the direction of wave propagation. For a standing wave there is no net energy flux because the currents and elevations are 90° out of phase, with maximum currents coinciding with the mid-tidal level. In the real world, a perfect standing wave cannot develop because there must be some energy lost at the reflection, and this energy must be supplied by a progressive wave component.

Calculation of the total energy flux due to combinations of all the tidal harmonic constituents is very easy: they may be added arithmetically in the same way as the variance at several frequencies in a time series may be added (see Section 1.6). In general terms the energy flux is proportional to the square of the constituent amplitudes, so that the S_2 energy flux is only about 10 per cent of the M_2 flux, and the energy flux due to other constituents is negligible.

Energy losses in shallow seas result in a systematic adjustment of the tidal patterns [29]. Consider the amphidromic system as illustrated in Figure 5.8. As discussed in Section 5.2.3, if the wave is not totally reflected at the head of a channel, the returning wave will have a smaller amplitude. As a result, in the northern hemisphere the amphidromic point will be displaced from the centre line of the channel towards the left of the direction of the ingoing wave. A very good example of this displacement is shown by the distribution of M_2 amphidromes in the North Sea; their displacement from the central axis (Figure 5.11) is due to energy losses.

If the incident and reflected Kelvin waves have amplitudes H_0 and αH_0 respectively, then the first amphidrome is displaced from the centre axis by a distance:

$$y = \frac{\sqrt{gD} \ln \alpha}{2f} \quad (\text{D.16})$$

Normally the positions of the amphidromes are plotted for individual harmonic tidal constituents. However, the amphidrome may also be considered as a time-dependent position of zero tidal range, determined on

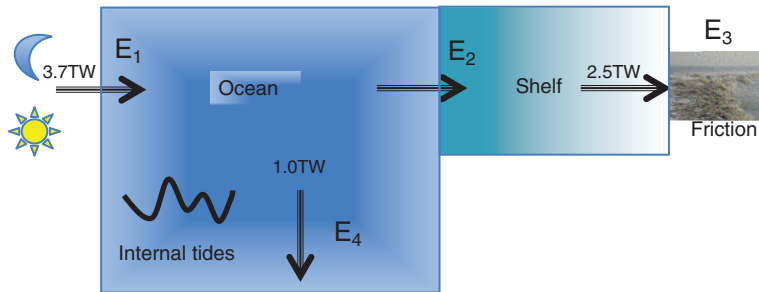


Figure 6.18 Detailed movements of the semidiurnal amphidrome at the entrance to the Irish Sea. The amphidrome occurs over land at spring tides (when it is known as a virtual or degenerate amphidrome), whereas it occurs in the ocean at neap tides (and is known as a real amphidrome). The positions of the time-averaged individual M_2 , S_2 and N_2 amphidromes are also shown.

a daily basis (D_2 in Section 6.3). Conceptually there are advantages in treating dissipation as a time-dependent rather than frequency-dependent phenomenon because of the strongly non-linear processes involved. When the daily positions of the D_2 amphidrome at the southern entrance to the Irish Sea are plotted (Figure 6.18) they are found to move regularly back and forth over 14.8 days within a narrow area: the range of the east–west movement exceeds 70 km, whereas the north–south movement is only 14 km. Figure 6.18 also shows the positions of the degenerate M_2 , S_2 and N_2 constituent amphidromes. The maximum displacement from the centre coincides with spring tides, whereas the minimum displacement occurs at neaps. For neap tides the D_2 amphidrome is real, with zero tidal range at a point within the Irish Sea. At spring tides the D_2 amphidrome is degenerate. The complicated tidal variations plotted in Figure 1.2a for Courtown are due to the sea/land mobility of this amphidrome.

This pattern of amphidrome movement is related to the cubic law of energy dissipation, which means that much more energy is absorbed from the Kelvin wave at spring tides than at neap tides. As a result, the reflection coefficient α for the wave is much less at spring tides, and so the amphidrome displacement from the centre is greater. In the case of the Irish Sea the reflection coefficient at neap tides is 0.65, but this reduces to 0.45 for average spring tides. Similar amphidrome mobility is expected in other seas where energy dissipation is high.

6.7.3 Global dissipation

Figure 6.17 summarises the sources and sinks of tidal energy. Tidal energy is dissipated by friction in shelf seas, and also by losses through internal tides in the deep ocean [30]. The locations of energy loss have been investigated empirically from accurate co-tidal maps generated from satellite altimetry [31]. Dissipation is calculated for each ocean element as the difference between work done against tidal forces and the net

input energy flux. The currents used to compute energy fluxes are derived by fitting the basic hydrodynamic tidal equations to the elevations; the work done directly against tidal forces allows for Earth tides.

About 1 TW of energy is lost in the deep ocean, generally near areas of rough seabed topography. This energy is thought to be lost through internal tide generation and dissipation, a process that substantially contributes to the energy needed to maintain the large-scale thermohaline circulation of the ocean [30]. Figure 6.19 confirms that there are major energy sinks in the southwest Pacific, the southwest Indian Ocean and along the Mid-Atlantic Ridge.

The dissipation in shallow water due to bottom friction is concentrated in areas of resonance and large tides. In order of importance, for M_2 , the first five areas are: Hudson Bay/Labrador (260 GW), European Shelf (210 GW), Yellow Sea (150 GW), northwest Australian Shelf (150 GW) and the Patagonian Shelf (110 GW). Together, these account for more than half the estimated 1.6 TW M_2 total shelf dissipation [31].

For the semidiurnal tides, about one-third of the energy is dissipated in the deep ocean. For the diurnal tides, the total dissipation is about 0.5 TW, of which 90 per cent is dissipated in shallow-water areas by friction [32]. The total diurnal and semidiurnal shelf dissipation is 2.5 TW. The total dissipation in the deep ocean due to internal tides and in the shallow-water areas due to bottom friction is estimated from altimeter modelling as 3.5 TW.

6.7.4 Astronomical energy sources

The energy losses due to tidal friction have gradually slowed down the rate of rotation of the Earth on its own axis, and so increased the length of the day. Microscopic studies of fossil corals show both yearly and daily cycles in their growth bands and careful analyses of the number of daily cycles in each yearly

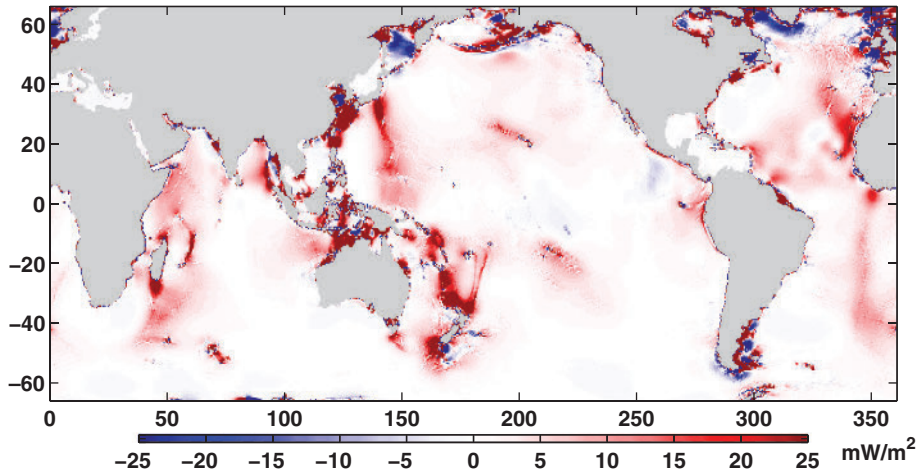


Figure 6.19 Map of areas of M_2 tidal energy dissipation derived from the TPXO.5 model (positive dissipation in red) [38].

cycle show that around 400 million years ago there were 400 days in a year, which means that the length of the day at that time was only 22 hours.

The ocean tide cannot respond instantly to the tidal potential forcing but must also adapt to other forces (e.g. friction) that contribute to its dynamics. The most obvious manifestation of tidal friction is the age of the tide, whereby spring tides occur typically 2 days later than the new or full Moon. Another consequence is a torque between the equivalent ‘tidal bulge’ of the real tide compared to that of the Equilibrium Tide, with angular momentum transferred from the Earth’s rotation to the Moon’s angular momentum.

Returning to [Figure 6.17](#), the loss of energy from the Moon–Earth system, represented by E_1 , may be calculated in several different ways. These include calculations based on the change in the length of the day, analyses of ancient eclipse data, and precise lunar laser ranging. The semi-major axis of the Moon’s orbit is increasing at 3.82 ± 0.07 cm per year [33]. The length of the day is increasing by about 2.4 ms per century, though over geological time the average increase rate is about half this. The best estimate for tidal energy dissipation, from astronomy, is 3.7 TW (2.5 TW from M_2 alone). This is in satisfactory agreement with the total global energy dissipation discussed above, allowing 0.2 TW for dissipation in the solid Earth.

The energy dissipated by the tides is small compared to that involved in some other natural processes. For example, the atmosphere and ocean redistribute the energy in the radiation received from the Sun and together transfer heat pole-ward at a rate of 5 PW (5×10^3 TW) at mid-latitudes [34], while the

warming of the lower layers of the ocean by geothermal heat flow from the solid Earth is thought to amount to some 30 TW [35] from a total global Earth’s surface heat flux of 47 ± 2 TW [36]. Nevertheless, tides (along with the winds) are a primary source of mechanical energy for mixing seas vertically, both in shelf seas and the deep ocean. They play a major role in global ocean circulation and climate.

References

1. Redfield, A. C. 1980. *The Tides of the Waters of New England and New York*. Woods Hole, MA: Woods Hole Oceanographic Institution.
2. Gallagher, B. S. and Munk, W. H. 1971. Tides in shallow water: spectroscopy. *Tellus*, **23**, 346–363, doi:10.1111/j.2153-3490.1971.tb00581.x.
3. Bowden, K. F. 1983. *The Physical Oceanography of Coastal Waters*. Chichester: Ellis Horwood.
4. Pingree, R. D. and Maddock, L. 1978. The M_4 tide in the English Channel derived from a non-linear numerical model of the M_2 tide. *Deep-Sea Research*, **25**, 53–63.
5. Prandle, D. 1984. A modelling study of the mixing of ^{137}Cs in the seas of the European continental shelf. *Philosophical Transactions of the Royal Society of London, A*, **310**, 407–436, doi:10.1098/rsta.1984.0002.
6. Mardell, G. T. and Pingree, R. D. 1981. Half-wave rectification of tidal vorticity near headlands as determined from current meter measurements. *Oceanologica Acta*, **4**, 63–68.
7. Bagnold, R. A. 1988. *The Physics of Sediment Transport by Wind and Water: A Collection of Hallmark Papers* (eds. C. R. Thorne, R. C. MacArthur and J. B. Bradley). New York: American Society of Civil Engineers.

8. Howarth, M. J. 1982. Tidal currents of the continental shelf. In *Offshore Tidal Sands* (ed. A. H. Stride), pp. 10–26. London: Chapman and Hall.
9. Roelvink, J. A. and Reniers, A. 2012. *A Guide to Modeling Coastal Morphology*. Singapore: World Scientific Publishing.
10. Ranasinghe, R. and Pattiaratchi, C. 2000. Tidal inlet velocity asymmetry in diurnal regimes. *Continental Shelf Research*, **20**, 2347–2366, doi:10.1016/S0278-4343(99)00064-3.
11. Hoitink, A. J. F., Hoekstra, P. and van Maren, D. S. 2003. Flow asymmetry associated with astronomical tides: implications for the residual transport of sediment. *Journal of Geophysical Research*, **108**, 3315, doi:10.1029/2002JC001539.
12. Jewell, S. A., Walker, D. J. and Fortunato, A. B. 2012. Tidal asymmetry in a coastal lagoon subject to a mixed tidal regime. *Geomorphology*, **138**, 171–180, doi:10.1016/j.geomorph.2011.08.032.
13. Woodworth, P. L., Blackman, D. L., Pugh, D. T. and Vassie, J. M. 2005. On the role of diurnal tides in contributing to asymmetries in tidal probability distribution functions in areas of predominantly semi-diurnal tide. *Estuarine, Coastal and Shelf Science*, **64**, 235–240, doi:10.1016/j.ecss.2005.02.014.
14. Hoitink, A. J. F., Hoekstra, P. and van Maren, D. S. 2006. Comment on “On the role of diurnal tides in contributing to asymmetries in tidal probability distribution functions in areas of predominantly semi-diurnal tide” by P. L. Woodworth *et al.* (2005). *Estuarine Coastal and Shelf Science*, **67**, 340–341, doi:10.1016/j.ecss.2005.10.008.
15. Song, D., Wang, X. H., Kiss, A. E. and Bao, X. 2011. The contribution to tidal asymmetry by different combinations of tidal constituents. *Journal of Geophysical Research*, **116**, C12007, doi:10.1029/2011JC007270.
16. Nidzicko, N. J. 2010. Tidal asymmetry in estuaries with mixed semidiurnal/diurnal tides. *Journal of Geophysical Research*, **115**, C08006, doi:10.1029/2009JC005864.
17. Savenije, H. H. G. 2005. *Salinity and Tides in Alluvial Estuaries*. Amsterdam: Elsevier.
18. Green, G. 1839. Note on the motion of waves in canals. *Transactions of the Cambridge Philosophical Society*, **7**, 87–96.
19. Lamb, H. 1932. *Hydrodynamics* (6th edition). Cambridge: Cambridge University Press.
20. Buschman, F. A., Hoitink, A. J. F., van der Vegt, M. and Hoekstra, P. 2009. Subtidal water level variation controlled by river flow and tides. *Water Resources Research*, **45**, W10420, doi:10.1029/2009WR008167.
21. Godin, G. 1999. The propagation of tides up rivers with special considerations on the Upper Saint Lawrence River. *Estuarine, Coastal and Shelf Science*, **48**, 307–324, doi:10.1006/ecss.1998.0422.
22. Gallo, M. N. and Vinzon, S. B. 2005. Generation of overtides and compound tides in Amazon estuary. *Ocean Dynamics*, **55**, 441–448, doi:10.1007/s10236-005-0003-8.
23. LeBlond, P. H. 1978. On tidal propagation in shallow rivers. *Journal of Geophysical Research*, **83**, 4717–4721, doi:10.1029/JC083iC09p04717.
24. Rowbotham, F. W. 1983. *The Severn Bore*. Newton Abbott, UK: David and Charles.
25. Tricker, R. A. R. 1964. *Bores, Breakers, Waves and Wakes*. London: Mills and Boon.
26. Jeffreys, H. 1976. *The Earth, Its Origin, History and Physical Constitution* (6th edition). Cambridge: Cambridge University Press.
27. Simpson, J. H. and Sharples, J. 2012. *Physical and Biological Oceanography of Shelf Seas*. Cambridge: Cambridge University Press.
28. Taylor, G. I. 1920. Tidal friction in the Irish Sea. *Philosophical Transactions of the Royal Society of London, A*, **220**, 1–33, doi:10.1098/rsta.1920.0001.
29. Pugh, D. T. 1981. Tidal amphidrome movement and energy dissipation in the Irish Sea. *Geophysical Journal of the Royal Astronomical Society*, **67**, 515–527, doi:10.1111/j.1365-246X.1981.tb02763.x.
30. Munk, W. H. 1997. Once again: Once again – tidal friction. *Progress in Oceanography*, **40**, 7–35, doi:10.1016/S0079-6611(97)00021-9.
31. Egbert, G. D. and Ray, R. D. 2001. Estimates of M2 tidal energy dissipation from TOPEX/Poseidon altimeter data. *Journal of Geophysical Research*, **106**, 22475–22502, doi:10.1029/2000JC000699.
32. Egbert, G. D. and Ray, D. R. 2003. Semi-diurnal and diurnal tidal dissipation from TOPEX/Poseidon altimetry. *Geophysical Research Letters*, **30**, 1907, doi:10.1029/2003GL017676.
33. Munk, W. and Wunsch, C. 1998. Abyssal recipes II: energetics of tidal and wind mixing. *Deep-Sea Research I*, **45**, 1977–2010, doi:10.1016/S0967-0637(98)00070-3.
34. Williams, R. G. and Follows, M. J. 2011. *Ocean Dynamics and the Carbon Cycle: Principles and Mechanisms*. Cambridge: Cambridge University Press.
35. Hofmann, M. and Morales Maqueda, M. A. 2009. Geothermal heat flux and its influence on the oceanic abyssal circulation and radiocarbon distribution. *Geophysical Research Letters*, **36**, L03603, doi:10.1029/2008GL036078.

36. Davies, J. H. and Davies, D. R. 2010. Earth's surface heat flux. *Solid Earth*, **1**, 5–24, www.solid-earth.net/1/5/2010/.
37. Woodworth, P. L., Blackman, D. L., Pugh, D. T. and Vassie, J.M. 2005. On the role of diurnal tides in contributing to asymmetries in tidal probability distribution functions in areas of predominantly semi-diurnal tide. *Estuarine, Coastal and Shelf Science*, **64**, 235–240, doi:10.1016/j.ecss.2005.02.014.
38. Egbert, G. D. and Ray, D. R. 2003. Semi-diurnal and diurnal tidal dissipation from TOPEX/Poseidon altimetry. *Geophysical Research Letters*, **30**, 1907, doi:10.1029/2003GL017676.

Storm surges, meteotsunamis and other meteorological effects on sea level

The olde sea wall (he cried) is downe,
The rising tide comes on apace,
And boats adrift in yonder towne
Go sailing uppe the marketplace.

Jean In gelow, The High Tide on the Coast of Lincolnshire

7.1 Introduction

This first part of this chapter discusses variations in sea level that occur at the coast and can contribute to flooding. Particularly important amongst these variations are storm surges, which are caused by the strong winds and low air pressures that occur during storms, and which are capable of being described by the ‘depth-averaged’ (or ‘two-dimensional’, ‘2-D’) equations. These equations are essentially the same as for tides but with gravitational forces replaced by meteorological ones. In shallow-water areas subject to the strong winds of violent storms, the sea-level variations can be very large due to a term in the equations involving wind stress (defined below) divided by water depth. The resulting storm surges can be many metres in magnitude and can cause major damage and loss of life, especially when they occur at the same time as the high water of the astronomical tide.

The chapter proceeds to describe other sea-level processes at the coast including seiches and meteotsunamis. Wave set-up is a process that can contribute significantly to coastal sea level, and yet is usually neglected in sea-level forecast schemes. The chapter concludes with discussion of 2-D (or ‘barotropic’) variations that occur for the deep ocean. These are also forced by winds and air pressures, and are understandable using similar 2-D models as for storm surges.

7.2 The depth-averaged (2-D) equations

We focus in this chapter on sea-level variations with timescales of hours through to weeks, which is a

timescale on which the ocean responds dynamically to changes in meteorological forcing (winds and air pressures). If one considers the air pressure forcing alone, and if the ocean adjusted instantly to air pressure change, then it could be said to have an isostatic response in which sea-level and air pressure changes, $\Delta\zeta$ and ΔP_A , are related by the local inverse barometer (LIB) equation:

$$\Delta\zeta = -\Delta P_A/(\rho g) \quad (7.1)$$

where ρ is water density and g is the acceleration due to gravity (Appendix A). In the LIB model a rise/fall of 1 mbar in air pressure results in a fall/rise of 1 cm in sea level to within approximately half a per cent [1]. In practice, when air pressure changes, the ocean does not adjust instantly, but approaches Equation 7.1 in what is called a ‘dynamical response’ [2]. Similarly, there are dynamical adjustments to changes in the wind.

It will be seen that the contribution of winds and air pressure changes to some of the aspects of sea-level variability discussed here can be studied adequately with the use of 2-D (or ‘barotropic’) models.¹ These aspects of sea-level variability are generally higher in frequency than those that require study of modifications of the ocean’s vertical density structure and, therefore, the use of three-dimensional (3-D, depth-dependent) ocean models [4].

The meteorological forcing in 2-D models is provided by air pressure and *wind stress*, that is the shear

¹ The word barotropic is here taken to indicate the depth-averaged components of motion [3].

force that the wind exerts on the ocean surface, and is parameterised in terms of the speed of the wind at a certain height (usually 10 m) above the surface in the form:

$$\begin{aligned}\tau_{sx} &= \rho_{\text{air}} C_d W_x \sqrt{W_x^2 + W_y^2} \text{ and} \\ \tau_{sy} &= \rho_{\text{air}} C_d W_y \sqrt{W_x^2 + W_y^2}\end{aligned}\quad (7.2)$$

where τ_{sx} and τ_{sy} are the components of wind stress in the x and y directions, ρ_{air} is the density of air, C_d is a dimensionless quantity called the drag coefficient, and W_x and W_y are the components of the total wind velocity W . A typical value for C_d as applied to 10 m winds (winds measured at 10 m above the sea surface) is $[0.8 + 0.065W]10^{-3}$, where W is wind speed in m/s, reflecting increasing roughness of the sea surface with a stronger wind [5].

The currents set in motion by the forces of air pressure gradient and wind stress are dissipated in a 2-D ocean by friction at the seabed, which can be written in a similar form:

$$\tau_{bx} = \rho C_b u \sqrt{u^2 + v^2} \text{ and } \tau_{by} = \rho C_b v \sqrt{u^2 + v^2}\quad (7.3)$$

where ρ is seawater density, C_b is the bottom drag coefficient, and u and v are the components of ocean current at the seabed, which are the same as throughout the water column in a 2-D ocean. In some models a linearised form of bottom stress is employed in which the stress is proportional to the current with a coefficient of linear friction that has the dimensions of velocity [6]. A typical value of C_b used in 2-D models is 0.0025.

The depth-averaged (2-D), non-linear shallow-water (NLSW) equations including air pressure and wind forcing are shown below. These are the same horizontal momentum and conservation of mass equations discussed in [Appendix A](#) but omitting the tidal forces [7, 8]:

$$\begin{aligned}\frac{\partial u}{\partial t} + u \frac{\partial u}{\partial x} + v \frac{\partial u}{\partial y} - f v &= -g \frac{\partial \zeta}{\partial x} - \frac{1}{\rho} \frac{\partial P_A}{\partial x} \\ &+ \frac{1}{\rho D} (\tau_{sx} - \tau_{bx})\end{aligned}\quad (7.4a)$$

$$\begin{aligned}\frac{\partial v}{\partial t} + u \frac{\partial v}{\partial x} + v \frac{\partial v}{\partial y} + f u &= -g \frac{\partial \zeta}{\partial y} - \frac{1}{\rho} \frac{\partial P_A}{\partial y} \\ &+ \frac{1}{\rho D} (\tau_{sy} - \tau_{by})\end{aligned}\quad (7.4b)$$

$$\frac{\partial \zeta}{\partial t} + \frac{\partial(Du)}{\partial x} + \frac{\partial(Dv)}{\partial y} = 0\quad (7.4c)$$

where the free surface elevation ζ is assumed to be smaller than the water depth D , and f is the Coriolis parameter:

$$f = 2\omega_s \sin \phi\quad (7.5)$$

where ω_s is the rotation rate of the Earth and ϕ is latitude ([Chapter 4](#)).

The equations are ‘non-linear’ primarily because of the products in the advection terms (the second and third terms on the left-hand side of Equations 7.4(a, b)). Also there is non-linearity in the equations due to the role of the reciprocal of depth times quadratic friction terms. It can be seen that, in the case of weak winds and currents, there is a balance between the first two terms on the right-hand side of [Equations 7.4\(a, b\)](#), representing the LIB.

A model may have an additional parameter in *horizontal eddy viscosity*, which has the role of spatially smoothing the model current fields. Such smoothing is often a crude attempt to account for the missing physics of energy dissipation in a simple 2-D description of the ocean (e.g. due to internal waves and tides) [7, 9]. In a realistic model, the bottom current should approximate the total current and not just that due to the meteorology. Therefore, the 2-D numerical models are usually run as combined tide+surge models, with the meteorological sea-level response (or ‘surge’) defined by the model output when run with both astronomical tide and meteorological forcing subtracted by the output from a run with tide forcing alone. More details of storm surge modelling are given below.

7.3 Storm surges

In the shallow waters of coastal seas, the acceleration terms in [Equations 7.4\(a, b\)](#) involving wind stress become more important due to the water depth denominator and, neglecting other terms, they result in sea-level gradients of the form:

$$\frac{\partial \zeta}{\partial x} = \frac{(\tau_s - \tau_b)}{\rho g D} \text{ or } \frac{\rho_{\text{air}} C_d W^2}{\rho g D}\quad (7.6)$$

when the bottom stress term is omitted, which is a reasonable assumption except for very shallow waters when bottom stress, and not the sea surface gradient, balances the wind stress.

This equation provides a simple means of estimating a *storm surge* when the wind blows over an

extensive region of shallow water.² For example, if a Strong Gale (Beaufort Force Nine, 22 m/s) blows over 200 km of water of depth 30 m (similar to the dimensions of the southern North Sea), then the increase in level will be 0.85 m. If the wind speed increases to a Storm (Beaufort Force Eleven, 30 m/s), the increase in level will be 1.6 m.

At its most extreme, a storm surge of many metres can result, which causes considerable damage and loss of life, for example in the 1953 and 1962 North Sea floods [10, 11, 12], in many Bay of Bengal surges [13], and in the Hurricane Katrina surge of 2005 at New Orleans (Figure 1.4b) [14], in the Hurricane Sandy surge at New York in 2012 [15], and, more recently, during Typhoon Haiyan in the Philippines in 2013. Figure 7.1 provides images associated with the 1953 event: a synoptic chart indicating intense northerly winds associated with a depression moving from west to east, the maximum computed surge, some of the flooding that it caused, and the considerable investment in coastal protection designed to guard against similar future events.

Reviews are available of the occurrence of such extreme events [16]. However, even under much less extreme weather conditions, surges can provide a signal of several decimetres in a tide gauge or altimeter time series, which can be considerably larger than other signals of interest. In some situations, the coastal dynamics can lead to a significant positive surge being generated at a point on the coast only a short distance from another area experiencing a significant negative surge [17].

Tropical and extra-tropical storms have different generation mechanisms and differ in their size and intensity. As a consequence, the storm surges caused by tropical cyclones are different in character to those produced by higher latitude storms. Tropical storm surges tend to be of smaller spatial scale (~500 km rather than ~1000 km), and have a shorter duration (hours to days rather than several days), but are much larger in amplitude (sometimes 5–10 m rather than typically 2–3 m) [18].

² The expression *storm surge* is used in different ways in the scientific literature. Usually, it is taken to mean the variation in sea level due to meteorological forcing, as in Equation 7.6, which forms part of the residuals of a tide gauge record discussed in Section 7.4. Other times, it refers to a particular *storm surge event*, sometimes called a *storm tide event*, both of which refer to times when a high sea level occurs due to the combination of tide and surge (a *storm tide*).

If the severity of a storm surge is measured in terms of the number of lives lost, then the most severe events have occurred in the Bay of Bengal, where extreme water levels are driven by tropical cyclones. According to one estimate, about 80 major tropical storms form in the world's ocean each year, and, even though only about 1 per cent of them impact Bangladesh, they result in over half of the world's deaths from cyclones and their associated surges [19]. There were at least 25 storm surge events in the Bay of Bengal between 1737 and 1985 in each of which over 10,000 people were killed, and several hundred thousand people (perhaps 300,000, although estimates vary) are thought to have been killed by the 1970 cyclone alone [13]. Cyclone Nargis, in which over 130,000 people were killed in Myanmar (Burma) in 2008, has provided a more recent example of major loss of life due to both the storm itself and the accompanying surge [20]. In spite of the importance of addressing this issue adequately, modelling of surges in the Bay of Bengal in the past has been difficult due to the lack of adequately precise meteorological and bathymetric information, especially given that the latter is subject to change with time in areas such as the Ganges–Brahmaputra delta [13].

7.3.1 Tide–surge interaction

The shallow-water dynamical processes that are manifested as interactions between the different tidal constituents, producing higher and lower harmonics, as discussed in Section 4.2.3, also cause the tidal and surge components of sea level to interact. This is clear from inspection of Equations 7.4(a, b) above, wherein the final terms on the right-hand side include a reciprocal of water depth. Wind stress will be more effective at generating a storm surge at low, rather than high, tide. In addition, the larger than normal water depth that is present when a surge occurs increases the speed of tidal propagation, both directly (\sqrt{gD} being the shallow-water wave speed) and because of reduced bottom friction, which is inversely proportional to depth [21].

Any sea-level record will differ from that predicted by considering only the astronomical tide at that location. The differences between the observed sea levels and the tide are called ‘residuals’ (their statistics are discussed in Section 7.4 below). At many locations, storm surges will be the main process responsible for residuals having large positive and negative values. As the storms that cause the surges can occur at any time

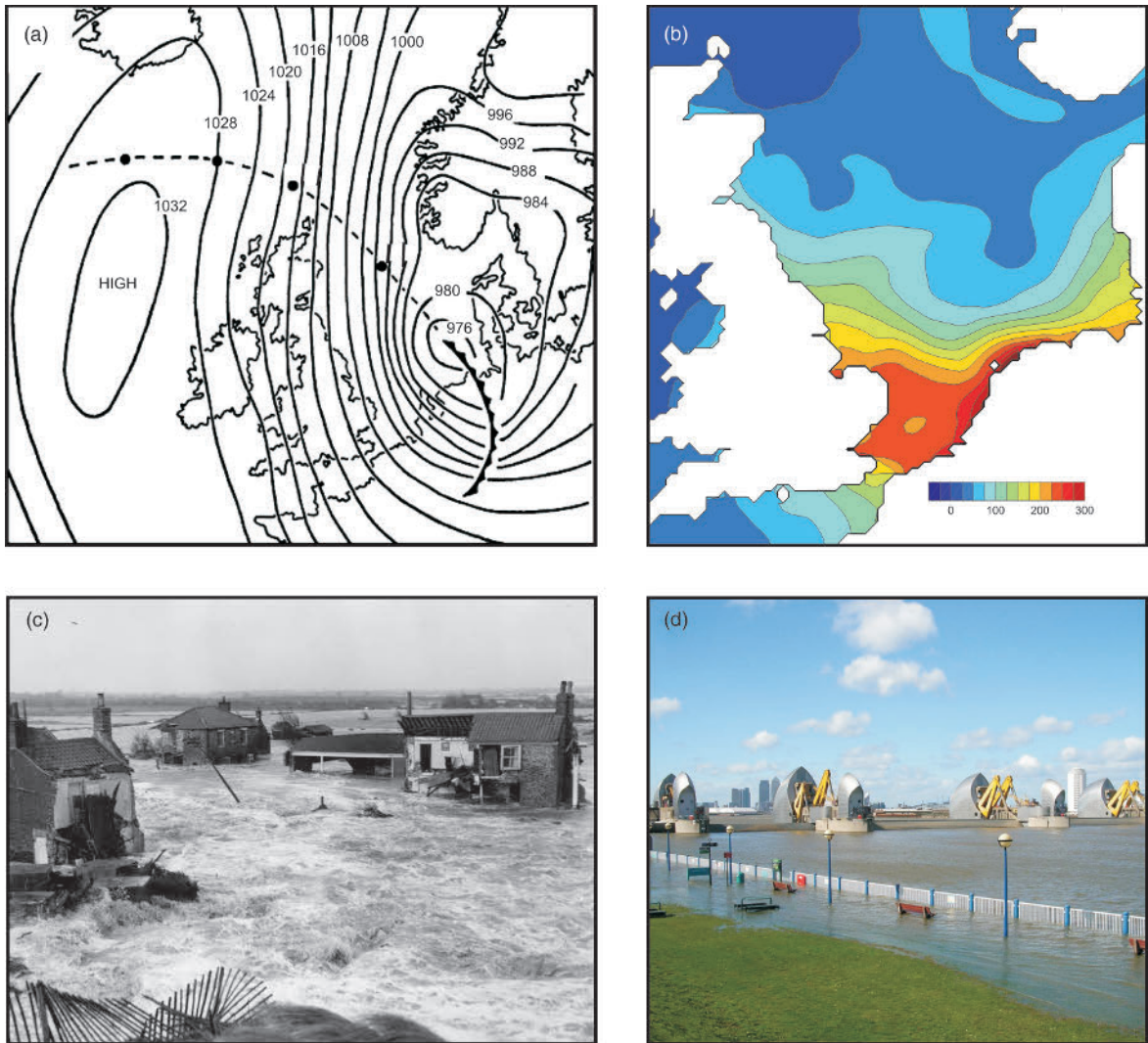


Figure 7.1 Images from the 1953 North Sea storm surge that resulted in over 2500 fatalities, mostly in the Netherlands and eastern England. (a) Meteorological chart for 1 February 1953 (0 hr GMT) with the track of the storm centre shown by black dots in 12-hour steps from 30 January (0 hr) to 1 February (0 hr); (b) maximum computed surge throughout the area (cm); (c) flooding at Sea Palling on the Norfolk coast of England; (d) the Thames Barrier, an example of the considerable investment in coastal protection in the United Kingdom and Netherlands following the 1953 storm. (a) and (b) from [11], (c) from Eastern Daily Press, and (d) from UK Environment Agency.

during the tidal cycle then, if observed sea level was simply a linear superposition of tide and surge, one would expect large residuals to occur at any time with respect to tidal high water (THW). In fact, an interesting consequence of interaction is the suppression of large residuals when water depth is largest, i.e. at astronomical tide high water.

Tide–surge interaction has been studied most intensively in the southern North Sea [22]. Figure 7.2 shows a distribution of residuals for Sheerness in the Thames Estuary for the 55 surge events with the largest

(top 1 per cent) residuals [23]. For each event, the maximum positive residual is identified and its time is plotted with respect to the nearest THW. The frequency of residuals is indeed dependent on the time of THW, most occurring about 4 hours before THW and a much smaller peak a similar time after THW. It demonstrates that the largest residuals tend to avoid THW and, therefore, do not usually result in as high an overall high water as one might expect, which is an important finding for flood risk managers and coastal engineers. Two-thirds of the events were associated

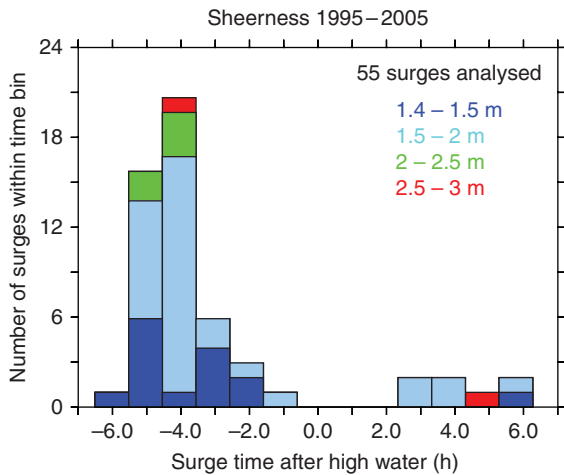


Figure 7.2 A distribution of times, with respect to the time of tidal high water, of the maximum positive residuals during the 55 surge events with the largest residuals in data from Sheerness spanning 1950–2005. Colours indicate the size of each of the maximum residuals. Following [21].

with a clear phase shift in the high water turning point of the observations with respect to the predicted tide. It turns out that the suppression of residuals at high tide is most easily explained as an artefact of the small advances in the timing of THW due to the increased water depth provided by the surge, and the definition of ‘residual’ by reference to the predicted (unadvanced) THW, combined with the fact that wind stress is most effective at generating a surge at low water [21, 24].

Interaction has been observed throughout the shallow northwest European shelf [25, 26], especially in estuaries [27]. It also occurs in other shelf areas around the world including Canada [28] and Australia [29], and was observed during Hurricane Sandy, the ‘storm of the century’ off the east coast of the United States [30]. In practice, the interactions at each location are difficult to describe fully by simple arguments, and they are best studied by means of numerical modelling, as discussed below. The fact that the time of the maximum residual within a storm surge event does not necessarily coincide with either THW or the time of the overall extreme sea level has led to a preference of describing an extreme in terms of the tide plus a *skew-surge* (see below).

There are further simple ways of presenting tide and surge statistics to demonstrate the interaction. One way is to calculate the standard deviation of residuals for different tidal levels. For example, in the Thames Estuary the standard deviation of the residuals

at mid-tide is approximately 0.27 m, compared with 0.19 m and 0.18 m at mean high water and mean low water spring tidal levels. Another method, which is adequate for a first scrutiny of data, is to plot each observed residual time series against the corresponding tidal level: any variation of residual with the tidal height is an indication of interaction.

Section 4.2.3 discussed the variation of tidal constituents through the year in shelf areas. For example, in the North Sea there is a 1–2 per cent seasonal modulation of M_2 amplitude [31]. This variation has a contribution from the astronomical tide, due to the Sun’s influence through the year on the Moon’s orbit. However, shallow-water interactions between tides and surges are likely to be primarily responsible for the variation, as a result of more energy being lost from tides and surges travelling together than would be lost if they were travelling separately [32]. Surges are larger in winter, so the winter amplitudes of M_2 should be less than those during the quieter summer months, and the observations are consistent with this behaviour.

7.3.2 Storm surge modelling

Many national meteorological agencies have coastal flood warning systems in which forecast meteorological information is used to predict storm surges. Early forecast schemes made use of empirical relationships between meteorological (especially sea-level pressure) fields and sea level in order to forecast local sea surface elevations [23, 33]. However, since the computer age a more rigorous approach has been possible through the use of numerical tide+surge barotropic models [34].³ The tide throughout the model domain and at its boundaries is provided by regional tide models, while the surges are generated in the models using wind and air pressure fields provided by meteorological agencies [6, 35].

As an example, the current UK operational surge model (CS3X) covers the entire northwest European continental shelf at 12 km horizontal resolution (Figure 7.3) and is forced by sea-level pressures and 10 m winds from an atmospheric model with a similar spatial resolution (0.11° longitude and latitude). Tidal input at the model open boundaries consists of the largest 26 constituents. To achieve greater resolution around coastlines, it is possible to nest finer grids within larger schemes [36] or to use finite-element

³ A list of agencies with models may be found in Reference 8.

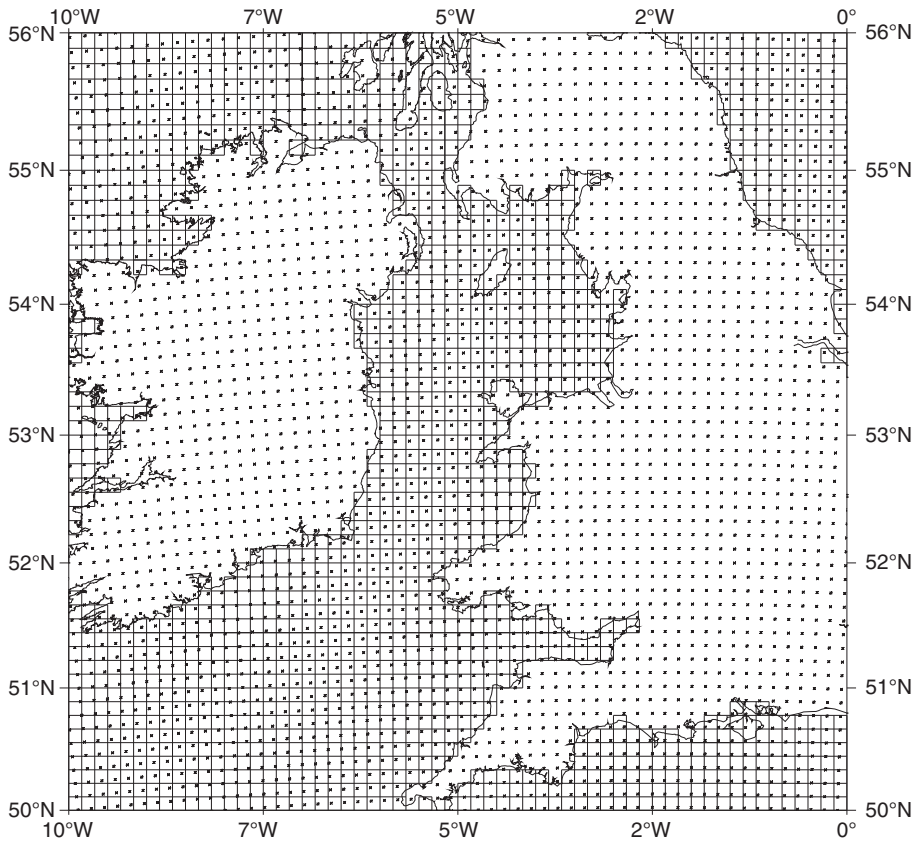


Figure 7.3 The grid used for the numerical tide–surge model (CS3X) employed in the current UK operational surge forecasting system. Only the Irish Sea section of the grid is shown to give an impression of model resolution and matching of a finite-difference grid to a coastline. The complete grid covers the entire northwest European continental shelf from 40° to 63° N and eastwards of 20° W. The model is forced by winds and air pressures covering the entire North Atlantic and Europe on a 0.11° grid indicated by dots.

techniques [37]. In the United Kingdom case, finer resolution models of critical areas, including the Bristol Channel and south coast of England, are nested within CS3X.

The models are usually run once in tide-only mode and then a second time with both tidal and meteorological forcings, with the difference between the two model outputs being the meteorologically forced ‘surge’ including its interaction with the tide. The UK models are run four times each day and simulations consist of a 6-hour hindcast portion followed by a 48-hour forecast. The ongoing performance of the modelling can be validated by comparison to real-time tide gauge data, and, if performance is satisfactory, then model predictions of water levels for several days ahead (i.e. the timescale for which weather forecasts have skill) can be provided to local and national governmental agencies in order to issue warnings to coastal industry and populations.

The conventional method to estimate model performance is to compare time series of tide gauge ‘residual’ during an event to that of model ‘surge’ obtained from the nearest model grid point. However, for flood warning we are interested primarily in the sea levels that occur around tidal high water, and we have seen that ‘residual’ as normally computed may not be the most appropriate parameter to use when tide–surge interaction occurs. A more practical comparison has been found to be with the use of the *skew-surge* (Figure 7.4), a parameter that was first employed in the Dutch operational system [38]. This is defined as the maximum observed sea level during the surge event minus the maximum predicted astronomical tide, where the two maxima would be during the same high tide but could be at slightly different times. The skew surge represents the mismatch between the observed sea level and the levels published in tide prediction tables, and is, in

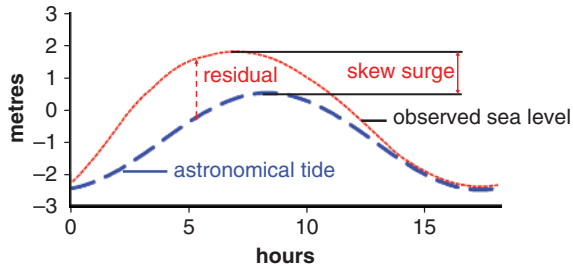


Figure 7.4 Definition of the skew surge.

practice, the parameter that coastal dwellers are most interested in.

A prediction of a surge model can represent only the meteorological contribution to sea level, rather than the ‘residual’ that one obtains in tidal analysis of tide gauge data and which operational agencies require in a forecast. A real residual will contain additional contributions from processes such as mean sea-level (MSL) change due to regional steric (density) variations, which are not included in the model but which can be assumed to persist for at least several days. Therefore, in addition to solving the above equations, some modelling schemes make use of the observed tide gauge residuals during the past 1–2 days in order to obtain a better idea of the likely residuals in the next few days [39]. This is one form of data assimilation in surge modelling.

Extensive reviews of modern storm surge modelling and forecasting are available [22, 40]. Most surge models are based on finite-difference techniques, which solve the above equations in discretised form. A smaller number employ finite-element methods, which allow complicated coastlines and bathymetry to be better resolved. For example, MOG2D (Modèle 2D d’Ondes de Gravité), now renamed T-UGO (Toulouse-Unstructured Grid Ocean model), is a finite-element 2-D model with a high spatial resolution at the coastline [37]. It uses 4 km elements for regional modelling while 15 km elements are used for its global version. The latter is used in routine processing of satellite altimeter data, in order to provide estimates of that part of the sea-level variability that can be accounted for by the 2-D equations. In practice, the model is used to describe variability with time-scales shorter than 20 days, lower frequencies being assumed to be represented by the inverse barometer.

Barotropic tide+surge models have also been used successfully in hindcast-mode for research purposes, using extended sets (order 50 years) of meteorological

reanalysis fields to compute variations in surge levels over a long period [41]. The accuracy of such computed surge fields is of the order of 0.1 m, although accuracy would be expected to be worse where model spatial and temporal resolution (either meteorological and/or surge) is insufficient. Examples of lower accuracy include surges initiated by tropical cyclones, or by polar lows.⁴

A fundamental requirement in all surge modelling, as in tide modelling, is the availability of accurate bathymetric information, particularly in shallow-water areas. In addition, surge modelling requires reliable air pressure and wind stress fields. If one assumes the meteorological fields to be accurate, then wind stress can be readily computed from wind velocity, as described above. The accuracy of that computation then depends on how well we know the drag coefficient [42]. In many cases, an average value for the coefficient will be assumed. However, the real value could depend upon wave conditions [43], and at the high wind speeds experienced in major storms and tropical cyclones its effective value may be less than that normally employed in models [44]. A similar consideration relates to whether the bottom drag parameterisation is suitable for the area under study [45]. The dependence of the accuracy of the surge computation on the accuracy of meteorological fields can be estimated with the use of ensemble techniques in which many surge estimates are made using air pressure and wind stress fields that differ within a range of their estimated accuracy [46].

Data assimilation provides a means to improve surge forecasts. At the present time, almost all real-time sea-level information comes from coastal tide gauges, although surge data are obtained from off-shore structures in some parts of the world. Satellite altimetry has been shown to be capable of observing storm surges to adequate accuracy and of contributing to understanding the reasons for their forcing (Figure 7.5) [47, 48]. However, the challenge of obtaining such data in real time, and the limitations of the spatial-temporal sampling of conventional nadir-pointing altimeters, have meant that altimetry has been of only modest benefit so far, although various projects are in progress [49]. The monitoring of storm surges and other coastal processes, and of short spatial-scale variability in the deep ocean, would

⁴ Polar lows are short-lived and small-scale low-pressure systems in polar areas usually with strong winds.

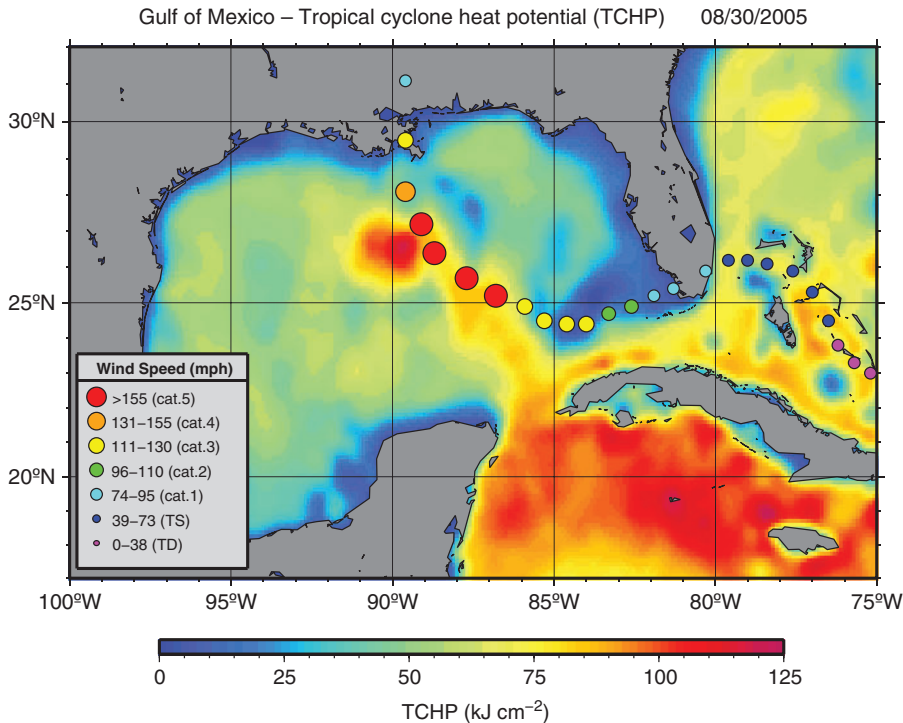


Figure 7.5 Track of Hurricane Katrina in the Gulf of Mexico during August 2005 indicating its intensification over areas of high tropical cyclone heat potential (TCHP) identified from altimeter data. The colour of the circles indicates storm category. From [46].

benefit from the improved sampling provided by constellations of satellites [50], or by altimeter data being obtained in a wide swath such in the SWOT (Surface Water Ocean Topography) mission proposed for launch after 2020 [51] (Chapter 9). Conceivably, other techniques, such as the measurement of the non-tidal loading of the solid Earth [52], may also be able to contribute in the future.

7.3.3 Changes in surges and extreme sea levels with time

Studies of changes in storm surges and extreme sea levels are based on the analysis of tide gauge data sets [15]. The observational evidence from tide gauge data, such as that shown in Figure 7.6, suggests that extreme sea levels have been increasing during the past few decades at many locations around the world. In addition, it indicates that a large part of the increase can be accounted for by changes in MSL rather than changes in the frequency and magnitude of storm surges [53]. However, there are locations that are exceptions to this conclusion [15]. In addition to any long-term changes in extreme sea levels, there are changes on interannual

and decadal timescales because of the nodal and perigean contributions to the astronomical tide (Chapter 3), and by a dependence of extremes on modes of climate variability such as the El Niño–Southern Oscillation (ENSO) and the North Atlantic Oscillation (NAO) [15, 54].

Studies of changes in extreme sea levels depend critically on the availability of suitable data sets. In some countries, access to high-frequency (hourly or more rapid sampling) tide gauge data is restricted for commercial or national security reasons. In others, many station-years of original records (tide gauge charts or tabulations) await reprocessing to modern standards. As a result, there are gaps in the data sets available for research even where the data themselves exist.

In addition, the largest extremes that lead to the most catastrophic flooding, and which are of most practical interest, might not always be represented adequately in the data sets. This reservation applies particularly for surges caused by tropical storms. These events are, by definition, rare ones, and when they do happen the highest sea level may not occur exactly at the gauge, rather than at some distance

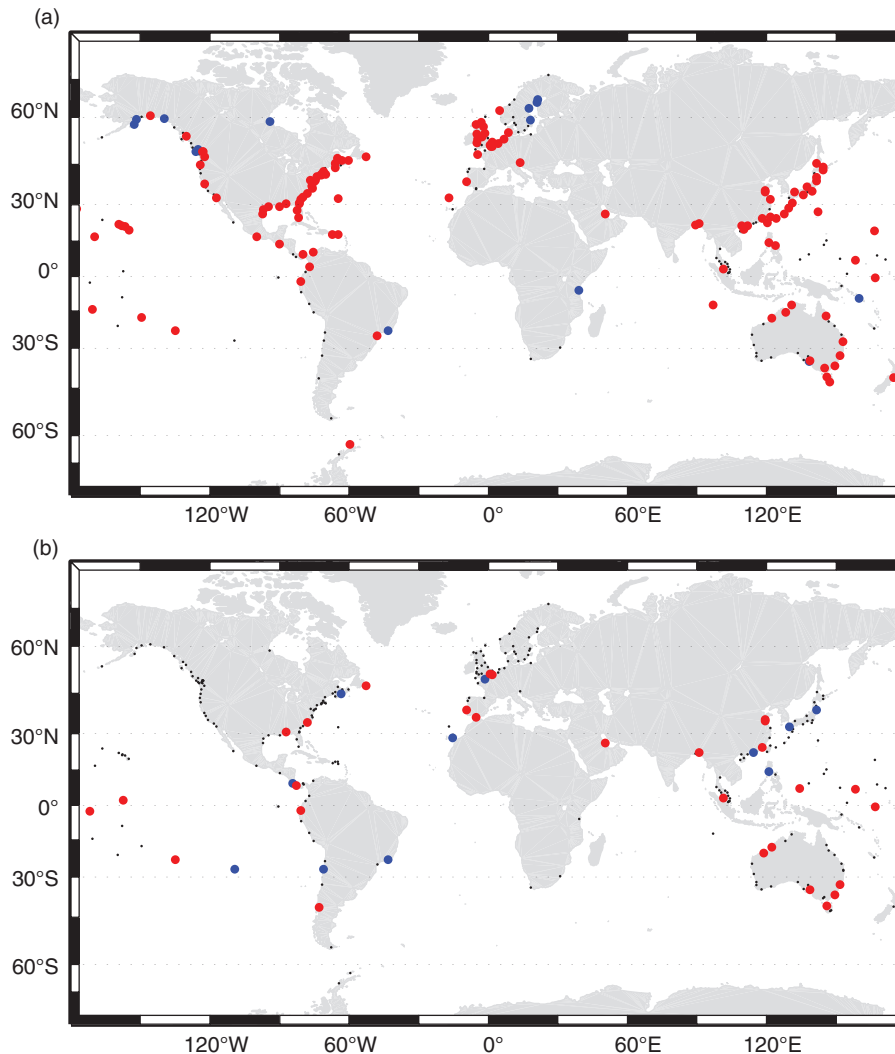


Figure 7.6 (a) Locations where estimated trends in the measured 99th percentile of sea level each year for 1970 onwards were found to be positive (red) or negative (blue) or not significantly different from zero (small black dots). (b) As plot (a) but with the median values of sea level for each year subtracted from the 99th percentile sea-level values. From [51].

along the coast. Therefore, these large events may not be sampled at all even in a record of many decades. In addition, some gauge technologies may not allow anomalously high sea levels to be recorded (e.g. if sea level were to exceed the height of a stilling well), and during the most energetic storms a gauge may be destroyed and so the extreme may not be recorded.

Changes in extremes have also been studied using multidecadal hindcasts of tide+surge models, such as those mentioned above [15, 40]. These have been important for demonstrating how changes in meteorology relate to trends in storm surges and extremes on

a regional basis, and for computing the return periods of sea-level exceedance levels. The same models have also been used to estimate the possible changes in storm surges and extremes due to future climate change by using the winds and air pressures provided by climate models [55]. Any future changes in extremes will result from a combination of regional MSL rise, including that due to changes in regionally important climate modes such as the NAO [56] as well as any related changes in storm surges [57]. Chapter 12 refers to how engineers might take all of these aspects into consideration when planning future coastal defences.

Table 7.1 Standard deviations of residuals of tidal analyses at several locations around the world*

Location	Standard deviation (m)	Latitude	Comments
Malé, Madive Islands	0.05	4° N	Indian Ocean tropical island
Halifax, Nova Scotia, Atlantic coast of Canada	0.12	47° N	Station in an inlet on a wide shelf
Cuxhaven, North Sea coast of Germany	0.39	54° N	Station in extensive area of shallow water prone to storm surges
Faraday/Vernadsky, west coast of Antarctic Peninsula	0.14	65° S	High-latitude station with longest record in Antarctica
San Francisco, Pacific coast of United States	0.11	38° N	Mid-latitude station on a narrow continental shelf

*Residuals were computed from 5 complete years of data from each station from the Research Quality Data set of the University of Hawaii Sea Level Center using a standard set of 63 tidal constituents. Such an analysis yields a common MSL (Z_0) for the 5 years and, in the case of Cuxhaven for example, leaves small shallow-water tidal signals in the residuals in addition to storm surge and other components. Nevertheless, the table provides a schematic appreciation of the variation in the magnitude of residuals at different stations.

7.4 Statistics of tidal residuals

A tide gauge record will differ from that expected from the astronomical tide because of additional contributions due to storm surges and other ocean processes. An analyst normally works by inspecting a year of data at a time and by separating the record into three components:

$$X(t) = Z_0 + T(t) + R(t) \quad (7.7)$$

where Z_0 is the MSL for the year, $T(t)$ is the tidal component and $R(t)$ is called confusingly by different authors either the ‘non-tidal residual’, ‘tidal-residual’ or, as we adopt here, simply the ‘residual’ time series (see also Section 1.6). Most analysts choose not to include long period tides, including the semi-annual and annual constituents, in such an analysis, so $T(t)$ and $R(t)$ have average values of zero over the year.

Inspection of time series of $R(t)$ can be informative for several reasons. Firstly, any instrumental errors resulting from data spikes or datum shifts or timing errors will be more apparent in the residuals than in the overall time series (Section 2.5). Instrumental errors aside, a residual time series will demonstrate an interesting spectrum of non-tidal sea-level variability. These variations can include low-frequency ones such as those due to seasonal variations in meteorological forcing (signals that are best studied if semi-annual and annual components are not included in $T(t)$, see Chapter 10 for discussion of the seasonal cycle of MSL). Higher-frequency components of the

residual time series will include storm surges, seiches and sometimes tsunamis.

In most cases, the variability in a residual time series will be due to the continuum of forcing from air pressures and winds, which is why some other authors refer to them as ‘meteorological residuals’ or even ‘surge residuals’, although the residuals may not be entirely due to meteorological effects. As a consequence, the standard deviation of a time series will, generally speaking, be smaller in tropical areas than at higher latitudes, and will be larger at continental shelf tide gauges, where processes such as storm surges and river runoff occur, than at ocean islands (Table 7.1).

At first sight, the distribution of residuals about zero may appear to approximate a normal (Gaussian) one. However, in reality residuals will not have a ‘noise-like’ random distribution, but will exhibit serial correlation with a timescale depending on the meteorological and oceanographic forcing responsible for sea-level variability in the region.⁵ For example, mid-latitude storms tend to last for a few days, and the residuals resulting from their anomalous winds and air pressures will persist for a similar time [56]. This is demonstrated by Figure 7.7, which shows the residuals at Sheerness in February 1993 when strong northerly winds resulted in a storm surge lasting for about one day [58].

⁵ Serial correlation means that the value of any one residual depends to some extent on previous and following values within a correlation timescale.

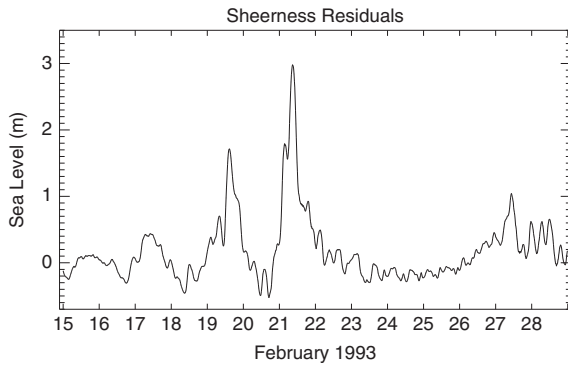


Figure 7.7 An example time series of residuals from Sheerness on the southern North Sea coast of England in February 1993 showing the large storm surge.

The distribution of residuals from a tide gauge in a shallow-water area prone to storm surges, such as at Sheerness, may exhibit much longer tails than a normal distribution, with the positive tails longer than the negative ones (Figure 7.8(a)). This contrasts with a distribution from a gauge nearer deeper water, such as Newlyn in southwest England, where the distribution is still skewed towards positive values but has shorter tails (Figure 7.8(b)) [59]. One reason for the skewness is the fact that there is an asymmetry in the meteorological forcing, with more energetic cyclones in the atmosphere than anticyclones [60]. The large positive tails at a location such as Sheerness correspond to the potentially damaging events that result in coastal flooding.

The distribution of residuals at any location will vary through the year owing to the seasonal cycle in the air pressures and winds and possibly other processes such as seasonal density changes and river runoff. Figure 7.9a shows that at Sheerness the largest residuals occur during winter months, as for other mid-latitude locations (December–January for North America and Europe and June–July south of 20 °S) (Figure 7.9b). Elsewhere, typhoons in the western Pacific are responsible for storm surges along the coasts of China and neighbouring countries in September. An August value for Bangladesh results from the extremes due to the Monsoon.

Bottom pressure records can be analysed in a similar way to tide gauge records, with their time series parameterised as a mean value of pressure together with tidal and residual components. However, their residuals will tend to be smaller than those of a nearby tide gauge, owing to at least part of the sea-level variability seen by the tide gauge being a consequence of

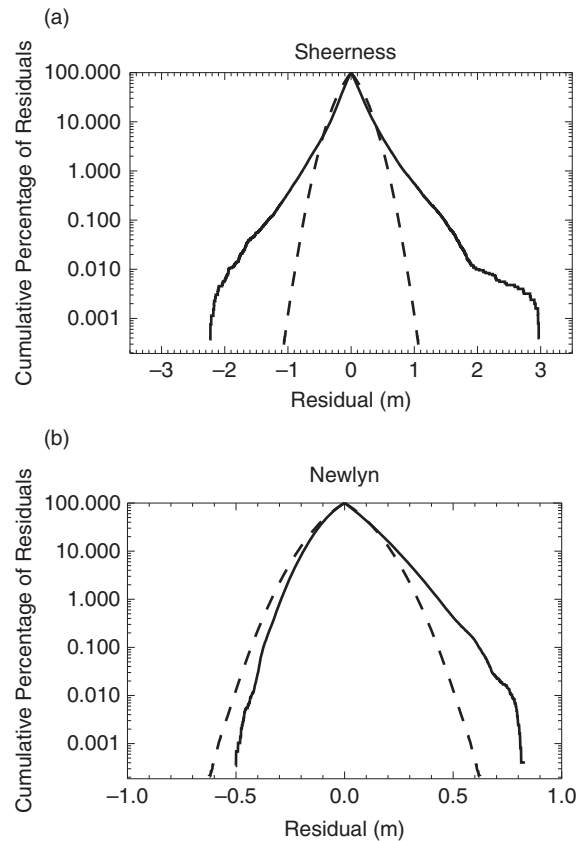


Figure 7.8 (a) Cumulative percentage of residuals over the period 1993–2008 from Sheerness in southeast England (solid line). Curves show the percentages of positive and negative residuals that have magnitudes larger than values shown on the abscissa, indicating the longer tail of larger positive residuals compared to negative ones. The dashed line indicates the curves one would have expected if the residuals had a normal distribution with an identical standard deviation. (b) The corresponding distribution over the same period at

air pressure changes. In an ideal LIB situation, the sea-level and air pressure contributions to bottom pressure will cancel out. This reduction of residual variance results in the use of bottom pressure often being preferable to that of sea level for the determination of tidal parameters, and for the detection of signals in the records such as those due to small tsunamis (Chapter 8).

7.5 Seiches

Anyone who has played with the water in a bath tub knows it is possible to set up resonant standing waves akin to the seiche phenomenon identified in Lake Geneva in the nineteenth century by Forel [61]. In fact, most inlets, bays and harbours on exposed coasts

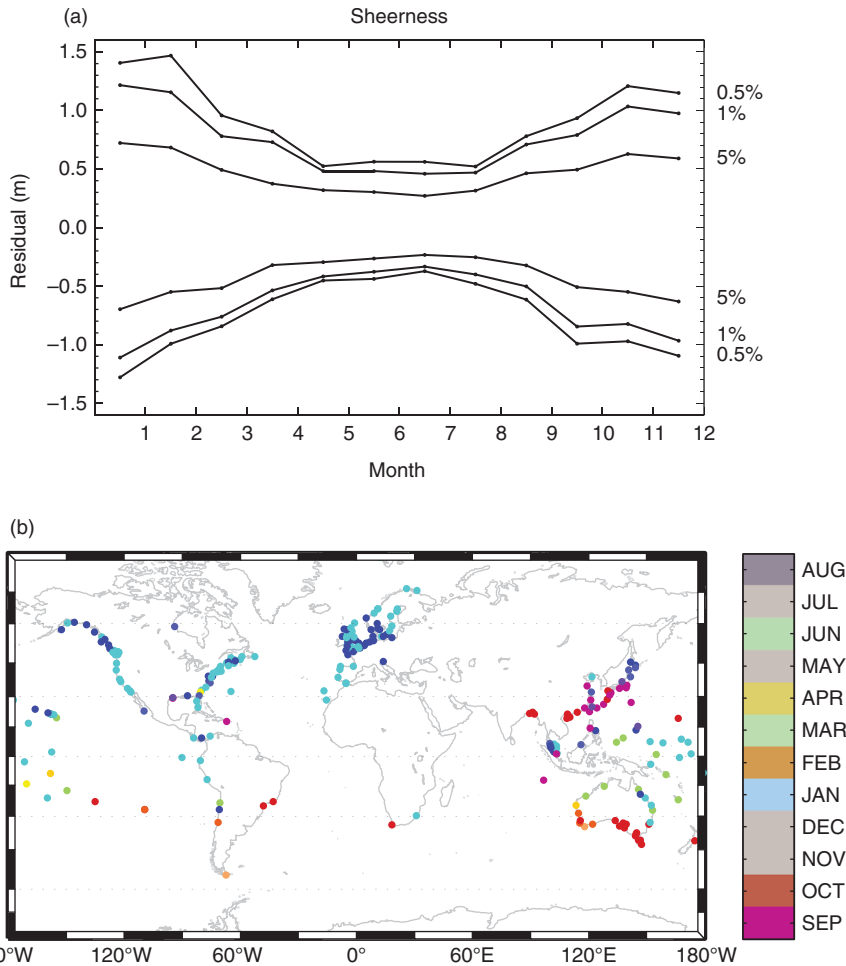


Figure 7.9 (a) Seasonal variation of the distribution of positive and negative residuals at Sheerness. The levels shown for each month correspond to those for which the indicated percentage of residuals is exceeded, demonstrating larger residuals in winter months. (b) Map showing the month at which the highest residual normally occurs. From [50].

demonstrate some form of seiche that is set in motion by the wind [62], changes in air pressure gradient [63], the ocean tide [64], the ocean internal tide [65], wave energy impinging on a harbour [66], earthquakes when water bodies are excited by ground motion such as during the 1755 Lisbon and 2011 Tōhoku earthquakes [67, 68], and, most dramatically, landslides or tsunamis [69]. The resonant periods of idealised harbours and inlets of simple shape can be determined straightforwardly [70, 71], and all periods are proportional to the reciprocal of the square-root of water depth.

As a simple example, consider the basin of Figure 5.4, as discussed in Section 5.2. Its natural period is the time taken for a wave to travel from one

end of the basin to the far end, and to return, after being reflected. This oscillation has one node in the centre, an antinode at each end, a wavelength twice the length of the basin, and a period as given by Merian's formula [71]:

$$\tau = \frac{2L}{\sqrt{gD}} \quad (7.8)$$

where L is the length of the harbour and D is its average depth, and g is acceleration due to gravity. Harmonics with periods half, third etc. of τ are allowed.

A second example is when the basin is open at one end, forming an inlet. In this case, the node can be located at the open entrance with an antinode at the closed end (Figure 5.5). This gives a natural period:

$$\tau = \frac{4L}{(2n-1)\sqrt{gD}} \quad (7.9)$$

or $4L/\sqrt{gD}$ for the fundamental mode ($n=1$) when the length of the bay corresponds to one-quarter of a wavelength [72]. In practice, the resonant periods can be calculated readily for any simple geometry of closed or open basins [68], and when basins have a non-uniform depth then the equations can be expressed in integral form, for example in this case

$$\tau = 4 \int_0^L \frac{dx}{\sqrt{gD(x)}}$$

Seiches observed in certain regions are mentioned below to provide examples of such phenomena that occur around the world. Many other examples may be found in the literature [73, 74].

An example of a basin such as Figure 5.4 is provided by the harbour of Port Stanley in the Falkland Islands (Malvinas), which is a one-dimensional almost-enclosed body of water (Figure 7.10a). A sea-level power spectrum shows two peaks centred on 2.3 and 0.69 cph (i.e. periods of 26 and 87 minutes) (Figure 7.10b) [72]. Both signals are always present with amplitudes of several centimetres, rising to 10 cm typically once or twice each month. The two signals have maximum amplitudes at almost the same times and their combined contribution can amount to approximately half of the tide. The most energetic seiching occurs following rapid changes in air pressure and winds associated with troughs and fronts. Merian's formula, using the known dimensions of the harbour, yields a period of 33 minutes, similar to the 26 minutes observed. Confirmation that this signal is indeed the standing wave of Figure 5.4, with an antinode at each end of the harbour and a node at the centre, was obtained by deploying three gauges with 1-minute sampling at each end of the harbour and at its centre (red dots in Figure 7.10a). Cross-spectral analysis confirmed that the two ends of the harbour co-oscillate with opposite phase and with little seiche energy at the centre. The $1/\sqrt{gD}$ dependence of seiche period was confirmed by studying the change in period at different states of the tide.

The 87-minute component had an entirely different character. The cross-spectral analysis of the three sensors showed that oscillations had similar amplitude and phase along the harbour, suggesting that they must be generated by exchanges through an inlet that connects the harbour to a basin called Port William which leads to the sea. A calculation of Port William's

resonant period, assuming a simplified rectangular (plan) and triangular (depth profile) description of its shape and bathymetry, gave a period of 73 minutes for a forced quarter-wave oscillatory system with an antinode at the head of the inlet, where it connects to Port Stanley harbour, and a node on the open boundary.

Every inlet in the Falkland Islands has its own seiche characteristics. North of Port Stanley is Berkeley Sound, which has seiches within a narrow frequency band centred on 0.46 cph (131 min). South of Port Stanley at Mare Harbour one observes oscillations centred on 0.58 cph (103 min). By contrast, data from Sea Lion Island, located on the open shelf and not in an inlet, displays a broad spectrum of variability but no specific peak. Stations near to Buenos Aires on the Argentine coast demonstrate seiche periods in the band 1.17–1.49 cph [76].

The Falklands have some similarity to the Shetland Islands, located at a similar latitude but in the northern hemisphere, and near to the edge of a wide continental shelf. Seiches there have been explained not by local resonance, but in terms of the production of edge waves trapped along the Shetlands east coast originating from long waves generated in the North Sea and associated with fast-moving meteorological fronts [77]. The similarity of the periods (28 min) observed at two locations (Baltasound and Lerwick, 65 km apart) lent support to this interpretation.

Different forcing mechanisms are responsible for seiches observed around the Sri Lanka coast, which have periods ranging from a few tens of minutes to 2 hours [78]. Those of the east coast are particularly interesting, varying fortnightly and seasonally in amplitude and being particularly large during neap tides in March–April and October–November (Figure 7.11a). Figure 7.11b shows that large seiche amplitudes can occur at any time of the day and any time after high tide, so they cannot be generated by a local daily cyclic forcing or at a particular tidal state. However, the clear inclined bands indicate that the large amplitudes occur at a particular time of day given a time of high tide, which corresponds at this location to the large amplitudes occurring during neaps. It has been suggested that these seiches are excited by internal waves originating as far away as the Andaman Sea during spring tides and travelling for 6–8 days to the Sri Lankan east coast where they arrive during neaps.

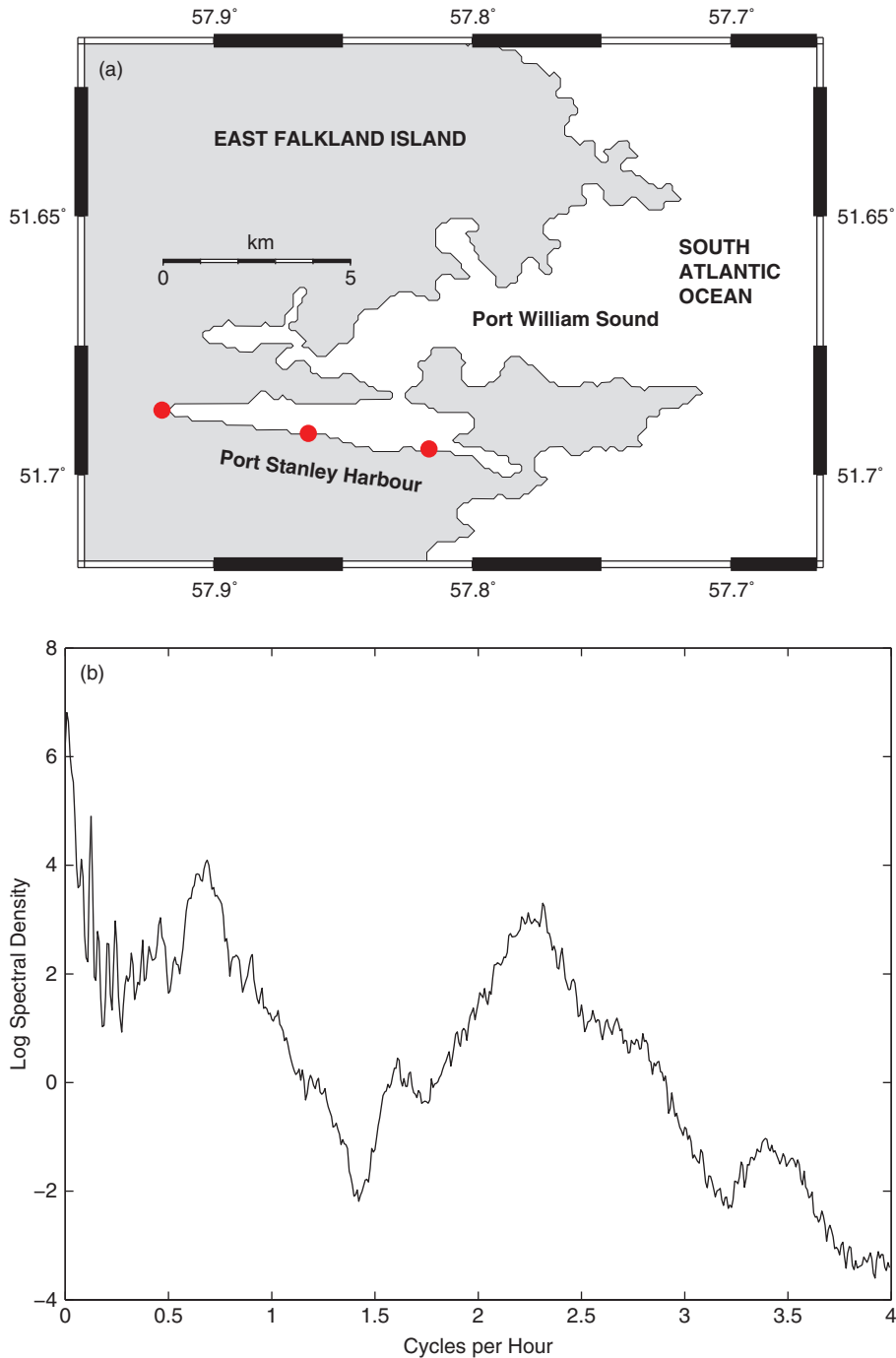


Figure 7.10 (a) Map of Port Stanley harbour in the Falkland Islands (Malvinas). The red dots indicate the locations of pressure sensors referred to in the text. (b) Power spectrum of sea-level variability in the harbour indicating the main seiche energy peaks centred at 2.3 and 0.69 cph (periods of 26 and 87 min) (arbitrary units). From [75].

Seiches are found all around the Indian Ocean with their individual periods. Periods of 10 and 50 minutes have been found at Mahé in the Seychelles, while at Aldabra, 1000 km to the south, periods of 25

to 50 minutes were observed intermittently. On the other hand, no seiching was observed at Mombasa on the Kenya coast [79]. At Mauritius, the main seiches have periods of 7 and 20 minutes at Port Louis on the

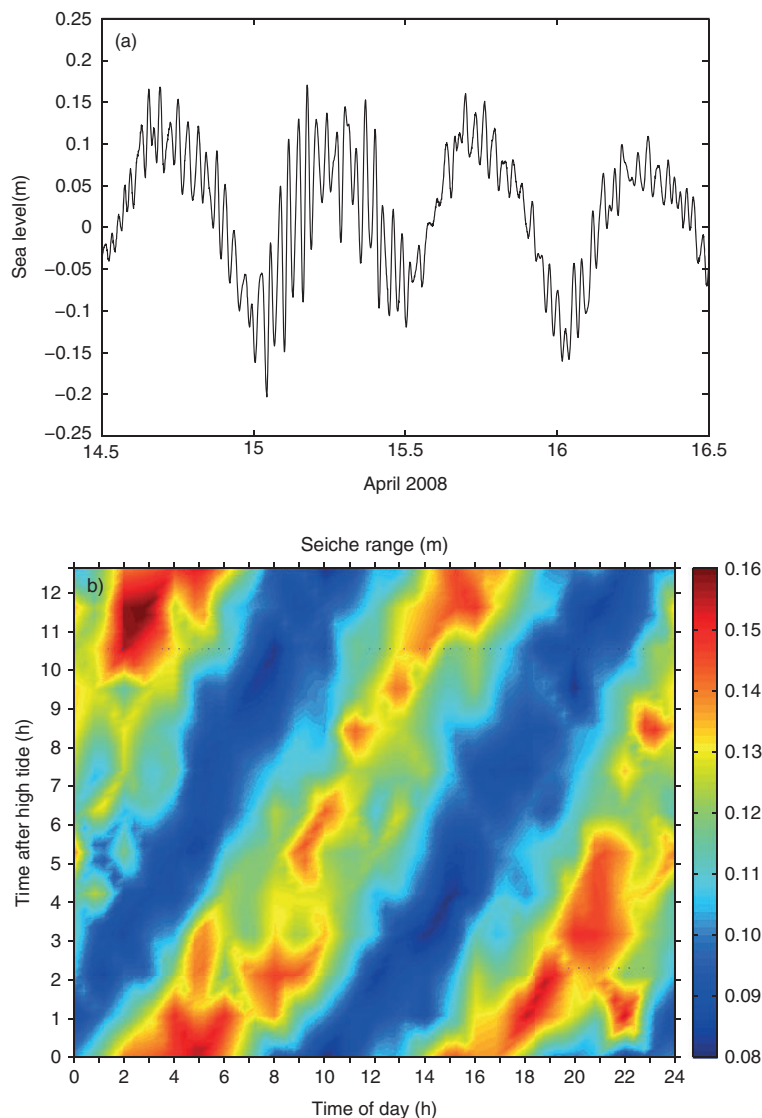


Figure 7.11 (a) Seiche variation for 2 days during neap tides at Trincomalee Bay on the east coast of Sri Lanka. (b) Variation in the range of the 42-minute seiche at Trincomalee as a function of time of day and time after high tide for the period 1 March to 30 May 2007 (range defined as the difference between a sea-level maximum and the following minimum). From [77].

west coast of the island but 32 minutes at Grand Gaube on the north coast. At Rodrigues, 25 and 18 minutes were found at Port Mathurin and Passe Demi located offshore of the north and west coasts, respectively [80]. Figure 7.12 shows a sea-level spectrum for Port Mathurin indicating a clear peak at 25 minutes which persists through the year. Seiche amplitudes there have a relationship to the tide, suggesting dynamical effects in the shallow channel to the open sea. For many Indian Ocean study sites, the observed seiche periods were longer than calculated from the dimensions of each harbour. Some differences might be expected from the use of simplified

geometry. However, discrepancies might also be accounted for by friction, loss of energy to the deep sea at the open boundary, and inertia of water at the mouth of the open basin, all of which would result in a longer period than for idealised cases [78]. An example of very short period seiches is provided by Esperance on the west coast of Australia, where energetic oscillations at 1–3 minutes are known to occur and cause excessive motion of moored ships; these seiches are thought to be associated with ocean swell [81].

Mediterranean islands are famous for their seiches. These include the Balearic Islands, where ‘rissaga’ with

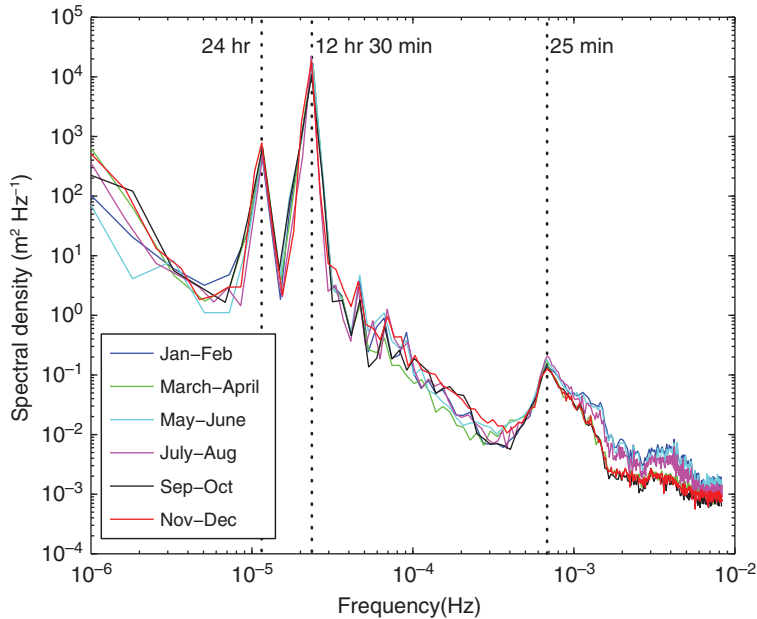


Figure 7.12 Seasonal variations of the seiche spectrum at Port Mathurin, Rodrigues Island, Mauritius. From [79].

wave heights more than 3–4 m have been observed in Ciutadella harbour in Menorca following meteotsunamis (see below), causing severe damage to the coastal area, ships and harbour constructions [82]. Similar oscillations occur in other harbours and inlets of the Balearic Islands and the Mediterranean coast of the Iberian Peninsula. Seiches are well known as ‘milghuba’ in Malta and consist of sea-level variations with periods ranging from a few minutes to several hours but mostly around 20 minutes [83]. Indeed, data from the Grand Harbour were included in one of the first scientific studies of seiches [84]. Weak seiching occurs along the north coast of Malta as background ‘noise’ in tidal records, but can have a range of over 1 m in bays at certain times when the associated currents can be comparable to those generated by tidal forcing. Analysis shows the seiches to be associated with shelf-scale resonances. Similar large-amplitude seiching, but at different period, occurs along the southern coast of Sicily [81].

Larger bodies of water can have seiches. For example, the Adriatic Sea has a seiche with a period of 21 hours, which compares well to 18.3 hours that one calculates from Merian’s formula for a quarter-wave resonance of a basin open at one end, the difference in period being accounted for by rotation effects [85]. Seiches there are triggered by a sudden change in the Sirocco (SE) wind and have been identified in current meter records as well as in multi-decimetric signals

in sea level. They contribute to the extreme sea levels observed at Venice [86]. The near-enclosed Baltic Sea has a uni-nodal oscillation of approximately 26 hours [87].

7.6 Meteotsunamis

The term ‘meteorological tsunamis’ or ‘meteotsunamis’ covers a wide range of phenomena in which meteorological disturbances (e.g. cyclones, frontal squalls, air pressure jumps, thunderstorms etc.) produce long waves in the ocean that propagate until they reach a coastline, where they are amplified by shoaling and local resonance that results in coastal flooding, in a similar way to the ‘seismic sea waves’ or tsunamis discussed in the next chapter [80, 88, 89]. Long waves for meteotsunamis are generated over minutes to hours, unlike the near-instantaneous wave generation of tsunami waves from earthquakes or landslides. However, the resulting meteotsunami and tsunami waves at the coast have similar temporal and spatial scales, and both can have amplitudes of many metres, so that different interpretations of particular historical flooding events are possible, especially when seismic information is lacking.

Many meteotsunamis are generated when the positive sea-level change caused by a low air pressure centre (cyclone or depression) is magnified when the

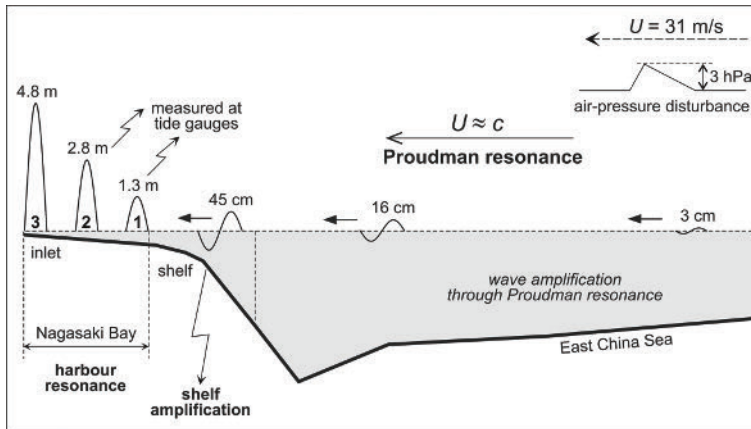


Figure 7.13 Schematic of the physical mechanism responsible for formation of the catastrophic meteotsunami at Nagasaki Bay (Japan) on 31 March 1979. The initial pressure jump over the western part of the East China Sea was about 3 hPa. The long waves generated by this event first amplified from 3 cm to 16 cm as a result of Proudman resonance, then to 45 cm due to the shelf amplification, and finally to 478 cm at the head of the bay due to the harbour resonance. From [86].

cyclone travels in the same direction and at the same speed of long progressive waves in the ocean (approximately \sqrt{gD}). In this situation, the LIB response is magnified by a factor $(1 - \frac{Q^2}{gD})$ where Q is the speed of the disturbance, in what is called a *Proudman resonance*, with most of the sea-level-raising force occurring in the back-right quadrant of the cyclone (as is also the case for normal storm surges in fact; back-left quadrant in the southern hemisphere) [90]. Although Proudman's theoretical calculation needs to be modified to include consideration of friction and diffusion processes [91] and, as a result, although in practice the magnification is rarely more than a factor of five, there are many examples of flooding events in which high sea levels have been produced this way. In the most damaging events, Proudman resonance is only part of the combination of reasons for flooding, by amplifying the sea-level signal along the path of the cyclone, followed by shoaling at the coast, and then by seiching within a harbour basin. An example of such an event occurred at Vela Luka, Croatia, in 1978, eventually resulting in a meteotsunami with a height of 6 m [92, 93]. The 'abiki' waves of Nagasaki Bay, Japan, including the damaging event of March 1979, tend to be caused not by cyclones but by several hPa positive pressure jumps that travel eastward across the East China Sea (Figure 7.13) [86, 94]. However, amplification provided by the Proudman resonance operates in a similar way. In notable flooding along the coast of Newfoundland, Canada, in 1999 and 2000, long waves are believed to have been generated by the 'barotropic wakes' (similar to the wake produced by a moving vessel) of the remains of tropical storms travelling across the Grand Banks at

speeds comparable to that required for Proudman resonance [95].

There are many other examples of long wave generation by different types of atmosphere–ocean interaction to be found in the literature [71, 72, 96]. The long waves need to be amplified by resonance to produce a meteotsunami at the coast. Proudman resonance, *Greenspan resonance*, wherein the speed of progressive edge waves (gravity waves constrained by refraction to propagate along a rigid boundary such as a shoaling beach) corresponds to the speed of the alongshore atmospheric disturbance [97], and *shelf resonances*, when the long waves have periods and wavelengths similar to the resonant period and wavelength of the shelf [71], provide suitable mechanisms. Further amplification is provided by shoaling (Section 8.4) and seiching in semi-enclosed bays, fjords or harbours (Section 7.5).

Some regions are represented in the literature more with regard to meteotsunamis than others. This will be primarily due to the particular combinations of regional meteorology and local coastal resonance such that rare and destructive events occur. For example, the meteotsunamis of the Croatian coast of the Adriatic are well documented [92]. The 'rissaga' events at Menorca island in the western Mediterranean are also well known, including that of June 2006 when an unusual air pressure jump resulted in 4–5 m waves at Ciutadella [98]. The northwest European continental shelf is another area where flooding events have been interpreted as due to meteotsunamis. These include the south coast of the United Kingdom where several events have been reported [99], including a recent meteotsunami in June 2011 [100]. 'Summer waves', short-lived large increases in sea level, are known on

the Danish North Sea coast and have been interpreted as due to Proudman-like resonance [101].

The similarities between meteotsunamis and tsunamis, and to some extent between meteotsunamis and storm surges, has created difficulties in the interpretation of some historical flooding events on the northwest European coast before seismic information became available and when meteorological data were incomplete [102]. There are also different conclusions drawn from some energetic events in more modern times, which have been interpreted as either a tsunami without a seismic signature or, alternatively, as a meteotsunami due to severe weather [103]. An example is an event in the North Sea in June 1858 that had a runup height on the Danish coast of 6 m [104].⁶ Meteotsunamis have been identified in many other parts of the world including the Pacific coast of Canada [105], Florida [106], Argentina [107], Japan [86] and Australia [108], and are probably more common than realised.

The many different physical processes in the atmosphere and ocean that contribute to flooding has led to an extensive literature that may not be best served by the single term ‘meteotsunami’, or the suggested ‘rissaga’ (a Catalan word for ‘drying’) as an alternative expression [86]. Nevertheless, there is no doubt that events occur in which there are rapid meteorological changes followed by large fluctuations of sea level that are not monitored and modelled adequately at present [90]. Consequently, the field of meteotsunamis continues to offer a range of interesting scientific and operational challenges.

7.7 Wave set-up and surf beat

Wave set-up is the increase of sea level in the surf zone due to the transfer of wave-related momentum to the water column during wave breaking (Figure 7.14). This process becomes particularly evident when wave heights are large during storms. Scientific studies of wave set-up began in the 1960s during theoretical investigations of the concept of radiation stress by Longuet-Higgins and Stewart [109], radiation stress being defined as the excess flow of momentum due to the waves. In addition, early field observations had shown sea levels measured exactly at the coast during

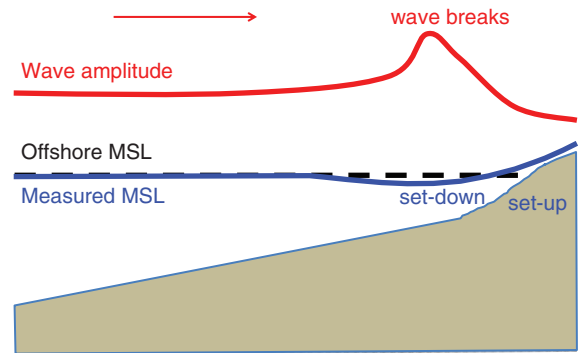


Figure 7.14 Schematic of the relationship between wave set-up and set-down and MSL near to a sloping beach.

storms to be higher than those recorded by tide gauges located a short distance offshore, such as at the end of a nearby pier. Wave set-up has since been investigated both theoretically and experimentally in laboratory and field studies [110, 111].

Wave set-up is normally considered to be capable of adding 10–20 per cent of the incident wave height to the sea level one would otherwise estimate using tide +surge models. However, larger percentages have been observed at tropical and sub-tropical islands [112] where time series of set-up, driven primarily by energetic swell, have been employed as indices of regional storminess [113]. Consequently, wave set-up can comprise many decimetres of water that can be an important factor in studies of coastal flooding. However, although numerical models show that wave set-up can be very significant during storms [41], to our knowledge there is no operational flood warning scheme that forecasts wave set-up alongside tide +surge levels. The reason is that, for any practical scheme, one would have to model the set-up in great detail for every sloping beach, and in every bay and harbour, along a coastline. For the same reason, the long hindcast runs of tide+surge models referred to above have not been complemented by long wave set-up time series.

Wave set-up is an important consideration in the scientific analysis of tide gauge data when a gauge has been installed at a location where set-up is particularly large. Although it may be largest during storms, set-up will always be present in the tide gauge record at some level. Therefore, if the incident wave climate changes, from season to season or from year to year, then the measured MSL will also change. When wave set-up is always low in amplitude it can be hard to distinguish from ‘surge’ in any tide gauge record.

⁶ This paper suggests, on balance, that the event was a tsunami. However, according to Dr David Long, British Geological Survey, there is a good set of newspaper reports supporting a meteorological (thunderstorm) cause.

On shorter timescales of minutes, a time series of the set-up can include a component that varies with the wave group period. This component can be amplified by near-shore resonances into sea-level variability called *surf beat*.⁷ These oscillations can be clearly seen by a tide gauge, or by a pressure recorder mounted offshore on the seabed. These surf beats may be refracted by the offshore topography to propagate along the coast as *edge waves* or other motions [71]. Where the coast has irregularities the edge waves may be reflected, establishing a pattern of trapped edge waves at some period that is a characteristic of the coast.

Wave set-up is a complicated subject which we can only summarise here with two examples. The first example concerns waves impinging on a long sloping beach at right angles to the beach. In this case, the radiation stress results in a *set-down* of sea level seaward of the breakers by an amount:

$$\Delta = -\left[\frac{1}{2}\right] \frac{A^2 k}{\sinh 2kD} \quad (7.10)$$

where A is wave amplitude (half the wave height), $k = 2\pi/\lambda$ is wave number, λ is wavelength and D is water depth: this reduces to $\Delta = -\left[\frac{1}{4}\right] \frac{A^2}{D}$ for small depths. This set-down becomes greater as the water shallows, reaching a maximum value just before the waves break. Experiments and theory show that waves tend to break when the water depth is approximately 2.6 times the wave amplitude [106, 111].

Inside the break point, the wave energy decreases shoreward and wave amplitude is proportional to depth, leading to a decrease in radiation stress. One obtains:

$$\frac{d\zeta}{dx} = -K \frac{dD}{dx} \quad (7.11)$$

where $\frac{d\zeta}{dx}$ is the gradient of sea level measured at distance x from the beach, $K = \frac{1}{1+8/(3\gamma^2)}$ and γ is the ratio of wave height to water depth $2A/D$. For small values of γ , then K approximates to $\frac{3\gamma^2}{8}$. There is an increase of sea level as the waves travel towards the beach, starting from the point where the waves break, and for a beach

of constant gradient the slope of sea level should be constant and proportional to the gradient [107, 108].

As an example, consider waves of 3 m amplitude and a beach with a constant slope of 1/30. These waves would tend to break at a water depth of $2.6 \times 3 = 7.8$ m, which is at 234 m offshore. The set-down at this point is 0.29 m. For this value of γ of 0.77, then K is 0.182 and the set-up gradient gives an increase of sea level from this point to the shoreline of $234 (1/30) 0.182$ or 1.42 m. This set-up can be combined with the seaward set-down to determine the overall change in sea level from the ocean to the coast during wave activity. As the wave amplitudes change in time, so the position of wave breaking is shifted nearer and further away from the shore, and set-down and set-up change accordingly.

A second example concerns the set-up that occurs in harbours, where permanent sea-level recorders are often located. As waves spread into a harbour from a narrow entrance, their amplitude decreases. Radiation stress arguments show that at distances within the harbour greater than a few times the width of the entrance, and for large long period waves, the MSL is higher than at the mouth by an amount:

$$\Delta = \frac{3}{4} \frac{A^2}{D} \quad (7.12)$$

where A is the wave amplitude at the entrance and D is the harbour depth (or 0.075 m for one metre waves in a 10 m deep harbour) [116]. Because the set-up is greater for lower mean water depths, the apparent amplitude of a measured tide can be reduced if waves increase measured low tide levels more than they increase high tide levels, perhaps by a few centimetres. Adjustment is not instantaneous as a few hours are necessary for the water transfer needed for full set-up to develop.

Wave set-up has been described as not being understood adequately for engineering design purposes [108], and we have shown that it represents a gap in understanding of sea level variability. Set-up and related processes such as over-topping of defences merit further consideration in sea-level and coastal research.

7.8 Air pressure-related changes of sea level in the world ocean

In this section, we mention briefly some features of sea-level variability in the world ocean that have been understood, at least partly, with the use of 2-D models such as those described above.

⁷ Surf beat describes wave motions with typical periods of 30 s to 3 min that are formed in the surf zone as a result of non-linear interaction of wind waves or swell. They were named as such by Munk [114]. A more general term, which also includes open-ocean waves of similar origin, is infragravity waves (IG-waves) as proposed by Kinsman [115].

It might have been thought that, while the shallow areas of coastal seas could be strongly affected by storm surges, most of the sea-level variability in the deep ocean should be describable to good approximation by the LIB response to air pressure and so to largely reflect air pressure variability as shown in Figure 7.15. However, the extent to which the LIB model provides a good description of the sea-level changes related to air pressure variability has been found to be strongly dependent on timescale and location [117]. The LIB is certainly not reliable anywhere for short periods (less than a few days) when dynamical factors are important. However, the LIB model also fails to apply to some extent over longer timescales and over extensive regions, as will be seen below.

The extent to which the LIB model applies across the world ocean at different timescales is summarised in Table 7.2. These statistics were obtained from a set of island tide gauges supplemented by a number of coastal sites where appropriate (e.g. in Antarctica) and by a number of bottom pressure recorders, and similar conclusions were also obtained using altimeter data [9]. Cross-spectral analysis was used to compare

sea-level and local air pressure variability in different frequency bands, and the table shows the average transfer function magnitudes, which are the average values in each band (in cm/mbar) by which sea level increases when local air pressure decreases. An abrupt change of regime can be identified at $\sim 20^{\circ}$ – 30° N/S with the observed response being less LIB-like in the tropics and at higher frequencies. A response of ~ 0.9 is typical in shelf areas where winds provide a

Table 7.2 Average transfer function magnitude in each frequency band (cm/mbar) [9]

Period	Tropics	Extratropics
2–3 days	0.59	0.94
3–4 days	0.65	0.99
4–6 days	0.66	1.01
6–10 days	0.78	0.97
10 days to 6 months	0.87	0.96
20 days and longer	0.91	0.96

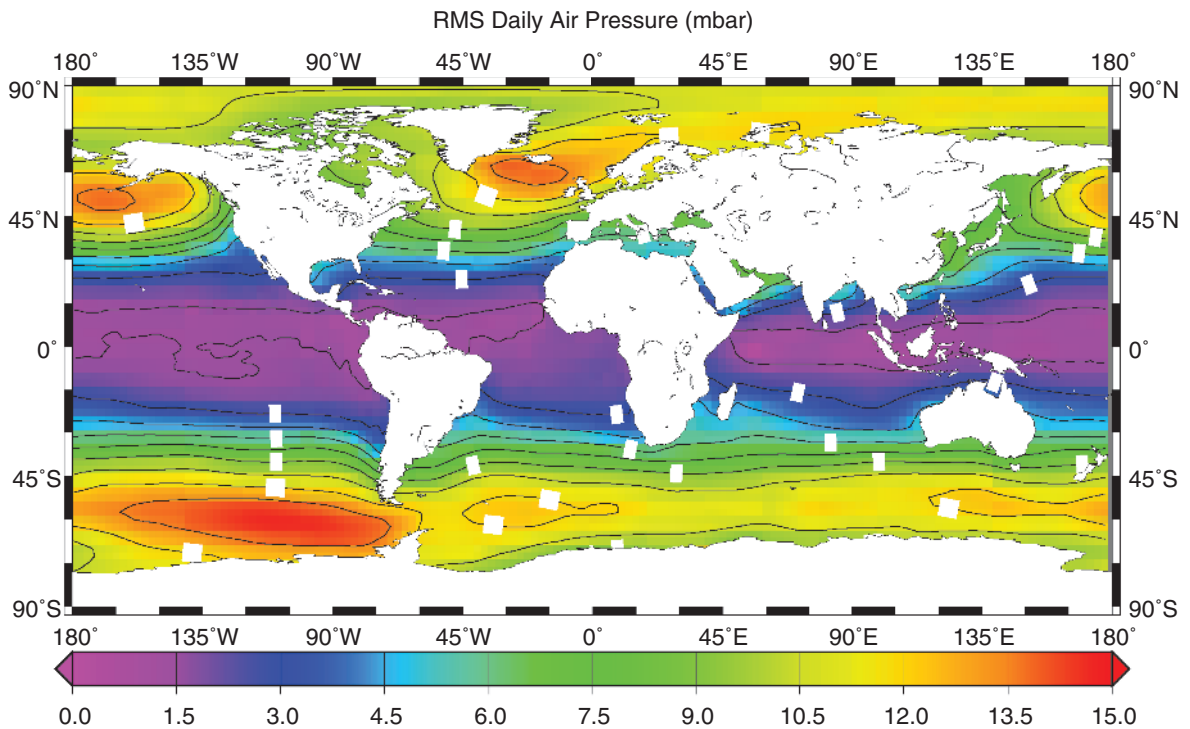


Figure 7.15 The standard deviation of air pressure variability around the world calculated from 10 years of daily mean values (2001–2010). Values vary from approximately 2 mbar in the tropics to over 15 mbar at higher latitudes. Data from National Centers for Environmental Prediction (NCEP) <http://www.cdc.noaa.gov/data/gridded/data.ncep.reanalysis.surface.html>.

comparable forcing to air pressures [118]. A similar response is obtained even in the deep ocean owing to Ekman pumping⁸ and other dynamical processes coherent with air pressure changes [119].

7.8.1 Modelling the effects of air pressure and winds with 2-D models: barotropic hot spots

The relationship between sea-level and air pressure variability at different locations around the world and at different timescales can best be investigated with a global 2-D (barotropic) ocean model. For example, Figure 7.16a shows maps of sea-level response to local air pressure (i.e. sea-level increase given an air pressure decrease) for variability in the bands 4–6, 11–15 and 20–30 days using air pressure forcing in the model alone [9]. In all three maps, the ocean's adjustment to the forcing results in significant departures from ~1 cm/mbar in the tropics, consistent with Table 7.2, with larger departures in the higher-frequency 4–6 day band in the Atlantic. The ocean becomes generally more LIB-like with increasing period. Nevertheless, the LIB continues to fail to some extent in the Southern Ocean.

Figure 7.16b has a second set of maps, this time for combined air pressure and wind stress forcing. Values for the 4–6-day band are similar to those with the air pressure forcing alone with major departures again in the tropics, and with some enhancement of LIB failure in parts of the Southern Ocean. At 11–15 and 20–30 days, qualitatively similar values are obtained in the tropics as for air pressure forcing alone. However, the Southern Ocean exhibits major differences to Figure 7.16a which are of greater importance at longer periods. The main areas affected by the wind include the southeast Pacific Basin and a basin in the Indian sector of the Southern Ocean to the southwest of Australia having the Kerguelen Plateau to its west and the southeast Indian Ridge to the north. Wind stress is also seen to play a role in the North Pacific and North Atlantic Oceans. These are extensive regions of deep abyssal plain surrounded by ridges or plateaus.

⁸ Cyclonic winds around areas of low air pressure induce Ekman transport (Appendix B) which pushes water away from beneath the cyclone centre, resulting in a divergence of water called Ekman pumping. The resulting sea-level change due to this effect is smaller than and opposite in sign to that of the LIB.

These areas are the so-called 'barotropic hot spots', which are areas of relatively high sea-level variability that were identified from the first few years of satellite altimetry [120] and have since been confirmed in space gravity information (Figure 7.17) [121], and by ocean modelling studies [122]. The 'hot spots' are driven by the action of wind stress curl (a measure of the angular momentum of the wind field that relates to the 'spinning up' of the ocean circulation) over regions of slowly varying f/D contours (f being the Coriolis parameter and D depth) and are highly damped geostrophic ocean modes, with decay times of about 2 and 3.5 days for the southeast Pacific and southwest of Australia respectively, that are continually excited by the wind (Figure 7.18) [123].

7.8.2 Variability over the Zapiola Rise

Less evident in Figure 7.17, because of the spatial smoothing applied to those figures, is another area of high sea-level variability in the Argentine Basin in the southwest Atlantic. This particular signal is one component of the generally high variability in that part of the ocean called the Brazil–Malvinas Confluence, which is very clear in plots of mesoscale variability observed by altimetry (Figure 10.2). This particular component results from a dipole pair of positive and negative sea-level anomalies that propagate anticlockwise around 45° S, 317° E at a bathymetric feature called the Zapiola Rise [124]. The dipole covers about 1000 km of ocean and rotates with a period of 20–25 days with a peak-to-trough amplitude of about 10 cm (Figure 7.19). This oscillation is another major barotropic component of the ocean circulation that is associated with a free barotropic mode of a basin, closed f/D contours providing a means to confine waves to the Rise. The transport associated with the variability is very large (about 50 Sv, where 1 sverdrup (Sv) is a unit of volume transport of 10^6 m³/s). However, unlike the previous examples of 'hot spots', this mode has been found to be only weakly excited by the wind in barotropic models, but to be strongly excited in a baroclinic model with a realistic eddy field. This suggests that the feature is intrinsically linked to interactions between eddies, mean flow and topography [125].

7.8.3 Annular modes of sea-level variability

Variability in sea level at high latitudes is closely associated with the two 'annular modes' of variability

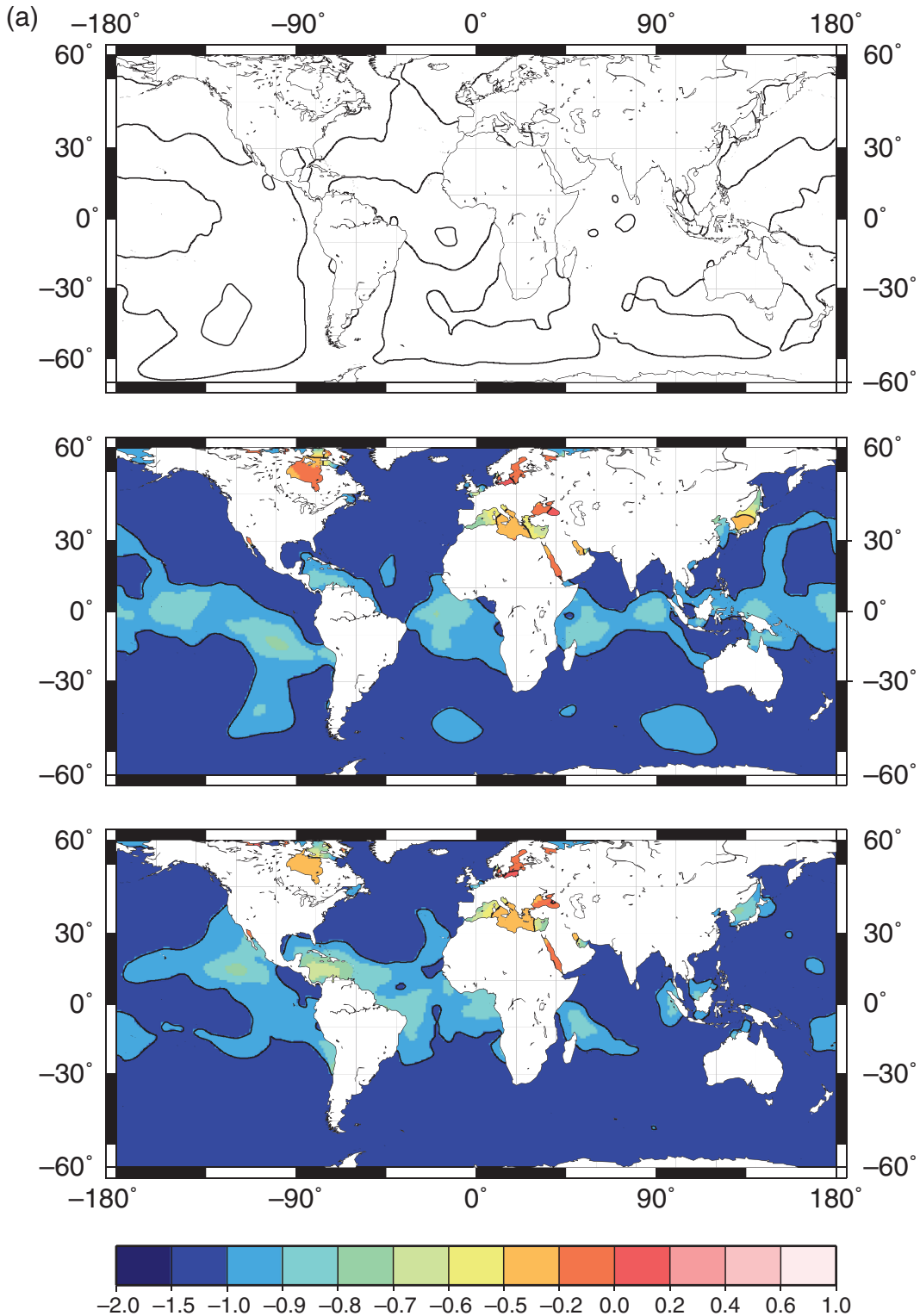
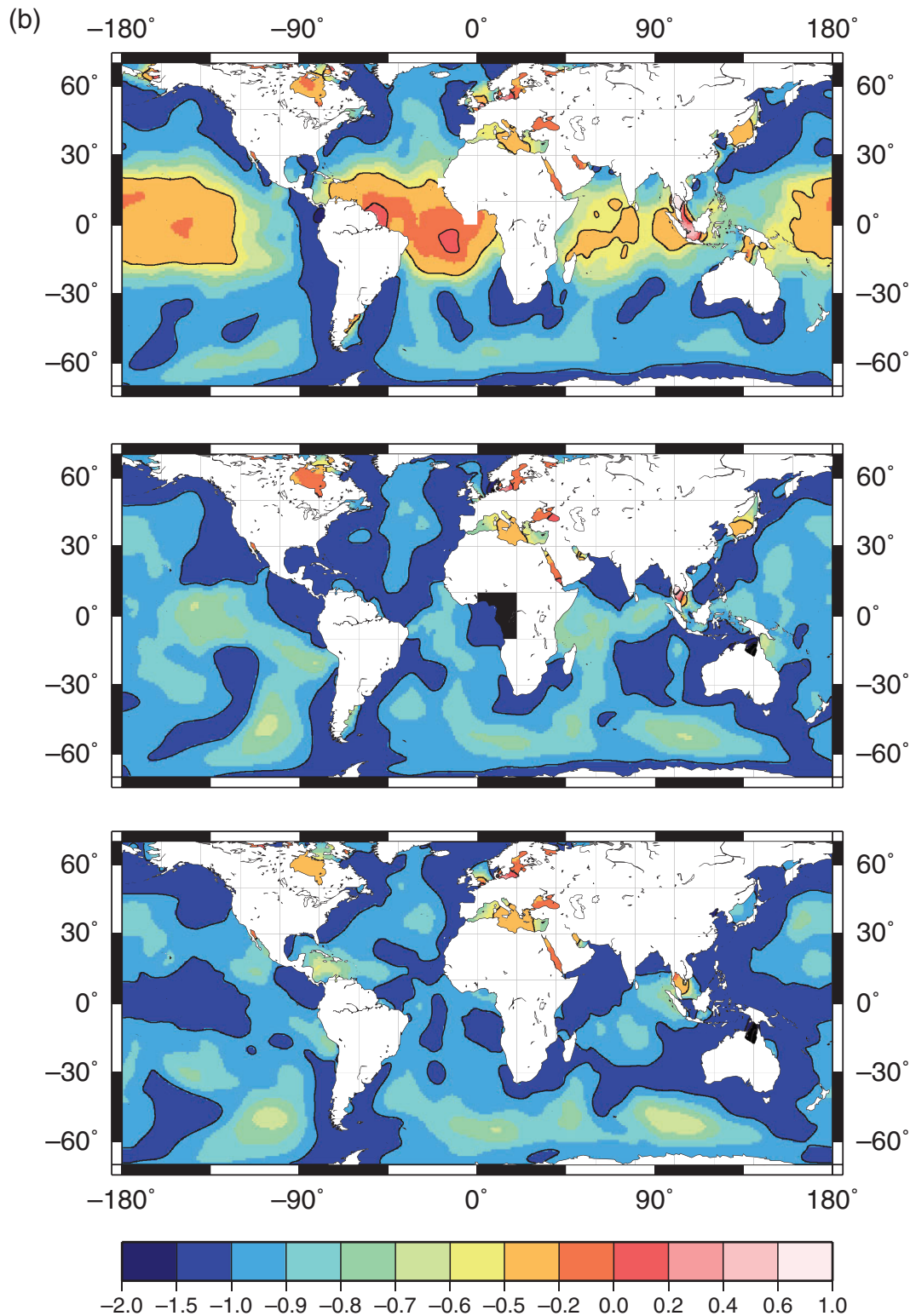


Figure 7.16 (a) Sea-level response to local air pressure forcing (cm/mbar) in the (a) 4–6, (b) 11–15 and (c) 20–30 day bands using a linear regression method and data from the numerical model of Reference 9. In these cases the model was forced by air pressure alone. (b) Sea-level response to local air pressure but using data from a model run with combined air pressure and wind stress forcing.



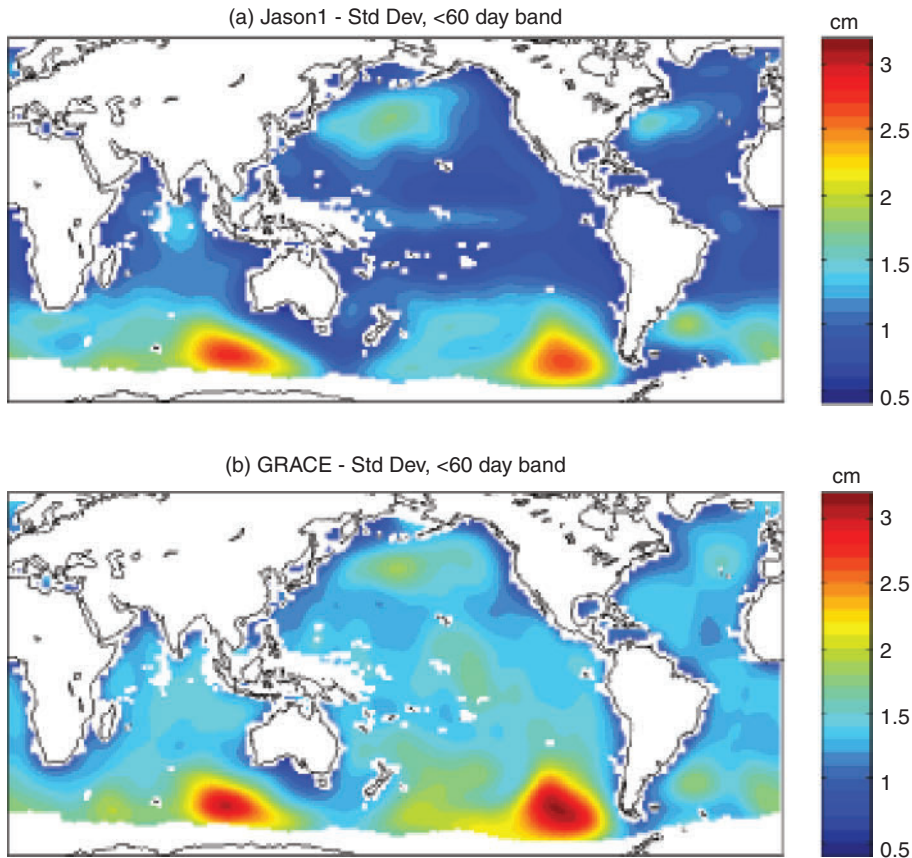


Figure 7.17 Standard deviations of centimetres of water for (a) Jason-1 altimeter sea-level and (b) GRACE space gravity data (the latter corresponding to bottom pressure data) filtered to show variability with periods less than 60 days. All data have been smoothed using a 750 km Gaussian filter to focus on long wavelength signals. From [118] using more recent GRACE (GFZ RL05) data.

in air pressure. They are called ‘annular’ to emphasise the primarily longitudinal symmetry of their variability around the two poles (see [Chapter 10](#) for more discussion of these modes). Each mode results in large-scale patterns of coherent sea-level variability that were unknown until recently, the sea levels of the ice-covered high latitudes presenting an environmental challenge to tide gauge operators and being unsampled by altimetry. The Arctic was also often excluded from ‘global’ ocean numerical models.

The Antarctic mode of sea-level variability was first identified in ocean models [126] and then observed in tide gauge, bottom pressure recorder (BPR) and satellite altimeter data [127, 128] (e.g. [Figure 7.20](#)). Coherent sea-level variations are observed around Antarctica that are correlated with the atmospheric mode of variability called the Southern Annular Mode (SAM). The SAM is a measure of the meridional

air pressure gradient in the Southern Ocean, and therefore of the strength of the westerly winds that drive the Antarctic Circumpolar Current (ACC) and thereby modulate sea level around the entire Antarctic coast.

An Arctic mode of sea-level variability is a more recent discovery [129], representing coherent variability across the entire Arctic on intraseasonal timescales (periods less than approximately 9 months) caused by winds blowing from the Atlantic Ocean that are in turn controlled by the Arctic Oscillation (AO), an atmospheric mode characterised by air pressure anomalies of one sign in the Arctic and one of opposite sign centred about 37–45° N. The evidence for the Arctic mode in sea level has been derived so far from tide gauge and numerical model information only, and clear evidence for its existence requires measurements in deep water, away from the shelf sea regions [126].

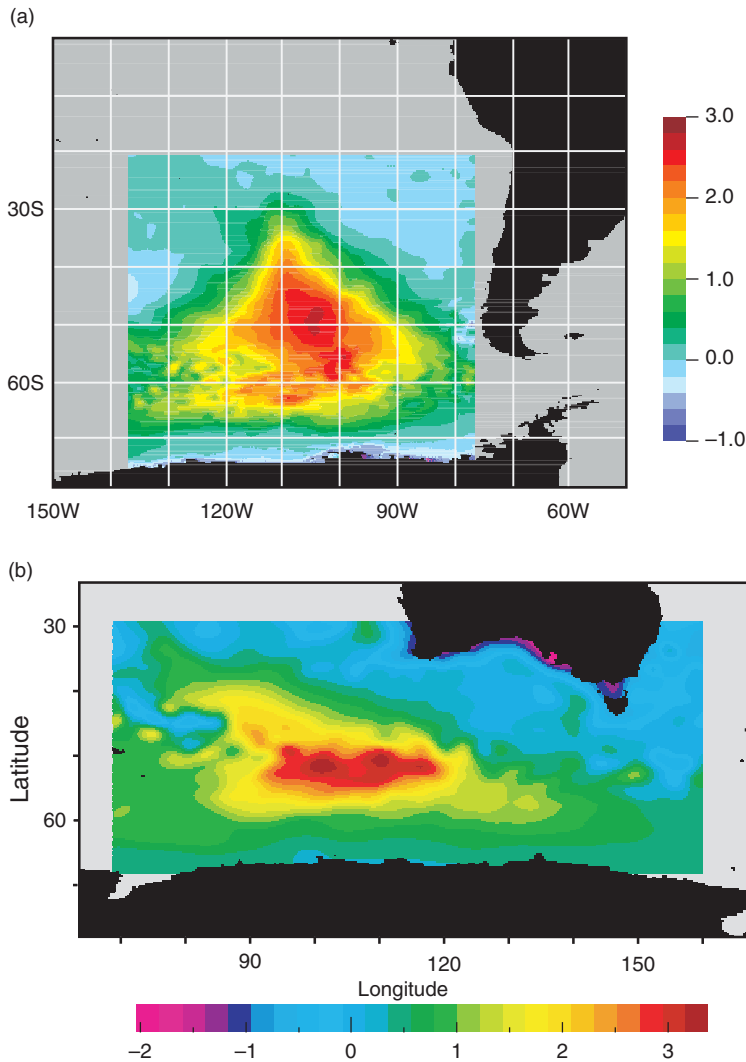


Figure 7.18 Amplitudes of the first mode of sea surface height variability in (a) the southeast Pacific and (b) Indian sector of the Southern Ocean using the OCCAM ocean model (normalised to have unit variance when averaged over the regions shown). From [122].

7.8.4 Five-day waves

An example of violation of the LIB model in the world ocean is provided by the ‘5-day’, or Madden–Julian, wave of air pressure that travels westwards around the world with a period of approximately 5 days [130].⁹ The wave is not confined to air pressure at sea level, but can be observed throughout the atmosphere [129]. It is not to be confused with the better-known

⁹ The 5-day wave is a westward propagating planetary wave, zonal wave number 1 (meaning that the wave has a wavelength equal to the Earth’s circumference at the equator) and is often referred to as a Rossby–Haurwitz normal-mode oscillation owing to its westward-propagating nature [3].

Madden–Julian Oscillation (MJO), which has a period of 40–50 days and is an eastward-propagating coupling between the atmospheric circulation and the tropical oceans [131]. The MJO is most clearly observed in fluctuations in tropical rainfall.

The 5-day wave at sea level has a maximum amplitude of about 1 mbar at approximately 50° N and S (Figure 7.21) [132, 133]. At these latitudes, its signal is masked by synoptic weather systems with air pressure variability of the order several tens of millibars. In contrast, the wave is clearly observed in the tropics, although its amplitude varies through the year, and from year to year [132]. In this region, the wave amplitude (approximately 0.7 mbar) is significant

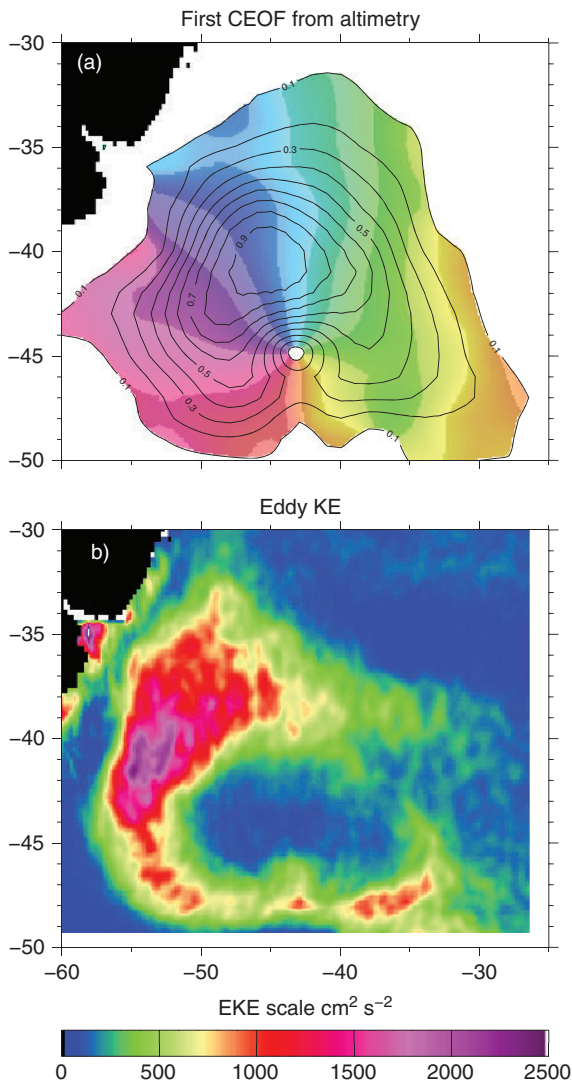


Figure 7.19 (a) The first complex mode of altimeter sea surface height variability in the Argentine Basin. Contours are amplitude, normalised to a maximum value of 1. Colours are phase, each colour band covering a 30° range. The natural direction of phase propagation for the mode follows the order red–yellow–green–blue (i.e. anticlockwise). Phase is only plotted where the amplitude is greater than 0.1. (b) Eddy kinetic energy in the same region. From [124].

when compared with the typically 2 mbar standard deviation of overall tropical air-pressure variability.

Five-day signals were first identified in sea-level records from Pacific islands and were shown to be very different from those that would be expected from an LIB response to the 5-day air pressure wave [130]. Similar LIB-violating signals at periods around

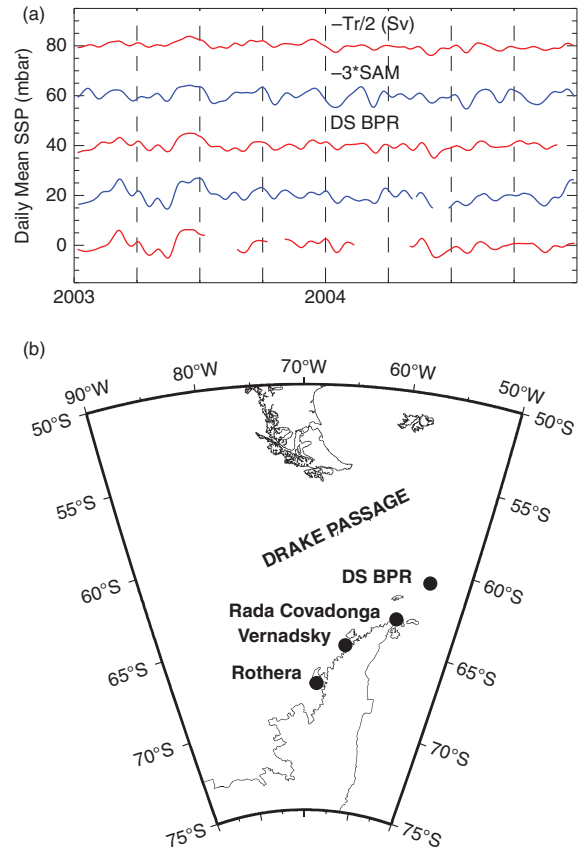


Figure 7.20 (a) Daily mean values of sub-surface pressure (sea level corrected for the inverse barometer) at the Vernadsky and Rothera coastal tide gauges and bottom pressure from a deployment in the southern Drake Passage at the locations in (b). Each record was low-pass filtered with a 30-day filter. Also shown are scaled values of the SAM index and an estimate of transport through the Drake Passage from a numerical model. Pairs of the various time series give zero-lag correlation coefficients around 0.7. Rada Covadonga station shown in (b) provided a shorter record from a third coastal site used in the analysis. From [125].

5 days were subsequently identified in tropical Atlantic sea levels [135] and in other tide gauge records from around the world [136]. They have also been investigated using altimeter data [137]. An explanation for the LIB violation comes from the large-scale character of the air pressure forcing at this period (Figure 7.21) as demonstrated by numerical modelling [129, 133, 138, 139]. Figure 7.22 shows the ocean response to the wave to be a complicated one, and to be very different from that expected from the LIB. Modelling has shown that the observed response results from the time taken for gravity waves to propagate between ocean basins leading to lags in the sea-level adjustment [129, 135], similar to the ocean's non-Equilibrium

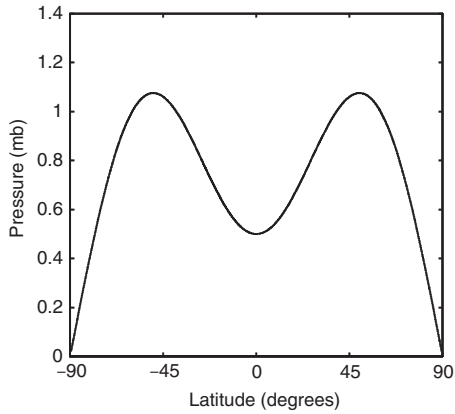


Figure 7.21 Schematic description of the latitudinal distribution of the Madden–Julian 5-day pressure wave. From [134].

response to astronomical tidal forcing at fortnightly period [140].

A complication to this topic is that there is another potential source of 4–6 day signals in equatorial sea levels due to resonant excitation of trapped baroclinic gravity waves [135, 141]. However, such signals are likely to be confined to within a few degrees of the equator, rather than span a large range of latitude as indicated by Figure 7.21. It was in the course of investigating equatorially trapped waves that the larger-scale barotropic signals associated with the 5-day wave were identified [130].

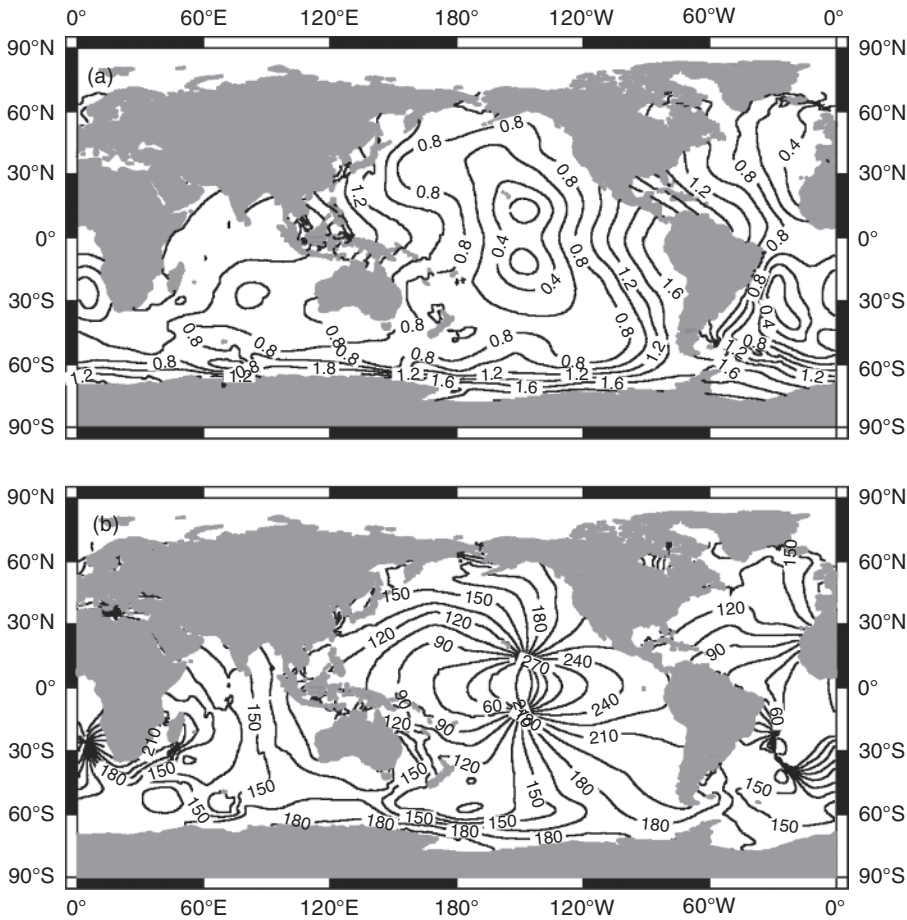


Figure 7.22 The sea-level response to the 5-day air pressure wave shown in Figure 7.21: (a) the magnitude of the response in cm/mbar, a uniform LIB response would have values of 1.0 throughout; (b) phase of the response, values of phase greater than 180° implying that sea level lags air pressure: a uniform LIB response would have values of 180° throughout. From [133].

References

1. Wunsch, C. and Stammer, D. 1997. Atmospheric loading and the oceanic “inverted barometer” effect. *Reviews of Geophysics*, **35**, 1, doi:10.1029/96RG03037.
2. Ponte, R. M., Salstein, D. A. and Rosen, R. D. 1991. Sea level response to pressure forcing in a barotropic numerical model. *Journal of Physical Oceanography*, **21**, 1043–1057, doi:10.1175/1520-0485(1991)021<1043:SLRTPF>2.0.CO;2.
3. Gill, A. E. 1982. *Atmosphere–Ocean Dynamics*. New York: Academic Press.
4. (1) Willebrand, J., Philander, S. G. H. and Pacanowski, R. C. 1980. The oceanic response to large-scale atmospheric disturbances. *Journal of Physical Oceanography*, **10**, 411–429, doi:10.1175/1520-0485(1980)010<0411:TORTLS>2.0.CO;2. (2) Vinogradova, N. T., Ponte, R. M. and Stammer, D. 2007. Relation between sea level and bottom pressure and the vertical dependence of oceanic variability. *Geophysical Research Letters*, **34**, L03608, doi:10.1029/2006GL028588.
5. Wu, J. 1982. Wind-stress coefficients over sea surface from breeze to hurricane. *Journal of Geophysical Research*, **87**, C12, doi:10.1029/JC087iC12p09704.
6. (1) Heaps, N. S. 1967. Storm surges. In *Oceanography and Marine Biology: An Annual Review: Volume 5* (ed. H. Barnes), pp. 11–47. London: Allen and Unwin. (2) Heaps, N. S. 1983. Storm surges 1967–1982. *Geophysical Journal of the Royal Astronomical Society*, **74**, 331–376, doi:10.1111/j.1365-246X.1983.tb01883.x.
7. Flather, R. A. 1988. *Storm surge modelling. Lecture notes during the Course on Ocean Waves and Tides at the International Centre for Theoretical Physics, Trieste*, 26 September–28 October 1988.
8. Woodworth, P. L. and Horsburgh, K. J. 2011. Surge models as providers of improved “inverse barometer corrections” for coastal altimetry users. In *Coastal Altimetry* (eds. S. Vignudelli, A. Kostianoy, P. Cipollini and J. Benveniste), pp. 177–189. Berlin: Springer-Verlag. doi:10.1007/978-3-642-12796-0_7.
9. Mathers, E. L. and Woodworth, P. L. 2001. Departures from the local inverse barometer model observed in altimeter and tide gauge data and in a global barotropic numerical model. *Journal of Geophysical Research*, **106** (C4), 6957–6972, doi:10.1029/2000JC000241.
10. (1) Baxter, P. J. 2005. The east coast Big Flood, 31 January–1 February 1953: a summary of the human disaster. *Philosophical Transactions of the Royal Society, A*, **363**, 1293–1312, doi:10.1098/rsta.2005.1569. (2) Gerritsen, H. 2005. What happened in 1953? The Big Flood in the Netherlands in retrospect. *Philosophical Transactions of the Royal Society, A*, **363**, 1271–1291, doi:10.1098/rsta.2005.1568. (3) McRobie, A., Spencer, T. and Gerritsen, H. 2005. The Big Flood: North Sea storm surge. *Philosophical Transactions of the Royal Society, A*, **363**, 1263–1270, doi:10.1098/rsta.2005.1567.
11. Wolf, J. and Flather, R. A. 2005. Modelling waves and surges during the 1953 storm. *Philosophical Transactions of the Royal Society, A*, **363**, 1359–1375, doi:10.1098/rsta.2005.1572.
12. Lamb, H. H. and Frydendahl, K. 2005. *Historic Storms of the North Sea, British Isles and Northwest Europe*. Cambridge: Cambridge University Press.
13. (1) Murty, T. S., Flather, R. A. and Henry, R. F. 1986. The storm surge problem in the Bay of Bengal. *Progress in Oceanography*, **16**, 195–233, doi:10.1016/0079-6611(86)90039-X. (2) Murty, T. S. and Flather, R. A. 1994. Impact of storm surges in the Bay of Bengal. *Journal of Coastal Research, Special Issue*, **12**, 149–161. (3) Flather, R. A. 1994. A storm surge prediction model for the northern Bay of Bengal with application to the cyclone disaster in April 1991. *Journal of Physical Oceanography*, **24**, 172–190, doi:10.1175/1520-0485(1994)024<0172:ASSPMF>2.0.CO;2. (4) Dube, S. K., Rao, A. D., Sinha, P. C., Murty, T. S. and Bahulayan, N. 1997. Storm surge in the Bay of Bengal and Arabian Sea: the problem and its prediction. *Mausam*, **48**, 283–304.
14. (1) FEMA. 2006. Reconstruction guidance using Hurricane Katrina surge inundation and advisory base flood elevation maps. Federal Emergency Management Agency. http://www.fema.gov/hazard/flood/recoverydata/katrina/katrina_about.shtm. (2) Needham, H. F. and Keim, B. D. 2012. A storm surge database for the US Gulf Coast. *International Journal of Climatology*, **32**, 2108–2123, doi:10.1002/joc.2425.
15. Sweet, W., Zervas, C., Gill, S. and Park, J. 2013. Hurricane Sandy inundation probabilities today and tomorrow. In *Explaining Extreme Events of 2012 from a Climate Perspective* (eds. T. C. Peterson, M. P. Hoerling, P. A. Stott and S. Herring), pp. 17–20. *Bulletin of the American Meteorological Society*, **94**, S1–S74. Available from www.ametsoc.org/2012extremeeventsclimate.pdf.
16. (1) Lowe, J. A., Woodworth, P. L., Knutson, T. *et al.* 2010. Past and future changes in extreme sea levels and waves. In *Understanding Sea-Level Rise and Variability* (eds. J. A. Church, P. L. Woodworth, T. Aarup and W. S. Wilson), Chapter 11. London: Wiley-Blackwell. (2) Woodworth, P. L., Menéndez, M. and Gehrels, W. R. 2011. Evidence for century-timescale acceleration in mean sea levels and for recent changes in extreme sea levels. *Surveys in Geophysics*, **32**(4–5), 603–618 (erratum p. 619), doi:10.1007/s10712-011-9112-8. (3) IPCC, 2012. *Managing the Risks of Extreme Events and Disasters to Advance Climate Change Adaptation. A Special Report of Working Groups I and II of the Intergovernmental Panel on Climate Change* (eds.

- C. B. Field, V. Barros, T. F. Stocker *et al.*). Cambridge: Cambridge University Press.
17. Pousa, J. L., D'Onofrio, E. E., Fiore, M. M. E. and Kruse, E. E. 2012. Environmental impacts and simultaneity of positive and negative storm surges on the coast of the Province of Buenos Aires, Argentina. *Environmental Earth Sciences*, **68**, 2325–2335, doi:10.1007/s12655-012-1911-9.
 18. von Storch, H. and Woth, K. 2008. Storm surges: perspectives and options. *Sustainability Science*, **3**, 33–43, doi:10.1007/s11625-008-0044-2.
 19. Ali, A. 1999. Climate change impacts and adaptation assessment in Bangladesh. *Climate Research*, **12**, 109–116.
 20. Wolf, J. 2009. Coastal flooding: impacts of coupled wave–surge–tide models. *Natural Hazards*, **49**, 241–260, doi:10.1007/s11069-008-9316-5.
 21. Wolf, J. 1981. Surge-tide interaction in the North Sea and River Thames. In *Floods Due to High Winds and Tides* (ed. D. H. Peregrine), pp. 75–94. New York: Elsevier.
 22. (1) Keers, J. F. 1968. An empirical investigation of interaction between storm surge and astronomical tide on the east coast of Great Britain. *Ocean Dynamics*, **21**, 118–125, doi:10.1007/BF02235726. (2) Prandle, D. and Wolf, J. 1978. The interaction of surge and tide in the North Sea and River Thames. *Geophysical Journal of the Royal Astronomical Society*, **55**, 203–216, doi:10.1111/j.1365-246X.1978.tb04758.x. (3) Prandle, D. and Wolf, J. 1978. Surge-tide interaction in the southern North Sea. *Hydrodynamics of Estuaries and Fjords (Proceedings of the 9th International Liege Colloquium on Ocean Hydrodynamics)*, pp. 161–185, doi:10.1016/S0422-9894(08)71277-7. (4) Wolf, J. 1978. Interaction of tide and surge in a semi-infinite uniform channel, with application to surge propagation down the east coast of Britain. *Applied Mathematical Modelling*, **2**, 245–253, doi:10.1016/0307-904X(78)90017-3.
 23. Horsburgh, K. J. and Wilson, C. 2007. Tide-surge interaction and its role in the distribution of surge residuals in the North Sea. *Journal of Geophysical Research*, **112**, C08003, doi:10.1029/2006JC004033.
 24. World Meteorological Organization. 2011. Guide to Storm Surge Forecasting. *WMO Report No. 1076*. Geneva: World Meteorological Organization. Available from <http://library.wmo.int/>.
 25. Amin, M. 1982. On analysis and forecasting of surges on the west coast of Great Britain. *Geophysical Journal of the Royal Astronomical Society*, **68**, 79–94, doi:10.1111/j.1365-246X.1982.tb06963.x.
 26. Woodworth, P. L. and Blackman, D. L. 2002. Changes in extreme high waters at Liverpool since 1768. *International Journal of Climatology*, **22**, 697–714, doi:10.1002/joc.761.
 27. (1) Proudman, J. 1955. The propagation of tide and surge in an estuary. *Proceedings of the Royal Society London, A*, **231**, 8–24, doi:10.1098/rspa.1955.0153. (2) Proudman, J. 1955. The effect of friction on a progressive wave of tide and surge in an estuary. *Proceedings of the Royal Society London, A*, **233**, 407–418, doi:10.1098/rspa.1955.0276. (3) Proudman, J. 1957. Oscillations of tide and surge in an estuary of finite length. *Journal of Fluid Mechanics*, **2**, 371–382, doi:10.1017/S002211205700018X.
 28. Bernier, N. B. and Thompson, K. R. 2007. Tide-surge interaction off the east coast of Canada and northeastern United States. *Journal of Geophysical Research*, **112**, C06008, doi:10.1029/2006JC003793.
 29. Haigh, I. D., MacPherson, L. R., Mason, M. S. *et al.* 2013. Estimating present day extreme water level exceedance probabilities around the coastline of Australia: tropical cyclone induced storm surges. *Climate Dynamics* (in press), doi:10.1007/s00382-012-1653-0.
 30. Valle-Levinson, A., Olabarrieta, M. and Valle, A. 2013. Semidiurnal perturbations to the surge of Hurricane Sandy. *Geophysical Research Letters*, **40**, 2211–2217, doi:10.1002/grl.50461.
 31. Pugh, D. T. and Vassie, J. M. 1976. Tide and surge propagation off-shore in the Dowsing region of the North Sea. *Deutsche Hydrographische Zeitschrift*, **29**, 163–213, doi:10.1007/BF02226659.
 32. Amin, M. 1982. On analysis and prediction of tides on the west coast of Great Britain. *Geophysical Journal of the Royal Astronomical Society*, **68**, 57–78, doi:10.1111/j.1365-246X.1982.tb06962.x.
 33. Rossiter, J. R. 1959. Research on methods of forecasting storm surges on the east and south coasts of Great Britain. *Quarterly Journal of the Royal Meteorological Society*, **365**, 262–277, doi:10.1002/qj.49708536508.
 34. Flather, R. A. 2000. Existing operational oceanography. *Coastal Engineering*, **41**, 13–40, doi:10.1016/S0378-3839(00)00025-9.
 35. Murty, T. S. 1984. *Storm Surges: Meteorological Ocean Tides*. Canadian Journal of Fisheries and Aquatic Sciences, Bulletin No. 12.
 36. For example, Greenberg, D. A. 1979. A numerical model investigation of tidal phenomena in the Bay of Fundy and Gulf of Maine. *Marine Geodesy*, **2**, 161–187, doi:10.1080/15210607909379345.
 37. For example, see Jones, J. E. and Davies, A. M. 1998. Storm surge computations for the Irish Sea using a three-dimensional numerical model including wave-current interaction. *Continental Shelf Research*, **18**, 201–251, doi:10.1016/S0278-4343(97)00062-9.
 38. de Vries, H., Breton, M., de Mulder, T. *et al.* 1995. A comparison of 2D storm surge models applied to three

- shallow European seas. *Environmental Software*, **10**, 23–42, doi:10.1016/0266-9838(95)00003-4.
39. Álvarez Fanjul, E., Pérez Gómez, B. and Rodríguez Sánchez-Arévalo, I. 2001. Nivmar: A storm surge forecasting system for Spanish Waters. *Scientia Marina*, **65** (Suppl. 1), 145–154.
 40. Gonnert, G., Dube, S. K., Murty, T. S. *et al.* 2001. *Global Storm Surges: Theory, Observations and Applications*. German Coastal Engineering Research Council.
 41. Examples include (1) Flather, R. A., Smith, J. A., Richards, J. D., Bell, C. and Blackman, D. L. 1998. Direct estimates of extreme storm surge elevations from a 40-year numerical model simulation and from observations. *The Global Atmosphere and Ocean System*, **6**, 165–176. (2) Bernier, N. B. and Thompson, K. R. 2006. Predicting the frequency of storm surges and extreme sea levels in the northwest Atlantic. *Journal of Geophysical Research*, **111**, C10009, doi:10.1029/2005JC003168. (3) Weisse, R. and Plüß, A. 2006. Storm-related sea level variations along the North Sea coast as simulated by a high-resolution model 1958–2002. *Ocean Dynamics*, **56**, 16–25, doi:10.1007/s10236-005-0037-y. (4) Haigh, I. D., Wijeratne, E. M. S., MacPherson, L. R. *et al.* 2013. Estimating present day extreme total water level exceedance probabilities around the coastline of Australia: tides, extra-tropical storm surges and mean sea level. *Climate Dynamics* (in press), doi:10.1007/s00382-012-1652-1.
 42. Munk, W. H. 1955. Wind stress on water: an hypothesis. *Quarterly Journal of the Royal Astronomical Society*, **81**, 320–332, doi:10.1002/qj.49708134903.
 43. (1) Mastenbroek, C., Burgers, G. and Janssen, P. A. E. M. 1993. The dynamical coupling of a wave model and a storm surge model through the atmospheric boundary layer. *Journal of Physical Oceanography*, **23**, 1856–1866, doi:10.1175/1520-0485(1993)023<1856:TDCOAW>2.0.CO;2. (2) Brown, J. M., Bolaños, R. and Wolf, J. 2011. Impact assessment of advanced coupling features in a tide-surge-wave model, POLCOMS-WAM, in a shallow-water application. *Journal of Marine Systems*, **87**, 13–24, doi:10.1016/j.jmarsys.2011.02.006. (3) Brown, J. M. and Wolf, J. 2009. Coupled wave and surge modelling for the eastern Irish Sea and implications for model wind-stress. *Continental Shelf Research*, **29**, 1329–1342, doi:10.1016/j.csr.2009.03.004. (4) Janssen, P. 2009. *The Interaction of Ocean Waves and Wind*. Cambridge: Cambridge University Press.
 44. Powell, M. D., Vickery, P. J. and Reinhold, T. A. 2003. Reduced drag coefficient for high wind speeds in tropical cyclones. *Nature*, **220**, 279–283, doi:10.1038/nature01481.
 45. Prandle, D. 1997. The influence of bed friction and vertical eddy viscosity on tidal propagation. *Continental Shelf Research*, **17**, 1367–1374, doi:10.1016/S0278-4343(97)00013-7.
 46. (1) Flowerdew, J., Horsburgh, K., Wilson, C. and Mylne, K. 2010. Development and evaluation of an ensemble forecasting system for coastal storm surges. *Quarterly Journal of the Royal Meteorological Society, Part B*, **136**, 1444–1456, doi:10.1002/qj.648. (2) Horsburgh, K. J., Williams, J. A., Flowerdew, J. and Mylne, K. 2008. Aspects of operational forecast model skill during an extreme storm surge event. *Journal of Flood Risk Management*, **1**, 213–221, doi:10.1111/j.1753-318X.2008.00020.x.
 47. (1) Madsen, K. S., Høyer, J. L. and Tscherning, C. C. 2007. Near-coastal satellite altimetry: sea surface height variability in the North Sea–Baltic Sea area. *Geophysical Research Letters*, **34**, L14601, doi:10.1029/2007GL029965. (2) Scharroo, R., Smith, W. H. F. and Lillibridge, J. L. 2005. Altimetry and the intensification of Hurricane Katrina. *Eos, Transactions of the American Geophysical Union*, **86**, 40, doi:10.1029/2005EO400004.
 48. Goni, G., DeMaria, M., Knaff, J. *et al.* 2009. Applications of satellite-derived ocean measurements to tropical cyclone intensity forecasting. *Oceanography*, **22**, 190–197, doi:10.5670/oceanog.2009.78.
 49. See www.storm-surge.info.
 50. For example, see Allan, T. 2005. Detecting tsunamis: calling in the satellites. *Marine Scientist*, **13**, 12–14.
 51. (1) Benveniste, J. 2011. Radar altimetry: past, present and future. In *Coastal Altimetry* (eds. S. Vignudelli, A. Kostianoy, P. Cipollini and J. Benveniste), pp. 1–17. Berlin: Springer-Verlag. doi:10.1007/978-3-642-12796-0_1. (2) Fu, L.-L., Chelton, D. B., Le Traon, P.-Y. and Morrow, R. 2010. Eddy dynamics from satellite altimetry. *Oceanography*, **23**, 14–25, doi:10.5670/oceanog.2010.02.
 52. Geng, J., Williams, S. D. P., Teferle, F. N. and Dodson, A. H. 2012. Detecting storm surge loading deformations around the southern North Sea using subdaily GPS. *Geophysical Journal International*, **191**, 569–578, doi:10.1111/j.1365-246X.2012.05656.x.
 53. Menéndez, M. and Woodworth, P. L. 2010. Changes in extreme high water levels based on a quasi-global tide-gauge dataset. *Journal of Geophysical Research*, **115**, C10011, doi:10.1029/2009JC005997.
 54. Abeyirigunawardena, D. S. and Walker, I. J. 2008. Sea level responses to climatic variability and change in Northern British Columbia. *Atmosphere-Ocean*, **46**, 277–296, doi:10.3137/ao.460301. (2) Haigh, I., Nicholls, R. and Wells, N. 2010. Assessing changes in extreme sea levels: application to the English Channel, 1900–2006. *Continental Shelf Research*, **30**, 1042–1055, doi:10.1016/j.csr.2010.02.002.

55. For example, Lowe, J. A., Gregory, J. M. and Flather, R. A. 2001. Changes in the occurrence of storm surges around the United Kingdom under a future climate scenario using a dynamic storm surge model driven by the Hadley Centre climate models. *Climate Dynamics*, **18**, 179–188, doi:10.1007/s003820100163.
56. For example see, Wakelin, S. L., Woodworth, P. L., Flather, R. A. and Williams, J. A. 2003. Sea-level dependence on the NAO over the NW European Continental Shelf. *Geophysical Research Letters*, **30**, 1403, doi:10.1029/2003GL017041.
57. For example see, Woodworth, P. L., Flather, R. A., Williams, J. A., Wakelin, S. L. and Jevrejeva, S. 2007. The dependence of UK extreme sea levels and storm surges on the North Atlantic Oscillation. *Continental Shelf Research*, **27**, 935–946. doi:10.1016/j.csr.2006.12.007.
58. Pratt, I. 1995. The storm surge of 21 February 1993. *Weather*, **50**, 42–48, doi:10.1002/j.1477-8696.1995.tb06075.x.
59. For an example of asymmetry between positive and negative surges in tropical areas, see Peng, M., Xie, L. and Pietrafesa, L. J. 2006. Tropical cyclone induced asymmetry of sea level surge and fall and its presentation in a storm surge model with parametric wind fields. *Ocean Modelling*, **14**, 81–101, doi:10.1016/j.ocemod.2006.03.004.
60. Bjerknes, J. and Solberg, H. 1922. Life cycle of cyclones and the polar front theory of atmospheric circulation. *Geofysiker Publikationer*, **3**, 3–18.
61. Forel, F.-A. 1901. *Handbuch der Seenkunde: Allgemeine Limnologie*. Stuttgart, Germany: J. Engelhorn.
62. Heaps, N. S., Mortimer, C. H. and Fee, E. J. 1982. Numerical models and observations of water motion in Green Bay, Lake Michigan. *Philosophical Transactions of the Royal Society of London, A*, **306**, 371–398, doi:10.1098/rsta.1982.0091.
63. Donn, W. L. and Wolf, D. M. 1972. Seiche and water level fluctuations in Grindavik Harbor, Iceland. *Limnology and Oceanography*, **17**, 639–643.
64. Golmen, L. G., Molvaer, J. and Magnusson, J. 1994. Sea level oscillations with super-tidal frequency in a coastal embayment of western Norway. *Continental Shelf Research*, **14**, 1439–1454, doi:10.1016/0278-4343(94)90084-1.
65. (1) Chapman, D. C. and Giese, G. S. 1990. A model for the generation of coastal seiches by deep sea internal waves. *Journal of Physical Oceanography*, **20**, 1459–1467, doi:10.1175/1520-0485(1990)020<1459:AMFTGO>2.0.CO;2. (2) Giese, G. S. and Chapman, D. C. 1993. Coastal seiches. *Oceanus*, **36**(1), 38–46.
66. Okihiro, M., Guza, R. T. and Seymour, R. J. 1993. Excitation of seiche observed in a small harbor. *Journal of Geophysical Research*, **98**, C10, doi:10.1029/93JC01760.
67. Muir-Wood, R. and Mignan, A. 2009. A phenomenological reconstruction of the M_w 9 November 1st 1755 earthquake source. In *The 1755 Lisbon Earthquake: Revisited* (eds. L. A. Mendes-Victor et al.), pp. 121–146. Geotechnical, Geological, and Earthquake Engineering 7, doi:10.1007/978-1-4020-8609-0_8. Springer Publishing.
68. Bondevik, S., Gjevik, B. and Sørensen, M. B. 2013. Norwegian seiches from the giant 2011 Tohoku earthquake. *Geophysical Research Letters*, **40**, 3374–3378, doi:10.1002/grl.50639.
69. Kulikov, E. A., Rabinovich, A. B., Thomson, R. E. and Bornhold, B. D. 1996. The landslide tsunami of November 3, 1994, Skagway Harbor, Alaska. *Journal of Geophysical Research*, **101**, C3, doi:10.1029/95JC03562.
70. (1) Wilson, B. W. 1972. Seiches. *Advances in Hydrosience*, **8**, 1–94. (2) Sorensen, R. M. 1978. *Basic Coastal Engineering*. Hoboken, NJ: John Wiley.
71. Proudman, J. 1953. *Dynamical Oceanography*. London: Methuen.
72. (1) Murty, T. S. 1977. *Seismic Sea Waves: Tsunamis*. Ottawa: Department of Fisheries and the Environment, Fisheries and Marine Service. (2) Giese, G. S., Chapman, D. C., Black, P. G. and Fornshell, J. A. 1990. Causation of large-amplitude coastal seiches on the Caribbean coast of Puerto Rico. *Journal of Physical Oceanography*, **20**, 1449–1458, doi:10.1175/1520-0485(1990)020<1449:COLACS>2.0.CO;2.
73. Rabinovich, A. B. 2010. Seiches and harbor oscillations. In *Handbook of Coastal Engineering* (ed. Y.C. Kim), pp. 193–236. Hackensack, NJ: World Scientific Publishing.
74. Joseph, A. 2011. *Tsunamis: Detection, Monitoring, and Early-Warning Technologies*. Burlington, MA: Academic Press.
75. Woodworth, P. L., Pugh, D. T., Meredith, M. P. and Blackman, D. L. 2005. Sea level changes at Port Stanley, Falkland Islands. *Journal of Geophysical Research*, **110**, C06013, doi:10.1029/2004JC002648.
76. Dragani, W. C., Mazio, C. A. and Nuñez, M. N. 2002. Sea level oscillations in coastal waters of the Buenos Aires province, Argentina. *Continental Shelf Research*, **22**, 779–790, doi:10.1016/S0278-4343(01)00096-36.
77. Cartwright, D. E. and Young, C. M. 1974. Seiches and tidal ringing in the sea near Shetland. *Proceedings of the Royal Society of London, A*, **338**, 111–128, doi:10.1098/rspa.1974.0077.
78. Wijeratne, E. M. S., Woodworth, P. L. and Pugh, D. T. 2010. Meteorological and internal wave forcing of seiches along the Sri Lanka coast. *Journal of Geophysical Research*, **115**, C03014, doi:10.1029/2009JC005673.

79. Pugh, D. T. 1979. Sea levels at Aldabra Atoll, Mombasa and Mahe, western equatorial Indian Ocean, related to tides, meteorology and ocean circulation. *Deep Sea Research Part A*, **26**, 237–258, doi:10.1016/0198-0149(79)90022-0.
80. Lowry, R., Pugh, D. T. and Wijeratne, E. M. S. 2008. Observations of seiche and tides around the islands of Mauritius and Rodrigues. *Western Indian Ocean Journal of Marine Science*, **7**, 15–28.
81. Morison, M. and Imberger, J. 1992. Water level oscillations in Esperance Harbour. *Journal of Waterway, Port, Coastal and Ocean Engineering*, **118**, 352–367, doi:10.1061/(ASCE)0733-950X(1992)118:4(352).
82. (1) Rabinovich, A. B. and Monserrat, S. 1996. Meteorological tsunamis near the Balearic and Kuril Islands: descriptive and statistical analysis. *Natural Hazards*, **13**, 55–90, doi:10.1007/BF00156506. (2) Rabinovich, A.B. and Monserrat, S. 1998. Generation of meteorological tsunamis (large amplitude seiches) near the Balearic and Kuril Islands. *Natural Hazards*, **18**, 27–55, doi:10.1023/A:1008096627047.
83. Drago, A. 2009. Sea level variability and the “Milghuba” seiche oscillations in the northern coast of Malta, Central Mediterranean. *Physics and Chemistry of the Earth*, **34**, 948–970, doi:10.1016/j.pce.2009.10.002.
84. Airy, G. B. 1878. On the tides at Malta. *Philosophical Transactions of the Royal Society of London*, **169**, 123–138, doi:10.1098/rstl.1878.0006.
85. Leder, N. and Orlić, M. 2004. Fundamental Adriatic seiche recorded by current meters. *Annales Geophysicae*, **22** 1449–1464.
86. Lionello, P., Cavaleri, L., Nissen, K. M. *et al.* 2012. Severe marine storms in the Northern Adriatic: characteristics and trends. *Physics and Chemistry of the Earth*, 40–41, 93–105, doi:10.1016/j.pce.2010.10.002.
87. Lisitzin, E. 1974. *Sea-Level Changes*. Amsterdam: Elsevier.
88. Defant, A. 1961. *Physical Oceanography* (Two volumes). Oxford: Pergamon Press.
89. Monserrat, S., Vilibić, I. and Rabinovich, A. B. 2006. Meteotsunamis: atmospherically induced destructive ocean waves in the tsunami frequency band. *Natural Hazards and Earth System Sciences*, **6**, 1035–1051, www.nat-hazards-earth-syst-sci.net/6/1035/2006/.
90. (1) Proudman, J. 1929. The effects on the sea of changes in atmospheric pressure. *Monthly Notices of the Royal Astronomical Society Geophysical Supplement No.2*, 197–209. (2) Doodson, A. T. and Warburg, H. D. 1941. *Admiralty Manual of Tides*. London: His Majesty’s Stationery Office. (3) Pugh, D. T. 1987. *Tides, Surges and Mean Sea-Level: A Handbook for Engineers and Scientists*. Chichester: Wiley.
91. Vilibić, I. 2008. Numerical simulations of the Proudman resonance. *Continental Shelf Research*, **28**, 574–581, doi:10.1016/j.csr.2007.11.005.
92. Orlić, M., 1980. About a possible occurrence of the Proudman resonance in the Adriatic. *Thalassia Jugoslavica*, **16**(1), 79–88.
93. Vilibić, I. and Šepić, J. 2009. Destructive meteotsunamis along the eastern Adriatic coast: overview. *Physics and Chemistry of the Earth*, **34**, 904–917, doi:10.1016/j.pce.2009.08.004.
94. Hibiya, T. and Kajiura, K. 1982. Origin of the Abiki phenomenon (a kind of seiche) in Nagasaki Bay. *Journal of the Oceanographical Society of Japan*, **38**, 172–182, doi:10.1007/BF02110288.
95. Mercer, D., Sheng, J., Greatbatch, R. J. and Bobanović, J. 2002. Barotropic waves generated by storms moving rapidly over shallow water. *Journal of Geophysical Research*, **107**, 3152, doi:10.1029/2001JC001140.
96. Vennell, R. 2007. Long barotropic waves generated by a storm crossing topography. *Journal of Physical Oceanography*, **37**, 2809–2823, doi:10.1175/2007JPO3687.1.
97. (1) Greenspan, H. P. 1956. The generation of edge waves by moving pressure disturbances. *Journal of Fluid Mechanics*, **1**, 574–592, doi:10.1017/S002211205600038X. (2) Donn, W. L. and Ewing, M. 1956. Stokes’ edge waves in Lake Michigan. *Science*, **124**, 1238–1242, doi:10.1126/science.124.3234.1238. (3) Liu, P.L.-F., Monserrat, S. and Marcos, M. 2002. Analytical simulation of edge waves observed around the Balearic Islands. *Geophysical Research Letters*, **29**, 1847, doi:10.1029/2002GL015555.
98. Jansa, A., Monserrat, S. and Gomis, D. 2007. The rissaga of 15 June 2006 in Ciutadella (Menorca), a meteorological tsunami. *Advances in Geosciences*, **12**, 1–4, doi:10.5194/adgeo-12-1-2007.
99. (1) Haslett, S. K. and Bryant, E. A. 2009. Meteorological tsunamis in southern Britain: an historical review. *The Geographical Review*, **99**, 146–163, doi:10.1111/j.1931-0846.2009.tb00424.x. (2) Haslett, S. K., Mellor, H. E. and Bryant, E. A. 2009. Meteo-tsunami hazard associated with summer thunderstorms in the United Kingdom. *Physics and Chemistry of the Earth*, **34**, 1016–1022, doi:10.1016/j.pce.2009.10.005.
100. Tappin, D. R., Sibley, A., Horsburgh, K. *et al.* 2013. The English Channel ‘tsunami’ of 27 June 2011: a probable meteorological source. *Weather*, **68**, 144–152, doi:10.1002/wea.2061.
101. See Chapter 5 of Huess, V. 2000. Sea level variations in the North Sea from tide gauges, altimetry and modelling. PhD Thesis, University of Copenhagen. Danish Meteorological Institute Scientific Report 01–08.

102. Horsburgh, K. and Horritt, M. 2006. The Bristol Channel floods of 1607: reconstruction and analysis. *Weather*, **61**, 272–277, doi:10.1256/wea.133.05.
103. DMI, 2005. *Tsunami Risk Assessment for Danish, Faroes and Greenland waters* (eds. E. Buch et al.). Danish Meteorological Institute Technical Report No. 05–08.
104. Newig, J. and Kelletat, D. 2011. The North Sea Tsunami of June 5, 1858. *Journal of Coastal Research*, **27**, 931–941, doi:10.2112/JCOASTRES-D-10-00098.1.
105. Thomson, R. E., Rabinovich, A. B., Fine, I. V. et al. 2009. Meteorological tsunamis on the coasts of British Columbia and Washington. *Physics and Chemistry of the Earth*, **34**, 971–988, doi:10.1016/j.pce.2009.10.003.
106. Churchill, D. D., Houston, S. H. and Bond, N. A. 1995. The Daytona Beach wave of 3–4 July 1992: a shallow-water gravity wave forced by a propagating squall line. *Bulletin of the American Meteorological Society*, **76**, 21–32, doi:10.1175/1520-0477(1995)076<0021:TDBWOJ>2.0.CO;2.
107. Dragani, W. C., Mazio, C. A. and Nuñez, M.N. 2002. Sea level oscillations in coastal waters of the Buenos Aires province, Argentina. *Continental Shelf Research*, **22**, 779–790, doi:10.1016/S0278-4343(01)00096-6.
108. Wijeratne, E. M. S., Pattiaratchi, C. B., Haigh, I. D. and Eliot, M. 2013. Observations and numerical modelling of meteotsunamis along the south-west Australian coast. (Submitted for publication.)
109. (1) Longuet-Higgins, M. S. and Stewart, R. W. 1963. A note on wave set-up. *Journal of Marine Research*, **21**, 4–10. (2) Longuet-Higgins, M. S. and Stewart, R. W. 1964. Radiation stresses in water waves; a physical discussion, with applications. *Deep-Sea Research*, **11**, 529–562.
110. Bowen, A., Inman, D. and Simmons, V. 1968. Wave ‘set-down’ and set-up. *Journal of Geophysical Research*, **73**, 8, doi:10.1029/JB073i008p02569.
111. (1) Dean, R. G. and Walton, T. L. 2009. Wave setup. Chapter 1 in *Handbook of Coastal and Ocean Engineering*. World Scientific. <http://www.worldscibooks.com/engineering/6914.html>. (2) Stockdon, H. F., Holman, R. A., Howd, P. A. and Sallenger, A. H. Jr. 2006. Empirical parameterization of setup, swash, and runup. *Coastal Engineering*, **53**, 573–588, doi:10.1016/j.coastaleng.2005.12.005.
112. (1) Tait, R. 1972. Wave set-up on coral reefs. *Journal of Geophysical Research*, **77**, 12, doi:10.1029/JC077i012p02207. (2) Vetter, O., Becker, J. M., Merrifield, M. A. et al. 2010. Wave setup over a Pacific Island fringing reef. *Journal of Geophysical Research*, **115**, C12066, doi:10.1029/2010JC006455.
113. Aucan, J., Hoeke, R. and Merrifield, M. A. 2012. Wave-driven sea level anomalies at the Midway tide gauge as an index of North Pacific storminess over the past 60 years. *Geophysical Research Letters*, **39**, L17603, doi:10.1029/2012GL052993.
114. Munk, W. H. 1949. Surf beats. *Eos, Transactions of the American Geophysical Union*, **30**, 849–854.
115. Kinsman, B. 1965. *Wind Waves: Their Generation and Propagation on the Ocean Surface*. Englewood Cliffs, NJ: Prentice Hall.
116. Thompson, R. O. R. Y. and Hamon, B. V. 1980. Wave setup of harbor water levels. *Journal of Geophysical Research*, **85**, C2, doi:10.1029/JC085iC02p01151.
117. Ponte, R. M. 1993. Variability in a homogeneous global ocean forced by barometric pressure. *Dynamics of Atmospheres and Oceans*, **18**, 209–234, doi:10.1016/0377-0265(93)90010-5.
118. See for example, Pugh, D. T. and Thompson, K. R. 1986. The subtidal behaviour of the Celtic Sea: I. Sea level and bottom pressures. *Continental Shelf Research*, **5**, 239–319, doi:10.1016/0278-4343(86)90001-4.
119. Ponte, R. 1994. Understanding the relation between wind- and pressure-driven sea level variability. *Journal of Geophysical Research*, **99**, C4, doi:10.1029/94JC00217.
120. (1) Chao, Y. and Fu, L.-L. 1995. A comparison between the TOPEX/POSEIDON data and a global ocean general circulation model during 1992–1993. *Journal of Geophysical Research*, **100**, C12, doi:10.1029/95JC02260. (2) Fu, L.-L. and Smith, R. D. 1996. Global ocean circulation from satellite altimetry and high-resolution computer simulation. *Bulletin of the American Meteorological Society*, **77**, 2625–2636, doi: [http://dx.doi.org/10.1175/1520-0477\(1996\)077<2625:GOCFSA>2.0.CO;2](http://dx.doi.org/10.1175/1520-0477(1996)077<2625:GOCFSA>2.0.CO;2).
121. Quinn, K. J. and Ponte, R. M. 2012. High frequency barotropic ocean variability observed by GRACE and satellite altimetry. *Geophysical Research Letters*, **39**, L07603, doi:10.1029/2012GL051301.
122. (1) Fukumori, I., Raghunath, R. and Fu, L.-L. 1998. Nature of global large-scale sea level variability in relation to atmospheric forcing: a modeling study. *Journal of Geophysical Research*, **103**, C3, doi:10.1029/97JC02907. (2) Stammer, D., Wunsch, C. and Ponte, R. M. 2000. De-aliasing of global high frequency barotropic motions in altimeter observations. *Geophysical Research Letters*, **27**(8), 1175–1178, doi:10.1029/1999GL011263.
123. (1) Webb, D. J. and de Cuevas, B. A. 2002. An ocean resonance in the Southeast Pacific. *Geophysical Research Letters*, **29**(8), 93-1-93-3, doi:10.1029/2001GL014259. (2) Webb, D. J. and de Cuevas, B. A. 2002. An ocean resonance in the Indian sector of the Southern Ocean. *Geophysical Research Letters*, **29**(14), 9-1-9-3, doi:10.1029/2002GL015270.
124. Fu, L.-L., Cheng, B. and Qui, B. 2001. 25-day period large-scale oscillations in the Argentine Basin revealed

- by the TOPEX/Poseidon altimeter. *Journal of Physical Oceanography*, **31**, 506–517, doi:10.1175/1520-0485(2001)031<0506:DPLSOI>2.0.CO;2.
125. Hughes, C. W., Stepanov, V. N., Fu, L.-L., Barnier, B. and Hargreaves, G. W. 2007. Three forms of variability in Argentine Basin ocean bottom pressure. *Journal of Geophysical Research*, **112**, C01011, doi:10.1029/2006JC003679.
126. (1) Woodworth, P. L., Vassie, J. M., Hughes, C. W. and Meredith, M. P. 1996. A test of the ability of TOPEX/POSEIDON to monitor flows through the Drake Passage. *Journal of Geophysical Research*, **101**, C5, doi:10.1029/96JC00350. (2) Hughes, C. W., Meredith, M. P. and Heywood, K. 1999. Wind-driven transport fluctuations through Drake Passage: a southern mode. *Journal of Physical Oceanography*, **29**, 1971–1992, doi:10.1175/1520-0485(1999)029<1971:WDTFTD>2.0.CO;2.
127. (1) Aoki, S. 2002. Coherent sea level response to the Antarctic Oscillation. *Geophysical Research Letters*, **29**, 1950, doi:10.1029/2002GL015733. (2) Hughes, C. W., Woodworth, P. L., Meredith, M. P. *et al.* 2003. Coherence of Antarctic sea levels, Southern Hemisphere Annular Mode, and flow through Drake Passage. *Geophysical Research Letters*, **30**(9), 1464, doi:10.1029/2003GL017240. (3) Hibbert, A., Leach, H., Woodworth, P. L., Hughes, C. W. and Roussenov, V. M. 2010. Quasi-biennial modulation of the Southern Ocean coherent mode. *Quarterly Journal of the Royal Meteorological Society*, **136**, 755–768, doi:10.1002/qj.581.
128. Woodworth, P. L., Hughes, C. W., Blackman, D. L. *et al.* 2006. Antarctic peninsula sea levels: a real time system for monitoring Drake Passage transport. *Antarctic Science*, **18**(3), 429–436, doi:10.1017/S0954102006000472.
129. Hughes, C. W. and Stepanov, V. N. 2004. Ocean dynamics associated with rapid J2 fluctuations: importance of circumpolar modes and identification of a coherent Arctic mode. *Journal of Geophysical Research*, **109**, C06002, doi:10.1029/2003JC002176.
130. (1) Deland, R. J. 1964. Travelling planetary waves. *Tellus*, **16**, 271–273, doi:10.1111/j.2153-3490.1964.tb00166.x. (2) Madden, R. A. and Julian, P. R. 1972. Further evidence of global scale, 5-day pressure waves. *Journal of the Atmospheric Sciences*, **29**, 1464–1469, doi:10.1175/1520-0469(1972)029<1464:FEOGSD>2.0.CO;2. (3) Rodgers, C. D. 1976. Evidence for the five-day wave in the upper stratosphere. *Journal of the Atmospheric Sciences*, **33**, 710–711, doi:10.1175/1520-0469(1976)033<0710:EFTFDW>2.0.CO;2. (4) Wu, D. L., Hays, P. B. and Skinner, W. R. 1994. Observations of the 5-day wave in the mesosphere and lower thermosphere. *Geophysical Research Letters*, **21**, 24, doi:10.1029/94GL02660.
131. Madden, R. A. and Julian, P. R. 1994. Observations of the 40–50-day tropical oscillation: a review. *Monthly Weather Review*, **122**, 814–837, doi:10.1175/1520-0493(1994)122<0814:OOTDIO>2.0.CO;2.
132. Ponte, R. M. 1997. Nonequilibrium response of the global ocean to the 5-day Rossby–Haurwitz wave in atmospheric surface pressure. *Journal of Physical Oceanography*, **27**, 2158–2168, doi:10.1175/1520-0485(0)027<2158:NROTGO>2.0.CO;2.
133. Luther, D. S. 1982. Evidence of a 4–6 day barotropic, planetary oscillation of the Pacific Ocean. *Journal of Physical Oceanography*, **12**, 644–657, doi:10.1175/1520-0485(1982)012<0644:EOADBP>2.0.CO;2.
134. (1) Hamilton, K. 1985. A possible relationship between tropical ocean temperatures and the observed amplitude of the atmospheric (1,1) Rossby normal mode. *Journal of Geophysical Research*, **90**, D5, doi:10.1029/JD090iD05p08071. (2) Weber, R. and Madden R. A. 1993. Evidence of traveling external Rossby waves in the ECMWF analyses. *Journal of the Atmospheric Science*, **50**, 2994–3007, doi:10.1175/1520-0469(1993)050<2994:EOTERW>2.0.CO;2.
135. Woodworth, P. L., Windle, S. A. and Vassie, J. M. 1995. Departures from the local inverse barometer model at periods of 5 days in the central South Atlantic. *Journal of Geophysical Research*, **100**, C9, 18281–18290, doi:10.1029/95JC01741.
136. Mathers, E. L. and Woodworth, P. L. 2004. A study of departures from the inverse barometer response of sea level to air pressure forcing at a period of 5 days. *Quarterly Journal of the Royal Meteorological Society*, **130**, 725–738, doi:10.1256/qj.03.46.
137. Hirose, N., Fukumori, I. and Ponte, R. M. 2001. A non-isostatic global sea level response to barometric pressure near 5 days. *Geophysical Research Letters*, **28**, 12, doi:10.1029/2001GL012907.
138. Stepanov, V. N. and Hughes, C. W. 2006. Propagation of signals in basin-scale ocean bottom pressure from a barotropic model. *Journal of Geophysical Research*, **111**, C12002, doi:10.1029/2005JC003450.
139. Carrère, L. and Lyard, F. 2003. Modeling the barotropic response of the global ocean to atmospheric wind and pressure forcing: comparisons with observations. *Geophysical Research Letters*, **30**, 1275, doi:10.1029/2002GL016473.
140. Egbert, G. D. and Ray, R. D. 2003. Deviation of long-period tides from equilibrium: kinematics and geostrophy. *Journal of Physical Oceanography*, **33**, 822–839, doi:10.1175/1520-0485(2003)33<822:DOLTFE>2.0.CO;2.
141. Wunsch, C. and Gill, A. E. 1976. Observations of equatorially trapped waves in Pacific sea level variations. *Deep Sea Research and Oceanographic Abstracts*, **23**, 371–390, doi:10.1016/0011-7471(76)90835-4.

Mere anarchy is loosed upon the world,
 The blood-dimmed tide is loosed, and everywhere
 The ceremony of innocence is drowned.
W. B. Yeats, The Second Coming

8.1 Introduction

In the past few years, two giant tsunamis caused by undersea earthquakes have caused major loss of life and damage to coastal infrastructure.¹ On 26 December 2004, a moment magnitude (M_w) 9.3 megathrust earthquake, the third largest on record, took place along 1600 km of the subduction zone from Sumatra to the Andaman Islands in the eastern Indian Ocean [1, 2].² The resulting tsunami waves caused enormous damage, particularly in Indonesia, India, Sri Lanka and Thailand, and killed more than 230,000 people (Figure 8.1) [3, 4]. On 11 March 2011, the Tōhoku (or Sendai) $M_w = 9.0$ megathrust earthquake, the fourth largest on record, occurred 70 km off the east coast of Japan leaving some 20,000 people dead or missing and tremendous destruction of coastal infrastructure (Figure 8.2), including a major nuclear emergency at the Fukushima Daiichi power plant [5]. These two catastrophic events have had many important consequences including, it will be seen, within sea-level research.

Major tsunamis have happened throughout history. The geological record contains evidence for events such as the Holocene Storegga slides, which were submarine landslides on the continental slope of Norway [6]. The

largest slide, in approximately 8100–8200 BP, generated a tsunami that impacted coasts from northeast England to north of the Arctic Circle in Norway, and left evidence of its extent in well-defined sand layers [7, 8, 9]. The eastern Mediterranean has been impacted by tsunamis many times. Events have included the tsunami responsible for the demise of the Minoan civilisation in Crete following the Santorini (or Thera) volcanic eruption between 1630 and 1550 BC [10], and those caused by submarine earthquakes that impacted Alexandria in 356 and 1303 [11]. Lisbon in Portugal was destroyed by an earthquake and tsunami in 1755, waves from the tsunami reaching the south coasts of Britain and Ireland [12, 13]. In the nineteenth century, there were two giant tsunami events caused by volcanism at Tambora [14] and Krakatoa [15]. In the modern era, a tsunami accompanied an earthquake-induced submarine landslide on the Grand Banks off the east coast of Canada in 1929 [16]. This event was notable because the landslide was one of the first to be timed accurately from the loss of signals in marine telegraph cables; the times when a dozen cables were cut allowed an estimate of the maximum speed of the turbidity current (the down-slope flux of a mixture of sediment and water) of about 28 m/s [16, 17].

These are just a few examples to demonstrate that, while tsunamis are infrequent, they cannot be considered as freak events. For example, major tsunamis, sometimes resulting in loss of life, have occurred at different locations along the Sumatra subduction zone roughly every other year since the 2004 event [18]. However, estimating their ‘return period’ can be difficult when major events occur only every few hundred years or so. For this reason, considerable efforts have been made in recent years to assemble national and international ‘tsunami catalogues’, which are lists of recorded

¹ We have used ‘tsunamis’ as the plural of ‘tsunami’ as now seems to be standard. ‘Tsu-nami’ is Japanese for ‘harbour-wave’, referring to a wave that appears at the coast, and is less evident offshore, following an earthquake. Earthquakes can also generate waves (seiches) in harbours.

² Moment magnitude is now the most common measure of the size of an earthquake in terms of the energy released. For medium-sized earthquakes it is equivalent to the more familiar Richter scale, but the M_w scale does not saturate at its upper end so there is no upper limit to its magnitude, see http://en.wikipedia.org/wiki/Moment_magnitude_scale.



Figure 8.1 The remains of the tourist resort of Hikkaduwa on the southwest coast of Sri Lanka following the Sumatra tsunami. Photograph by Mr Jagath Rajapaksha, National Aquatic Resources Research and Development Agency, Sri Lanka, provided by Dr E. M. S. Wijeratne, University of Western Australia.



Figure 8.2 An aerial view of damage to Sukuiso, Japan, a week after the Tohoku earthquake and subsequent tsunami devastated the area. Sukuiso is located on the east coast of Japan, north of Sendai. Photograph by Dylan McCord, U.S. Navy, obtained from www.ngdc.noaa.gov.

events, estimates of their magnitudes, and assessments of the damage caused [19, 20]. Cataloguing smaller tsunami events can be difficult when they occur at higher latitudes during storms [21].

Major tsunamis occur most often in the Pacific Ocean caused by submarine earthquakes around the

'Ring of Fire' (Figure 8.3). An example includes the April 1946 tsunami following an earthquake near the Aleutian Islands that killed 160 people in Hilo, Hawaii, and led to the establishment of a Hawaiian Tsunami Warning Center [22]. In May 1960, the Valdivia earthquake, the largest earthquake of the

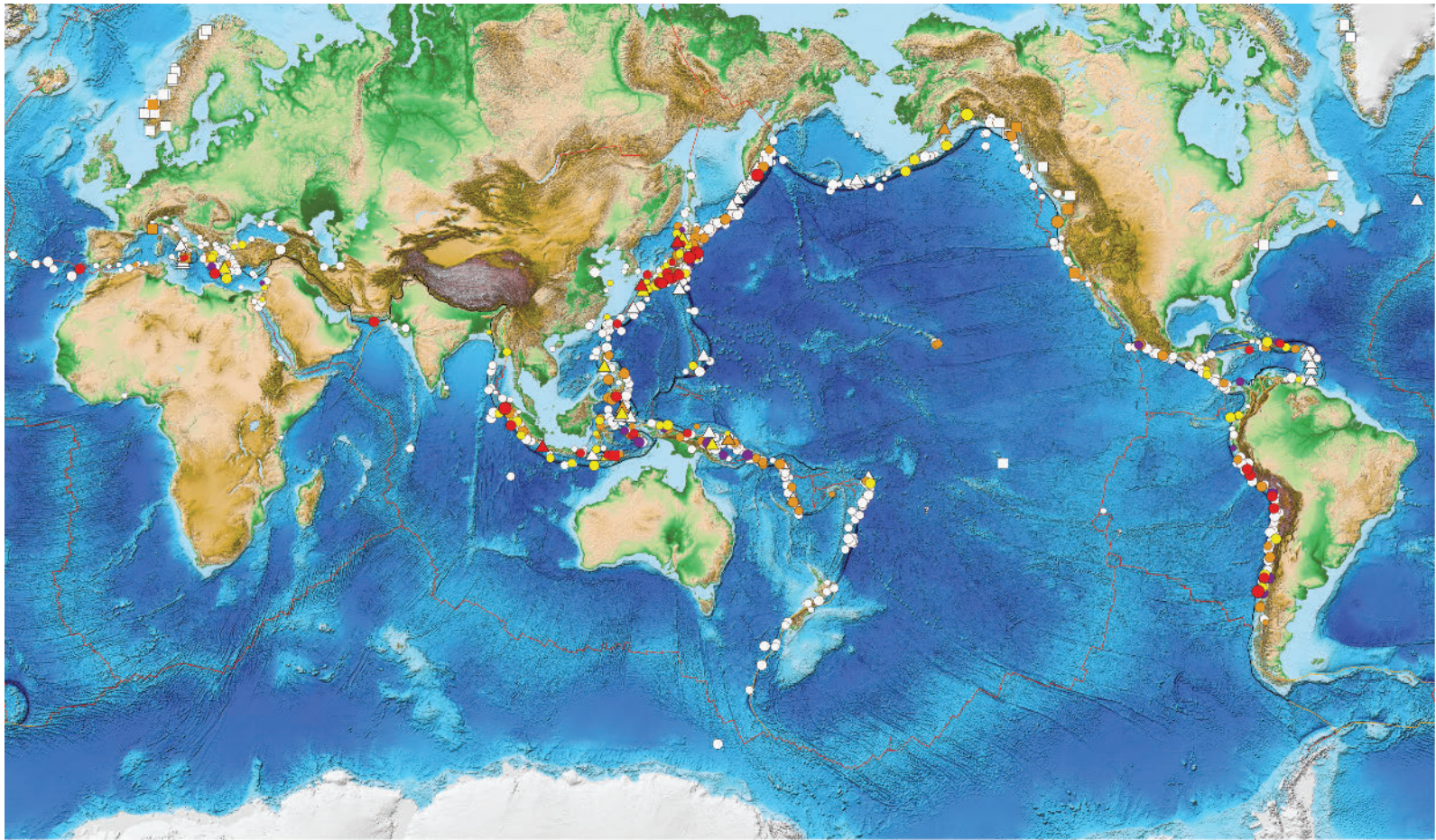


Figure 8.3 Map of tsunami sources around the world since 1410 BC from the Intergovernmental Tsunami Information Center catalogue (<http://itic.ioc-unesco.org>) and NGDC/NOAA (<http://www.ngdc.noaa.gov>). Symbols indicate volcanic eruption (triangle), landslide (square), unknown (?) and earthquake (circle) with small to large circles for magnitudes 6 to 9. Colours indicate number of deaths: none (white), up to 50 (brown), up to 100 (purple), up to 1000 (yellow) and over 1000 (red). The two websites and also textbooks on tsunamis [20, 27] contain lists of major events in terms of earthquake magnitude and number of deaths. Map provided by Paula Dunbar, NGDC.

twentieth century ($M_w = 9.5$), occurred off the coast of Chile, producing a transoceanic tsunami that killed thousands around Pacific coastlines, particularly in Chile, Hawaii and Japan. The Hawaii facility was afterwards renamed the Pacific Tsunami Warning Center (PTWC), as the operational headquarters for the Pacific Tsunami Warning System (PTWS) [22, 23]. The PTWS became the model for warning systems in other areas as we describe in Chapter 12. Their centres depend primarily upon seismic information for warnings, although all earthquakes do not result in tsunamis and all tsunamis are not caused by earthquakes. Other important components of the PTWS and other regional systems are networks of tide gauges and, more recently, pressure sensors on the seabed which report their data via surface buoys, to provide confirmation of a tsunami's existence [24].

Many of the tide gauges used for tsunami warning are also part of conventional sea-level networks used for tidal measurements, flood warning or climate research. The technical requirements for conventional gauges are primarily ones of accuracy and long-term stability of datum control, with sampling (or integration) of sea level every 6 or 15 minutes or even hourly at some sites (Chapter 2). These requirements contrast with those of a tsunami station, which are primarily to do with reliability and redundancy of instrumentation, rapid transmission of data to a centre, and high-rate sampling of sea level at typically once per minute or faster [25]. Nevertheless, many sea-level stations are equipped to accommodate both sets of requirements.

In this chapter, we explain why tsunamis happen, how they propagate from their source, and how they are seen in tide gauge and other sea-level data. In addition, we describe the technologies available for monitoring tsunamis. There are other overviews of tsunamis available [26], and more detailed treatments [20, 27, 28, 29, 30]. However, it is necessary for sea-level scientists to be aware of the possibility of tsunamis in their records, so the present chapter forms an important complement to others in this book. In addition, it is a recognition of the fact that the organisation of international sea-level programmes, such as the Global Sea-Level Observing System (GLOSS), is becoming more closely coordinated with developments in tsunami warning systems [31].

8.2 Why tsunamis happen

Tsunamis occur whenever large volumes of water are displaced and equilibrium is restored by the propagation of long waves across the ocean. There are six main

reasons for them, as discussed below: a seventh concerning 'meteotsunamis', which are meteorological in origin, is discussed in Chapter 7.

We can divide tsunamis, somewhat arbitrarily, into two categories, *transoceanic* ones and *local* ones, with the distinctions between them being determined primarily by their energy and period. These two parameters can be related as the largest undersea earthquakes that produce the most energetic and longer distance tsunamis tend to have displacements occurring across a larger area of seabed which, as shown below, determines the wavelength and period of the tsunami. The periods of tsunami waves are within the range of minutes to an hour (10^2 – 10^4 seconds). For example, the 2004 Sumatra tsunami was an extremely energetic event that was able to propagate around the world and had a predominant period of approximately 40 minutes [33].³ The 2011 Tōhoku event had a predominant period of approximately 25 minutes and crossed the Pacific into the Atlantic and Indian Oceans [34]. However, the tsunami waves associated with the underwater landslides following the $M_w = 7.1$ earthquake at Papua New Guinea in 1998 had shorter periods of the order of minutes [35], and they would have dispersed rapidly with distance.⁴ Of course, both categories of tsunami can result in major loss of life near their source: for example, over 2200 people were killed at Papua New Guinea [37].⁵

³ Although a tsunami may have a predominant period, its spectrum will be far from monochromatic, and will encompass a broad range of periods that can be related to the geological characteristics of the source. Examples of spectra for the 2004 Sumatra tsunami can be found in Reference 32.

⁴ A weak tsunami signal was detected at tide gauges at several distant western Pacific islands and in Japan, see http://nctr.pmel.noaa.gov/PNG/png_pmel.html. These signals contain a longer period component associated with the first tsunami waves from the earthquake itself (Dr A. B. Rabinovich, private communication and see also Reference 36).

⁵ The National Geophysical Data Center/World Data Service for Geophysics (NGDC/WDS) database contains 1192 confirmed tsunami events between 1410 BC and AD 2012. Of these, 236 events are known to have caused deaths and the actual numbers are known for 181 events containing a total of 559,358 deaths. The majority occurred in the local region, within one hour of the source event. In the Mediterranean, Atlantic and Caribbean, 100 per cent of fatalities have occurred locally. In the Pacific, 99 per cent of deaths have occurred in the local region (<1 hour) and 1 per cent in the far field (>3 hours or >1000 km from the source). In the Indian Ocean, primarily because of the large contribution from the 2004 Sumatra event, 78, 3 and 19 per cent of deaths have occurred during <1 hour, between 1–3 hours and >3 hours, respectively, compared to 89, 1 and 10 per cent distributed globally. Note that far-field deaths in the 2004 Sumatra event occurred when no tsunami warning system was in place. (Information from Paula Dunbar, NGDC/WDS.)

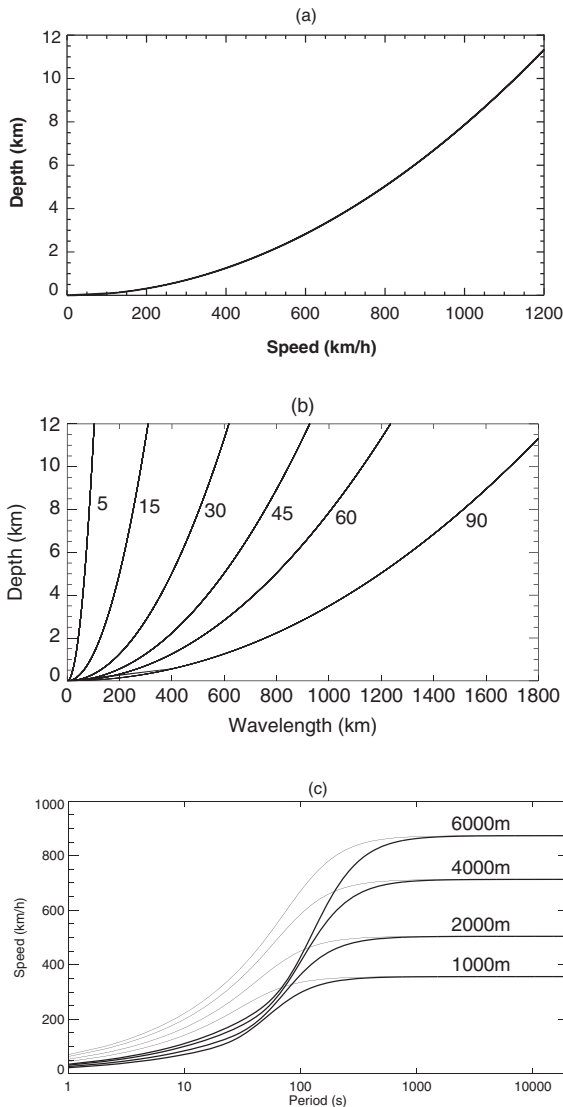


Figure 8.4 The relationships between (a) water depth and velocity of a long wave in deep water, (b) water depth and wavelength of waves with a specified period (in minutes), and (c) velocity and period for different water depths. In (c), the thin and thick lines show the phase and group velocities respectively.

The period of the tsunami wave can be considered to have approximately the same value as it travels across the ocean, whereas its wavelength and speed will vary depending upon the ocean depth (Figure 8.4a, b). The wavelength at its source is determined by the spatial scale of the displacement, and the period can be calculated by $\tau = c/\lambda$, where λ is the wavelength and c is the phase velocity at the source given approximately by $c = \sqrt{gD_L}$, g being the acceleration due to gravity and D_L the local water depth.⁶ The amplitude of the tsunami

will be determined by the magnitude of the displacement [38].

As mentioned above, the importance of a tsunami at some distance from its source depends on two related parameters. The first and most important is its initial energy, which diminishes with distance from the source. Its period enters into consideration via a property of water waves called *dispersion* or, more precisely, *frequency dispersion* [39, 40, 41, 44]. A tsunami wave will not contain a single wavelength but a spectrum with a range of wavelengths larger and smaller than an average one. The phase velocity of an individual component along the tsunami's path is given by the dispersion relation $\omega^2 = gk \tanh(kD)$, where $\omega = 2\pi/\tau$ is its angular frequency, $k = 2\pi/\lambda$ is its wave number and D is water depth, leading to:

$$c = \frac{\omega}{k} = \sqrt{\frac{g \tanh(kD)}{k}} \quad (8.1)$$

At long wavelength, then $c = \sqrt{gD}$, and within a spectrum of similarly large wavelengths, phase velocity will not depend on wavelength or period and will have the same value. The overall wave is said to be *non-dispersive*. However, for a shorter period such that $\lambda \sim D$, then it is clear from Equation 8.1 that phase velocity does depend on wavelength and that longer wavelengths will travel faster than shorter ones. In this case, the overall wave is *dispersive*. By spreading the energy out as it progresses, the eventual tsunami impact on a distant shore is much reduced. We return to the issues of tsunami propagation and modelling below.

8.2.1 Submarine earthquakes

Most tsunamis are caused by submarine earthquakes. Specifically, over half of tsunamis worldwide occur in the Pacific Ocean and over 80 per cent of those are due to submarine earthquakes [19, 27].⁷ In some cases, a tsunami can originate from an earthquake that has an epicentre that is actually on land near the coast, with the seismic waves disturbing the nearby water. However, most tsunamis occur due to earthquakes

⁶ The parameter c might be better called phase speed. However, many tsunami authors refer to it as velocity.

⁷ Tsunami statistics are best for the Pacific where earthquakes over the past 2000 years have been responsible for approximately 82 per cent of tsunamis, landslides (submarine and subaerial) approximately 5 per cent, volcanoes 5 per cent, and about 8 per cent of unclear origin [27]. Meteotsunamis (Chapter 7) are relatively rare events worldwide and correspond to perhaps several per cent of the number of tsunamis [20].

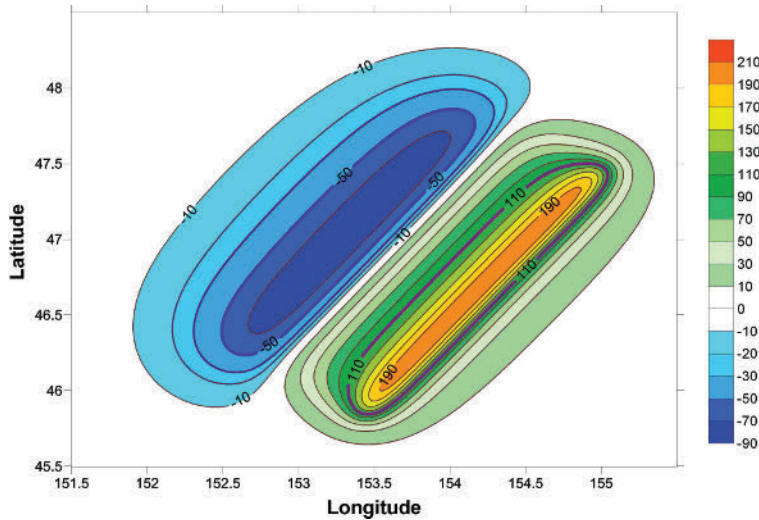


Figure 8.5 An example of a source function (bottom deformation), in this case shown in centimetres for the Kuril Islands tsunami of November 2006. From [115].

beneath the sea floor (submarine earthquakes), and especially due to the seismic activity at subduction zones such as that near Sumatra [42]. The release of energy stored elastically in a fault can result in a rapid vertical displacement of the sea floor and the water above it, with about 1 per cent of the total energy released by the earthquake going into tsunami generation, the majority of the energy being transmitted as seismic vibrations in the solid Earth [43].⁸

The energy of the tsunami can be calculated from the change in potential energy of the water due to the assumed near-instantaneous displacement:⁹

$$S = \frac{1}{2} \rho g \int_S b^2 dS \quad (8.2)$$

where ρ is water density, g is acceleration due to gravity and a vertical displacement b occurs over an area element dS [44]. A map of b is called a *source function* (Figure 8.5).

For the study of historical events, a source function can sometimes be inferred from general knowledge of the geology of the region. However, its exact form remains uncertain for some important historical tsunamis, such as the 1755 Lisbon event [13]. Surveys of the seabed can provide direct evidence of larger

displacements in an area. For more recent events, characteristics of the source functions have been obtained by inverse modelling techniques, employing oceanographic measurements of the resulting tsunamis [45].

The energy available to the Sumatra tsunami was calculated using best estimates of the probable source function as approximately 4.1 or 5.4 times 10^{15} J [2, 46, 47], which corresponds to less than 0.5 per cent of the strain energy released by the faulting [2]. However, an important aspect of the Sumatra event was that it was not instantaneous but had the longest recorded duration for an earthquake rupture (>1000 s). The rupture propagated along the length of the ~200 km wide Andaman fault at a speed of approximately 1.7 km/s, with the vertical displacement exceeding 10 m in some places (more than 20 m horizontally) [48, 97]. Consequently, modelling of the resulting tsunami has been more challenging than implied by simple inspection of Equation 8.2, and we refer to the success of this modelling below. Altimeter observations have suggested that horizontal as well as vertical forces contributed to the tsunami energy [49].

The Tōhoku event represented 250 km³ of displaced water within an area of rupture 300–400 km long and 100 km wide [34]. The spatial extent of the rupture determined the predominant tsunami period of approximately 25 minutes compared to 40 minutes for the Sumatra event, while the magnitude of the rupture determined the tsunami amplitude [50]. Deep-sea pressure gauges, or ‘tsunameters’, together with satellite altimetry, have suggested that the energy of the Tōhoku tsunami was about a fifth of that in the Sumatra event (3×10^{15} and 1.7×10^{16} J respectively) [34].

⁸ Note that not all fault movements have a vertical component. For example, the large submarine earthquake ($M_w = 8.6$) that occurred 600 km from the Indonesian coast on 11 April 2012, produced little in the way of a tsunami as faulting was primarily a lateral strike-slip movement.

⁹ Most earthquakes occur over several, or several tens, of seconds. However, this is considerably shorter than tsunami periods and so can be considered near-instantaneous.

Methods for calculating source functions have changed radically following the development of national networks of GPS stations that can provide real-time data on high-frequency land movements.¹⁰ These data, combined with seismic information from around the world, enable a first estimate of an earthquake's magnitude to be determined accurately and rapidly [51], after which there are established techniques for estimating the resulting displacements and, thereby, the tsunami at its source [52]. If a first estimate of the size of a submarine earthquake can be made with an uncertainty in M_w of 0.2, then the resulting tsunami amplitude should be determined to within a factor of two [30, 34]. Numerical tsunami models based on this approach have been shown to give good results when compared to observations. In parallel, a complementary real-time method for estimating the energy of the tsunami uses data from tsunameters located near the source together with combinations of pre-computed possible source functions [34, 53].

General constraints on tsunami generation due to sea-floor displacements are that the earthquakes must be larger than a threshold M_w of about 7.5 for events in the regions discussed above, although the threshold will vary depending on the local geological context. The tsunamis must have wavelengths at least three times the ocean depth at source because waves with shorter wavelengths cannot be generated by rapid movements of the sea floor [30].

Sea floor displacements that have a much shorter spatial scale than Sumatra or Tōhoku can still generate tsunamis that have major coastal impacts when they occur nearby. In this case they are called *local* (or *regional*) tsunamis. A devastating local tsunami was caused by a $M_w = 7.0$ earthquake to the north of Flores Island in Indonesia in December 1992 in which 2000 people were killed. The sea-floor displacement, which was ~100 km in size, and also coastal landslides caused by the earthquake produced a tsunami reported as having a wave height of up to 25 m. That value could have been an overestimate, but certainly runup of that size was observed at some locations (runup being the maximum height above MSL that the tsunami flooded the land, see below) [54]. The larger observed values of runup have proved hard to model adequately,

probably because of the difficulty of parameterising the coastal slumping adequately. Babi Island, a small near-circular island to the north of Flores, was particularly badly affected on its south coast even though the tsunami source was to its north. This has been explained by multiple-reflected waves captured by the waveguide of the local shelf and converging from both sides of the island [55].

8.2.2 Submarine landslides

Submarine landslides are often associated with earthquakes. The Grand Banks event, for example, consisted of a tsunami caused by a landslide of 200 km³ of sediment induced by an earthquake. Sometimes it is difficult to know whether a sea-floor displacement or an earthquake-induced landslide was the trigger for the tsunami, as for the case of the Messina, Sicily tsunami of 1908 [56]. The Storegga slide was a gigantic event in which over 3500 km³ of sediment (enough to bury Scotland to a depth of about 50 m), which had been deposited rapidly on the Norwegian continental slope during the preceding ice age, became unstable on a gradient of around 1° (Figure 8.6) [57].¹¹ Runup values on the east coast of Scotland were estimated at approximately 5 m [7], while those for the Norwegian coast directly opposite the slide region were of the order of 10–12 m [58], with 20 m in the Shetland Islands [8]. The dynamics of the slide are interesting in that sediment on such a gentle gradient would be considered stable on dry land [59]. Gas hydrate dissociation has been proposed as the cause of the slide and its tsunami instead of an earthquake [60]. Gas hydrates are stable at high pressures and low temperatures, but ocean warming could have caused expansion of their methane leading to an increase in pore pressure within the sediment [61]. Some submarine landslide tsunamis are not obviously related to any trigger, an example being the Corinth submarine landslide and tsunami of 1963 which, although located in a seismic area, was apparently an aseismic event [62].

Two tsunami trains are produced by submarine landslides, one towards the shore and the other seaward and parallel to the slide. Their amplitudes depend upon the amount of sediment moved, its depth and the speed of the landslide. Wavelengths and periods tend to be

¹⁰ For example, the Geospatial Information Authority of Japan operates a network of approximately 1200 GPS stations at about 20 km spacing for land survey applications. Data from these stations are now being applied in real time to tsunami warnings issued by the Japan Meteorological Agency.

¹¹ The Holocene Storegga event is just the most recent massive slide that has affected the Norwegian continental slope. There has been at least one such slope failure during each interglacial over the last half million years (Dr David Long, British Geological Survey, private communication).



Figure 8.6 A picture of the Storegga sand layer at Maggie Kettle's Loch, near Sullom Voe, Shetland Islands. The layer sits just above water level and extends vertically to a few centimetres above the metal end of the spade. The layer is overlain by peat and woody material that extend up to the ground surface. The sand layer has black 'lumps' scattered throughout it which are clasts of peat ripped from a pre-existing land surface by the tsunami, transported, and then deposited in association with the sand and other material. Photograph by Professor Alastair Dawson, University of Aberdeen.

1–10 km and 1–5 minutes respectively, although the Grand Banks tsunami period was considered to have larger values depending on the location where it was observed [16]. However, in general the periods of submarine landslide tsunamis are much shorter than for sea-floor earthquake events. Wavelength increases with slide size and with decreasing slope, independent of water depth [27].

Underwater landslides can initiate local tsunamis in fjords. Examples include tsunami waves in Resurrection Bay in Prince William Sound, Alaska, in 1964 caused by a 211 million cubic metre landslide following the Great Alaskan Earthquake ($M_w = 9.2$), which was the largest earthquake recorded in North America [63]. Over 120 people were killed, with most fatalities due to the local tsunamis. The main tsunami associated with the earthquake travelled a great distance, its period appearing to be over half an hour in many tide gauge records [64]. It caused major damage along the Canadian and United States coasts. Waves exceeding 6 m, at the time the largest in Canadian history, were recorded at Alberni Inlet on the west coast of Vancouver Island [65], and the 6.4 m wave at Crescent City was the largest tsunami recorded on the west coast of the United States caused by a distant earthquake [65]. (The record for the largest tsunami on the west coast of Canada during the past 200 years, but caused by an $M_w = 7.7$ submarine earthquake, was set in October 2012 on the Queen Charlotte fault offshore of Haida Gwaii island. Runup is estimated as more than 7 m, fortunately in an

unpopulated area. Tide gauges in Hawaii recorded a tsunami amplitude of 0.8 m [66].)

There are many examples of locally destructive tsunamis generated by underwater landslides throughout Alaska and British Columbia [67]. An interesting example is that at Skagway Harbour, Alaska, in 1994 when a tsunami with waves over 10 m high followed an underwater slide that had been initiated by the collapse of a dockside at a time of extreme low water [68]. There are many other examples of landslide tsunamis occurring near to low spring tide in this region, the stability of accumulated sediments being much reduced when partially exposed at low sea level [69]. Another example of a landslide without an earthquake, but in a different region, occurred in October 1979, at Nice airport in France, when a submarine slide, set in motion by the collapse of a landfill platform, was followed by a several-metre tsunami that caused extensive coastal flooding [70].

8.2.3 Terrestrial landslides

Terrestrial (subaerial) landslides have been shown by theoretical and laboratory studies to be much more effective as tsunami generators than submarine landslides [71]. The most famous example of a subaerial landslide, which generated the largest tsunami recorded in modern times, was that of 9 July 1958 in Lituya Bay, Alaska. An earthquake ($M_w = 8.3$) on the Fairweather fault resulted in an estimated 30 million cubic metres

of rock and ice falling into the bay with a subsequent megatsunami wave of hundreds of metres.¹² The wave washed over the opposite slope of the inlet to a height of 524 m above sea level [72].

Similar local tsunamis are known to have occurred in Lituya Bay before, and at other inlets and fjords especially in Alaska, British Columbia and Norway [27, 73]. On 7 April 1934, over two million cubic metres of rock fell into the Tafjorden in Norway, generating a local tsunami over 60 metres high that killed 47 people, and concern remains about future rock falls there [74]. Slightly further south is the tourist destination and UNESCO World Heritage Site of Geirangerfjord, which is similarly threatened [75]. In April 2007, almost 20 million cubic metres of rock fell into the Aysén fjord in Chile following earthquake activity producing tsunami waves up to 10 m in height [76].

One much-discussed potential subaerial landslide is that which could occur if an eruption of the Cumbre Vieja volcano at La Palma in the Canary Islands were to cause a failure of its west flank, releasing 150–500 km³ of rock into the sea in a similar way to when its flank last failed 550,000 years ago [30], and is thought to have occurred in dozens of similar lateral collapses at volcanic islands in the Atlantic during the past million years. Although modelling studies vary, it is thought that tsunami waves with heights of many hundreds of metres could occur along the local island coasts and could impact the coastlines of the Americas, north and south, with wave heights of tens of metres [77, 78, 79].

8.2.4 Volcanic eruptions

Bryant [27] lists ten mechanisms by which volcanic eruptions can result in tsunamis including the associated earthquakes, pyroclastic flows, submarine explosions, landslides and caldera collapses. The most violent event in recent history, equivalent to 400 megatons of TNT, was the eruption of Krakatoa in 1883, which resulted in at least 36,000 deaths, primarily due to the tsunamis caused by pyroclastic flows [80]. Cubic kilometres of volcanic material falling into the ocean produced tsunami waves that destroyed coastal towns including Anjer and Merak, where the wave was over 40 m high [15]. Some reports mention that the Krakatoa tsunami travelled around the world, and indeed its signal is seen in many tide gauge records [81]. It has been calculated as

having a period less than 5 minutes and wavelength less than 7 km [15]. The Batavia (Jakarta) gauge indicated an amplitude of 2.4 m but an unusually large period of 122 minutes, which has been attributed to modification of the original wave due to resonance effects [82].¹³ While there were certainly large tsunami waves throughout the Indian Ocean as far as India and South Africa, the signals detected by many distant tide gauges, such as those in the United Kingdom, were undoubtedly due to the associated air pressure wave, which would have excited transient sea-level responses in shelf areas [83] and the reported flooding of Cardiff in Wales has been associated with such an excitation [83]. Indonesia contains many volcanoes capable of producing tsunamis. In 1815, Mount Tambora erupted with tens of thousands of deaths and with major global climatic consequences. Pyroclastic flows spread at least 20 km from the volcano to the ocean and were most likely the cause of the resulting tsunami. However, the tsunami's height was less than 4 m and it had considerably less impact than that of Krakatoa [14].

8.2.5 Asteroid and comet impacts

There have been no recorded examples in modern times of asteroid or comet impacts on the ocean that have produced a tsunami, although examples are known from the geological past and it is impossible to rule them out in the future. For example, from knowledge of the number of comets and Earth-crossing objects, it can be calculated that New York has a 1 in 47 chance of experiencing a 5 m tsunami due to an impact during the next millennium [84].

The most well-known impact is that at the end of the Cretaceous Period, about 65 million years ago, when a 10 km wide bolide (asteroid or comet) impacted offshore of the Yucatan peninsula of Mexico, producing a 180 km crater named after the nearby town of Chicxulub [85]. That impact is credited with the demise of the dinosaurs following the subsequently unleashed climatic changes that would have lasted decades. One of the largest megatsunamis in Earth's history with kilometre-scale wave height would have been produced, flooding large areas of North and Central America and the Caribbean [86]. The only remotely comparable

¹² The term 'megatsunami' is used variously in the literature to mean tsunamis with wave heights of tens or hundreds of metres or more.

¹³ The Winchester and Pararas-Carayannis publications together give an excellent overview of the Krakatoa explosion. In fact it is clear that there was a sequence of explosions and tsunamis of which the 10 am (local time) 27 August explosion (that Winchester calls the fourth) was the cataclysmic one.

event in recent times was the Tunguska air burst in 1908 in eastern Russia, in which an approximately 100 m bolide exploded at an altitude of 5–10 km with energy released in the blast equivalent to 10–15 megatons of TNT [87]. If the bolide had impacted the ocean, then a tsunami with an initial wave height of 900 m would have followed [27]. The Tunguska bolide exploded over land but, of course, any future similar object would have a 70 per cent chance of occurring over the ocean and generating a tsunami. Tunguska has been estimated as a ‘1000 year event’ [87].

Simulations of impacts on the ocean have been made by several authors using insight from known impacts such Chicxulub and Eltanin (a several kilometres-wide asteroid that impacted the South Pacific 2.15 million years ago) [88]. Objects can be considered to be 100–1000 m wide, made of different materials (e.g. comet ‘snowball’ or stony or iron meteorite type), and be travelling at around 20 km/s. Simulations can be made for impacts at various angles from the vertical and the different resulting tsunamis compared. Figure 8.7 shows one simulation of the vertical impact of a 200 m bolide that produces an underwater ‘crater’ with near-vertical walls that collapse and throw water into the atmosphere. A tsunami with an initial height of over 2 km is

generated with waves of a far more complex character than normal shallow-water waves. However, their wavelengths are shorter than those of earthquake tsunamis, and so decay roughly as $(1/\text{distance})$, giving amplitudes of only a few metres at 1000 km from the impact [30].

8.2.6 Man-made explosions

An explosion in a confined space can generate a local tsunami. An example is the detonation in 1917 in the harbour of Halifax, Nova Scotia, of the SS Mont Blanc, which was loaded with wartime explosives. Considerable damage was caused to the town [89]. The explosion caused a ‘crater’ in the harbour waters, exposing the harbour floor, and producing a tsunami estimated as 18 m above the harbour’s high water mark [90]. Similar size waves were produced following the underwater explosions produced by the nuclear tests of the second half of the twentieth century, many of which took place at Pacific islands [91]. In April 1958, one of the world’s largest non-nuclear explosions of 1400 tons of explosive removed the submarine twin peaks of the Ripple Rock in the Seymour Narrows navigation channel on the west coast of Canada. Some reports give the

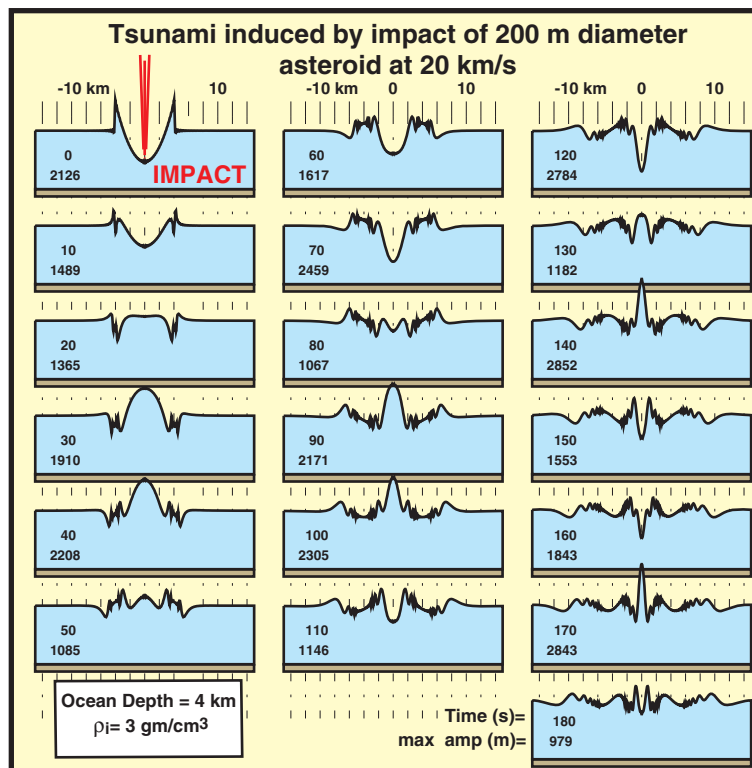


Figure 8.7 Simulation of the impact of a 200 m diameter asteroid of density 3 g/cm^3 travelling at 20 km/s on an ocean 4000 m deep. The waveforms show tsunami waves expanding from the impact site at intervals of 10 s. The maximum amplitude (m) at any time is shown on the bottom left of each panel. From [30].

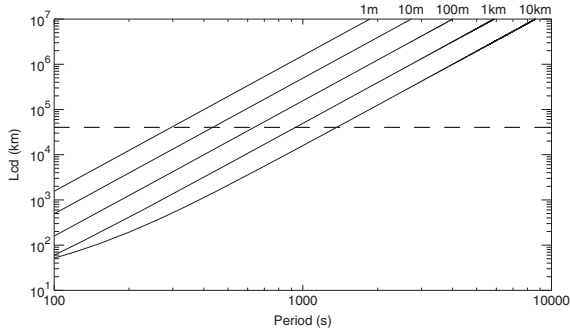


Figure 8.8 Distance of dispersive destruction of a tsunami wave as a function of period and ocean depth (number at the top end of each curve). The dotted line represents a distance equal to the circumference of the Earth's equator, as a measure of a limiting distance that can be travelled by a tsunami wave. The non-linear behaviour for 10 km depth at short period occurs when wavelength becomes smaller than water depth. Based on a similar figure in [28].

initial tsunami wave height as many metres, with measurements several kilometers away showing its attenuation to the order of 0.5 m [92].

8.3 Tsunami propagation across the ocean

Although frequency dispersion is a secondary factor, and tends to become important only for relatively intensive tsunamis with smaller source areas (e.g. 2006 Kuril Islands or 2009 Samoa events), its role in propagation across the ocean can be appreciated by considering the difference between the phase velocity for a given wavelength and depth, described by Equation 8.1, and the group velocity of the overall wave packet:

$$c_g = \frac{\partial \omega}{\partial k} = \frac{\omega}{2k} \left[1 + \frac{2kD}{\sin h(2kD)} \right] \quad (8.3)$$

When $\lambda \gg D$, as for the longest gravity waves in shallow water, then the phase and group velocities are the same:

$$c_g = c = \sqrt{gD} \quad (8.4)$$

The differences between the phase and group velocities for different depths and periods are shown in Figure 8.4c. In 4000 m depth the wave will travel at about 200 m/s, or over 700 km/h, which is similar to the speed of an aeroplane. It is also similar to the speed of the tide. A distance of dispersive destruction [28] can be defined as the time required for a wave packet to lag behind the front of the wave by a distance equal to the wavelength multiplied by the velocity of a long wave:

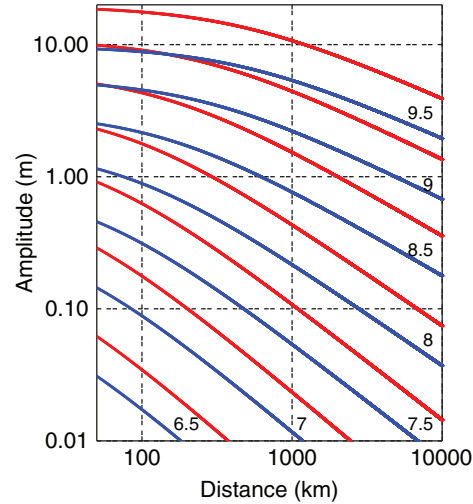


Figure 8.9 A schematic description of maximum open-ocean tsunami height versus distance for 'typical' submarine earthquakes of magnitudes 6.5 to 9.5 (blue lines), and a factor of two allowance for most anomalously large earthquakes (red lines). Ocean depth of 4000 m assumed. For the largest earthquakes the height decays roughly like $r^{-1/2}$, while tsunamis from smaller earthquakes decay faster due to dispersion. Based on parameterisation in [30].

$$L_{cd} = \frac{\lambda \sqrt{gD}}{\sqrt{gD} - c_g} \quad (8.5)$$

and when $\lambda \gg D$ this becomes:

$$L_{cd} \sim \lambda \left(\frac{\lambda}{D} \right)^2 \quad (8.6)$$

This parameter is shown in Figure 8.8 for different water depths, while the dashed line indicates the size of the Earth's circumference. Consider any one water depth (say 1 km), then a wave with a period less than 10^3 seconds, on the left-hand side of the figure, travels only 1000 km or so before 'dispersive destruction' occurs, whereas waves with much longer periods, such as those of the 2004 Sumatra or 2011 Tōhoku events, on the right-hand side of the figure, will travel around the world and longer before significant dispersion happens.¹⁴

As a tsunami propagates away from its source, its height will diminish for two general reasons. The first reason is due to a simple $r^{-1/2}$ geometrical spreading factor (where r is the distance from the source). The second factor is an $r^{-\psi}$ diminution due to frequency dispersion, where ψ varies from approximately zero for the longest periods to $1/2$ for the shortest [30]. Figure 8.9

¹⁴ As all tsunami periods are considerably shorter than a day, Earth rotation has no effect on tsunami propagation [40].

shows schematically an overall amplitude reduction with distance for tsunamis following submarine earthquakes: the amplitude at source in this case is assumed to be comparable to the sea-floor displacement.

These general considerations assume a uniform ocean depth, but bathymetry (ocean depth distribution throughout the ocean) influences the tsunami propagation in several ways. Consider first its energy flux (i.e. total influx of energy per unit width of the ocean per unit time), which can be taken to be that of a progressive wave of amplitude H_0 :

$$E = \frac{1}{2} \rho g H_0^2 \sqrt{gD} \quad (8.7)$$

(This is the same equation as used for tides [93, 94], see Appendix D.) The energy flux vector for a progressive wave is always perpendicular to the wave front, so if \sqrt{gD} decreases, then H_0^2 has to increase to preserve energy flux. A second depth-related factor is refraction. Refraction occurs because of the long wavelength, as different parts of the wave are at different depths and travel at different speeds (Section 5.4.1). The tsunami wave will, therefore, refract, just as light does when passing from one medium to another (Snell's law). For this reason, a tsunami experiences focusing and defocusing along its path due to bathymetry.

A proper understanding of tsunami generation, propagation and impact on a distant coast can be obtained only with the use of combinations of numerical models (Figure 8.10). 'Forward modelling' requires a model of the initial displacement (source function in the case of a sea-floor earthquake, as described above), a model for the propagation across the open ocean, and models for shoaling and runup at a far coastline. The opposite of this form of modelling is

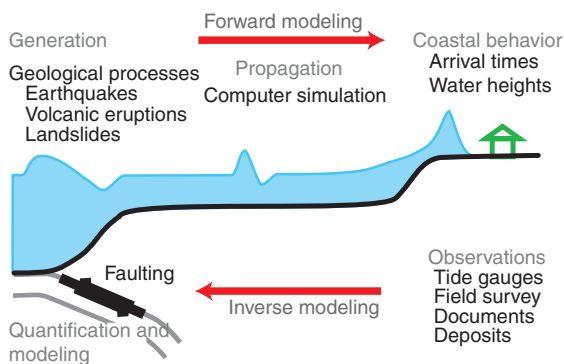


Figure 8.10 Schematic of tsunami generation, propagation and coastal behaviour. Forward modelling starts from the tsunami source and forecasts the coastal behaviour, while inverse modelling starts from observed data to estimate the tsunami source. From [53].

'inverse modelling', wherein data from tide gauges and other instruments are used to learn about the initial displacement [53].

Many of the numerical models used to simulate tsunami propagation across the open ocean employ the same non-linear shallow water (NLSW) schemes used to model tides and storm surges as described in Chapter 7, although with smaller spatial grids and time stepping. For example, a recent successful simulation of the Lisbon tsunami employed a $1/30^\circ$ by $1/20^\circ$ (latitude by longitude) grid and 10-second timestep in what was otherwise a standard operational finite-difference, depth-averaged, tide-surge model [13]. A similar scheme is used by the most well-known model used in tsunami research called MOST (Method Of Splitting Tsunami) [95] and there are several other finite-difference and finite-element models used by other groups [28, 96]. Most of these NLSW models cannot adequately simulate dispersive waves, which limits their ability to simulate short-wavelength tsunamis.

The sophistication of modern tsunami modelling from both geological and ocean modelling perspectives was demonstrated by the Sumatra event. In particular, it revealed the main factors responsible for the rupture [97] and for the direction of the tsunami waves [98]. In the near field, the linear seafloor deformation of the rupture (its source function) produced the highest amplitude waves perpendicular to the source (i.e. in the zonal direction) with smaller waves in the meridional direction. It also generated a first wave with a frontal crest that propagated westward and a frontal trough that went east due to the rapid uplift on the western side of the source area and subsidence on its eastern side [32, 99]. Modelling of the tsunami's propagation [94, 99] demonstrated the importance of multiple refraction at the mid-ocean ridges, which acted as waveguides, efficiently transmitting the tsunami wave energy by slower but more economic (energy conserving) routes, with the southwest Indian Ridge and the Mid-Atlantic Ridge serving as waveguides into the Atlantic Ocean and the southeast Indian Ridge, Pacific–Antarctic Ridge, and East Pacific Rise acting as waveguides to the Pacific (Figure 8.11). Tide gauge and altimeter information [32, 100, 101] provided a general validation of model simulations.

The MOST model demonstrated that ridges act as waveguides only until their curvature exceeds critical angles. For example, the large amplitudes observed along the coast of Brazil [102] can be explained by the sharp bend of the Mid-Atlantic Ridge in the South Atlantic, which results in the tsunami path departing

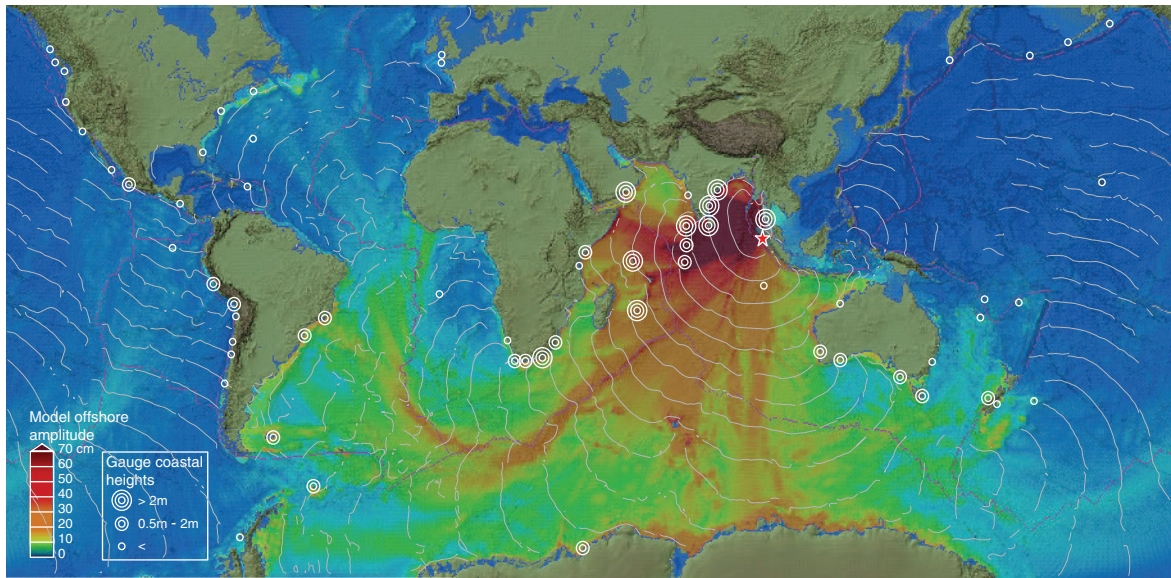


Figure 8.11 Energy propagation of the 2004 Sumatra tsunami calculated from the MOST model. Filled colours show maximum computed tsunami heights during 44 hours of wave propagation. Contours show computed arrival time of tsunami waves. Circles denote the locations and amplitudes of tsunami waves in three range categories for selected tide gauge stations. From [99]. Reprinted with permission from AAAS.

from the ridge near 40° S. Amplitudes at other Atlantic locations were smaller [103, 104, 105, 106], although there were exceptions, presumably owing to local resonances [107].

Model simulations of tsunami propagation over a great distance from the source are the most sensitive way to test for the effects of errors in the bathymetric information used by the model, and for its limitations in handling wave dispersion; it being recalled that MOST is based on a non-dispersive shallow-water approximation. However, neither of these potential deficiencies were apparent in an investigation of very distant data. Figure 8.12 shows locations and data from two bottom pressure recorders acquired during the Sumatra event at depths of over 1000 m in the Drake Passage. The tsunami had amplitudes at these locations of only several centimetres but the signals were measured accurately in terms of amplitude and timing. Comparison of the observed records and those simulated by MOST showed clearly that the identified tsunami waves were due to the second (main) train of waves propagating along the energy-conserving route of the mid-ocean ridges, while the first train of waves travelling by the fastest route across the deeper ocean were unrecognisable due to their tiny amplitudes compared to the background variability [108].

Owing to the geographical location of the Tōhoku earthquake in 2011 and to the vast extent of the Pacific Ocean, the resulting tsunami was largely confined to that ocean basin (Figure 8.13(a)) [34, 109, 110]. Waveguides in this case were provided by the seamount chains that enabled the tsunami to reach Chile in 20 hours. Waves of over 4 m amplitude were observed at certain points on the California coast, which are considered to have been due to wave refraction and focusing of energy into relatively narrow sections of coast where local shelf resonance also occurred [111], in a similar manner to observations along the United States coast of the 2006 Kuril Islands tsunami [112]. Similarly large values were observed at certain locations along the Pacific coast of South America, and some energy propagated through the Drake Passage into the South Atlantic (Figure 8.13b) [34]. On the Japanese coast itself, the maximum inundation height is known to have been 19.5 m on the Sendai Plain with the tsunami bore propagating 5 km inland [113], and runups in excess of 30 m were reported on the Sanriku coastline, the fjordic area to the north of the Sendai Plain [114]. All tide gauges in the area of interest were destroyed but simulated sea level time series have been computed [115]. All studies of the event point to the need for adequate deep ocean instrumentation including ‘tsunameters’ (see below)

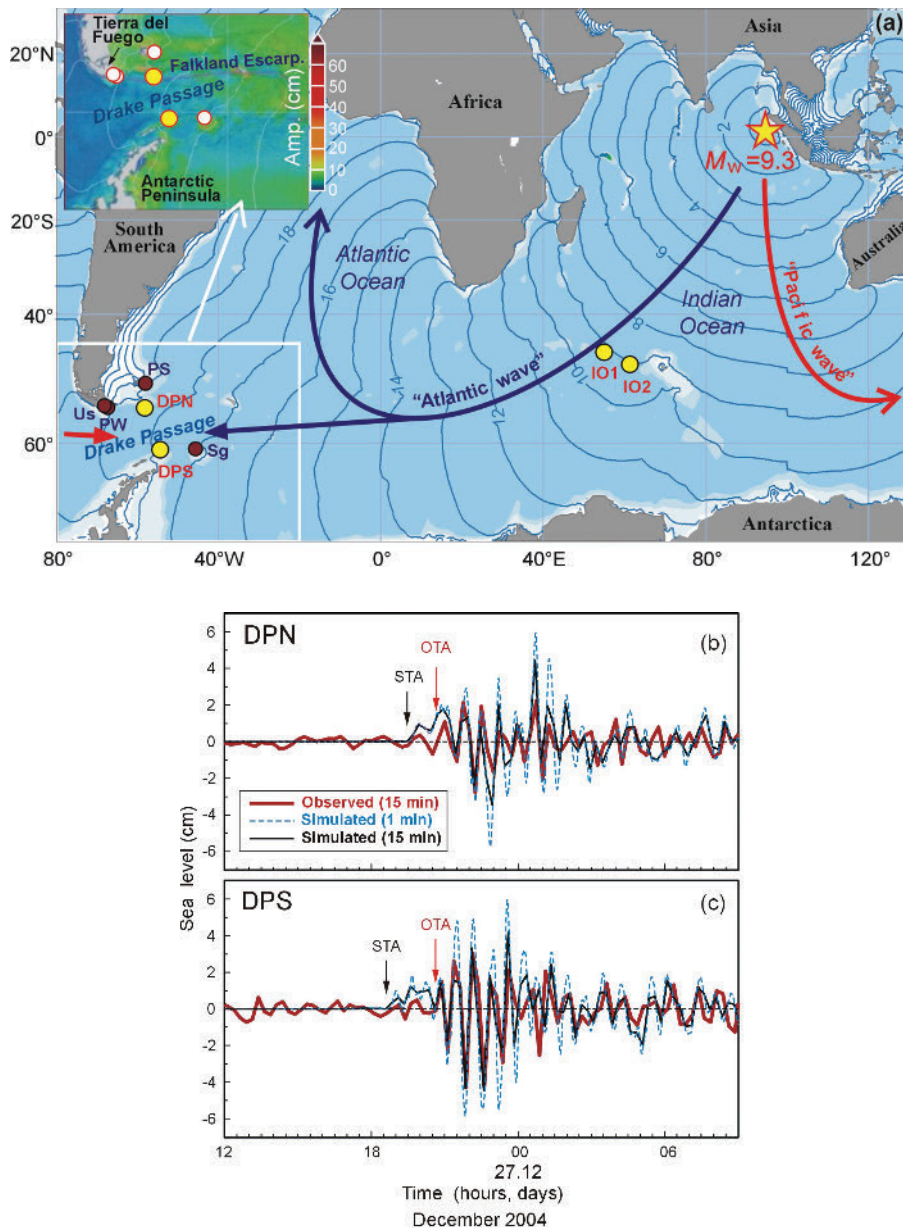


Figure 8.12 (a) Propagation of the 2004 Sumatra tsunami waves from the source area (yellow star) into the Drake Passage region (white box); a dark blue curved arrow indicates the 'Atlantic wave', a red arrow indicates the 'Pacific wave'. Yellow circles mark bottom pressure recorders IO1, IO2, DPN and DPS; brown (white in the insert) circles mark coastal tide gauges Signy, South Orkney Islands (Sg), Port Stanley, Falkland Islands (PS), Puerto Williams, Chile (PW) and Ushuaia, Argentina (Us). The small insert shows simulated tsunami wave heights for the region along with the locations of certain topographic features.

(b) Numerically simulated (dashed blue line with 1-minute sampling and solid black line with 15-minute sampling) and observed with 15-minute sampling tsunami records at DPN and (c) DPS stations. For best fitting the data, the simulated records are shifted by 15 minutes (DPN) and 10 minutes (DPS). The black arrow denotes the simulated shifted tsunami arrival time (STA) of the first train of waves, which has not been identified in the observations, and the red arrow denotes the observed detected tsunami arrival (OTA). From [108].

together with improved modelling schemes to prepare for future events [116].

The complexity of the propagation of a tsunami wave, refracting and reflecting, as it travels across the ocean is apparent in the *travel-time chart* of an event, or even better in an animation [117]. The role of refraction in leading to mid-ocean ridges acting as waveguides in the 2004 Sumatra event can be

appreciated readily from Figure 8.12. Charts and animations for the Sumatra and other events also demonstrate how continental shelves can also act as waveguides, notably along the Pacific coasts of North and South America [99, 118], and how refractive focusing of energy into 'beams' when the tsunami crosses onto a continental shelf can result in considerably different amplitudes at locations only a short

distance apart [13]. A tsunami wave can also reflect off a coastline, retaining significant amounts of energy that can travel great distances to impact on other coastlines, thereby complicating the initial picture of energy distribution from the event. For example, tide gauge data from the west and south coasts of Sri Lanka during the Sumatra event demonstrated the importance of reflections from the Maldiv Islands chain [119].

As mentioned above, the Sumatra wave contained an eastward-propagating frontal trough due to the way that the sea-floor displacement occurred. Where the trough met the coast, such as in Thailand, then the first evidence for a tsunami was a *withdrawal* (or *draw-back*) of the water exposing normally submerged areas (Figure 8.14) [120]. Initial withdrawal of the ocean (IWO) can occur over hundreds of metres where the coast has a gentle gradient and can last for many minutes (i.e. a quarter to a half of the wave period). There are many famous examples of IWO (e.g. during the Lisbon tsunami of 1755) but it does not always happen, and whether the first sign of a tsunami at any location is represented by a positive or negative change in sea level depends on the particular event.

We have described tsunamis so far as if they were simple sinusoidal waves. However, in some events, such as that of Sumatra in 2004, they are better described as steeper N-waves, reflecting to some extent the shape of the source function [99].¹⁵ Tsunami waves tend to become more peaked as they enter shallow waters, with their shape approaching that of solitary waves that in some circumstances can also be modified into an N-shape [27, 121]. In the case of a propagating frontal trough, an N-wave represents better an IWO and subsequent ‘wall’ of incoming water (Figure 8.15). The particular deep-ocean characteristics of the wave do not affect the various formulae for propagation given above.

8.4 Coastal shoaling and runup

The wave height of a transoceanic tsunami may be modest in the open sea but will be amplified considerably from when it enters depths of 100 m or so, typical of a continental shelf, up until the time it impacts a

distant shoreline. This process is called *shoaling*. For simplicity, assume that the wave direction is perpendicular to the shore. Then the leading part of this long wave will sample shallower water, where phase velocity is smaller, before its trailing part, so the wave will compress. Kinetic energy will be converted into potential energy, and the wavelength will shorten while wave period remains the same. We showed above that the energy flux for a progressive wave must be preserved, so that amplitudes can be expected to increase by a factor:

$$S = \sqrt[4]{\frac{D_{ocean}}{D_{coast}}} \quad (8.8)$$

where D_{ocean} and D_{coast} refer to water depths in the open sea and near the coast. This is known as Green’s formula (Section 6.6). However, it is more accurate to express the increase in amplitude as the ratio of group velocities [30]:

$$S = \sqrt{\frac{c_g(ocean)}{c_g(coast)}} \quad (8.9)$$

This amplification can be multiplied by two where the wave is reinforced by constructive reflection from the shoreline [122].

As the wave height increases, a second type of dispersion called *amplitude dispersion* becomes more important, in which velocity depends on amplitude as well as depth. This is a function of the non-linearity of the wave, defined as the ratio of wave height to water depth. When this quantity is small, as in the open ocean, the wave is linear and no amplitude dispersion occurs. In a similar way to above, we can introduce a *distance of non-linear destruction* of a wave [28]:

$$L_{cn} = \frac{\lambda\sqrt{gD}}{\sqrt{g(D + H_0)} - \sqrt{gD}} \quad (8.10)$$

and if the wave amplitude $H_0 \ll D$ then this becomes:

$$L_{cn} \sim \lambda\left(\frac{D}{H_0}\right) \quad (8.11)$$

and for any reasonable values of H_0 and D then L_{cn} will be much larger than the circumference of the Earth, and so non-linear effects can be neglected. However, as the tsunami enters shallower water, the ratio $\frac{H_0}{D}$ approaches unity and L_{cn} is much smaller. The wave is non-linear and undergoes significant transformation depending on the bathymetric distribution of the near-shore area and on the wave itself. Velocity at

¹⁵ A familiar example of an N-wave is the shock wave of a sonic boom, see http://en.wikipedia.org/wiki/Sonic_boom. The parameters of an N-wave can be chosen to select either a leading frontal trough or elevation and their relative amplitudes [121].

(a)

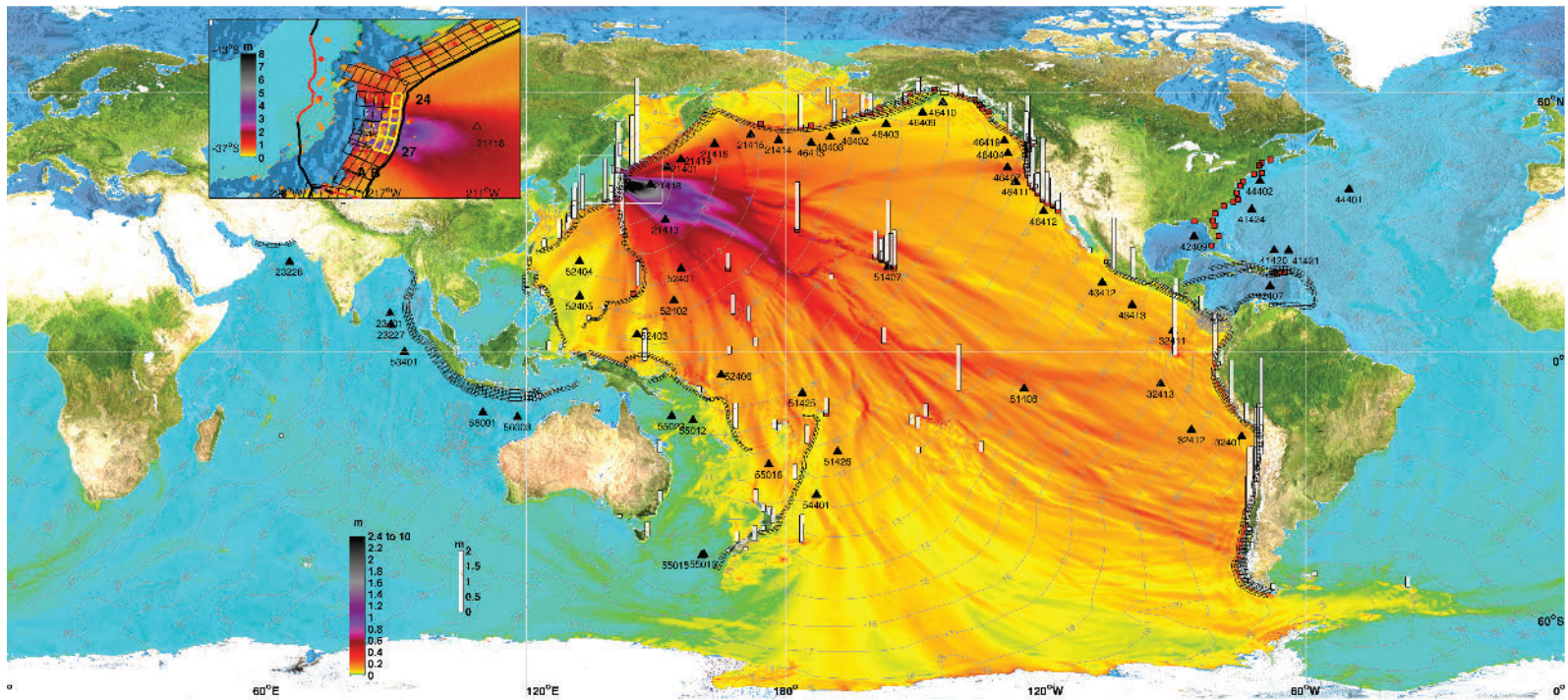


Figure 8.13 (a) Energy propagation patterns guided by seafloor topography during the Tohoku tsunami. Filled colours show the maximum offshore elevation in metres during 48 hours of wave propagation. Contours indicate computed arrival time in hours. White bars represent the maximum wave crests at coastal tide gauges. The inset shows the source geometry of pre-computed tsunami source functions. From [34].

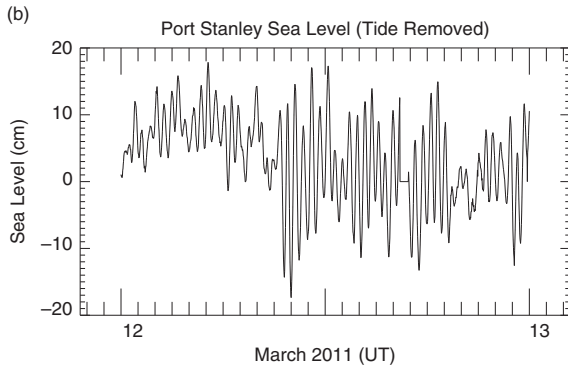


Figure 8.13 (b) Sea level at Port Stanley, Falkland Islands, on 12 March 2011 showing first the several centimetres background variability due to the local seiche and then the tsunami arrival at approximately 09:00 hours UT with a wave height of approximately 20 cm, demonstrating that some of the Tōhoku tsunami energy entered the South Atlantic.

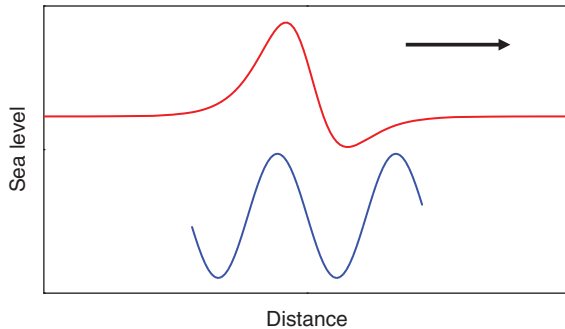


Figure 8.15 Schematic of a simple N-wave travelling to the right with a leading depression wave followed by a larger elevation wave, compared to a sinusoidal wave of similar amplitude and wavelength.

a point in the wave group where sea level is ζ will be more like $\sqrt{g(D + \zeta)}$ than \sqrt{gD} , focusing energy at the wave front and in some circumstances leading to a bore effect [30] (see also Section 6.6.2).

At this point, the ability to explain the tsunami's progress becomes much more difficult, and impossible to simulate with the models used for the open sea. Turbulence, friction and interaction with the coastline become more important, and refraction and reflection become even greater issues. As for all waves, a tsunami wave will break when its height becomes comparable to the water depth, but the energy dissipated in tsunami breaking is usually inadequate to halt it and it will move onto the land as far as its *runup height* at its landward limit (measured as a height above MSL) (Figure 8.16). A *runup factor* is defined by the ratio of runup height to open ocean amplitude.



Figure 8.14 A photograph of a beach in Thailand in 2004 where IWO has occurred prior to the arrival of the tsunami. Photograph from Getty/Agence France-Presse.

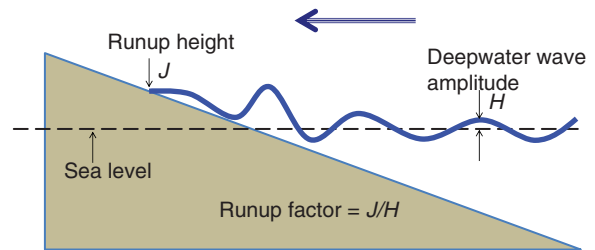


Figure 8.16 Schematic figure illustrating the amplification of tsunami wave height due to coastal shoaling.

The near-shore slope of the ocean bottom determines the character of the runup with 'surging' (non-breaking) runup for steep slopes, 'plunging' (crest surpassing foot of the wave) runup for medium inclined slopes and 'spilling' (wave breaking and foaming) runup for gentler slopes [28]. Reviews are available of the moving shoreline, or runup, algorithms required to simulate the evolution of the wave (of whatever type) from deep ocean to shallow water and onto the land using combinations of NLSW techniques, Boussinesq models (models that include some frequency dispersion) and more rigorous but computationally intensive models based on the Navier-Stokes equations (the full equations of fluid motion) [28, 96]. One complication in simulating the most energetic events is that tsunami waves can do so much damage to a coast (erosion of the coastline, destruction of infrastructure etc.) that subsequent waves can meet with a modified environment. This complexity of interaction with the coast is the reason why damage and loss of life can vary so much within

short distances [3, 123]. The ability of models to simulate future tsunami inundations can be tested by comparing their outputs to field surveys of past events and to laboratory experiments.

8.5 Tsunami signals in sea-level and bottom pressure data

Examples of tsunami signals in tide gauge records are included in many papers and websites, so we only give examples here [124]. Figure 8.17a shows large amplitude tsunami signals from the Indian Ocean during the Sumatra event [32], while Figure 8.17b demonstrates a more modest signal at another location during the same event. Three points may be made about the latter.

A first point is that, although the signal is smaller, it is clearly detected. Therefore, Port Stanley, located near the edge of the continental shelf, could provide confirmation of the approach of distant tsunamis an hour or more before they impact the Argentine coast [103, 106, 125]. A second point is that, although the signal is clear, it is not as well resolved with the 15-minute averaging then used at that location as it would have been with higher-frequency sampling. A third observation is to recognise that tsunami signals must exist in the tide gauge records available from data centres and that many of the smaller ones will be unflagged. Therefore, analysts of extreme levels or non-tidal sea-level variability must always be aware of the possibility of tsunamis in their data sets.

Figure 8.18a shows a tsunami signal in a bottom pressure record from an instrument in the North Pacific during the Gulf of Alaska tsunami in 1988 [126]. The pressure signal from the Rayleigh seismic pulse from the earthquake can be seen ahead of the pressure variations due to the tsunami itself; both features are not observed in all events. Although tsunami signals in the deep ocean tend to be measured in centimetres, as in this case, bottom pressure time series are much quieter than those from coastal tide gauges, as sea-level variability due to the ‘inverse barometer’ has no signal in bottom pressure (Chapter 7). Consequently, oceanic bottom pressure measurements are highly desirable as part of tsunami monitoring and warning systems, as demonstrated by the many deployments of DART (Deep-ocean Assessment and Reporting of Tsunami) tsunameters described below. By contrast, Figure 8.18b shows a pair of quite different bottom pressure records obtained during the Tōhoku tsunami [45]. These are from two

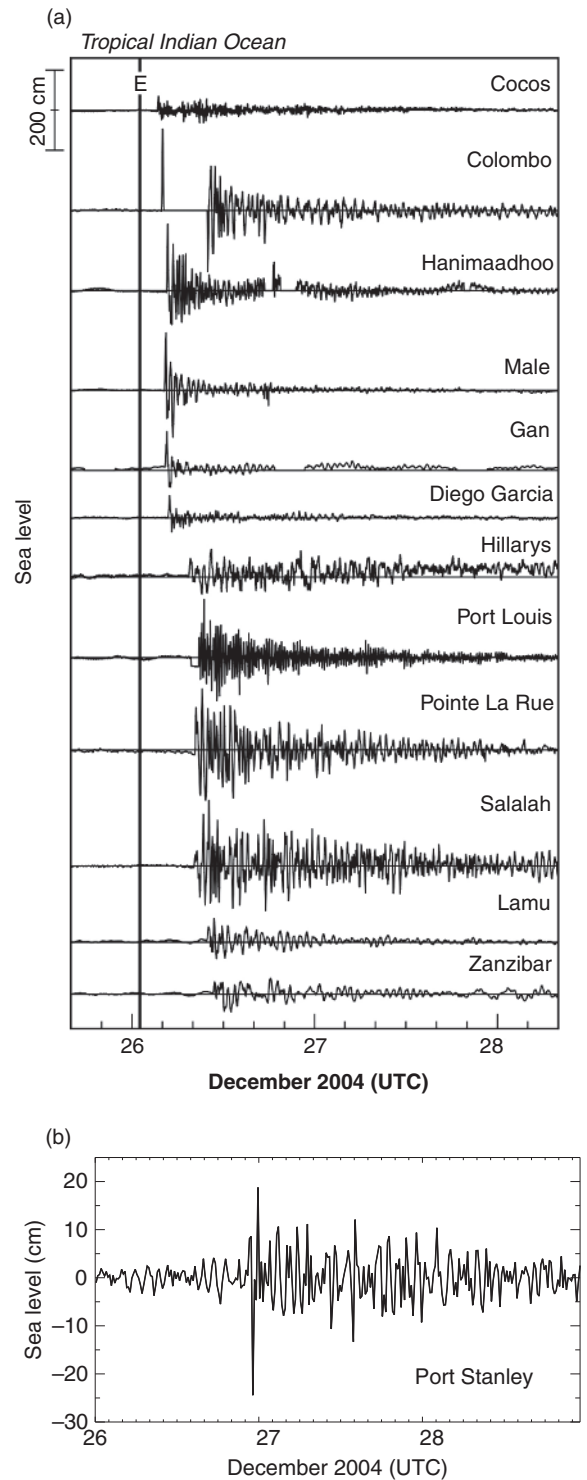


Figure 8.17 (a) Tsunami signals in tide gauge records from the Indian Ocean during the Sumatra event. The vertical solid line labelled ‘E’ denotes the time of the main earthquake shock. From [32]. (b) Tsunami signal during the same event from Port Stanley, Falkland Islands, re-plotted from [103].

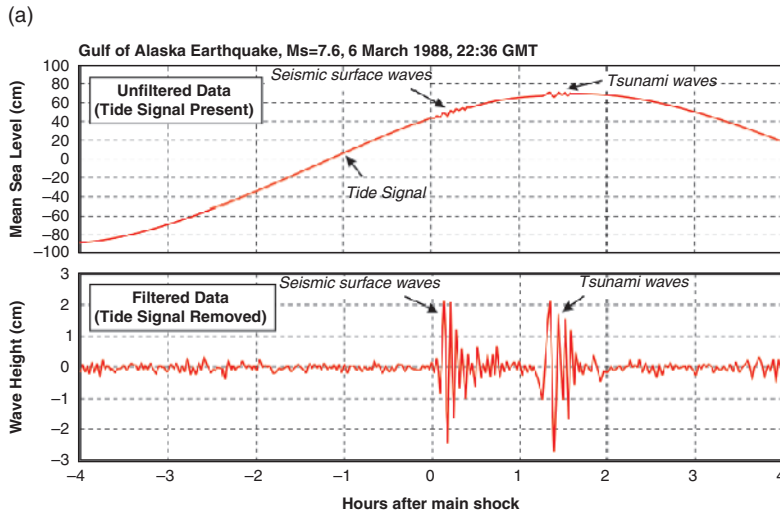
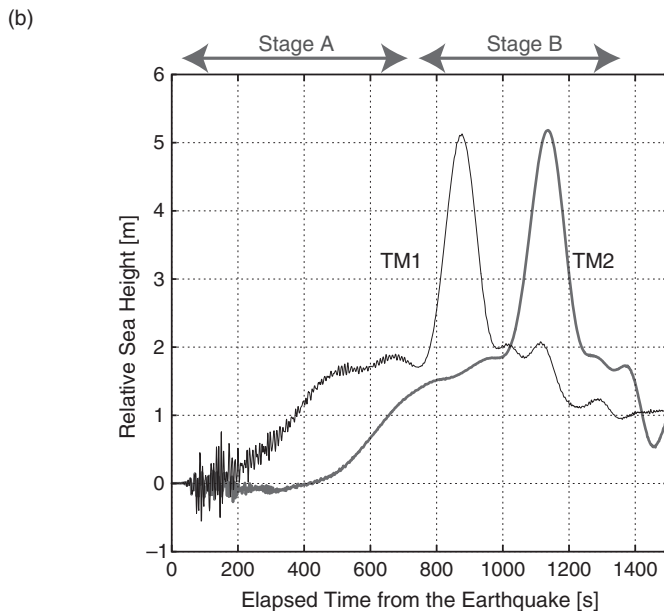


Figure 8.18 (a) A bottom pressure record from a deployment in the northern Pacific following the Gulf of Alaska earthquake in 1988. From [127].

(b) Bottom pressure records from two pressure sensors off the east coast of Japan during the 2011 Tōhoku tsunami. From [45].



pressure sensors TM1 and TM2 located 75 and 45 km from the east coast of Japan in 1600 and 1000 m depth respectively. The gigantic tsunami passed these locations as a smoothly increasing wave, reaching 2 m during the first 800 seconds followed by a pulse amounting to more than 5 m.

At many locations, coastal tide gauge records will also exhibit high-frequency variability during and after tsunami events due to local resonances of the harbours, bays and continental shelves near to which they are located (Figure 8.19). Seiches are excited by the incoming tsunami and, at other times, can also be excited at similar high frequencies by strong winds or rapid air pressure changes (Chapter 7). They are

important for two reasons. One is that the additional ‘noise’ complicates the tsunami interpretation of the record. A second reason is that the currents associated with such rapid changes of sea level can inflict damage to shipping and port infrastructure additional to that of the tsunami itself. Any modelling of tsunami impact must take seiching into account.

8.6 Sea-level and related technologies for tsunami monitoring

The 2004 Sumatra tsunami forced agencies in many parts of the world to consider if their oceanographic infrastructure was adequate for the purpose of tsunami

Table 8.1 Other uses of equipment that could form part of a tsunami warning system identified in a study of tsunami risks to Europe [128]

Technology	Alternative use
Deep ocean DART systems	Pressure data for studies of ocean dynamics and tides Focus for deep ocean observatories
Shallow water pressure sensors on oil rigs and cables	Shelf circulation studies Storm surge and wave data Benthic observatory developments
Coastal tide gauge pressure sensors	Storm surge and coastal wave data
HF radars	Offshore currents and waves Coastal observatory studies (e.g. water quality monitoring)
GPS buoys	Altimeter calibration and geodetic studies
Pressure sensors on dedicated cables	Ocean circulation variability monitoring
GPS reflection	Not clear, but receivers would provide data for GPS applications in meteorology
Advanced altimetry	A wide range of oceanographic research

detection and onward transmission of data to warning centres. In many cases, the conclusion was that the infrastructure was both unsuitable or incomplete, requiring investment in new equipment. This investment could be considered expensive and unnecessary, especially where tsunamis are rare events, although in many cases the instrumentation can be used in other applications (Table 8.1). In this section, we discuss the sea-level and related ocean instrumentation that could contribute to a tsunami warning system [127].

8.6.1 Coastal tide gauges

In Chapter 2, we described how tide gauge technology has evolved with the addition of acoustic, pressure and radar techniques to the traditional float and stilling-well method of measuring sea level. When the measurement of tsunamis is added as a monitoring requirement, then it is clear that some techniques are more suitable

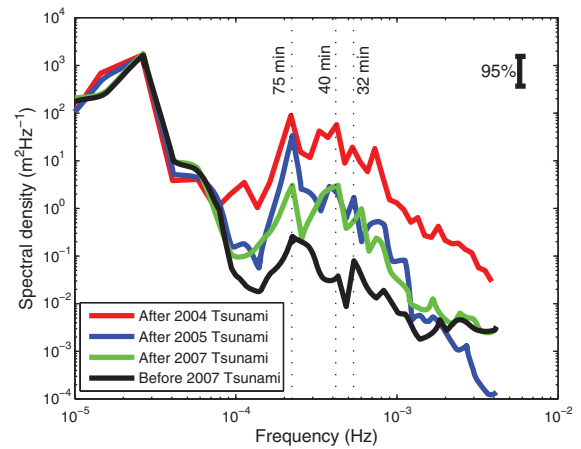


Figure 8.19 Sea-level spectra from Colombo during the 2004, 2005 and 2007 tsunamis showing the spectral energy after the tsunamis; spectral energy before the 2007 tsunami is also shown. The plot demonstrates the presence of high-frequency oscillations which persist for several days after the tsunamis. From [120].

than others for meeting all requirements. Alternatively, separate tsunami instrumentation can be provided alongside conventional technologies.

For tsunami monitoring, any device should be exposed as little as possible and be robust enough to survive an energetic event. It should be able to sample sea level rapidly enough to resolve the passage of the wave, and to measure as much of the wave's full height as possible. This points to the value of pressure sensors located as securely as possible on the seabed with armoured cables connecting them to a protected data logger and transmission system. In addition, it indicates the importance of several methods of transmitting data to warning centres.

These requirements contrast with those for MSL monitoring, which are focused more on datum stability. In addition, they contrast to some extent with those for storm surge measurements. Surge monitoring also requires timely data transmission to a centre but in general not as rapidly as for tsunamis, and also in most cases it does not need as rapid a sampling of sea level. In addition, storm surges at most locations have amplitudes measured in decimetres or one or two metres, except in the most energetic events during tropical storms. Consequently, surges can usually be monitored adequately with the same instrumentation used for tides and MSL.

Since the Sumatra tsunami, there has been consideration given to the provision of 'multi-use' or 'multi-hazard' instrumentation at sea-level stations. However, from the above discussion, it can be seen that it is the

station that should be considered as providing the ‘multi-use’ rather than the specific instrumentation. There is a recommendation that a sea-level station be equipped with a combination of sensors [25]. The primary sea-level sensor could be a pulsed radar, with sampling fast enough (e.g. 3-minute averages or shorter) to serve also as a secondary tsunami sensor. The primary tsunami sensor would be a vented pressure transducer reporting 1-minute or shorter averages, with the pressure time series, converted to water level, used to fill short gaps in the radar record. Existing float gauges would be retained as backups. While there are certain types of radar gauges that aim to satisfy almost all the requirements of sea-level and tsunami monitoring, the multi-sensor approach is the more resilient.

Access to real-time sea-level data is essential. A regional warning centre will issue an alert called a ‘tsunami watch’ when seismic information of earthquake activity suggests a tsunami might be possible, and then national authorities will provide a ‘tsunami warning’ when the alert is confirmed on the basis of tide gauge data (warnings being usually a national responsibility). If no tsunami exists, then the alert is cancelled. International collaboration is the key to building a network of sea-level stations for tsunami warning. A tide gauge that records a tsunami is of interest not only locally but also to coastal communities downstream of the wave. Similarly, a country cannot rely just on its own sea-level stations for information but must have access to data from countries nearer the source.

Difficulties with existing sea-level networks concern whether their hardware and data transmission methods are suitable for tsunami monitoring, and whether they are complete enough. For example, in the Mediterranean where many tsunamis occur, the existing sea-level network has major gaps along the North African coastline [128]. Another difficulty concerns whether neighbouring countries are willing and able to exchange data in real time; this is an organisational and political issue [129]. One beneficial by-product of the Sumatra disaster was that it stimulated international exchange of real-time data within the framework of regional tsunami warning systems, as we describe in Chapter 12.

The telemetry used in most tsunami applications worldwide is based on the use of the Global Telecommunications System (GTS) [130]. However, its limited transmission rate and bandwidth has meant that alternative systems have been investigated for tsunami warning, so as to minimise the delay with which information is received at warning centres

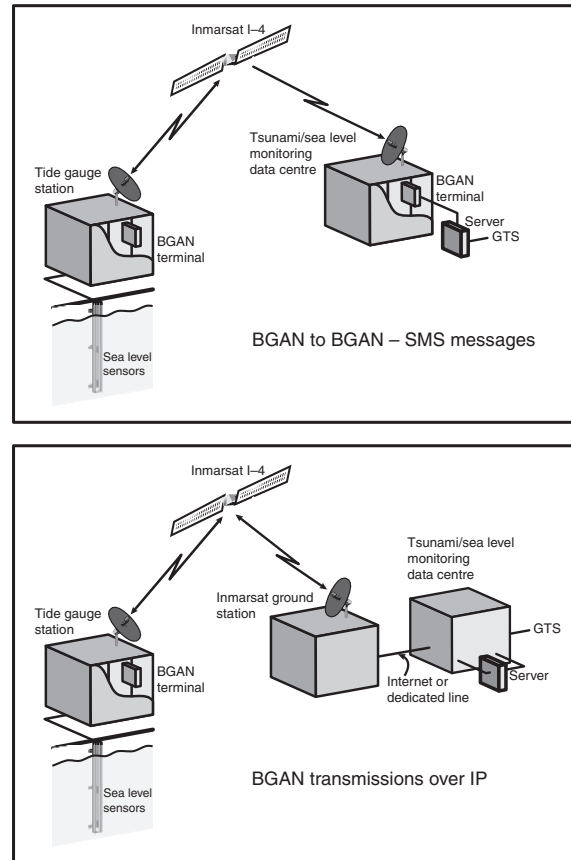


Figure 8.20 Schematic of a tide gauge station linked via an Inmarsat BGAN terminal to the Internet and tsunami warning centre with onward data distribution to the GTS (an alternative is a dedicated line to the GTS and onward distribution to warning centres). From [133]. ©American Meteorological Society. Used with permission.

[131, 132, 133]. Particular types of telemetry may be appropriate depending on the local circumstances. It can comprise fixed line or mobile telephony or Internet connections, while satellite-based broadband is available worldwide through the Inmarsat BGAN (Broadband Global Area Network) (Figure 8.20) and other systems.

A large fraction of the tsunami-relevant near real-time sea-level data from around the world is transmitted to the Intergovernmental Oceanographic Commission monitoring facility at the Flanders Marine Institute (VLIZ; <http://www.ioc-sealevelmonitoring.org/>). This facility exists only as a monitor of network status; it does not provide tsunami warning or validation. The latter roles are the responsibility of various tsunami warning centres now being established (Chapter 12). Any operational tsunami centre needs algorithms to

detect potential tsunami signals in the high-rate tide gauge data that they receive and various sets of software are now available [134].

8.6.2 Tide gauges on offshore platforms

A number of continental shelves have offshore structures owned by the oil and gas industry that have tide gauges for monitoring of water depth beneath the platforms and such data are sometimes used for ocean research. Examples include the Gulf of Mexico and Celtic Sea. In these cases, it would be possible to install additional pressure sensors and telemetry suitable for tsunami monitoring. The oil and gas industry is generally willing to make its offshore platforms available to ocean monitoring where possible [135]. An advantage of an offshore platform is that it has continuous mains electricity and telecommunications. However, appropriate ‘platforms’ could also include small islands or rocky outcrops equipped with pressure sensors and telemetry powered by a solar panel.

8.6.3 Deep ocean bottom pressure measurements using buoys

Real-time information from a bottom pressure sensor requires either an undersea cable or acoustic transmission between the sensor and a surface buoy such as in the DART equipment (Figure 8.21) [24]. The pressure sensors in tsunameters such as the DARTs can monitor the rate of change of sea level and software can decide if a tsunami (or, occasionally, the Rayleigh wave that precedes the tsunami) has been detected. The DART system is expensive but is essential if, following a seismic alert, authorities are to be able to verify the existence of a tsunami while it is still in the deep sea and before it reaches the coast. Data from regular sampling of the pressure sensors is available in real time, while sampling switches to higher rate in the event of a potential tsunami being detected in the pressure data.

A total of 55 DART buoys and similar tsunameters are now operational (Figure 8.22). The first ones were deployed in the Pacific by the United States National Oceanic and Atmospheric Administration (NOAA) and the Pacific boundary coasts are now reasonably well represented with instruments. Buoys have also been deployed in the Indian Ocean through collaboration between Germany and Indonesia [136] and also by the governments of Australia, Thailand

and India. One focus is clearly on warning of any repeat of the Sumatra event in the eastern Indian Ocean, although tsunami hazard in the northern Bay of Bengal [137] and in the Arabian Sea near the Makran subduction zone is a concern. One buoy is at present deployed to monitor the latter possibility, a $M_w = 8.1$ earthquake having occurred in the area in November 1945 which produced a tsunami that caused widespread damage around Arabian Sea coasts [138]. Buoys have also been deployed at seven sites in the Caribbean and western part of the North Atlantic.

DART-like tsunameters complemented by coastal tide gauges have been proposed for a western Mediterranean warning system, where there is also recent experience of tsunamis [139], and where distances between tsunami source and impacted coastlines are much shorter than in other ocean areas. Every minute counts for effective warning [140].

8.6.4 Bottom pressure measurements using cabled submarine networks

Cabled submarine networks exist as operational or demonstration projects in many parts of the world (e.g. ESONET in Europe, <http://www.esonet-noe.org/>, and the Neptune Network off the Pacific coast of Canada, <http://www.neptunecanada.com>) and their expansion complements the development of deep-ocean observatories (e.g. EuroSITES, <http://www.eurosites.info/>). Cabled networks provide great advantages over the use of buoys by supplying power and high-bandwidth, real-time communications connected to multiple sensors including bottom pressure gauges for tsunami detection. Japanese groups have for many years made pressure measurements using former telephone cables at considerable distances from the coast [140]. Seven tsunami-related cable systems are believed to be operational in Japan [24] with considerable investment in cable networks planned for the future involving 100s of pressure sensors.

8.6.5 GPS technology

Many tide gauges around the world are equipped with GPS receivers. A GPS receiver provides many benefits to a sea-level station (as described in Chapter 11) including the measurement of long-term vertical land movement at the site. If the receiver samples land level rapidly enough (e.g. 1 Hz), then its data can also

(a)

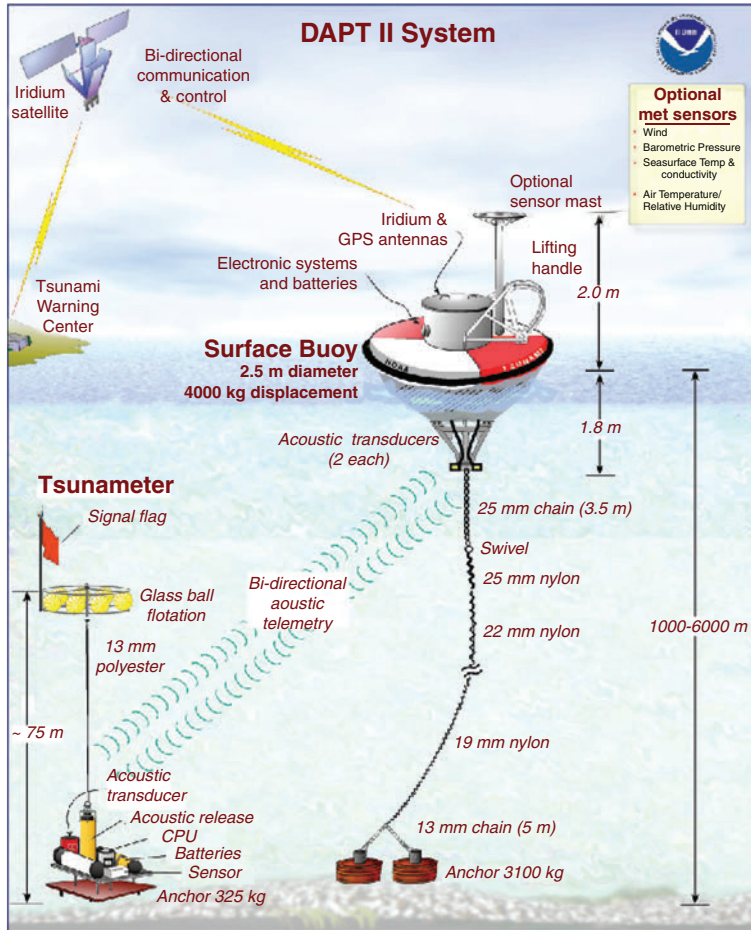


Figure 8.21 (a) Schematic of the second generation DART system from the Pacific Marine Environment Laboratory of NOAA (<http://nctr.pmel.noaa.gov/Dart/>). (b) Most recent variant of the DART surface buoy (the Easy to Deploy Buoy).

(b)



provide a tsunami warning centre important seismic information in the event of an earthquake [51].

GPS on ocean buoys can be used to measure tsunamis. Several such buoys in operation in Japanese waters delivered excellent time series showing

fluctuations of sea surface height of over 5 m during the Tōhoku event (Figure 8.23) [142, 143]. They have also been installed as part of the Indian Ocean Tsunami Warning System [137]. The GPS receiver, together with motion and dipping sensors, monitors

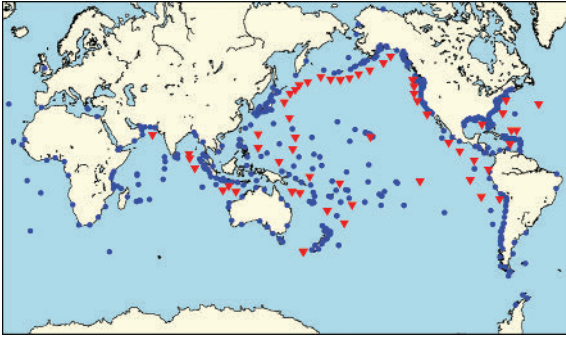


Figure 8.22 Map of DART and similar tsunameter deployments around the world (red triangles) together with sea-level stations (blue dots) that are presently monitored in real time by the Pacific Tsunami Warning Center. From [26].

sea level in real time and transmits data to a warning centre for further processing. Although the accuracy of GPS is not as good as ocean bottom pressure sensors, the technique is able to provide complementary information.

GPS installed on commercial ships has also been shown to be capable of detecting tsunamis, and it has been suggested that it should be possible to equip a significant fraction of the world's shipping fleet with GPS systems and create a cost-effective complement to other components of a tsunami warning system. Such a system would have detected the 2004 Sumatra tsunami in less than an hour, validating any warnings issued to distant coastlines such as Sri Lanka [144].

GPS can also be used to measure sea level near the coast by comparing GPS signals received directly from navigation satellites to those reflected off the nearby sea surface using a technique called reflectometry. Various experiments have been made, giving particular consideration to different antenna arrangements, and time series of sea level that have been produced compare well to those from nearby conventional tide gauges [145]. It is not clear if such a technology would have advantages over tide gauges in tsunami monitoring.

However, GPS, or more generally Global Navigation Satellite System (GNSS), reflectometry can also be used in space. The technique uses all available GNSS signal sources from navigational satellites, i.e. from GPS (United States) and GLONASS (Russia) at present, to be complemented by 2020 by COMPASS (China) and GALILEO (Europe). A constellation of perhaps 50 Low Earth Orbit (LEO) satellites equipped with multi-frequency receivers should be able to record reflections of GNSS signals from the sea surface and thereby rapidly provide maps of sea surface height

with decimetre precision in which a tsunami should be observable [146].

8.6.6 Coastal radars

High-frequency (HF) radars measure surface current by Bragg reflection of the radar waves. The technology can provide measurements of current approximately 200 km out to sea with accuracy better than 0.1 m/s depending on the spatial and temporal averaging employed [147]. The distance offshore at which a tsunami can be detected, and hence the warning time provided, depends on the width and depth of the continental shelf, the wider the shelf the greater the time. For example, a tsunami with a period of 40 minutes that is 1 metre high in water depth of 500 m has a wavelength of 168 km and a current (orbital velocity) of 0.14 m/s. As the depth decreases, orbital velocity increases as the inverse three-quarters power of depth, so at 200, 100 and 50 m depth the current is about 0.3, 0.5 and 0.8 m/s respectively. After the Sumatra event, it was proposed that such changes in current should be detectable before a large tsunami meets the coast [148], and they were indeed observed during the Tōhoku event in 2011 [149].

Others ways of measuring currents include current meters in the form of moored instruments or bottom-mounted Acoustic Doppler Current Profilers (ADCPs). However, they have disadvantages in measuring only at point locations, in being at risk of loss or damage in a violent event, and in needing effective means of transmitting their data. Novel methods for measuring currents have been proposed including the use of near-stationary un-manned stratospheric airships to carry a variety of radars for measurement of tsunami radar cross-section, wave height and orbital velocity [150]. These are particularly desirable for the detection of near- rather than far-field tsunamis.

8.6.7 Satellite altimetry

Radar altimetry has a long history in measuring global sea-level variability (Chapters 9 and 10). Each mission has its own orbit parameters leading to a specific sampling of the global sea surface. The Sumatra tsunami in 2004 was sampled by TOPEX/Poseidon, Jason-1, Envisat and GEOSAT Follow On, showing for the first time the capability of this technique to monitor rapid sea-level changes [101]. The Tōhoku tsunami in 2011 was also sampled by at least three altimeter satellites (Jason-1, Jason-2 and Envisat) with one recording

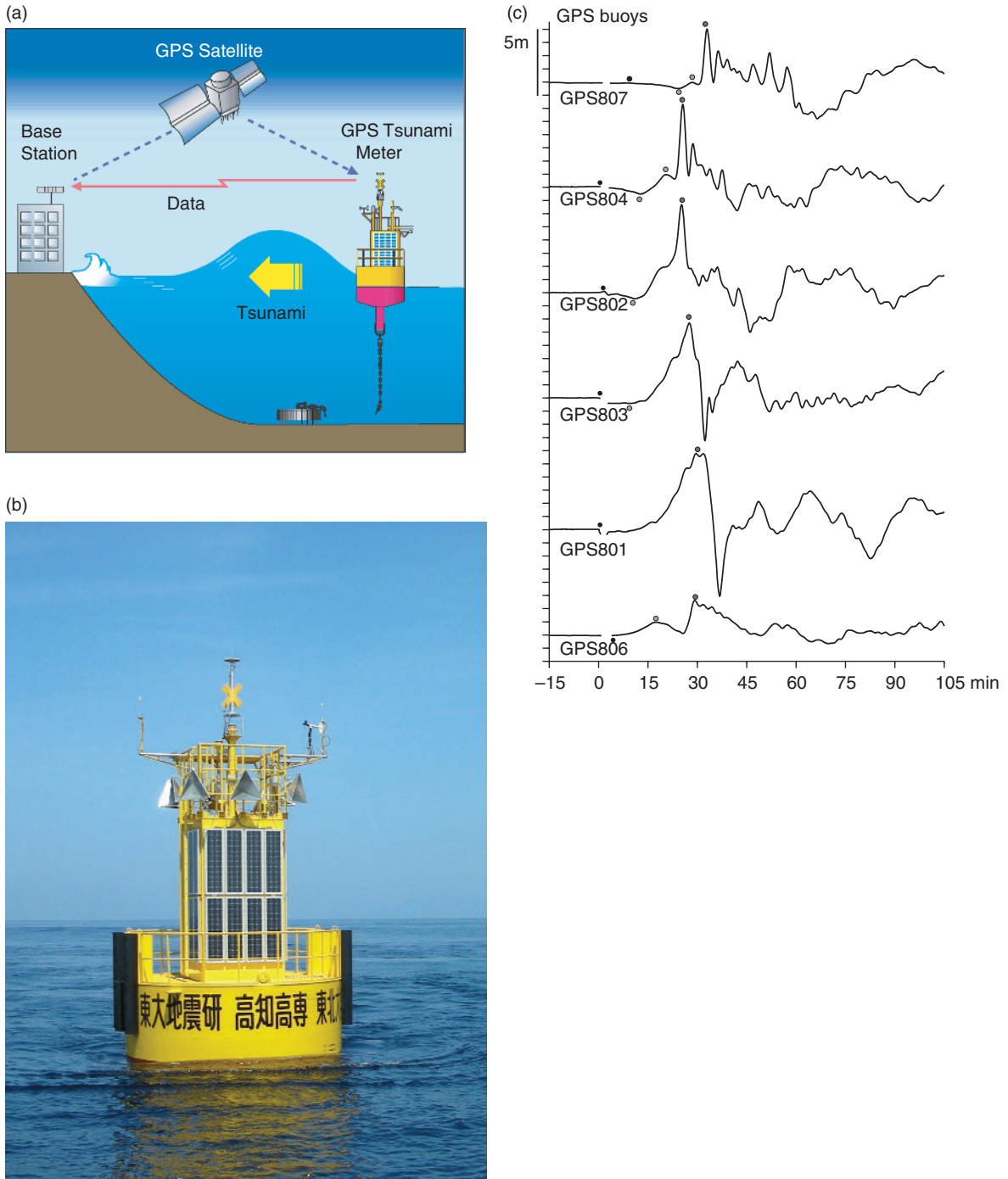


Figure 8.23 (a) Schematic of the Japanese GPS-buoy system. (b) GPS buoy located west of Cape Muroto, southwest Japan. From [142]. (c) Time series of sea surface height (slightly smoothed) from GPS-buoys off the east coast of Japan during the 2011 Tōhoku tsunami; dots indicate times of tsunami arrival, initial trough, a local crest and primary crest. From [143].

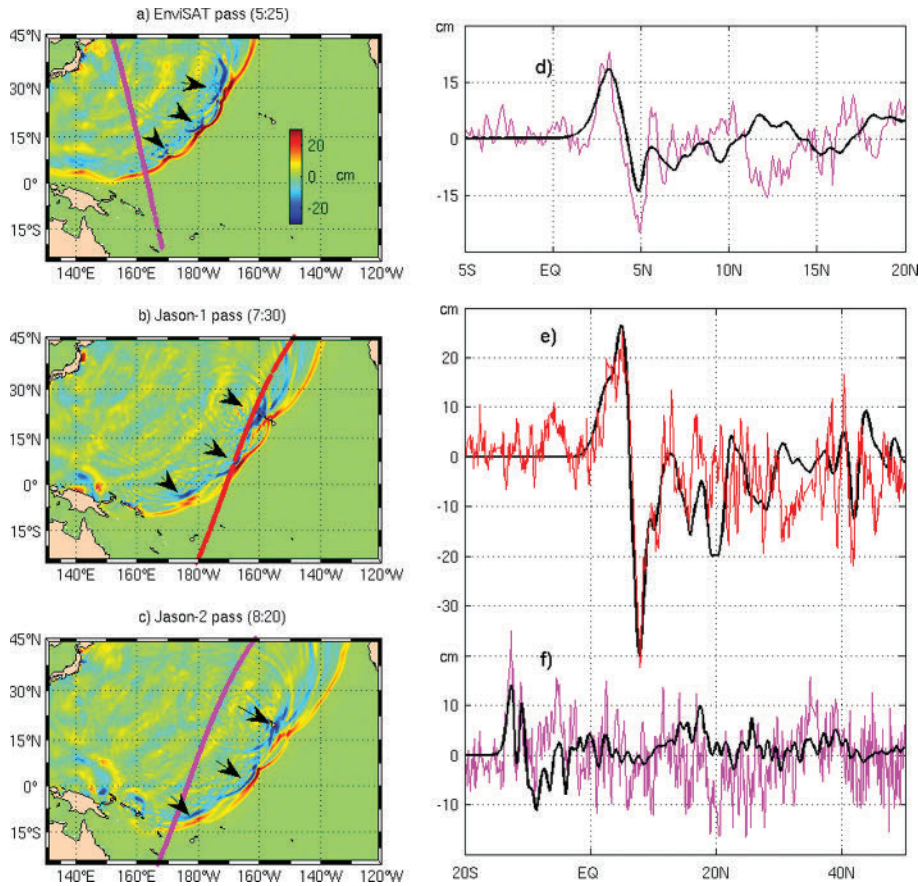


Figure 8.24 Altimeter passes by (a) Envisat at 5:25 hours after the Tohoku earthquake, (b) Jason-1 at 7:30 hours, and (c) Jason-2 at 8:20 hours. (d)–(f) show corresponding modelled tsunami heights (black) and altimeter measurements (red). Black arrows indicate areas of higher tsunami amplitude in particular parts of the ocean due to the merging of refracted waves; these larger amplitudes were observed only in the Jason-1 profile. From [151].

twice the wave height of the other two missions and thereby helping to identify the focusing of energy into jets by topographic refraction (Figure 8.24) [151].

A good development of modern altimetry is that missions now have real-time data capability [152]. However, the coarse spatial–temporal sampling of nadir-pointing altimeters means that they are unlikely to detect most tsunamis apart from basin-wide events [153]. If satellites were to be developed with wide-swath altimeters [154] and/or if constellations of conventional altimeter satellites could be deployed [155], together with real-time data processing, then there would be a possibility of constructing an operational altimeter tsunami observation system.

The 2004 Sumatra earthquake resulted in changes to the Earth’s gravity field that were detected by another satellite, the Gravity Recovery And Climate Experiment (GRACE) space gravity mission (Chapter 9 and Figure 10.27) [156]. However, it is not feasible at

present to include real-time space gravity data in an operational tsunami warning system.

8.6.8 Acoustic measurements

Infrasound refers to atmospheric sound waves with frequencies lower than the 20 Hz hearing threshold of the human ear and can be produced by the displacements of the Earth’s surface caused by earthquakes, tsunamis and volcanoes. Infrasound detection arrays exist in the Pacific and Indian Oceans and they recorded the low-frequency emissions of the Sumatra earthquake and tsunami, although interpretation of the various signals remains a research topic [157]. Acoustic signals with frequencies exceeding 100 Hz were recorded in hydrophone arrays in the Indian Ocean, with arrival times compared to those from tide gauge data [158]. The feasibility of using both types of acoustic measurements were also tested

during the 2011 Tōhoku event [159], demonstrating that both may eventually prove useful in providing ancillary information in tsunami warning. In addition, variations of air density and vertical acceleration at an altitude of approximately 270 km stemming from the infrasound wave fronts of the Tōhoku event were detected by the GOCE space satellite [160].

8.7 Tsunami further reading

The research literature is replete with studies of tsunamis, especially since the Sumatra and Tōhoku events [161]. This chapter has concentrated on providing an overview to complement other chapters in this book, but there is much more to read concerning the geology, oceanography and coastal and civil defence aspects of tsunamis. Particularly interesting areas include lessons learned for the rapid forecasting of local impacts once an earthquake has occurred and scenario planning based on experience of past events [162]. Many countries have made assessments of what they have to do to be better prepared for tsunamis [163] and studies have been made of risks to strategic global assets [164]. It is clear that tide gauge, GPS and other specialists have a large part to play in ensuring that the world has an effective and sustained future tsunami warning system.

References

1. Details of the 2004 Sumatra and other earthquakes may be found at <http://earthquake.usgs.gov/earthquakes/>.
2. Lay, T., Kanamori, H., Ammon, C. J. *et al.* 2005. The Great Sumatra-Andaman earthquake of 26 December 2004. *Science*, **308**, 1127–1133, doi:10.1126/science.1112250.
3. Rossetto, T., Peiris, N., Pomonis, A. *et al.* 2007. The Indian Ocean tsunami of December 26, 2004: observations in Sri Lanka and Thailand. *Natural Hazards*, **42**, 105–124, doi:10.1007/s11069-006-9064-3.
4. <http://tsun.ssc.ru/tsulab/20041226fat.htm>.
5. Lay, T. and Kanamori, H. 2011. Insights from the great 2011 Japan earthquake. *Physics Today*, **64**, 33–39, doi:10.1063/PT.3.1361.
6. Solheim, A., Berg, K., Forsberg, C. F. and Bryn, P. 2005. The Storegga Slide complex: repetitive large scale sliding with similar cause and development. *Marine and Petroleum Geology*, **22**, 97–107, doi:10.1016/j.marpetgeo.2004.10.013.
7. Smith, D. E., Shib, S., Cullingford, R. A. *et al.* 2004. The Holocene Storegga Slide tsunami in the United Kingdom. *Quaternary Science Reviews*, **23**, 2291–2321, doi:10.1016/j.quascirev.2004.04.001.
8. Bondevik, S., Mangerud, J., Dawson, S., Dawson, A. and Lohne, Ø. 2005. Evidence for three North Sea tsunamis at the Shetland Islands between 8000 and 1500 years ago. *Quaternary Science Reviews*, **24**, 1757–1775, doi:10.1016/j.quascirev.2004.10.018.
9. Romundset, A. and Bondevik, S. 2011. Propagation of the Storegga tsunami into ice-free lakes along the southern shores of the Barents Sea. *Journal of Quaternary Science*, **26**, 457–462, doi:10.1002/jqs.1511.
10. Goodman-Tchernov, B. N., Dey, H. W., Reinhardt, E. G., McCoy, F. and Mart, Y. 2009. Tsunami waves generated by the Santorini eruption reached Eastern Mediterranean shores. *Geology*, **37**, 943–946, doi:10.1130/G25704A.
11. Hamouda, A. Z. 2006. Numerical computations of 1303 tsunamigenic propagation towards Alexandria, Egyptian Coast. *Journal of African Earth Sciences*, **44**, 37–44, doi:10.1016/j.jafrearsci.2005.11.005.
12. Dawson, A. G., Musson, R. M. W., Foster, I. D. L. and Brunnsden, D. 2000. Abnormal historic sea-surface fluctuations, SW England. *Marine Geology*, **170**, 59–68, doi:10.1016/S0025-3227(00)00065-7.
13. Horsburgh, K. J., Wilson, C., Baptie, B. J. *et al.* 2008. Impact of a Lisbon-type tsunami on the U.K. coastline and the implications for tsunami propagation over broad continental shelves. *Journal of Geophysical Research*, **113**, C04007, doi:10.1029/2007JC004425.
14. Stothers, R. B. 1984. The Great Tambora eruption in 1815 and its aftermath. *Science*, **224**, 1191–1198, doi:10.1126/science.224.4654.1191.
15. Mader, C. L. and Gittings, M. L. 2006. Numerical model for the Krakatoa hydrovolcanic explosion and tsunami. *Science of Tsunami Hazards*, **24**, 174–182.
16. Fine, I. V., Rabinovich, A. B., Bornhold, B. D., Thomson, R. E. and Kulikov, E. A. 2005. The Grand Banks landslide-generated tsunami of November 18, 1929: preliminary analysis and numerical modeling. *Marine Geology*, **215**, 45–57, doi:10.1016/j.margeo.2004.11.007.
17. (1) Heezen, B. C. and Ewing, W. M. 1952. Turbidity currents and submarine slumps and the 1929 Grand Banks earthquake. *American Journal of Science*, **250**, 849–873, doi:10.2475/ajs.250.12.849. (2) Piper, D. J. W., Shor, A. N. and Hughes Clarke, J. E., 1988. The 1929 Grand Banks earthquake, slump and turbidity current. In *Sedimentologic Consequences of Convulsive Geologic Events* (ed. H. E. Clifton), pp. 77–92. Special Papers of the Geological Society of America, 229, doi:10.1130/SPE229-p77.
18. See the NOAA Center for Tsunami Research website http://nctr.pmel.noaa.gov/database_devel.html.
19. Cataloguesinclude: (1) NOAA/WDC Global Historical Tsunami Database at NGDC <http://www.ngdc.noaa.gov/>

- hazard/tsu_db.shtml; (2) The International Tsunami Information Centre catalogue <http://itic.ioc-unesco.org/index.php> and see also <http://www.ioc-tsunami.org/>; (3) Tinti, S., Maramai, A. and Graziani, L. 2004. The new catalogue of Italian tsunamis. *Natural Hazards*, **33**, 439–465, doi:10.1023/B:NHAZ.0000048469.51059.65; (4) Papadopoulos, G. A., Daskalaki, E., Fokaefs, A. and Giraleas, N. 2007. Tsunami hazards in the Eastern Mediterranean: strong earthquakes and tsunamis in the East Hellenic Arc and Trench system. *Natural Hazards and Earth System Sciences*, **7**, 57–64, <http://www.nat-hazards-earth-syst-sci.net/7/57/2007/>; (5) Pasarić, M., Brizuela, B., Graziani, L., Maramai, A. and Orlić, M. 2012. Historical tsunamis in the Adriatic Sea. *Natural Hazards*, **61**, 281–316, doi:10.1007/s11069-011-9916-3; (6) Long, D. and Wilson, C. K. 2007. *A Catalogue of Tsunamis in the UK*. British Geological Survey Commissioned Report, CR/07/077; (7) Soloviev, S. L., Solovieva, O. N., Go, C. N., Kim, K. S. and Shchetnikov, N. A., 2000. *Tsunamis in the Mediterranean Sea 2000 B.C.–2000 A.D.* Advances in Natural and Technological Hazards Research, 13. Dordrecht: Kluwer, (8) A review of catalogues can also be found in Joseph (2011), see below.
20. Joseph, A. 2011. *Tsunamis: Detection, Monitoring, and Early-Warning Technologies*. Burlington, MA: Academic Press.
 21. Horsburgh, K. and Horritt, M. 2006. The Bristol Channel floods of 1607: reconstruction and analysis. *Weather*, **61**, 272–277, doi:10.1256/wea.133.05.
 22. The PTWC website is <http://ptwc.weather.gov/>
 23. Igarashi, Y., Kong, L., Yamamoto, M. and McCreery, C. S. 2011. Anatomy of historical tsunamis: lessons learned for tsunami warning. *Pure and Applied Geophysics*, **168**, 2043–2063, doi:10.1007/s00024-011-0287-1.
 24. Mofjeld, H. O. 2009. Tsunami measurements. In *The Sea. Volume 15: Tsunamis*, pp. 201–235. Cambridge, MA and London, UK: Harvard University Press.
 25. IOC, 2006. *Manual on Sea-Level Measurement and Interpretation. Volume 4: An Update to 2006* (eds. T. Aarup, M. Merrifield, B. Perez, I. Vassie and P. Woodworth). Intergovernmental Oceanographic Commission Manuals and Guides No. 14. Paris: UNESCO/Intergovernmental Oceanographic Commission.
 26. IOC, 2013. *Tsunami Glossary* (Revised edition). Intergovernmental Oceanographic Commission Technical Series, 85 (IOC/2008/Ts/85rev). Paris: UNESCO/Intergovernmental Oceanographic Commission.
 27. Bryant, E. 2008. *Tsunami: The Underrated Hazard* (2nd edition). Chichester: Springer Praxis Books.
 28. Levin, B. and Nosov, M. 2010. *Physics of Tsunamis*. Springer.
 29. Kowalik, Z. 2012. Introduction to numerical modeling of tsunami waves. Available from <http://www.sfos.uaf.edu/directory/faculty/kowalik/>.
 30. Ward, S. N. 2011. Tsunami. In *The Encyclopedia of Solid Earth Geophysics* (ed. H. Gupta), pp.1473–1493. Dordrecht: Springer. doi:10.1007/978-90-481-8702-7.
 31. IOC, 2012. *The Global Sea Level Observing System (GLOSS) Implementation Plan – 2012*. UNESCO/Intergovernmental Oceanographic Commission (IOC Technical Series No. 100). Available from ioc.unesco.org.
 32. Rabinovich, A. B. and Thomson, R. E. 2007. The 26 December 2004 Sumatra tsunami: analysis of tide gauge data from the World Ocean. Part 1. Indian Ocean and South Africa. *Pure and Applied Geophysics*, **164**, 261–308, doi:10.1007/s00024-006-0164-5.
 33. Abe, K. 2006. Dominant periods of the 2004 Sumatra tsunami and the estimated source size. *Earth, Planets and Space*, **58**, 217–221.
 34. Tang, L., Titov, V. V., Bernard, E. N. *et al.* 2012. Direct energy estimation of the 2011 Japan tsunami using deep-ocean pressure measurements. *Journal of Geophysical Research*, **117**, C08008, doi:10.1029/2011JC007635.
 35. Tappin, D. R., Watts, P. and Grilli, S. T. 2008. The Papua New Guinea tsunami of 17 July 1998: anatomy of a catastrophic event. *Natural Hazards and Earth System Sciences*, **8**, 243–266, www.nat-hazards-earth-syst-sci.net/8/243/2008/.
 36. Tanioka, Y. 1999. Analysis of the far-field tsunamis generated by the 1998 Papua New Guinea earthquake. *Geophysical Research Letters*, **26**, 3393–3396, doi:10.1029/1999GL005392.
 37. González, F. I. 1999. Tsunami! *Scientific American*, **280**, 56–65, doi:10.1038/scientificamerican0599-56.
 38. Mader, C. L. 2001. Modeling the 1755 Lisbon tsunami. *Science of Tsunami Hazards*, **19**, 93–98.
 39. Lighthill, M. J. 1978. *Waves in Fluids*. Cambridge: Cambridge University Press.
 40. For a general treatment of ocean waves see, LeBlond, P. H. and Mysak, L. A. 1978. *Waves in the Ocean*. Amsterdam: Elsevier Scientific Publishing.
 41. Faber, T. E. 1995. *Fluid Dynamics for Physicists*. Cambridge: Cambridge University Press.
 42. McCaffrey, R. 2009. The tectonic framework of the Sumatran Subduction Zone. *Annual Review of Earth and Planetary Sciences*, **37**, 345–366, doi:10.1146/annurev.earth.031208.100212.
 43. Certain earthquakes such as Tōhoku can be associated with a release of gravitational energy as well as elastic strain, see McKenzie, D. and Jackson, J. 2012. Tsunami earthquake generation by the release of

- gravitational potential energy. *Earth and Planetary Science Letters*, 345–348, 1–8, doi:10.1016/j.epsl.2012.06.036.
44. Murty, T. S. 1977. *Seismic Sea Waves: Tsunamis*. Ottawa: Department of Fisheries and the Environment, Fisheries and Marine Service.
 45. Maeda, T., Furumura, T., Sakai, S. and Shinohara, M. 2011. Significant tsunami observed at the ocean-bottom pressure gauges at 2011 off the Pacific coast of Tohoku earthquake. *Earth, Planets and Space*, **63**, 803–808, doi:10.5047/eps.2011.06.005.
 46. Geist, E. L., Bilek, S. L., Arcas, D. and Titov, V. V. 2006. Differences in tsunami generation between the December 26, 2004 and March 28, 2005 Sumatra earthquakes. *Earth, Planets and Space*, **58**, 185–193.
 47. (1) Kowalik, Z., Logan, T., Knight, W. and Whitmore, P. 2005. Numerical modeling of the global Indonesian tsunami of 26 December 2004. *Science of Tsunami Hazards*, **23**, 40–56. (2) Nirupama, N., Murty, T. S., Bistor, I. and Rao, A. D. 2006. Energetics of the tsunami of 26 December 2004 in the Indian Ocean: a brief review. *Marine Geodesy*, **29**, 39–47, doi:10.1080/01490410600582346.
 48. Tanioka, Y., Yudhicara, Kususose, T. *et al.* 2006. Rupture process of the 2004 great Sumatra-Andaman earthquake estimated from tsunami waveforms. *Earth, Planets and Space*, **58**, 203–209.
 49. (1) Song, Y. T., Ji, C., Fu, L.-L. *et al.* 2005. The 26 December 2004 tsunami source estimated from satellite radar altimetry and seismic waves. *Geophysical Research Letters*, **32**, L20601, doi:10.1029/2005GL023683. (2) Song, Y. T., Fu, L.-L., Zlotnicki, V. *et al.* 2008. The role of horizontal impulses of the faulting continental slope in generating the 26 December 2004 tsunami. *Ocean Modelling*, **20**, 362–379, doi:10.1016/j.ocemod.2007.10.007. (3) Song, Y. T. and Han, S.-C. 2011. Satellite observations defying the long-held tsunami genesis theory. In *Remote Sensing of the Changing Oceans* (ed. D. Tang), pp. 327–342. Berlin: Springer-Verlag, doi:10.1007/978-3-642-16541-2_17.
 50. In the geological modelling of long period tsunami generation one also has to consider the structure of the solid Earth and its normal modes, see Ward, S. N. 1980. Relationships of tsunami generation and an earthquake source. *Journal of Physics of the Earth*, **28**, 441–474.
 51. (1) Blewitt, G., Kreemer, C., Hammond, W. C. *et al.* 2006. Rapid determination of earthquake magnitude using GPS for tsunami warning systems. *Geophysical Research Letters*, **33**, L11309, doi:10.1029/2006GL026145. (2) Murray-Moraleda, J. 2009. GPS: applications in crustal deformation monitoring. In *Encyclopedia of Complexity and Systems Science* (ed. R. A. Myers), pp. 4249–4283. Springer, doi:10.1007/978-0-387-30440-3_250.
 52. Okada, Y. 1985. Surface deformation due to shear and tensile faults in a half-space. *Bulletin of the Seismological Society of America*, **75**, 1135–1154.
 53. Satake, K. 2009. Tsunamis, inverse problem of. In *Encyclopedia of Complexity and Systems Science* (ed. R. A. Myers), pp. 1022–1034. Springer, doi:10.1007/978-1-4419-7695-6_54.
 54. Yeh, H., Imamura, F., Synolakis, C. *et al.* 1993. The Flores Island Tsunamis. *Eos, Transactions of the American Geophysical Union*, **74**(33), 369 and 371–373.
 55. Imamura, F., Gica, E., Takahashi, T. and Shuto, N. 1995. Numerical simulation of the 1992 Flores tsunami: interpretation of tsunami phenomena in Northeastern Flores Island and damage at Babi Island. *Pure and Applied Geophysics*, **144**, 555–568, doi:10.1007/BF00874383.
 56. Billi, A., Funicello, R., Minelli, L. *et al.* 2008. On the cause of the 1908 Messina tsunami, southern Italy. *Geophysical Research Letters*, **35**, L06301, doi:10.1029/2008GL033251.
 57. Bondevik, S., Løvholt, F., Harbitz, C. *et al.* 2005. The Storegga Slide tsunami: comparing field observations with numerical simulations. *Marine and Petroleum Geology*, **22**, 195–208, doi:10.1016/j.marpetgeo.2004.10.003.
 58. Weninger, B., Schulting, R., Bradtmöller, M. *et al.* 2008. The catastrophic final flooding of Doggerland by the Storegga Slide tsunami. *Documenta Praehistorica*, **35**, 1–24.
 59. Masson, D. G., Wynn, R. B. and Talling, P. J. 2010. Large landslides on passive continental margins: processes, hypotheses and outstanding questions. In *Submarine Mass Movements and Their Consequences* (eds. D. C. Mosher *et al.*), pp. 153–165. Advances in Natural and Technological Hazards Research, Volume 28, Berlin: Springer-Verlag.
 60. Vogt, P. R. and Jung, W.-Y. 2002. Holocene mass wasting on upper non-polar continental slopes: due to post-glacial ocean warming and hydrate dissociation? *Geophysical Research Letters*, **29**, 9, doi:10.1029/2001GL013488.
 61. Kvenvolden, K. A. 1988. Methane hydrates: a major reserve of carbon in the shallow geosphere? *Chemical Geology*, **71**, 41–51, doi:10.1016/0009-2541(88)90104-0.
 62. Lobkovsky, L. I., Mazova, R. K., Garagash, I. A. and Kataeva, L. Y. 2006. Numerical simulation of the 7 February 1963 tsunami in the Bay of Corinth, Greece. *Russian Journal of Earth Sciences*, **8**, ES5003, doi:10.2205/2006ES000210.
 63. Suleimani, E., Hansen, R. and Haessler, P. J. 2009. Numerical study of tsunami generated by multiple submarine slope failures in Resurrection Bay, Alaska, during the M_w 9.2 1964 earthquake. *Pure and Applied*

- Geophysics*, **166**, 131–152, doi:10.1007/s00024-004-0430-3.
64. Lander, J. F., Lockridge, P. A. and Kozuch, M. J. 1993. *Tsunamis Affecting the West Coast of the United States 1806–1992*. National Geophysical Data Center Key to Geophysical Records Documentation No. 29.
 65. Fine, I. V., Cherniawsky, J. Y., Rabinovich, A. B. and Stephenson, F. 2008. Numerical modeling and observations of tsunami waves in Alberni Inlet and Barkley Sound, British Columbia. *Pure and Applied Geophysics*, **165**, 2019–2044, doi:10.1007/s00024-008-0414-9.
 66. James, T., Rogers, G., Cassidy, J. et al. 2013. Field studies target 2012 Haida Gwaii earthquake. *Eos, Transactions of the American Geophysical Union*, **94**, 197–198, doi:10.1002/2013EO220002.
 67. Rabinovich, A. B., Thomson, R. E., Bornhold, B. D., Fine, I. V. and Kulikov, E. A. 2003. Numerical modelling of tsunamis generated by hypothetical landslides in the Strait of Georgia, British Columbia. *Pure and Applied Geophysics*, **60**, 1273–1313, doi:10.1007/s000240300006.
 68. (1) Kulikov, E. A., Rabinovich, A. B., Thomson, R. E. and Bornhold, B. D. 1996. The landslide tsunami of November 3, 1994, Skagway Harbor, Alaska. *Journal of Geophysical Research*, **101**, C3, doi:10.1029/95JC03562. (2) Rabinovich, A. B., Thomson, R. E., Kulikov, E. A., Bornhold, B. D. and Fine, I. V. 1999. The landslide-generated tsunami of November 3, 1994 in Skagway Harbor, Alaska: a case study. *Geophysical Research Letters*, **26**, 19, doi:10.1029/1999GL002334. (3) Thomson, R. E., Rabinovich, A. B., Kulikov, E. A., Fine, I. V. and Bornhold, B. D. 2001. On numerical simulation of the landslide-generated tsunami of November 3, 1994 in Skagway Harbor, Alaska. In *Tsunami Research at the End of a Critical Decade* (ed. G. Hebenstreit), pp. 243–282. Dordrecht: Kluwer Academic Publishers.
 69. Kulikov, E. A., Rabinovich, A. B., Fain, I. V., Bornhold, B. D. and Thomson, R. E. 1998. Tsunami generation by landslides at the Pacific coast of North America and the role of tides. *Oceanology*, **38**, 323–328.
 70. Labbé, M., Donnadiou, C., Daubord, C. and Hébert, H. 2012. Refined numerical modeling of the 1979 tsunami in Nice (French Riviera): comparison with coastal data. *Journal of Geophysical Research*, **117**, F01008, doi:10.1029/2011JF001964.
 71. Fine, I. V., Rabinovich, A. B., Thomson, R. E. and Kulikov, E. A. 2003. Numerical modeling of tsunami generation by submarine and subaerial landslides. In *Submarine Landslides and Tsunamis* (eds. A. C. Yalciner, E. N. Pelinovsky, C. E. Synolakis and E. Okal), pp. 69–88. NATO Advanced Series, Volume 21, Dordrecht: Kluwer Academic Publishers.
 72. (1) Weiss, R., Fritz, H. M. and Wünnemann, K. 2009. Hybrid modeling of the mega-tsunami runup in Lituya Bay after half a century. *Geophysical Research Letters*, **36**, L09602, doi:10.1029/2009GL037814. (2) Fritz, H. M., Mohammed, F. and Yoo, J. 2009. Lituya Bay landslide impact generated mega-tsunami 50th anniversary. *Pure and Applied Geophysics*, **166**, 153–175, doi:10.1007/s00024-008-0435-4.
 73. Bornhold, B. D., Harper, J. R., McLaren, D. and Thomson, R. E. 2007. Destruction of the first nations village of Kwalete by a rock avalanche-generated tsunami. *Atmosphere-Ocean*, **45**, 123–128, doi:10.3137/ao.450205.
 74. Panthi, K. K. and Nilsen, B. 2006. Numerical analysis of stresses and displacements for the Tafjord slide, Norway. *Bulletin of Engineering Geology and the Environment*, **65**, 57–63, doi:10.1007/s10064-005-0009-y.
 75. <http://en.wikipedia.org/wiki/Geirangerfjord>
 76. Naranjo, J. A., Arenas, M., Clavero, J. and Munoz, O. 2009. Mass movement-induced tsunamis: main effects during the Patagonian Fjordland seismic crisis in Aisén (45° 25'S), Chile. *Andean Geology*, **36**, 137–145. www.scielo.cl/rgch.htm.
 77. Ward, S. N. and Day, S. 2001. Cumbre Vieja Volcano: potential collapse and tsunami at La Palma, Canary Islands. *Geophysical Research Letters*, **28**, 17, doi:10.1029/2001GL013110.
 78. Løvholt, F., Pedersen, G. and Gisler, G. 2008. Oceanic propagation of a potential tsunami from the La Palma Island. *Journal of Geophysical Research*, **113**, C09026, doi:10.1029/2007JC004603.
 79. Abadie, S. M., Harris, J. C., Grilli, S. T. and Fabre, R. 2012. Numerical modeling of tsunami waves generated by the flank collapse of the Cumbre Vieja Volcano (La Palma, Canary Islands): tsunami source and near field effects. *Journal of Geophysical Research*, **117**, C05030, doi:10.1029/2011JC007646.
 80. (1) Winchester, S. 2004. *Krakatoa: The Day the Earth Exploded: August 27, 1883*. London: Penguin Books. (2) Maeno, F. and Imamura, F. 2011. Tsunami generation by a rapid entrance of pyroclastic flow into the sea during the 1883 Krakatau eruption, Indonesia. *Journal of Geophysical Research*, **116**, B09205, doi:10.1029/2011JB008253.
 81. (1) <http://www.ipfran.ru/pp/Pelinovsky/krakatau/> (2) Pelinovsky, E., Choi, B. H., Stromkov, A., Didenkulova, I. and Kim, H.-S. 2005. Analysis of tide-gauge records of the 1883 Krakatau tsunami. In *Tsunamis: Case Studies and Recent Developments* (ed. K. Satake), pp. 57–78. Dordrecht: Springer.
 82. Pararas-Carayannis, G. 2003. Near and far-field effects of tsunamis generated by the paroxysmal eruptions, explosions, caldera collapses and massive slope failures of the Krakatau volcano in Indonesia on August 26–27, 1883. *Science of Tsunami Hazards*, **21**, 191–211.

83. See extended discussion of the role of the air pressure wave in Murty (1977) [44] and also Garrett, C. J. R. 1970. A theory of the Krakatoa tide gauge disturbances. *Tellus*, **22**, 43–52, doi:10.1111/j.2153-3490.1970.tb01935.x.
84. Ward, S. N. and Asphaug, E. 2000. Asteroid impact tsunami: a probabilistic hazard assessment. *Icarus*, **145**, 64–78, doi:10.1006/icar.1999.6336.
85. Schulte, P. *et al.* 2010. The Chicxulub asteroid impact and mass extinction at the Cretaceous-Paleogene boundary. *Science*, **327**, 1214–1218, doi:10.1126/science.1177265.
86. Toon, O. B., Zahnle, K., Morrison, D., Turco, R. P. and Covey, C. 1997. Environmental perturbations caused by the impacts of asteroids and comets. *Reviews of Geophysics*, **35**, 1, doi:10.1029/96RG03038.
87. Shoemaker, E. M. 1983. Asteroid and comet bombardment of the Earth. *Annual Review of Earth and Planetary Sciences*, **11**, 461–94, doi:10.1146/annurev.ea.11.050183.002333.
88. (1) Ward, S. N. and Asphaug, E. 2002. Impact tsunami: Eltanin. *Deep-Sea Research II*, **49**, 1073–1079, doi:10.1016/S0967-0645(01)00147-3. (2) Gislser, G., Weaver, R., Mader, C. and Gittings, M. L. 2003. Two- and three-dimensional simulations of asteroid ocean impacts. *Science of Tsunami Hazards*, **21**, 119–134. (3) Weiss, R., Wünnemann, K. and Bahlburg, H. 2006. Numerical modelling of generation, propagation and runup of tsunamis caused by oceanic impacts: model strategy and technical solutions. *Geophysical Journal International*, **167**, 77–88, doi:10.1111/j.1365-246X.2006.02889.x.
89. http://en.wikipedia.org/wiki/Halifax_Explosion
90. MacDonald, L. M. 2005. *Curse of the Narrows*. New York: Walker and Company.
91. http://en.wikipedia.org/wiki/Underwater_explosion
92. Rutley, J. I. A. 1959. The demolition of Ripple Rock. *International Hydrographic Review*, **36**, 19–28.
93. Kowalik, Z., Knight, W., Logan, T. and Whitmore, P. 2007. The tsunami of 26 December, 2004: numerical modeling and energy considerations. *Pure and Applied Geophysics*, **164**, 379–393, doi:10.1007/s00024-006-0162-7.
94. Henry, R. F. and Foreman, M. G. G. 2001. A representation of tidal currents based on energy flux. *Marine Geodesy*, **24**, 139–152, doi:10.1080/01490410152494718.
95. Titov, V. V. and Synolakis, C. E. 1998. Numerical modeling of tidal wave runup. *Journal of Waterway, Port, Coastal, and Ocean Engineering*, **124**, 157–171, doi:10.1061/(ASCE)0733-950X(1998)124:4(157) and see also many references in <http://nctr.pmel.noaa.gov/most-pubs.html>.
96. Lynett, P. J. 2009. Tsunami inundation, modeling of. In *Encyclopedia of Complexity and Systems Science* (ed. R. A. Myers), pp. 9618–9631. Springer, doi:10.1007/978-0-387-30440-3_569.
97. Ammon, C. J., Ji, C., Thio, H.-K. *et al.* 2005. Rupture process of the 2004 Sumatra-Andaman earthquake. *Science*, **308**, 1133–1139, doi:10.1126/science.1112260.
98. Titov, V., Rabinovich, A. B., Mofjeld, H. O., Thomson, R. E. and González, F. I. 2005. The global reach of the 26 December 2004 Sumatra tsunami. *Science*, **309**, 2045–2048, doi:10.1126/science.1114576.
99. Fine, I. V., Rabinovich, A. B. and Thomson, R. E. 2005. The dual source region for the 2004 Sumatra tsunami. *Geophysical Research Letters*, **32**, L16602, doi:10.1029/2005GL023521.
100. Merrifield, M. A., Firing, Y. L., Aarup, T. *et al.* 2005. Tide gauge observations of the Indian Ocean tsunami, December 26, 2004. *Geophysical Research Letters*, **32**, L09603, doi:10.1029/2005GL022610.
101. (1) Gower, J. 2005. Jason 1 detects the 26 December 2004 tsunami. *Eos, Transactions American Geophysical Union*, **86**, 37–38, doi:10.1029/2005EO040002. (2) Smith, W. H. F., Scharroo, R., Titov, V. V., Arcas, D. and Arbic, B. K. 2005. Ocean news: Satellite altimeters measure tsunami: early model estimates confirmed. *Oceanography*, **18**(2), 11–13, doi:10.5670/oceanog.2005.62. (3) Song, Y. T., Ji, C., Fu, L.-L. *et al.* 2005. The 26 December 2004 tsunami source estimated from satellite radar altimetry and seismic waves. *Geophysical Research Letters*, **32**, L20601, doi:10.1029/2005GL023683. (4) Ablain, M., Dorandeu, J., Le Traon, P.-Y. and Sladen, A. 2006. High resolution altimetry reveals new characteristics of the December 2004 Indian Ocean tsunami. *Geophysical Research Letters*, **33**, L21602, doi:10.1029/2006GL027533. (5) Hayashi, Y. 2008. Extracting the 2004 Indian Ocean tsunami signals from sea surface height data observed by satellite altimetry. *Journal of Geophysical Research*, **113**, C01001, doi:10.1029/2007JC004177.
102. França, C. A. S. and De Mesquita, A. R. 2007. The December 26th 2004 tsunami recorded along the southeastern Coast of Brazil. *Natural Hazards*, **40**, 209–222, doi:10.1007/s11069-006-0010-1.
103. Woodworth, P. L., Blackman, D. L., Foden, P. *et al.* 2005. Evidence for the Indonesian tsunami in British tidal records. *Weather*, **60**, 263–267. doi:10.1256/wea.59.05.
104. (1) Rabinovich, A. B., Thomson, R. E. and Stephenson, F. E. 2006. The Sumatra tsunami of 26 December 2004 as observed in the North Pacific and North Atlantic oceans. *Surveys in Geophysics*, **2**, 647–677, doi:10.1007/s10712-006-9000-9. (2) Thomson, R. E., Rabinovich, A. B. and

- Krassovski, M. V. 2007. Double jeopardy: Concurrent arrival of the 2004 Sumatra tsunami and storm-generated waves on the Atlantic coast of the United States and Canada. *Geophysical Research Letters*, **34**, L15607, doi:10.1029/2007GL030685.
105. Candella, R. N., Rabinovich, A. B. and Thomson, R. E. 2008. The 2004 Sumatra tsunami as recorded on the Atlantic coast of South America. *Advances in Geosciences*, **14**, 117–128, www.adv-geosci.net/14/117/2008/.
106. Dragani, W. C., D'Onofrio, E. E., Grismeyer, W. and Fiore, M. E. 2006. Tide gauge observations of the Indian ocean tsunami, December 26, 2004, in Buenos Aires coastal waters, Argentina. *Continental Shelf Research*, **26**, 1543–1550, doi:10.1016/j.csr.2006.03.002.
107. Joseph, A., Odamety, J. T., Nkebi, E. K. *et al.* 2006. The 26 December 2004 Sumatra tsunami recorded on the coast of West Africa. *African Journal of Marine Science*, **28**(3–4), 705–712.
108. Rabinovich, A. B., Woodworth, P. L. and Titov, V. V. 2011. Deep-sea observations and modeling of the 2004 Sumatra tsunami in Drake Passage. *Geophysical Research Letters*, **38**, L16604, doi:10.1029/2011GL048305.
109. Stimpson, I. 2011. Japan's Tohoku earthquake and tsunami. *Geology Today*, **27**, 96–98.
110. Grilli, S. T., Harris, J. C., Bakhsh, T. S. T. *et al.* 2013. Numerical simulation of the 2011 Tohoku tsunami based on a new transient FEM co-seismic source: comparison to far- and near-field observations. *Pure and Applied Geophysics*, **170**, 1333–1359, doi:10.1007/s00024-012-0528-y.
111. Allan, J. C., Komar, P. D., Ruggiero, P. and Witter, R. 2012. The March 2011 Tōhoku tsunami and its impacts along the U.S. west coast. *Journal of Coastal Research*, **28**(5), 1142–1153, doi:10.2112/JCOASTRES-D-11-00115.1.
112. Kowalik, Z., Horrillo, J., Knight, W. and Logan, T. 2008. Kuril Islands tsunami of November 2006: 1. Impact at Crescent City by distant scattering. *Journal of Geophysical Research*, **113**, C01020, doi:10.1029/2007JC004402.
113. Mori, N., Takahashi, T., Yasuda, T. and Yanagisawa, H. 2011. Survey of 2011 Tohoku earthquake tsunami inundation and run-up. *Geophysical Research Letters*, **38**, L00G14, doi:10.1029/2011GL049210.
114. Private communication from Dr David Long, British Geological Survey.
115. Tsushima, H., Hirata, K., Hayashi, Y. *et al.* 2011. Near-field tsunami forecasting using offshore tsunami data from the 2011 off the Pacific coast of Tohoku Earthquake. *Earth, Planets and Space*, **63**, 821–826, doi:10.5047/eps.2011.06.052.
116. Wei, Y., Chamberlain, C., Titov, V. V., Tang, L. and Bernard, E. N. 2012. Modeling of the 2011 Japan tsunami: lessons for near-field forecast. *Pure and Applied Geophysics*, **170**(6–8), 1309–1331. doi:10.1007/s00024-012-0519-z.
117. Travel time charts and movies can be found at the NOAA Center for Tsunami Research web site <http://nctr.pmel.noaa.gov> and travel time charts also at http://www.ngdc.noaa.gov/hazard/tsu_travel_time.shtml.
118. González, F. I., Satake, K., Boss, E. F. and Mofjeld, H. O. 1995. Edge wave and non-trapped modes of the 25 April 1992 Cape Mendocino tsunami. *Pure and Applied Geophysics*, **144**, 409–426, doi:10.1007/BF00874375.
119. Pattiaratchi, C. B. and Wijeratne, E. M. S. 2009. Tide gauge observations of 2004–2007 Indian Ocean tsunamis from Sri Lanka and Western Australia. *Pure and Applied Geophysics*, **166**, 233–258, doi:10.1007/s00024-008-0434-5.
120. Ioualalen, M., Asavanant, J., Kaewbanjak, N. *et al.* 2007. Modeling the 26 December 2004 Indian Ocean tsunami: case study of impact in Thailand. *Journal of Geophysical Research*, **112**, C07024, doi:10.1029/2006JC003850.
121. (1) Tadepalli, S. and Synolakis, C. E. 1994. The run-up of N-waves on sloping beaches. *Proceedings of the Royal Society of London A*, **445**, 99–112, doi:10.1098/rspa.1994.0050. (2) Tadepalli, S. and Synolakis, C. E. 1996. Model for the leading waves of tsunamis. *Physical Review Letters*, **77**, 2141–2144, doi:10.1103/PhysRevLett.77.2141.
122. Baba, T., Hirata, K. and Kaneda, Y. 2004. Tsunami magnitudes determined from ocean-bottom pressure gauge data around Japan. *Geophysical Research Letters*, **31**, L08303, doi:10.1029/2003GL019397.
123. Choi, B. H. and Imamura, F. (eds.) 2005. Sumatra tsunami on 26th December 2004. In *Proceedings of the Special Asia Tsunami Session at the Asia and Pacific Coast (APAC) Conference*, 4–8 September 2005, Jeju-do, Korea. Seoul: Hanrimwon Publishing Co.
124. Many tide gauge records from the Sumatra tsunami can be found at <http://www.pac.dfo-mpo.gc.ca/science/oceans/tsunamis/tsunami-asia-asie-eng.htm>.
125. Okal, E. A. and Hartnady, C. J. 2009. The South Sandwich Islands earthquake of 27 June 1929: seismological study and inference on tsunami risk for the South Atlantic. *South African Journal of Geology*, **112**, 359–370, doi:10.2113/gssajg.112.3-4.359.
126. Milburn, H. B., Nakamura, A. I. and Gonzalez, F. I. 1996. Real-time tsunami reporting from the deep ocean. *Proceedings of the Oceans '96 MTS/IEEE Conference*, Fort Lauderdale, Florida, 23–26 September 1996. Available from <http://nctr.pmel.noaa.gov/milburn1996.html>.

127. This section is based on work undertaken for the European Union TRANSFER project www.transferproject.eu.
128. Woodworth, P. L., Rickards, L. J. and Pérez, B. 2009. A survey of European sea level infrastructure. *Natural Hazards and Earth System Science*, **9**, 927–934, <http://www.nat-hazards-earth-syst-sci.net/9/927/2009/>.
129. For example, for a discussion of the need for data exchange along the Atlantic coastline see: Defra, 2005. *The Threat Posed by Tsunami to the UK* (ed. D. Kerridge). Study commissioned by Defra Flood Management and produced by British Geological Survey, Proudman Oceanographic Laboratory, Met Office and HR Wallingford.
130. WMO, 2004. *Manual on the Global Telecommunications System. Volume 1: Global Aspects. Volume 2: Regional Aspects*. World Meteorological Organization report 386. http://www.wmo.ch/web/www/ois/Operational_Information/WMO386/ManOnGTS.html.
131. Holgate, S. J., Foden, P. and Pugh, J. 2007. Tsunami monitoring system: implementing global real time telemetry. *Sea Technology*, **48**(3), 37–40.
132. Holgate, S., Foden, P., Pugh, J. and Woodworth, P. 2008. Real time sea level data transmission from tide gauges for tsunami monitoring and long term sea level rise observations. *Journal of Operational Oceanography*, **1**, 3–8.
133. Holgate, S. J., Woodworth, P. L., Foden, P. R. and Pugh, J. 2008. A study of delays in making tide gauge data available to tsunami warning centres. *Journal of Atmospheric and Oceanic Technology*, **25**, 475–481, doi:10.1175/2007JTECHO544.1.
134. (1) Horsburgh, K. J., Bradley, L., Angus, M. *et al.* 2009. *High Frequency Sea Level Recording for Tsunami Warning and Enhanced Storm Surge Monitoring at UK Sites*. Proudman Oceanographic Laboratory, Internal Document 190. (2) Bressan, L. and Tinti, S. 2012. Detecting the 11 March 2011 Tohoku tsunami arrival on sea-level records in the Pacific Ocean: application and performance of the Tsunami Early Detection Algorithm (TEDA). *Natural Hazards and Earth System Sciences*, **12**, 1583–1606, doi:10.5194/nhess-12-1583-2012. (3) Software developed through the European Union TRANSFER project by Puertos del Estado in Spain is now being applied to 1-minute sampling and latency data across the REDMAR network: see <http://www.puertos.es>.
135. As demonstrated by the OGP/JCOMM/WCRP Workshop on Climate Change and the Offshore Industry at the World Meteorological Organization, Geneva, 27–29 May 2008.
136. See the German–Indonesian Tsunami Early Warning System pages www.gitews.de.
137. Cummins, P. R. 2007. The potential for giant tsunamigenic earthquakes in the northern Bay of Bengal. *Nature*, **449**, 75–78, doi:10.1038/nature06088.
138. Neetu, S., Suresh, I., Shankar, R. *et al.* 2011. Trapped waves of the 27 November 1945 Makran tsunami: observations and numerical modeling. *Natural Hazards*, **59**, 1609–1618, doi:10.1007/s11069-011-9854-0.
139. Alasset, P.-J., Hébert, H., Maouche, S., Calbini, V. and Meghraoui, M. 2006. The tsunami induced by the 2003 Zemmouri earthquake ($M_w = 6.9$, Algeria): modelling and results. *Geophysical Journal International*, **166**, 213–226, doi:10.1111/j.1365-246X.2006.02912.x.
140. Schindelé, F., Loevenbruck, A. and Hébert, H. 2008. Strategy to design the sea-level monitoring networks for small tsunamigenic oceanic basins: the Western Mediterranean case. *Natural Hazards and Earth System Sciences*, **8**, 1019–1027, www.nat-hazards-earth-syst-sci.net/8/1019/2008/.
141. Tsushima, H., Hino, R., Fujimoto, H. and Tanioka, Y. 2007. Application of cabled offshore ocean bottom tsunami gauge data for real-time tsunami forecasting. *Underwater Technology and Workshop on Scientific Use of Submarine Cables and Related Technologies*. Symposium 17–20 April 2007, pp. 612–620.
142. Kato, T., Terada, Y., Nishimura, H., Nagai, T. and Koshimura, S. 2011. Tsunami records due to the 2010 Chile Earthquake observed by GPS buoys established along the Pacific coast of Japan. *Earth, Planets and Space*, **63**, e5–e8, doi:10.5047/eps.2011.05.001.
143. Hayashi, Y., Tsushima, H., Hirata, K., Kimura, K. and Maeda, K. 2011. Tsunami source area of the 2011 off the Pacific coast of Tohoku Earthquake determined from tsunami arrival times at offshore observation stations. *Earth, Planets and Space*, **63**, 809–813, doi:10.5047/eps.2011.06.042.
144. Foster, J. H., Brooks, B. A., Wang, D., Carter, G. S. and Merrifield, M. A. 2012. Improving tsunami warning using commercial ships. *Geophysical Research Letters*, **39**, L09603, doi:10.1029/2012GL051367.
145. (1) Löfgren, J. S., Haas, R., Scherneck, H.-G. and Bos, M. S. 2011. Three months of local sea level derived from reflected GNSS signals. *Radio Science*, **46**, RS0C05, doi:10.1029/2011RS004693. (2) Larson, K. M., Löfgren, J. and Haas, R. 2013. Coastal sea level measurements using a single geodetic GPS receiver. *Advances in Space Research*, **51**(8), 1301–1310, doi:10.1016/j.asr.2012.04.017.
146. Helm, A., Stosius, R., Montenbruck, O. *et al.* 2008. Utilizing ocean reflected GPS L1 C/A and the new GPS L2C signals for tsunami detection from space: possible small satellite constellations and the GORS instrument. *International Conference on Tsunami Warning (ICTW)*, Bali, Indonesia, November 12–14, 2008.

147. Essen, H.-H., Gurgel, K.-W. and Schlick, T. 2000. On the accuracy of current measurements by means of HF radar. *IEEE Journal of Oceanic Engineering*, **25**, 472–480, doi:10.1109/48.895354.
148. Lipa, B. J., Barrick, D. E., Bourg, J. and Nyden, B. D. 2006. HF radar detection of tsunamis. *Journal of Oceanography*, **62**, 705–716.
149. Lipa, B., Isaacson, J., Nyden, B. and Barrick, D. 2012. Tsunami arrival detection with high frequency (HF) radar. *Remote Sensing*, **4**, 1448–1461, doi:10.3390/rs4051448.
150. Börner, T., Galletti, M., Marquart, N. P. and Krieger, G. 2010. Concept study of radar sensors for near-field tsunami early warning. *Natural Hazards and Earth System Sciences*, **10**, 1957–1964, doi:10.5194/nhess-10-1957-2010.
151. Song, Y. T., Fukumori, I., Shum, C. K. and Yi, Y. 2012. Merging tsunamis of the 2011 Tohoku-Oki earthquake detected over the open ocean. *Geophysical Research Letters*, **39**, L05606, doi:10.1029/2011GL050767.
152. For example, see <http://www.avisio.oceanobs.com/en/data/product-information/duacs/>.
153. Hamlington, B. D., Leben, R. R., Godin, O. A. *et al.* 2012. Could satellite altimetry have improved early detection and warning of the 2011 Tohoku tsunami? *Geophysical Research Letters*, **39**, L15605, doi:10.1029/2012GL052386.
154. For example, see the Surface Water and Ocean Topography website <http://swot.jpl.nasa.gov>.
155. Allan, T. 2005. Detecting tsunamis: calling in the satellites. *Marine Scientist*, **13**, 12–14.
156. (1) Han, S.-C., Shum, C. K., Bevis, M., Ji, C. and Kuo, C.-Y. 2006. Crustal dilatation observed by GRACE after the 2004 Sumatra-Andaman earthquake. *Science*, **313**, 658–662, doi:10.1126/science.1128661. (2) Chen, J. L., Wilson, C. R., Tapley, B. D. and Grand, S. 2007. GRACE detects coseismic and postseismic deformation from the Sumatra-Andaman earthquake. *Geophysical Research Letters*, **34**, L13302, doi:10.1029/2007GL030356.
157. Garces, M. and Le Pichon, A. 2009. Infrasonic sound from earthquakes, tsunamis and volcanoes. In *Encyclopedia of Complexity and Systems Science* (ed. R. A. Myers), pp. 663–679. Springer, doi:10.1007/978-1-4419-7695-6_35.
158. Hanson, J. A. and Bowman, J. R. 2005. Dispersive and reflected tsunami signals from the 2004 Indian Ocean tsunami observed on hydrophones and seismic stations. *Geophysical Research Letters*, **32**, L17606, doi:10.1029/2005GL023783.
159. (1) Arai, N., Iwakuni, M., Watada, S. *et al.* 2011. Atmospheric boundary waves excited by the tsunami generation related to the 2011 great Tohoku-Oki earthquake. *Geophysical Research Letters*, **38**, L00G18, doi:10.1029/2011GL049146. (2) Prior, M., Salzberg, D. and Brogan, R. 2011. Pressure signals on IMS hydrophones at Wake Island due to the M9.0 event on March 11th 2011 off the coast of Japan. Presentation JS-P1, in Book of Abstracts. *Comprehensive Nuclear-Test-Ban Treaty: Science and Technology Conference*, 8–10 June 2011, Vienna, Austria. Available from <http://www.ctbto.org/>.
160. Garcia, R. F., Bruinsma, S., Lognonné, P., Doornbos, E. and Cachoux, F. 2013. GOCE: The first seismometer in orbit around the Earth. *Geophysical Research Letters*, **40**, 1015–1020, doi:10.1002/grl.50205.
161. Examples include *Surveys in Geophysics*, 27(6), 2006; *Pure and Applied Geophysics*, 168(6–7), 2011; *Natural Hazards*, 63(1), 2012.
162. Geist, E. L., Titov, V. V. and Synolakis, C. E. 2006. Tsunami: wave of change. *Scientific American*, **294**, 56–63, doi:10.1038/scientificamerican0106–56.
163. (1) Defra, 2005. *The Threat Posed by Tsunami to the UK* (ed. D. Kerridge). Study commissioned by Defra Flood Management and produced by British Geological Survey, Proudman Oceanographic Laboratory, Met Office and HR Wallingford. (2) DMI, 2005. *Tsunami Risk Assessment for Danish, Faroes and Greenland Waters* (eds. E. Buch *et al.*). Danish Meteorological Institute Technical Report No. 05–08.
164. Finkl, C. W., Pelinovsky, E. and Cathcart, R. B. 2012. A review of potential tsunami impacts to the Suez Canal. *Journal of Coastal Research*, doi:10.2112/JCOASTRES-D-12A-00002.1.

Spatial variations in sea level

But who would say that a sea surface is inclined?

Strabo, Geography

9.1 Introduction

Geodesy is a branch of science that is concerned with the Earth's time-dependent geometric shape, gravitational field and rotation. Over 70 per cent of our planet is covered by ocean, and its shape is largely defined by the mean sea surface, so geodesy and sea-level science are intimately connected. A number of classic texts on geodesy are available [1, 2], and also excellent reviews of modern geodetic techniques [3]. In this chapter, we confine ourselves to a description of some of the main developments in geodesy that relate to understanding the spatial variations in the sea surface. In the [next chapter](#) we discuss its temporal variations.

9.2 The International Terrestrial Reference Frame

A principal goal of geodesy is to assign coordinates to points on the Earth's surface as a function of time. Such a time series could be, for example, the height of sea level at a particular location (latitude, longitude) in the ocean, or the height of a benchmark on land. It is important to know something of the geodetic framework within which many of the sea- and land-level measurements described later in this chapter are made.

A geodetic reference *system* is a set of definitions and mathematical models that allow such geodetic measurements to be related to each other in a systematic fashion, while a geodetic reference *frame* is the practical realisation of a system in terms of coordinates and motions of networks of Reference Stations. The latest International Terrestrial Reference Frame (ITRF) is the ITRF2008 [4], which is defined by four geodetic techniques: the Global Positioning System (GPS), Doppler Orbitography and Radiopositioning Integrated by Satellite (DORIS), Satellite Laser Ranging (SLR) and Very Long Baseline

Interferometry (VLBI). The ITRF2008 comprises 934 stations at 580 sites, of which 463 and 117 are in the northern and southern hemispheres, respectively (Figure 9.1).

An important issue is the ability of one technique to complement others within the ITRF. For example, SLR is the only technique that can contribute to a monitor of the time-varying motion of the origin of the reference frame (relative to the Earth centre-of-mass), and in combination with VLBI (the only non-satellite technique) to a determination of its physical scale. VLBI, together with GPS, DORIS and other techniques in combination, provide Earth Orientation Parameters (EOPs) including polar motion and length of day (LOD). GPS and DORIS provide an essential densification of the global coverage of Reference Stations in the ITRF. In addition, these two latter techniques play an important role in the determination of satellite orbits, as described below.

The maintenance of the ITRF origin at the mean Earth system centre of mass (CM) is critical to all geodetic measurements and especially important for sea-level studies. Although the ITRF combines data from the four techniques, its origin is currently realised by SLR only. Consequently, it is difficult to evaluate the origin accuracy independently. At the present time it is thought that the ITRF2008 origin is consistent with the mean CM at the level of 0.5 mm/yr, while the mean radius of the Earth is not changing within a measurement uncertainty of 0.2 mm/yr [5]. This is a significant improvement on the situation just a few years ago with the use of the ITRF2000. However, the target accuracy requirement for 'geocentre stability' for long-term sea-level studies is 0.1 mm/yr, requiring an ITRF that is more robust and stable over decades and longer [6].

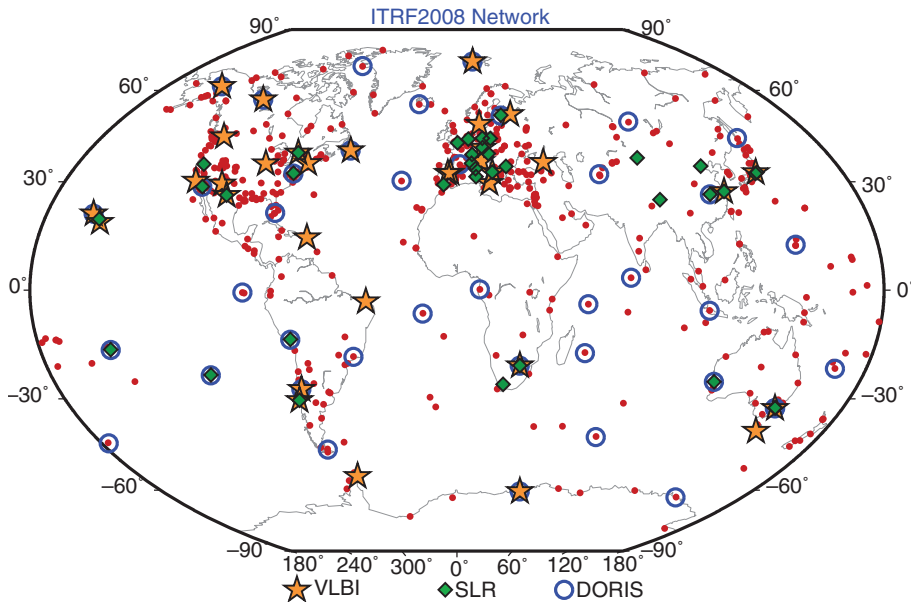


Figure 9.1 The ITRF2008 network highlighting VLBI, SLR and DORIS sites co-located with GPS. From [4].

Although the ITRF is becoming a mature system, investments in the networks that contribute to it are required in some parts of the world, including both polar regions and the whole southern hemisphere. Such developments are the responsibility of the Global Geodetic Observing System (GGOS) of the International Association of Geodesy (IAG) [3]. The various techniques with which GGOS is concerned are shown in Figure 9.2. It can be appreciated that, if one is interested in time series of heights on the Earth's surface, such as sea or land level, then it is essential that the ITRF be completed and maintained with the accuracy and stability required [6, 7].

9.3 The Global Positioning System

Descriptions of each of the geodetic techniques mentioned above are available [3]. However, a particularly important one for sea-level studies is the Global Positioning System (GPS). GPS together with the Russian GLONASS (Globalnaya Navigatsionnaya Sputnikovaya Sistema), followed by the European GALILEO and Chinese COMPASS systems, which are in stages of becoming fully operational, are denoted as Global Navigation Satellite System (GNSS) technologies and operate on similar principles.

GPS has revolutionised navigation and surveying by providing positions on the Earth's surface to

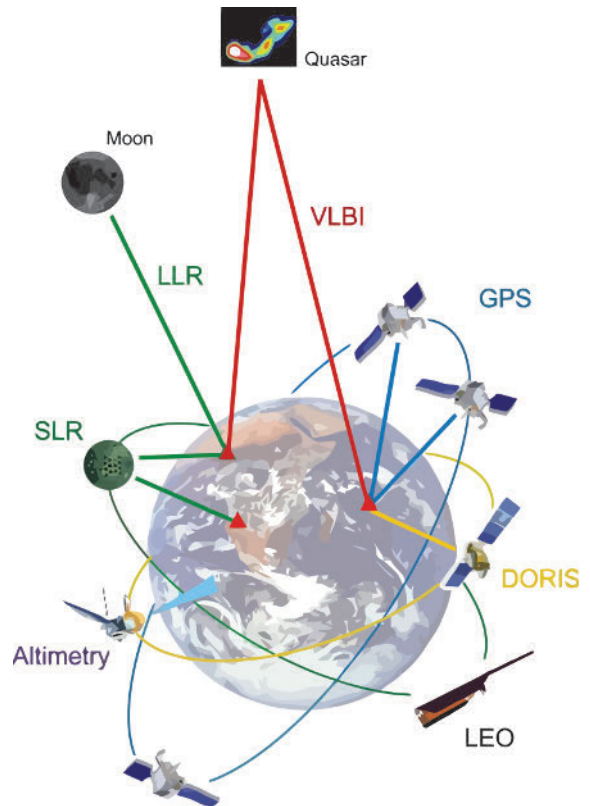


Figure 9.2 The various techniques with which the Global Geodetic Observing System (GGOS) is associated. Lunar Laser Ranging (LLR) and Low Earth Orbiter (LEO). For other acronyms, see the text.

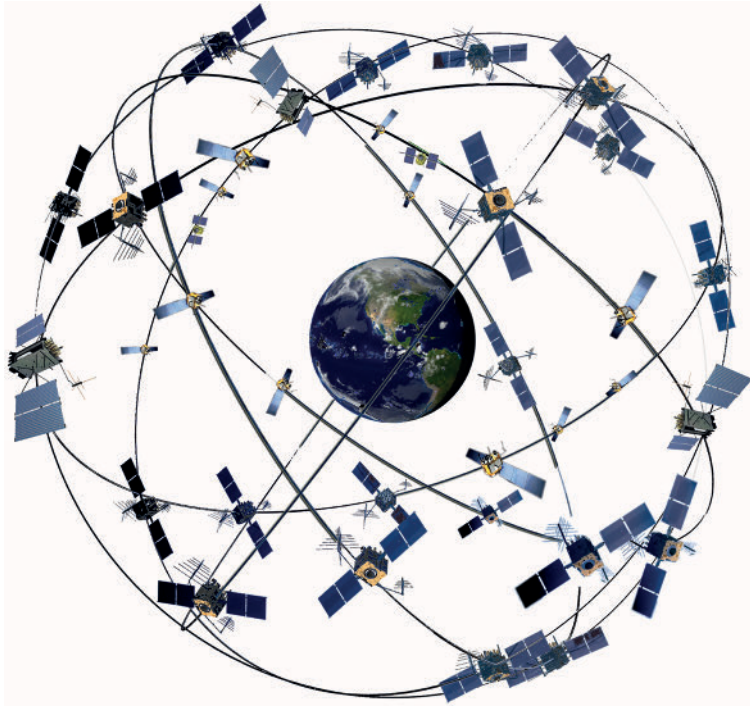


Figure 9.3 The GPS constellation to be expected by 2015. From [8]. Figure courtesy of Lockheed Martin.

decimetre accuracy.¹ It has also been applied with millimetric precision to many important areas of scientific research. For example, long-term monitoring by GPS of the position of a benchmark has shown how the land may move horizontally, as a result of continental plate movements, and vertically, as a consequence of processes such as Glacial Isostatic Adjustment (GIA) or earthquakes. Within sea-level research, GPS is an essential technique for determining the rate of vertical land movement at a tide gauge site, and for positioning tide gauge data within the same geodetic reference frame as used for altimetry. More details on the use of GPS at tide gauges, in order to monitor the movement of the Tide Gauge Bench Marks (TGBMs) and so to learn more of the temporal changes in sea and land levels, are given in Chapter 11.

GPS is the American military GNSS and has been operational since the 1980s. It consists of space, ground and user components. The space component is currently composed of 30 satellites at altitudes of

approximately 20,200 km, grouped in six orbital planes, such that a minimum of four satellites is visible from any location on the ground at any time, and will shortly be enhanced with the GPS III generation of satellites (Figure 9.3) [8]. The ground component consists of a small number of control stations which upload to each satellite a best estimate of its orbital position (its 'broadcast ephemeris'), the state of its satellite clock, and general housekeeping data. All of this information is in turn downloaded from the satellites to the user component, which consists of an unlimited number of receivers on the ground. No transmission takes place from receiver to satellite and so the network of receivers may be as large as desired. A programme within each receiver records the GPS data (time-tagged, pseudo-ranges and carrier phases) at two frequencies ($L1 = 1575$ MHz and $L2 = 1240$ MHz) for as long as each satellite is in view, and data from each, or combinations of, receiver are subsequently analysed in order to provide station coordinates.

A user's GPS equipment will consist of an antenna located on a special pillar or, less ideally, on the roof of a building. The antenna is connected by a cable to the receiver, which may be operated using either mains, solar or battery power. The analysis of GPS data comprises study of the time series of the codes and phases obtained by a receiver from each satellite,

¹ GPS users should be aware of different definitions of reference meridian and longitude. Satellite systems such as GPS use the International Earth Rotation and Reference Systems Service (IERS) reference meridian, which is at present approximately 100 m to the east of the historical Greenwich meridian at Greenwich's latitude. See for example http://en.wikipedia.org/wiki/Prime_meridian.

together with the downloaded information on the orbits (broadcast ephemerides) and clocks of each satellite. Such broadcast information is adequate for many real-time GPS positioning applications. However, for the most precise scientific studies, more accurate ephemerides and clock information are required, which are obtained from specialist centres with a time delay of several days. Data from the receivers of interest, together with data from other stations in a regional or global network, are analysed in order to determine the antenna coordinates within a geodetic reference frame using the techniques of Double Differencing (DD) or Precise Point Positioning (PPP). Conventional levelling can then be used to relate antenna height to that of nearby benchmarks such as a TGBM.

Details of the DD and PPP techniques need not concern us, except to note that the carrier phase information is the essential quantity that provides their precision. GPS data analysis has many similarities, and important differences, to the processing of satellite radar altimeter data (see below) [9]. The electromagnetic signals that pass between GPS satellites and receivers travel slower than the speed of light because the composition of the lower (troposphere) and upper (ionosphere) atmosphere results in an effective refractive index larger than 1. Moreover, the composition varies considerably. For example, the free electrons in the ionosphere that slow the radar wave propagation have a concentration that varies from day to night (few electrons at night), seasonally, and with the sunspot cycle (few electrons at solar minimum).

Therefore, both GPS and altimeter data have to be corrected for the effects of the ‘dry’ and ‘wet’ troposphere and for the ionosphere. The dry correction depends on the amount of atmospheric ‘dry gas’ (i.e. excluding water vapour) between the satellite and the receiver, while the wet correction is related to the amount of water vapour and cloud liquid water in the atmosphere. The ionospheric correction takes into account the Total Electron Content (TEC) of the ionosphere and is proportional to the reciprocal of the radar frequency squared.

However, there are important differences in the processing of GPS and altimeter data. One is that GPS satellites are much higher than altimeter ones, and so the average corrections are larger. Another difference is that the radar signals in altimetry are transmitted and received at nadir (i.e. directly beneath the satellite, from satellite to sea surface and back), but GPS signals arrive at the ground receiver from the satellite at all elevation angles above a certain cut-off

(typically $\geq 15^\circ$ to the horizon). This means that the signals pass through a varying thickness of atmosphere as the satellite moves across the sky, with the signals refracted (i.e. bent) as well as delayed.

As the ionospheric correction is a function of frequency, data at the two frequencies used by GPS can be combined in such a way that ionospheric effects can be accounted for almost completely. However, the dry (often called ‘hydrostatic’ in GPS literature) and wet corrections are independent of frequency and must be determined differently. A measurement of air pressure at the GPS station provides the ‘zenith dry’ (or hydrostatic) delay, which can be used to provide estimates of dry correction at all elevations with the use of ‘mapping functions’ derived from simulations of electromagnetic ray tracing within three-dimensional numerical models of the atmosphere. The remaining part of the tropospheric delay is then estimated along with the station coordinates as part of the GPS processing solution, resulting in an estimate of ‘zenith wet’ delay which, when determined in real time, has application to operational weather forecasting.

Uncertainty in estimation of the wet correction determines to a large extent the accuracy of the station coordinates, and in particular the vertical component [10]. In some installations, the wet correction can be measured directly with the use of a ground-based water vapour radiometer. However, such expensive equipment cannot be installed alongside all of the many GPS receivers around the world, or even at the several hundred used for monitoring vertical land movement near tide gauges discussed in [Chapter 11](#).

GPS heights are geocentric (Earth-centred) ones and are expressed relative to a *standard ellipsoid* (or *reference ellipsoid*) which is a first-order description of the shape of the Earth described by an equatorial radius a_e and flattening coefficient f ([Figure 9.4](#)):

$$f = \frac{(a_e - a_p)}{a_e} \quad (9.1a)$$

where the polar radius a_p is given by:

$$a_p = a_e(1 - f) \quad (9.1b)$$

Such heights, relative to the Earth-centred ellipsoid, are called ellipsoidal heights.

The flattening of the planet at the poles had been suggested by Newton and led to extensive research in the eighteenth century [11]. The flattening results in a polar radius 21 km smaller than the equatorial one. GPS uses the World Geodetic System (WGS)-84

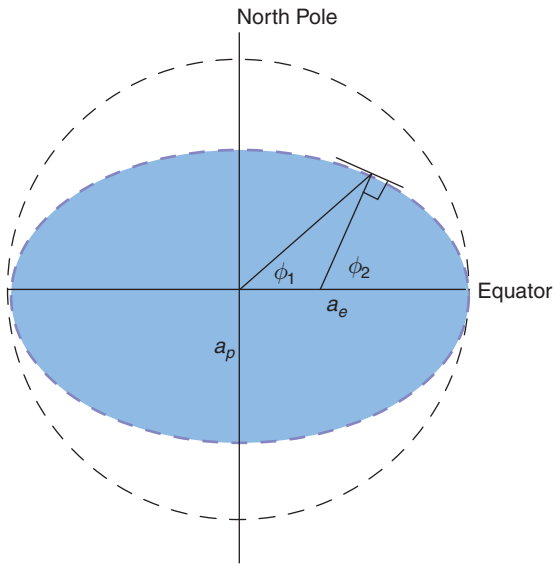


Figure 9.4 Schematic of a standard ellipsoid defined by an equatorial radius a_e and flattening coefficient $f = \frac{(a_e - a_p)}{a_e}$. ϕ_1 and ϕ_2 indicate geocentric and geodetic latitude.

ellipsoid, which has parameters $a_e = 6378.137$ km and $f = 1/298.257\,223\,563$, and thereby $a_p = 6356.752$ km. **Figure 9.4** also indicates the two latitudes associated with an ellipsoid: geocentric and geodetic (or geographic) latitude. The two latitudes differ by approximately 0.19° at 45° N/S, the exact value depending on the flattening coefficient.²

GPS heights are conventionally expressed in a ‘tide free’ system, unlike altimeter data which are expressed in a ‘mean tide’ system (see further below). This somewhat abstruse feature becomes important when one undertakes a detailed comparison of heights determined by the different techniques.

9.4 DORIS

DORIS was designed by the Centre National d’Études Spatiales (CNES), the French Space Agency, primarily as a system for determining precisely the orbits of satellites, including those with radar altimeters discussed below. It has a heritage in the earlier Doppler systems used for satellite tracking. It consists of a network of ground beacons with near-global coverage, each dual-frequency beacon transmitting signals at

² The usual meaning of ‘latitude’ on maps is geodetic latitude, being measured conventionally by finding the angle between the vertical and the pole star (in the northern hemisphere). The choice of which latitude to use in various aspects of ocean science is discussed in Reference 12.

known frequencies (2036.25 and 401.25 MHz) to an antenna, radio receiver and ultra-stable oscillator on board the satellite (**Figure 9.5**). Owing to the Doppler effect, the signals received are shifted in frequency, and analysis of these shifts enables the satellite’s orbit to be determined precisely.

Additional products of the analysis are the time-mean station coordinates of each beacon, together with a time series of the three-dimensional motion of each beacon, which may be studied alongside corresponding time series provided by GPS. DORIS has become an important additional technique that contributes to maintaining the stability of the ITRF, while its data have been applied to the measurement of continental drift and sea- and land-level change as described in **Chapter 11**.

9.5 Satellites and the Mean Sea Surface

The 1970s saw the start of what has been called the ‘era of satellite altimetry’, which had been foreseen by geodesists for many years previously [13]. Since that time, the measurement of sea level from space by altimeters has contributed enormously to studies of the solid Earth and the ocean circulation [14, 15], while altimeters now routinely provide operational significant wave height (SWH) and wind speed products to meteorological agencies [16]. A ‘nadir-pointing’ radar altimeter satellite orbits the Earth transmitting a narrow beam of radar pulses onto a small area of the ocean surface beneath it called its ‘footprint’, which is typically several kilometres wide. The pulses are transmitted many times per second and are reflected off the ocean and received back at the satellite. The times of flight of the individual pulses are usually grouped together into 1-second averages. After various environmental corrections are applied as described below, these average values provide a one per second sampling of the distance between the satellite and the ocean, called the ‘altimeter range’. If one knows the height of the satellite above the ellipsoid, then one can subtract the range to give a 1-second average of the ellipsoidal sea surface height (SSH). In that one second, the satellite will have moved across the ocean by about 6 km and a new measurement of SSH will begin.

Knowledge of the height of the satellite is obtained from several types of satellite tracking systems. For the first altimeter satellites, tracking was provided primarily by a ground network of SLR stations with incomplete

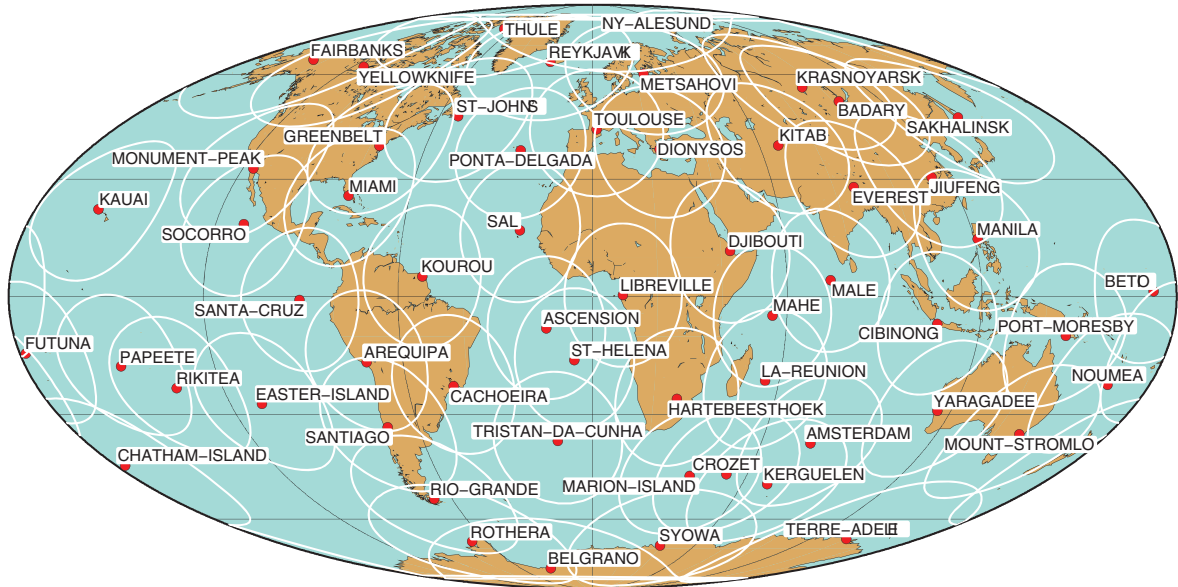


Figure 9.5 Map of the DORIS network of Doppler tracking beacons showing the ‘circles’ around each station in which the Envisat satellite was above the horizon and so could be tracked by the beacon. Larger circles, and so more continuous tracking, apply for higher-flying satellites such as Jason-1. From <http://ids-doris.org>.

global coverage. The accuracy of a satellite’s orbit then depended on how well computer models could use the SLR information together with knowledge of the Earth’s gravity field at that altitude and with parameterisations of the various atmospheric and radiational forces on the spacecraft. The orbit accuracies at that time were of the order of a metre. More recent satellites now employ the near-continuous tracking afforded by GPS and DORIS, together with SLR tracking and with much improved models of the gravity field. As a consequence, altimeter satellite orbits now have an accuracy better than 2 cm [17].

An altimeter satellite has a near-circular orbit, which means that it completes one revolution of the Earth in:

$$T_{rev} = 84.4 \left[\frac{r}{a} \right]^{\frac{3}{2}} \text{minutes} \quad (9.2)$$

where r is the mean radius of the satellite orbit and a is the Earth’s mean radius, or approximately 112 minutes for the TOPEX/Poseidon altitude of 1336 km. Near-circularity (near zero ‘eccentricity’) is required not only for simplicity, but also to minimise uncertainties in assigning a precise time to each altimeter range measurement, and to maintain the rate of change of range within a limit imposed by the radar return signal-following algorithms on board the satellite. Altitudes between approximately 780 and 1330 km are optimal. At lower altitudes, atmospheric drag increases and

gravity field uncertainties are a greater consideration. The satellite also has to carry more fuel to maintain a given height. At higher altitudes, the radar altimeter design (power requirements, antenna size etc.) is more complex and the satellite has greater exposure to the Earth’s damaging Van Allen radiation belts.

The other important parameter to describe the satellite’s orbit, in addition to altitude, is its inclination i . This is the angle at which the plane of the satellite orbit cuts the equator and is measured at the ‘ascending node’, when the satellite crosses the equator travelling north. Inclination is measured anticlockwise from east and can have values between 0 and 180°, with the maximum latitude surveyed by the nadir-pointing altimeter being i when $i < 90^\circ$ and $180 - i$ when $i > 90^\circ$. In the former case, the satellite is travelling west to east in a ‘prograde orbit’, while in the latter it is moving east to west and is in a ‘retrograde orbit’ (as is the Moon in fact). Owing to the Earth’s equatorial bulge, the orbital plane of a satellite will rotate in the opposite direction to the satellite’s motion at a rate of:

$$X = 9.97 \left(\frac{a}{r} \right)^{3.5} \cos i \text{ degrees per day} \quad (9.3)$$

If this rate equals $(360/365.25)^\circ/\text{day}$, then the orbital plane will have the same orientation with respect to a line drawn between the Sun and the Earth throughout the year. This results in the satellite having a

‘sun-synchronous orbit’ which will necessarily be a retrograde one (so that X has the correct sign). This choice of orbit is much preferred by engineers as solar panels can be fixed in alignment with the Sun and so do not require regular readjustment as occurs for non-sun-synchronous orbits. The requirement for a satellite to be sun-synchronous is why the choice of $i = 98^\circ$ was made for ERS-1, ERS-2 and Envisat along with altitudes of approximately 800 km. An inclination as near to 90° as possible was also required for these missions so as provide data for polar research.

Engineers can make choices of altitude and inclination such that the satellite can be placed into an orbit that traces out a path over the Earth’s surface that eventually repeats itself. This ‘repeat period’ is necessarily an exact number of days for a sun-synchronous orbit. The choice of repeat period is primarily one for the scientists in charge of the mission, depending on the sampling required to study the processes of interest in the ocean. A choice of a short repeat period means that one has to be satisfied with a coarse spatial sampling, and vice versa.

TOPEX/Poseidon was designed to fly at a high altitude of over 1300 km, so as to benefit from the more precise orbit determination provided by lower gravity and less atmospheric drag, the size of the latter being dependent on solar activity which varies throughout the sunspot cycle (Table 9.1). Sun-synchronicity was undesirable if the mission was to provide data suitable for detailed study of the solar, as well as the lunar, components of the ocean tide. The selected altitude and inclination ($i = 66^\circ$) resulted in a repeat period of 9.9156 days, which was ideal for providing regular coverage of the large-scale ocean circulation at a high enough inclination to include the Drake Passage (Figure 9.6a). The sampling provided a suitable aliasing of the eight main components of the ocean tide, such that precise tidal models could be determined from the quantity of data to be obtained during the first years of the mission [18].

ERS-1, ERS-2 and Envisat had altitudes of approximately 800 km, and were operated with different repeat periods at different times, but mostly with a choice of 35 days (Table 9.1). This repeat provides higher spatial resolution sampling (at the expense of reduced temporal sampling) of SSH variability including the eddy field (Figure 9.6b). ERS-1 and some other satellites have had long or non-repeat orbits yielding a fine spatial sampling most useful for geophysical studies; these are known as Geodetic Missions.

The environmental corrections to the altimeter range mentioned above include three that are similar to those described for GPS. They are the ‘dry’ correction for the amount of atmospheric ‘dry gas’ between the satellite and the ocean. This is the largest of the various corrections but can be readily parameterised to first order simply in terms of air pressure. The ‘wet’ correction is obtained from either measurements by a radiometer on the satellite, or meteorological models, or coastal GPS measurements. The ‘ionospheric’ correction is obtained with the use of either dual-frequency altimeter range measurements, if the altimeter instrument is a dual-frequency one, or from DORIS and GPS information.³

Finally, a ‘sea state bias’ correction is required, which stems from the fact that the radar pulses are reflected from small wave facets within the antenna footprint that are perpendicular to the incident radiation. As a result, the shape of the returned waveforms is determined by the distribution of these specular scatterers rather than by the actual SSH in the footprint. The sea state bias can be expressed as the sum of two terms: the ‘electromagnetic bias’, which arises because of greater backscattered power per unit surface area from wave troughs rather than wave crests; and the ‘skewness bias’, which stems from the difference between the mean and median scattering surfaces. The mean surface is the relevant one for specifying SSH, but the median surface determines the recorded altimeter range. Sea state bias is usually determined by means of empirical studies of the relationship of range to wave height for a given altimeter, and in most parts of the world the accuracy of this correction is the dominant factor in the accuracy of a SSH measurement.

When altimeter SSH values have been corrected for all instrumental and environmental factors, they will also usually be adjusted for the ocean tide using tidal models, and for the ‘inverse barometer’ effect of air pressure on the ocean. The heights can then be averaged into optimum longitude–latitude boxes so as to define a Mean Sea Level (MSL) for the box, with the average heights in all boxes contributing to a Mean Sea Surface (MSS).

³ The dry, wet and ionospheric corrections for TOPEX/Poseidon had typical values of 226, 10–24 and 6–12 cm respectively, with the dry an order of magnitude larger than the others. However, each can be measured or modelled to cm accuracy [14]. The sea state bias correction had a larger uncertainty, possibly 1% of significant wave height or 2–3 cm on average, and is still a topic of research.

Table 9.1 Chronological list of the main past, present and planned altimeter missions as of February 2013

Mission	Agency	Inclination (deg), height (km), sun-synchronous?	Repeat period (days)	Dates of operation	Comments
Skylab	NASA (USA)	50, 435, No	None	1973–4	Proof of concept of altimetry
GEOS-3	NASA	115, 845, No	Non-repeat ground track although many near-repeat passes occurred	1975–8	First mission to yield useful measurements of sea level and its variability
Seasat	NASA	108, 800, Approx.	Near 17 day repeat and then near 3 day repeat during the last 25 days	June-Oct 1978 (105 days)	First mission to provide global data sets of ocean variability and ocean topography for geophysics
Geosat	U.S. Navy	108, 800, Approx.	None 17.05	1985–6 (18 months), 1986–90	Geodetic Mission Exact Repeat Mission The first mission to provide extended high quality altimeter data
Geosat Follow-On (GFO)	U.S. Navy	108, 800, Approx.	17.05	1998–2008	Same parameters as for Geosat
ERS-1	ESA (Europe)	98.52, 785, Yes	3, 35 and 168	1991–6	First of the ESA altimeter missions
ERS-2	ESA	98.52, 785, Yes	35	1995–2011	Similar to ERS-1 with which it overlapped during 1995–6
Envisat	ESA	98.52, 785, Yes	35	2002–12	Envisat carried a wide range of instrumentation
TOPEX/Poseidon	NASA/CNES (USA/France)	66, 1336, No	9.9156	1992–2005	The first dual-frequency altimeter The most successful altimeter mission for sea-level studies to date
Jason-1	NASA/CNES	66, 1336, No 66, 1324, No	9.9156 406 (nominally) geodetic orbit	2001–12 May 2012–June 2013	Same ground track as TOPEX/Poseidon
Ocean Surface Topography Mission (OSTM)/Jason-2	NASA/CNES	66, 1336, No	9.9156	2008–ongoing	Same ground track as TOPEX/Poseidon

Cryosat-2	ESA	92, 717, No	369 with 30 day sub-cycle	2010–ongoing	Primarily an ice mission but with good ocean coverage Carries a SIRAL (SAR/Interferometric Radar Altimeter) altimeter capable of operating in conventional mode or in SAR and Interferometric modes
HY-2A (Hai Yáng meaning Ocean)	NSOAS (China)	99.35, 971, Yes	14 day cycle for 2 years then 168 day geodetic mission for 1 year	2011–ongoing	Co-operation with CNES
SARAL (Satellite with ARGos and ALtika) [means 'Simple' in Hindi]	ISRO (India) and CNES	98.52, 785, Yes	35 day cycle as for Envisat	Launched February 2013	A Ka-band altimeter (Altika) with a smaller footprint than the conventional Ku and C band instruments
<i>Future missions</i>	<i>Planned launch</i>				
Jason-3	EUMETSAT (Europe)/ NOAA/NASA/ CNES	66, 1336, No	9.9156	Dec. 2014	Continuation of the Jason series. Same ground track as TOPEX/Poseidon
Sentinel-3	ESA	98.65, 800, Yes	27	Sentinel-3A and 3B in 2014–15	A pair of satellites with SAR-mode SIRAL altimeters derived from Cryosat-2
Geosat Follow-On (GFO) - 2	U.S. Navy	Under discussion		After 2016	Presumably similar mission as Geosat and GFO
Jason-CS (Jason Continuity of Service)	EUMETSAT/ NOAA	66, 1336, No	9.9156	2018	Altimeter derived from those on Cryosat-2 and Sentinel-3
SWOT (Surface Water and Ocean Topography)	USA/France	Under discussion		After 2020	Altimeter mission measuring along a ±60 km swath for observing small-scale ocean processes and land water changes

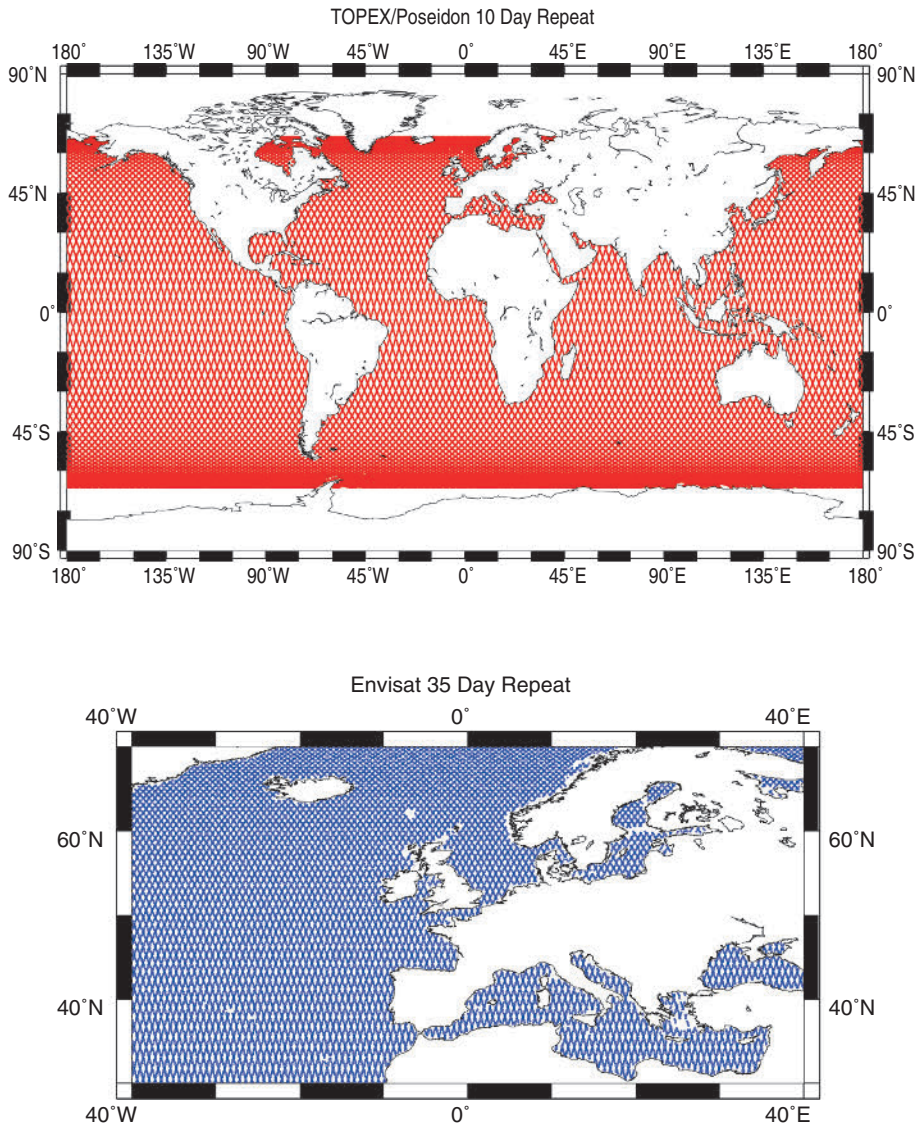


Figure 9.6 (a) Ground track of the 10-day repeat TOPEX/Poseidon, Jason-1 and Jason-2 missions, and (b) of the 35-day repeat ERS-1, ERS-2 and Envisat missions in the northeast Atlantic. Each map was made using along-track data from www.aviso.oceanobs.com.

Altimeter SSH values are expressed not as radial distances from the centre of the Earth, but rather as heights above a reference ellipsoid, as discussed for GPS above. The ellipsoid used for most altimeter missions is the TOPEX ellipsoid, which has a 70 cm radial offset from the WGS-84 ellipsoid used for GPS.⁴ A conversion of heights measured relative to one

ellipsoid can be made readily to heights relative to any other. Altimeter heights are effectively in a ‘mean tide’ system and differ from those in a ‘tide free’ system as used by GPS by:

$$0.198h\left(\frac{3}{2}\sin^2\phi - 0.5\right) \text{ metres} \quad (9.4)$$

where f is latitude and the Love number h is 0.6090 [13, 19, 20, 21]. These different tide systems represent alternative approaches to the specification of geocentric coordinates when one has to consider the permanent (zero frequency) tidal deformation of the Earth

⁴ The TOPEX ellipsoid is defined by $a_e = 6378.1363$ km and $f = 1/298.257$. The similar flattening coefficient to the WGS-84 ellipsoid means that the two ellipsoids are almost exactly 70 cm apart at all latitudes.

due to the gravitational potentials of the Moon and Sun. In the ‘tide-free’ approach, an attempt is made to remove this permanent part of the tidal potential from the measurements made on the mean tide crust; they are ‘attempts’ because h is not known accurately at zero frequency [21]. Heights in a mean tide system have values higher at the equator (i.e. further from the centre of the Earth) than in a tide-free system. If heights obtained from tide gauge plus GPS measurements are to be compared to altimeter ones, care must be taken to ensure that the same ellipsoid and tide system are being used.

Altimetric heights are monitored with the use of tide gauges and GPS measurements. GPS enables the tide gauge data to be expressed as ellipsoidal heights which can be compared to the altimetry. Any offsets (called ‘biases’) in the altimeter measurements can then be calculated (Figure 9.7). Long-term calibration sites have been established, such as the Harvest platform off the California coast [22], and at various tide gauge sites around the world [25, 24, 25]. Knowledge of each mission’s bias (usually assumed constant for each mission) can be used to combine the sea-level data from different missions into long time series.

A larger subset of the global tide gauge network is used to monitor the temporal stability of an individual altimeter’s SSH measurement system, which is

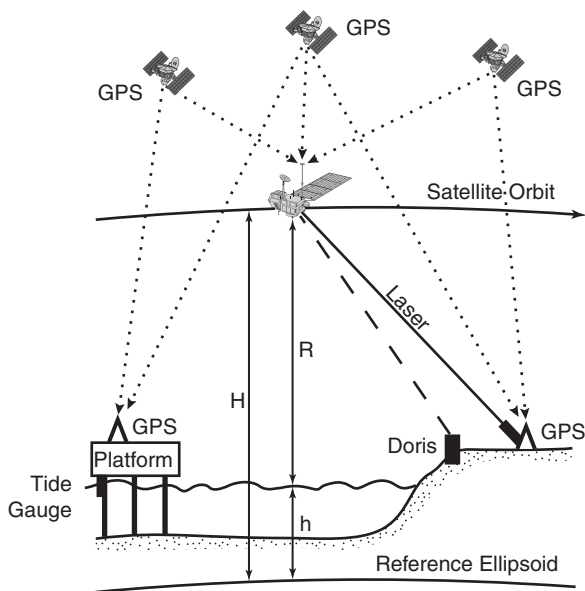


Figure 9.7 Schematic of the absolute calibration of an altimeter satellite (TOPEX/Poseidon near to the Harvest platform in this case) by means of laser ranging, GPS and DORIS with *in situ* measurements of sea level made by tide gauges on the platform. From [14].

particularly important for long-term sea-level change studies [26]. The method has been optimised for monitoring missions in repeat orbits, such as TOPEX/Poseidon and the Jason series. Such comparisons of altimeter and tide gauge data led to an identification of a major error in the range measurements of TOPEX/Poseidon, which had been responsible for incorrect findings of sea-level rise in the early years of the mission [27]. The method is used only for validation, and not calibration, of the altimeter data, and altimeter time series are not constrained to agree with those from the tide gauges.

Altimetry is now one of the main Earth observing techniques, with a succession of new missions planned over the next few years (Table 9.1). Although each mission has its particular features, they may be divided into two general classes: the ‘reference’ series of high-flying satellites comprising TOPEX/Poseidon and the Jason missions, which have provided a record of precise altimetry since 1992 utilising the same 10-day repeat ground track over the tropical and mid-latitude oceans within 66° N/S, and a set of sun-synchronous missions, which have provided a densification of the ocean sampling and access to higher latitude areas of the ocean (Figure 9.8).

9.6 Satellites and the geoid

If there were no oceanographic contributions to the MSS, then that surface would be equivalent to (or technically closely parallel to) the surface that geodesists call the *geoid*.⁵ This is an equipotential surface of the gravity field, defined by a potential that geodesists denote as W_0 . The gravity field is a combination of the gravitational field, due to the mass composition of the Earth, and the centrifugal forces due to Earth rotation. This potential has a value of 62,636,856.0 m^2/s^2 in the International Earth Rotation and Reference Systems Service (IERS) conventions [21]. The geoid would be a sphere if the Earth had a composition that was spherically symmetric and if it did not rotate.⁶ The difference between the MSS and the geoid is called the Mean

⁵ The word ‘geoid’ was first used by Listing in 1893. A review of the concept of the geoid and the development of early models is given in Reference 27.

⁶ The geoid can also be expressed using different tide systems: ‘mean tide’, ‘tide free’ and also a third called ‘zero tide’ [12]. A geoid model provided in one system can be converted to another system using standard formulae [19, 20]. For most research in oceanography it is best to work throughout with a single (usually mean tide) system.

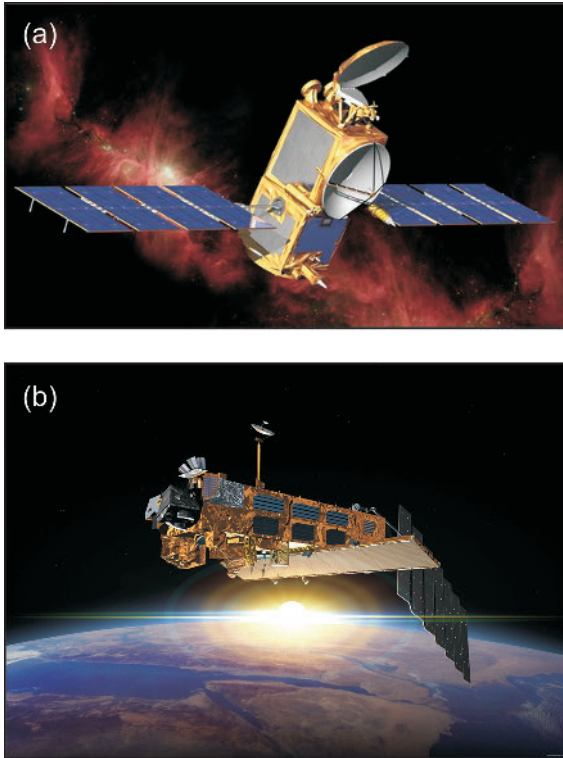


Figure 9.8 Examples of the ‘reference’ and sun-synchronous series of altimeter satellites (a) Jason-2 (also called the Ocean Surface Topography Mission, OSTM) and (b) Envisat. Images provided by NASA/JPL-Caltech and European Space Agency.

Dynamic Topography (MDT) (Figure 9.9), which is discussed in more detail below.

A determination of the shape of the geoid surface can be obtained only from gravity measurements, although models of the geoid over the ocean often also employ altimeter SSH data as proxy-gravity measurements at short wavelengths. Gravity measurements are obtained in many ways. Copious terrestrial gravity data are available from each continent and are archived by the Bureau Gravimétrique International (BGI), which is a component of the IAG’s International Gravity Field Service (IGFS) [29]. However, the spatial density and the accuracy of terrestrial measurements varies considerably, and data are either absent or have restricted availability in some countries. Gravity has also been measured from ships using marine gravity meters, beneath the sea surface using submarines [30], and as airborne gravity using aircraft. The last is particularly important in polar regions [31]. However, it is clear that any global gravity data set collected with these techniques will always be inhomogeneous in both coverage,

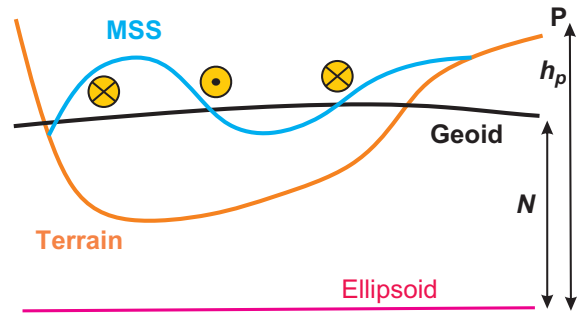


Figure 9.9 Schematic showing the geoid and Mean Sea Surface (MSS). The geoid would correspond to the surface of a theoretical ocean at rest. The difference between the real MSS and the geoid is the Mean Dynamic Topography (MDT). N indicates the height of the geoid above the ellipsoid at point P , while h_p is its ellipsoidal height. P may be a point on land, as shown, as would be measured by a GPS receiver, or a point on the MSS, as measured by altimetry. A geostrophic ocean current flows in an anticyclonic (clockwise) direction around regions of positive MDT anomaly, and in a cyclonic (anticlockwise) direction around negative MDT anomalies in the northern hemisphere (cyclonic and anticyclonic circulations are clockwise and anticlockwise respectively in the southern hemisphere). Terrain indicates the land surface or seabed.

spatial resolution and quality (Figure 9.10). For this reason, measurements of gravity from space have for many years been recognised as being the best means to obtain a uniform, and ultimately a precise, model of the geoid.

The orbit of any satellite will be perturbed by the Earth’s gravity field, and inferences can be made on how gravity varies around the world by means of accurate observations of the satellite’s path. An important factor is that the small-scale components of the gravitational potential decrease with altitude by a term $(\frac{a}{r})^{l+1}$, where r is distance from the centre of the Earth and l is spherical harmonic degree. Values of l correspond to spatial scales of $2\pi a/l$ at the Earth’s surface, or approximately 200 km for degree 200. Therefore, if a satellite is to provide information on the small-scale, high-degree components of the gravity field, then its altitude must be as low as possible. This presents major technical challenges.

Geodesists have tracked satellites since the launch of the first Sputniks [32] using a variety of optical (photographic), radar and radio tracking techniques, the latter being the predecessors of today’s GPS and DORIS technologies. Later, dedicated research satellites such as LAGEOS and Starlette were tracked accurately by means of the global network of SLR stations (Figure 9.11). These space techniques provided long-wavelength geoid information that remains the most accurate today. To make models of the geoid, it was

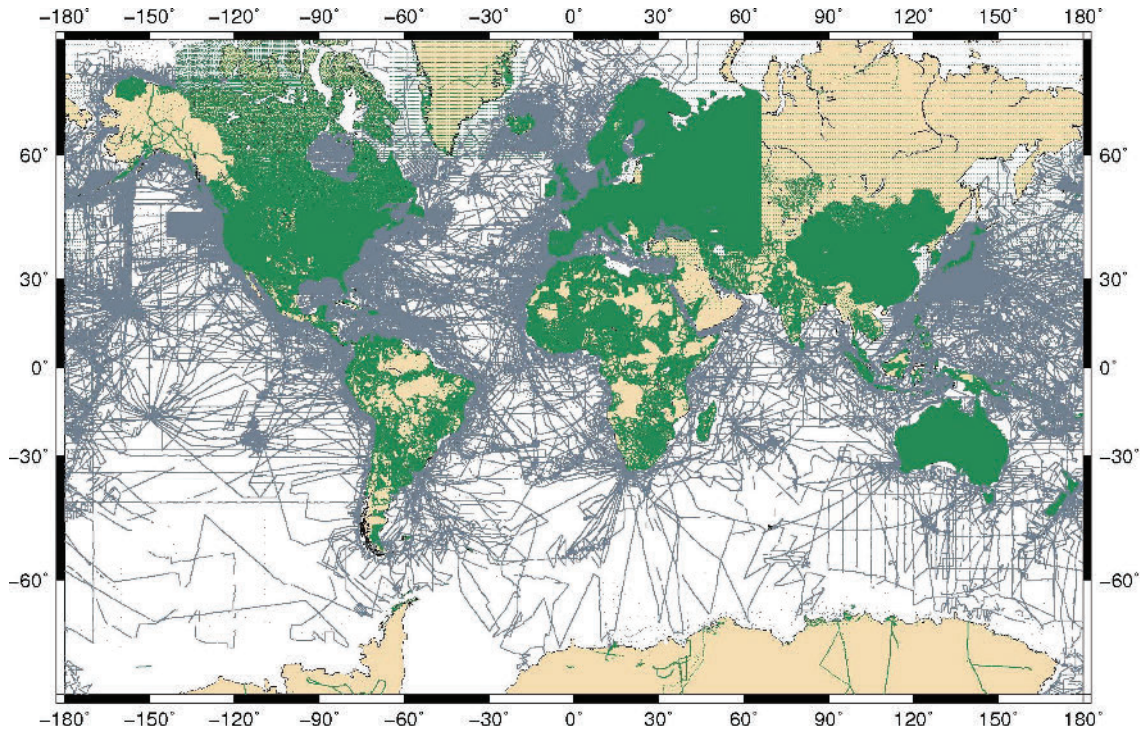


Figure 9.10 Distribution of presently available gravity measurements from land and marine surveys in the database of the Bureau Gravimétrique International. Figure from Dr Sylvain Bonvalot, Director BGI.

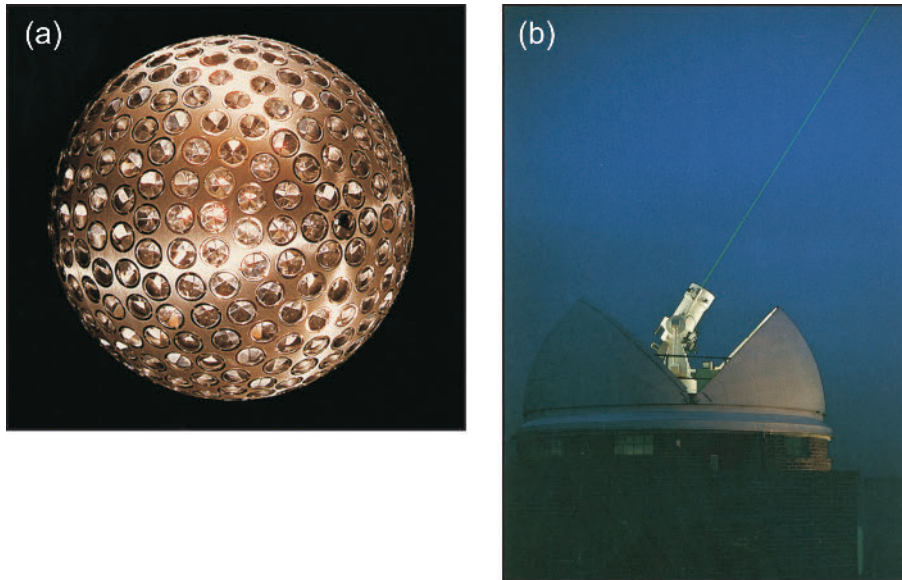


Figure 9.11 (a) One of the two LAGEOS geodetic satellites that consist of a 60 cm diameter, 400 kg aluminium-covered brass sphere covered in over 400 corner-cube reflectors which can be readily tracked from the Earth's surface using satellite laser ranging. The high mass-to-area of the satellites and their high altitude (6000 km) means that they have a highly stable orbit that is affected by the long-wavelength components of the Earth's gravity field only. Photograph by NASA obtained from Wikimedia Commons. (b) The Herstmonceux satellite laser ranging station in the south of England. Photograph by David Calvert, Herstmonceux.

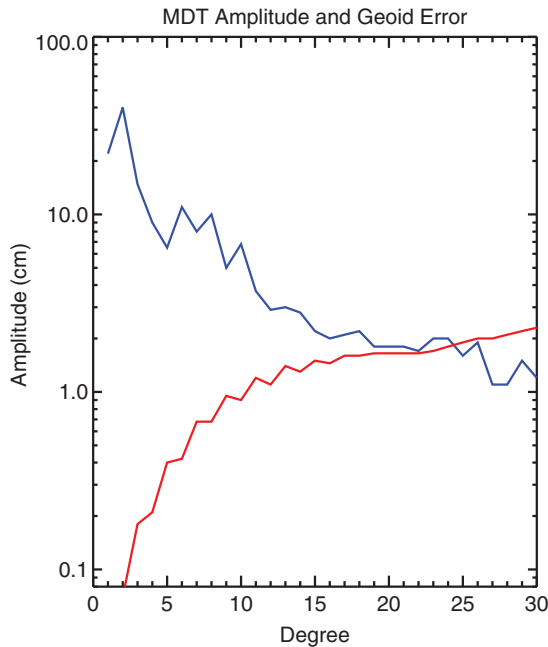


Figure 9.12 A figure made in the mid-1990s showing the power spectra of the MDT derived from TOPEX/Poseidon altimetry (blue) compared to the estimated uncertainty of a state-of-the-art geoid model at the time (EGM-96) (red). The crossover of the MDT and EGM-96 curves occurs around degree 20, which was consequently the limit at which the MDT could be measured as the difference of MSS and geoid. Adapted from a figure in [56].

blended with terrestrial and marine information, where such information was available. However, knowledge of the geoid at intermediate and short scales remained imprecise worldwide, while terrestrial and marine gravity were anyway sparse in many areas (Figure 9.10). As a consequence, until the launch of the new space gravity missions described below, the geoid was known well enough only to allow the MDT to be calculated up to degree 20 or so (wavelength approximately 2000 km) (Figure 9.12).

Figure 9.13 shows recent satellite missions devoted to obtaining a vastly improved knowledge of the gravity field and geoid, particularly at intermediate and short scales. Figure 9.14a indicates the concept of satellite-to-satellite tracking in the ‘satellite-to-satellite high-low’ mode (SST-hl), as used for the German CHAMP mission. Mass anomalies within the Earth result in spatial variations in the gravity field which are experienced by the satellite as it flies along its orbit. As a consequence, the orbit departs from that which would have been expected without the spatial variations in gravity, and precise measurements of the orbit by means of the constellation of GPS satellites and network of ground

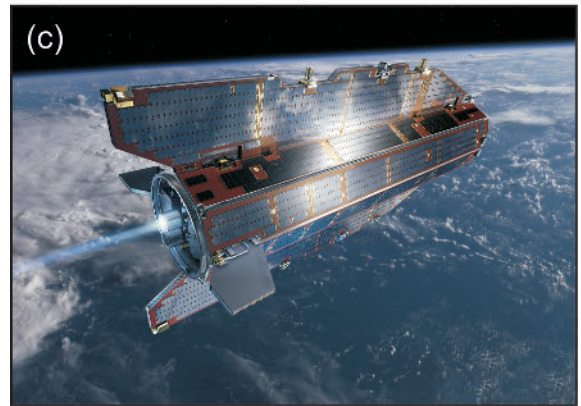
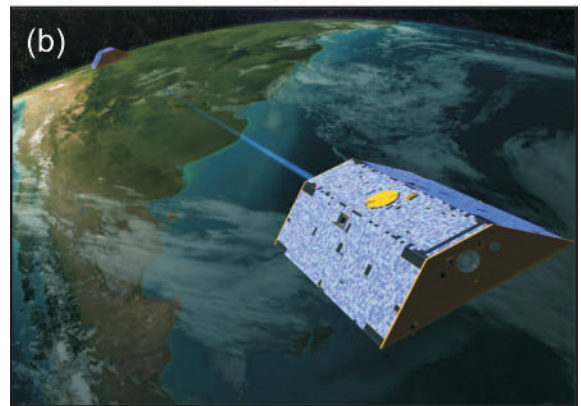
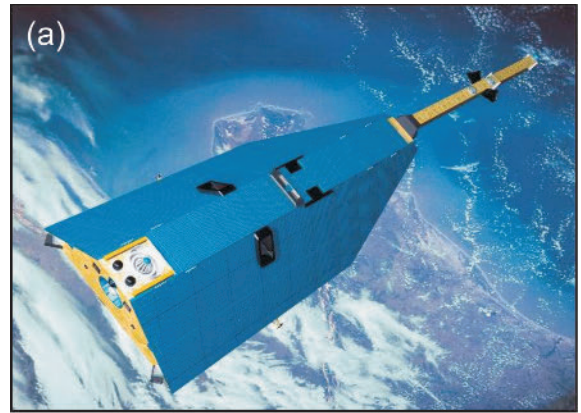


Figure 9.13 Gravity satellites (a) CHAMP, (b) GRACE, which consists of two CHAMP-like satellites, and (c) GOCE. Images from Deutsches GeoForschungsZentrum Helmholtz Centre Potsdam, the GRACE mission home page <http://www.csr.utexas.edu/grace/>, and European Space Agency – AOES Medialab.

stations can be used to infer those variations. The satellite’s orbit is also perturbed by non-gravitational forces (e.g. atmospheric drag). However, these can be measured and accounted for by means of an accelerometer placed at the satellite’s centre of mass.

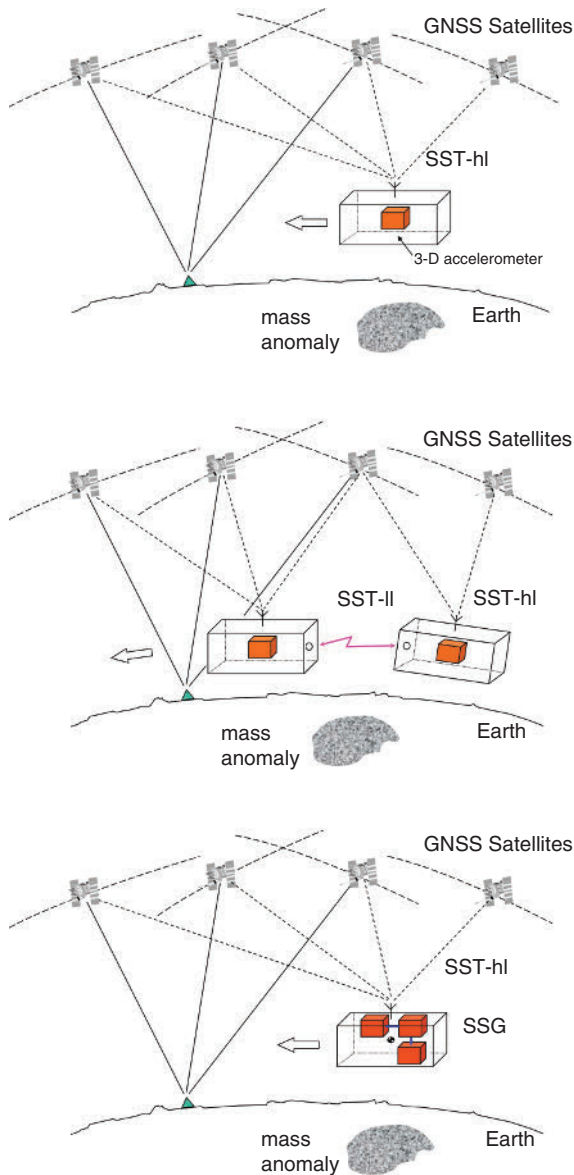


Figure 9.14 (a) Concept of satellite-to-satellite tracking in high-low mode (SST-hl). A low Earth orbiter is tracked by the high orbiting GNSS satellites relative to a network of ground stations. Non-gravitational forces on the low orbiter are measured by an accelerometer.

(b) Tracking in the low-low mode (SST-II) combined with SST-hl. The relative motion between two low orbiters following each other in the same orbit at a distance of a few hundred kilometres is measured by an inter-satellite link.

(c) Concept of satellite gradiometry combined with SST-hl. The second-order derivative of the gravitational potential of the Earth is measured in a low orbiting satellite by a gravity gradiometer (differential accelerometer). Figures adapted from those in [57].

Figure 9.14b shows the concept of satellite-to-satellite tracking in the ‘low-low’ mode (SST-II), which employs an inter-satellite link between a pair of satellites

separated by a few 100 km. The pair are also tracked in SST-hl mode. It can be imagined that, as the first satellite passes through a spatial variation in the gravity field, it is accelerated slightly differently from the second satellite, and as a result the distance between them is continuously modified as the pair orbit in tandem. These modifications can again be used to infer the spatial variations in gravity. The highly successful United States–German Gravity Recovery and Climate Experiment (GRACE) mission launched in 2002 was of this type, comprising a pair of CHAMP-like satellites orbiting at an altitude of 500 km and separated by 220 km [33]. A microwave ranging system, accurate to 10 micrometres, measured the rate of change of separation between them (low-low) while both were tracked by GPS (high-low). The relatively high altitude of GRACE, compared to GOCE discussed below, was designed with the aim of achieving a mission lasting many years so as to be able to monitor time-dependent components of the gravity field as well as the time-mean geoid. GRACE is expected to continue in operation until approximately 2017. A similar mission to GRACE, with a pair of satellites called GRAIL (Gravity Recovery and Interior Laboratory), was employed in lunar orbit during 2012 to determine the Moon’s gravity field and learn more of its origin.

Figure 9.14c shows the concept of gravity gradiometry as used in the Gravity Field and Steady-State Ocean Circulation Mission (GOCE) of the European Space Agency, which was launched in 2009 [34, 35, 36]. This mission employed a single satellite at a low altitude of 260 km, which was much lower than GRACE and was the lowest altitude ever employed for a scientific satellite. As a result, the satellite was much more sensitive to the shorter wavelength components of the gravity field. GOCE was also tracked by GPS, but most importantly carried a three-axis gravity gradiometer. This instrument consists of three pairs of electrostatic servo-controlled accelerometers with 0.5 m baselines. The slightly different gravity measured by the two accelerometers in each pair enabled the gravity gradient to be measured, and the three pairs together provided a complete measurement of the three components of gravity field gradient (**Figure 9.15a, b**).

Each of the high-low, low-low and gradiometry techniques has advantages with regard to measuring different components of the power spectrum of the gravity field or geoid. The geoid, measured relative to the ellipsoid, can be parameterised as:

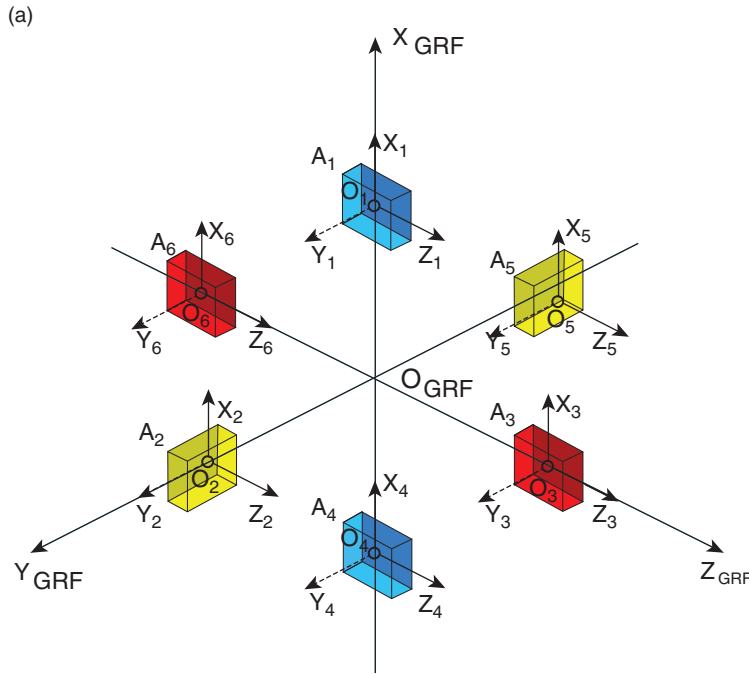
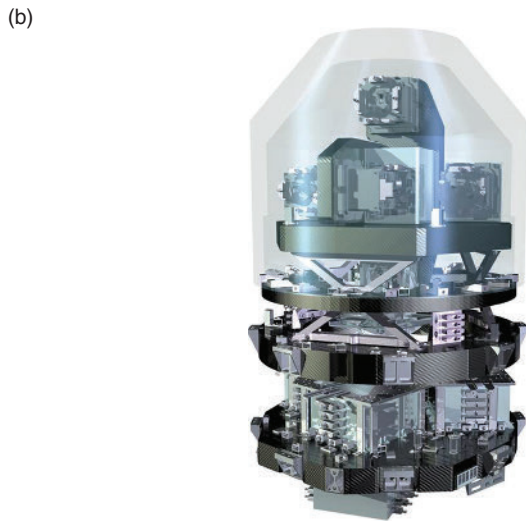


Figure 9.15 (a) Schematic description of the principle of measurement of gravity gradients by means of three pairs of accelerometers housed within a gravity gradiometer. Each accelerometer measures a slightly different gravity, enabling gravity gradients to be computed. Figure provided by Professor Reiner Rummel, Technical University of Munich.

(b) Picture of the GOCE gradiometer. Image from the European Space Agency – AOES Medialab.



$$N(\theta, \lambda) = a \sum_{l=2}^L \sum_{m=0}^l \overline{P}_{lm}(\sin \theta) [\overline{C}_{lm} \cos(m\lambda) + \overline{S}_{lm} \sin(m\lambda)] \quad (9.5)$$

where the \overline{P}_{lm} are fully normalised associated Legendre polynomials of degree l and order m , and θ , λ are colatitude⁷ and longitude [37]. The \overline{C}_{lm} and

\overline{S}_{lm} are coefficients to be determined. The sum starts at degree 2 because degree 1 terms vanish by taking the origin at the centre of the Earth, while a degree zero term would represent a simple spherically symmetric dependence. The sum runs up to a maximum degree (shortest spatial scale) shown by L . The dimensionless quantity:

$$\sigma_l^2 = \sum_{m=0}^l [\overline{C}_{lm}^2 + \overline{S}_{lm}^2] \quad (9.6)$$

⁷ Colatitude is given by $(90^\circ - \text{latitude})$.

is called degree variance and studies of gravity anomalies for many years have suggested that its square root, called degree amplitude, must be approximated by the formula:

$$\frac{\sigma_l}{\sqrt{2l+1}} \approx \frac{10^{-5}}{l^2} \quad (9.7)$$

This rule of thumb is called Kaula's Rule [38]. A plot of σ_l versus l , called a degree amplitude spectrum, is shown in Figure 9.16a, demonstrating the Kaula Rule as a function of spherical harmonic degree, together with what was our best (but rather inaccurate) idea of the real spectrum from a model of the geoid dating from before the recent space gravity missions (the EGM2008 model).⁸ What the new missions have done is given us the ability to measure the real spectrum to great accuracy. The green, red and blue curves in Figure 9.16a indicate the accuracies of measurement of each degree amplitude by each mission. GRACE can be seen to have provided the most accurate measurements to about degree 100 (wavelength of approximately 400 km), improving considerably on the earlier measurements by CHAMP, while GOCE provided the most accurate measurements at higher degree. At long wavelengths (low degree) the information from the dedicated research satellites such as LAGEOS and Starlette remains the most important. The colour bar at the top of Figure 9.16a indicates which technique contributes to each part of the spectrum.

Models of the geoid with names like 'GOCO03S' are now available that employ data from both GRACE and GOCE in an optimal combined way [39]. The *cumulative uncertainty* of a geoid model is calculated by integrating the uncertainties at each degree up to a maximum degree value (L). GRACE and GOCE have together revolutionised our knowledge of the detailed shape of the geoid by so much that the cumulative uncertainty of such combined (or even GOCE-only) models is now known to be centimetric for a value of L of 200 or so (i.e. wavelengths of approximately 200 km and larger) (Figure 9.16b). Geodesists often prefer to quote spatial scales as half-wavelengths, so they would say that the geoid is nowadays known with an accuracy of a few centimetres for scales of ~ 100 km and larger. Several accurate altimetric MSS models are available

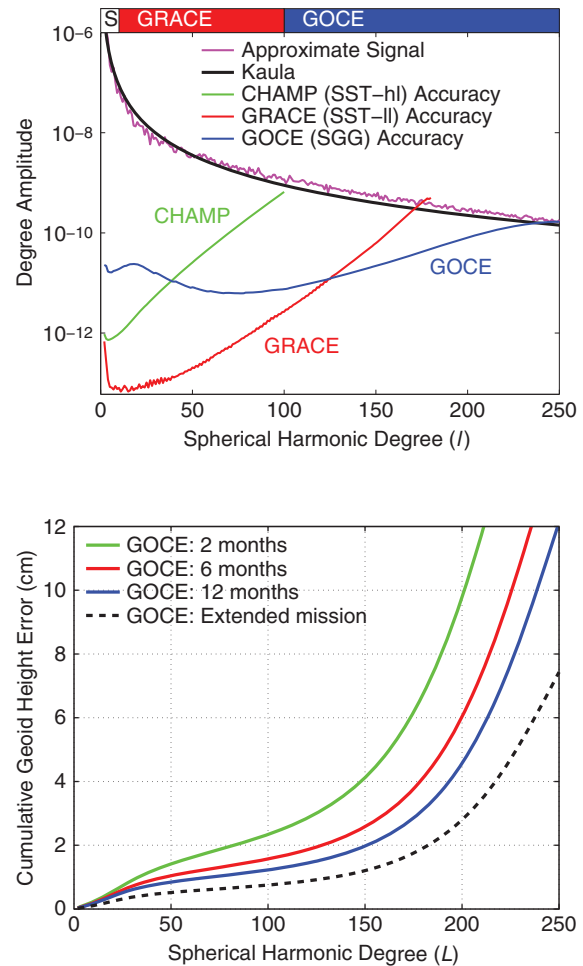


Figure 9.16 (a) A degree amplitude spectrum of the Earth's gravity field estimated from the EGM2008 model (purple) and from the Kaula Rule (black) compared to the accuracy of measurement at each degree of the CHAMP (green), GRACE (red) and GOCE (blue) missions. The main technique contributing to measurement of components of the gravity field are given by the bands at the top of the figure: Satellite laser ranging of geodetic satellites such as LAGEOS (S), and then GRACE and GOCE.

(b) Improvement in the cumulative uncertainty in the geoid as a function of maximum degree (L) as more data from GOCE become available, showing that an overall accuracy of better than 3 cm for $L = 200$ (i.e. wavelengths of approximately 200 km and larger) should be achievable by the end of the extended mission. Figures based on information from Professors Reiner Rummel and Roland Pail, Technical University of Munich.

down to this scale, and knowledge of both MSS and geoid at this short scale and larger is adequate for many aspects of oceanographic research.

To map the geoid from space at even higher spatial resolution would require another low-flying satellite with more precise instrumentation, or an intensive worldwide campaign for the collection of considerable

⁸ Note that this plot shows the more customary 'root power at degree l ', which is the same as degree amplitude but divided by $\sqrt{(2l+1)}$.

amounts of terrestrial, marine and airborne gravity. In that way the ‘omission errors’ in geoid models, which are the uncertainties in knowledge of the height of the geoid at any one location (such as at a tide gauge) due to the lack of information at spherical harmonic degree values larger than L , would be considerably reduced.

9.7 Models of the MSS, geoid and MDT

The accuracy of the GPS and other satellite tracking methods, of the various environmental corrections and, of course, of the altimetric measurements themselves means that there is now excellent knowledge (~2 cm accuracy) of the global MSS averaged over a number of years [40]. Figure 9.17 shows an image of the MSS obtained by combining data from several altimeter missions. As each mission had a different ground track, it was possible to map the MSS at high spatial resolution (1 minute), while the surface of the Arctic, located at latitudes higher than the inclinations of radar altimeter satellites, was provided by the ICESat laser altimeter mission. Long wavelength, large amplitude signals are evident, such as the low to the south of India associated with a deep-seated mass deficiency in the mantle in this region [41], while closer inspection shows short spatial scale features associated with seamounts, trenches and mid-ocean ridges (Figure 9.18).

These spatial variations in the MSS can be used to compute maps of *gravity anomalies*, which are short-wavelength variations of the gravity field [42]. Such maps demonstrate a wealth of geophysical information that has potential commercial and practical value as well as scientific interest. In particular, by using models of isostatic compensation of seafloor topography that provide spectral transfer functions to calculate the gravity anomalies to be expected from sea-floor topography, one can compute detailed maps of the ocean bathymetry (Figure 9.19) [43].

Figure 9.20 shows a picture of the geoid obtained from satellite information only (i.e. from the space gravity missions and from the tracking of geodetic satellites). The model shown here is truncated at degree 250 (wavelength approximately 160 km) so does not have as much detail as the MSS, but otherwise many of its features are similar. In particular, it shows the geoid high (relative to the ellipsoid) in the North Atlantic and the low in the Indian Ocean which are

related to the large-scale composition of the Earth’s mantle and crust [44].

The difference between MSS and geoid (i.e. the MDT) has been calculated by various researchers [45, 46]. An example is shown in Figure 9.21a as a map and in Figure 9.21b as a power spectrum, for which the latter may be compared to the historical example in Figure 9.12. In this case, the MDT is defined as the difference between the Technical University of Denmark DTU10 model of the MSS and the GOCO03S model of the geoid. Thanks to the new gravity missions, the two surfaces are now separable down to approximately degree 180 when uncertainties in the geoid are larger than any signal in the difference. The most obvious aspects of the MDT are the metre-size features associated with the large ocean currents (Gulf Stream, Kuroshio, Antarctic Circumpolar Current). However, close inspection shows many other features with amplitudes of decimetres related to smaller current systems. Maps of the MDT can be expected to improve further as researchers continue to work with the recently available space data sets. For the fullest resolution of ocean circulation features, one will need to use models of the geoid that also incorporate all terrestrial, marine and airborne gravity information then available so as to represent its local short-wavelength components as well as possible.

Until such maps could be produced as MSS-geoid differences, the only empirical way to learn about the global ocean circulation was by means of hydrographic measurements of temperature and salinity from ships. At each point in the ocean one can compute a *dynamic height* relative to a given pressure surface (e.g. 1500 dbar, which is approximately 1500 m depth) that is assumed to be a ‘level of no motion’. The resulting map of dynamic height could then be interpreted as an MDT due to the baroclinic component of the ocean circulation (motions in the ocean that are different at different depths). Figure 9.22 shows a recent computation of dynamic height computed in this way, which can be seen to have many similarities to Figure 9.21a, indicating that a large part of the mean ocean circulation is baroclinic.⁹

From many years of study of altimeter data, we know that models of the MSS will have an accuracy of

⁹ One can see significant differences between the figures in the Southern Ocean where a large part of the mean circulation is more barotropic, i.e. more uniform with depth. (Note that there is an overall offset between values in Figures 9.21a and 9.22 that is not important in the present discussion.)

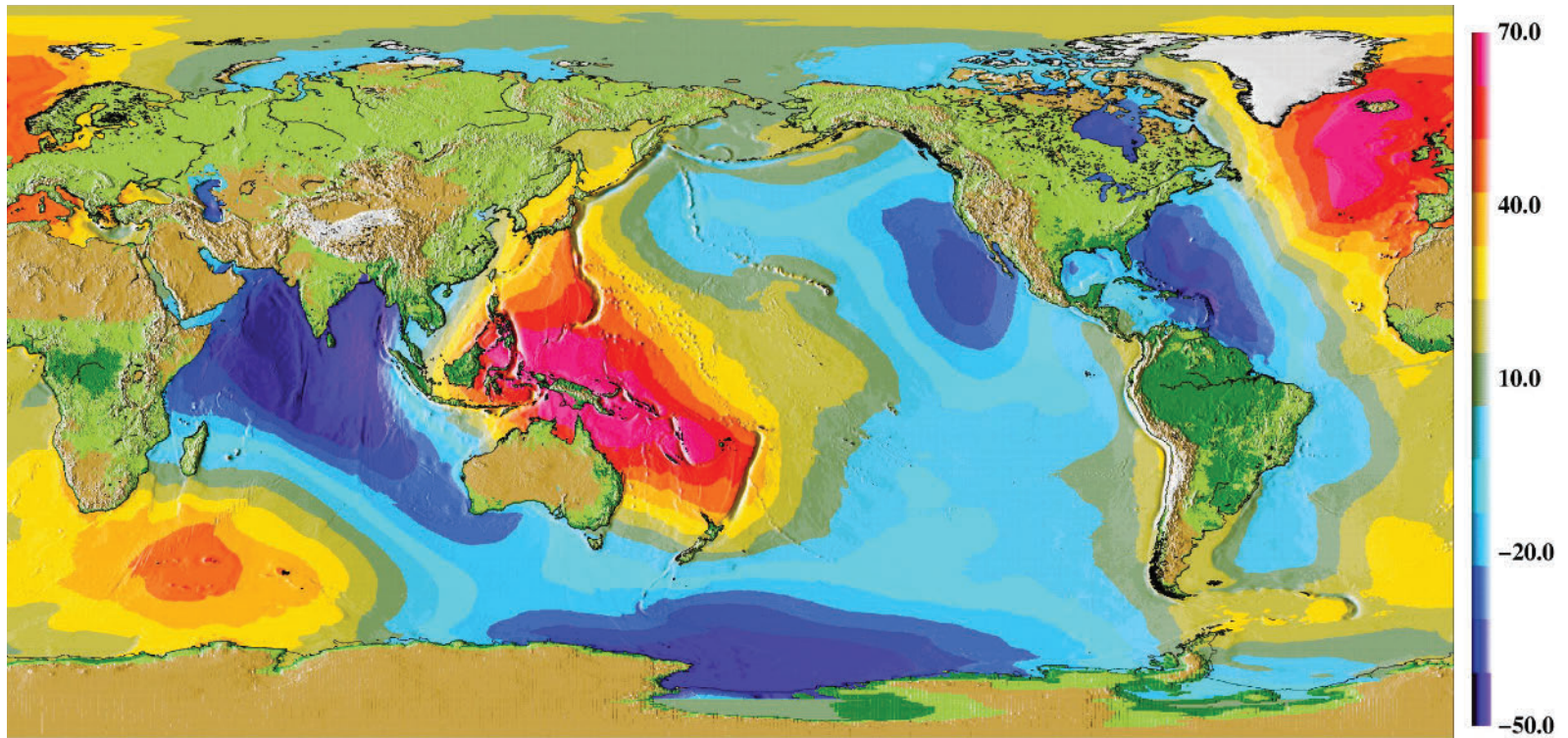


Figure 9.17 The DTU10 model of the global mean sea surface (MSS), which is an updated version of the DNSC08 model [39]. Colour scale in centimetres. Figure from Dr Ole Andersen, Technical University of Denmark.

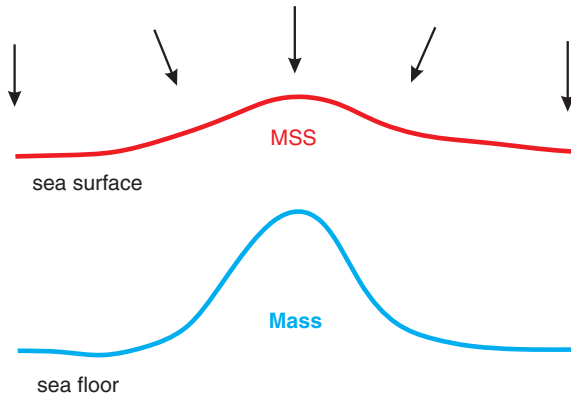


Figure 9.18 A schematic of how a positive mass anomaly (e.g. a submerged seamount) can produce a short-spatial-scale signal in the MSS (and geoid). In this case, the mass of the seamount results in the geopotential surface being further from the centre of the Earth than it would have been otherwise, corresponding to an increase in the height of the MSS. Conversely, the mass deficiency of an ocean trench reduces the height of the MSS. Seamounts can be ~2 km high (and trenches kilometres deep), with a spatial scale of order 100 km, while the corresponding excursions in the MSS (and geoid) are typically a few metres. The arrows indicate how the seamount increases local gravity, causing a plumb line at the sea surface (which defines the vertical) to be deflected towards the seamount.

several centimetres [41]. However, how can one have confidence in the accuracy of models of the geoid and, thereby, MDT? One way, of course, is to compare MDT models produced by different groups of scientists. However, all such studies will have used similar sources of altimeter and gravity information. An independent method nowadays is to use numerical ocean circulation models that employ the data sets of ocean information (temperature, salinity) mentioned above for dynamic height, together with meteorological (winds, air pressures) and sometimes hydrological (river runoff) information, in combination with knowledge of ocean dynamics, to determine the MDT and its associated currents in a dynamically consistent way. There are many such numerical ocean models of the MDT constructed by different groups and with different spatial resolutions, and Figure 9.23 shows the root-mean-square (rms) difference between the MDT values for a set of six of the most modern for the common 5-year epoch 1996–2000 [45]. It can be seen that rms values are less than 10 cm in most parts of the ocean, including the coastal oceans, apart from bands of higher rms along the trajectories of the major currents and in Hudson Bay. There are even significant, large regions where the rms difference is less than 2.5 cm. Consequently, even though the determination of the MDT continues

to be an active area of research, we are starting to have a good insight into its spatial distribution to much better than a decimetre.

Accurate knowledge of the MDT is important as it implies that we know well the mean surface circulation of the ocean and, with help of hydrographic information and models, the circulation at all depths. This is essential information on a major component of the Earth's climate system which can be included in the numerical models used to study climate change. The mean value also determines the rate at which eddies and other instabilities in the circulation occur; the effective monitoring and prediction of this 'ocean weather' is important to many operational uses of the ocean [48].

It is less straightforward to determine geoid model accuracy over land, especially when all available space and terrestrial gravity information has been included in the model. The different models can be tested by comparison to the heights of benchmarks determined by conventional levelling within a national geodetic network. The ellipsoidal heights of the benchmarks obtained from GPS, expressed relative to the geoid (known as *orthometric heights*), should correspond to their levelled heights apart from an overall offset [49]. Networks of benchmarks are better maintained in some countries than others and the quality of the benchmark network is a limiting factor in any comparison to geoid information; those networks that contain fundamental benchmarks (FBMs), marks buried deep in solid rock so as to be as stable as possible, are of particular interest in these studies [50].

In spite of the enormous recent improvement in knowledge of the MDT demonstrated by Figures 9.21 and 9.23, there remains a need to know how the MDT (or 'sea level') can change over shorter distances than can presently be resolved using geoid models derived using satellite data alone. For example, sea level can change by several decimetres or a metre in a short distance as one crosses ocean fronts such as that of the Gulf Stream. In addition, one would like to use MSS and geoid information to measure accurately the transport of currents through narrow straits such as at Gibraltar. Sea level (relative to the geoid) can also change when one crosses a short stretch of land separating different oceanographic régimes; the Isthmus of Panama is such an example, with MSL at the Pacific end of the Panama Canal some 0.2 m higher than that at the Atlantic end with only 60 km between them. The example of Panama demonstrates the continued utility of conventional levelling in many

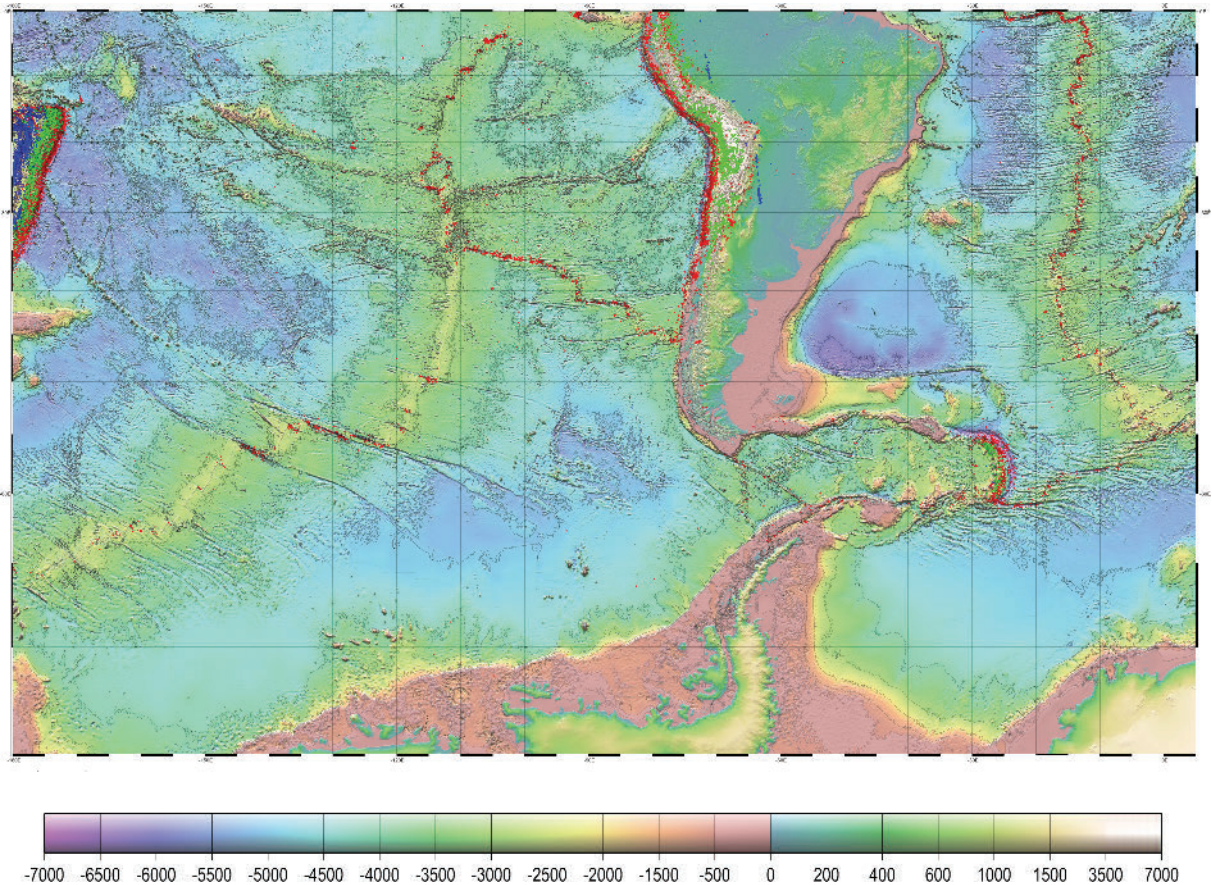


Figure 9.19 Bathymetry of the southeast Pacific and South Atlantic in the latest version of such maps based on altimeter data and ship soundings from [43]. Depths in metres. Figure from Professor David Sandwell, Scripps Institution of Oceanography.

surveying applications requiring geoid-difference information over short distances.

9.8 A comment on epochs

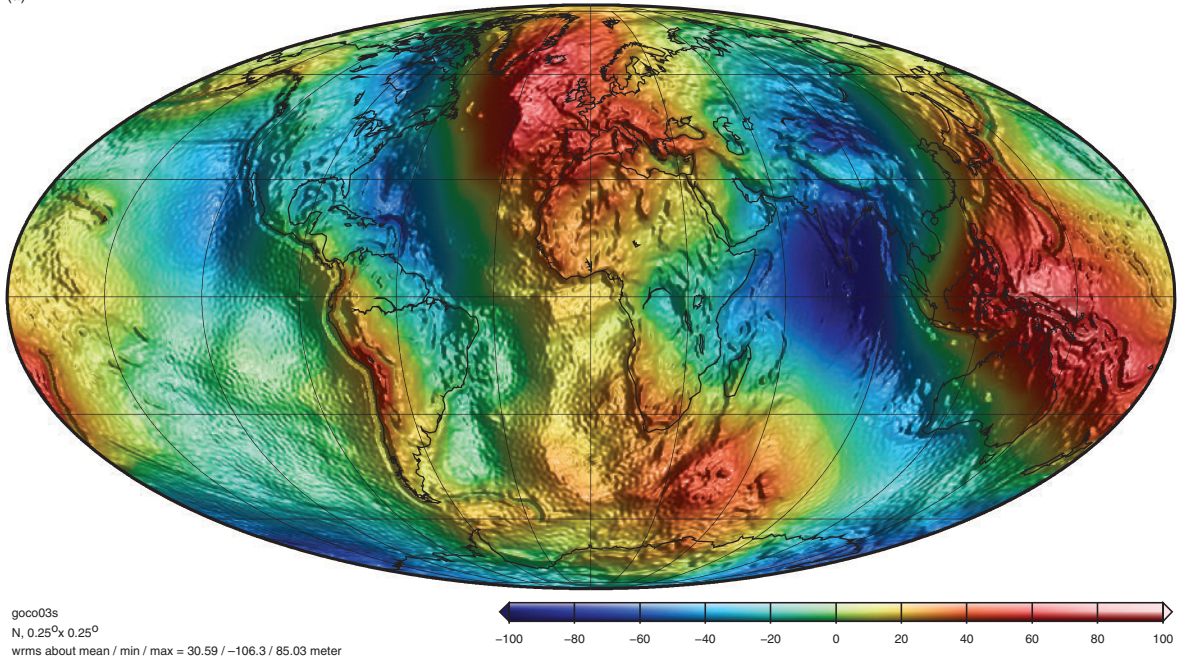
This chapter has focused on the way that sea level varies in space, while temporal changes in sea level are discussed in detail in the [next chapter](#). However, it is important to realise that there are aspects of sea level that vary in both space and time. For example, a MSS is computed from altimeter information collected over a certain number of years, and MSSs computed over different epochs will differ due to changes in the ocean circulation and global sea-level change. Therefore, it is important to note that any ‘mean’ quantity (e.g. MSL, MSS or MDT) requires a statement of the epoch over which it is measured. In addition, the geoid has been discussed in this chapter with an implicit assumption that the Earth’s gravity field does not change, but of

course it does. Its last period of glaciation was only 20,000 years ago, and the continued response of the solid Earth to the removal of the great ice sheets, and the accompanying change in the gravity field, results in a GIA signal in the geoid of several tenths of a millimetre per year [51]. Significant changes to the geoid will also occur as hydrological and glaciological loads on the solid Earth change and, locally, whenever large earthquakes take place [52]. Consequently, gravity missions like GOCE will be required at regular intervals in the future in order to obtain the most precise and up-to-date information on the shape of the geoid surface.

9.9 Towards a global vertical datum

Until the satellite era, the main link between sea-level science and geodesy was in the definition of an official MSL at the most suitable station in a country. This

(a)



(b)

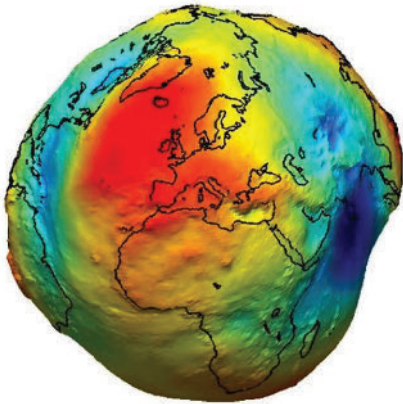


Figure 9.20 (a) Map of the GOCO03S model of the geoid derived from satellite (primarily space gravity) data obtained from <http://icgem.gfz-potsdam.de/ICGEM/>.

(b) An alternative view of the variation of the geoid around the world, exaggerating its long wavelength features. Image from the European Space Agency.

value of MSL would then be adopted as the national datum (reference level) and would be transferred to other locations by means of conventional levelling. In this way, all points could be expressed as ‘heights above sea level’. The MSL used in this way was usually an average value of sea level (relative to land) recorded over an extended period, traditionally chosen to be a lunar nodal period of 18.61 years, although in practice much shorter periods were employed. Occasionally,

very short samples of sea level were used; for example only 10 days of measurements were used in March 1844 in the definition of Ordnance Datum Liverpool (ODL) in the United Kingdom [52]. This datum was subsequently replaced by Ordnance Datum Newlyn (ODN) defined in terms of MSL measured at Newlyn in southwest England during May 1915–April 1921. Other examples of European national datums include Normaal Amsterdams Peil (NAP) in the Netherlands

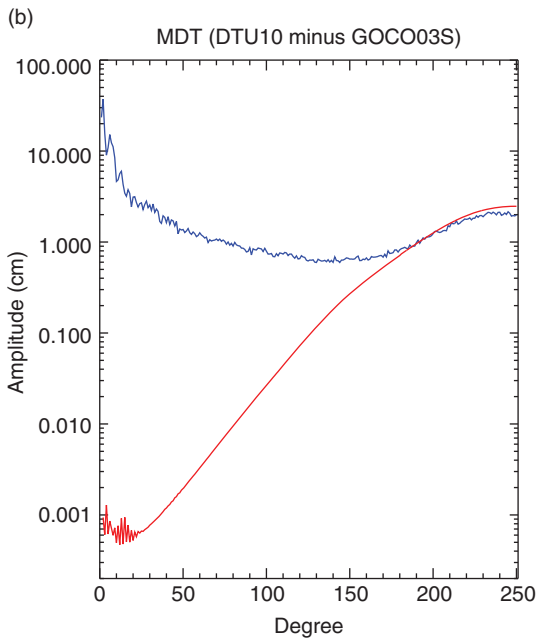
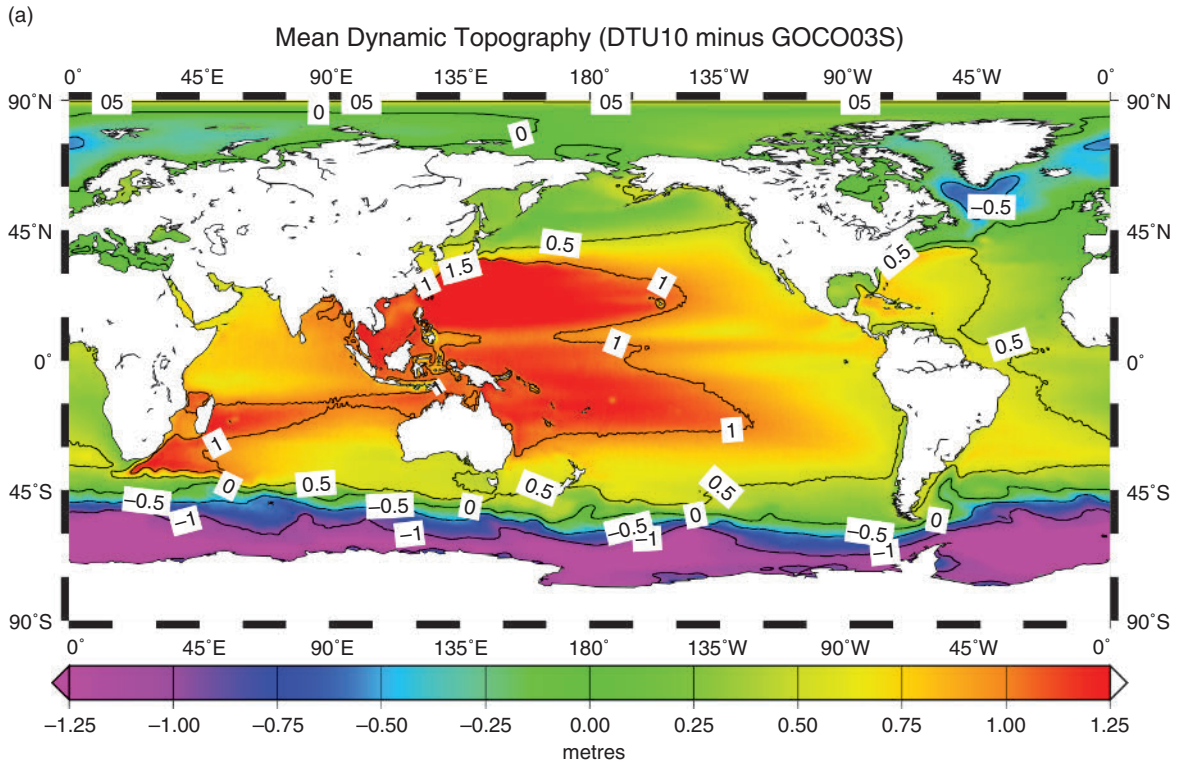


Figure 9.21 (a) The mean dynamic topography (MDT) of the ocean determined as the difference between the mean sea surface (MSS) and geoid to degree 250 (the Technical University of Denmark DTU10 model and GOCO03S geoid model respectively). Slight smoothing has been applied. Computed by Dr Rory Bingham, University of Newcastle.

(b) A modern version of Figure 9.12, demonstrating that it is now feasible to derive the MDT as the difference between MSS and geoid up to approximately degree 180. The blue curve shows the MDT spectrum derived as in (a) while the formal errors of GOCO03S are shown in red.

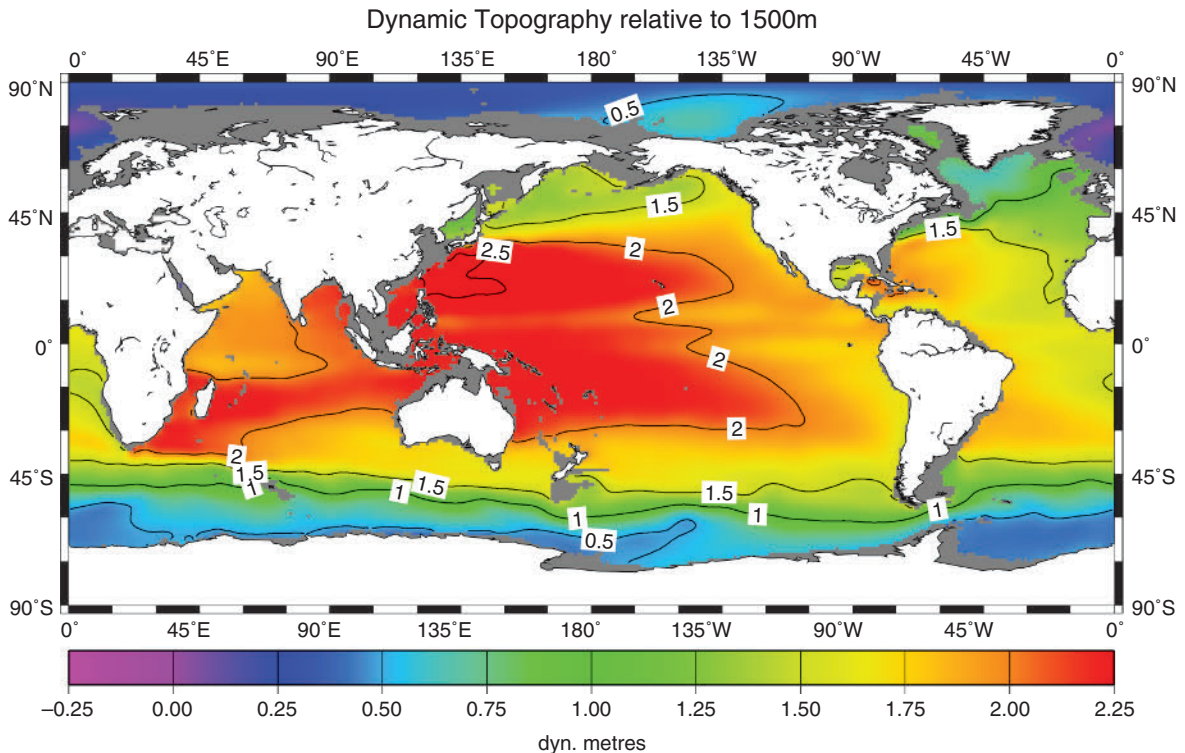


Figure 9.22 Map of the dynamic topography of the ocean relative to 1500 m reference level derived from temperature and salinity data in the World Ocean Database 2009. National Oceanic and Atmospheric Administration National Oceanographic Data Center http://www.nodc.noaa.gov/OC5/WOA09/pr_woa09.html.

and Nivellement Général de la France (NGF) in France. All of these datums, when originally established approximately a century ago, were close approximations of the then MSL at Newlyn, Amsterdam and Marseille respectively. The later Canadian Geodetic Vertical Datum 28 (CGVD28) and North American Vertical Datums 1929 and 1988 (NAVD29 and NAVD88) used in the United States were also related to MSL, in both cases to that at Rimouski in Québec.

The problem with any datum tied to a historical MSL measurement is that MSL, measured relative to a datum, will change after the datum is established. For example, sea level has risen by almost 0.2 m at Newlyn since the datum was first defined [54]. Nevertheless, these national datums remain as important reference levels in each country, even though they might be (and might always have been) at a different geopotential because of the spatial variation of the mean sea surface relative to the geoid. National datums remain of great practical (and legal) importance and cannot be disregarded now, even if we know that they do not represent exactly the same geopotential (or 'level').

Methods for relating one national datum to another have been studied for many years and it is known that there are significant differences between them (e.g. Figure 9.24). Knowledge of the differences is needed most obviously whenever it is necessary to consider a bridge or tunnel spanning adjacent countries. On those occasions, conventional levelling can provide a suitable connection between datums for adjacent continental countries [55], while various types of ocean (hydrodynamic) levelling can be used to relate datums between countries separated by water [56]. However, there has never been a single suitable method for relating all national datums until now [48].

Improvements in datum information are needed not only *between* countries but also *within* them, as many of the national levelling networks mentioned above were known to contain significant spatially dependent (often latitudinal) biases [57]. For example, Figure 9.25 shows a determination of the apparent north-south slope of MSL along the Atlantic coast of North America measured with respect to national datums in the United States and Canada (red and blue

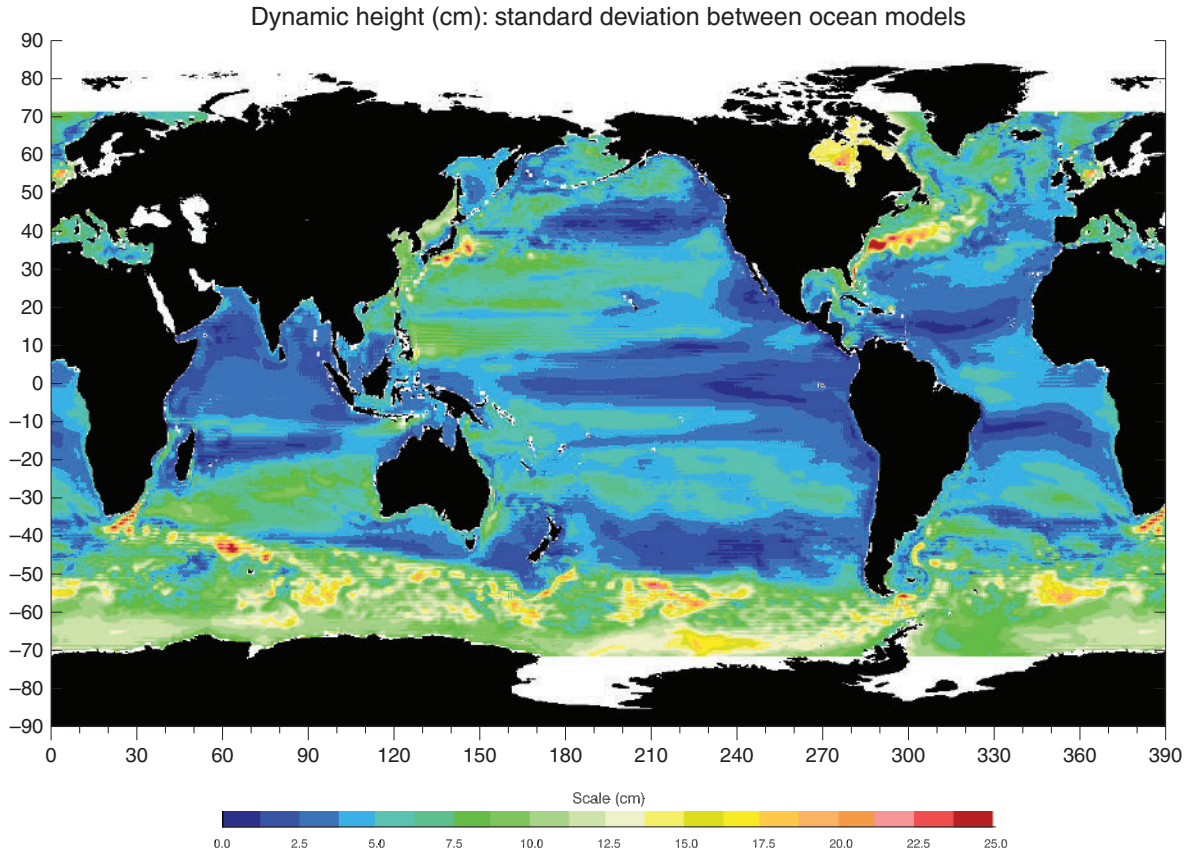


Figure 9.23 Rms difference between the MDT values for a set of six modern numerical ocean models for the common 5-year epoch 1996–2000. The good agreement between models provides a working estimate of their accuracy when they are used in height system unification. From [46].

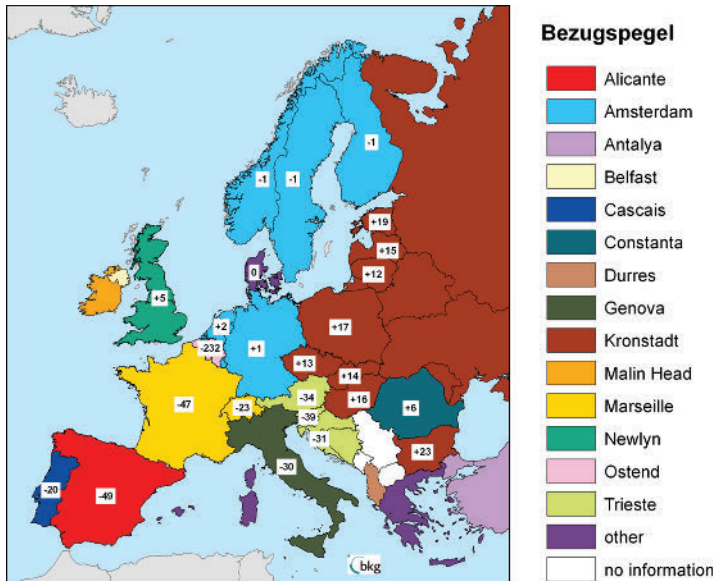


Figure 9.24 Estimated biases (in centimetres) between the national datums used in Europe provided by the Bundesamt für Kartographie und Geodäsie, Germany (www.bkg.bund.de). The numbers are mean offsets in the ‘middle’ of each country between national heights and those of the European Vertical Reference Frame (EVRF2007), which is a pan-European conventional levelling programme. Offsets have to be added to national heights to obtain heights in EVRF2007. This figure does not demonstrate the significant spatial dependence of biases within each country.

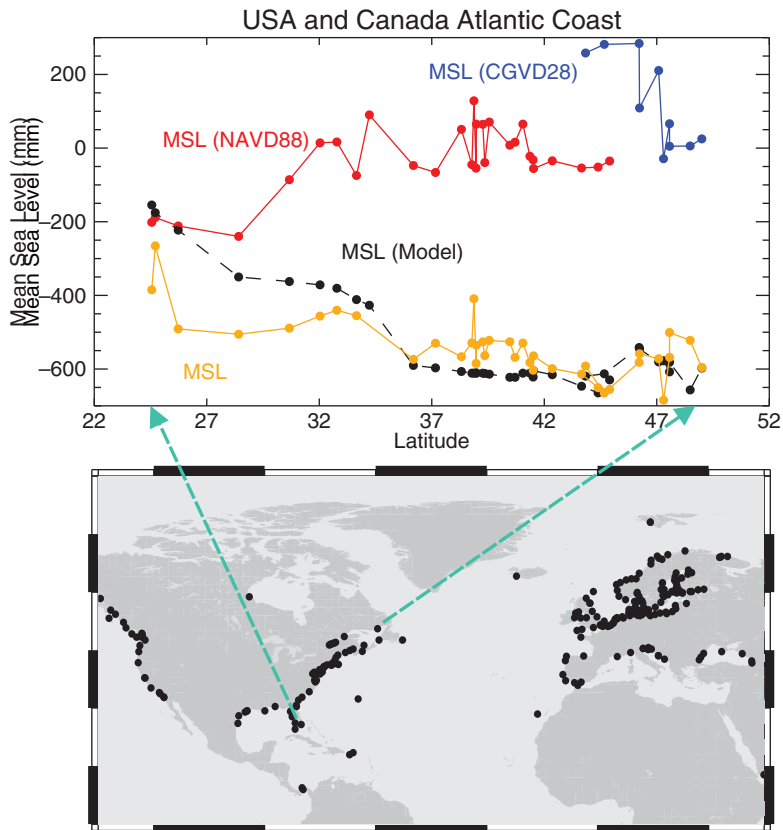


Figure 9.25 The apparent north–south slope of MSL along the Atlantic coast of North America derived by three different methods: measured at tide gauges with respect to national datums in the United States and Canada (red and blue dots, respectively); determined at the same locations by calculating MSL above the geoid using a state-of-the-art geoid model (yellow dots); and as inferred from a numerical ocean circulation model (black dots). Based on a figure in [46].

dots, respectively). At first sight, these data would suggest that the height of the sea increases travelling north from Florida to Canada. However, most modern numerical models of ocean circulation (black dots) demonstrate that the slope of the sea actually decreases travelling north, primarily due to the effects of the Gulf Stream in this region of the Atlantic Ocean. New models of the geoid, such as those discussed above, have resolved this long-standing controversy by providing conclusive proof that the height of the sea does, indeed, fall going north along the coast (yellow dots) [46].

It is now universally recognised that the only true datum (or ‘level’) is the geoid and that the relationships between national datums can be determined best by comparison to a state-of-the-art geoid model, with the model itself validated by means of combined oceanographic and terrestrial data sets containing tide gauge, altimeter, ocean model, GPS and levelling information. The goal is to have eventually a model of the geoid that will be considered accurate enough to be adopted as a universal Global Vertical Datum, which can meet all the many requirements for vertical reference around the world [3].

References

1. Bomford, G. 1980. *Geodesy*. Oxford: Clarendon Press.
2. Hofmann-Wellenhof, B. and Moritz, H. 2006. *Physical Geodesy*. New York: Springer.
3. Plag, H.-P. and Pearlman, M. (eds.) 2009. *Global Geodetic Observing System: Meeting the Requirements of a Global Society on a Changing Planet in 2020*. Berlin: Springer Geoscience.
4. Altamimi, Z., Collilieux, X. and Métivier, L. 2011. ITRF2008: an improved solution of the International Terrestrial Reference Frame, *Journal of Geodesy*, **85**, 457–473, doi:10.1007/s00190-011-0444-4.
5. Wu, X., Collilieux, X., Altamimi, Z. *et al.* 2011. Accuracy of the International Terrestrial Reference Frame origin and Earth expansion. *Geophysical Research Letters*, **38**, L13304, doi:10.1029/2011GL047450.
6. Blewitt, G., Altamimi, Z., Davis, J. *et al.* 2010. Geodetic observations and global reference frame contributions to understanding sea-level rise and variability. In *Understanding Sea-Level Rise and Variability* (eds. J. A. Church, P. L. Woodworth, T. Aarup and W. S. Wilson), pp. 256–284. London: Wiley-Blackwell.

7. (1) Teferle, F. N., Bingley, R. M., Williams, S. D. P., Baker, T. F. and Dodson, A. H. 2006. Using continuous GPS and absolute gravity to separate vertical land movements and changes in sea-level at tide-gauges in the UK. *Philosophical Transactions of the Royal Society*, **364**, 917–930, doi:10.1098/rsta.2006.1746. (2) Mazzotti, S., Lambert, A., Henton, J., James, T. S. and Courtier, N. 2011. Absolute gravity calibration of GPS velocities and glacial isostatic adjustment in mid-continent North America. *Geophysical Research Letters*, **38**, L24311, doi:10.1029/2011GL049846.
8. Marquis, W. and Shaw, M. 2011. GPS-III. Bringing new capabilities to the global community. *Inside GNSS*, 34–48, September–October. www.insidegnss.com.
9. Blewitt, G. 1998. GPS data processing methodology: from theory to applications. In *GPS for Geodesy* (eds. P. J. G. Teunissen and A. Kleusberg), pp. 231–270. Berlin: Springer-Verlag.
10. Tregoning, P. and Herring, T. A. 2006. Impact of a priori zenith hydrostatic delay errors on GPS estimates of station heights and zenith total delays. *Geophysical Research Letters*, **33**, L23303, doi:10.1029/2006GL027706.
11. Hoare, M. R. 2005. *The Quest for the True Figure of the Earth: Ideas and Expeditions in Four Centuries of Geodesy*. Aldershot: Ashgate Publishing Limited.
12. Hughes, C. W. and Bingham, R. J. 2008. An oceanographer's guide to GOCE and the geoid. *Ocean Science*, **4**, 15–29, doi:www.ocean-sci.net/4/15/2008/.
13. Kaula, W. M. 1970. *The Terrestrial Environment: Solid Earth and Ocean Physics*. Report of the Williams College, Williamstown meeting in August 1969. NASA Report CR-1579. Washington, D.C.: National Aeronautics and Space Administration.
14. Fu, L.-L. and Cazenave, A. (eds.) 2001. *Satellite Altimetry and Earth Sciences: A Handbook of Techniques and Applications*. San Diego, CA: Academic Press.
15. Robinson, I. S. 2010. *Discovering the Ocean from Space: The Unique Applications of Satellite Oceanography*. Berlin: Springer-Verlag.
16. For many references on the history and technology of satellite radar altimetry and on the areas of science that have benefitted from it, see the *Proceedings of the Symposium on 20 Years of Progress in Radar Altimetry*, Venice, September 2012. www.altimetry2012.org.
17. Lemoine, F. G., Zelensky, N. P., Chinn, D. S. *et al.* 2010. Towards development of a consistent orbit series for TOPEX, Jason-1, and Jason-2. *Advances in Space Research*, 1513–1540, doi:10.1016/j.asr.2010.05.007.
18. Parke, M. E., Stewart, R. H., Farless, D. L. and Cartwright, D. E. 1987. On the choice of orbits for an altimetric satellite to study ocean circulation and tides. *Journal of Geophysical Research*, **92**, C11, doi:10.1029/JC092iC11p11693.
19. Ekman, M. 1989. Impacts of geodynamic phenomena on systems for height and gravity. *Bulletin Géodésique (Journal of Geodesy)*, **63**, 281–296, doi:10.1007/BF02520477.
20. Rapp, R. H., Nerem, R. S., Shum, C. K., Klosko, S. M. and Williamson, R. G. 1991. *Consideration of Permanent Tidal Deformation in the Orbit Determination and Data Analysis for the TOPEX/POSEIDON Mission*. NASA Technical Memorandum 100775. Greenbelt, MD: Goddard Space Flight Center.
21. IERS, 2010. *IERS Conventions (2010)*. International Earth Rotation and Reference Systems Service (IERS) Technical Note No. 36 (eds. G. Petit and B. Luzum). Frankfurt am Main: Verlag des Bundesamts für Kartographie und Geodäsie. Available from <http://www.iers.org/IERS/EN/Publications/TechnicalNotes/tn36.html>.
22. Haines, B. J., Desai, S. D. and Born, G. H. 2010. The Harvest Experiment: calibration of the climate data record from TOPEX/Poseidon, Jason-1 and the Ocean Surface Topography Mission. *Marine Geodesy*, **33**(S1), 91–113, doi:10.1080/01490419.2010.491028.
23. Bonnefond, P., Exertier, P., Laurain, O. and Jan, G. 2010. Absolute calibration of Jason-1 and Jason-2 altimeters in Corsica during the Formation Flight Phase. *Marine Geodesy*, **33**, Supplement 1, 80–90, doi:10.1080/01490419.2010.487790.
24. Mertikas, S. P., Ioannides, R. T., Tziavos, I. N. *et al.* 2010. Statistical models and latest results in the determination of the absolute bias for the radar altimeters of Jason Satellites using the Gavdos Facility. *Marine Geodesy*, **33**, Supplement 1, 114–149, doi:10.1080/01490419.2010.488973.
25. Watson, C., White, N., Church, J. *et al.* 2010. Absolute calibration in Bass Strait, Australia: TOPEX, Jason-1 and OSTM/Jason-2. *Marine Geodesy*, **34**, 242–260, doi:10.1080/01490419.2011.584834.
26. Mitchum, G. T. 2000. An improved calibration of satellite altimetric heights using tide gauge sea levels with adjustment for land motion. *Marine Geodesy*, **23**, 145–166, doi:10.1080/01490410050128591.
27. Nerem, R. S. 1997. Global mean sea level change: correction. *Science*, **275**, 1049–1053, doi:10.1126/science.275.5303.1049i.
28. Amalvict, M. and Boavida, J. 1993. The geoid: from geodesy to geophysics and from geophysics to geodesy. *Surveys in Geophysics*, **14**, 477–494, doi:10.1007/BF00690573.
29. The IGFS website is www.igfs.net.
30. Vening Meinesz, F. A. 1931. Gravity anomalies in the East Indian archipelago. *The Geographical Journal*, **77**, 323–332, doi:www.jstor.org/stable/1784280.
31. Forsberg, R., Olesen, A. V., Yildiz, H. and Tscherning, C. C. 2011. Polar gravity fields from GOCE

- and airborne gravity. *Proceedings of the Fourth International GOCE User Workshop*, Munich, Germany, 31 March–1 April 2011. European Space Agency Report ESA SP-696.
32. King-Hele, D. G., 1960. *Satellites and Scientific Research*. London: Routledge and Kegan Paul.
 33. Tapley, B. D., Bettadpur, S., Watkins, M. and Reigber, C. 2004. The gravity recovery and climate experiment: mission overview and early results. *Geophysical Research Letters*, **31**, L09607, doi:10.1029/2004GL01992.
 34. Visser, P. N. A. M., Rummel, R., Balmino, G. *et al.* 2002. The European Earth Explorer Mission GOCE: impact for the geosciences. In *Ice Sheets, Sea Level and the Dynamic Earth* (eds. J. Mitrovica and L. L. A. Vermeersen), pp. 95–107. Geodynamics Series 29, American Geophysical Union.
 35. Rummel, R. 2010. GOCE: gravitational gradiometry in a satellite. In *Handbook of Geomathematics. Volume 2* (eds. W. Freeden, M. Z. Nashed and T. Sonar), pp. 93–103. Berlin: Springer. doi:10.1007/978-3-642-01546-5-4.
 36. Many papers on the GOCE mission are included in a special issue of the *Journal of Geodesy*, **85**(11), 2011, while related papers on regional and global geoid-based vertical datums can be found in the *Journal of Geodetic Science*, Number 4, December 2012.
 37. Heiskanen, W. A. and Moritz, H. 1967. *Physical Geodesy*. San Francisco: Freeman.
 38. Kaula, W. M. 1966. *Theory of Satellite Geodesy*. Waltham, MA: Blaisdell Publishing Company.
 39. (1) Pail, R., Goiginger, H., Schuh, W.-D. *et al.* 2010. Combined satellite gravity field model GOCO01S derived from GOCE and GRACE. *Geophysical Research Letters*, **37**, L20314, doi:10.1029/2010GL044906. (2) Pail, R. 2013. Global gravity field models and their use in Earth System Research. In *Earth Observation of Global Changes (EOGC)* (eds. J. M. Krisp, L. Meng, R. Pail, and U. Stilla), pp. 3–20. Berlin: Springer-Verlag.
 40. Andersen, O. B. and Knudsen, P. 2009. The DNSCO8 mean sea surface and mean dynamic topography. *Journal of Geophysical Research*, **114**, C11, doi:10.1029/2008JC005179.
 41. Banerjee, P. 2011. Geoid. In *Encyclopedia of Solid Earth Geophysics* (electronic book), pp. 353–358. Dordrecht: Springer. doi:10.1007/978-90-481-8702-7_101.
 42. Andersen, O. and Knudsen, P. 1998. Global marine gravity field from the ERS-1 and Geosat geodetic mission altimetry. *Journal of Geophysical Research*, **103**, C4, doi:10.1029/97JC02198.
 43. Smith, W. H. F. and Sandwell, D. T. 1997. Global sea floor topography from satellite altimetry and ship depth soundings. *Science*, **277**, 1956–1962, doi:10.1126/science.277.5334.1956.
 44. Ihnen, S. M. and Whitcomb, J. H. 1983. The Indian ocean gravity low: evidence for an isostatically uncompensated depression in the upper mantle. *Geophysical Research Letters*, **10**, 421–423, doi:10.1029/GL010i006p00421.
 45. Bingham, R. J., Knudsen, P., Andersen, O. and Pail, R. 2011. An initial estimate of the North Atlantic steady-state geostrophic circulation from GOCE. *Geophysical Research Letters*, **38**, L01606, doi:10.1029/2010GL045633.
 46. Higginson, S., Thompson, K. R., Huang, J., Véronneau, M. and Wright, D. G. 2011. The mean surface circulation of the North Atlantic subpolar gyre: a comparison of estimates derived from new gravity and oceanographic measurements. *Journal of Geophysical Research*, **116**, C08016, doi:10.1029/2010JC006877.
 47. Woodworth, P. L., Hughes, C. W., Bingham, R. J. and Gruber, T. 2012. Towards worldwide height system unification using ocean information. *Journal of Geodetic Science*, **2**(4), 302–318, doi:10.2478/v10156-012-004-8.
 48. Le Traon, P. Y., Hernandez, F., Rio, M. H. and Davidson, F. 2003. How operational oceanography can benefit from dynamic topography estimates as derived from altimetry and improved geoid. *Space Science Reviews*, **108**, 239–249, doi:10.1023/A:1026111006289.
 49. Featherstone, W. E. and Filmer, M. S. 2012. The north-south tilt in the Australian Height Datum is explained by the ocean's mean dynamic topography. *Journal of Geophysical Research*, **117**, C08035, doi:10.1029/2012JC007974.
 50. Ziebart, M. K., Iliffe, J. C., Forsberg, R. and Strykowski, G. 2008. Convergence of the UK OSGM05 GRACE-based geoid and the UK fundamental benchmark network. *Journal of Geophysical Research*, **113**, B12401, doi:10.1029/2007JB004959.
 51. Tamisiea, M. E. and Mitrovica, J. X. 2011. The moving boundaries of sea level change: understanding the origins of geographic variability. *Oceanography*, **24**, 24–39, doi:10.5670/oceanog.2011.25.
 52. Han, S.-C., Shum, C. K., Bevis, M., Ji, C. and Kuo, C.-Y. 2006. Crustal dilatation observed by GRACE after the 2004 Sumatra-Andaman earthquake. *Science*, **313**, 658–662, doi:10.1126/science.1128661.
 53. Close, C. 1922. *The Second Geodetic Levelling of England and Wales 1912–1921*. London: His Majesty's Stationery Office.
 54. Woodworth, P. L., Teferle, N., Bingley, R., Shennan, I. and Williams, S. D. P. 2009. Trends in

- UK mean sea level revisited. *Geophysical Journal International*, **176**, 19–30, doi:10.1111/j.1365-246X.2008.03942.x.
55. Papers on the European levelling activity called the United European Levelling Network (UELN) can be downloaded from <http://www.bkg.bund.de/geodIS/EVRS/>. A classic example of the use of continent-wide levelling information in combination with tide gauge data is given by Rossiter, J. R. 1967. An analysis of annual sea level variations in European waters. *Geophysical Journal of the Royal Astronomical Society*, **12**, 259–299, doi:10.1111/j.1365-246X.1967.tb03121.x.
56. Cartwright, D. E. and Crease, J. 1962. A comparison of the geodetic reference levels of England and France by means of the sea surface. *Proceedings of the Royal Society of London, A*, **273**, 558–580, doi:10.1098/rspa.1963.0109.
57. Thompson, K. R. 1980. An analysis of British monthly mean sea level. *Geophysical Journal of the Royal Astronomical Society*, **63**, 57–73, doi:10.1111/j.1365-246X.1980.tb02610.x.
58. ESA, 1999. *The Gravity Field and Steady-State Ocean Circulation Mission*. Reports for Mission Selections. ESA Report SP-1233(1). Noordwijk, the Netherlands: European Space Agency.

Mean sea-level changes in time

And Noah he often said to his wife when he sat down to dine,
 ‘I don’t care where the water goes if it doesn’t get into the wine.’
G. K. Chesterton, Wine and Water

10.1 Introduction

This chapter discusses a number of aspects of variability and long-term change in mean sea level (MSL). The changes take place on timescales of months through to centuries and can be studied with tide gauge, altimeter and some other data types, combined with different types of numerical modelling. The variations considered have amplitudes measured in centimetres or decimetres for most timescales and at most places. However, much larger variations do take place at some locations. For example, seasonal sea-level changes of around a metre are observed in certain parts of the Bay of Bengal in the Indian Ocean, and variations of several decimetres to a metre occur approximately every 3–7 years in the Pacific during El Niño events. A similarly large rise may occur throughout the world ocean during the next 100 years if some predictions of anthropogenic climate change prove correct.

Many aspects of sea-level variability can be investigated with the use of data sets that can be obtained from international centres.¹ The main data sets are introduced below, followed by a description of a number of topics of sea-level variability and long-term change that can be studied with them.

¹ Variability is often defined by timescale. Seasonal variability usually refers to changes through the year, with annual variability referring to the 12-month component. Interannual variability refers to changes from year to year or on timescales of several years, while decadal variability refers to changes from one decade to the next. Secular sea-level change refers to the linear rate of change of sea level between specified dates.

10.2 Sea-level data

10.2.1 MSL data from tide gauges

There are many different types of tide gauge (Chapter 2) and each type delivers sea-level data in different ways. Historically, the most common data type comprised spot values of sea level every hour, obtained from inspection of the ink trace on a tide gauge chart. An analyst would smooth through any high-frequency variability in the trace due to seiche before estimating the hourly values. Nowadays, the data loggers of tide gauges provide their data electronically. These data can be either spot values, integrated (averaged) values over specified periods (e.g. 6 minutes), or integrated over a specified period within a longer sampling period (e.g. averaged over 3 minutes every 6 minutes).

The Permanent Service for Mean Sea Level (PSMSL) recommends that all data be filtered to provide hourly values, hourly values then filtered to make so-called daily mean values, followed by an arithmetic averaging of the daily means to derive monthly and annual values of MSL. The choice of the first filter, to provide hourly values from the tide gauge measurements, depends on the particular way that the measurements were obtained. The most common filters used to convert hourly values to daily means are the Doodson- X_0 and University of Hawaii filters [1]. The former is a simple 39-point moving arithmetic filter, while the latter performs a tidal reduction for four constituents (M_2 , S_2 , O_1 and K_1) for each month of data and then low-pass filters the residuals using a 119-point filter [1]. Whichever filter is employed, or even if the hourly values are simply averaged arithmetically into monthly and

annual means, monthly MSL values are usually the same to within several mm.

A closely related parameter to MSL is Mean Tide Level (MTL). This quantity is obtained by averaging values of high and low water into monthly and annual mean high and low waters (MHW and MLW) and then by averaging those two quantities into MTL. Tabulations of MTL are often found in archives when port operators recorded only the highs and lows of the tide rather than the full tidal curve. There is a systematic offset between the two quantities which depends upon the shallow-water tide (Appendix C). Consequently, time series of MTL must be stored in data banks separately from those of MSL so as to avoid confusion between them, and an allowance for the offset must be made when the two quantities are combined in research [2].

10.2.2 The PSMSL and other MSL data sets

The PSMSL is the global data bank for long-term sea-level information from tide gauges [3, 4]. It was founded in 1933 and operates under the auspices of the International Council for Science. Its data sets are used intensively in research including the regular research assessments of the Intergovernmental Panel on Climate Change (IPCC). The PSMSL currently holds over 60,000 station-years of monthly and annual means of sea level, of which the earliest dates from 1807. Station records in the Revised Local Reference (RLR) subset are measured to a consistent datum (benchmark height) and so can be analysed to determine sea-level trends and variability. Figure 10.1a

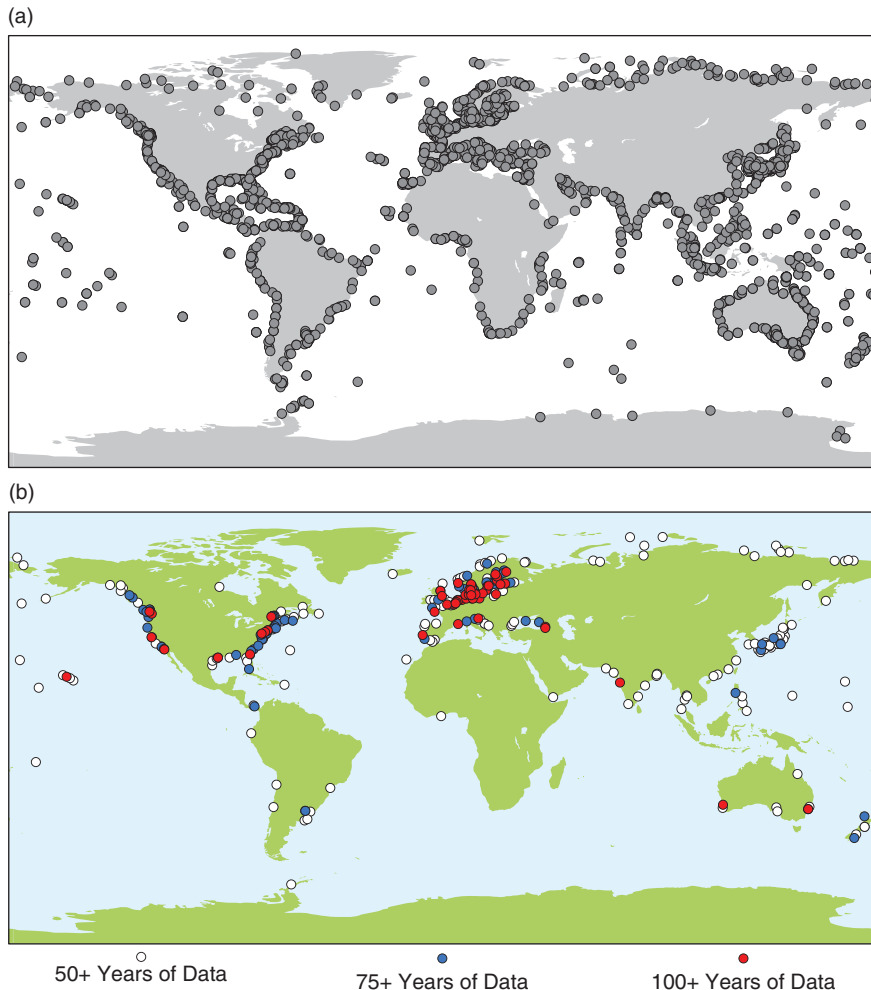


Figure 10.1 Distributions of (a) all PSMSL stations including both research quality (RLR) and non-datum controlled stations (known as 'Metric only' stations) and (b) long, research-quality records in the PSMSL RLR subset. From [4].

shows a map of all stations represented in the [PSMSL](#) data set while [Figure 10.1b](#) shows stations with long records in the RLR subset. The [PSMSL](#) website (www.psmsl.org) contains a considerable amount of training material and related information. Much of the science discussed in this chapter is based on the [PSMSL](#) data set.

MSL information can also be obtained from other international centres, notably the University of Hawaii Sea Level Center (uhslc.soest.hawaii.edu) and from a number of national data banks. The [PSMSL](#) website contains a list of the various other sources of sea-level information

10.2.3 Sea-level data from altimetry

[Chapter 9](#) has explained how the orbit of an altimeter satellite is usually selected so as to trace out a track over the ocean that is repeated at regular intervals (e.g. 9.9156 days in the case of TOPEX/Poseidon and Jason-1 and -2). In most analyses, sea surface heights are calculated at defined ‘reference points’ along the track (e.g. incremental values of latitude) by interpolation between the original 1-second altimeter measurements. The heights can subsequently be converted to height anomalies by subtraction of the long-term average height along the track. Time series of sea-level anomalies at each reference point can then be analysed in a similar way to the study of tide gauge records and a pseudo-mean sea-level time series generated. An alternative method bins and optimally interpolates height anomalies into regular latitude–longitude grids using data acquired from single or multiple missions over a short period such as a week [5].

There are differences between the ‘sea level’ discussed by scientists in the tide gauge and altimeter communities. One difference is that an altimeter measurement is a *geocentric* one, with sea level measured with respect to the centre of the Earth, or to an Earth-centred standard ellipsoid ([Chapter 9](#)). However, a tide gauge measurement, and also archaeological and geological sea-level measurements, are *relative* ones, with sea level measured with respect to the height of a benchmark on the nearby land ([Chapter 2](#)). GPS can be used to convert a relative measurement into a geocentric one. The difference between the two types of sea level is especially important when one discusses long-term sea-level change at a particular location. A second difference is that ‘sea level’ for the altimeter community usually means the measured sea surface height corrected for the inverse barometer effect (see below), yielding a parameter akin to sub-surface pressure. On the other

hand, for the tide gauge community, ‘sea level’ has always meant the physical ‘still water level’. These different conventions have caused confusion at times and it is always important to verify whether any reported ‘sea level’ has been adjusted for air pressure or not.

Properly corrected, tide gauge and altimeter data complement each other well, with the former having ideal temporal sampling but at a single point, and the latter a mixed temporal and spatial sampling on a quasi-global basis. Altimeter data obtained from the area of ocean near to a sea-level station usually agree well with those from the tide gauge for the timescales of sea-level variability it is reasonable to compare them over (i.e. several days and longer). This is particularly true for mid-ocean islands, although lower correlation might be expected for some islands in particular frequency bands [6]. However, agreement can be good or bad along continental coastlines, depending on whether local variability in coastal sea level exists, associated with processes such as coastally trapped circulation, western boundary currents and their eddy regimes, or river runoff [7].

10.3 Mesoscale variability in sea level

The ocean circulation is a turbulent system. ‘Mesoscale variability’ is the name given to the variations in sea level on timescales of 10–100 days and space scales of 50–500 km associated with isolated eddies, meanders of ocean currents and instabilities of frontal systems [8]. Mesoscale variability occurs throughout the ocean. However, until the advent of satellite altimetry, this important component of sea-level variability was largely under-appreciated. The fact that most tide gauges are located on continental coastlines, rather than in the path of the major ocean currents, together with the fact that dynamics prevents simple propagation of eddies to the coast, meant that the mesoscale sea-level variability was largely unreported in tide gauge data, apart from that obtained from particular ocean islands [9].

[Figure 10.2a](#) shows a map of the standard deviation of sea surface height obtained from almost a year of data from four altimeter satellites operating simultaneously [10]. (Similar information was obtained from only 25 days of the first Seasat altimetry in 1978 [11]). The areas of intense mesoscale variability such as the Antarctic Circumpolar Current and the major western boundary currents (Gulf Stream, Kuroshio and

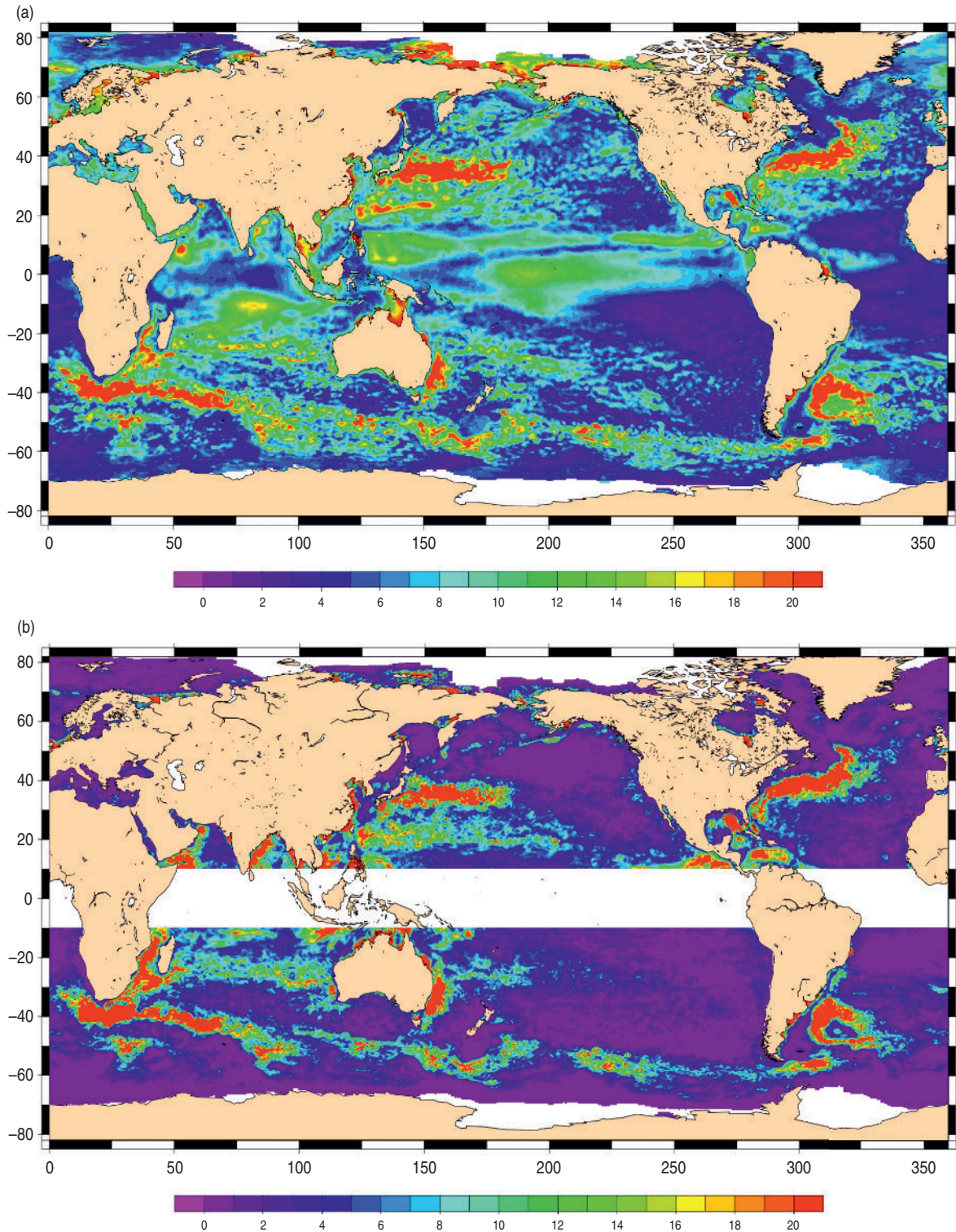


Figure 10.2 (a) Standard deviation of sea surface height variability in the ocean mesoscale obtained from four altimeters (TOPEX/Poseidon, Jason-1, ERS-2/Envisat and Geosat Follow On) operating simultaneously [10]. Units cm. (b) Eddy kinetic energy from the same data set. Units cm^2/s^2 .

Brazil–Malvinas Confluence Region) are clearly identified by having standard deviation higher than 0.2 m.

Oceanographers often prefer to consider an alternative parameter called eddy kinetic energy (EKE), which represents the variance (energy) in the meso-scale, which is constructed as follows [12]. Consider anomalies of sea-level gradient at each point along the ground track of the altimeter (where ‘anomaly’ means with respect to the time mean): these anomalous gradients correspond to anomalous currents across-track according to:

$$\Delta v_y = \frac{g}{f} \frac{\partial \zeta}{\partial x} \quad (10.1)$$

where Δv_y is the anomalous across-track current, $\frac{\partial \zeta}{\partial x}$ is the anomalous along-track gradient in sea level, f is the Coriolis parameter and g is acceleration due to gravity. The EKE is then the variance of this parameter (usually computed assuming an isotropic distribution of energy). Figure 10.2b shows a map of EKE, with maximum values concentrated in the vicinity of the major ocean currents [10]. EKE varies seasonally and from year to year, particularly in equatorial regions [8, 13]. In parts of the ocean, it can be related to the intensity of the wind forcing responsible for the variability in ocean currents [14].

Mesoscale variability is of great interest in its own right in studies of the ocean circulation but, in the context of this chapter, its existence has to be recognised as a strong component of sea surface height variability that is averaged in the computation of any altimetric ‘mean’ values.

10.4 The seasonal cycle of MSL

The seasonal cycle of sea level is an obvious feature in all MSL records and has been studied for many years [15]. At some locations it can have an amplitude comparable to that of the tide. The reasons for seasonal variations are different between low and high latitudes, between shallow waters and the deep ocean, and in many cases can depend on very local factors. Nevertheless, there are several well-understood reasons for such variations. These include air pressure changes and winds both in shallow water areas and in the deep ocean, local surface heating density effects, and advected density changes due to the seasonality of the ocean circulation. Glaciological and hydrological contributions to the cycle will also be present, including seasonal melting of ice at high latitudes and run-off from gauges located near to large rivers. Wave set-up in

small harbours may also contribute to the observed seasonal cycle, as may even a variety of instrumental effects, depending on tide gauge technology.

While the seasonal cycle in MSL is primarily forced by oceanographic and meteorological processes, the cycle also contains small annual and semi-annual astronomical tidal contributions (S_a and S_{sa}) which are two of the long period tides. If one assumes that these tides have their Equilibrium form (see discussion below under Nodal Tide) then Equation 3.12 shows that they have their maximum amplitudes at the poles, where the latitude term is unity. The varying distance to the Sun over a year, R_s , produces the annual harmonic, while the semi-annual component stems from the $(\frac{3}{2} \sin^2 d_s - \frac{1}{2})$ term as solar declination d_s varies between $23^\circ 27'$ north and south of the equator. The term $(\frac{3}{2} \sin^2 \phi - \frac{1}{2})$ is common to all long period tides and results in zero amplitude at a latitude ϕ of $35^\circ 16'$ N/S. During the annual cycle, the value of R_s varies by ± 1.7 per cent of its mean value. At present the nearest approach of the Earth to the Sun, called perihelion, occurs early in January. Amplitudes for S_a and S_{sa} in mm are:

$$H_{Sa} = -3.1 \left(\frac{3}{2} \sin^2 \phi - \frac{1}{2} \right) \cos(h - p') \quad (10.2a)$$

and

$$H_{Ssa} = -19.5 \left(\frac{3}{2} \sin^2 \phi - \frac{1}{2} \right) \cos(2h) \quad (10.2b)$$

where h is the mean longitude of the Sun, which increases by 0.0411° per mean solar hour and which is zero at the equinox on 21 March and $\pi/2$ on 21 June; p' is the mean longitude of the solar perigee, which changes over a cycle of 21,000 years and has a present value (year 2000) of 283° . Even these small amplitudes must be reduced to allow for the elastic response of the solid Earth to the tidal forces, and for the gravitational attraction of the tidal bulge on itself. This is done by multiplying the above values by a ‘diminishing factor’ of 0.69, which is a combination of geophysical ‘Love numbers’ (Section 5.7), giving final amplitudes of 1.1 and 6.7 mm for the gravitational S_a and S_{sa} components at the equator.

The observed annual and semi-annual variations in MSL are very different, and generally much larger, than their astronomical components due to the influence of the many seasonal climatic forcings. The PSMSL data set shows the distribution of the seasonal cycle of MSL around the world [16]. For each site, average MSL was determined for each month of the year, using stations with at least three complete years of data. The resulting

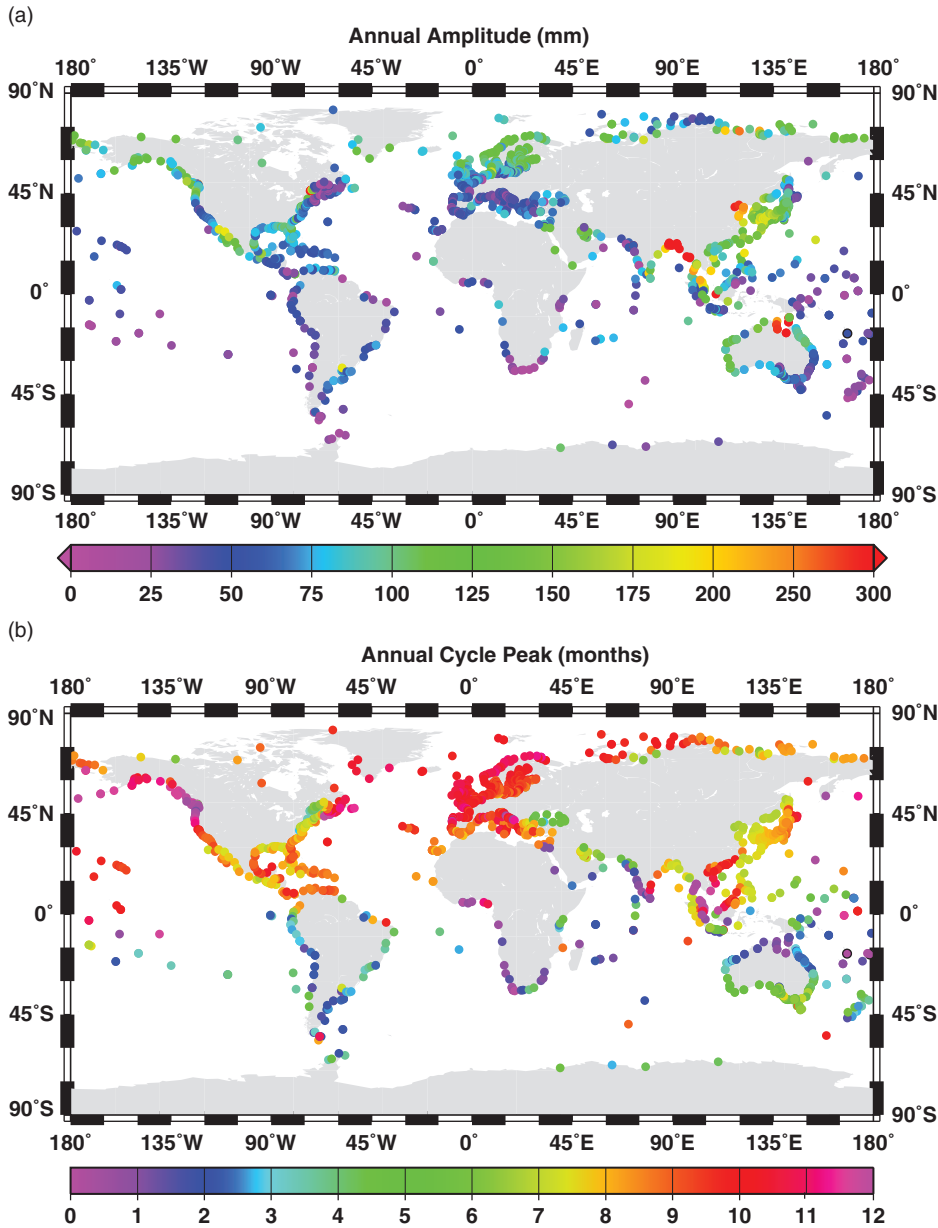


Figure 10.3 (a) Amplitude and (b) peak month of the annual cycle of MSL from tide gauges having at least three complete years of data. Data from the PSMSL. Updated from [16].

12-monthly values were then subjected to a simple harmonic analysis to obtain the amplitude and phase (peak month) of the observed annual and semi-annual components of the cycle. Parameters for the annual component are shown in Figure 10.3 and some general observations are made below; more detailed regional and local descriptions of seasonal variability may be found in the literature [16, 17].

The annual amplitude can reach several decimetres near to river outflows (Figure 10.3a). Examples include the Bay of Bengal where the amplitude can exceed 1000 mm in the Ganges Delta, the Gulf of Bohai, where the Yellow River outflows, the St Lawrence River in Canada, and along the Uruguay and La Plata rivers in South America [16]. Amplitudes at most other locations are less than 150 mm with the southern

hemisphere tending to have lower values than in the north, especially in the south of South America, in South Africa, southern Australia and southern New Zealand. Major variations are observed in Australia with larger amplitudes in the west to northeast parts, with the western-most amplitudes possibly affected by the Leeuwin current. Amplitudes in Europe are small around Portugal and in the Mediterranean and increase northwards to Scandinavia. By contrast, the American side of the North Atlantic has slightly larger amplitudes in the Gulf of Mexico and along the south-east Atlantic coast which reduce moving northwards. Larger annual amplitudes (over 80 mm) are obtained for stations inside the Chesapeake and Delaware Bays than for neighbouring stations on the open coast. The Pacific American coast contains a set of higher amplitudes in the Gulf of California, values around 50 mm along the Californian coast itself, then increasing amplitudes at higher latitude towards Alaska owing to the enhanced meteorological forcing. Large values are observed in the south of Japan and reduce moving north. Amplitudes on the western side of Korea are twice those on the eastern side. The island stations in the Pacific and other ocean basins give, in general, small annual amplitudes (≤ 75 mm).

The autumn–spring difference in annual phase between the two hemispheres is particularly evident (Figure 10.3b). A large difference can be observed between stations near rivers and those along the coast. Particularly striking is the Black Sea difference from the Mediterranean and European Atlantic stations. The annual phase on the northern European Atlantic coast is approximately constant as far south as 45° N peaking in mid-November, while the annual cycle in the Baltic has approximately the same amplitude as for neighbouring stations on the Atlantic coast but the phase is one month earlier. A smooth variation of phase can be noted around Australia and along the coastlines of North America. Different annual phases are observed between the west and east coasts of the Malayan peninsula and those of India, while opposite annual phase is obtained for stations at the north and south ends of the west coast of the Indonesian islands.

The semi-annual amplitude is in general much smaller than the annual. Most open-ocean island stations exhibit values less than 20 mm. In areas of very large annual variation, the semi-annual amplitude also becomes large, and one concludes that one is really observing a harmonic of the annual cycle rather than a semi-annual term *per se*. Stations with large

amplitudes are in the Gulf of Mexico, the southeast United States, Venezuela, the Pacific coasts of Colombia and Panama, the Baltic Sea, the Black Sea, northern Red Sea (Suez), equatorial West Africa, eastern India, Indonesia, southern China and northern Australia.

The seasonal cycle observed in any one tide gauge record can differ considerably from year to year, and at some locations there can be said to be no stable cycle at all [18]. Most studies require several years of data before computing a ‘mean seasonal cycle’ [16]. Although there is evidence that the cycle can be affected by the large-scale climate processes discussed below [19, 20], there is practical value in having some idea of the mean seasonal cycle, to include it in tidal predictions for future years.

Satellite altimetry has enabled the seasonal cycle to be mapped across most of the world ocean (Figure 10.4). The cycle in inverse barometer (IB)-corrected information is shown, rather than observed sea level from the tide gauges in Figure 10.3. Annual amplitudes (Figure 10.4a) are mostly less than 10 cm with the largest in western boundary currents and narrow zonally elongated bands in the tropical Pacific between 5–15° N. In the tropical Indian Ocean, high amplitudes are found near the Cocos Islands and in the Arabian Sea associated with the annual cycle of the Monsoon. Elevated amplitudes can also be found in shallow semi-enclosed seas and coastal regions. Moderate values (3–6 cm) can be found in mid-latitudes in the North Atlantic and Pacific and in the Mediterranean. Most of the Southern Ocean south of 45° has a weak annual signal (<2 cm). The phases show the reversal of seasons between northern and southern hemispheres, and within each hemisphere phases are essentially the same (Figure 10.4b). From space gravity data (Chapter 9) and ocean models, we know that part of the annual cycle comes from an exchange of water between the ocean and the cryosphere and hydrosphere equivalent to about 1 cm of sea level with peak mass in the ocean in late September [21].

Altimetry can be used in combination with tide gauges to study how well the latter, which are necessarily located at the coast, measure the open ocean seasonal variability. Annual amplitudes measured by tide gauges have been shown to be comparable to, but larger than, those in the nearby shallow ocean (<200 m depth), and the cycle in shallow areas is in most locations enhanced relative to the open ocean, apart from areas with strong western boundary currents offshore [22].

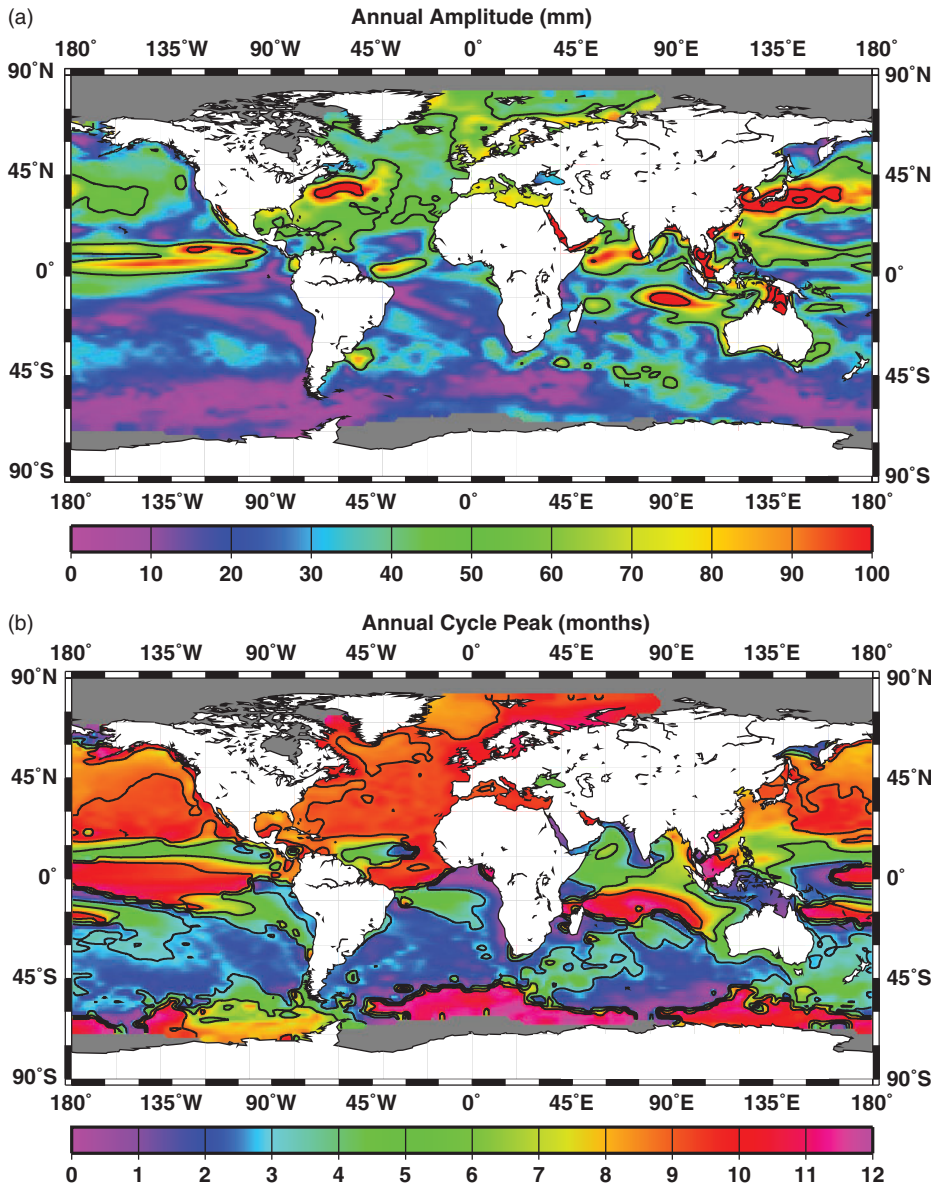


Figure 10.4 (a) Amplitude of the annual cycle of IB-corrected sea level obtained from 15 years (1993–2007) of altimetry. Contours every 50 mm. (b) Phase of the annual cycle indicating the month at which the cycle peaks. Contours every 3 months. Computed from the merged sea-level anomalies of multiple missions from www.aviso.oceanobs.com.

Substantial differences are found near to river outflows and where strong narrow coastal currents occur. Differences of 1–2 months in annual phases for coastal, shallow and deep ocean are found at many places.

Altimetry and tide gauge data can also be combined in ocean models to study the seasonal cycle in even greater detail [23]. An advantage of models is their ability to diagnose the contributions to the annual cycle from changes in density due to temperature and

salinity variations and mass redistribution, and thereby make progress in understanding as well as observing the seasonal cycle [23].

10.5 Pole tide

The angular displacements of the Earth's axis of rotation around its mean geographic pole can be described to good approximation in terms of components with

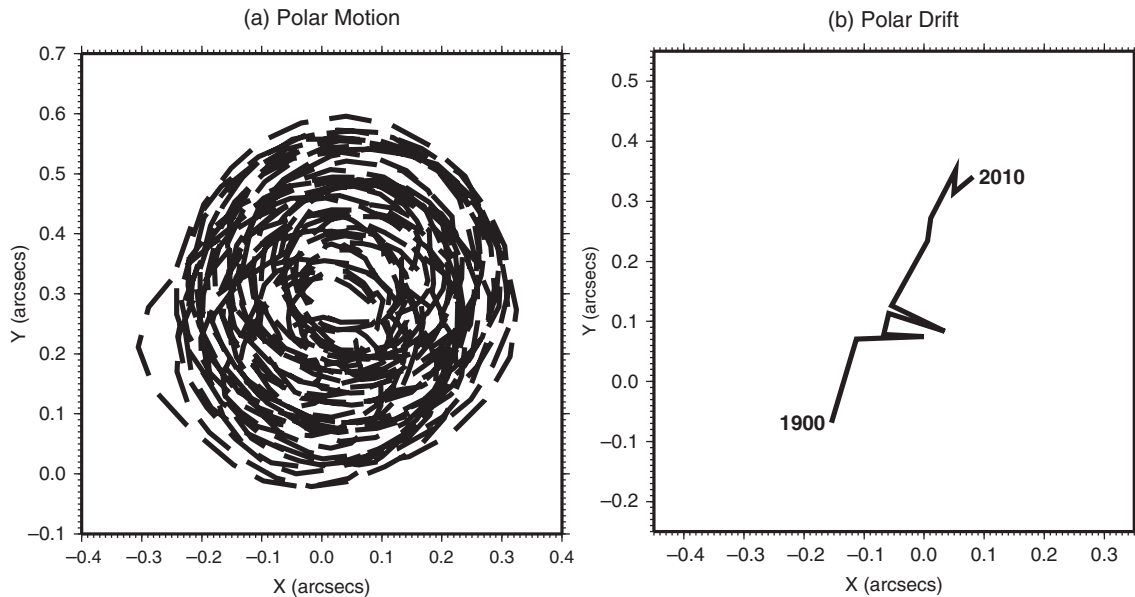


Figure 10.5 (a) Polar motion between 1962 and 2012. The X axis points towards Greenwich and the Y axis towards 90° W. (b) Polar drift demonstrated by the annual mean values of X and Y plotted every 10 years between 1900 and 2010. Data from the International Earth Rotation and Reference Systems Service (www.iers.org).

periods of 14 and 12 months. This polar motion is a consequence of the rotational axis not coinciding with the principal axis of the Earth's ellipsoid (Chapter 9). The 14-month (435 days) component is the larger, with an amplitude that can reach 0.3'' (10 m), and is called the Chandler Wobble (Figure 10.5a) [24]. The mean poles are not fixed either, with the mean north pole moving slowly at 0.3 arcseconds (10 m) per century in the direction of eastern Canada; this is called polar drift (Figure 10.5b).

The centrifugal potential of the Earth can be written as $V = \frac{1}{2} \omega^2 a^2 \sin^2 \theta$, where ω is rotational velocity, a is the radius of the Earth, and θ is colatitude. The wobble corresponds to a small change in θ , $d\theta$, which produces a small change in V of $dV = \frac{1}{2} \omega^2 a^2 \sin 2\theta d\theta$ [25]. As a consequence, the 14-month *pole tide* is generated in the ocean with a maximum at 45° latitude. A corresponding pole tide is also observed in the solid Earth.

At this long period there is little horizontal motion in the ocean associated with the tide, and it is expected that its amplitude should be close to its Equilibrium value of approximately $5 \sin 2f|m| 10^6$ mm where $|m|$ is the angle of polar displacement in radians (see Equation 6.4.9 of [24]). This latitudinal dependence differs from those of the Equilibrium long period tides due to the Moon and Sun (i.e. the astronomical

components of S_a and S_{sa} discussed above or the nodal tide discussed below). Instead, the pole tide has the same dependence as the Equilibrium diurnal tides (Equation 3.12).

The amplitude is of the order of 5 mm at 45° N/S, which is observable in MSL records that do not contain significant additional variability around the same frequency (Figure 10.6). Analysis of the pole tide signal in the complete set of PSMSL records confirmed that the response over most of the ocean must indeed be near Equilibrium [26]. In addition, analysis of almost 9 years of sea surface height information from TOPEX/Poseidon satellite altimetry demonstrated consistency with the theoretical 'self-consistent' form of the geocentric (ocean plus solid Earth) pole tide [27]. (The 'self-consistent' form is mentioned further below.)

For many years, much larger signals with a period around 14 months, several time larger than the Equilibrium pole tide value, have been observed in the North and Baltic Seas and have been interpreted in various ways, including basin resonance at the pole tide frequency [28]. This possibility was largely discounted by two studies [29, 30] that made use of numerical tide and surge models driven by air pressure and wind field data sets spanning several decades. The conclusion was that the observed 'anomalous pole tide'

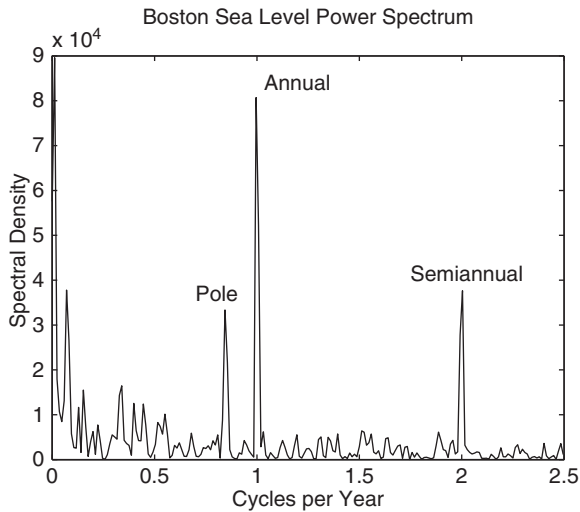


Figure 10.6 Spectrum of sea-level variability at Boston, United States, comparing the pole tide component in the record with the annual and semi-annual components (arbitrary units of power). Boston's latitude of 42.4° N is near to 45° where maximum pole tide amplitude would be expected if the ocean has an Equilibrium response to the Chandler Wobble.

was entirely due to wind forcing, without a need for local resonance.

However, this conclusion raises 'an even more difficult problem than the one it solves' [31] as the issue then is how to explain the existence of the 14-month periodicity in the regional wind field. It has been speculated [32] that the regional winds, as part of the North Atlantic Oscillation system, contain periodicities that just happen to match those of the pole tide, but no further research has been done on this topic in recent years. The history of tidal research by Cartwright [33] contains interesting sections on this topic.

10.6 Nodal tide

The nodal tide is an astronomical tide with a period of 18.61 years. There are few low-frequency lines in the spectrum of the tidal potential (Figure 4.1) between the annual and nodal terms; these consist primarily of low amplitude harmonics of the nodal term and lunar perigeon terms [34]. Similarly, there are no lines lower in frequency than the nodal one if one neglects consideration of variations in solar perigee (perihelion) which take place over a cycle of 21,000 years.

The nodal tide, as a long period astronomical tide, is discussed in Chapter 3. However, it is important to mention it here also, so as to have an appreciation of its

amplitude and spatial distribution and its contribution to MSL records. If the nodal tide were to be large in amplitude, then its signal in either tide gauge or altimeter data could be misinterpreted as significant ocean decadal variability, or even secular trend and acceleration in shorter records [35].

There is a long-standing belief that as the period of a long period tide increases, then its spatial dependence should become more like that expected from the Equilibrium Tide. Proudman [36] argued on general principles that:

- (i) the constituent whose period is nearly 19 years will certainly follow the Equilibrium law;
- (ii) the semi-annual and annual constituents will probably follow the Equilibrium law;
- (iii) the fortnightly and monthly constituents will probably not follow the Equilibrium law.

By 'following the Equilibrium law', Proudman meant a long period tide with an amplitude simply proportional to $(\frac{3}{2} \sin^2 \phi - \frac{1}{2})$, and so maximum amplitude at the poles, zero at $35^\circ 16' \text{ N/S}$, out-of-phase between poles and equator and with no zonal dependence. If the nodal tide conformed to classical Equilibrium expectations then its amplitude in mm would be $0.69 \times 17.6(\frac{3}{2} \sin^2 \phi - \frac{1}{2})$ and the 18.61-year cycle would peak at the equator in the years $1922.7 \pm n \times 18.61$ (and be a minimum at the poles at the time) [34, 37]. The amplitude is similar to that of the semi-annual astronomical tide S_{sa} . The amplitude given here is multiplied by a solid Earth elastic response factor (diminishing factor or combination of Love Numbers) of $(1 + k - h)$ or approximately 0.69 to account for the change in potential and elastic response of the solid Earth (Section 5.7).

However, loading and self-attraction and mass conservation will modify the simple spatial dependence of any long period tide that would otherwise 'follow the Equilibrium law' [38]. These two factors combine to provide the 'self consistent Equilibrium Tide' distribution of Figure 10.7, from which the nodal tide distribution may be obtained by multiplying throughout by 0.44 [39]. It is this distribution that is more suitable for 'correcting' MSL records rather than the classical Equilibrium form, which underestimates the nodal signal at higher altitudes by about 25 per cent because of the loading term, although in tropical areas the self-consistent response is within 5–10 per cent of the classical calculation.

Attempts to extract nodal tide signals from individual MSL records have had limited success, owing to

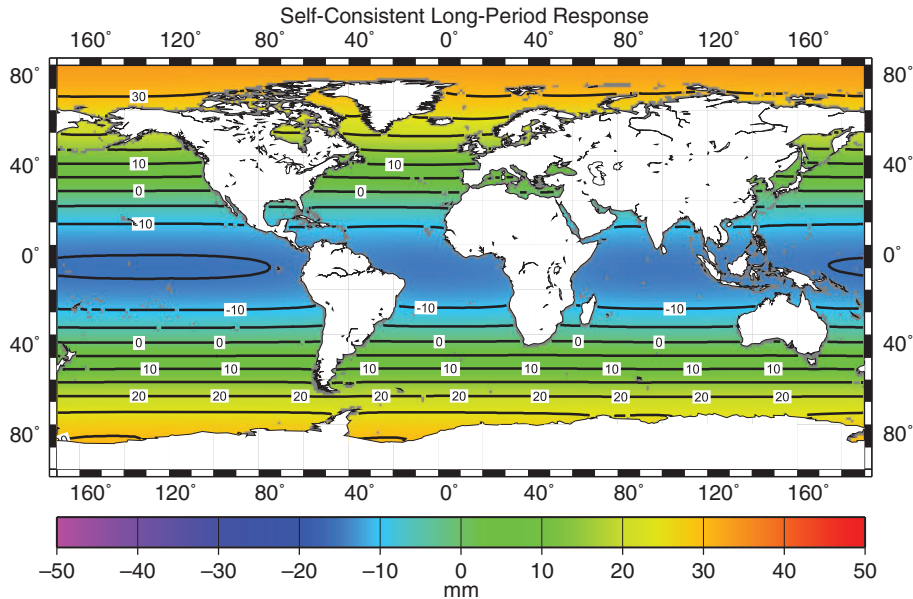


Figure 10.7 The spatial dependence of the generic self-consistent Equilibrium long period tide following Reference 38. Nominal units of mm. From [39].

their small amplitude compared to those of other ocean processes at similar period [40]. The one study that has any plausibility for identifying a nodal signal employed a global ‘stack’ of records (as in seismic research) rather than individual ones, concluding that the aggregate nodal signal was consistent with Equilibrium expectations [26]. The question of whether the nodal tide in MSL departs from its classical or self-consistent form remains.

It is important not to confuse this long period tide in MSL with nodal variations in other mean quantities such as MHW, MLW or Mean Tidal Range, which arise from 18.61-year variations in the main diurnal and semidiurnal components of the ocean tide (Section 3.4.5). Such variations have been suggested as contributing to nodal variations in shallow water temperatures via modulations in tidal currents and mixing [41]. In addition, nodal variations in MHW play an important role in some coastal processes (Section 11.7).

10.7 Air pressure-related sea-level variability

Chapter 7 has explained how sea level responds to wind stress and air pressure forcing on timescales of hours and days, leading to the development of storm

surges in shallow waters. Such a response depends on the dynamics (physical laws) encapsulated in Equations 7.4 which describe a system that is continuously evolving rather than in equilibrium. However, when wind and air pressure changes occur over longer timescales, the ocean has time to move and for sea level to adjust to the applied forces.

The relative importance of air pressure and winds in sea-level variability depends on location (e.g. latitude) and timescale [42]. The role of air pressure is the more simple to demonstrate. Over timescales of several days or longer (the timescale will depend on the location), the sea surface will rise (fall) in response to a drop (increase) in local air pressure by approximately $\frac{\Delta P_A}{\rho g}$ where P_A is air pressure, ρ is water density and g is the acceleration due to gravity. This expression corresponds to 1 cm/mbar to within about half a per cent. This process is called the local inverse barometer (LIB) and, in this *isostatic* adjustment of the sea surface, the consequence is no change in *sub-surface pressure* (pressure that would be measured by a sensor at a level in the ocean just below low tide) or *bottom pressure* (pressure measured by a sensor located on the seabed) (see also Chapter 7).

The LIB was first observed in the Baltic Sea in the eighteenth century by the Swede Nils Gissler [43, 44]. The British polar explorer James Clark Ross is

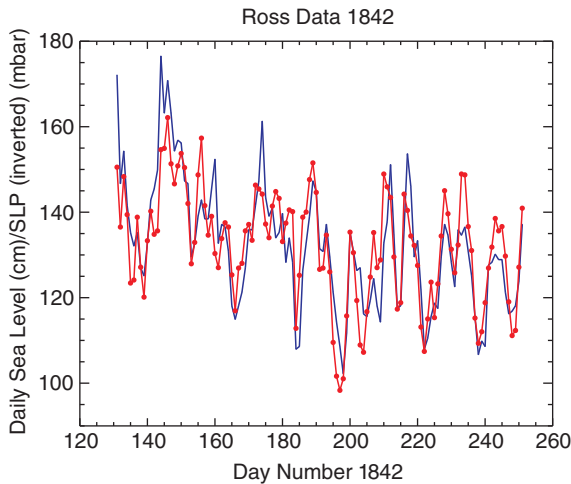


Figure 10.8 Daily values of mean tide level (MTL) measured in 1842 at Port Louis, Falkland Islands, by James Clark Ross (blue) together with his daily values of air pressure (red). Air pressure values are shown inverted and their average adjusted to equal that in MTL. The MTL daily values are defined as the average of the average of high waters and average of low waters recorded each day. From [135].

sometimes credited as the first to record the effect at Port Leopold in Canada in 1848–9 [45], although it had been observed in the United Kingdom many years before at Liverpool [46] and was even recorded by Ross himself at Port Louis in the Falkland Islands in 1842 (Figure 10.8). The LIB model works well for most parts of the ocean, less so in the tropics where the amplitude of air pressure variability is low, where the role of winds is more important and where baroclinic processes dominate the sea-level spectrum. Outside of the tropics the observed response is typically 90–95 per cent of the LIB [47] owing to the effect of Ekman pumping (see Chapter 7) [48].

It is often difficult to assess the quality of a historical sea-level record. However, if air pressure data are also available, and if we know from more recent data that the LIB model works well at that location, then the two records can be compared to see how well they are correlated. That provides confidence in the quality of both records. An example is provided by the daily sea-level and air pressure data in Figure 10.8. An even earlier example concerns one of the first sea-level records, that of monthly mean high water (MHW) for 1768–93 from Liverpool [49]. The availability of air pressure information from the port enabled a regression analysis between the two parameters, yielding a coefficient of -0.897 ± 0.074 cm/mbar, consistent with knowledge of monthly sea-level variability on the

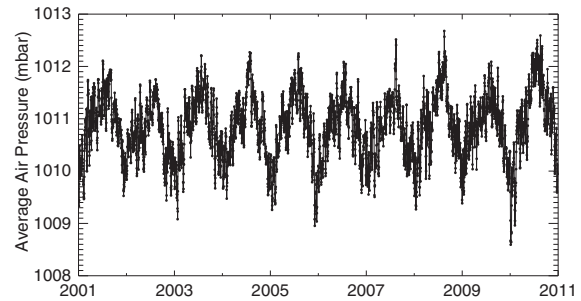


Figure 10.9 Daily average air pressure over the global ocean using National Centers for Environmental Prediction (NCEP) daily grids from <http://www.cdc.noaa.gov/data/gridded/data.ncep.reanalysis.surface.html>.

west coast of England, and thereby validating both time series.

Oceanographers usually refer to the inverse barometer (IB) model in their research rather than the LIB. The IB model is similar to the LIB but with an additional term that accounts for the average air pressure over the global ocean, i.e. ΔP_A is replaced by $\Delta P_A - \Delta P_A^{av}$. Global ocean average air pressure ΔP_A^{av} has a root-mean-square variation of approximately 0.6 mbar and contains a large annual component that peaks in July–August [50, 51](Figure 10.9).

However, air pressure changes are not the only meteorological forcing responsible for sea-level variability. Winds blowing over the shallow waters of continental shelves result in wind set-up (or ‘surge’) as described in Chapter 7, which can be an important signal in MSL records even at timescales of weeks or months. Winds also play a major role in driving the large-scale ocean circulation that contains sea-level variability on short (e.g. eddies) and long (climate change related) space and time scales.

MSL researchers tend to account for meteorological effects in their tide gauge records in two ways. The first method adopts an empirical approach and parameterises a record in a form such as:

$$\text{MSL}(t) = at + b(\Delta P_A - \Delta P_A^{av}) + c\tau_x + d\tau_y + \varepsilon(t) \quad (10.3)$$

where t is time, τ_x and τ_y are local wind stress in the long- and cross-shore directions, a , b , c and d are parameters determined by linear regression, and $\varepsilon(t)$ represents the residuals to the regression fit [52]. The at term accounts for secular trends due to long-term changes in the ocean and to vertical land movement of the land upon which the tide gauge is located, while the

terms involving b, c and d parameterise the meteorological effects on MSL. Often a choice is made to work with the mean seasonal cycle removed from each quantity, so that the regression parameters are more representative of a spectrum of variability rather than simply of the sometimes dominant seasonal cycle.

Many variations of such regression fits can be found in the literature, involving the use of both local and distant wind and wind stress, wind stress curl (a measure of the angular momentum of the wind field which relates to the ‘spinning up’ of the ocean circulation), air temperature (which is frequently correlated with wind direction), sea surface temperature (associated with heat content) and rainfall (related to river flow).

A second method of accounting for meteorology in MSL records is provided by regional or global barotropic (‘two-dimensional’ or ‘depth-averaged’) ocean numerical models, similar to those used for operational storm surge prediction. The models require long time series of high spatial resolution air pressure and wind information, and detailed maps of ocean bathymetry, so as to provide time series of MSL throughout the model grid, including at the grid points near to tide gauge locations. In this way, time series of model MSL can be used to simulate the contribution of air pressures and winds to the MSL record from the tide gauge [53, 54].

While the first method remains an important tool for understanding relationships between parameters, the second method tends to be more powerful as it takes into account both local and distant meteorological forcings in a rigorous way, as well as providing information on the spatial scales of variability. Whichever method is used, once the contributions from air pressure, winds and other factors are accounted for, an analysis can progress to studying the residuals of the regression fit, which may contain interesting information on other ocean processes.

10.8 Large-scale patterns of interannual variability

Examination of global data sets of any of the main climate parameters (air and sea temperatures, air pressure, sea level etc.) demonstrates the importance of the major modes of variability of the climate system. Each of these modes is the subject of an enormous amount of research for which reviews are available [55]. We shall refer briefly to connections between some of these main climate modes and sea level.

In what might be called ‘normal’ years in the Pacific, the Walker circulation in the atmosphere produces easterly trade winds that result in warm water being moved to the ‘warm pool’ in the west of the ocean. This raises the sea surface topography in the western tropical Pacific by several decimeters. Winds also associated with the circulation result in upwelling off the coasts of Peru and Ecuador and thereby an increase in fishing productivity. In this situation, the Southern Oscillation Index (SOI), measured in terms of air pressure difference between Tahiti and Darwin, is positive. During El Niño–Southern Oscillation (ENSO) events, which occur approximately every 3–7 years, the SOI is negative and the trade winds relax. Equatorial Kelvin waves transfer water from the ‘warm pool’ to the eastern side of the basin (Figure 1.8e). In addition, they deepen the thermocline (the depth of warm surface waters) in the eastern part of the ocean [56]. The changes in ocean and meteorological conditions result in modified regional ocean currents and dampen upwelling along the coast, with a negative impact on fish catches. At the eastern boundary, the equatorial waves are converted into coastally trapped poleward-propagating Kelvin waves, which can be observed clearly along the entire American Pacific coastline (Figure 10.10) [57]. The ENSO event is then followed by ‘La Niña’ conditions during which the Pacific recovers its normal state until the next event.

ENSO-related signals can be found around the globe in modification of weather patterns and ocean circulation. The Pacific Decadal Oscillation (PDO) [58] takes place in the same ocean as ENSO but on much longer timescales (20–30 years) as reflected in sea surface temperatures north of 20° N. The Indian Ocean Dipole [59] is a quasi-periodic oscillation of sea surface temperatures between the western and eastern tropical Indian Ocean which impacts significantly on the regional monsoonal weather. Major IOD events occur less frequently than ENSO ones, but the two phenomena are clearly linked components of the climate system. The North Atlantic Oscillation (NAO) [60] is a measure of the air pressure gradient between the Icelandic low and the Azores high and, therefore, of the strength and direction of westerly winds and storm tracks across the North Atlantic. It is closely related to the Arctic Oscillation (AO) [61], which is characterised by air pressure anomalies of one sign in the Arctic and one of opposite sign centred about 37–45° N. The NAO and AO vary with no particular periodicity and so could be said not to be true

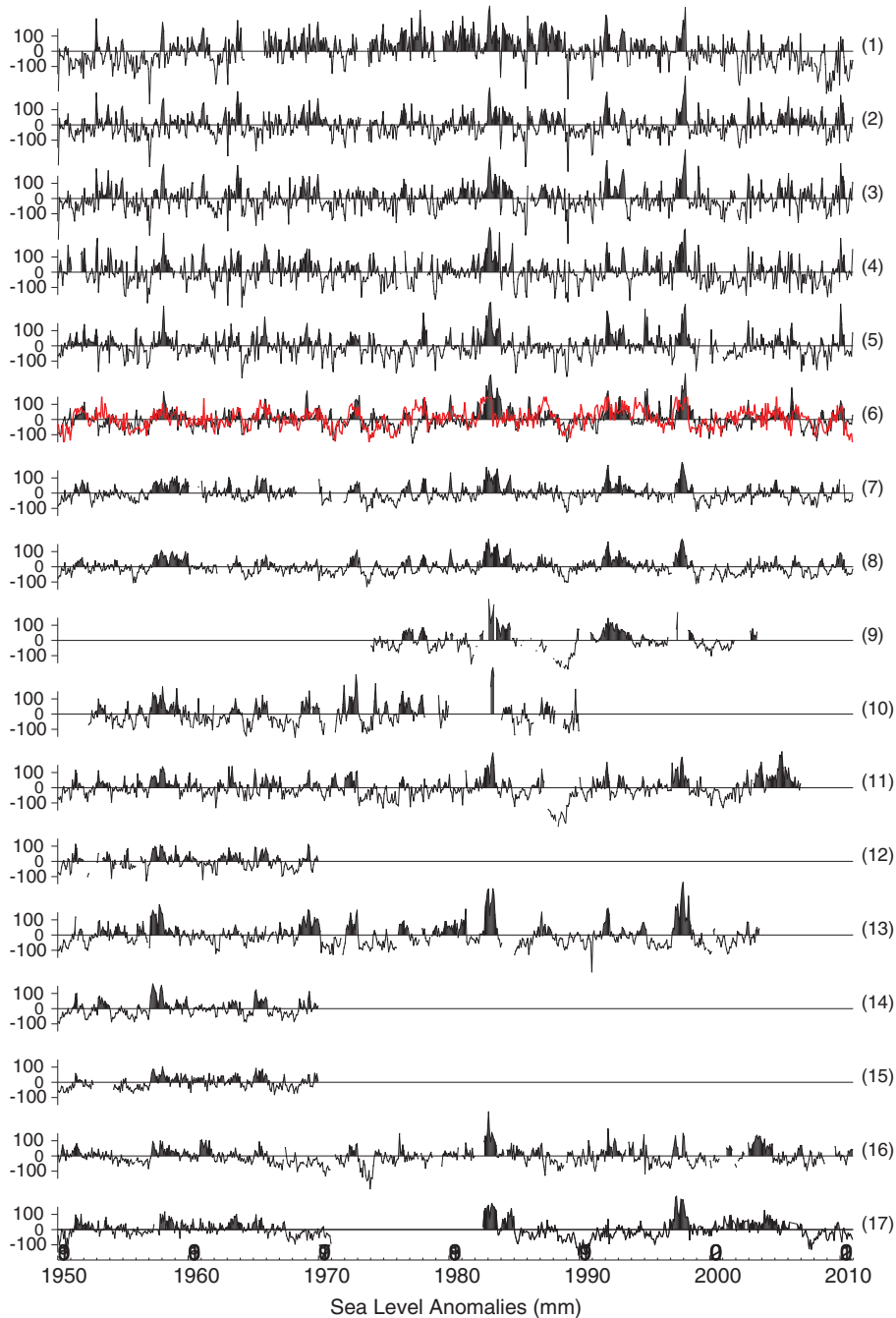


Figure 10.10 Time series of monthly MSL anomalies from north to south along the Pacific coasts of the Americas updating a similar plot in [57]. Positive anomalies are shaded black. Anomalies are defined by the MSL in each record after detrending and removal of the mean seasonal cycle. Stations are (1) Yakutat and (2) Sitka, Alaska, (3) Prince Rupert, Canada, (4) Neah Bay, (5) Crescent City, (6) San Francisco, (7) Port San Luis and (8) San Diego, United States, (9) Cabo San Lucas and (10) Salina Cruz, Mexico, (11) Balboa, Panama, (12) Buenaventura, Colombia, (13) La Libertad, Ecuador, (14) Talara and (15) Matarani, Peru, (16) Antofagasta and (17) Valparaiso, Chile. The red line in (6) is the negative of the SOI scaled to have the same variance as the sea level. Data from the PSMML and Climatic Research Unit, University of East Anglia.

'oscillations'. The NAO is best defined in the winter months when it has large effects on European winters. The NAO and AO can be considered to be components of a Northern Annular Mode (NAM) in the atmospheric circulation.

The Southern Annular Mode (SAM), or Antarctic Oscillation, is an oscillation in sea-level pressure between a node centred over Antarctica and an annulus encircling the Southern Ocean [62, 63] and is a measure of the meridional air pressure gradient in the Southern Ocean, and therefore of the strength of the westerly winds that drive the Antarctic Circumpolar Current (ACC). The ACC is one of the world's major ocean currents, enabling transfers of heat, salt and other properties between the Atlantic, Pacific and Indian Oceans. The Atlantic Multidecadal Oscillation (AMO) [64] takes place on timescales of decades. It is thought to be due to the variability of the Atlantic Meridional Overturning Circulation (AMOC), and is associated with warming of the North Atlantic with especially pronounced warm anomalies in the subtropical North Atlantic (hurricane generation region) and in the northern part of the North Atlantic near the southern tip of Greenland. The PDO and AMO might be related due to teleconnections between ocean basins [65].

The time series of each mode is described, at least to first order, in terms of a simple index based on sea surface temperatures (for ENSO, PDO, IOD and AMO) and/or air pressures (ENSO, NAO, AO, SAM) which can be related to sea-level time series either from altimetry or tide gauges; one can mention examples relating to ENSO (Figure 10.10), IOD [18] (Figure 10.11), NAO [54, 66], SAM [67, 68, 69, 70, 71] (Figure 7.20) and AMO [72]. Time series of extreme sea levels may also be related to indices such as the NAO [73, 74, 75].

Any time series of MSL will contain variability on timescales of more than one year owing to variability on similar timescales in the forcing factors (temperatures, air pressures etc.) whether that variability is associated with the various climate modes or not. Also there will be some low-frequency variability due to dynamical modes of variation in the ocean itself. Whatever the source of this interannual and decadal variability, it means that in a time series analysis any one annual MSL value cannot be considered as independent of the value from the year earlier or later. This feature is known as 'serial correlation' and means that, when calculating a rate of sea-level change from a time series, then a standard error of the rate calculated by an ordinary least-squares procedure that treats each annual mean as independent will be underestimated. This complication in estimating the significance of secular trends in sea level has been discussed many times [76], and is particularly relevant to trends calculated at tropical locations where ENSO and other low-frequency variations are large. Figure 10.12 demonstrates the relative magnitudes of interannual variability and 'underlying trend' by considering the length of record needed to provide a given standard error on the trend in an ocean with the variability spectrum of the existing altimetric data set [77]. For example, in the Chagos area of the Indian Ocean (approximately 7° S, 72° E) a data set of several decades would be required to obtain a standard error of 1 mm/yr (with a further implicit assumption that the spectrum of variability does not change over many decades).

Numerical modelling of the ocean has made great advances in the past two decades. Many models have been constructed by different groups and for different operational and research applications [78, 79]. One example is the Massachusetts Institute of Technology (MIT) general circulation model [80].

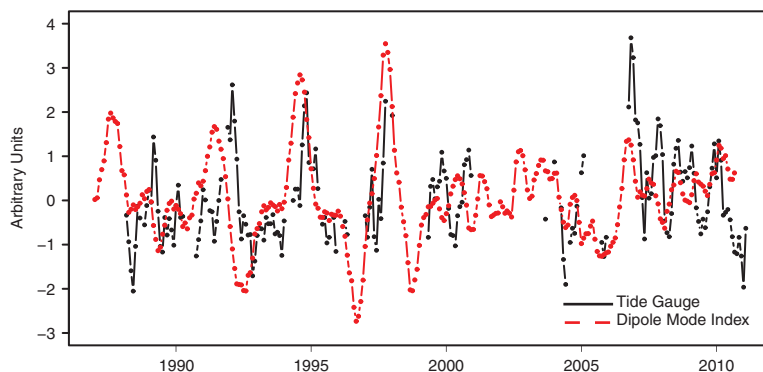


Figure 10.11 Comparison of monthly MSL since 1988 from Diego Garcia, in the Chagos Archipelago in the western tropical Indian Ocean, to the Indian Ocean Dipole (IOD) index. The IOD is a measure of the oscillation between sea surface temperatures in the western and eastern Indian Ocean, with positive IOD corresponding to higher temperatures in the west. The sea-level time series has been scaled to have the same standard deviation as the IOD index. From [18].

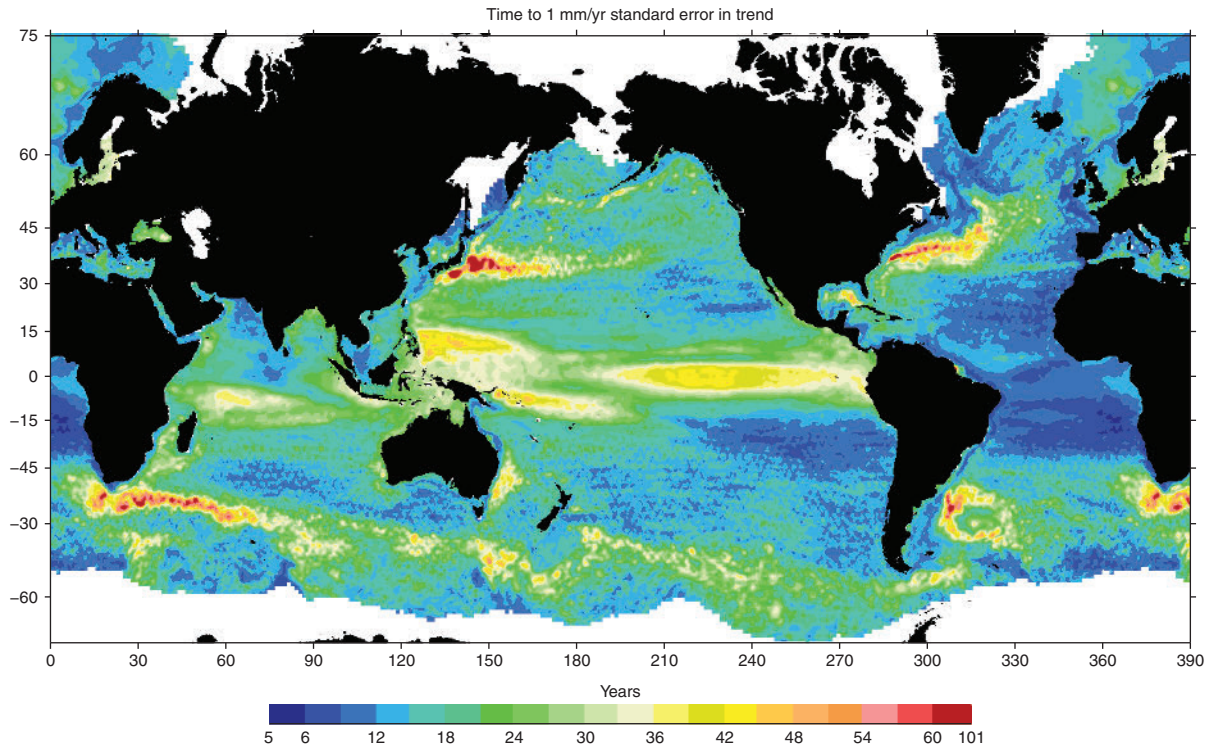


Figure 10.12 The implied length of a sea-level time series that would be necessary for the statistical error in sea-level trend to reduce to 1 mm/yr, based on the analysis of 12 years of altimeter data. From [77].

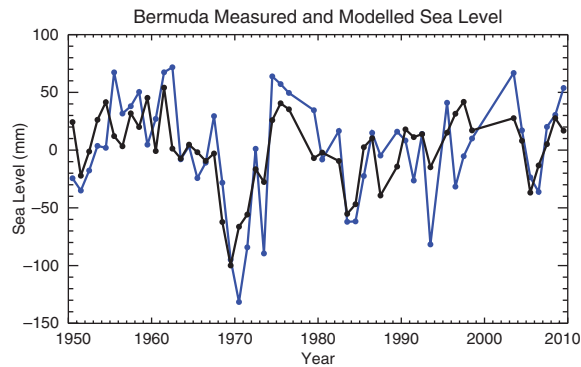


Figure 10.13 Sea level at Bermuda in the centre of the North Atlantic sub-tropical gyre. Data from PSMML (blue) corrected for atmospheric pressure compared to a simulation by the MIT-Liverpool ocean model (black). Both time series have been detrended and have a zero-lag correlation coefficient of 0.71.

This was used in one study [81] with a 1° global grid and 23 vertical levels to describe the ocean, with the ocean circulation forced by twice-daily wind stresses and heat and fresh-water fluxes obtained from a meteorological agency. The model was run for 50

years (1948–97) and the resulting sea levels at many locations around the world compared to PSMML data from tide gauges with some success. A more recent example is from the Liverpool adaptation of the MIT global model, which has $1/5^\circ \times 1/6^\circ$ longitude–latitude resolution in the North Atlantic, and is constrained by hydrographic fields provided by the UK Met Office [82]. Figure 10.13 compares 60 years of model and PSMML sea levels at Bermuda in the centre of the North Atlantic sub-tropical gyre, indicating that the model can account for a large part of inter-annual variability at that location (the sea-level fall around 1970 corresponds to cooler conditions at that time [83]); comparisons at other locations are discussed in References 18 and 84.

However, such an ocean model will not account completely for long-term sea-level change as it does not consider changes in ocean mass due to exchanges between the ocean and cryosphere or terrestrial hydrosphere. Modelling of longer-term changes requires the use of Atmosphere–Ocean General Circulation Models (AOGCMs) [85], intensive use of which is made in IPCC research assessments.

10.9 Long-term changes in sea level

For much of the past two and a half million years, in what geologists call the Pleistocene Epoch, the Earth has experienced extended periods of glaciation, during which the polar ice sheets expanded and sea levels fell, separated by warmer intervals called interglacials with smaller ice sheets and higher sea levels (Figure 10.14) [86]. The interglacial that the Earth is enjoying now corresponds to what geologists call the Holocene Epoch, commencing approximately 12,000 years ago, with a climate that has some similarities to that during the previous interglacial, called the Eemian, about 130,000–114,000 years ago.

Figure 10.14 demonstrates that sea level fluctuated by over 100 m throughout the last half-million years of the Pleistocene with a dominant timescale of

approximately 125,000 years. Sea level was at its lowest in its recent geological history during the Last Glacial Maximum (LGM, 25,000–20,000 years ago). Thereafter, it rose at times at rates of the order of several tens of mm/yr [87] and increased overall by over 130 m (Figure 10.15) [88]. Melting of the great ice sheets was largely complete by 6000 years ago, and various studies have concluded that sea level has risen relatively slowly in the past 3000 years at a rate not exceeding 0.2 mm/yr [89, 90], with fluctuations in this interval not exceeding ± 25 cm on timescales of a few hundred years [91, 92], although these conclusions may not apply regionally [93].

Although detailed discussion of these large fluctuations in sea level in the geological past is beyond the scope of this chapter, it is important to know something

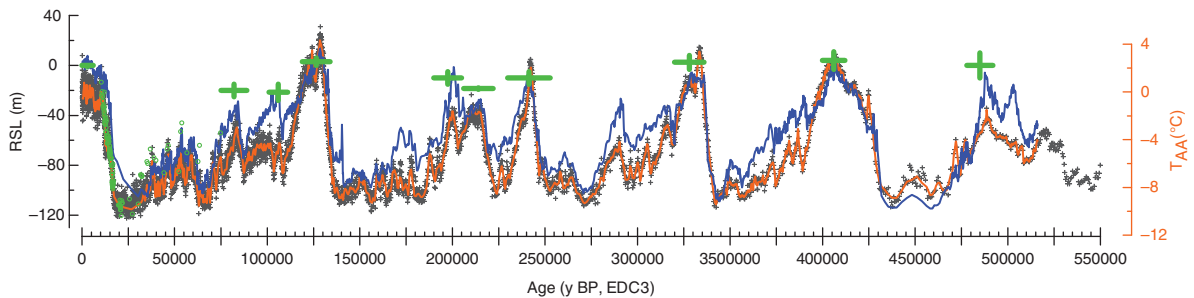


Figure 10.14 Sea-level change (blue) derived from Red Sea cores, demonstrating the association of sea level and temperature anomaly (in this case Antarctic) for the past half-million years (grey dots, with orange line subsampled at the same times as sea level). Green symbols are coral and speleothem-based sea-level markers; EDC3 refers to the dating calibration. From [86].

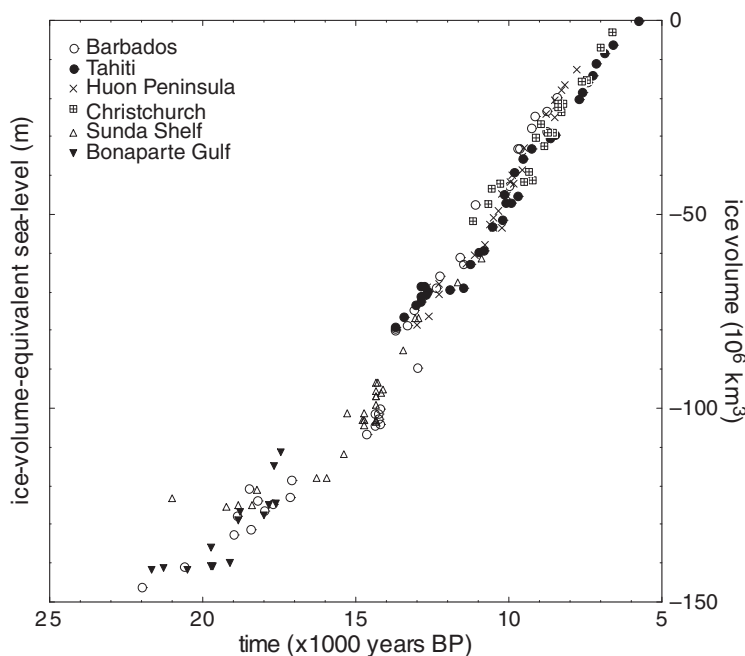


Figure 10.15 Ice-volume equivalent sea-level change during and after the Last Glacial Maximum inferred from coral, sedimentary and palaeontological data. From [88].

of them for two main reasons. One reason is simply to recognise the fact that sea level has always changed throughout the Earth's history, and sometimes at high rates. Therefore, it should not be too great a surprise to learn that it is continuing to change today, albeit at much lower rates. A second reason is that, although much of the ice that existed at the time of LGM has now disappeared, there is a 'memory' of its existence in the ongoing visco-elastic response of the solid Earth to the removal of the major ice loads. This long-term memory means that sea level, measured relative to a land level, will appear to be changing differently at different locations today, even if there were to be no present-day increase in ocean volume (Chapter 11). Therefore, the Earth's glaciological history continues to influence our interpretation of sea-level measurements today.

This brings us to the particular focus of this section, which is concerned with the changes in sea level that have occurred during recent centuries and decades. These changes are often parameterised as linear, quadratic or low-order polynomials of time. It will be seen that these observed 'secular changes', and those anticipated in the next century, are considerably smaller than those of Figure 10.15. Nevertheless, it is important that we understand them as well as possible so as to have some insight into predicting potentially larger changes in the future [91, 94].

All methods of sea-level measurement are of interest but in this chapter we focus on three of them. These methods use salt marsh, tide gauge and space (altimetry and space gravity) data, so providing knowledge of how sea level has changed on typical timescales of several hundred, hundred-tens, and tens of years respectively [95]. The fact that salt marsh records can span several centuries means that they are particularly interesting in providing an idea of the rate of sea-level change before the instrumental era when tide gauge measurements became available. In certain cases, their time series overlap with records from a nearby tide gauge, thereby providing a comparison and validation of data sets. The study of corals, in particular micro-atolls, can also provide information on sea-level change in tropical areas during the past few centuries [88]. Other relevant fields of research include archaeology wherein historical constructions such as Roman and medieval fish ponds, quaysides or wells can be related to both former and present sea levels [96, 97, 98, 99] or can at least provide upper or lower limits on change. Novel ideas, such as study of paintings or early photographs that record historical sea levels can also be useful [100].

10.9.1 Long-term sea-level information from salt marshes

Salt marshes are intertidal areas in which layers of sediments have accreted and now support a wide variety of rushes, sedges and grasses. As an example, Figure 10.16 shows a pristine marsh, at Sanborn Cove in Maine, United States, at high and low tide. If one extracts cores of sediment at different distances from the sea at points spanning the high to the low marsh, then microfossils (foraminifera and diatoms) within different layers of the sediment can be used as indicators of sea-level change. Figure 10.17 provides a schematic description of the method.

Salt marsh records are obtained primarily from mid-latitude locations with some records spanning many hundreds or a thousand years [101, 102, 103]. The temporal resolution of a record depends on the rate of sedimentation in the marsh. For marshes with a high rate, shorter timescale changes can be resolved in the cores, and the records can be compared to information from nearby tide gauges. Figure 10.18 shows that in most cases where data exist there is reasonable similarity between methods.

Different methods have to be used for dating the layers of a core, depending upon where the core was obtained. Methods include radiometric analyses (^{14}C , ^{210}Pb) and stratigraphic marker techniques (e.g. ^{137}Cs , pollen, charcoal, Pb isotopes, metal concentrations). For example, the ^{137}Cs method can be used to detect the time in the mid-1960s when nuclear bomb testing was at its peak. Along some coasts (e.g. those of the southwest Pacific), pollen in the cores can provide markers of times in the eighteenth and nineteenth centuries by indicating changes in vegetation following settlement by Europeans [104, 105, 106, 107]. Many salt marsh records that span the nineteenth and twentieth centuries show a marked inflexion in the late 1800s or the early 1900s, although the exact timing of the inflexion differs between them [108, 109, 110] (Figure 10.18). Such inflexions are, however, qualitatively consistent with the accelerations in sea level observed from tide gauge data over the same period, as discussed further below.

The salt marsh technique is a relatively new source of sea-level information with many complications and requiring considerable experience in interpretation of information from the cores. Where both salt marsh and tide gauge information exist, then overall confidence in findings can be obtained from comparison of data sets. Salt marsh data in those cases can be

(a)



(b)



Figure 10.16 Sanborn Cove salt marsh in eastern Maine, United States, at (a) high tide and (b) low tide. Salt marshes are vegetated tidal flats that are submerged during spring tides, when a thin layer of mud is deposited. Over time, mud and peat build up with rising sea level. The speed of this accumulation can be dated and thus represents a proxy for the rate of sea-level rise. Photographs by Professor Roland Gehrels, University of York.

considered as an extension back in time of the tide gauge information. In addition, the technique can be applied to parts of the world without tide gauge records, notably in the southern hemisphere, thereby extending the geographical coverage of our knowledge of sea level change.

10.9.2 Long-term sea-level information from tide gauges

Measurements of sea level were made at a number of locations in Europe in the eighteenth and nineteenth centuries using ‘tide gauges’, graduated markings on

the stone walls of docks or ‘sluices’ (gated passages between the sea and inland waters) intended to show water depth over an entrance sill. Alternatively, wooden measuring rods called ‘tide-poles’ or ‘tide-staffs’ were used. Tabulated observations were usually of the heights and times of high and low waters, or sometimes high waters alone [25, 44, 111, 112, 113]. The first automatic (or ‘self-registering’) tide gauges were developed in the mid-nineteenth century [114]. These installations have provided the nineteenth-century MSL data to be found in the [PSMSL](#).

[Figure 10.19](#) shows time series of sea level from a small number of sites in northern Europe at which historical measurements were made and where

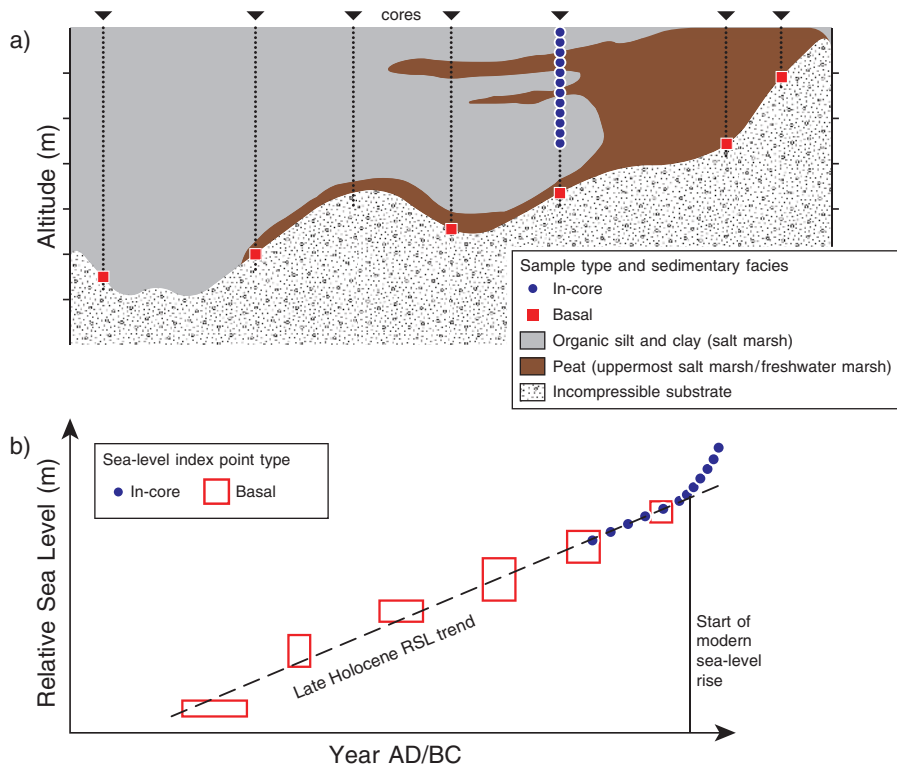


Figure 10.17 Schematic of the salt marsh technique showing stratigraphy and sea-level index points. (a) Dates on basal sediments (squares) provide a long-term (millennial-scale) trend of sea-level change. The most recent record of sea-level change is captured by the upper part of the salt-marsh stratigraphy (dots). (b) Age–altitude graph of sea-level index points. The squares and dots correspond to the basal points and upper salt marsh points in (a). The sizes of the boxes reflect age and altitudinal errors. For the recent record (dots), errors are typically much smaller. Figure from [110] adapted from [102].

recording has continued into modern times [115]. If one applies a simple second-order fit ($a + bt + ct^2$ where t is time) to each time series shown, then quadratic coefficients ‘ c ’ of order 0.005 mm/yr^2 are obtained, all the records shown providing evidence for a long-term acceleration in sea level and suggestive that the twentieth century rise started at around the end of the nineteenth century. There are no records of comparable length elsewhere, but the evidence from a small number of shorter records from North America is consistent with a similar acceleration [115]. These long-term accelerations seen in tide gauge data are similar to those seen in the salt marshes but have less of the character of the inflexion seen in the latter. Nevertheless, the two data types together are suggestive of the nineteenth–twentieth-century acceleration being more global than just European.

More copious data have been available since the nineteenth century and many such records are included in the **PSMSL** data set. They provide the

main evidence that sea level is rising (Figure 10.20). Many authors have attempted to combine individual records into ‘global average’ curves (sometimes called ‘reconstructions’) in spite of the spatial and temporal limitations of the data set evident in Figure 10.1. The simplest method is just to average all the available individual tide gauge records, with each record corrected for vertical land movement using a geodynamic model of Glacial Isostatic Adjustment [116]. That method clearly biases the resulting average time series towards regions with most records (i.e. Europe, North America and Japan). A second approach involves the combining of regional-average time series into a global-average one [117, 118], or of averages in latitude bands into global averages [119]. Inevitably, these methods cannot take into consideration the possible sea-level changes that have occurred either in coastal regions not represented in the **PSMSL** data set, or across the vast areas of the deep ocean.

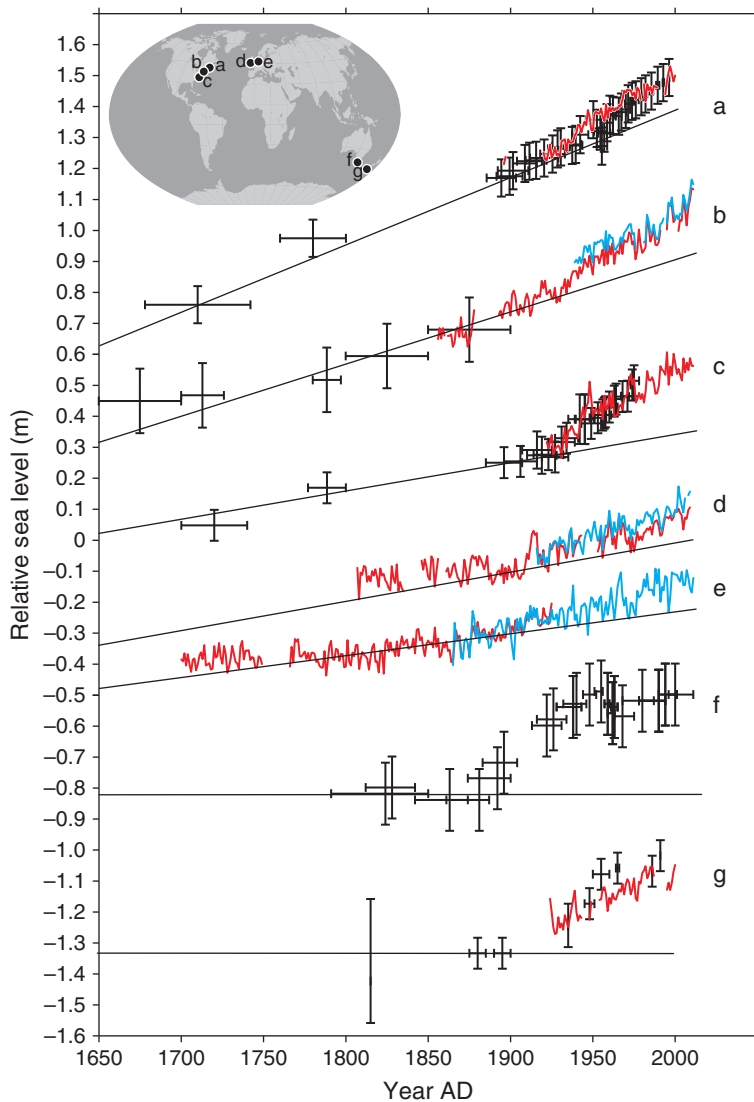


Figure 10.18 Sea-level changes in the last 200–350 years obtained from salt marsh data (black points) at six marshes around the world (inset map). The individual late-Holocene trends in sea level have been superimposed in each case. For comparison, red and blue lines show MSL data from nearby tide gauges. Each salt marsh record has an arbitrary offset for presentation purposes. From [110].

Efforts to at least partly account for sea-level variations in a more spatially representative fashion include the use of low degree and order spherical harmonics to parameterise sea-level changes worldwide [120]; empirical orthogonal functions (EOFs) of known modes of ocean variability since the 1990s since when quasi-global sea-level coverage has been available from satellite altimetry [121, 122]; EOFs based on modes of variability in ocean circulation models with model runs performed over many decades and therefore, in principle, capable of representing lower-frequency sea-level changes more reliably than the EOFs based on altimetry [123]; and cyclo-stationary EOFs to represent

progressive motions in sea-level variations instead of the standing waves of conventional EOFs [124]. Each of these methods has drawbacks that are inevitable when using a sparse data set [122, 125].

Sophisticated ways have also been designed to average individual records in a region, or globally, without consideration of particular modes of variability. These methods include the ‘virtual station’ technique [126] wherein individual records, which may be quite short, are successively combined into regional and global time series, or a neural network technique [127] which connects coastal sea level with the regional and global mean via a non-linear empirical relationship.

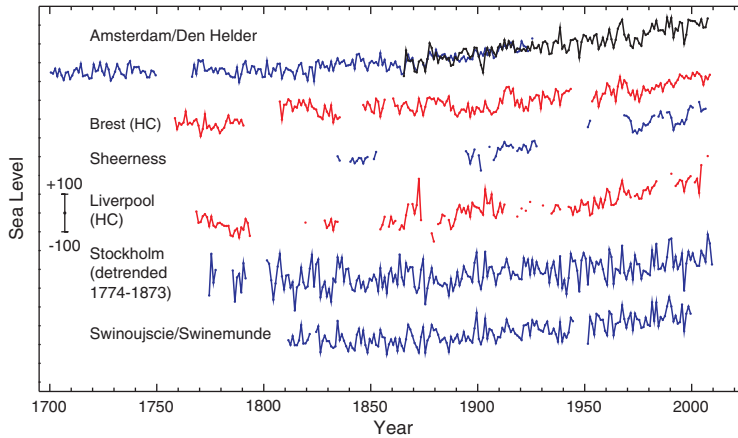


Figure 10.19 Long sea-level records from northern Europe. The Brest and Liverpool records are derived from mean high waters. They are denoted by ‘HC’ (‘high water computation’) and are shown in red. The Den Helder record shown in black has been adjusted to have the same mean value as Amsterdam for the period of overlap. The vertical scale is indicated by the ± 100 mm error bars. From [115].

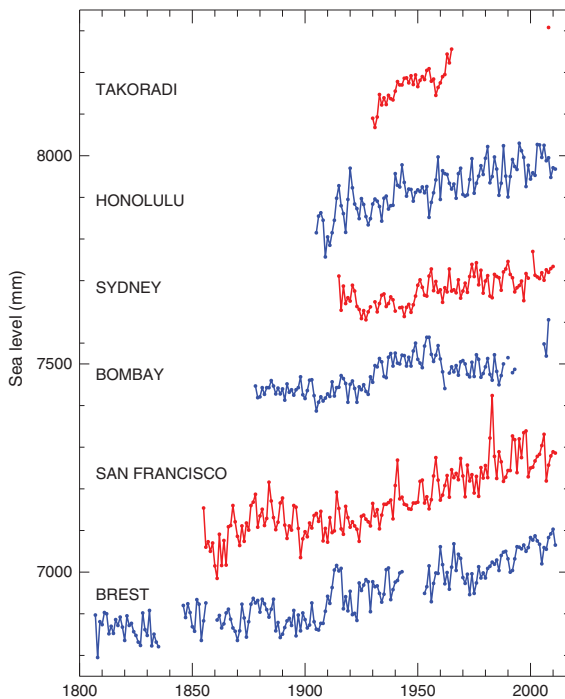


Figure 10.20 Typical long records in the PSMSL data set from different regions of the world. The Takoradi (Ghana) record, one of the longest in Africa, has recently been restarted after many years. Each record has an arbitrary offset for presentation purposes.

One can make some general observations about all these methods. A first is that, while there is an interesting range of different statistical techniques employed, there is little oceanographic science behind any of them. For example, the sea-level variations of the central North Atlantic are dominated by the strength of the sub-tropical and sub-polar gyres including the Gulf

Stream, so how can such complicated patterns of variability be parameterised by a limited number of base functions (EOFs)? A second observation is that, in spite of concern about individual methods, it is interesting that they result in similar global sea-level time series, with the ‘accelerations’ and ‘inflexions’ discussed above (cf. Figure 3 of Reference 128). An exception might be the time series of Reference 127, which appears more linear than the others. This apparently reassuring conclusion has to be qualified by the realisation that the same data set (PSMSL) has been used in all the analyses.

Figure 10.21 summarises our knowledge of how global sea level changed since the end of the nineteenth century for three of the ‘reconstruction’ exercises described above. The changes have been largely monotonic with an average rate of rise of 1.63, 1.70 and 1.94 mm/yr for the CW, RD and J curves respectively. The three are very similar for the period after 1940 and show differences only for the earlier years when the global data set was sparser. For each of them, it can be seen that there were higher rates during the 1920–30 period and since 1990, and lower values in the decades following approximately 1960 [128]. The short periods with higher rates may have been related to high rates of melting in Greenland glaciers [110]. They, and the short periods with lower rates, together make up the long-term acceleration mentioned above. The higher and lower rates at different times have been suggested as being partly due to a 60-year cycle similar to that observed in climate indices such as the AMO and PDO [129].

The high rate since 1990 (2.6, 3.3 and 3.1 mm/yr respectively for the three reconstructions) has been confirmed by measurements over a similar period by

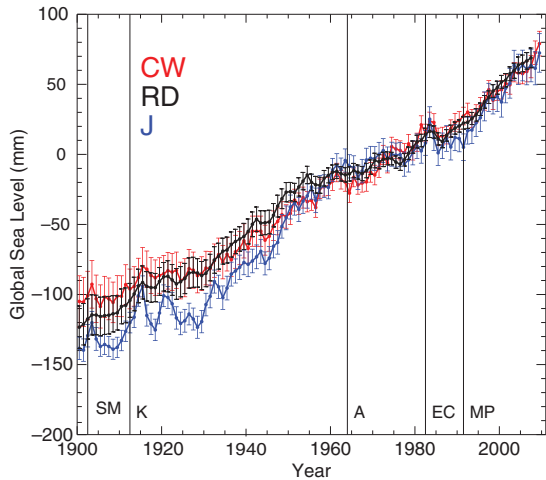


Figure 10.21 Three ‘reconstructions’ of global sea-level change from Church and White [121], Ray and Douglas [122] and updated from Jevrejeva *et al.* [126] shown by ‘CW’, ‘RD’ and ‘J’ respectively. Each record has an average value of zero over the baseline period 1960–90. The vertical lines indicate the times of the major volcanic eruptions of Santa Maria (SM), Katmai (K), Agung (A), El Chichón (EC) and Mount Pinatubo (MP).

satellite altimetry (see below). It is well known that the ocean is variable on many timescales, particularly on those from years to decades owing to large-scale processes discussed above, and there are corresponding short-term accelerations in sea level [130]. Therefore, a question is whether this recent high rate is unusual, or whether it is similar to previous high rates [121, 131, 132]. Several studies have indicated that there were indeed similarly high rates earlier in the twentieth century [118, 126, 133, 134].

However, the higher rate since the 1990s is unusual in having taken place in the tropics and higher southern latitudes as well as in the northern hemisphere [119]. Recent ‘data archaeology’ exercises support this picture. For example, measurements made by James Clark Ross in the 1840s at Port Louis in the Falkland Islands, together with more recent measurements, yielded an average long-term rate of approximately 1.0 mm/yr after correction for vertical land movements (Figure 10.22) [135]. This provided a baseline to which the present day rate at Port Stanley (near to Port Louis) could be compared. The conclusion was that the rate in the past two decades was significantly higher than the average rate since the 1840s. Ross was associated with similar sea-level measurements in the 1840s at Port Arthur, Tasmania [136], and our inspection of modern data from nearby Spring Bay gives a similar conclusion

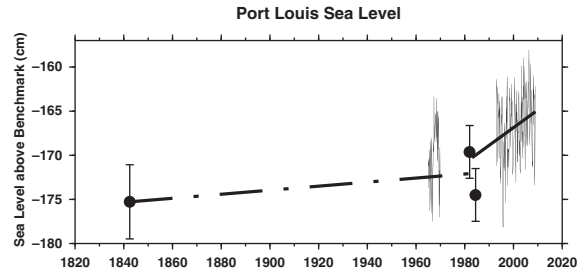


Figure 10.22 Values of MSL at locations near to Port Louis in the Falkland Islands, adjusted for air pressure changes and the seasonal cycle of sea level. All sea levels are measured with respect to the same benchmark. The 1842 dot is derived from measurements between May and August by James Clark Ross. The dots in the 1980s are from similar short-term measurements at nearby locations. The lines show data from permanent tide gauges at Port Stanley: a conventional float gauge during the 1960s, and a modern pressure-based gauge since 1992. The solid line is a fit to the near continuous record of the modern gauge extrapolated back to the early 1980s; the dashed line connects the Ross 1842 data point to the centre of the 1980s short-term measurements. The higher rate of sea-level change in recent years compared to the average rate since 1842 can be seen. Following [135].

of a recent higher rate. These findings are consistent with the picture of a general recent global acceleration with particular contributions from higher southern latitudes [119]. It will clearly be of great interest to see if the recent high global-average rate persists, or increases, in the future.

It is important to emphasise that any computed rate of sea-level change or of acceleration applies only to the epoch of the data from which it was computed and any such value cannot be assumed to be the same over another epoch. This is particularly true for the short-term accelerations mentioned above. However, it also applies to discussion at longer timescales. For example, it has been known for many years that records from Europe, North America and Australia exhibit an overall negative acceleration (deceleration) during the twentieth century [76, 137, 138, 139] whereas, if earlier data from the nineteenth century are included, then a small positive acceleration is apparent [115]. This important fact is sometimes ignored in the headline reporting of some studies of accelerations in sea level.

In spite of the general agreement on global-average sea-level change in the different analyses, there remains considerable uncertainty regarding reliable regional information using the methods described above, especially for those coastal regions where few or

no historical data exist and for the deep ocean [140]. This inability is hardly unexpected if analyses use methods that have a statistical, rather than an oceanographic, basis.

One region where plentiful historical tide gauge data exist is the Atlantic coast of North America. Accelerated sea-level rise along this coastline has been suggested as being related to a slowdown of the Atlantic Meridional Overturning Circulation [141, 142]. If this interpretation is correct, this would be an example of an ‘ocean fingerprint’ (Chapter 11).

However, similar studies in other regions can only take place if we have access to the maximum possible amount of historical tide gauge information. Major campaigns in sea-level ‘data archaeology’ are needed in many countries where such potentially important archives exist, before valuable historical information in the form of paper charts or tabulations is lost. The results of some data archaeology activities are represented in Figure 10.19, and more recent ones have confirmed how valuable historical data can be to the science of this chapter [143]. Worldwide catalogues of potentially important information are needed followed by computerisation and analysis of the resulting data sets [144].

10.9.3 Long-term sea-level change from altimetry

The TOPEX/Poseidon mission (launched 1992), together with Jason-1 (2001) and Jason-2 (2008), has provided one of the most valuable oceanographic data sets, measurements of near-global (within $\pm 66^\circ$ N/S) MSL change every 10 days [95]. Figure 10.23 shows that global sea level has risen at an average rate of 3.2 ± 0.4 mm/yr in the period 1992–2013, with systematic errors on this estimate of the order of 0.4 mm/yr [145, 146]. Major variations in this rate occurred around 1997–8, which are thought to be due to the hydrological processes associated with ENSO at that time, and around 2010–11, when the ocean experienced a relative cooling due to an extended La Niña period (Figure 10.24) [147].

However, sea-level rise has not been the same in all parts of the ocean during the past two decades. In some areas of the western equatorial Pacific, rates have been approximately three times the global average, while off the Pacific coast of North America sea level has actually fallen (Figure 10.25a, b) [148]. A large part of the spatial variability in the observed sea-level change can be explained in terms of its ‘thermsteric’ component, the change in sea level due to the change in density

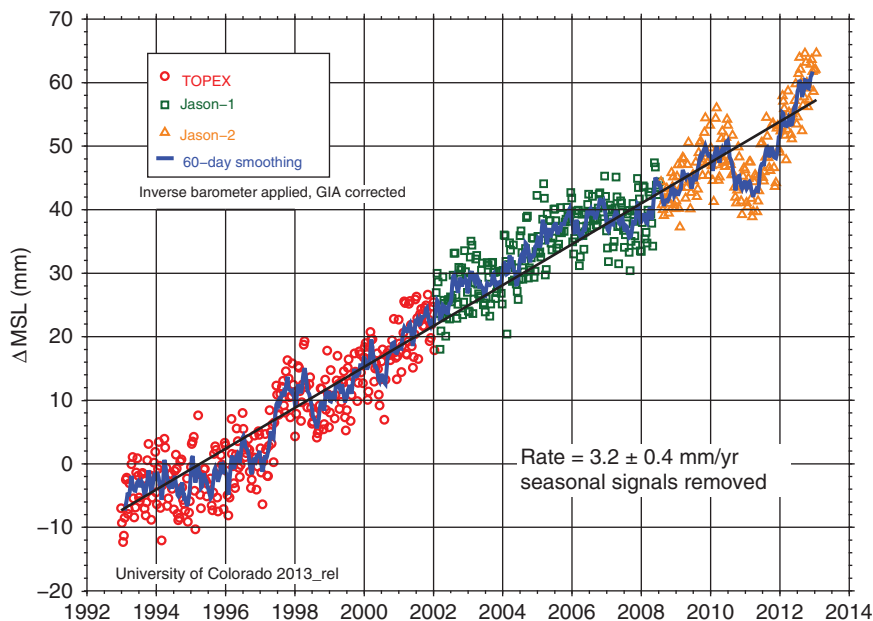


Figure 10.23 Variations in global MSL from a combination of TOPEX/Poseidon, Jason-1 and Jason-2 altimeter measurements, using 60-day and annual smoothing of 10-day average values. A Glacial Isostatic Adjustment correction of 0.3 mm/yr has been applied. Figure from Professor Steve Nerem, University of Colorado (sealevel.colorado.edu).

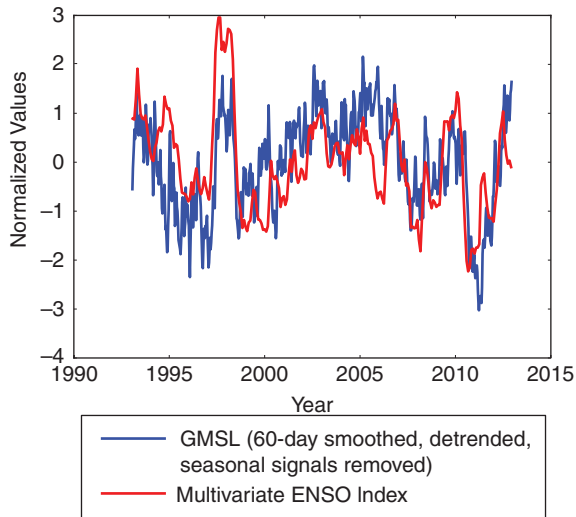


Figure 10.24 Global MSL change from altimetry (60-day smoothed and with the mean, linear trend and seasonal signals removed) compared to the Multivariate ENSO Index (MEI) which is one of the Pacific ENSO indices. Each time series is normalised by dividing by its standard deviation. The two series are clearly related, with the global MSL often lagging changes in the MEI. The large ENSO-related excursions are related to changes in global precipitation and land water storage. From sealevel.colorado.edu.

associated with temperature (Figure 10.25c). In turn, a large part of the thermosteric pattern is clearly ENSO-related. Unfortunately, it is not possible to produce a corresponding global map for ‘halosteric’ sea-level change (the change in sea level due to the change in density associated with salinity) owing to the lack of reliable historical salinity measurements worldwide. Halosteric change could be very important for sea level regionally but will not contribute to global-average sea-level change [149].²

10.10 Understanding sea-level change

10.10.1 Understanding sea-level change in the last century

It is generally believed that sea levels have changed during the past century primarily because the Earth’s

² Adding or removing fresh water from an ocean where salt is conserved does not result in an overall change in sea level due to halosteric change because (in the case of adding fresh water) the dilution of the original seawater and the salinisation of the added fresh water contribute equally to halosteric change but with opposite sign. The global-average change in sea level is then just determined by the volume of fresh water alone. See Appendix A of Reference 149.

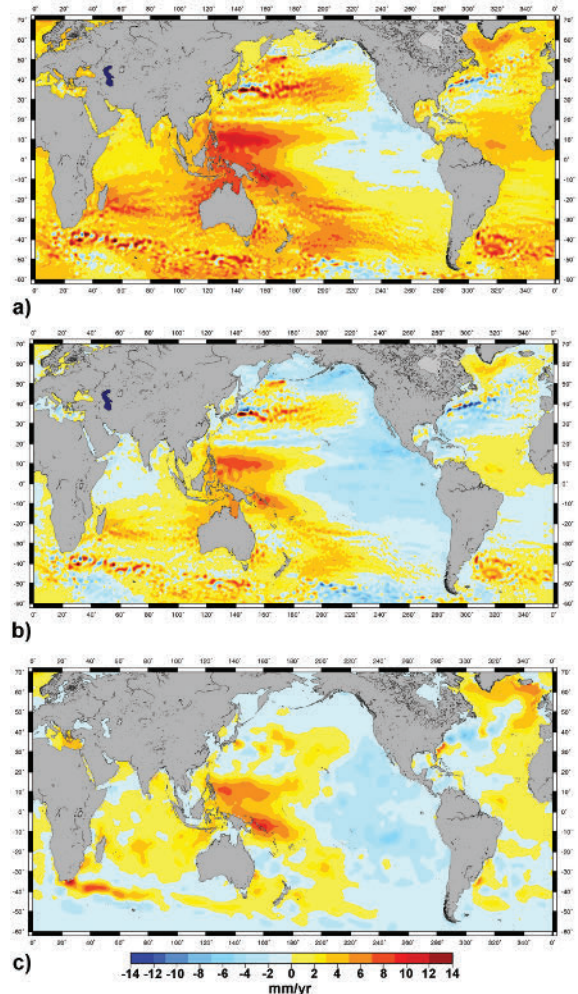


Figure 10.25 (a) Spatial trends patterns in the rate of sea-level change around the world from satellite altimetry data over 1993–2011. (b) As figure (a) but with a global mean trend of 3.2 mm/yr removed. (c) Spatial trend patterns in thermosteric sea level in a similar period. Figure from Dr Benoit Meyssignac, Observatoire Midi-Pyrénées, Toulouse updated from a similar figure in [148].

climate has warmed [91]. However, understanding which processes have contributed to the observed changes is a complex task [150]. The procedure for determining the magnitude of the various contributions (thermal expansion, glacier melting, ice sheet mass balance etc.) involves both measurements and modelling and is called ‘estimating a budget’. Examples can be found in each of the IPCC research assessments and other reports. Most of these attempts yielded an overall budget for twentieth-century sea-level rise lower than that observed, resulting in a

‘sea-level rise enigma’ [151]. The budget discrepancy presented a particular difficulty with regard to prediction of future sea-level rise, for without a proper understanding of the changes of the past, how can one reliably predict those of the future?

The problem becomes worse as one goes back in time from the relatively well-instrumented modern era, back to the start of the twentieth century when observations were sparser, both of sea level itself (Figure 10.1) and of the oceanographic, cryospheric and hydrological parameters required to understand the budget. In recent years, attempts have been made to construct more complete data sets for many of these parameters, models have been improved, and more convincing budget estimates have been made [152].

Figure 10.26 shows how one reconstruction of twentieth-century global sea-level change [121] might be parameterised as the sum of thermal expansion, glacier melting, Greenland mass balance, groundwater depletion and reservoir storage, together with a ‘residual trend’ of 0.19 mm/yr, the latter being an attempt to account for the budget discrepancy [153]. (Antarctica is not included owing to the difficulty of constructing a twentieth-century time series of its contribution.) In this example, thermal expansion and glaciers can be seen to be the main contributors. However, there are other published reconstructions of global sea-level change, as discussed above, and of each individual contributing term. As a result, there are a number of plausible budget combinations, and a conclusion on the most likely mix of terms becomes a

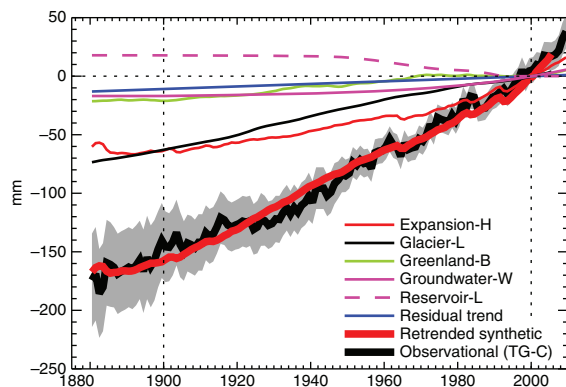


Figure 10.26 An example of parameterising a reconstruction of global sea-level change for the twentieth century (black line) in terms of various contributing terms including a ‘residual trend’. The sum of the contributors and residual trend gives the ‘retrended synthetic’ time series (red line). From [153]. © American Meteorological Society. Used with permission.

matter of judgement of the uncertainties involved in each case.

This procedure is discussed at some length in the IPCC Fifth Assessment Report (AR5) [91], which made a best estimation of global sea-level rise between 1901 and 1990 (average rate 1.5 mm/yr) as having received contributions from thermal expansion (0.37 mm/yr), glaciers (0.70 mm/yr) and land water (−0.11 mm/yr) and with a ‘residual’ of 0.5 mm/yr. The authors concluded that, for this and all other periods studied, the residuals are small enough to be accounted for by changes in the ice sheets. The AR5 also concluded that, as ocean warming will have resulted in the thermosteric sea-level change, and as it is likely that the substantial mass loss of glaciers and possibly also Greenland is also due to human influence, then a large part of the observed sea-level rise during the twentieth century can be confidently claimed to have had an anthropogenic cause [154].

The twentieth century contained several large volcanic eruptions (Figure 10.21) which could have temporarily offset the impact of global warming and sea-level rise, by injecting aerosols into the stratosphere, reflecting some of the incoming solar radiation. Climate modelling suggests that the eruption of Krakatoa in 1883 would have caused a substantial ocean cooling and immediate thermosteric sea-level fall of 5–10 mm, with the cooling persisting for many decades in the deep layers of the ocean and a remnant signal even into the late twentieth century [155]. However, there are fewer sea-level records available from that period to investigate such a sea-level fall (Figure 10.1). The effects of the earlier but larger Tambora eruption in 1815 are also considered to have persisted in the ocean into the twentieth century [156]. For the twentieth century itself, modelling indicates that a global sea-level fall of several millimetres could have occurred in the years immediately following the Mount Pinatubo eruption, followed by a longer recovery to previous conditions [157]. Smaller falls might have followed Agung and El Chichón. However, while Figure 10.21 shows similar sea-level falls in all three reconstructions after the Agung eruption, there are none after Mount Pinatubo. Consequently, it is difficult to confirm the existence of the small volcano signals from the observations. Changes in the global hydrological cycle caused by the eruptions have been suggested to lead to a more complicated global sea-level response than that due to thermosteric change alone [158].

As explained above, ocean data sets become increasingly sparse as one goes back in time. Consequently, climate modelling is often used to provide estimates of thermal expansion instead of observations (cf. Table 13.1 of Reference 91). Such models are usually ‘spun-up’ for several hundred years until a time, such as the late nineteenth century, when they can be driven by known climate and volcanic forcings. However, it has recently been realised that the twentieth-century thermal expansion simulated by climate models may previously have been underestimated owing to their not including volcanic forcing in their spin-up period [152]. The switching-on of volcanic forcing in the late nineteenth century would have simulated a cooler ocean and a lower thermal expansion into the twentieth century. It is important, therefore, to have a fuller appreciation, at least on a statistical basis, of the role of volcanoes in climate through history if one is to understand the sea-level changes of the past century.

Changes in global average sea level are usually discussed in terms of its changing budget, as discussed above. However, an important question is whether, given that there has been only a partial monitoring system based on tide gauges for most of the twentieth century, water may have simply been redistributed around the ocean, and that the apparent rise is an artefact of sampling. For example, one study of sea-level acceleration between the nineteenth and twentieth centuries [159] considered the evidence for a long-term deceleration in North Atlantic gyre strength (spin down), represented by decreasing air pressures near to the centre of the sub-tropical gyre, and for a connection to an acceleration in the rate of sea-level change at the eastern boundary (see also Reference 160). A similar inference was made from the North Pacific data, although the poorer quality air pressure fields available for that ocean prevented as firm a set of conclusions as for the North Atlantic. A subsequent study showed that the relationship holds, at a qualitative level for the North Atlantic, for the last two and a half centuries [161]. The accelerations observed by tide gauges in this case would have nothing to do with sea-level rise.

The question of water redistribution is also relevant to discussion of sea-level changes in the past two decades by altimetry, when we have had a quasi-global monitoring system. As shown above, the high global rate in this period contains a major contribution from the equatorial western Pacific where sea level has been rising at ~10 mm/yr since the beginning of the altimeter era. In an analysis of tide gauge data from this

region [162], it was found that sea level was relatively stable prior to the altimeter era, and then began to rise rapidly in the early 1990s due to an increase in the speed of the trade winds. The importance of wind field changes has been shown by several other studies to be responsible for anomalous (compared to the global average) regional sea-level trends in recent decades in both the Pacific [163, 164] and Indian Oceans [165]. These aspects stress the importance of considering ‘trends’ and ‘accelerations’ in sea level alongside those of large-scale patterns of ocean variability. It is clear that a considerable amount of ocean, climate and geophysical modelling remains to be performed in order to understand better the various contributors to regional and global-average sea-level rise during the last century.

10.10.2 Understanding sea-level change in recent years

In Chapter 9, we described the GRACE space gravity mission which was launched in 2002 [166]. This highly successful mission has since provided monthly time series of mass changes around the world, which are conventionally expressed as changes in water-equivalent as the satellite has no way of distinguishing between different types of mass change. Figure 10.27 shows the trend in water-equivalent in cm/yr between 2003 and 2013 [167]. One can see a large signal to the west of Indonesia which stems from the change in the local gravity field following the Sumatra earthquake in 2004, and a similar smaller signal is perhaps present to the east of Japan associated with the Tōhoku earthquake in 2011. Elsewhere, there are large negative values over Greenland and the West Antarctic Ice Sheet (WAIS), and other negative signals over the Alaskan, Andean and Himalayan glaciers. Positive values reflect increased water storage in the Congo and Amazon basins. The positive signals over Hudson Bay and Scandinavia are due to GIA (Chapter 11) and can be removed with the use of a GIA model.

GRACE has also provided information that can be interpreted as changes in ocean mass, once the data have been corrected for GIA (Figure 11.10d) [168]. Time series of mass change at each point in the ocean in effect provide a global set of records of ocean bottom pressure, complementing the data from deep-sea tide gauges described in Chapter 2. Figure 10.28c shows that the trends in these records from the mission so far are of the order of 1 mm/yr

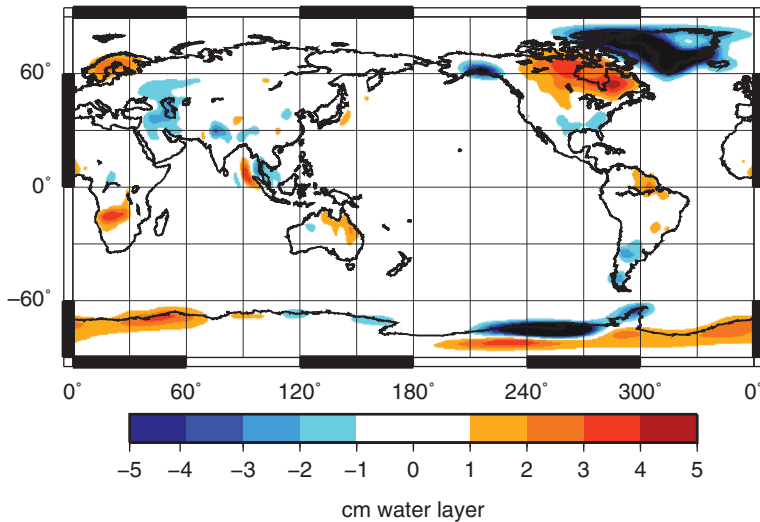


Figure 10.27 Trends in mass change around the world estimated from GRACE time-variable gravity data (CSR RL05) for the period March 2003 – November 2012, smoothed with a 300 km Gaussian filter. Units are cm/yr of equivalent water height. Data have been processed as described in [167], except no GIA signal was removed. Figure provided by Drs Jenni Bonin and Don Chambers, University of South Florida.

(this ocean information is not represented in the processing of Figure 10.27). When summed over the entire ocean, they provide evidence for significant variation in ocean mass, as discussed below.³

The early 2000s also saw the start of cooperation by over 40 countries to construct a global network of over 3000 Argo floats (Figure 10.29(a)) [169]. The floats are battery-powered autonomous instruments that drift at ~1000 m depth for approximately 9 days when a pump transfers a fluid between a reservoir inside the instrument and an external bladder enabling them to sink to 2000 m and then to ascend to the surface recording temperature and salinity. At the surface, their position is determined and data transmitted to data centres using the Argos satellite system (Figure 10.29b). Their temperature and salinity information is then used to compute steric sea-level changes (changes in sea level due to the combined thermosteric and halosteric effects) throughout most of the world ocean.

Altimetry, Argo and GRACE complement each other perfectly in a sea-level monitoring system. The first provides a direct measurement of sea-level change, the second an assessment of steric change, and the third a measure of the change in ocean mass (Figure 10.28). The first two maps in Figure 10.28 are

similar to those in Figure 10.25, but for the shorter recent period for which GRACE data are available. Figure 10.30 shows how, when summed over the whole ocean, most of the variation in the global sea-level change in recent years can be parameterised as the sum of its steric and mass components [170]. The IPCC AR5 concluded that, although these records are short at present, the current ocean observing system comprising altimetry, Argo and GRACE is capable of resolving the components of long-term sea-level rise, assuming continued measurements [171].

The large signals seen in Figure 10.27 indicate how GRACE can provide a means of understanding the origins of changes in ocean mass. Their detailed analysis has provided insight into fluctuations in ice sheets [172, 173], glaciers [174, 175, 176] and terrestrial water storage [177]. Figure 10.31 provides examples of three of the most important signals, with each time series corrected for GIA [178], showing changes in the amount of ice stored in Greenland, Antarctica and coastal Alaskan glaciers. These are potentially the largest contributors to a future sea-level rise: Antarctica, Greenland and glaciers containing ice equivalent to 58, 7.4 and 0.4 m global-average sea-level rise respectively [179]. All three records present evidence for melting (primarily in West Greenland and the WAIS for the first two), with possible accelerations in melting suggested by the quadratic components of the orange lines in Figures 10.31a, b. Over the period 2003–10, the Greenland and Antarctic ice sheets contributed 1.06 mm/yr to sea-level rise, with an additional 0.41 mm/yr from glaciers and ice caps, including those from Alaska [176].

³ Some of the oceanographic literature refers to ocean mass change as a 'eustatic' one, whereas other literature, such as IPCC reports, uses the term 'eustatic' to mean change in ocean volume. Most of the sea-level community have agreed that the term should no longer be used. However, if it is used, it must be clearly defined. Some authors have suggested the term 'barystatic' for ocean mass change where 'bary' has connotations of mass.

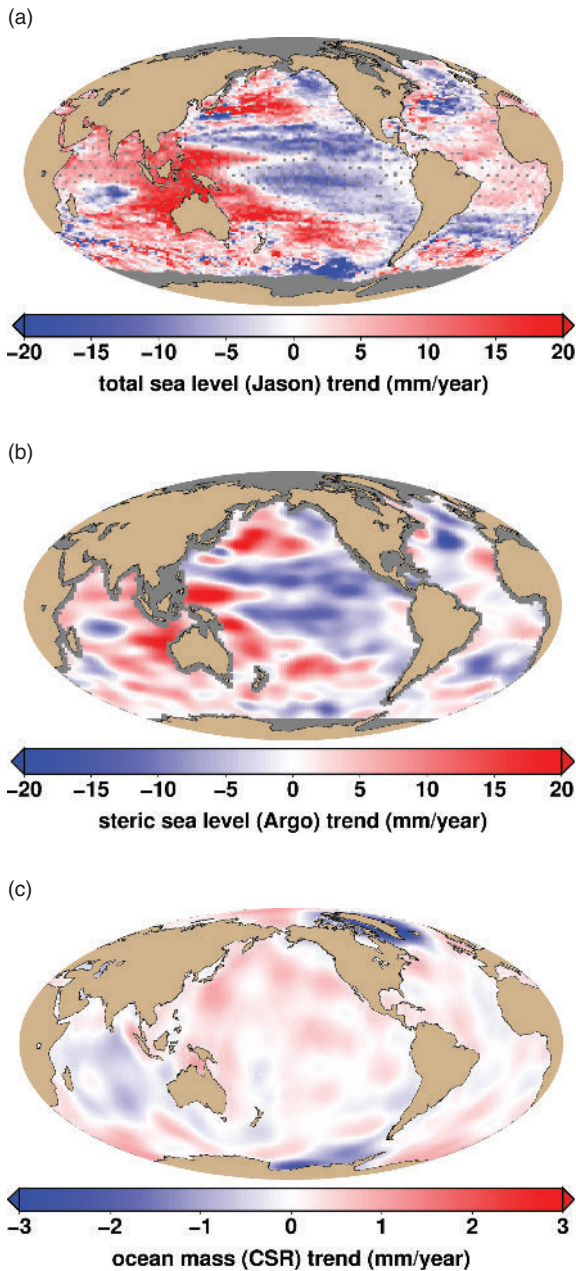


Figure 10.28 Spatial distribution of the trends from January 2005 to December 2011 in (a) sea level from altimetry, (b) steric sea level from Argo, and (c) ocean mass from GRACE determined by the University of Texas Center for Space Research (CSR). Figure provided by Dr Eric Leuliette, NOAA updated from information in [170].

GRACE and Argo have made major contributions to the studies of the ocean circulation and sea-level change. As a result, arguments have been made for their continuation and technical development so that the community can have ongoing information on

mass and steric changes. A GRACE Follow-On mission is planned for launch by 2017, with a microwave system for inter-satellite ranging similar to that on GRACE complemented by a technical demonstration of a laser system. The shorter wavelength of the laser will provide an order of magnitude improvement in ranging accuracy and lead to more precise gravity measurements. Meanwhile, efforts are being made to extend Argo monitoring to ice-covered parts of the ocean and to greater depths [180].

Comprehensive summaries are available of all the *in situ* and remotely sensing observing systems needed for a better understanding of sea-level change [181]. These systems include both existing techniques, which must be sustained, and new ones, which need to be developed. Satellite observations generally need to be as continuous as possible, with overlap between successive missions and coincident with the collection of appropriate *in situ* observations. Further identified requirements include the need for more data archaeology, so that the record of the past can be better documented and understood. An overarching requirement is the need for national agencies to operate an open data policy and enable timely, unrestricted access for all researchers.

10.11 Future rise in mean and extreme sea levels

Future sea-level rise is one of the most publicised aspects of climate change owing to its potential impact on coastal zones (Chapters 12 and 13). Two general approaches are followed for estimating the likely rise, and rate of rise, of future global sea level. One is by comparison of the temperatures and sea levels of previous interglacials to those of today, and thereby to obtain estimates on possible limits of change in a warming world. The other involves the use of climate modelling of various kinds, which takes advantage of our experience in understanding sea-level variability in the past to predict that in the future.

In the first line of research, comparisons are made between the present Holocene, the previous Eemian and even earlier interglacials [182]. Sea levels are known to be highly correlated with high-latitude temperatures during interglacials. Polar temperatures in the Eemian are generally considered to have been 3–5 °C higher than today, while sea levels were between 5 and 10 m higher [91, 183, 184]. An increase in steric height cannot account for such a large rise [185], so a

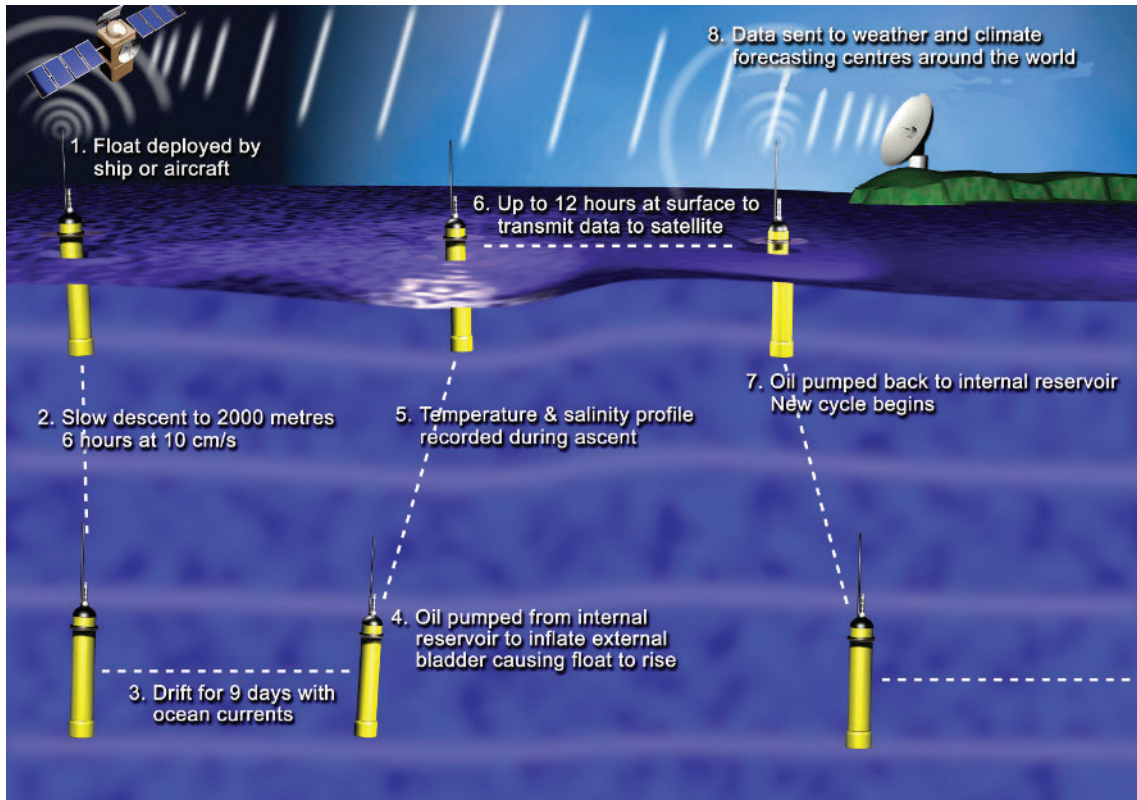


Figure 10.29 (a) Distribution of over 3500 Argo floats as of February 2013. The colour of each dot indicates the country that deployed the float. From the Argo Information Centre at www.jcommops.org. (b) Schematic description of the normal 10-day cycle of operation of an Argo float. From www.argo.ucsd.edu/.

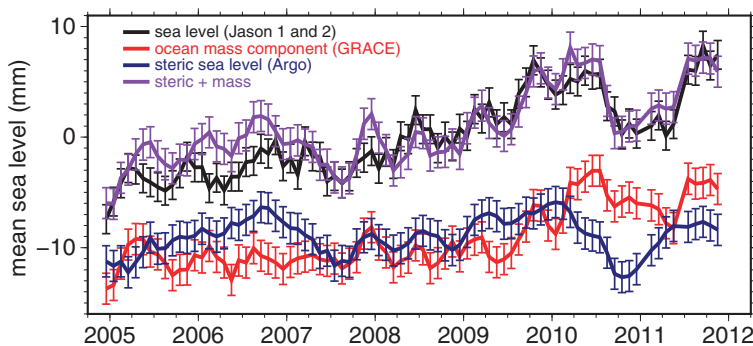


Figure 10.30 Monthly estimates from Jason-1 and Jason-2 of global MSL for areas greater than 200 km from the coast (black), which are in general agreement with the sum (purple) of the ocean mass component from GRACE (blue) and the steric component of the upper 900 m from Argo (red). Each time series has been deseasonalised and slightly smoothed. Figure from Dr Eric Leuliette, NOAA updated from information in [170].

significant ice sheet melting is required, primarily from the WAIS as a Greenland contribution is thought to be limited to approximately 2 m [186]. This melting would have taken place while polar temperatures were comparable to those predicted during the next 100 years due to anthropogenic climate change [91]. Consequently, the

climate of the Eemian could serve as an indicator of how sea level might rise in coming years in response to future higher temperatures. Some authors [187] have even suggested that the Eemian was not in fact significantly warmer than today, increasing the possibility of a future rise due to modest warming.

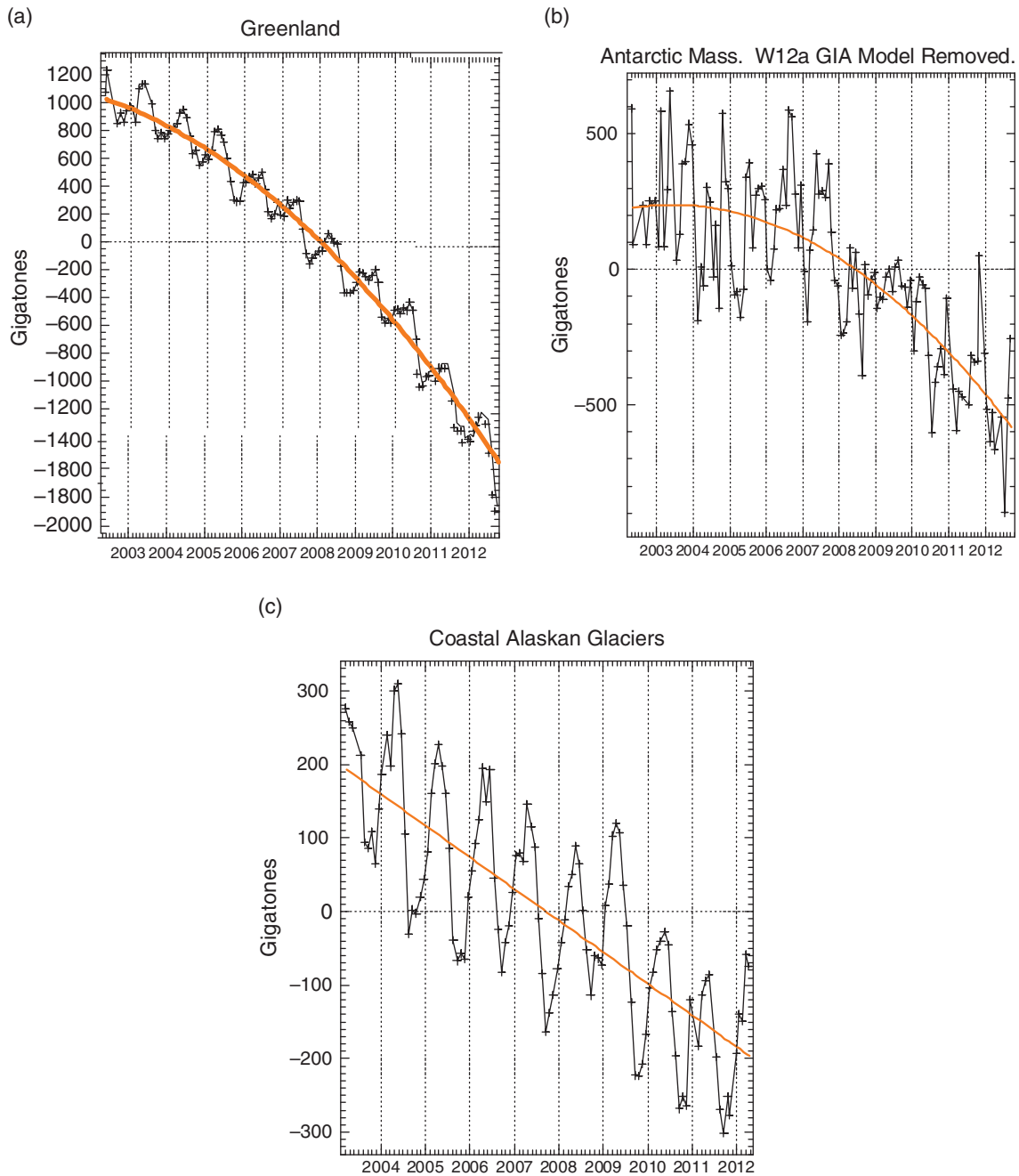


Figure 10.31 (a) Mass balance of Greenland during April 2002 – September 2012 observed by GRACE indicating a possible acceleration in the overall rate (orange quadratic line); (b) corresponding time series of mass balance for Antarctica; (c) time series of mass balance of coastal Alaskan glaciers for March 2003 – April 2012. Each figure adjusted for GIA as appropriate. 360 gigatons of ice corresponds to 1 mm of sea level. Figures provided by Professor John Wahr, University of Colorado.

For many processes that involve adaptation to sea-level rise, the important issue is not so much the magnitude of any rise but its likely rate of rise. It has been estimated that, during that part of the Eemian

when sea level was comparable to that of today, the rate of rise averaged over periods of 1000 years could have reached 5.6 mm/yr but was unlikely to have exceeded 9.2 mm/yr (the available data are not suitable

for estimating rates of change over shorter periods) [183]. A different study concluded that average rates during the interglacial were about 16 mm/yr [188], although their uncertainties are such that the authors estimate that the real rate could have been in the range 6–25 mm/yr. The IPCC AR5 concluded that the maximum 1000-year average rate, for the time interval in the Eemian when global-average sea level was above that at present, exceeded 2 mm/yr but did not exceed 7 mm/yr. Therefore, there must have times when the rate exceeded that during the twentieth century [91].

A second direction of research in providing estimates of future sea-level rise involves the use of AOGCM (sometimes called ‘process-based’) modelling. In brief, these studies start with ‘greenhouse gas emission scenarios’, which are estimates of the concentrations of carbon dioxide and other greenhouse gases in the atmosphere in the future. Knowledge is then required of the ‘climate sensitivity’, the expected long-term change in temperature for a doubling of carbon dioxide concentration (typically 3 °C) [189]. The models, which for the ocean employ finite-difference 3-D grids similar to the 2-D grids discussed in Chapter 7 but with an additional dimension to allow for the dependence of ocean temperatures and salinities on depth, then attempt to simulate the resulting changes in the ocean circulation due to the fluxes of heat and fresh water exchanged between the atmosphere and the ocean. The consequent changes in the temperature, salinity and density fields in the model ocean can then be analysed to estimate changes in regional and global-average ‘steric’ sea level and heat content. Additional changes in sea level can be estimated from the changes in mass balance of glaciers and ice sheets parameterised in terms of their sensitivity to regional temperature change, and from separately modelled variations in exchanges of water between the terrestrial hydrosphere and ocean. These various changes in sea level can then be combined to provide a projection of future global and regional sea-level change [190].⁴

⁴ Climate change terminology distinguishes between *prediction* and *projection*. A climate prediction (or forecast) is the result of an attempt to produce an estimate of the actual evolution of the climate in the future. Since that evolution may be sensitive to initial conditions, predictions are usually probabilistic in nature. A climate projection is the simulated response of the climate system to a *scenario* of future emissions of greenhouse gases and aerosols, usually by means of numerical simulations by climate models. Climate projections are distinguished from climate predictions by their dependence on the forcing scenario used, which is in turn

Large integrated studies of this kind are conducted every few years within the scientific assessments of the IPCC. In the Third Assessment Report (TAR) [89], global average sea level was predicted to rise between 20 and 70 cm between 1990 and 2100 using the full range of greenhouse gas scenarios and climate models. An additional uncertainty for land-ice changes widened the range to 9 to 88 cm. The Fourth Assessment Report (AR4) used a larger set of models and settled on a range of 18 to 59 cm sea-level rise for the period 1980–99 to 2090–99. Ocean thermal expansion was determined to be the largest contributor followed by glaciers and ice caps. Consideration of an additional uncertainty in the stability of ice sheets increased the upper limit by 17 cm, giving an overall range of 17 to 76 cm [90]. Even higher values were considered possible, but the difficulty of predicting future contributions of the ice sheets, particularly those grounded below sea level, meant that a quantitative upper bound could not be determined [191].

The IPCC AR5 estimated that global sea level is likely to rise by between 28 and 97 cm by 2100, compared to a 1986–2005 baseline, depending upon a low or high gas emission scenario, these values including a term for rapid, dynamical changes in ice-sheet outflow (Figure 10.32) [91]. Although the TAR, AR4 and AR5 projections differed in how they treated ice sheet uncertainties, their conclusions are similar, with projected increases in global sea level for the twenty-first century in the range one to five times that of the twentieth century (Figure 10.33). The ‘headline’ projections of global-average sea-level rise to 2100 have in fact been similar in all five IPCC assessments (Table 10.1).

There are likely to be many regional differences in the future rates of sea-level change, due partly to the variability of the ocean circulation [192] and also due to geophysical ‘fingerprints’ associated with changes in the mass loads on the planet (Chapter 11) [193, 194]. However, regional differences are expected to become smaller, relative to the global average, as time goes on.

Several scientists have adopted a different approach to estimating future sea-level rise by using ‘semi-empirical’ models as alternatives to AOGCMs. This approach arose partly because the observed rate of sea-level rise since 1990 has exceeded that projected by the AOGCMs [118, 195]. The analyses establish a

based on assumptions of economic and technological development [190].

Table 10.1 Projections of future sea-level rise obtained using AOGCMs in the IPCC assessments

IPCC assessment	Year of assessment	Reference epoch	Projected epoch	Range of sea-level rise (central value) Units: metres	Comments
1	1990	1990	2100	0.31 (0.66) 1.10 0.15–1.10	Using the Business As Usual emission scenario Using four scenarios
2	1995	1990	2100	0.20 (0.49) 0.86 0.13–0.94	Using the IS92a emission scenario Using all six IS92 scenarios
3	2001	1990	2100	0.11 (0.44) 0.77 0.09 (0.48) 0.88	Using the IS92a scenario Using 35 SRES scenarios and including land ice uncertainty
4	2007	1980–1999	2090–2099	0.18 (0.38) 0.59 0.17 (0.46) 0.76	Based on six SRES ‘marker scenarios’ but without inclusion of rapid ice-sheet dynamical change (estimated at between –0.01 and 0.17) Including rapid ice-sheet dynamical change
5	2014	1986–2005	2100	0.28 (0.63) 0.97	Using four RCP scenarios and including rapid dynamical changes in ice sheets

Notes:

1. The above projections are the ‘headline’ ones from each assessment. However, there are many details behind all projections and each assessment report should be consulted for more details.
2. There are detailed differences between the scenarios used in each assessment (SRES: IPCC Special Reports of Emission Scenarios. RCP: Representative Concentration Pathways for greenhouse gas concentrations).
3. Projections in assessments 3–5 were obtained using a number of AOGCMs from different centres, information on particular models can be found in each report. Assessments 1–2 used simple models for projections together with a range of climate sensitivity.
4. The table shows the range across all scenarios for assessments 4 and 5; the reports give ranges for individual scenarios. Deriving a combined range requires assumptions on the relative probabilities of scenarios.
5. There are statistical differences between assessments in how ‘range’ is defined (e.g. 5–95 per cent probability).

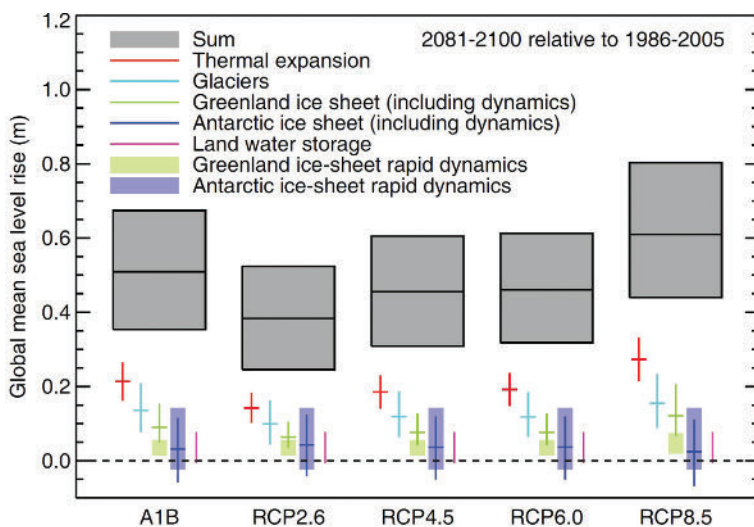


Figure 10.32 Projections of global sea-level change from the IPCC AR5 using AOGCMs. The likely ranges and median values for sea-level rise are shown together with their contributions. The period considered is 1986–2005 to 2081–2100, using four RCP scenarios and the scenario A1B used in the AR4. Contributions from ice sheet dynamical change, which are also shown separately, and anthropogenic land water storage are included in each sum and are independent of scenario. From [91].

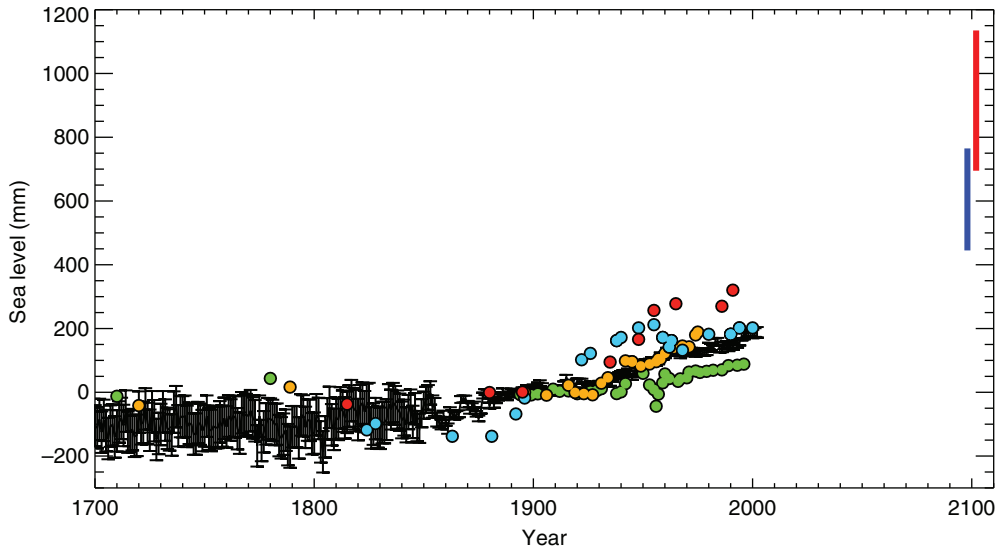


Figure 10.33 An indication of how sea level has changed in the recent past using a sea-level reconstruction based on tide gauge data [210] (black line). Also shown is information from salt marsh data [110] (dots). Each time series has been adjusted to zero for the baseline period 1870–1930. The figure also gives an indication of how sea level could change by 2100; the blue and red lines are projections for the RCP2.6 (low) and RCP8.5 (high) emission scenarios of the IPCC AR5 [91].

relationship between sea-level change and global temperature (or a climate forcing parameter), and make use of the fact that most components of sea-level rise (e.g. glacier melting) are related to temperature somehow. The parameters describing the relationship can be determined from historical sea-level and temperature information for the nineteenth to twenty-first centuries [196, 197, 198], or longer term with the use of geological information [199]. The parameters can then be used to predict the rate of future sea-level rise based on IPCC estimates of future global temperature change in various greenhouse gas emission scenarios. Such methods can lead to projections of sea-level rise of more than 1 m by 2100, exceeding by approximately 0.2 m the upper bound of projections from AOGCMs under the same emission scenario (Figure 12.12 of Reference 91). The semi-empirical projections have been criticised as being unreliable if the main contributors to sea-level rise are different in the future from those in the past [200, 201, 202]. However, the reasons for the systematic differences in projections between the two sets of modelling are complex [91].

Even if greenhouse gas emissions are stabilised at some point during the twenty-first century, global temperatures will continue to rise [203]. The deeper parts of the ocean will carry on warming for many hundreds of years, resulting in an on-going thermos-teric sea-level rise called a ‘sea-level commitment’ [91,

204]. Glaciers, especially those at lower altitude and latitude, will melt but there is a limit of the order of 0.4 m on their potential sea-level contribution. The IPCC AR5 suggested (with medium confidence) that global-average sea level could increase by 1–3 m by 2300 depending on greenhouse gas concentrations [91]. Another estimate suggests that we are committed to sea-level rise of approximately $2.3 \text{ m } ^\circ\text{C}^{-1}$ within the next 2000 years [205].

If emissions cease at some point in the future, then climate and sea level can be expected to reach a new equilibrium, but only after many centuries. At that time, the part of sea-level rise due to thermal expansion in the intervening period will depend upon the integrated amount of carbon (and its equivalent from other greenhouse gases) burned since industrialisation. The rise could be expected to be in the range 0.7–5 m if all of the world’s carbon store (some 5000 PgC) were to be consumed [206]. However, this amount does not include additional contributions from changes in ice sheets and other water sources; the loss of Greenland alone could amount to 7 m of sea-level rise. If temperatures over Greenland exceed a threshold for surface melting to permanently dominate over precipitation, and if that situation is maintained for several millennia, a virtual elimination of the Greenland ice sheet and a global-average sea-level rise of metres will result [207].

While climate scientists are interested primarily in future MSL change, the question of how extreme sea levels of the future will differ from those today is of far more interest to people who live at the coast, and for those interested in impacts on coastal infrastructure and environment. As mentioned in [Chapter 7](#), the available evidence suggests that extremes have changed in recent decades as one would expect due to changes in MSL, and the IPCC AR5 concluded that this situation will continue in the future. If MSL change is indeed the only factor contributing to changes in extremes, effective planning of future coastal defences will be more straightforward ([Chapter 12](#)) [208]. However, that assumes that the climatology of the storms that lead to extremes will remain the same. Unfortunately, there is little insight into how storminess, and the associated surges and sea-level extremes, might change, including on how the magnitude and frequency of large tropical cyclones such as Nargis, Katrina or Haiyan will be modified, or whether at mid-latitudes the depth of depressions and of storm tracks will change [115, 209]. We return to the question of how coastal dwellers may adapt to future higher sea levels in [Chapters 12 and 13](#).

References

- IOC, 2002. *Manual on sea-level measurement and interpretation. Volume III: Reappraisals and recommendations as of the year 2000* (ed. P. L. Woodworth), Intergovernmental Oceanographic Commission, Manuals and Guides, No 14. Paris: UNESCO/Intergovernmental Oceanographic Commission. Available from ioc.unesco.org.
- An example is the use of MSL and MTL data from several UK stations referred to in Woodworth, P. L., Teferle, N., Bingley, R., Shennan, I. and Williams, S. D. P. 2009. Trends in UK mean sea level revisited. *Geophysical Journal International*, **176**, 19–30, doi:10.1111/j.1365-246X.2008.03942.x.
- Woodworth, P. L. and Player, R. 2003. The Permanent Service for Mean Sea Level: an update to the 21st century. *Journal of Coastal Research*, **19**, 287–295.
- Holgate, S. J., Matthews, A., Woodworth, P. L. *et al.* 2013. New data systems and products at the Permanent Service for Mean Sea Level. *Journal of Coastal Research*, **29**, 493–504, doi:10.2112/JCOASTRES-D-12-00175.1.
- Altimeter data can be obtained from several agencies including Archiving, Validation et Interprétation de données des Satellites Océanographiques (AVISO, www.aviso.oceanobs.com), Physical Oceanography Distributed Active Archive Center (PO.DAAC, podaac.jpl.nasa.gov), Radar Altimeter Database System at the Delft University of Technology (RADS, rads.tudelft.nl/rads), University of Colorado Sea Level Research Group (sealevel.colorado.edu) and Commonwealth Scientific and Industrial Research Organisation (CSIRO, www.cmar.csiro.au/sealevel).
- Williams, J. and Hughes, C. W. 2013. The coherence of small island sea level with the wider ocean: a model study. *Ocean Science*, **9**, 111–119, doi:10.5194/os-9-111-2013.
- Vinogradov, S. V. and Ponte, R. M. 2011. Low-frequency variability in coastal sea level from tide gauges and altimetry. *Journal of Geophysical Research*, **116**, C07006, doi:10.1029/2011JC007034.
- Morrow, R. and Le Traon, P.-Y. 2012. Recent advances in observing mesoscale ocean dynamics with satellite. *Advances in Space Research*, **50**, 1062–1076, doi:10.1016/j.asr.2011.09.033.
- For example, Firing, Y. L. and Merrifield, M. A. 2004. Extreme sea level events at Hawaii: the influence of mesoscale eddies. *Geophysical Research Letters*, **31**, L24306, doi:10.1029/2004GL021539.
- Pascual, A., Faugère, Y., Larnicol, G. and Le Traon, P.-Y. 2006. Improved description of the ocean mesoscale variability by combining four satellite altimeters. *Geophysical Research Letters*, **33**, L02611, doi:10.1029/2005GL024633.
- Cheney, R. E., Marsh, J. G. and Beckley, B. D. 1983. Global mesoscale variability from collinear tracks of SEASAT altimeter data. *Journal of Geophysical Research*, **88**, C7, doi:10.1029/JC088iC07p04343.
- (1) Menard, Y. 1983. Observations of eddy fields in the Northwest Atlantic and Northwest Pacific by SEASAT altimeter data. *Journal of Geophysical Research*, **88**, C3, doi:10.1029/JC088iC03p01853. (2) Shum, C. K., Werner, R. A., Sandwell, D. T. *et al.* 1990. Variations of global mesoscale eddy energy observed from Geosat. *Journal of Geophysical Research*, **95**, 17865–17876, doi:10.1029/JC095iC10p17865. (3) Heywood, K., McDonagh, E. and White, M. 1994. Eddy kinetic energy of the North Atlantic subpolar gyre from satellite altimetry. *Journal of Geophysical Research*, **99**, C11, doi:10.1029/94JC01740.
- Fu, L.-L., Chelton, D. B., Le Traon, P.-Y. and Morrow, R. 2010. Eddy dynamics from satellite altimetry. *Oceanography*, **23**, 14–25, doi:10.5670/oceanog.2010.02.
- Meredith, M. P. and Hogg, A. M. 2006. Circumpolar response of Southern Ocean eddy activity to a change in the Southern Annular Mode. *Geophysical Research Letters*, **33**, L16608, doi:10.1029/2006GL026499.
- Pattullo, J. G., Munk, W. H., Revelle, R. and Strong, E. 1955. The seasonal oscillation in sea level. *Journal of Marine Research*, **14**, 88–155.

16. Tsimplis, M. N. and Woodworth, P. L. 1994. The global distribution of the seasonal sea level cycle calculated from coastal tide gauge data. *Journal of Geophysical Research*, **99**, C8, doi:10.1029/94JC01115.
17. (1) Marcos, M. and Tsimplis, M. N. 2007. Variations of the seasonal sea level cycle in southern Europe. *Journal of Geophysical Research*, **112**, C12011, doi:10.1029/2006JC004049. (2) Wijeratne, E. M. S., Woodworth, P. L. and Stepanov, V. N. 2008. The seasonal cycle of sea level in Sri Lanka and Southern India. *Western Indian Ocean Journal of Marine Science*, **7**, 29–43. (3) Zhang, C., Wang, B. and Chen, G. 2006. Annual sea level amphidromes in the South China Sea revealed by merged altimeter data. *Geophysical Research Letters*, **3**, L14606, doi:10.1029/2006GL026493. (4) Torres, R. R. and Tsimplis, M. N. 2012. Seasonal sea level cycle in the Caribbean Sea. *Journal of Geophysical Research*, **117**, C7, doi:10.1029/2012JC008159.
18. Dunne, R. P., Barbosa, S. M. and Woodworth, P. L. 2012. Contemporary sea level in the Chagos Archipelago, central Indian Ocean. *Global and Planetary Change*, **82–83**, 25–37, doi:10.1016/j.gloplacha.2011.11.009.
19. Meyers, G. 1982. Interannual variation in sea level near Truk Island: a bimodal seasonal cycle. *Journal of Physical Oceanography*, **12**, 1161–1168, doi:10.1175/1520-0485(1982)012<1161:IVISLN>2.0.CO;2.
20. Plag, H. P. and Tsimplis, M. N. 1999. Temporal variability of the seasonal sea-level cycle in the North Sea and the Baltic Sea in relation to climate variability. *Global and Planetary Change*, **20**, 173–203, doi:10.1016/S0921-8181(98)00069-1.
21. Hughes, C. W., Tamisiea, M. E., Bingham, R. J. and Williams, J. 2012. Weighing the ocean: using a single mooring to measure changes in the mass of the ocean. *Geophysical Research Letters*, **39**, 17, doi:10.1029/2012GL052935.
22. Vinogradov, S. V. and Ponte, R. M. 2010. Annual cycle in coastal sea level from tide gauges and altimetry. *Journal of Geophysical Research*, **115**, C04021, doi:10.1029/2009JC005767.
23. Vinogradov, S. V., Ponte, R. M., Heimbach, P. and Wunsch, C. 2008. The mean seasonal cycle in sea level estimated from a data-constrained general circulation model. *Journal of Geophysical Research*, **113**, C03032, doi:10.1029/2007JC004496.
24. Lambeck, K. 1980. *The Earth's Variable Rotation: Geophysical Causes and Consequences*. Cambridge: Cambridge University Press.
25. Ekman, M., 1988. The world's longest continued series of sea level observations. *Pure and Applied Geophysics*, **127**, 73–77, doi:10.1007/BF00878691.
26. Trupin, A. and Wahr, J. 1990. Spectroscopic analysis of global tide gauge sea level data. *Geophysical Journal International*, **100**, 441–453, doi:10.1111/j.1365-246X.1990.tb00697.x.
27. Desai, S. 2002. Observing the pole tide with satellite altimetry. *Journal of Geophysical Research*, **107**, 3186, doi:10.1029/2001JC001224.
28. Wunsch, C. 1986. Dynamics of the North Sea pole tide revisited. *Geophysical Journal of the Royal Astronomical Society*, **87**, 869–884, doi:10.1111/j.1365-246X.1986.tb01974.x.
29. Tsimplis, M. N., Flather, R. A. and Vassie, J. M. 1994. The North Sea pole tide described through a tide-surge numerical model. *Geophysical Research Letters*, **21**, 6, doi:10.1029/94GL00181.
30. O'Connor, W. P., Chao, B. F., Zheng, D. and Au, A. Y. 2000. Wind stress forcing of the North Sea 'pole tide'. *Geophysical Journal International*, **142**, 620–630, doi:10.1046/j.1365-246x.2000.00184.x.
31. Wunsch, C. 2001. Comments on 'Windstress forcing of the North Sea "pole tide"', by W. P. O'Connor, B. F. Chao, D. Zheng and A. Y. Au. *Geophysical Journal International*, **146**, 264–265, doi:10.1046/j.1365-246X.2001.00455.x.
32. Chao, B. F., O'Connor, W. P., Zeng, D. and Au, A. Y. 2001. Reply to comment by C. Wunsch on 'Wind stress forcing of the North Sea "Pole Tide"'. *Geophysical Journal International*, **146**, 266, doi:10.1046/j.0956-540x.2001.01454.x.
33. Cartwright, D. E. 1999. *Tides: a Scientific History*. Cambridge: Cambridge University Press.
34. (1) Cartwright, D. E. and Tayler, R. J. 1971. New computations of the tide-generating potential. *Geophysical Journal of the Royal Astronomical Society*, **23**, 45–74, doi:10.1111/j.1365-246X.1971.tb01803.x. (2) Cartwright, D. E. and Edden, A. C. 1973. Corrected tables of tidal harmonics. *Geophysical Journal of the Royal Astronomical Society*, **33**, 253–264, doi:10.1111/j.1365-246X.1973.tb03420.x.
35. Iz, H. B. 2006. How do unmodeled systematic mean sea level variations affect long-term sea level trend estimates from tide gauge data? *Journal of Geodesy*, **40**, 40–46, doi:10.1007/s00190-006-0028-x.
36. Proudman, J. 1960. The condition that a long-period tide shall follow the equilibrium-law. *Geophysical Journal of the Royal Astronomical Society*, **3**, 244–249, doi:10.1111/j.1365-246X.1960.tb00392.x.
37. Doodson, A. T. and Warburg, H. D. 1941. *Admiralty Manual of Tides*. London: His Majesty's Stationery Office.
38. Agnew, D. C. and Farrell, W. E. 1978. Self-consistent equilibrium ocean tides. *Geophysical Journal of the*

- Royal Astronomical Society*, **55**, 171–181, doi:10.1111/j.1365-246X.1978.tb04755.x.
39. Woodworth, P. L. 2012. A note on the nodal tide in sea level records. *Journal of Coastal Research*, **28**, 316–323, doi:10.2112/JCOASTRES-D-11A-00023.1.
 40. Rossiter, J. R. 1967. An analysis of annual sea level variations in European waters. *Geophysical Journal of the Royal Astronomical Society*, **12**, 259–299, doi:10.1111/j.1365-246X.1967.tb03121.x.
 41. Loder, J. W. and Garrett, C. 1978. The 18.6-year cycle of sea surface temperature in shallow seas due to variations in tidal mixing. *Journal of Geophysical Research*, **83**, 1967–1970. doi:10.1029/JC083iC04p01967.
 42. Ponte, R. 1994. Understanding the relation between wind- and pressure-driven sea level variability. *Journal of Geophysical Research*, **99**, C4, doi:10.1029/94JC00217.
 43. Roden, G. I. and Rossby, H. T. 1999. Early Swedish contribution to oceanography: Nils Gissler (1715–71) and the inverted barometer effect. *Bulletin of the American Meteorological Society*, **80**, 675–682.
 44. Ekman, M. 2009. *The Changing Level of the Baltic Sea During 300 Years: A Clue to Understanding the Earth. Åland Islands: Summer Institute for Historical Geophysics (www.historicalgeophysics.ax).*
 45. Ross, J. C. 1854. On the effect of the pressure of the atmosphere on the mean level of the ocean. *Philosophical Transactions of the Royal Society of London*, **144**, 285–296, doi:10.1098/rstl.1854.0013.
 46. Lubbock, J. W. 1836. On the tides at the port of London. *Philosophical Transactions of the Royal Society of London*, **126**, 217–266, doi:10.1098/rstl.1836.0017.
 47. Mathers, E. L. and Woodworth, P. L. 2001. Departures from the local inverse barometer model observed in altimeter and tide gauge data and in a global barotropic numerical model. *Journal of Geophysical Research*, **106**, 6957–6972, doi:10.1029/2000JC000241.
 48. Stewart, R. E. 2005. Vorticity in the ocean. In *Introduction to Physical Oceanography*. Available from oceanworld.tamu.edu/home/course_book.htm.
 49. Woodworth, P. L. 2006. The meteorological data of William Hutchinson and a Liverpool air pressure time series spanning 1768–1999. *International Journal of Climatology*, **26**, 1713–1726, doi:10.1002/joc.1335.
 50. Ponte, R. M. 1993. Variability in a homogeneous global ocean forced by barometric pressure. *Dynamics of Atmospheres and Oceans*, **18**, 209–234, doi:10.1016/0377-0265(93)90010-5.
 51. Wunsch, C. and Stammer, D. 1997. Atmospheric loading and the oceanic “inverted barometer” effect. *Reviews of Geophysics*, **35**, 1, doi:10.1029/96RG03037.
 52. Thompson, K. R., 1986. North Atlantic sea-level and circulation. *Geophysical Journal of the Royal Astronomical Society*, **87**, 15–32, doi:10.1111/j.1365-246X.1986.tb04543.x.
 53. Marcos, M. and Tsimplis, M. N. 2008. Coastal sea level trends in Southern Europe. *Geophysical Journal International*, **175**, 70–82, doi:10.1111/j.1365-246X.2008.03892.x.
 54. Wakelin, S. L., Woodworth, P. L. Flather, R. A. and Williams, J. A. 2003. Sea-level dependence on the NAO over the NW European Continental Shelf, *Geophysical Research Letters*, **30**(7), 1403, doi:10.1029/2003GL017041.
 55. Trenberth, K. E., Jones, P. D., Ambenje, P. et al. 2007. Observations: Surface and Atmospheric Climate Change. In *Climate Change 2007: The Physical Science Basis. Contribution of Working Group I to the Fourth Assessment Report of the Intergovernmental Panel on Climate Change* (eds. S. Solomon, D. Qin, M. Manning et al.). Cambridge: Cambridge University Press.
 56. McPhaden, M. J., Busalacchi, A. J., Cheney, R. et al. 1998. The Tropical Ocean-Global Atmosphere observing system: a decade of progress. *Journal of Geophysical Research*, **103**, C7, doi:10.1029/97JC02906.
 57. Enfield, D. B. and Allen, J. S. 1980. On the structure and dynamics of monthly mean sea level anomalies along the Pacific coast of North and South America. *Journal of Physical Oceanography*, **10**, 557–578, doi:10.1175/1520-0485(1980)010<0557:OTSADO>2.0.CO;2.
 58. Mantua, N. J. and Hare, S. R. 2002. The Pacific Decadal Oscillation. *Journal of Oceanography*, **58**, 35–44.
 59. Saji, N. H. and Yamagata, T. 2003. Possible impacts of Indian Ocean Dipole Mode events on global climate. *Climate Research*, **25**, 151–169.
 60. Pinto, J. G. and Raible, C. C. 2012. Past and recent changes in the North Atlantic Oscillation. *Climate Change*, **3**, 79–90, doi:10.1002/wcc.150.
 61. Thompson, D. W. J. and Wallace, J. M. 1998. The Arctic oscillation signature in the wintertime geopotential height and temperature fields. *Geophysical Research Letters*, **25**, 9, doi:10.1029/98GL00950.
 62. Thompson, D. W. J. and Wallace, J. M. 2000. Annular modes in the extratropical circulation. Part I: Month-to-month variability. *Journal of Climate*, **13**, 1000–1016, doi:10.1175/1520-0442(2000)013<1000:AMITEC>2.0.CO;2, and Thompson, D. W. J., Wallace, J. M. and Hegerl, G. C. 2000. Annular modes in the extratropical circulation. Part II: Trends. *Journal of Climate*, **13**, 1018–1036, doi:10.1175/1520-0442(2000)013<1018:AMITEC>2.0.CO;2.
 63. Marshall, G. J. 2003. Trends in the Southern Annular Mode from observations and reanalyses. *Journal of*

- Climate*, **16**, 4134–4143, doi:10.1175/1520-0442(2003)016<4134:TITSAM>2.0.CO;2.
64. Parker, D., Folland, C., Scaife, A. *et al.* 2007. Decadal to multidecadal variability and the climate change background. *Journal of Geophysical Research*, **112**, D18115, doi:10.1029/2007JD008411.
 65. d'Orgeville, M. and Peltier, W. R. 2007. On the Pacific Decadal Oscillation and the Atlantic Multidecadal Oscillation: might they be related? *Geophysical Research Letters*, **34**, L23705, doi:10.1029/2007GL031584.
 66. Woolf, D. K., Shaw, A. G. P. and Tsimplis, M. N. 2003. The influence of the North Atlantic Oscillation on sea level variability in the North Atlantic Region. *The Global Atmosphere and Ocean System*, **9**(4), 145–167, doi:10.1080/10236730310001633803.
 67. Aoki, S. 2002. Coherent sea level response to the Antarctic Oscillation. *Geophysical Research Letters*, **29**, 1950, doi:10.1029/2002GL015733.
 68. Hughes, C. W., Woodworth, P. L., Meredith, M. P. *et al.* 2003. Coherence of Antarctic sea levels, Southern Hemisphere Annular Mode, and flow through Drake Passage. *Geophysical Research Letters*, **30**(9), 1464, doi:10.1029/2003GL017240.
 69. Hibbert, A., Leach, H., Woodworth, P. L., Hughes, C. W. and Roussenov, V. M. 2010. Quasi-biennial modulation of the Southern Ocean coherent mode. *Quarterly Journal of the Royal Meteorological Society*, **136**, 755–768, doi:10.1002/qj.581.
 70. Meredith, M. P., Woodworth, P. L., Hughes, C. W. and Stepanov, V. 2004. Changes in the ocean transport through Drake Passage during the 1980s and 1990s, forced by changes in the Southern Annular Mode. *Geophysical Research Letters*, **31**, L21305, doi:10.1029/2004GL021169.
 71. Woodworth, P. L., Hughes, C. W., Blackman, D. L. *et al.* 2006. Antarctic peninsula sea levels: a real time system for monitoring Drake Passage transport. *Antarctic Science*, **18**(3), 429–436, doi:10.1017/S0954102006000472.
 72. Bingham, R. J. and Hughes, C. W. 2009. Signature of the Atlantic meridional overturning circulation in sea level along the eastcoast of North America. *Geophysical Research Letters*, **36**, L02603, doi:10.1029/2008GL036215.
 73. Woodworth, P. L., Flather, R. A., Williams, J. A., Wakelin, S. L. and Jevrejeva, S. 2007. The dependence of UK extreme sea levels and storm surges on the North Atlantic Oscillation. *Continental Shelf Research*, **27**, 935–946, doi:10.1016/j.csr.2006.12.007.
 74. Menéndez, M. and Woodworth, P. L. 2010. Changes in extreme high water levels based on a quasi-global tide-gauge dataset. *Journal of Geophysical Research*, **115**, C10011, doi:10.1029/2009JC005997.
 75. Marcos, M., Tsimplis, M. N. and Shaw, A. G. P. 2009. Sea level extremes in southern Europe. *Journal of Geophysical Research*, **114**, C01007, doi:10.1029/2008JC004912.
 76. Douglas, B. C. 1992. Global sea level acceleration. *Journal of Geophysical Research*, **97**, C8, doi:10.1029/92JC01133.
 77. Hughes, C. W. and Williams, S. D. P. 2010. The color of sea level: importance of spatial variations in spectral shape for assessing the significance of trends. *Journal of Geophysical Research*, **115**, C10048, doi:10.1029/2010JC006102.
 78. Kantha, L. H. and Clayson, C. A. 2000. *Numerical Models of Oceans and Oceanic Processes*. International Geophysics Series, Volume 66. San Diego, CA: Academic Press.
 79. Griffies, S. M. 2004. *Fundamentals of Ocean Climate Models*. Princeton, New Jersey: Princeton University Press.
 80. Marshall, J., Hill, C., Perelman, L. and Adcroft, A. 1997a. Hydrostatic, quasi-hydrostatic, and nonhydrostatic ocean modelling. *Journal of Geophysical Research*, **102**, C3, doi:10.1029/96JC02775102, and Marshall, J., Adcroft, A., Hill, C., Perelman, L. and Heisey, C. 1997b. A finite-volume, incompressible Navier-Stokes model for studies ocean on parallel computers. *Journal of Geophysical Research*, **102**, C3, doi:10.1029/96JC02776.
 81. Hill, E. M., Ponte, R. M. and Davis, J. L. 2007. Dynamic and regression modeling of ocean variability in the tide-gauge record at seasonal and longer periods. *Journal of Geophysical Research*, **112**, C05007, doi:10.1029/2006JC003745.
 82. Smith, D. M. and Murphy, J. M. 2007. An objective ocean temperature and salinity analysis using covariances from a global climate model. *Journal of Geophysical Research*, **112**, C02022, doi:10.1029/2005JC003172.
 83. Joyce, T. M. and Robbins, P. 1996. The long-term hydrographic record at Bermuda. *Journal of Climate*, **9**, 3121–3131, doi:10.1175/1520-0442(1996)009<3121:TLTHRA>2.0.CO;2.
 84. Woodworth, P. L., Foden, P. R., Jones, D. S. *et al.* 2012. Sea level changes at Ascension Island in the last half century. *African Journal of Marine Science*, **34**, 443–452, doi:10.2989/1814232X.2012.689623.
 85. Gregory, J. M., Church, J. A., Boer, G. J. *et al.* 2001. Comparison of results from several AOGCMs for global and regional sea-level change 1900–2100. *Climate Dynamics*, **18**, 225–240, doi:10.1007/s003820100180.
 86. Rohling, E. J., Grant, K., Bolshaw, M. *et al.* 2009. Antarctic temperature and global sea level closely

- coupled over the past five glacial cycles. *Nature Geoscience*, **2**, 500–504, doi:10.1038/ngeo557.
87. Deschamps, P., Durand, N., Bard, E. *et al.* 2012. Ice-sheet collapse and sea-level rise at the Bølling warming 14,600 years ago. *Nature Climate Change*, **483**, 559–564, doi:10.1038/nature10902.
 88. Lambeck, K., Woodroffe, C. D., Antonioli, F. *et al.* 2010. Palaeoenvironmental records, geophysical modelling and reconstruction of sea-level trends and variability on centennial and longer time scales. In *Understanding Sea-Level Rise and Variability* (eds J. A. Church, P. L. Woodworth, T. Aarup and W. S. Wilson), pp. 61–121. London: Wiley-Blackwell.
 89. Church, J. A., Gregory, J. M., Huybrechts, O. *et al.* 2001. Changes in sea level. In *Climate Change 2001: The Scientific Basis. Contribution of Working Group I to the Third Assessment Report of the Intergovernmental Panel on Climate Change* (eds J. T. Houghton, Y. Ding, D. J. Griggs *et al.*). Cambridge: Cambridge University Press.
 90. Bindoff, N., Willebrand, J., Artale, V. *et al.* 2007. Observations: oceanic climate change and sea level. In *Climate Change 2007: The Physical Science Basis. Contribution of Working Group I to the Fourth Assessment Report of the Intergovernmental Panel on Climate Change* (eds S. Solomon, D. Qin, and M. Manning). Cambridge: Cambridge University Press.
 91. Church, J. A. *et al.* 2014. Sea level change. In *Climate Change 2013: The Physical Science Basis. Working Group I Report of the Fifth Scientific Assessment of the Intergovernmental Panel on Climate Change*. Cambridge: Cambridge University Press.
 92. Masson-Delmotte, V. *et al.* 2014. Information from paleoclimate archives. In *Climate Change 2013: The Physical Science Basis. Working Group I Report of the Fifth Scientific Assessment of the Intergovernmental Panel on Climate Change*. Cambridge: Cambridge University Press.
 93. Cronin, T. M. 2012. Was pre-twentieth century sea level stable? *Eos, Transactions of the American Geophysical Union*, **92**, 455–456.
 94. Williams, R. G. and Follows, M. J. 2011. *Ocean Dynamics and the Carbon Cycle: Principles and Mechanisms*. Cambridge: Cambridge University Press.
 95. Woodworth, P. L., Gehrels, W. R and Nerem, R. S. 2011. Nineteenth and twentieth century changes in sea level. *Oceanography*, **24**(2), 80–93, doi:10.5670/oceanog.2011.29.
 96. Lambeck, K., Anzidei, M., Antonioli, F., Benini, A. and Esposito, E. 2004. Sea level in Roman time in the central Mediterranean and implications for modern sea level rise. *Earth and Planetary Science Letters*, **224**, 563–575, doi:10.1016/j.epsl.2004.05.031.
 97. Flemming, N. C. 1978. Holocene eustatic changes and coastal tectonics in the north east Mediterranean: implications for models of crustal consumption. *Philosophical Transactions of the Royal Society of London, A*, **289**, 405–458, doi:10.1098/rsta.1978.0065.
 98. Sivan, D., Wdowinski, S., Lambeck, K., Galilid, E. and Raban, A. 2001. Holocene sea-level changes along the Mediterranean coast of Israel, based on archaeological observations and numerical model. *Palaeogeography, Palaeoclimatology, Palaeoecology*, **167**, 101–117, doi:10.1016/S0031–0182(00)00234–0.
 99. Toker, E., Sivan, D., Stern, E. *et al.* 2012. Evidence for centennial scale sea level variability during the Medieval Climate Optimum (Crusader Period) in Israel, eastern Mediterranean. *Earth and Planetary Science Letters*, **315–316**, 51–61, doi:10.1016/j.epsl.2011.07.019.
 100. Camuffo, D. and Sturaro, G. 1983. Sixty-cm submersion of Venice discovered thanks to Canaletto's paintings. *Climatic Change*, **58**, 333–343, doi:10.1023/A:1023902120717.
 101. Kemp, A. C., Horton, B. P., Donnelly, J. P. *et al.* 2011. Climate related sea-level variations over the past two millennia. *Proceedings of the National Academy of Sciences*, **108**, 11017–11022, doi:10.1073/pnas.1015619108.
 102. Engelhart, S. E., Horton, B. P. and Kemp, A. C. 2011. Holocene sea-level changes along the United States' Atlantic Coast. *Oceanography* **24**, 70–79, doi:10.5670/oceanog.2011.28.
 103. Long, A. J., Woodroffe, S. A., Milne, G. A. *et al.* 2012. Relative sea-level change in Greenland during the last 700 yrs and ice sheet response to the Little Ice Age. *Earth and Planetary Science Letters*, **315–316**, 76–85, doi:10.1016/j.epsl.2011.06.027.
 104. Gehrels, W. R., Kirby, J., Prokoph, A. *et al.* 2005. Onset of recent rapid sea level rise in the western Atlantic Ocean. *Quaternary Science Reviews*, **24**, 2083–2100.
 105. Gehrels, W. R., Hayward, B. W., Newnham, R. M. and Southall, K. E. 2008. A 20th century sea-level acceleration in New Zealand. *Geophysical Research Letters*, **35**, L02717, doi 10.1029/2007GL032632.
 106. Kemp, A. C., Horton, B. P., Culver, S. J. *et al.* 2009. Timing and magnitude of recent accelerated sea-level rise (North Carolina, United States). *Geology*, **37**, 1035–1038, doi:10.1130/G30352A.1.
 107. Gehrels, W. R., Callard, S. L., Moss, P. T. *et al.* 2012. Nineteenth and twentieth century sea-level changes in Tasmania and New Zealand. *Earth and Planetary*

- Science Letters*, **315**–316, 94–102, doi:10.1016/j.epsl.2011.08.046.
108. Donnelly, J. P., Cleary, P., Newby, P. and Ettinger, R. 2004. Coupling instrumental and geological records of sea level change: evidence from southern New England of an increase in the rate of sea level rise in the late 19th century. *Geophysical Research Letters*, **31**, L05203, doi:10.1029/2003GL018933.
109. Leorri, E., Horton, B. P. and Ceareta, A. 2008. Development of a foraminifera-based transfer function in the Basque marshes, N. Spain: implications for sea-level studies in the Bay of Biscay. *Marine Geology*, **251**, 60–74, doi:10.1016/j.margeo.2008.02.005.
110. Gehrels, W. R. and Woodworth, P. L. 2013. When did modern rates of sea-level rise start? *Global and Planetary Change*, **100**, 263–277, doi:10.1016/j.gloplacha.2012.10.020.
111. van Veen, J. 1945. Bestaat er een geologische bodemdaling te Amsterdam sedert 1700? *Tijdschrift Koninklijk Nederlandsch Aardrijkskundig Genootschap*, 2nd Series, Part 62.
112. Woodworth, P. L. 1999. High waters at Liverpool since 1768: the UK's longest sea level record. *Geophysical Research Letters*, **26**, 11, doi:10.1029/1999GL900323.
113. Wöppelmann, G., Pouvreau, N., Coulomb, A., Simon, B. and Woodworth, P. 2008. Tide gauge datum continuity at Brest since 1711: France's longest sea-level record. *Geophysical Research Letters*, **35**, L22605, doi:10.1029/2008GL035783.
114. The first such tide gauge is often credited to Palmer, H. R. 1831. Description of a graphical register of tides and winds. *Philosophical Transactions of the Royal Society of London*, **121**, 209–213. However, the same ideas were being pursued at many places at around the same time. The first self-registering tide gauge in the United States was made by Joseph Saxton for the U.S. Coast Survey in 1851. For a history see: Matthäus, W. 1972. On the history of recording tide gauges. *Proceedings of the Royal Society of Edinburgh, B*, **73**, 26–34, doi:10.1017/S0080455X00002083.
115. Woodworth, P. L., Menéndez, M. and Gehrels, W. R. 2011. Evidence for century-timescale acceleration in mean sea levels and for recent changes in extreme sea levels. *Surveys in Geophysics*, **32**(4–5), 603–618 (erratum page 619), doi:10.1007/s10712-011-9112-8.
116. Peltier, W. R. 2004. Global glacial isostasy and the surface of the ice-age Earth: the ICE-5G (VM2) model and GRACE. *Annual Review of Earth and Planetary Sciences*, **32**, 111–149, doi:10.1146/annurev.earth.32.082503.144359.
117. Douglas, B. C. 1991. Global sea level rise. *Journal of Geophysical Research*, **96**, C4, doi:10.1029/91JC00064.
118. Holgate, S. J. and Woodworth, P. L. 2004. Evidence for enhanced coastal sea level rise during the 1990s. *Geophysical Research Letters*, **31**, L07305, doi:10.1029/2004GL019626.
119. Merrifield, M. A., Merrifield, S. T. and Mitchum, G. T. 2009. An anomalous recent acceleration of global sea level rise. *Journal of Climate*, **22**, 5772–5781, doi:10.1175/2009JCLI2985.1.
120. Nakiboglu, S. M. and Lambeck, K. 1991. Secular sea-level change. In *Glacial Isostasy, Sea-Level and Mantle Rheology* (eds. R. Sabadini *et al.*), pp. 237–258. Dordrecht: Kluwer Academic Publishers.
121. Church, J. A. and White, N. J. 2011. Sea-level rise from the late 19th to the early 21st century. *Surveys in Geophysics*, **32**, 585–602, doi:10.1007/s10712-011-9119-1.
122. Ray, R. D. and Douglas, B. C. 2011. Experiments in reconstructing twentieth-century sea levels. *Progress in Oceanography*, **91**, 496–515, doi:10.1016/j.pcean.2011.07.021.
123. Llovel, W., Cazenave, A., Rogel, P., Lombard, A. and Nguyen, M. B. 2009. Two-dimensional reconstruction of past sea level (1950–2003) from tide gauge data and an Ocean General Circulation Model. *Climate of the Past*, **5**, 217–227, doi:www.clim-past.net/5/217/2009/.
124. Hamlington, B. D., Leben, R. R., Nerem, R. S., Han, W. and Kim, K.-Y. 2011. Reconstructing sea level using cyclostationary empirical orthogonal functions. *Journal of Geophysical Research*, **116**, C12015, doi:10.1029/2011JC007529.
125. Christiansen, B., Schmith, T. and Thejll, P. 2010. A surrogate ensemble study of sea level reconstructions. *Journal of Climate*, **23**, 4306–4326, doi:10.1175/2010JCLI3014.1.
126. Jevrejeva, S., Grinsted, A., Moore, J. C. and Holgate, S. J. 2006. Nonlinear trends and multiyear cycles in sea level records. *Journal of Geophysical Research*, **111**, C09012, doi:10.1029/2005JC003229.
127. Wenzel, M. and Schröter, J. 2010. Reconstruction of regional mean sea level anomalies from tide gauges using neural networks. *Journal of Geophysical Research*, **115**, C08013, doi:10.1029/2009JC005630.
128. Woodworth, P. L., White, N. J., Jevrejeva, S. *et al.* 2009. Evidence for the accelerations of sea level on multi-decade and century timescales. *International Journal of Climatology*, **29**, 777–789, doi:10.1002/joc.1771.
129. Chambers, D. P., Merrifield, M. A. and Nerem, R. S. 2012. Is there a 60-year oscillation in global mean sea level? *Geophysical Research Letters*, **39**, 18, doi:10.1029/2012GL052885.
130. Douglas, B. C., Kearney, M. S. and Leatherman, S. P. (eds.) 2000. *Sea-Level Rise: History and Consequences*. San Diego, CA: Academic Press.
131. Holgate, S. J. and Woodworth, P. L. 2004. Evidence for enhanced coastal sea level rise during the 1990s.

- Geophysical Research Letters*, **31**, L07305, doi:10.1029/2004GL019626.
132. Prandi, P., Cazenave, A. and Becker, M. 2009. Is coastal mean sea level rising faster than the global mean? A comparison between tide gauges and satellite altimetry over 1993–2007. *Geophysical Research Letters*, **36**, L05602, doi:10.1029/2008GL036564.
 133. Holgate, S. J. 2007. On the decadal rates of sea level change during the twentieth century. *Geophysical Research Letters*, **34**, L01602, doi:10.1029/2006GL028492.
 134. Church, J. A., White, N. J., Aarup, T. *et al.* 2008. Understanding global sea levels: past, present and future. *Sustainability Science*, **3**, 9–22, doi:10.1007/s11625-008-0042-4.
 135. Woodworth, P. L., Pugh, D. T. and Bingley, R. M. 2010. Long term and recent changes in sea level in the Falkland Islands. *Journal of Geophysical Research*, **115**, C09025, doi:10.1029/2010JC006113. Correction in *JGR*, **116**, C11030, doi:10.1029/2011JC007685.
 136. Hunter, J., Coleman, R. and Pugh, D. 2003 The sea level at Port Arthur, Tasmania, from 1841 to the present. *Geophysical Research Letters*, **30**, 1401, doi:10.1029/2002GL016813.
 137. Woodworth, P. L. 1990. A search for accelerations in records of European mean sea level. *International Journal of Climatology*, **10**, 129–143, doi:10.1002/joc.3370100203.
 138. Tsimplis, M. N. and Baker, T. F. 2000. Sea level drop in the Mediterranean Sea: an indicator of deep water salinity and temperature changes? *Geophysical Research Letters*, **27**, 12, doi:10.1029/1999GL007004.
 139. Watson, P. J. 2011. Is there evidence yet of acceleration in mean sea level rise around mainland Australia? *Journal of Coastal Research*, **27**, 368–377, doi:10.2112/JCOASTRES-D-10-00141.1.
 140. Stammer, D. and Gregory, J. 2011. Understanding processes contributing to regional sea level change. *Eos, Transactions American Geophysical Union*, **92**(39), 328, doi:10.1029/2011EO390004. (This is a Meeting Report of a World Climate Research Programme/ Intergovernmental Oceanographic Commission conference on regional sea level change. A fuller report is available from http://www.wcrp-climate.org/documents/Regional_SeaLevel_workshop.pdf.)
 141. Boon, J. D. 2012. Evidence of sea level acceleration at U.S. and Canadian tide stations, Atlantic coast, North America. *Journal of Coastal Research*, **28**, 1437–1445, doi:10.2112/JCOASTRES-D-12-00102.1.
 142. Sallenger, A. H. Jr, Doran, K. S. and Howd, P. A. 2012. Hotspot of accelerated sea-level rise on the Atlantic coast of North America. *Nature Climate Change*, **2**, 884–888, doi:10.1038/NCLIMATE1597.
 143. (1) Testut, L., Wöppelmann, G., Simon, B. and Techine, P. 2006. The sea level at Port-aux-Français, Kerguelen Island, from 1950 to the present. *Ocean Dynamics*, **56**, 464–472, doi:10.1007/s10236-005-0056-8. (2) Testut, L., Martin Miguez, B., Wöppelmann, G. *et al.* 2010. Sea level at Saint Paul Island, southern Indian Ocean, from 1874 to the present. *Journal of Geophysical Research*, **115**, C12028, doi:10.1029/2010JC006404. (3) Marcos, M., Puyol, B., Wöppelmann, G., Herrero, C. and García-Fernández, M. J. 2011. The long sea level record at Cadiz (southern Spain) from 1880 to 2009. *Journal of Geophysical Research*, **116**, C12003, doi:10.1029/2011JC007558. (4) Araújo, I. B., Bos, M. S., Bastos, L. C. and Cardoso, M. M. 2013. Analysing the 100 year sea level record of Leixões, Portugal. *Journal of Hydrology*, **481**, 76–84, doi:10.1016/j.jhydrol.2012.12.019. (5) Gouriou, T., Martin Miguez, B. and Wöppelmann, G. 2013. Reconstruction of a two-century long sea level record for the Pertuis D'Antioche (France). *Continental Shelf Research*, 61–62, 31–40, doi:10.1016/j.csr.2013.04.028.
 144. Caldwell, P. C. 2013. Tide gauge data rescue. In *Proceedings of the UNESCO Conference on The Memory of the World in the Digital Age: Digitization and Preservation* (eds. L. Duranti and E. Shaffer), pp. 134–149. 26–28 September 2012, Vancouver, British Columbia, Canada. Available from www.unesco.org.
 145. Ablain, M., Cazenave, A., Valladeau, G. and Guinehut, S. 2009. A new assessment of the error budget of global mean sea level rate estimated by satellite altimetry over 1993–2008. *Ocean Science*, **5**, 193–201, www.ocean-sci.net/5/193/2009/.
 146. (1) Leuliette, E. W., Nerem, R. S. and Mitchum, G. T. 2004. Calibration of TOPEX/Poseidon and Jason altimeter data to construct a continuous record of mean sea level change. *Marine Geodesy*, **27**, 79–94, doi:10.1080/01490410490465193. (2) Nerem, R. S., Chambers, D., Choe, C. and Mitchum, G. T. 2010. Estimating mean sea level change from the TOPEX and Jason altimeter missions. *Marine Geodesy*, **33**, Supplement 1, 435–446, doi:10.1080/01490419.2010.491031.
 147. Boening, C., Willis, J. K., Landerer, F. W., Nerem, R. S. and Fasullo, J. 2012. The 2011 La Niña: So strong, the oceans fell. *Geophysical Research Letters*, **39**, L19602, doi:10.1029/2012GL053055.
 148. Meyssignac, B. and Cazenave, A. 2012. Sea level: a review of present-day and recent-past changes and variability. *Journal of Geodynamics*, **58**, 96–109, doi:10.1016/j.jog.2012.03.005.
 149. Lowe, J. A., and Gregory, J. M. 2006. Understanding projections of sea level rise in a Hadley Centre coupled climate model. *Journal of Geophysical Research*, **111**, C11014, doi:10.1029/2005JC003421.

150. Milne, G. A., Gehrels, W. R., Hughes, C. W. and Tamisiea, M. E. 2009. Identifying the causes of sea-level change. *Nature Geoscience*, **2**, 471–478, doi:10.1038/ngeo544.
151. Munk, W., 2002. Twentieth century sea level: an enigma. *Proceedings of the National Academy of Sciences*, **99**, 6550–6555, doi:10.1073/pnas.092704599.
152. Church, J. A., White, N. J., Konikow, L. F. *et al.* 2011. Revisiting the Earth's sea-level and energy budgets from 1961 to 2008. *Geophysical Research Letters*, **38**, L18601, doi:10.1029/2011GL048794.
153. Gregory, J. M., White, N. J., Church, J. A. *et al.* 2012. Twentieth-century global-mean sea-level rise: is the whole greater than the sum of the parts? *Journal of Climate*, **26**, 4476–4499, doi:10.1175/JCLI-D-12-00319.1.
154. Bindoff, N. L. *et al.* 2014. Detection and attribution of climate change: from global to regional. In *Climate Change 2013: The Physical Science Basis. Working Group I Report of the Fifth Scientific Assessment of the Intergovernmental Panel on Climate Change*. Cambridge: Cambridge University Press.
155. (1) Gleckler, P. K., AchutaRao, K., Gregory, J. M. *et al.* 2006. Krakatoa lives: the effect of volcanic eruptions on ocean heat content and thermal expansion. *Geophysical Research Letters*, **33**, L17702, doi:10.1029/2006GL026771. (2) Gregory, J. M., Lowe, J. A. and Tett, S. F. B. 2006. Simulated global-mean sea level changes over the last half-millennium. *Journal of Climate*, **19**, 4576–4591, doi:10.1175/JCLI3881.1.
156. Stenchikov, G., Delworth, T. L., Ramaswamy, V. *et al.* 2009. Volcanic signals in oceans. *Journal of Geophysical Research*, **114**, D16104, doi:10.1029/2008JD011673.
157. Church, J. A., White, N. J. and Arblaster, J. M. 2005. Significant decadal-scale impact of volcanic eruptions on sea level and ocean heat content. *Nature*, **433**, 74–77, doi:10.1038/nature04237.
158. Grinsted, A., Moore, J. C. and Jevrejeva, S. 2007. Observational evidence for volcanic impact on sea level and the global water cycle. *Proceedings of the National Academy of Sciences*, **104**, 19730–19734, doi:10.1073/pnas.0705825104.
159. Miller, L. and Douglas, B. C. 2007. Gyre-scale atmospheric pressure variations and their relation to 19th and 20th century sea level rise. *Geophysical Research Letters*, **34**, L16602, doi:10.1029/GL030862.
160. Sturges, W. and Douglas, B. C. 2011. Wind effects on estimates of sea level rise. *Journal of Geophysical Research*, **116**, C06008, doi:10.1029/2010JC006492.
161. Woodworth, P. L., Pouvreau, N. and Wöppelmann, G. 2010. The gyre-scale circulation of the North Atlantic and sea level at Brest. *Ocean Science*, **6**, 185–190, doi: www.ocean-sci.net/6/185/2010/.
162. (1) Merrifield, M. A., 2011. A shift in western tropical Pacific sea-level trends during the 1990s. *Journal of Climate*, **24**, 4126–4138, doi:10.1175/2011JCLI3932.1. (2) Merrifield, M. A., Thompson, P. R. and Lander, M. 2012. Multidecadal sea level anomalies and trends in the western tropical Pacific. *Geophysical Research Letters*, **39**, L13602, doi:10.1029/2012GL052032.
163. Timmermann, A., McGregor, S. and Jin, F. F., 2010. Wind effects on past and future regional sea level trends in the southern Indo-Pacific. *Journal of Climate*, **23**, 4429–4437, doi:10.1175/2010JCLI3519.1.
164. Bromirski, P. D., Miller, A. J., Flick, R. E. and Auad, G. 2011. Dynamical suppression of sea level rise along the Pacific coast of North America: indications for imminent acceleration. *Journal of Geophysical Research*, **116**, C07005, doi:10.1029/2010JC006759.
165. Han, W., Meehl, G. A., Rajagopalan, B. *et al.* 2010. Patterns of Indian Ocean sea-level change in a warming climate. *Nature Geoscience*, **3**, 546–550, doi:10.1038/ngeo901.
166. Tapley, B. D., Bettadpur, S., Watkins, M. and Reigber, C. 2004. The gravity recovery and climate experiment: mission overview and early results. *Geophysical Research Letters*, **31**, L09607, doi:10.1029/2004GL01992.
167. Chambers, D. P. and Bonin, J. A. 2012. Evaluation of Release 05 time-variable gravity coefficients over the ocean. *Ocean Science*, **8**, 859–868, www.ocean-sci.net/8/859/2012.
168. (1) Chambers, D. P., Wahr, J., Tamisiea, M. E. and Nerem, R. S. 2010. Ocean mass from GRACE and glacial isostatic adjustment. *Journal of Geophysical Research*, **115**, B11415, doi:10.1029/2010JB007530. (2) Tamisiea, M. E. 2011. Ongoing glacial isostatic contributions to observations of sea level change. *Geophysical Journal International*, **186**, 1036–1044, doi:10.1111/j.1365-246X.2011.05116.x. (3) Peltier, W. R., Drummond, R. and Roy, K. 2012. Comment on “Ocean mass from GRACE and glacial isostatic adjustment” by D. P. Chambers *et al.* *Journal of Geophysical Research*, **117**, B11403, doi:10.1029/2011JB008967.
169. Gould, J. *et al.* 2004. Argo profiling floats bring new era of in situ ocean observations. *Eos, Transactions of the American Geophysical Union*, **85**(19), 185, doi:10.1029/2004EO190002.
170. (1) Leuliette, E. and Miller, L. 2009. Closing the sea level budget with altimetry, Argo and GRACE. *Geophysical Research Letters*, **36**, L04608, doi:10.1029/

- 2008GL036010. (2) Leuliette, E. W. and Willis, J. K. 2011. *Balancing the sea level budget*. *Oceanography*, **24**, 122–129, doi:10.5670/oceanog.2011.32.
171. Rhein, M. *et al.* 2014. Observations: ocean. In *Climate Change 2013: The Physical Science Basis. Working Group I Report of the Fifth Scientific Assessment of the Intergovernmental Panel on Climate Change*. Cambridge: Cambridge University Press.
172. Velicogna, I. 2009. Increasing rates of ice mass loss from the Greenland and Antarctic ice sheets revealed by GRACE. *Geophysical Research Letters*, **36**, L19503, doi:10.1029/2009GL040222.
173. Schrama, E. J. O. and Wouters, B. 2011. Revisiting Greenland ice sheet mass loss observed by GRACE. *Journal of Geophysical Research*, **116**, B02407, doi:10.1029/2009JB006847.
174. Chen, J. L., Wilson, C. R., Tapley, B. D., Blankenship, D. D. and Ivins, E. R. 2007. Patagonia icefield melting observed by Gravity Recovery and Climate Experiment (GRACE). *Geophysical Research Letters*, **34**, L22501, doi:10.1029/2007GL031871.
175. Luthcke, S. B., Arendt, A. A., Rowlands, D. D., McCarthy, J. J. and Larsen, C. F. 2008. Recent glacier mass changes in the Gulf of Alaska region from GRACE mascon solutions. *Journal of Glaciology*, **54**, 767–777, doi:10.3189/002214308787779933.
176. Jacob, T., Wahr, J., Pfeffer, W. T. and Swenson, S. 2012. Recent contributions of glaciers and ice caps to sea level rise. *Nature*, **482**, 514–518, doi:10.1038/nature10847.
177. Llovel, W., Becker, M., Cazenave, A., Crétaux, J. F. and Ramillien, G. 2010. Global land water storage change from GRACE over 2002–2009: inference on sea level. *Comptes Rendus Geoscience*, **342**, 179–188, doi:10.1016/j.crte.2009.12.004.
178. Whitehouse, P. L., Bentley, M. J., Milne, G. A., King, M. A. and Thomas, I. D. 2012. A new glacial isostatic adjustment model for Antarctica: calibrated and tested using observations of relative sea-level change and present-day uplift rates. *Geophysical Journal International*, **190**, 1464–1482, doi:10.1111/j.1365-246X.2012.05557.x.
179. Comiso, J. C. *et al.* 2014. Observations: cryosphere. In *Climate Change 2013: The Physical Science Basis. Working Group I Report of the Fifth Scientific Assessment of the Intergovernmental Panel on Climate Change*. Cambridge: Cambridge University Press.
180. Roemmich, D. and the Argo Steering Team. 2009. Argo: the challenge of continuing 10 years of progress. *Oceanography*, **22**, 46–55, doi:10.5670/oceanog.2009.65.
181. Wilson, W. S., Abdalati, W., Alsdorf, D. *et al.* 2010. Observing systems needed to address sea-level rise and variability. In *Understanding Sea-Level Rise and Variability* (eds. J. A. Church, P. L. Woodworth, T. Aarup and W. S. Wilson), pp. 376–401. London: Wiley-Blackwell.
182. Roberts, D. L., Karkanis, P., Jacobs, Z., Mearns, C. W. and Roberts, R. G. 2012. Melting ice sheets 400,000 yr ago raised sea level by 13 m: past analogue for future trends. *Earth and Planetary Science Letters*, **357–358**, 226–237, doi:10.1016/j.epsl.2012.09.006.
183. Kopp, R. E., Simons, F. J., Mitrovica, J. X., Maloof, A. C. and Oppenheimer, M. 2009. Probabilistic assessment of sea level during the last interglacial stage. *Nature*, **462**, 863–867, doi:10.1038/nature08686.
184. Dutton, A. and Lambeck, K. 2012. Ice volume and sea level during the last interglacial. *Science*, **337**, 216–219, doi:10.1126/science.1205749.
185. McKay, N. P., Overpeck, J. T. and Otto-Bliesner, B. L. 2011. The role of ocean thermal expansion in Last Interglacial sea level rise. *Geophysical Research Letters*, **38**, L14605, doi:10.1029/2011GL048280.
186. NEEM community members. 2013. Eemian interglacial reconstructed from a Greenland folded ice core. *Nature*, **493**, 489–494, doi:10.1038/nature11789.
187. Hansen, J. E. and Sato, M. 2012. Paleoclimate implications for human-made climate change. In *Climate Change: Inferences From Paleoclimate and Regional Aspects* (eds. A. Berger, F. Mesinger and D. Šijački), pp. 21–48. Berlin: Springer, doi:10.1007/978-3-7091-0973-1_2.
188. Rohling, E. J., Grant, K., Hemleben, Ch. *et al.* 2008. High rates of sea-level rise during the last interglacial period. *Nature Geoscience*, **1**, 38–42, doi:10.1038/ngeo.2007.28.
189. Knutti, R. and Hegerl, G. C. 2008. The equilibrium sensitivity of the Earth's temperature to radiation changes. *Nature Geoscience*, **1**, 735–743, doi:10.1038/ngeo337.
190. Planton, S. (ed). 2014. Glossary. In *Climate Change 2013: The Physical Science Basis. Working Group I Report of the Fifth Scientific Assessment of the Intergovernmental Panel on Climate Change*, Annex III. Cambridge: Cambridge University Press.
191. Church, J. A., Gregory, J. M., White, N. J., Platten, S. M. and Mitrovica, J. X. 2011. Understanding and projecting sea level change. *Oceanography*, **24**, 130–143, doi:10.5670/oceanog.2011.33.
192. Yin, J., Griffies, S. M. and Stouffer, R. J. 2010. Spatial variability of sea level rise in twenty-first century projections. *Journal of Climate*, **23**, 4585–4607, doi:10.1175/2010JCLI3533.1.
193. Tamisiea, M. E. and Mitrovica, J. X. 2011. The moving boundaries of sea level change: understanding the

- origins of geographic variability. *Oceanography*, **24**, 24–39, doi:10.5670/oceanog.2011.25.
194. Church, J. A., Aarup, T., Woodworth, P. L. *et al.* 2010. Sea-level rise and variability: synthesis and outlook for the future. In *Understanding Sea-Level Rise and Variability* (eds. J. A. Church, P. L. Woodworth, T. Aarup and W. S. Wilson), pp. 402–419. London: Wiley-Blackwell.
195. Rahmstorf, S., Cazenave, A., Church, J. A. *et al.* 2007. Recent climate observations compared to projections. *Science*, **316**, 709, doi:10.1126/science.1136843.
196. Rahmstorf, S. 2007. A semi-empirical approach to projecting future sea-level rise. *Science*, **315**, 368–370, doi:10.1126/science.1135456.
197. Horton, R., Herweijer, C., Rosenzweig, C. *et al.* 2008. Sea level rise projections for current generation CGCMs based on the semi-empirical method. *Geophysical Research Letters*, **35**, L02715, doi:10.1029/2007GL032486.
198. Vermeer, M. and Rahmstorf, S. 2009. Global sea level linked to global temperature. *Proceedings of the National Academy of Sciences*, **106**, 21527–21532, doi:10.1073/pnas.0907765106.
199. Grinsted, A., Moore, J. C. and Jevrejeva, S. 2010. Reconstructing sea level from paleo and projected temperatures 200 to 2100. *Climate Dynamics*, **34**, 461–472, doi:10.1007/s00382-008-0507-2.
200. Holgate, S., Jevrejeva, S., Woodworth, P. and Brewer, S. 2007. Comment on “A semi-empirical approach to projecting future sea-level rise”. *Science*, **317**, 1866, doi:10.1126/science.1140942.
201. Schmith, T., Johansen, S. and Thejll, P. 2007. Comment on “A semi-empirical approach to projecting future sea-level rise”;. *Science*, **317**, 1866, doi:10.1126/science.1143286.
202. von Storch, H., Zorita, E. and González-Rouco, J. F. 2008. Relationship between global mean sea-level and global mean temperature in a climate simulation of the past millennium. *Ocean Dynamics*, **58**, 227–236, doi:10.1007/s10236-008-0142-9.
203. Gillett, N., Arora, V., Zickfeld, K., Marshall, S. and Merryfield, A. 2011. Ongoing climate change following a complete cessation of carbon dioxide emissions. *Nature Geoscience*, **4**, 83–87, doi:10.1038/ngeo1047.
204. Church, J. A., White, N. J., Aarup, T. *et al.* 2008. Understanding global sea levels: past, present and future. *Sustainability Science*, **3**, 9–22, doi:10.1007/s11625-008-0042-4.
205. Levermann, A., Clark, P. U., Marzeion, B. *et al.* 2013. The multimillennial sea-level commitment of global warming. *Proceedings of the National Academy of Sciences*, **110**, 13745–13750, doi:10.1073/pnas.1219414110.
206. Williams, R. G., Goodwin, P., Ridgwell, A. and Woodworth, P. L. 2012. How warming and steric sea level rise relate to cumulative carbon emissions. *Geophysical Research Letters*, **39**, 19, doi:10.1029/2012GL052771.
207. Ridley, J., Gregory, J. M., Huybrechts, P. and Lowe, J. 2010. Thresholds for irreversible decline of the Greenland ice sheet. *Climate Dynamics*, **35**, 1065–1073, doi:10.1007/s00382-009-0646-0.
208. Hunter, J. 2012. A simple technique for estimating an allowance for uncertain sea-level rise. *Climatic Change*, **113**, 239–252, doi:10.1007/s10584-011-0332-1.
209. Lowe, J. A., Woodworth, P. L., Knutson, T. 2010. Past and future changes in extreme sea levels and waves. In *Understanding Sea-Level Rise and Variability* (eds. J. A. Church, P. L. Woodworth, T. Aarup and W. S. Wilson), pp. 326–375. London: Wiley-Blackwell.
210. Jevrejeva, S., Moore, J. C., Grinsted, A. and Woodworth, P. L. 2008. Recent global sea level acceleration started over 200 years ago? *Geophysical Research Letters*, **35**, L08715, doi:10.1029/2008GL033611.

Sea-level changes in time to do with the solid Earth

Whatever motion appears in the firmament arises not from any motion of the firmament, but from the earth's motion.

Nicolaus Copernicus, The Commentariolus

11.1 Introduction

Mean sea level (MSL) records contain many examples of relative sea level being affected by geology as much as by the oceanography and climate discussed in the [previous chapter](#).¹ [Figure 11.1](#) shows three examples; many more can be found in the scientific literature [1]. Unlike the sea-level rise experienced during the twentieth century at most locations around the world, the MSL record at Stockholm in Sweden shows a sea-level fall of approximately 4 mm/yr, which is a consequence of the land on which the tide gauge is situated experiencing a high rate of crustal uplift due to Glacial Isostatic Adjustment (GIA) [2, 3]. The record from Nezugaseki shows an example of a near-instantaneous change of MSL of about 20 cm due to the 1964 Niigata earthquake off the west coast of Japan [4]. Both of these examples are due to natural processes in the solid Earth. The third example is of a change in land level (and so relative sea level) due to an anthropogenic process, in this case groundwater pumping under Bangkok, Thailand [5]. Any analyst of MSL records will be aware of such large signals. However, the possibility of other, smaller and more subtle, signals in the data set cannot be excluded, and anyone who uses the records primarily for ocean or climate research must always be aware of them.

Monitoring the rate of vertical land movement at a tide gauge, irrespective of the reasons for it, allows the relative sea level record to be adjusted to reflect ocean change. In this chapter, we show how great progress has been made in developing techniques such as the

Global Positioning System (GPS) to meet this requirement. Without them, analysts of the global MSL data set have had to infer vertical land movements from the long-term baseline of relative sea-level change provided by geological information obtained near to the tide gauges, where such information exists [6]. Alternatively they have had to employ predictions of relative sea level obtained from geodynamic models of GIA [7], which is the only geological process for which suitable global models exist. However, it is clear that their use will account for only one component of overall vertical land movement, albeit a large one in the case of a location like Stockholm.

The chapter then goes on to describe some of the main geophysical processes that lead to signals in sea-level records and which can be as important as climate-related signals in interpreting those records. More details of the role of such processes on long-term sea-level change may be found in the literature [8]. However, some appreciation of them is a necessary complement to the discussion of [Chapter 10](#), and in understanding how sea-level changes have resulted in present-day coastlines.

11.2 Techniques for measuring vertical land movement

11.2.1 GPS at tide gauges

Many tide gauge stations are now equipped with GPS receivers and an objective of the Global Sea Level Observing System (GLOSS) is that all stations in its core network (GCN) will be equipped with them within a short time [9]. Receivers are sometimes

¹ Relative sea level being sea level measured with respect to the height of the nearby land.

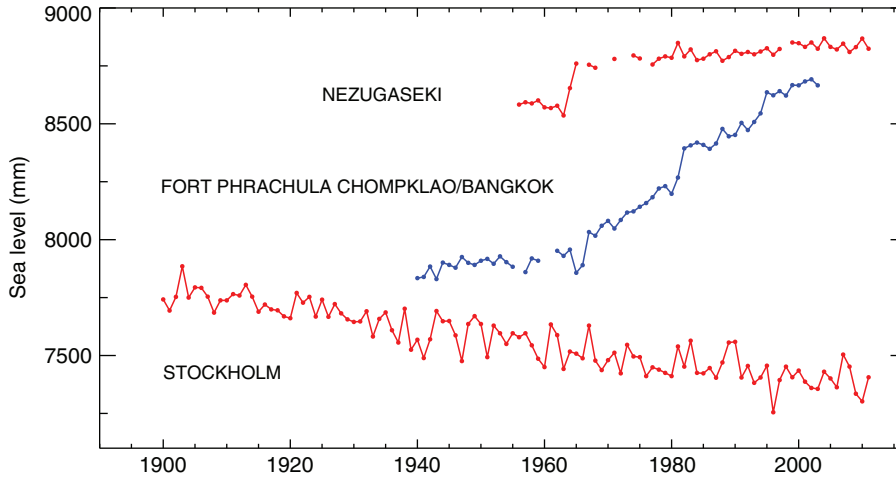


Figure 11.1 Time series from Stockholm, Sweden, indicating the contribution of Glacial Isostatic Adjustment to a MSL record; Nezugaseki, Japan, indicating an earthquake; and Bangkok, Thailand, showing local subsidence under a major Asian city. Data from the PSMSL.

located on geodetic pillars at a short distance from the gauge, such that conventional levelling can be readily used to provide a geodetic connection between them. At other sites the receivers are, less ideally, installed on the roofs of the buildings nearby.

Advice on the operation of GPS equipment at tide gauges is readily available [10, 11]. Important issues concern requirements for antenna monumentation (the type of pillar) and the methods of transmission of the receiver's data to a centre for analysis. The GPS antenna should be mounted as close as possible to the tide gauge, or even fixed to it if the installation allows (Figure 11.2). Regular levelling should be made between the antenna and the local benchmark network, including the main Tide Gauge Bench Mark, so that a time series of vertical land movement (sometimes referred to as vertical crustal movement) can be combined with relative sea level change measured by the tide gauge. The time series of vertical land movement will then include contributions from any local processes, such as sinking of a pier on which the gauge is located, as well as regional ones such as GIA. This recommendation contrasts with that provided by the geophysics community, which usually prefers GPS equipment to be installed on solid ground, and therefore probably at some distance from a gauge, so that information on regional vertical land movement can be obtained. In this case, any levelling between GPS and tide gauge becomes a larger undertaking. Ideally, at important tide gauge installations, one would like to see two receivers employed, one 'on' and one 'off' the

gauge, such that information of use to both oceanographers and geophysicists is obtained.

Also to be stressed is the importance of GPS equipment being installed continuously at tide gauges (this is often denoted as CGPS@TG), rather than being used in campaigns of a few days separated by long periods of time (called 'epochal' or 'episodic' GPS, EGPS). CGPS is now affordable for major tide gauge installations as the cost of receivers falls. A continuous GPS time series is much superior to an EGPS one in allowing fuller appreciation of the spectra of signals.

A GPS receiver brings many benefits to tide gauge operations. One is that the receiver provides an accurate time standard which can be used in control of other clocks in the tide gauge hardware. In addition, its precise positional information can be added to the station's metadata documentation, enabling the tide gauge's position to be shown accurately on maps. However, there are other scientific and practical benefits beyond the routine operational ones. Firstly, sea levels recorded by the gauge can be expressed as ellipsoidal heights for direct comparison to those obtained from space by satellite altimetry (Chapter 9). In addition, sea levels expressed in geocentric coordinates can be applied to modern methods of hydrographic chart production [12]. Secondly, GPS provides a time series of vertical crustal movement at the site which can be employed in studies of the reasons for the observed relative sea-level change. Thirdly, at some locations, if operated at high sampling rate and connected to high-bandwidth telemetry, the receivers can contribute

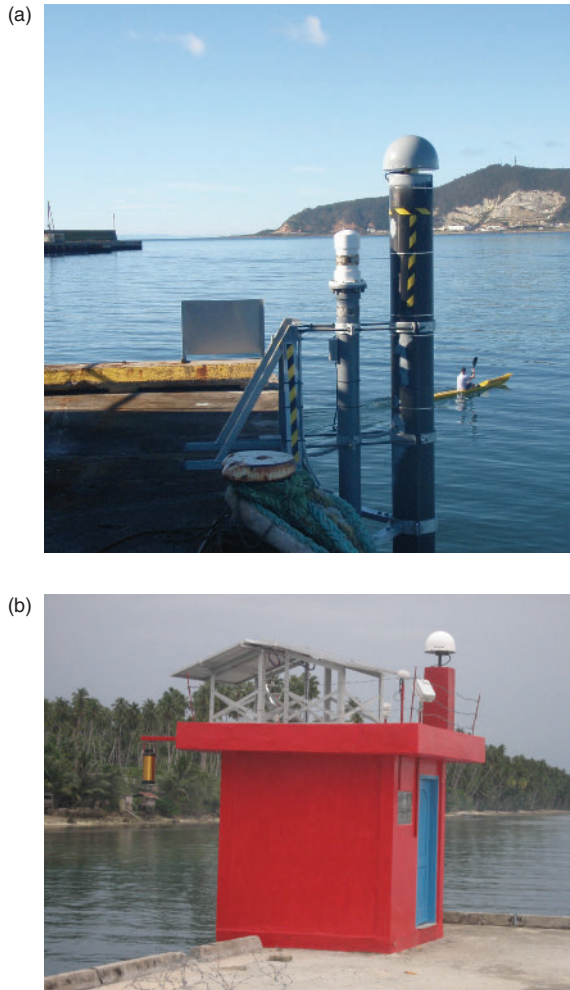


Figure 11.2 (a) An acoustic tide gauge at Burnie in northern Tasmania, Australia, and, to its right, a special pillar with a GPS receiver on top. Photograph courtesy of Geoscience Australia. (b) An Indonesian tide gauge installation with radar gauge at the left and GPS receiver on top right of the roof of the tide gauge building. This station provides data for both sea-level studies and tsunami warning. Photograph by Tilo Schöne, GeoForschungsZentrum, Germany.

seismic information to regional warning centres for determination of earthquake magnitudes and calculation of near real-time tsunami alerts [13].

GPS data of the quality required for vertical crustal movement studies started to become available in the latter half of the 1990s when CGPS receivers were installed at many tide gauge sites. Time series of a decade or more are now available from many locations, and their vertical rates can account for a large part of the land movement signals in sea-level records [14]. For example, Figure 11.3 shows MSL records from three regions: Northern Europe, Northwest

America and the Gulf of Mexico. The left panels show the original tide gauge records, while the middle panels show each record adjusted for GIA contributions to relative sea level using the ICE-5G (VM2) model 6. Much more complete adjustment, resulting in the trends in the records within each region becoming more similar, is shown in the right panels, which make use of GPS information at each site.

In spite of these and other encouraging results [15, 16] much remains to be understood concerning the operation of GPS at the coast and the ultimate utility of GPS to sea-level studies. The quality of a GPS time series depends on many local factors (continuity of antennas, cabling etc.) and global ones (especially stability of the reference frame as discussed in Chapter 9). A programme called TIGA (Tide GAuge) [17] of the International GNSS Service (IGS) is tasked with undertaking such studies, and an international centre for GPS data from tide gauge sites called SONEL (Système d'Observation du Niveau des Eaux Littorales) has been established at the University of La Rochelle. Data from this centre are freely available to any researcher [18].

Before leaving GPS, it is important to point out that, although we have talked about its data being used to 'adjust' a tide gauge record, that is not the complete story. The rate of relative sea-level change (SL^*), as would be measured by a tide gauge, is related to the rate of vertical land movement (R^*), as measured by GPS, via:

$$SL^* = G^* - R^* \quad (11.1)$$

where G^* is the rate of change of the gravitational equipotential surface over the ocean, which would correspond to the sea surface if there were no ocean currents. G^* and R^* are both geocentric parameters while SL^* is relative to the crust. Any geophysical process that results in crustal motion will also produce a change in the equipotential surface, and in principle that change will be worldwide. However, processes with short spatial scales, such as anthropogenic hydrocarbon extraction, will not produce a significant worldwide signal. In practice, most of G^* will be due to GIA, which is the predominant global-scale geological process, with a value of approximately -0.3 mm/yr over most of the ocean (see Figure 11.10c discussed below) [19, 20]. Some studies [14] have not considered this factor so far because it is small compared to the uncertainties in GPS measurement. However, it will be important to include as measurements become more accurate in the future.

One way to validate the rates of vertical land movement measured by GPS is to compare:

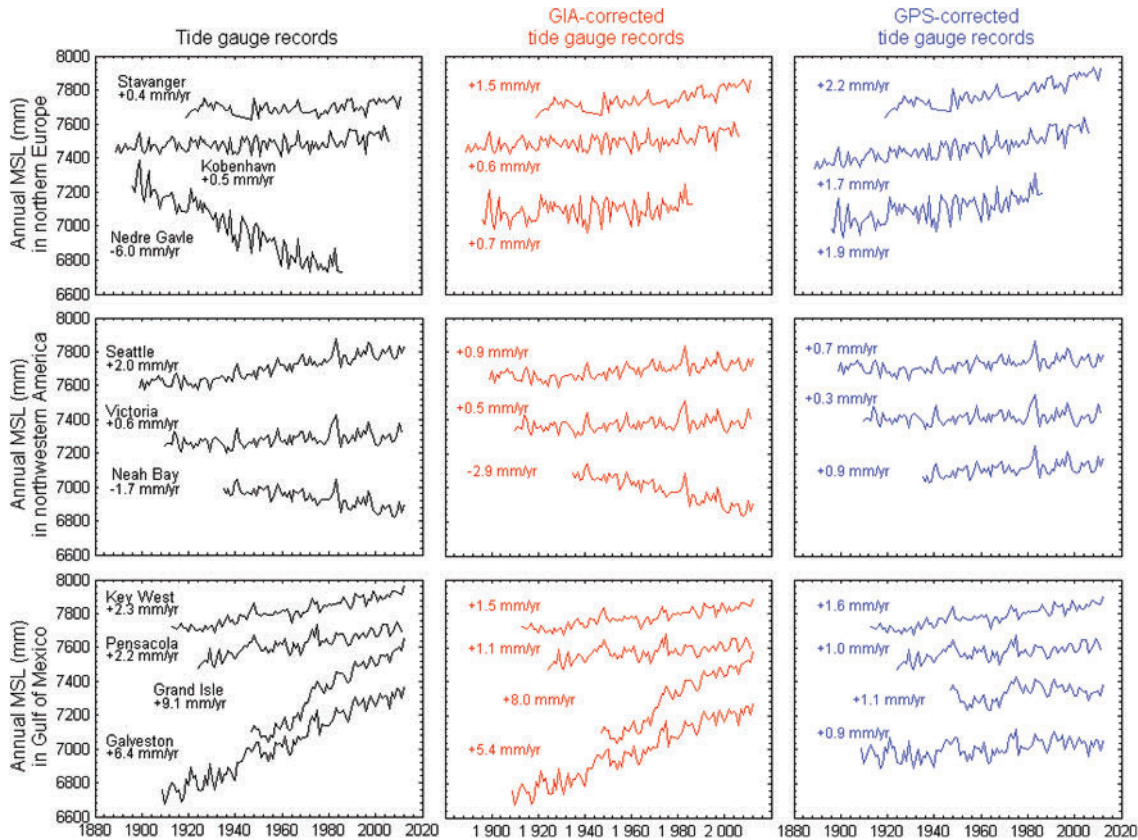


Figure 11.3 Time series of annual MSL from (left) tide gauge records, (middle) tide gauge records with GIA contributions to relative sea level removed using the Peltier ICE-5G (VM2) model, and (right) GPS-adjusted tide gauge records; in (top) Northern Europe, (middle) Northwest America, and (bottom) Gulf of Mexico. The time series are displayed with arbitrary offsets for presentation purposes. Units mm. Figure from Dr Guy Wöppelmann, University of La Rochelle.

$$SLA^* = R^* + SL^* \quad (11.2)$$

where SLA^* is the rate of sea-level change measured by an altimeter, SLA^* and R^* being geocentric parameters. The difference between the rates measured by the altimeter and tide gauge should then correspond to the GPS rate. Several studies have made such comparisons of data sets [21] with results consistent at approximately 0.4 mm/yr.

11.2.2 Absolute Gravity

An alternative technique for inferring vertical land movement is Absolute Gravity. An absolute gravimeter measures the acceleration of a corner-cube reflector in free fall in a vacuum using an iodine-stabilised laser interferometer with an accuracy of typically 1–2 μgal (or 1–2 times 10^{-9} of the acceleration due to gravity, 'g')

(Figure 11.4a). This corresponds to an accuracy in height of the order of 5–10 mm based on a formula dependent on upper mantle density [22].

The Micro-g LaCoste FG5 gravimeter shown in Figure 11.4b is a portable instrument that makes typically 200 'drops' (i.e. 200 independent measurements of 'g') every hour within campaigns of several days at a location near to each tide gauge. It is usually not desirable to operate the instrument at the coast itself due to noise from microseisms.² Older buildings (churches, schools etc.) are preferred that have dry basements and that are unlikely to be modified significantly in the future. 'Monumentation' is again an important issue, with the instrument required to be

² Microseisms are a background noise of small seismic signals caused by waves in the nearby ocean.

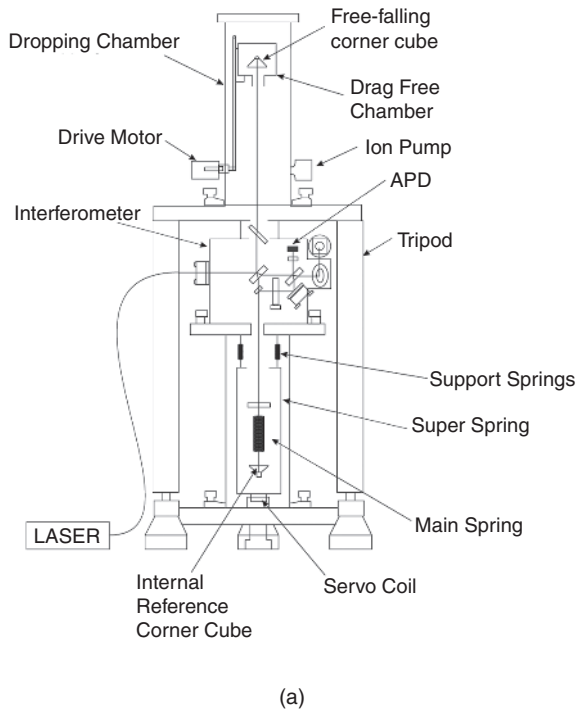


Figure 11.4 (a) Schematic of an Absolute Gravity meter indicating the dropping chamber and laser measurement system. (b) The Micro-g LaCoste FG5-X Absolute Gravity meter, the latest in the FG5 series. Pictures from Micro-g LaCoste.

installed on solid bedrock for which the vertical crustal movement is representative of the surrounding area.

Several factors limit the use of Absolute Gravity compared to that of GPS. One concerns the cost of the instruments, which is many times that of a GPS receiver. A second is that data can be obtained only for short campaign periods, and not continuously, due to the limited lifetime of the laser and other components. A third consideration concerns the fact that the gravity measured may not be due entirely to vertical land movement but to changes in groundwater or to surrounding buildings etc. Nevertheless, Absolute Gravity is important as a completely independent check on findings derived from GPS and, once it has been established that findings from the two techniques are consistent, their data sets may be analysed in combination [15, 23, 24].

11.2.3 DORIS

DORIS can also provide information on vertical land movement near to a tide gauge (Figure 11.5) and there are several examples of such applications in the

literature [25, 26]. However, DORIS has been applied to sea-level studies much less than GPS, owing to the limited number of beacons that can be employed in the global network, compared to the unlimited number of GPS receivers. In addition, few DORIS beacons are deployed near to tide gauges, their main role being for operational satellite tracking.

11.2.4 InSAR

Many tide gauges are installed at locations where the rate of vertical land movement could vary significantly over a short distance. Some are located in ports constructed on reclaimed land or are near to cities where groundwater pumping is taking place. Consequently, even though GPS measurements are now being made at many tide gauge stations, if the GPS equipment is some distance from the gauge then it could, in theory, measure a different vertical rate than at the gauge itself. One way to monitor this possibility is to have repeated levelling campaigns in an extended region around the station, or to install a dense network of GPS receivers, in order to keep a check on differential

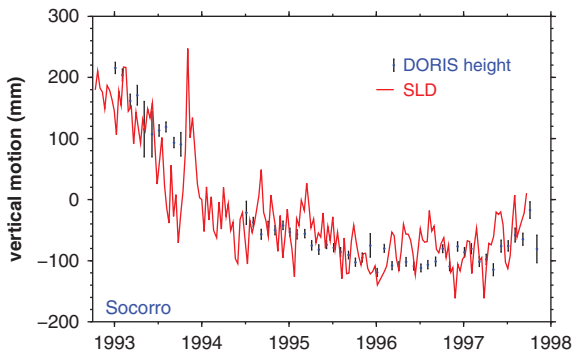


Figure 11.5 Time series of sea-level difference (SLD) between altimeter sea surface height and sea level measured by a tide gauge compared to the geocentric height of the crust measured by DORIS. Socorro Island is in the eastern Pacific Ocean and the time series reflect the adjustment of the crust following a nearby submarine volcanic eruption in early 1993. From [25].

land movement. An alternative recent development is the use of Synthetic Aperture Radar Interferometry (InSAR) from space [27].

InSAR employs the phase-differences between repeated SAR images of an area and reconstructs the displacements in the Earth's surface as measured along the radar's line-of-sight (LOS) which is $\sim 23^\circ$ from vertical for the ERS-1 and -2 satellites. As an example, Figure 11.6 shows findings for the Los Angeles basin demonstrating considerable spatial variability (+3.4 to -4.3 mm/yr during 1992–2000), a large part of which is due to groundwater and oil extraction [28]. As a consequence, it is almost certain that the long-term sea-level trend estimated from the Los Angeles tide gauge (0.8 mm/yr) has been affected by such local land motions.

11.3 Glacial Isostatic Adjustment

The solid Earth can be pictured as containing a mechanically stiff but elastic outer layer, called the lithosphere, on top of its upper and lower mantle and core (Figure 11.7). The lithosphere can be subdivided into its oceanic and continental parts. The main geodynamical processes that involve the oceanic lithosphere are spreading at the ocean ridges and subduction at the active continental margins. The continental lithosphere is where the periodic glaciations and deglaciations have occurred during the Pleistocene geological period (the last 2.5 million years up to the start of the Holocene Epoch approximately 12,000 years ago). Figure 10.15 shows how sea

level rose by ~ 130 m since the LGM and the Earth is still recovering its isostatic equilibrium after the melting of the great ice sheets in a process called Glacial Isostatic Adjustment (GIA). The response of the lithosphere and ocean to the removal of the great loads of ice is shown by raised beaches in former glaciated areas (Figure 11.8a), while evidence that the process is still ongoing has been obtained from regular observations of historical coastal benchmarks (Figure 11.8b). The data sets of the instrumental era also show evidence of GIA. Figure 11.9 shows rates of relative sea-level change from tide gauges and vertical land movements from GPS from Scandinavia [29] and Hudson Bay [30, 31], where the large GIA component dominates the geological signal [32]. In these cases, the spatial pattern of the GIA rates can be seen to explain a large part of the tide gauge observations.

Several comprehensive reviews of the modelling of GIA are available [7, 19, 33]. The modelling involves four main components: a global Late Pleistocene history of the ice load on the Earth; a spherically symmetric (i.e. depth-varying) visco-elastic Earth model to simulate the deformational response of the Earth to the loads; an algorithm called the 'sea-level equation' to compute the resulting redistribution of water in the ocean [34]; and a method for computing the consequent changes in Earth rotation and the further sea-level changes associated with this mechanism [50]. Data sets of Holocene sea-level information for comparison to model findings comprise a fifth important component. The models provide maps of rates of change of relative sea level and crustal movement arising from GIA, as would contribute to tide gauge and GPS measurements respectively, at every point on the globe for any time in the past or future (e.g. Figures 11.10a, b)). In the models, relative sea level at any point on the coast depends upon several things: the amount of water transferred from the ice sheets to the ocean; the response of the solid Earth to the removal of the ice loads in northern America, Europe and Antarctica and the consequent loading of the ocean basins; and the change in the gravitational potential due to the redistributions of mass. The solid Earth response is computed using similar Green's functions as employed in tidal loading described in Section 5.7 but for the visco-elastic response of the Earth rather than the elastic response. As water is free to move, the resulting sea surface at any point in time is by construction a geopotential surface (Figure 11.10c).

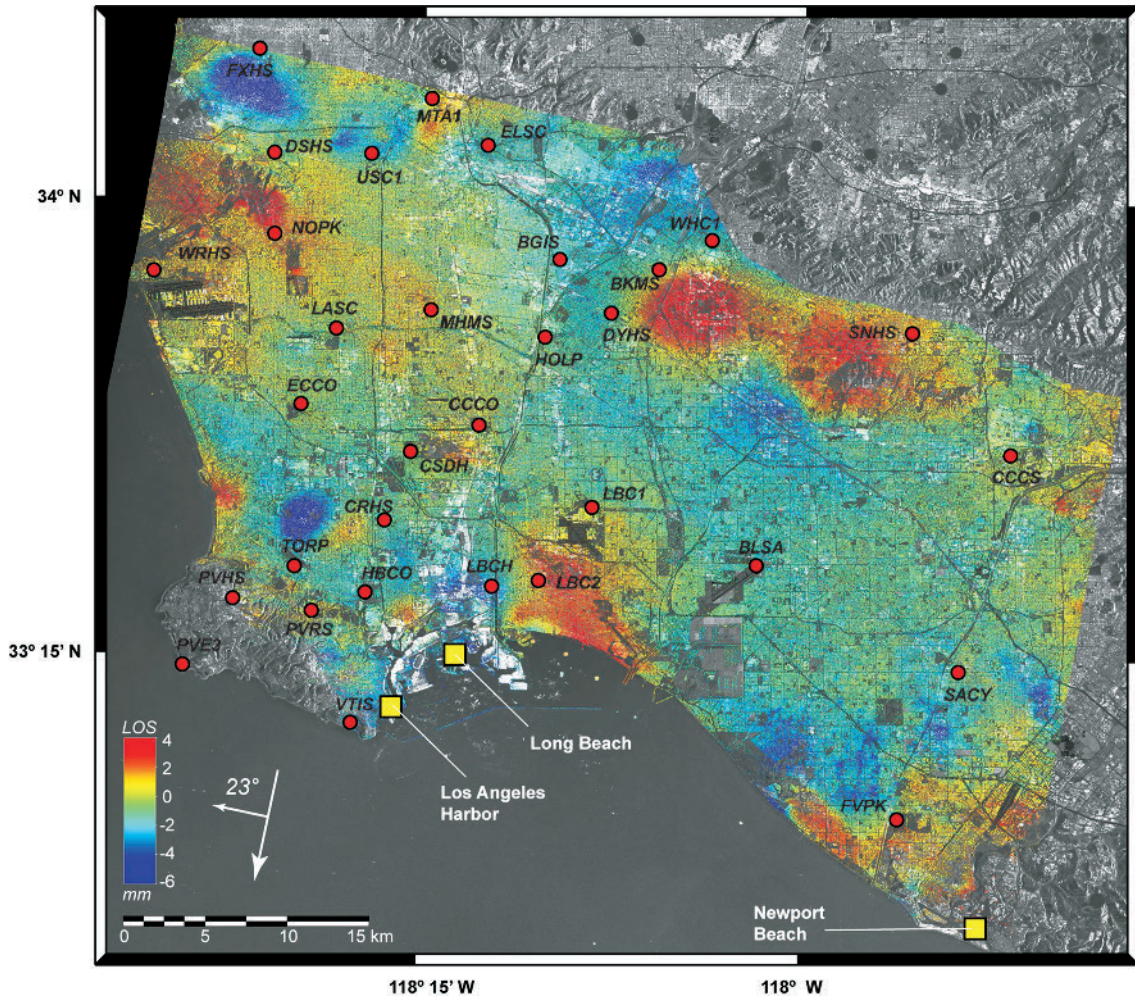


Figure 11.6 Linear line-of-sight (LOS) velocity, which for present purposes can be regarded as the rate of vertical land movement, for the period 1992–2000 using ERS-1 descending passes across the Los Angeles basin. Continuous GPS stations used in the analysis (red circles) and tide gauge stations (yellow squares) are shown. The legend arrow shows ERS LOS azimuth and inclination (23°). From [28].

The evolution of this surface is sometimes referred to as ‘change in the geoid’ although it is less confusing to reserve the term ‘geoid’ for the particular surface corresponding to a specified potential (Chapter 9).

Such a model of GIA provides a picture of what the Earth would have been like without other processes occurring, such as recent climate change. Consequently, the modelled rates of relative sea-level change have been applied routinely in sea-level studies as baselines to which recent tide gauge measurements of sea-level change can be compared.³ Similarly, their modelled rates of crustal movement can be compared to GPS

measurements [16]. As the models are global ones, they can be applied to any record or combinations of records. In the ‘far field’ (i.e. in mid-latitude or tropical areas far from the former ice sheets), the present-day rates of relative sea-level change or crustal movement due to GIA are of the order of several tenths of a millimetre per year (Figure 11.10a, b). Those for relative sea level are similar and negative across a large part of the ocean (Figure 11.10a), implying a small positive correction to most sea-level trends, given the present geographical distribution of long records [35]. Uncertainties in GPS rates in the far field are probably comparable to or larger than the modelled GIA values [16], unlike the cases shown in Figure 11.3 where land movement rates are larger, so it is not surprising that comparison

³ Rates of present-day relative sea-level change due to GIA as computed in the models of Professor Richard Peltier can be obtained via the PSMSL website www.psmsl.org.

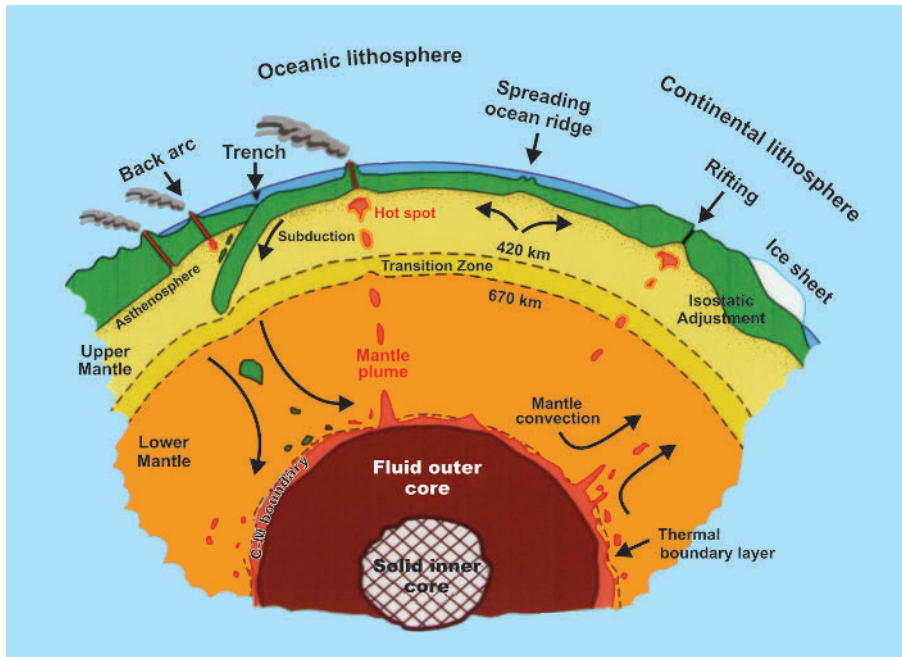


Figure 11.7 The major dynamic processes of plate tectonics and the layers into which the Earth is differentiated (not to scale). The outer lithosphere is divided into the ocean and continental sections, the upper mantle, the transition zone and the lower mantle. The fluid outer core and solid inner core are also indicated. From left to right are portrayed subduction and related back arc opening, hot spots and a spreading ocean ridge. For the continental lithosphere, Glacial Isostatic Adjustment following post-glacial rebound is suggested. Adapted from a figure in [91].

between the two does not as yet yield a close correspondence.

The ellipsoidal heights of sea level that are measured by altimetry (Chapter 9) contain a contribution from GIA that is the potential surface change mentioned above (Figure 11.10c). The global average of this signal is approximately -0.3 mm/yr, which constitutes a correction to be applied to an altimetric global-average sea-level change estimate in order to infer a change in ocean volume [19, 20, 33]. This is a relatively small correction compared to the estimate of global sea-level rise of approximately 3 mm/yr since the early 1990s [36]. However, the corresponding correction for GIA that must be applied to the sea-level change inferred from temporal space gravity measurements is a comparatively large value (~ 1 mm/yr) (Figure 11.10d) [37, 38, 39]. The importance of these corrections can be further appreciated from the discussion in Chapter 10.

The use of a spherically symmetric Earth model in GIA modelling can be extended to consider lateral variation (3-D modelling), which includes the variations in lithospheric structure associated with, amongst other factors, the transitions from ocean to

continents and plate boundaries [40]. The spatial variations in present-day relative sea-level change associated with such models do not as yet appear to result in better comparison to tide gauge information [41], although this remains an important area of research.

Similar modelling to GIA is necessary in regional contexts wherever there have been changing loads on the Earth's crust. Notably, this involves study of sedimentary loading of river deltas where the history of deposition of sediment was itself affected by sea-level rise [42], leading to major subsidence in the present day and large rates of local relative sea-level rise [1]. These large rates, coupled with the fact that deltas are necessarily low-lying areas often with high populations and industry, makes them vulnerable to coastal flooding [5, 43].

11.4 Tectonic sea-level changes

The Earth's crust and upper part of the mantle, together called the lithosphere, are composed of a set of continental plates that are in constant relative motion, resulting in much of the mountain building, volcanism and seismicity on our planet [44]. Active

(a)



(b)



Figure 11.8 (a) Raised beaches in the Hudson Bay Lowlands of Manitoba, Canada, demonstrating Glacial Isostatic Adjustment in North America. Photograph by Linda Dredge, National Resources, Canada. (b) The Celsius rock at the island of Lövgrund in the southwest part of the Gulf of Bothnia, the most famous of several such rocks around the Baltic coast, which demonstrates uplift due to GIA in Scandinavia. Three marks can be seen in the photograph. One made by Celsius in 1731 when the rock was only half a metre or so above sea level, one in 1831 shortly before a visit by Lyell to the rock [92], and a third in 1931. From [3].

convergence between plates can result in vertical crustal motions along continental margins that can manifest themselves as changes in relative sea level. For example, one study considered the sea-level changes to be expected in the Adriatic region due to the convergence of the Africa and Eurasian plates and associated subduction in the Tyrrhenian area [45]. Long-term sea-level information from archaeological surveys of

Roman remains were used to validate modelled spatial patterns of sea-level change due to tectonics, superimposed upon those anticipated from a general sea-level rise and GIA.

At some locations, very large displacements have taken place due to the slow but sustained movements of tectonic change over many thousands of years. A good example is provided by the Huon Peninsula in

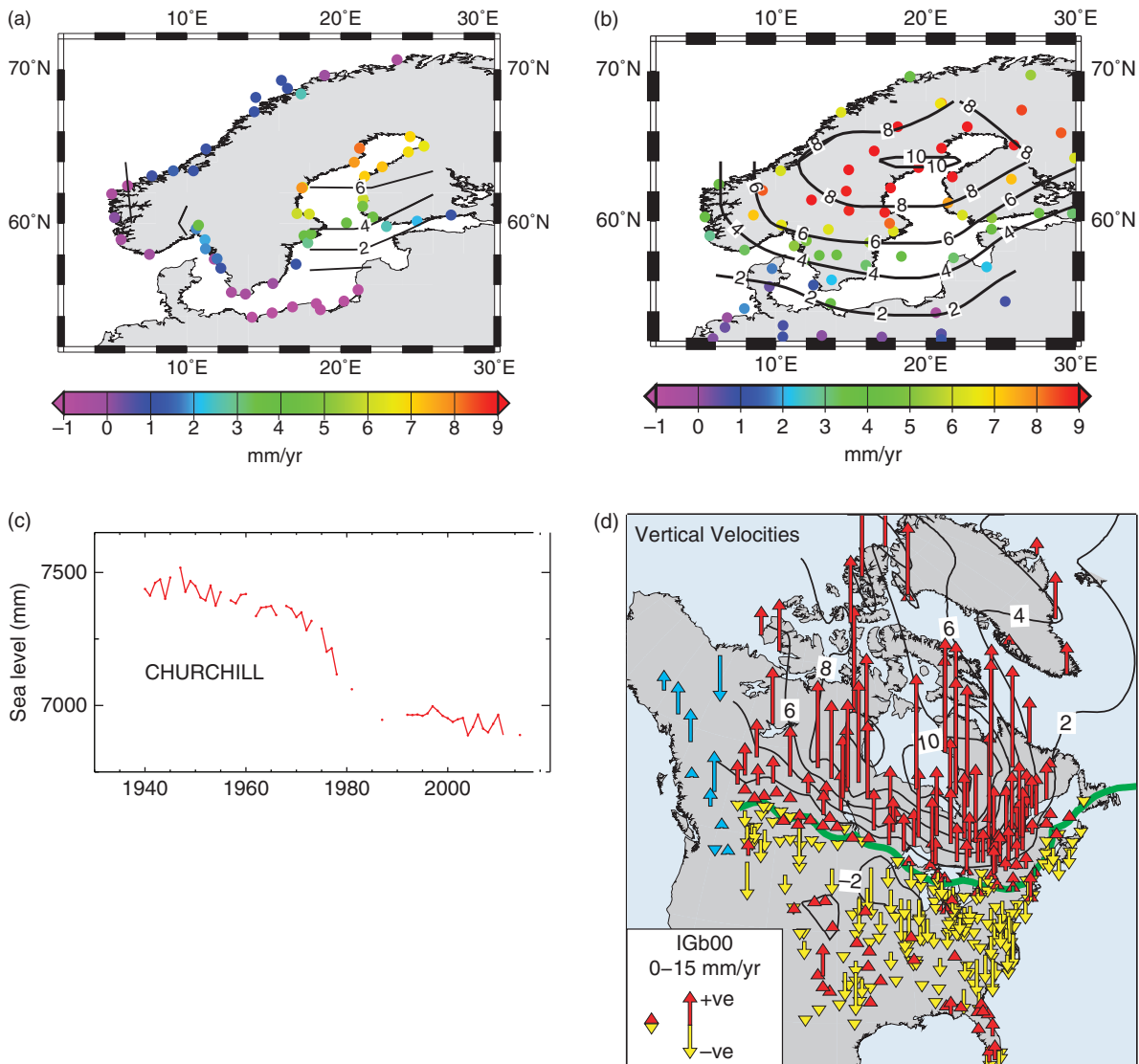


Figure 11.9 (a) Rates of sea-level change in Scandinavia selecting PSMSL stations with at least 40 years of data since 1900. Rates have been multiplied by -1 so as to allow direct comparison to (b). (b) Rates of vertical crustal movement in the same area as measured by GPS. Re-plotted from information in Lidberg *et al.* (2010) [29]. (c) Sea level recorded by the tide gauge at Churchill on the southwest coast of Hudson Bay demonstrating an average trend of -9.4 mm/yr in the period 1940–2011. (d) Rates of vertical crustal movement in North America as measured by GPS. The rates in the latter are relative to a global set of reference GPS stations (IGb00). The green line shows the ‘hinge line’ between areas of uplift (red) and subsidence (yellow) in central and eastern North America. From [31].

Papua New Guinea (Figure 11.11). This coastline consists of 125,000 year old coral terraces that have uplifted several hundred metres above present sea level. The intermediate terraces shown in the photograph were formed at times when the tectonic uplift rates and sea-level rise were similar. Modern analysis shows that the long-term rate of uplift has been between 2 and 4 mm/yr with episodic displacements of about 1 m occurring every 1000 years [46, 47]. Such long-term processes

have been known for many years. During the voyage of the *Beagle*, Charles Darwin reported on the vertical land movements following the earthquake at Concepción, Chile, in 1835 [48]. Putrid mussel shells were found 10 feet above the high water mark, for which the inhabitants had previously dived at low water spring tides. However, equally interesting, Darwin also referred to the discovery of sea shells several hundreds of feet above sea level, evidence that the

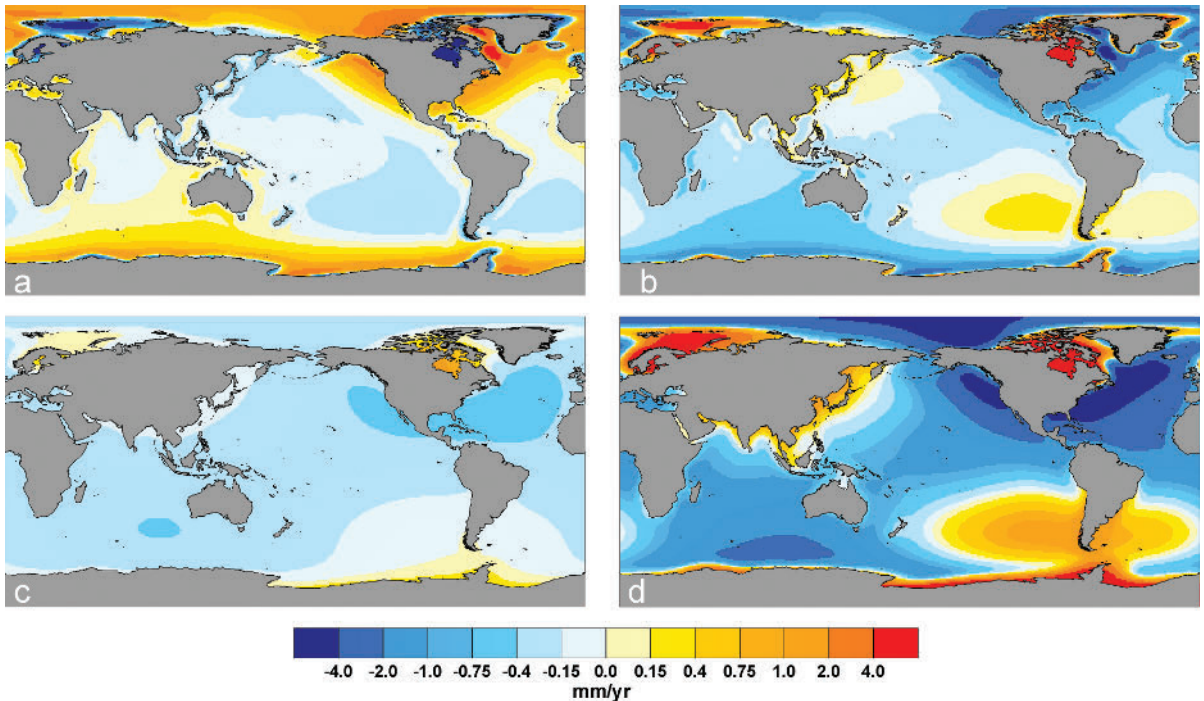


Figure 11.10 Predictions from a GIA model of the present-day rates of change of (a) relative sea level as would be measured by a tide gauge, (b) vertical crustal movement as would be measured by GPS, (c) geocentric sea surface height as would be measured by an altimeter, and (d) estimated change in water thickness as would be inferred from a gravity satellite mission. The non-linear colour scale has been chosen to highlight the far-field changes. Figures by Mark Tamisiea, National Oceanography Centre following [19] and [38].



Figure 11.11 The emergent terraces on the Huon peninsula in Papua New Guinea, which have risen to more than 100 m above sea level as a result of co-seismic uplift. The arrow indicates the last interglacial (Eemian) shoreline. From [8]. Photograph by Professor Sandy Tudhope, Edinburgh University.

whole Andes chain was formed by intermittent systematic uplift over geological timescales.

The sometimes dramatic changes in mean sea level (MSL) that occur during earthquakes are

indicated by Figure 11.1 and in a wide range of other sea-level research [8]. These vertical (and horizontal) crustal motions can nowadays be monitored using GPS receivers [49], which may also provide the

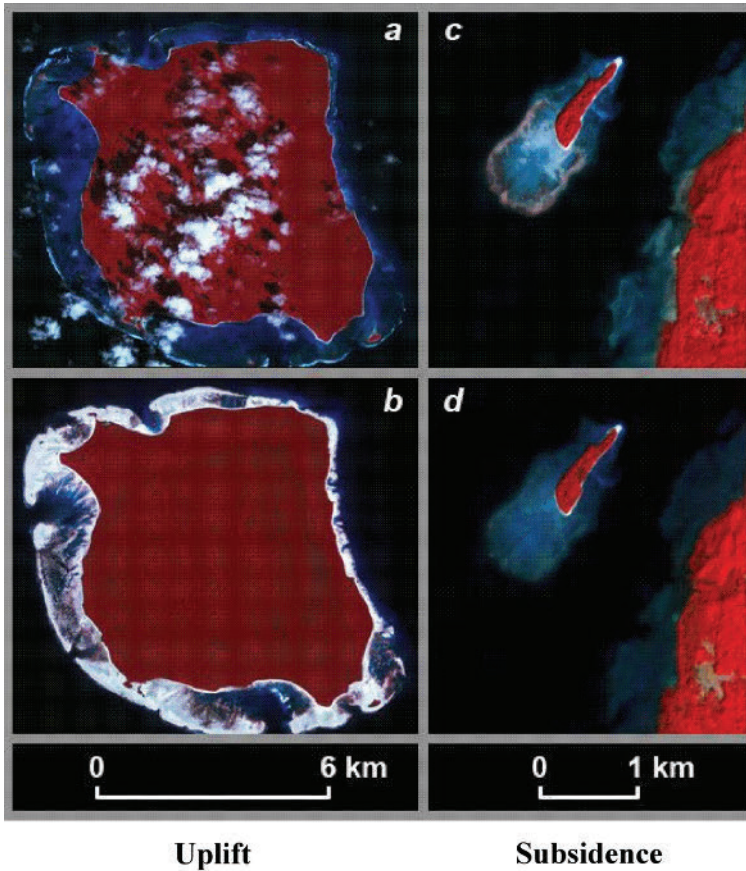


Figure 11.12 (a) Pre- and (b) post-earthquake images from space of North Sentinel Island in the Andaman Islands in the Bay of Bengal, indicating a sea-level lowering and coral reef emergence of 1–2 m after the 2004 Sumatra earthquake. (c) Pre- and (d) post-earthquake images for a small island 38 km east of North Sentinel Island indicating submergence of the reef. Both locations are about 50 km from the rupture. From [50] and [51].

real-time seismic information required for tsunami warning (Chapter 8). The largest earthquakes can affect relative sea level hundreds of kilometres away from the epicentre [50]. For example, Figure 11.12 shows the changes in coastal land elevations associated with the 26 December 2004 Indian Ocean earthquake in Sumatra, Indonesia within 100 km of the rupture, demonstrating major emergence and submergence at different locations [51]. Some estimates of global sea-level change in recent decades based on the PSMSL data set could have been biased by one or two tenths of a millimetre per year due to earthquakes around the world [52].⁴

However, all earthquakes do not result in an observed change in MSL. This is partly due to the fact that, if the tide gauge is some distance from the epicentre and if the crustal movement is small, then any small change in relative sea level will have to be

identified within a time series containing other sources of variability. For example, on 27 February 2010 there was a magnitude 8.8 earthquake off the coast of central Chile, which is ranked as the sixth largest on record. The earthquake was followed by a tsunami that devastated a number of coastal towns and damaged the port of Talcahuano approximately 100 km to the south. However, monthly MSL values registered by the port tide gauge for March 2010 and later were similar to those for January–February [53]. In these cases, the danger of tsunamis from submarine earthquakes and the associated affects of harbour seiching (Chapters 7 and 8) is of far greater consequence to coastal dwellers than any long-term changes in MSL.

11.5 Man-made crustal movements

Anthropogenic reasons for relative sea-level change exist alongside the natural ones. In particular, there are a large number of major coastal cities that are known to be submerging due to groundwater extraction. Consequently, they will exhibit higher

⁴ This finding relates to the sampling of global sea-level change provided by the present tide gauge network. The total water volume itself does not change due to earthquakes.

rates of MSL change than neighbouring stations. For example, this is known to be a long-standing problem at Galveston in the Gulf of Mexico, which has one of the longest tide gauge records in the United States and which exhibits a significantly higher rate of sea-level rise than other locations in the Gulf of Mexico, other than in Louisiana where the high rate is to do with sedimentary loading [54]. Several Asian cities are also known to have been sinking in recent decades for the same reason. These include Osaka and Toyko (up to 3 and 5 m subsidence respectively over the twentieth century), Shanghai (3 m) and parts of Bangkok (2 m) [5] although subsidence for the latter is now reduced [55]. Jakarta is similarly affected as is Manila, where the higher rate of sea-level rise after 1960 correlates with records of groundwater withdrawal, floods and increased pollution [56].

Venice is one of the most famous of submerging cities. Sea level has been rising for many years [57] but increased markedly during 1950–70 due to groundwater extraction for industry [58]. Since that time extraction has been reduced and the tide gauge records for Venice and Trieste are now similar (Figure 11.13) [59]. That may be not the end of the story, however. Recent geodetic research suggests that Venice may be continuing to sink at a rate of 1–2 mm/yr due to soil compaction and may also be tilting due to regional differential crustal movement of tectonic origin, as discussed above [60].

Anthropogenic submergence that takes place over a small area can occur for other reasons and can be represented in tide gauge records. Examples include gauges situated over coal mines with shafts that extend under the sea [61]. In addition, many gauges are located in modern port areas that have been constructed on reclaimed land that compacts over many years. Such considerations underline

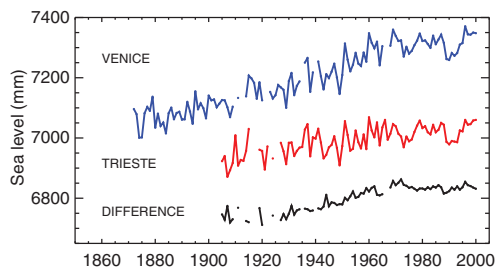


Figure 11.13 Annual MSL time series from Venice and Trieste and their difference. Each record has been offset vertically for presentation purposes. From [59].

the need for monitoring by modern geodetic techniques.

11.6 Geophysical fingerprints of sea-level change

The spatial pattern of relative sea-level change to be expected from GIA (Figure 11.10a) provides an example of a spatial ‘fingerprint’ of a geological process. GIA occurs primarily as a result of the viscous flow of the solid Earth and so takes place over timescales of thousands of years. Figure 11.14 explains the fingerprint of GIA further by means of profiles of the crust and sea surface in the past and present day for (a) near to the centre of a former loading region and (b) from a far-field continental region into the adjacent ocean [19].

However, when a load is removed (or added) there is also an *elastic* response, which is essentially instantaneous and is more relevant to discussion of changes in loads on the decadal and centennial timescales associated with present-day climate change. The elastic response is proportional to the size of the load change so any spatial pattern of sea-level change predicted using an elastic model can simply be scaled accordingly. Figure 11.15 shows a classic calculation of the fingerprint of relative sea-level change that would be expected as a result of an elastic response to the removal of loads from Greenland, Antarctica and mountain glaciers [62]. In each case, the sea-level equation is used to compute the change in the equipotential surface of the ocean arising from water added to it.

In each panel of Figure 11.15, the patterns of sea-level change have been adjusted to correspond to a global-average change of 1 mm/yr. It can be seen that relative sea level actually falls in the area near to the load, as a consequence of the elastic response of the solid Earth to the load removal and to a reduction in the gravitational attraction of the ocean by the ice masses, as explained further by the profiles in Figure 11.14c. On the other hand, sea level rises by more than average in the far field, so that, for example, the two coasts of the United States experience a larger than average rate of sea-level rise from an unloading of Antarctica.

Sea-level fingerprints can also be computed for changes in the hydrological loads on the continents. These loads can vary significantly seasonally and on longer timescales (cf. Figure 11.14d) [19]. As an example, Figure 11.16a shows the spatial distribution of

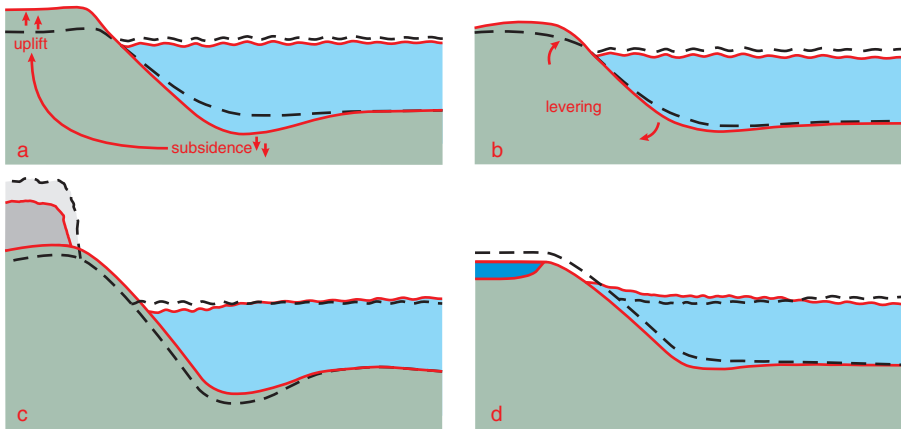


Figure 11.14 Mechanisms by which crustal motion and changes in gravity contribute to sea-level variations. Black lines show the crust and sea surface at some point in the past, red lines represent present-day positions. (a) and (b) show mechanisms associated with GIA while (c) and (d) illustrate the effect of present-day mass changes. (a) Profile from the centre of a former loading region into the surrounding ocean. The centre is uplifting while the nearby crustal forebulge in the ocean collapses as mantle flows back to previously glaciated areas. (b) Profile from a continental region into the adjacent ocean in an area at great distance from the centres of glaciations (the ‘far field’). As the ocean basins are now loaded with meltwater, offshore regions are levered downward and the adjacent continent upward as mantle material flows from under the former to under the latter. (c) Profile from the middle of a rapidly melting ice sheet into the surrounding ocean. The reduced mass of the ice sheet allows the crust to rebound and reduces the gravitational force that attracted ocean water towards the ice sheet. (d) Profile of a river basin exhibiting an increase in water storage. Opposite to (c), the additional mass on the continent attracts water toward the shore and depresses the crust. From [19].

relative sea-level change during 2003–9 due to changes in land hydrology [63]. The figure was obtained by scaling the expected sea-level fingerprints for hydrological loading at each location by the measured mass changes over the continents observed by GRACE (cf. Figure 10.27). This contribution to sea-level change can be combined with those from ice sheets and glaciers, using fingerprints similar to those of Figure 11.15 scaled by the GRACE information, to give the total estimated spatial pattern in sea-level change due to the various changes in loads (Figure 11.16b). The contribution of the ice sheets to Figure 11.16b can be clearly seen. The global average of the sum of the various contributions amounts to approximately 1 mm/yr. One can see that while hydrology did not contribute significantly to global average sea-level change in this period, it did its spatial variation.

The above studies are all concerned with understanding the geophysical signals in sea-level data due to changing loads on the solid Earth. However, there are potentially other kinds of sea-level fingerprints. For example, changes in the AMOC (Chapter 10) caused by meltwater forcing in the subpolar North Atlantic have been suggested as being responsible for a fingerprint of sea-level change in the North Atlantic, particularly along the Northeast American

coast [64, 65, 66]. In addition, climate models of thermosteric sea-level change have often suggested a fingerprint of lower than average sea-level changes in the Southern Ocean during the twenty-first century and higher ones in the Arctic [67]. Although these are examples of ocean processes, their fingerprints may involve changes of mass and therefore, for completeness, the loading of the solid Earth and change in the gravity field need to be considered. Such a calculation has been made for thermosteric sea-level change in the twenty-first century, with the conclusion that the predicted rates are modified by between -4 and $+14$ per cent, with the largest modifications in the Arctic seas of Eurasia, with overall gravitational and self-attraction effects amounting to approximately 3 per cent of that part of the global rise due to thermal expansion (or of the order of 1 per cent of the total) [68].

There is now a considerable literature on the use of fingerprints in sea-level studies [69]. Estimates have been made of the uncertainties in such calculations [70], and fingerprints have been computed for specific processes such as the changing loads of water trapped in dams [71]. The fingerprints of a process will differ depending whether one is studying tide gauge (relative sea level), altimeter (geocentric sea level) or space gravity data, so it will always be beneficial to use data sets in

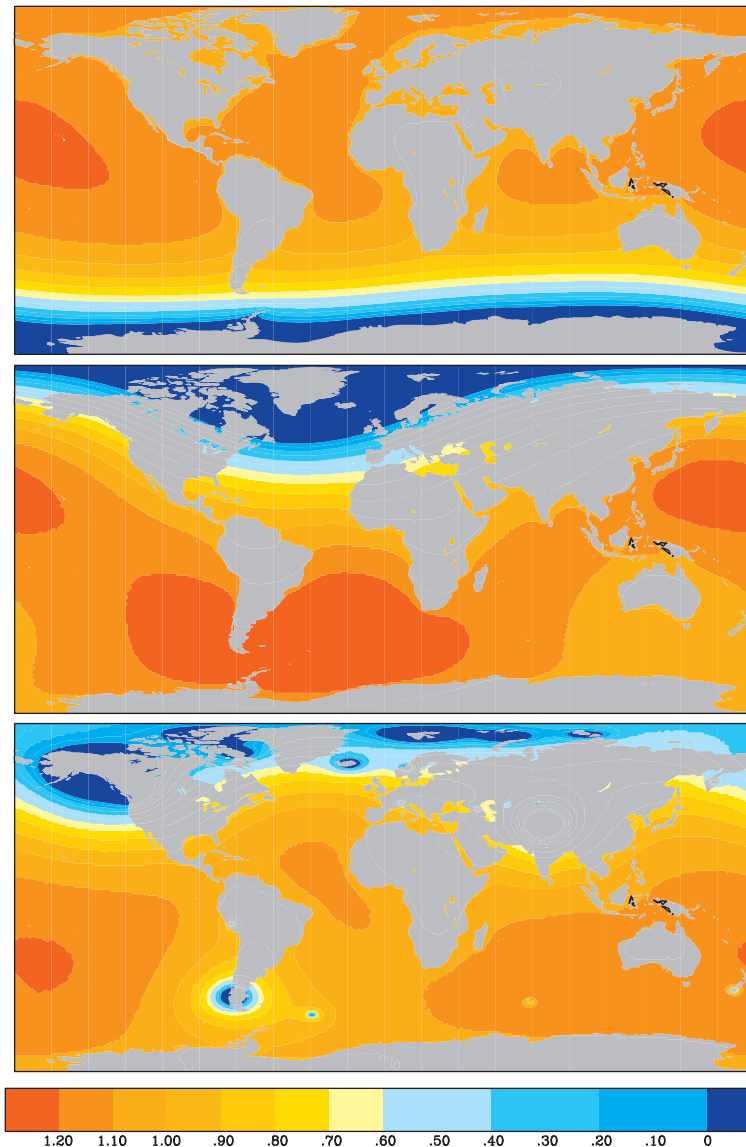


Figure 11.15 Sea-level changes due to present-day ice mass variations in (top) Antarctica, (middle) Greenland and (bottom) mountain glaciers. Each panel has been normalised so as to correspond to 1 mm/yr global average sea-level change, so that departures from a contour value of 1.0 reflect departures from an assumption that the sea-level distribution accompanying the mass flux is uniform. From [62].

combination. The fingerprints of each process in sea-level data should become clearer as available time series lengthen, as their identification is largely one of extraction of signal from noise.

11.7 Coastal processes

In the coastal and near-shore environment, tides and waves work together to produce very complicated and dynamic geomorphology [72]. Characteristic features include estuarine deposits, lagoons, barrier islands and coastal sand banks. The role played by waves in the development of coastal features is not part of this

account, but cannot be overemphasised: breaking waves are very effective agents of erosion and for driving sediments along the coast. For any particular length of coast there is usually a direction of net long-shore sediment transport, the magnitude of which depends on the supply of sedimentary material and the direction of wave attack along the shore. If an asymmetry exists between ebb and flood currents, the direction of the resulting residual tidal flow will also influence the direction and extent of the long-shore transport.

For these reasons, sea level is one of the major controllers of coastal evolution. Sea-level change raises

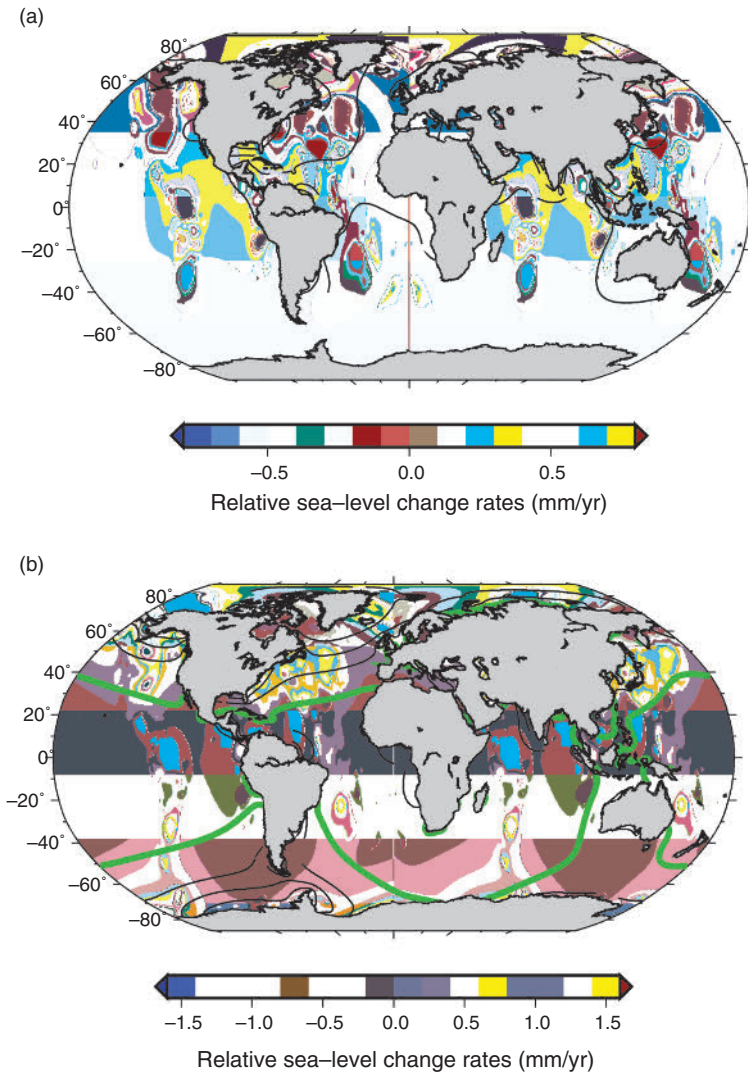


Figure 11.16 (a) The estimated land hydrological component of relative sea-level change during 2003–9 calculated from GRACE information and knowledge of the fingerprint in sea level of changing loads around the world; (b) the total relative sea-level changes due to cryological and hydrological processes. Units are mm/yr. From [63].

or lowers the level at which wave attack occurs and causes erosion. Sea level (water depth) determines tidal wavelength and hence the spatial pattern of the tides in shallow waters. It modifies the magnitude of storm surges that result in coastal flooding. These different processes in the ocean can interact with each other and with others that affect the coast from the land side, such as river flow and fluvial sediment supply. As a consequence, the modelling and prediction of coastal evolution present a formidable challenge that, nevertheless, can be simulated in general terms [73, 74]. The challenge is even greater when coastal constructions, including flood defence schemes, mineral extraction

and energy generation, are imposed on natural processes.

The role of the tides within a number of coastal processes has been discussed previously [75] and in those processes the role of sea level is implicit for the above reasons. However, the role of sea level in coastal evolution becomes more explicit over longer time-scales. The most obvious concerns the rise of sea level after the Last Glacial Maximum (Figures 10.15 and 11.17) when the continental shelves were flooded and tides were modified throughout the world ocean [76]. The tides of the newly flooded shelves were especially sensitive to depth changes (e.g. Figure 4 of

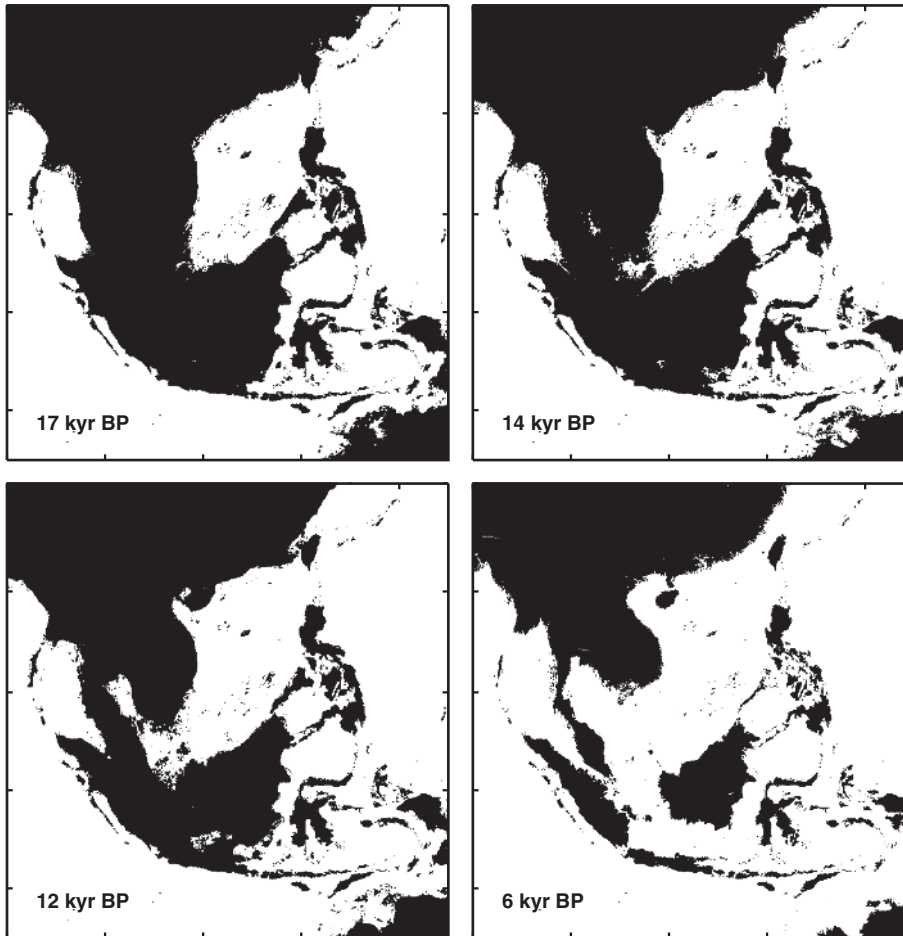


Figure 11.17 Maps of shoreline evolution in Southeast Asia according to GIA. Maps are shown for 17, 14, 12 and 6K BP after which the shoreline was much like that of today. Figure by Professor Glenn Milne, University of Ottawa.

Reference 77). As the diurnal, semidiurnal and higher-frequency composition of the tide changed, then factors such as tidal asymmetry that control sediment transport will also have changed, thereby in itself contributing to a modification of bathymetry and the coastal topography [78, 79, 80]. The tides of coastal lagoons, estuaries and embayments continue to evolve when depths change either naturally or through coastal engineering [81]. Dredging of shipping channels of estuary ports has a particularly marked effect of lowering low waters but leaves high waters unchanged, with a resulting increased tidal range and modified MSL [82].

Connections between MSL change and coastal change in recent history are less clear. The IPCC Fifth Research Assessment (AR5) [83] concluded that, while many coasts are eroding, few studies have

unambiguously quantified the relationships between observed coastal land loss, the rate of sea-level rise, and local anthropogenic drivers of change. One exception relates to sandy shorelines and dunes for which there is evidence of general retreat [83, 84]. In addition, muddy mangrove shorelines seem clearly to migrate with interannual changes in mean high water [85], and might be expected to retreat with a rise in sea level. Coastal steepening, the process whereby a cross-shore profile becomes steeper, is also considered to be widespread as demonstrated by the east coast of the United Kingdom, where 67 per cent of the coastline experienced a landward retreat of the low water mark over the past century [86].

Any acceleration in sea-level rise is expected to exacerbate beach erosion around the world, although the local response will depend on the total sediment budget.

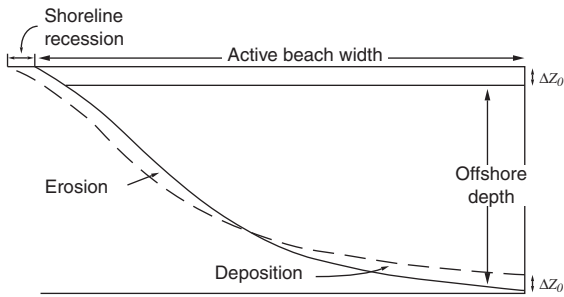


Figure 11.18 The basis for the Bruun Rule of coastal evolution as a consequence of sea-level change. As sea level rises, the shoreline recedes and the beach profile is modified from the solid to the dashed lines.

One widely used tool to estimate the response of a beach profile to a change in the MSL, assuming a closed sediment system, is called the 'Bruun Rule' named after the Danish coastal engineer Per Bruun [87] (Figure 11.18). A closed system means that there is no loss or additional supply of sediment except from the beach and near-shore, over the active beach width. By equating the sediment volumes in the erosion and deposition zones it may be shown that the shoreline recession resulting from an increase of MSL ΔZ_0 is given by:

$$\begin{aligned} \text{Shoreline recession} \\ = (\text{Active beach width} / \text{Offshore depth}) \times \Delta Z_0 \end{aligned} \quad (11.3)$$

irrespective of the detailed shape of the profile.

The Bruun Rule does not suggest that MSL rise itself causes erosion, rather than resulting from processes such as waves attacking further up the beach and transporting sand offshore. Even when there are coastal cliffs, if these are formed of soft materials, they can be eroded progressively as the waves undermine their base more frequently.

Equation 11.3 tends to predict shoreline recession in the range 50 to 200 times the rise in relative sea level. Despite the limiting two-dimensional assumptions, it has been applied with some success in near-ideal circumstances for beaches along the east coast of the United States [88]. However, the wider use of the rule is controversial. For example, the infilling of coastal embayments as sea level rises, acting as a sink of sand from the open coast, could result in erosion an order of magnitude or more greater than that predicted by the Bruun model [89], suggesting the potential for major coastal instability due to sea-level rise in the vicinity of tidal inlets.

There are many factors other than MSL changes that may be responsible for coastal erosion, including the loss of sediment supply due to construction of defences elsewhere and changing patterns of beach use. The many drivers of coastal change, the effects of sea-level rise on different types of coast, and the management of coastal change have been discussed elsewhere [90].

References

1. Emery, K. O. and Aubrey, D. G. 1991. *Sea Levels, Land Levels, and Tide Gauges*. New York: Springer-Verlag.
2. Ekman, M., 1988. The world's longest continued series of sea level observations. *Pure and Applied Geophysics*, **127**, 73–77, doi:10.1007/BF00878691.
3. Ekman, M. 2009. *The Changing Level of the Baltic Sea During 300 Years: A Clue to Understanding the Earth*. Åland Islands: Summer Institute for Historical Geophysics (www.historicalgeophysics.ax).
4. Details of the Niigata earthquake can be found at http://earthquake.usgs.gov/earthquakes/world/events/1964_06_16.php. This submarine earthquake generated a several metre tsunami that impacted the west coast of Japan.
5. Nicholls, R. J. 2010. Impacts of and responses to sea-level rise. In *Understanding Sea-Level Rise and Variability* (eds. J. A. Church, P. L. Woodworth, T. Aarup and S. Wilson), pp. 17–51. London: Wiley-Blackwell.
6. Shennan, I. and Woodworth, P. L. 1992. A comparison of late Holocene and twentieth century sea-level trends from the UK and North Sea region. *Geophysical Journal International*, **109**, 96–105, doi:10.1111/j.1365-246X.1992.tb00081.x.
7. Peltier, W. R. 2004. Global glacial isostasy and the surface of the ice-age Earth: the ICE-5G (VM2) model and GRACE. *Annual Review of Earth and Planetary Sciences*, **32**, 111–149, doi:10.1146/annurev.earth.32.082503.144359.
8. Lambeck, K., Woodroffe, C. D., Antonioli, F. *et al.* 2010. Palaeoenvironmental records, geophysical modelling and reconstruction of sea-level trends and variability on centennial and longer time scales. In *Understanding Sea-Level Rise and Variability* (eds. J. A. Church, P. L. Woodworth, T. Aarup and W. S. Wilson), pp. 61–121. London: WileyBlackwell.
9. Intergovernmental Oceanographic Commission. 2012. *The Global Sea Level Observing System (GLOSS) Implementation Plan – 2012*. IOC Technical Series No. 100. Paris: UNESCO/Intergovernmental Oceanographic Commission. Available from ioc.unesco.org.

10. Bevis, M., Scherer, W. and Merrifield, M. 2002. Technical issues and recommendations related to the installation of continuous GPS Stations at tide gauges. *Marine Geodesy*, **25**, 87–99, doi:10.1080/014904102753516750.
11. Intergovernmental Oceanographic Commission. 2006. *Manual on Sea-level Measurements and Interpretation. Volume IV: An Update to 2006*. (IOC Manuals and Guides No.14, Vol. IV; JCOMM Technical Report No.31; WMO/TD. No. 1339). Paris: UNESCO/ Intergovernmental Oceanographic Commission. Available from www.psmsl.org/train_and_info/.
12. Iliffe, J. C., Ziebart, M. K. and Turner, J. F. 2007. A new methodology for incorporating tide gauge data in sea surface topography models. *Marine Geodesy*, **30**, 271–296, doi:10.1080/01490410701568384.
13. Blewitt, G., Kreemer, C., Hammond, W. C. *et al.* 2006. Rapid determination of earthquake magnitude using GPS for tsunami warning systems. *Geophysical Research Letters*, **33**, L11309, doi:10.1029/2006GL026145.
14. (1) Wöppelmann, G., Letetrel, C., Santamaria, A. *et al.* 2009. Rates of sea-level change over the past century in a geocentric reference frame. *Geophysical Research Letters*, **36**, L12607, doi:10.1029/2009GL038720. (2) Santamaria-Gómez, A., Gravelle, M., Collilieux, X. *et al.* 2012. Mitigating the effects of vertical land motion in tide gauge records using a state-of-the-art GPS velocity field. *Global and Planetary Change*, 98–99, 6–17, doi:10.1016/j.gloplacha.2012.07.007.
15. Teferle, F. N., Bingley, R. M., Orliac, E. J. *et al.* 2009. Crustal motions in Great Britain: evidence from continuous GPS, Absolute Gravity and Holocene sea-level data. *Geophysical Journal International*, **178**(1), 23–46, doi:10.1111/j.1365-246X.2009.04185.x.
16. Bouin, M. N. and Wöppelmann, G. 2010. Land motion estimates from GPS at tide gauges: a geophysical evaluation. *Geophysical Journal International*, **180**, 193–209, doi:10.1111/j.1365-246X.2009.04411.x.
17. The TIGA website is adsc.gfz-potsdam.de/tiga/.
18. The SONEL website is www.sonel.org.
19. Tamisiea, M. E. and Mitrovica, J. X. 2011. The moving boundaries of sea level change: understanding the origins of geographic variability. *Oceanography*, **24**, 24–39, doi:10.5670/oceanog.2011.25.
20. Shennan, I., Milne, G. and Bradley, S. 2012. Late Holocene vertical land motion and relative sea-level changes: lessons from the British Isles. *Journal of Quaternary Science*, **27**, 64–70, doi:10.1002/jqs.1532.
21. (1) Nerem, R. S. and Mitchum, G. T. 2002. Estimates of vertical crustal motion derived from differences of TOPEX/POSEIDON and tide gauge sea level measurements. *Geophysical Research Letters*, **29**, 1934, doi:10.1029/2002GL015037. (2) Kuo, C. Y., Shum, C. K., Braun, A., Cheng, K.-C. and Yi, Y. 2008. Vertical motion determined using satellite altimetry and tide gauges. *Terrestrial, Atmospheric and Oceanic Sciences*, **19**, 21–35, doi:10.3319/TAO.2008.19.1–2.21(SA). (3) Ostanciaux, É., Husson, L., Choblet, G., Robin, C. and Pedoja, K. 2012. Present-day trends of vertical ground motion along the coast lines. *Earth-Science Reviews*, **110**, 74–92, doi:10.1016/j.earscirev.2011.10.004. (4) Wöppelmann, G. and Marcos, M. 2012. Coastal sea level rise in southern Europe and the nonclimate contribution of vertical land motion. *Journal of Geophysical Research*, **117**, C01007, doi:10.1029/2011JC007469. (5) King, M. A., Keshin, M., Whitehouse, P. L. *et al.* 2012. Regional biases in absolute sea-level estimates from tide gauge data due to residual unmodeled vertical land movement. *Geophysical Research Letters*, **39**, L14604, doi:10.1029/2012GL052348.
22. Farrell, W. E. 1972. Deformation of the Earth by surface loads. *Reviews of Geophysics*, **10**, 3, doi:10.1029/RG010i003p00761.
23. Teferle, F. N., Bingley, R. M., Williams, S. D. P., Baker, T. F. and Dodson, A. H. 2006. Using continuous GPS and absolute gravity to separate vertical land movements and changes in sea-level at tide-gauges in the UK. *Philosophical Transactions of the Royal Society*, **364**, 917–930, doi:10.1098/rsta.2006.1746.
24. Mazzotti, S., Lambert, A., Henton, J., James, T. S. and Courtier, N. 2011. Absolute gravity calibration of GPS velocities and glacial isostatic adjustment in mid-continent North America. *Geophysical Research Letters*, **38**, L24311, doi:10.1029/2011GL049846.
25. Cazenave, A., Soudarin, L., Cretaux, J.-F. and Le Provost, C. 1999. Sea level changes from Topex-Poseidon altimetry and tide gauges, and vertical crustal motions from DORIS. *Geophysical Research Letters*, **26**, 14, doi:10.1029/1999GL900472.
26. Ray, R. D., Beckley, B. D and Lemoine, F. G. 2010. Vertical crustal motion derived from satellite altimetry and tide gauges, and comparisons with DORIS measurements. *Advances in Space Research*, **45**, 1510–1522, doi:10.1016/j.asr.2010.02.020.
27. Hannsen, R. F. 2001. *Radar Interferometry: Data Interpretation and Error Analysis*. Dordrecht: Kluwer Academic Publishers.
28. Brooks, B. A., Merrifield, M. A., Foster, J. *et al.* 2007. Space geodetic determination of spatial variability in relative sea level change, Los Angeles basin. *Geophysical Research Letters*, **34**, L01611, doi:10.1029/2006GL028171.
29. (1) Milne, G. A., Mitrovica, J. X., Scherneck, H.-G. *et al.* 2004. Continuous GPS measurements of postglacial adjustment in Fennoscandia: 2. Modeling results. *Journal of Geophysical Research*, **109**, B02412, doi:10.1029/2003JB002619. (2) Lidberg, M., Johansson, J. M., Scherneck, H.-G. and Milne, G. A. 2010. Recent results based on continuous GPS

- observations of the GIA process in Fennoscandia from BIFROST. *Journal of Geodynamics*, 50, 8–18, doi:10.1016/j.jog.2009.11.010.
30. (1) Wolf, D., Klemann, V., Wunsch, J. and Zhang, F.-P. 2006. A reanalysis and reinterpretation of geodetic and geological evidence of glacial-isostatic adjustment in the Churchill Region, Hudson Bay. *Surveys in Geophysics*, 27, 19–61, doi:10.1007/s10712-005-0641-x. (2) Henton, J. A., Craymer, M. R., Ferland, R. *et al.* 2006. Crustal motion and deformation monitoring of the Canadian landmass. *Geomatica*, 60, 173–191.
 31. Sella, G. F., Stein, S., Dixon, T. H. *et al.* 2007. *Geophysical Research Letters*, 34, L02306, doi:10.1029/2006GL027081.
 32. Hillaire-Marcel, C. and Fairbridge, R. W. 1978. Isostasy and eustasy of Hudson Bay. *Geology*, 6, 117–122.
 33. Peltier, W. R., 2001. Global glacial isostatic adjustment. In *Sea level rise: history and consequences* (eds. B. C. Douglas, M. S. Kearney and S. P. Leatherman), pp. 65–95. San Diego, CA: Academic Press.
 34. (1) Woodward, R. S. 1888. On the form and position of mean sea level. *United States Geological Survey Bulletin*, 48, 87–170. (2) Farrell, W. E. and Clark, J. A. 1976. On postglacial sea level. *Geophysical Journal of the Royal Astronomical Society*, 46, 647–667, doi:10.1111/j.1365-246X.1976.tb01252.x. (3) Mitrovica, J. X. and Milne, G. A. 2003. On post-glacial sea level: I. General theory. *Geophysical Journal International*, 154, 253–267, doi:10.1046/j.1365-246X.2003.01942.x.
 35. Douglas, B. C. 1991. Global sea level rise. *Journal of Geophysical Research*, 96, C4, doi:10.1029/91JC00064.
 36. Woodworth, P. L., Gehrels, W. R. and Nerem, R. S. 2011. Nineteenth and twentieth century changes in sea level. *Oceanography*, 24, 80–93, doi:10.5670/oceanog.2011.29.
 37. Chambers, D. P., Wahr, J., Tamisiea, M. E. and Nerem, R. S. 2010. Ocean mass from GRACE and glacial isostatic adjustment. *Journal of Geophysical Research*, 115, B11415, doi:10.1029/2010JB007530.
 38. Tamisiea, M. E. 2011. Ongoing glacial isostatic contributions to observations of sea level change. *Geophysical Journal International*, 186, 1036–1044, doi:10.1111/j.1365-246X.2011.05116.x.
 39. Peltier, W. R., Drummond, R. and Roy, K. 2012. Comment on “Ocean mass from GRACE and glacial isostatic adjustment” by D. P. Chambers *et al.* *Journal of Geophysical Research*, 117, B11403, doi:10.1029/2011JB008967.
 40. Steffen, H. and Wu, P. 2011. Glacial isostatic adjustment in Fennoscandia: a review of data and modeling. *Journal of Geodynamics*, 52, 169–204, doi:10.1016/j.jog.2011.03.002.
 41. Kendall, R. A., Latychev, K., Mitrovica, J. X., Davis, J. E. and Tamisiea, M. E. 2006. Decontaminating tide gauge records for the influence of glacial isostatic adjustment: The potential impact of 3-D Earth structure. *Geophysical Research Letters*, 33, L24318, doi:10.1029/2006GL028448.
 42. Syvitski, J. P. M. 2008. Deltas at risk. *Sustainability Science*, 3, 23–32, doi:10.1007/s11625-008-0043-3.
 43. Syvitski, J. P. M., Kettner, A. J., Overeem, I. *et al.* 2009. Sinking deltas due to human activities. *Nature Geoscience*, 2, 681–686, doi:10.1038/ngeo629.
 44. Bird, P. 2003. An updated digital model of plate boundaries. *Geochemistry, Geophysics and Geosystems*, 4, 1027, doi:10.1029/2001GC000252.
 45. Di Donato, G., Negredo, A. M., Sabadinai, R. and Vermeersen, L. L. A. 1999. Multiple processes causing sea-level rise in the Central Mediterranean. *Geophysical Research Letters*, 26, 12, doi:10.1029/1999GL900258.
 46. Chappell, J., Ota, Y. and Berryman, K. 1996. Late Quaternary coseismic uplift history of Huon Peninsula, Papua New Guinea. *Quaternary Science Reviews*, 15, 7–22, doi:10.1016/0277-3791(95)00062-3.
 47. Church, J. A., Gregory, J. M., Huybrechts, O. *et al.* 2001. Changes in sea level. In *Climate Change 2001: The Scientific Basis. Contribution of Working Group I to the Third Assessment Report of the Intergovernmental Panel on Climate Change* (eds. J. T. Houghton, Y. Ding, D. J. Griggs *et al.*). Cambridge: Cambridge University Press.
 48. Darwin, C. 1845. A naturalist’s voyage: journal of researches into the natural history and geology of the countries visited during the voyage of H.M.S. *Beagle Round the World* (2nd edition). London: John Murray. (Note that the texts of versions of this book are freely available on the internet.)
 49. As one of many examples, see Nishimura, T., Munekane, H. and Yurai, H. 2011. The 2011 off the Pacific coast of Tohoku Earthquake and its aftershocks observed by GEONET. *Earth, Planets and Space*, 63, 631–636, doi:10.5047/eps.2011.06.025.
 50. Mitrovica, J. X., Tamisiea, M. E., Ivins, E. R. *et al.* 2010. Surface mass loading on a dynamic Earth: complexity and contamination in the geodetic analysis of global sea-level trends. In *Understanding Sea-Level Rise and Variability* (eds. J. A. Church, P. L. Woodworth, T. Aarup and W. S. Wilson), pp. 289–325. London: Wiley-Blackwell.
 51. Meltzner, A. J., Sieh, K., Abrams, M. *et al.* 2006. Uplift and subsidence associated with the great Aceh-Andaman earthquake of 2004. *Journal of Geophysical Research*, 111, B02407, doi:10.1029/2005JB003891.
 52. Melini, D. and Piersanti, A. 2006. Impact of global seismicity on sea level change assessment. *Journal of*

- Geophysical Research*, **111**, B03406, doi:10.1029/2004JB003476.
53. Centro Nacional de Datos Hidrográficos y Oceanográficos de Chile (CENHOC) of the Servicio Hidrográfico y Oceanográfico de la Armada de Chile (SHOA), www.shoa.cl/cendhoc_php/.
 54. Penland, S. and Ramsey, K. E. 1990. Relative sea-level rise in Louisiana and the Gulf of Mexico: 1908–1988. *Journal of Coastal Research*, **6**, 323–342.
 55. Phien-Wej, N., Giao, P. H. and Nutalaya, P. 2006. Land subsidence in Bangkok, Thailand. *Engineering Geology*, **82**, 187–201, doi:10.1016/j.enggeo.2005.10.004.
 56. Jacinto, G. S., Azanza, R. V., Velasquez, I. B and Siringan, F. P. 2006. Manila Bay: environmental challenges and opportunities. In *The Environment in Asia Pacific Harbours* (ed. E. Wolanski), pp. 309–328. Berlin: Springer.
 57. Camuffo, D. and Sturaro, G. 1983. Sixty-cm submersion of Venice discovered thanks to Canaletto's paintings. *Climatic Change*, **58**, 333–343, doi:10.1023/A:1023902120717.
 58. Pirazzoli, P. A. 1991. Possible defenses against a sea-level rise in the Venice Area, Italy. *Journal of Coastal Research*, **7**, 231–248.
 59. Woodworth, P. L. 2003. Some comments on the long sea level records from the northern Mediterranean. *Journal of Coastal Research*, **19**, 212–217.
 60. Bock, Y., Wdowinski, S., Ferretti, A., Novali, F. and Fumagalli, A. 2012. Recent subsidence of the Venice Lagoon from continuous GPS and interferometric synthetic aperture radar. *Geochemistry, Geophysics, Geosystems*, **13**, doi:10.1029/2011GC003976.
 61. Humphries, L. 2001. A review of relative sea level rise caused by mining-induced subsidence in the coastal zone: some implications for increased coastal recession. *Climate Research*, **18**, 147–156, doi:10.3354/cr018147.
 62. Mitrovica, J. X., Tamisiea, M. E., Davis, J. L. and Milne, G. A. 2001. Recent mass balance of polar ice sheets inferred from patterns of global sea-level change. *Nature*, **409**, 1026–1029, doi:10.1038/35059054.
 63. Riva, R. E. M., Bamber, J. L., Lavallée, D. A. and Wouters, B. 2010. Sea-level fingerprint of continental water and ice mass change from GRACE. *Geophysical Research Letters*, **37**, L19605, doi:10.1029/2010GL044770.
 64. Yin, J. J., Schlesinger, M. E. and Stouffer, R. J. 2009. Model projections of rapid sea level rise on the northeast coast of the United States. *Nature Geoscience*, **2**, 262–266, doi:10.1038/ngeo462.
 65. Lorbacher, K., Dengg, J., Böning, C. W. and Biastoch, A. 2010. Regional patterns of sea level change related to interannual variability and multidecadal trends in the Atlantic Meridional Overturning Circulation. *Journal of Climate*, **23**, 4243–4254, doi:10.1175/2010JCLI3341.1.
 66. (1) Sallenger, A. H. Jr, Doran, K. S. and Howd, P. A. 2012. Hotspot of accelerated sea-level rise on the Atlantic coast of North America. *Nature Climate Change*, **2**, 884–888, doi:10.1038/NCLIMATE1597. (2) Boon, J. D. 2012. Evidence of sea level acceleration at U.S. and Canadian tide stations, Atlantic coast, North America. *Journal of Coastal Research*, **28**, 1437–1445, doi:10.2112/JCOASTRES-D-12-00102.1.
 67. Meehl, G. A., Stocker, T. F., Collins, W. *et al.* 2007. Global climate projections. In *Climate Change 2007: The Physical Science Basis. Contribution of Working Group 1 to the Fourth Assessment Report of the Intergovernmental Panel on Climate Change* (eds. S. Solomon, D. Qin and M. Manning). Cambridge: Cambridge University Press.
 68. Gregory, J. M., White, N. J., Church, J. A. *et al.* 2012. Twentieth-century global-mean sea-level rise: is the whole greater than the sum of the parts? *Journal of Climate*, **26**, 4476–4499, doi:10.1175/JCLI-D-12-00319.1.
 69. (1) Plag, H.-P. 2006. Recent relative sea-level trends: an attempt to quantify the forcing factors. *Philosophical Transactions of the Royal Society of London A*, **364**, 821–844, doi:10.1098/rsta.2006.1739. (2) Wake, L. M., Milne, G. A. and Leuliette, E. 2006. 20th Century sea-level change along the eastern US: unravelling the contributions from steric changes, Greenland ice sheet mass balance and Late Pleistocene glacial loading. *Earth and Planetary Science Letters*, **250**, 572–580, doi:10.1016/j.epsl.2006.08.006. (3) Marcos, M. and Tsimplis, M. N. 2007. Forcing of coastal sea level rise patterns in the North Atlantic and the Mediterranean Sea. *Geophysical Research Letters*, **34**, L18604, doi:10.1029/2007GL030641 (4) Engelhart, S. E., Horton, B. P., Douglas, B. C., Peltier, W. R. and Trnqvist, T. E. 2009. Spatial variability of late Holocene and 20th century sea-level rise along the Atlantic coast of the United States. *Geology*, **37**, 1115–1118, doi:10.1130/G30360A.
 70. Mitrovica, J. X., Gomez, N., Morrow, E., *et al.* 2011. On the robustness of predictions of sea level fingerprints. *Geophysical Journal International*, **187**, 729–742, doi:10.1111/j.1365-246X.2011.05090.x.
 71. Fiedler, J. W. and Conrad, C. P. 2010. Spatial variability of sea level rise due to water impoundment behind dams. *Geophysical Research Letters*, **37**, L12603, doi:10.1029/2010GL043462.
 72. Dyer, K. R. 1997. *Estuaries: A Physical Introduction*. Chichester: John Wiley and Sons.
 73. Dearing, J. A., Richmond, N., Plater, A. J. *et al.* 2006. Modelling approaches for coastal simulation based on cellular automata: the need and potential. *Philosophical*

- Transactions of the Royal Society A*, **364**, 1051–1071; doi:10.1098/rsta.2006.1753 1471–2962.
74. Mokrech, M., Hanson, S., Nicholls, R. *et al.* 2011. The Tyndall coastal simulator. *Journal of Coastal Conservation*, **15**, 325–335, doi:10.1007/s11852-009-0083-6.
 75. Pugh, D. T. 1987. *Tides, Surges and Mean Sea-Level: A Handbook for Engineers and Scientists*. Chichester: Wiley. This book may be downloaded from www.psmssl.org.
 76. Hill, D. F., Griffiths, S. D., Peltier, W. R., Horton, B. P. and Törnqvist, T. E. 2011. High-resolution numerical modeling of tides in the western Atlantic, Gulf of Mexico, and Caribbean Sea during the Holocene. *Journal of Geophysical Research*, **116**, C10014, doi:10.1029/2010JC006896.
 77. Uehara, K., Scourse, J. D., Horsburgh, K. J., Lambeck, K. and Purcell, A. 2006. Tidal evolution of the northwest European shelf seas from the last glacial maximum to the present. *Journal of Geophysical Research*, **111**, C09025, doi:10.1029/2006JC003531.
 78. Hoitink, A. J. F., Hoekstra, P. and van Maren, D. S. 2003. Flow asymmetry associated with astronomical tides: implications for the residual transport of sediment. *Journal of Geophysical Research*, **108**, 3315, doi:10.1029/2002JC001539.
 79. Van Maren, D. S., Hoekstra, P. and Hoitink, A. J. F. 2004. Tidal flow asymmetry in the diurnal regime: bed load transport and morphologic changes around the Red River Delta. *Ocean Dynamics*, **54**, 424–434, doi:10.1007/s10236-003-0085-0.
 80. Woodworth, P. L., Blackman, D. L., Pugh, D. T. and Vassie, J. M. 2005. On the role of diurnal tides in contributing to asymmetries in tidal probability distribution functions in areas of predominantly semi-diurnal tide. *Estuarine, Coastal and Shelf Science*, **64**, 235–240, doi:10.1016/j.ecss.2005.02.014.
 81. Araújo, I. B., Dias, J. M. and Pugh, D. T. 2008. Model simulations of tidal changes in a coastal lagoon, the Ria de Aveiro (Portugal). *Continental Shelf Research*, **28**, 1010–1025, doi:10.1016/j.csr.2008.02.001.
 82. (1) Woodworth, P. L., Shaw, S. M. and Blackman, D. B. 1991. Secular trends in mean tidal range around the British Isles and along the adjacent European coastline. *Geophysical Journal International*, **104**, 593–610, doi:10.1111/j.1365-246X.1991.tb05704.x. (2) Wahl, T., Jensen, J. and Frank, T. 2010. On analysing sea level rise in the German Bight since 1844. *Natural Hazards and Earth System Sciences*, **10**, 171–179, www.nat-hazards-earth-syst-sci.net/10/171/2010/.
 83. Wong, P. P. *et al.* 2014. Coastal systems and low-lying areas. In *Climate Change 2013: Impacts, Adaptation and Vulnerability. Working Group II Report of the Fifth Scientific Assessment of the Intergovernmental Panel on Climate Change*, Chapter 5. Cambridge: Cambridge University Press.
 84. Bird, E. C. F. 1985. *Coastline Changes: A Global Review*. Chichester: John Wiley and Sons.
 85. Gratiot, N., Anthony, E. J., Gardel, A. *et al.* 2008. Significant contribution of the 18.6 year tidal cycle to regional coastal changes. *Nature Geoscience*, **1**, 169–172, doi:10.1038/ngeo127.
 86. Taylor, J. A., Murdock, A. P. and Pontee, N. I. 2004. A macroscale analysis of coastal steepening around the coast of England and Wales. *Geographical Journal*, **170**, 179–188, doi:10.1111/j.0016-7398.2004.00119.x.
 87. Bruun, P. 1962. Sea-level rise as a cause of shore erosion. *Journal of the Waterways and Harbors Division*, **88**, 117–130.
 88. Zhang, K. Q., Douglas, B. C. and Leatherman, S. P. 2004. Global warming and coastal erosion. *Climatic Change*, **64**, 41–58, doi:10.1023/B:CLIM.0000024690.32682.48.
 89. Woodworth, P. L., Gregory, J. M. and Nicholls, R. J. 2004. Long term sea level changes and their impacts. In *The Sea: Volume 13* (eds. A. R. Robinson and K. H. Brink), pp. 715–753. Cambridge, MA: Harvard University Press.
 90. Plater, A. J. and Kirby, J. R. 2011. Sea-level change and coastal geomorphic response. In *Treatise on Estuarine and Coastal Science: Volume 3* (eds. E. Wolanski and D. S. McLusky), pp. 39–72. Waltham, MA: Academic Press.
 91. ESA, 1999. *The Gravity Field and Steady-State Ocean Circulation Mission*. Reports for Mission Selections. ESA Report SP-1233(1). Noordwijk, the Netherlands: European Space Agency.
 92. Lyell, C. 1835. On the proofs of a gradual rising of the land in certain parts of Sweden. *Philosophical Transactions of the Royal Society of London*, **125**, 1–38, doi:10.1098/rstl.1835.0002.

Sea-level applications

... we cannot tell
 When any given tide on the heart's shore
 Comes to the full.
 ... Few could endure
 That knowledge, and not die.
 It is better to be unsure.
Jan Struther, High Tide

The application of sea-level and tidal knowledge to the design and construction of useful marine structures and systems includes:

- harbour design and operation,
- design of coastal defences to resist flooding,
- coastal sediment control, groynes,
- flood warning systems,
- estuary, wetland, lagoon and inlet management,
- offshore structures for gas and oil extraction,
- schemes for generating power,
- cooling water intakes, effluent discharges to the sea,
- climate change forecasts and planning.

Tides offer many invaluable on-going environmental services that are not costed or charged. Ship routing between ports has used tides since historical times. Most of the great ports of the world are situated near the mouths of large rivers and many are a considerable distance inland. London, on the River Thames, and Hamburg, on the River Elbe, are good examples of inland ports. By travelling inward on a flooding tide and outward on an ebbing tide, ships can make considerable savings of fuel and time. The vigorous tidal currents serve to keep channels deep. The tidal flows can also prevent harbours freezing during winter, for example in New York, both by their mixing action and by the introduction of salt water which lowers the freezing point. Pollution, inevitably associated with large industrial developments and centres of population, is also more readily diluted and discharged to sea where there are regular exchanges of tidal water. The

conditions for ports where tidal ranges are relatively large may be contrasted favourably with those, for example Marseilles, where tides are small. The pollution problems are much greater in the Mediterranean, and despite their high rates of fresh-water discharge, neither the Rhone nor the Nile have proved navigable for any but the smallest sea-going vessels.

When planning marine engineering works, the design parameters include not only sea-level changes: tides, surges, tsunamis and mean sea level (MSL), but also waves, winds, earthquakes, sediment movement, marine fouling and ice movement. Here we focus only on the sea-level aspects of the design engineer's considerations.

12.1 Design parameters

The environmental parameters for the design engineer to consider will depend on the system being designed. Statistical analyses are most common, and fall into two general classes, those that deal with the normal operational conditions, and those that describe the extreme conditions that a structure must survive. The relative importance of these two aspects will depend on the type of project. Coastal defences must be high enough to protect against the highest expected levels; here normal conditions are less relevant but may have to be considered when adding amenities such as public paths. Conversely, although tidal power schemes and harbours must survive the most extreme conditions, they must also be carefully designed to work efficiently during normal operating conditions.

Authorities that have a statutory responsibility to give approval for new schemes issue guidelines for the design engineer. These publications are often phrased in general terms because each proposed construction is slightly different, and because the relative importance of the several environmental parameters depends on the location. It is very unusual to have access to the quantity (or quality) of data that many of the theoretical techniques described in this chapter require. Estimates of the statistics of the relevant tidal and other parameters are usually based on only limited observations at the site proposed, so that extrapolation of the available data in both time and space is inevitable. It is necessary to decide how valid it will be to use data from another location, and the best way to make this transfer.

The patterns of normal tidal behaviour at a site have been considered in [Chapter 1](#). [Figure 1.5](#) shows the probability density function (pdf) of tidal levels at both Newlyn and Karumba, derived from hourly height predictions. The common terms ([Section 1.5](#) and [Appendix C](#)) such as Mean High Water Spring and Mean Low Water Spring, Highest and Lowest Astronomical Tide and Mean Sea Level have all been developed over many years because of their practical use in approximately defining the tidal environment.

The best way to determine the tidal parameters at a site is to analyse a year, or if this is not possible at least a month, of hourly observations of the levels or currents. Many parameters may then be determined directly from the resulting harmonic constituents. If only a month of data is available, a tidal analysis that makes use of the known tidal characteristics at a nearby site, either as related harmonic constituents or computed through intermediate response functions, may be adequate. The most difficult parameters to estimate from only short periods of data are [MSL](#) and the probability distribution of the non-tidal (mainly meteorological) residuals, because both of these change seasonally. In the case of [MSL](#) the monthly mean level may be adjusted by comparison of simultaneous [MSLs](#) at a nearby permanent station with long-term information. Any differences may then be used to adjust the mean level at the secondary site: such a transfer is acceptable because seasonal changes of sea level are similar over long distances [[1](#)]. Extrapolating the statistics of meteorological residuals from one site to another is less reliable because topography, weather and other local effects can result in important local differences over a short distance.

Tidal parameters are also summarised in national tide tables. The basic parameters obtained from the published charts and tables are adequate for most straightforward applications, but more elaborate engineering systems may require further specific details. An example might be the engineer who needs to relate elevations and currents along a complicated route for towing a structure from a fabricating yard to an offshore site during a particular month of the year. Sometimes these questions may be answered by scrutiny of the harmonic constituents, but in general it is better to make observations and to then generate the required information numerically from tidal predictions and modelling.

12.2 Extreme conditions

Coastal defences are designed to protect against flooding from very high sea levels, and accompanying waves. By definition these occur very rarely. Assuming the individual extreme events are independent of each other, useful statistics can be derived. Later we look specifically at standard analyses used by design engineers. Here we outline briefly the general use of sea-level data to estimate the likelihood of flooding. Essentially, analyses seek to define the likelihood of sea levels reaching or exceeding specific design levels, either in a calendar year or, more specifically, over a structure's lifetime. Obviously the higher the level, the better the protection; but also, the higher the construction costs, and the probable losses of visual amenities.

Sometimes the term *risk* is used just to describe the flooding event likelihood, but this is incorrect. The *risk* is here defined as the probability or likelihood of an event, multiplied by the consequential costs, or impacts on what is at risk. Planners assessing total *risk* need to know both the flooding likelihood and the value of the assets that might be impacted. Standards for risk assessment and management have been internationally agreed [[2](#)].

There is a necessary and important distinction between knowing the risks and ignoring them. Known risks can be assessed from observations using probability theory, and knowing the value of what is being protected. These can be incorporated into planning, investment, and defence design; if the risks are not known there is no basis for making decisions, other than 'trusting to luck'.

The methods that we discuss here are most effective for calculating extremes for extratropical regions,

outside areas influenced by hurricanes. In these extra-tropical regions extreme sea levels are usually due to a combination of high astronomical tides and extreme weather effects. In the tropics particularly violent hurricanes can result in statistical outliers in the measured extremes, which make statistical modelling and extrapolation less reliable.

It is assumed that MSL trends have been removed from the data before analysis. For details of the application of the following methods readers should consult specialised publications [3, 4, 5].

For each high water extreme level it may be possible to estimate the Average Recurrence Interval (ARI) of exceedance. The higher the level, the longer is the ARI. Hence, for a level with an exceedance ARI of T years, the *expected* number of occurrences (N) of exceedance over M years will be $N = M/T$. However, over different periods of M years, the actual number of occurrences will vary above and below this expected average. Statistically this scatter is a binomial distribution, and in the case of large ARIs this converges to the Poisson distribution, with the property that the probability of exactly x occurrences over an interval M is:

$$\text{Probability}(x, N) = \exp(-N) \frac{N^x}{x!} \quad (12.1)$$

This applies for zero, and for all positive integer values of x . For extreme levels, in any chosen single ARI period, there is a 37 per cent chance of no event, a 37 per cent chance of a single event, 18 per cent of two events and 6 per cent of three events. More than three events will happen on only 2 times in a hundred.

We are particularly interested in the likelihood of *no exceedance* ($x = 0$) in a specified design period. For this simple case of no exceedance events over a period, the probability is $\exp(-N)$. Further, the probability of exceedance is:

$$F = 1 - \exp(-N)$$

If a structure has a lifetime of $M = 100$ years and the ARI of the design level is $T = 200$ years, the probability of non-exceedance is $\exp(-100/200) = 0.61$; and of exceedance is 0.39. This exceedance figure is called the design encounter probability. As shown in Figure 12.1, a structure designed to protect against a level with a return period equal to its design life ($N = 1$) will have a 63 per cent likelihood of being reached or exceeded in its lifetime.

Clearly, designing for a level of protection that has an expected lifetime equal to the ARI is generally not

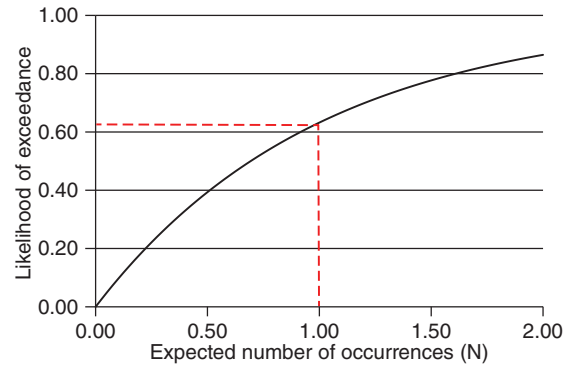


Figure 12.1 The likelihood of encountering an extreme level as a function of the expected number of such events (N) in a period. For example, the dotted line shows that if the structure is to last for 100 years then there is a 0.63 probability of encountering the 100-year level ($N = 1$) during its lifetime.

acceptable. For good design, the *design level* must have an ARI that considerably exceeds the expected lifetime of the structure. As an example, suppose that the envisaged life of a structure is 100 years, then for probability of 0.1 of exceedance during this period, the design level should have $N = 0.1053$, equivalent to an ARI of 950 years.

Although widely used, the term ‘return period’ for ARIs should be avoided. It is often misunderstood in popular thinking to imply regularly occurring flood levels once every return period, or that after a flood there will be no further floods until a further return period has elapsed. The alternative, *recurrence interval*, is similarly misunderstood.

12.2.1 Regional factors

The simplest approach to estimating extreme level probabilities is to compute the ratio between some normal tidal parameter and the level having a specified ARI of years for a Standard Port in a region and some defined tidal parameter. For values relative to MSL, one such factor, shown in Figure 12.2, is defined as:

$$\gamma_1 = \frac{\text{One year highest sea level}}{\text{Mean high water spring level}} \quad (12.2)$$

An alternative for longer periods and more extreme levels is:

$$\alpha_{100} = \frac{100\text{-year highest sea level}}{\text{HAT} + 100\text{-year surge}} \quad (12.3)$$

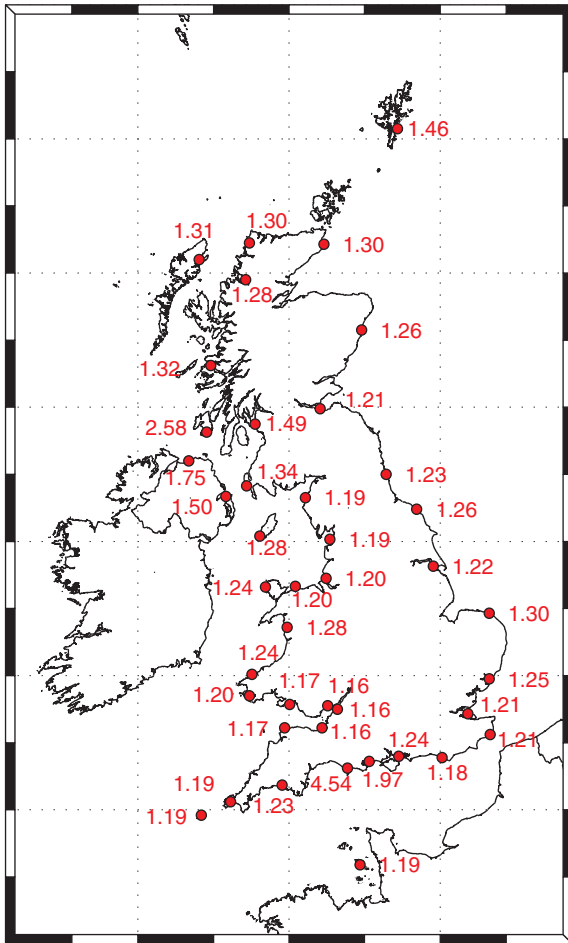


Figure 12.2 Ratio (γ_1) of the 1-year return level to MHWS at tide gauges in the UK network.

The 100-year surge levels may be estimated from a long series of non-tidal residuals, or by analytical or numerical models, which relate them to 100-year winds. Clearly α_{100} , the most pessimistic case where the 100-year surge level is assumed always to coincide with Highest Astronomical Tide, has a maximum value of 1.0. Building structures for $\alpha_{100} = 1.0$ will almost certainly lead to expensive over-design. In practice the values are lower than this because extreme surges will probably occur with more normal tidal levels. Around the British Isles α_{100} is typically in the range 0.8 to 0.9, except in the southern North Sea, where the value falls to around 0.72. This reduction is because the local shallow water dynamics, discussed in [Chapter 7](#), cause large surges to avoid times of high water of astronomical tides ([Section 7.3.1](#)); this is a very fortunate interaction as it substantially lowers the

levels of potential flooding of London and the Netherlands.

12.2.2 Analysis of annual extreme values

Design engineers traditionally prefer to work with annual likelihood statistics, $Q(z)$, noting their close link with ARIs. Working with annual likelihoods avoids any complications of seasonal changes in flooding probabilities: both tides and surges have strong seasonal variations so extreme levels have a seasonal cycle (weather effects are generally greatest in winter, and the semidiurnal tides are often biggest in March and September). In order to determine the value of $Q(z)$, the annual likelihood of exceedance of a level z , from which flooding probabilities and risks may be estimated, it is first necessary to tabulate the maximum levels reached in each of as many years as possible.

The annual maxima for 84 years of Newlyn data are plotted as a histogram in [Figure 12.3](#). The level of Highest Astronomical Tide (3.0 m) was exceeded in only 28 of the years. The broken curve in [Figure 12.3](#) shows the probability of a particular level (z) being exceeded in any single year. For example, the probability of an annual maximum level exceeding 3.0 m at Newlyn is 0.33, because 28-yearly maxima in the set of 84 were higher than this. Expressed in a different way, an annual maximum in excess of 3.0 m has an ARI of 3 years. Plots like [Figure 12.3](#) are useful for representing the general characteristics of annual maxima, but they cannot be used for the extrapolations necessary when estimating for extreme events, which by definition have a very low likelihood, $Q(z)$.

If the probability of a level z being exceeded in a single year is $Q(z)$, that level is often (and misleadingly, see above) said to have a return period, which is the inverse of $Q(z)$ in years; we have called this the ARI. For example, a sea level having a probability of being exceeded in a single year of 0.05 has an ARI 20 years.

This inversion of annual exceedance probabilities to give an ARI makes the implicit assumption that the same statistics are valid for the whole period specified. For very small probabilities, where this may be many tens or hundreds of years, this can be a very big assumption. It would be absurd to say the 10^{-4} flood level has a 10,000-year return period, because climate and MSL conditions have changed substantially over that period, and will do so in future.

The appropriate value of $Q(z)$ and hence z chosen for coastal planning will depend on the value of the property at risk. Nuclear power stations may specify

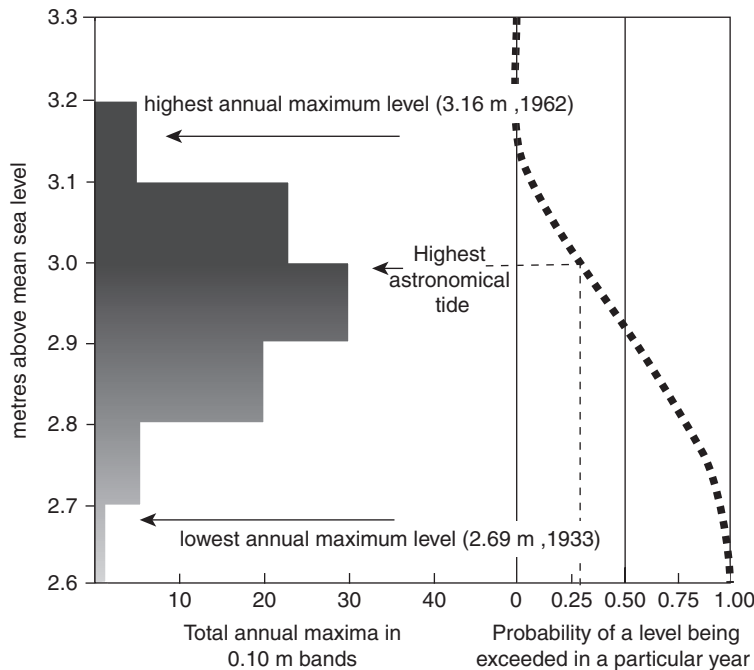


Figure 12.3 The observed annual maximum sea levels at Newlyn relative to MSL, 1916–2000, and the probability of a level being exceeded in a particular year. MSL trends are removed from the data. The most probable annual maximum level lies in the band 2.9 to 3.0 m above MSL. The fine dotted line shows that the highest astronomical tide (3.0 m) has a probability of 0.3 of being exceeded in a particular year.

10^{-5} or 10^{-6} . For the coastal protection of the Netherlands a value of 10^{-4} is adopted, but for many British coastal protection schemes values of 10^{-3} or greater are accepted.

One way of presenting the likelihoods of extreme still water levels is as the probability that a stated extreme level will be exceeded at least once during the specified design life of the structure. This factor, which depends on N (see above), is called the *design encounter probability*. For the first year the likelihood of reaching z is $Q(z)$, and the probability of *not* reaching that level is $F(z) = (1 - Q(z))$. The probability of not reaching an extreme level, z , in either of the first two years is $(1 - Q(z))^2$ and the likelihood of reaching the level is $[1 - (1 - Q(z))^2]$. As a simple comparison, this is the same as calculating the chance of throwing two dice and not showing a six on either. For a sea-level example, if $Q(z)$ is 0.1, the risk of exceeding the level z in the first two years is 0.19.

We can continue these arguments, to understand the statistics, taking a specific semidiurnal tidal regime example for illustration. Suppose a level has an ARI of $R(z)$ years. This means that *on average* one high water out of $705R(z)$ will exceed z . This makes use of the fact that there are 705 semidiurnal tidal high waters in a year. Hence the probability of a particular high water, chosen at random, failing to reach z is $\left(1 - \frac{1}{705R(z)}\right)$

and the probability that all 705 high waters in a year will fail to reach the level is $\left(1 - \frac{1}{705R(z)}\right)^{705}$. For such a large exponent, the series and hence the annual *non-exceedance* probability approximates the Poisson distribution described above, to give $\exp\left(-\frac{1}{R(z)}\right) = \exp(-Q(z))$. This is, of course, a specific case of Equation 12.1.

The usual procedure is next to fit a curve to values of z plotted against the probability of annual exceedance, as in Figure 12.3 [3, 4]. Plotting the levels against the X-axis logarithmic scale for probability has the advantages of opening out the two ends of the probability curve ($P = 0$ and $P = 1$) relative to its central position, and of making the transformed curve approximately linear (Figure 12.4a). The family of curves used for fitting and extrapolating to very low probability events is known as the Generalised Extreme Value (GEV) distribution. The most appropriate curve is usually fitted to the data using either least-squares or maximum likelihood methods.

A widely applied function to fit to these extremes is the Gumbel cumulative distribution, which may be expressed [4] as:

$$\exp\left[-\exp\left(\frac{\mu - z}{\lambda}\right)\right] \quad (12.4)$$

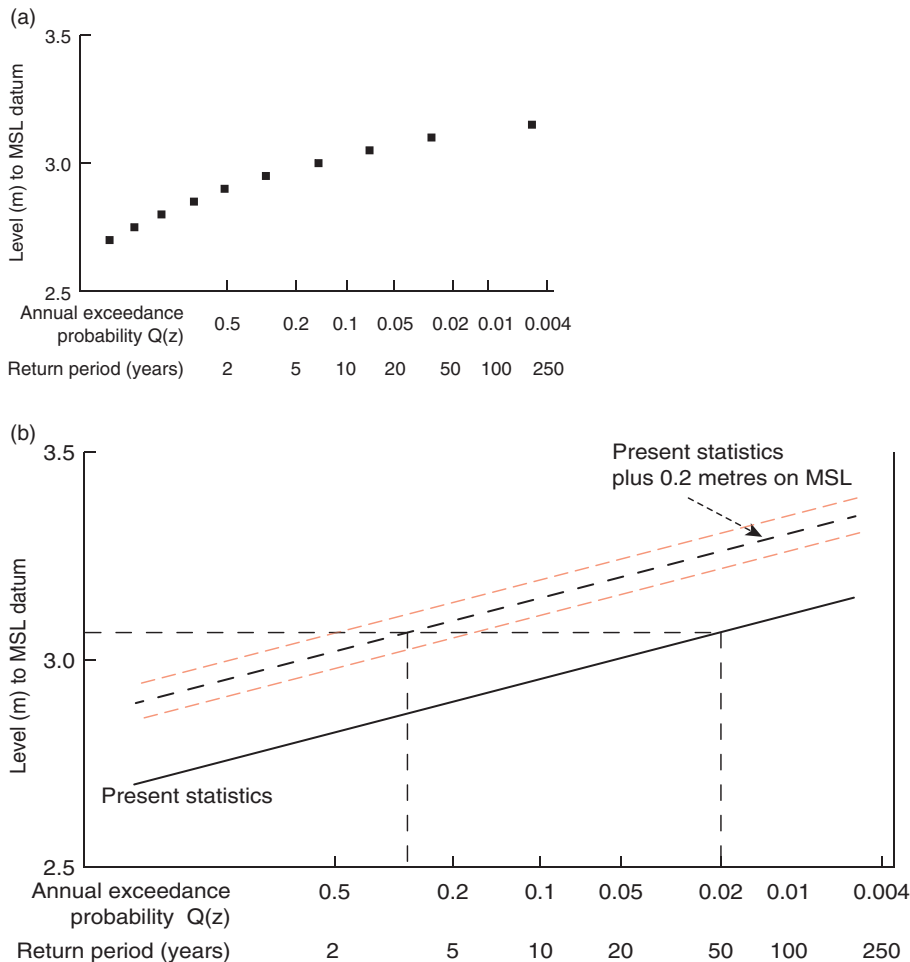


Figure 12.4 (a) A different way of showing the information in Figure 12.3. This shows the probabilities of annual maximum levels at Newlyn falling below a specified level. *MSL* trends have been removed. (b) This shows the effects of a *MSL* rise on flooding risks. The solid line is a simplified version of the curve plotted in (a). The heavy dashed line adjusts the 1916–2000 statistics for a 0.2 m rise in *MSL*. The fine dashed line shows that a level of 3.1 m at Newlyn, now reached once every 50 years, will then be reached approximately every 4 years. The red dashed lines show a possible range of uncertainty in future sea-level rises (see Section 12.2.5).

where z is the level, μ is a location parameter, and λ is a scale parameter; all three have units of length. These parameters, μ and λ , are determined in the fitting process; μ is the level for which the average number of exceedances, N , in a period, T , is unity. For example, for a curve of annual maximum levels, μ is the level with an ARI of a year; λ describes the variability in the distribution of the extremes of sea level (not in the total sea-level variability) [6].

Although as few as ten annual maxima have been used to compute probability curves, experience suggests that at least 25 annual values are needed for a satisfactory analysis. As a general rule extrapolation should be limited to return periods not longer than four times the

period of annual maximum levels available for analysis, but even within this limit extrapolated values should be interpreted with caution. Experience also shows that the form of the extrapolated curve is almost always strongly controlled by the last few points of the plotted values; it is often found that one or two extreme levels observed during the period appear to lie outside the usual distribution pattern. As mentioned above, tropical storms are particularly prone to this under-sampling problem because of their concentrated local impacts. The degree of weight given to these becomes a matter for subjective judgement. They cannot be discounted easily: the dangers of omitting the most extreme, genuine sea-level values from an analysis are obvious.

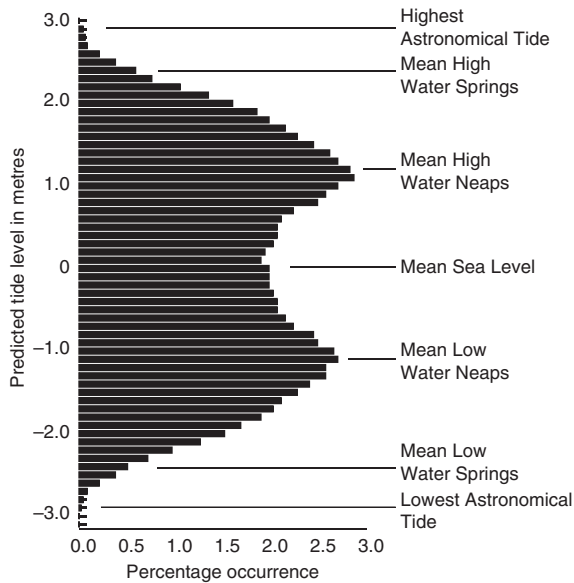


Figure 12.5 The frequency distribution of hourly tidal levels at Newlyn over an 18-year nodal period. The intervals are 0.1 m. The most probable levels are at mean high water neaps and mean low water neaps. This shows in bar form the distribution in Figure 1.5a.

The major disadvantage of the annual maxima method is the waste of data, because a complete year of observations is being represented by a single value. If the largest non-tidal surge for the year coincides with a low tidal level, the information is ignored despite its obvious relevance to the problem of estimating extreme level probabilities. Other techniques, which avoid this, are described below.

12.2.3 Joint tide–surge probability estimates

An alternative way of estimating probabilities of extreme levels is to make use of the separate distribution of tidal and surge frequencies. Tidal probabilities can be determined from quite short periods of data by tidal analysis because the range of tidal forcing is well known from the astronomy. Figure 12.5 shows the statistical distribution of predicted tidal level at Newlyn over an 18-year period; the same information is in a different form in Figure 1.5a. The double-humped distribution, with the most frequent levels near to mean high and mean low water on neap tides is typical of semidiurnal tidal regimes. The frequency distribution of non-tidal (surge) levels is plotted in a similar way in Figure 7.8b. Figure 12.6 shows the variability from year to year in the surge extremes.

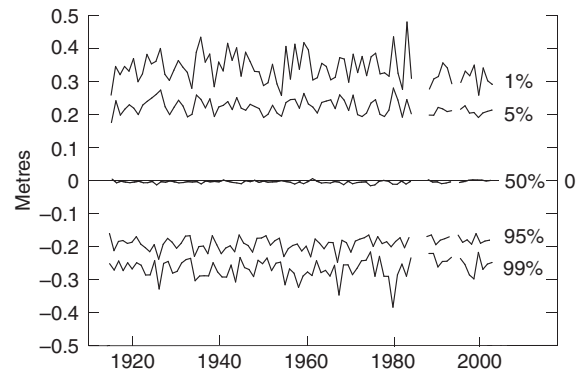


Figure 12.6 Annual exceedance percentile levels of non-tidal sea-level residuals at Newlyn, 1916–2000. Annual MSLs have been removed in the analysis. These curves show the levels, with the stated percentage of time for which they are exceeded. For example, residuals are more negative than the values in the 99 per cent curve for only 1 per cent of the time.

Table 12.1 shows how joint tide–surge probabilities can be calculated in practice. In this example we assume that the extreme sea levels occur on a high tide, when there is also a large positive surge. The residual (surge) and predicted (tidal) high water levels over a complete number of years are tabulated to produce normalised frequency distributions. An appropriate tabulating interval is 0.1 m. In the example shown in Table 12.1 the tidal high water levels and the meteorological distributions have been artificially restricted to five 0.1 m class intervals in each case. Forty per cent of the observed residuals are in the range of -0.05 m to $+0.05$ m, whereas 10 per cent are in the range 0.15 m to 0.25 m. The highest tides lie in the range 3.15 m to 3.25 m above the defined datum, represented by the 3.2 m band.

The frequency distributions of the surge observations and the tidal predictions are then assumed to be representative of the probability of future events. This is not a trivial assumption, particularly in the context of climate change. The joint probability of a 3.2 m predicted tide and a 0.0 m surge is 0.04, the product of their individual probabilities. Similarly, a 3.1 m tide and a 0.1 m residual have a joint probability of 0.04. For a 3.0 m tide with a 0.2 m residual the probability is 0.03. Any of these three joint events will produce a total observed high water level of 3.2 m, and so the total probability of a 3.2 m level, obtained by scanning along the dashed diagonal, is the sum of the three probabilities, 0.11. Eleven per cent of all observed sea levels will lie between 3.15 m and 3.25 m.

In this example the highest total level, 3.4 m, can only occur when a 3.2 m tide and a 0.2 m residual

Table 12.1 Examples of high water and high water residual probabilities for calculating joint probabilities. For example, a surge of 0.1 m represents all surges in the range 0.05 to 0.15 m.

Tidal HW levels (m)	Normalised frequency	Non-tidal residuals (m)				
		-0.2	-0.1	0.0	0.1	0.2
3.2	0.1	0.01	0.02	0.04	0.02	0.01
3.1	0.2	0.02	0.04	0.08	0.04	0.02
3.0	0.3	0.03	0.06	0.12	0.06	0.03
2.9	0.3	0.03	0.06	0.12	0.06	0.03
2.8	0.1	0.01	0.02	0.04	0.02	0.01

coincide, which has a joint probability of 0.01. When this method is applied to real data, much smaller probabilities of extreme joint events are calculated, because the probabilities are distributed over many more class intervals.

In this case there is a natural way of relating these probabilities to the time interval between high waters. For example, 3.4 m levels occur on average once in every 100 tidal periods. More generally, these dimensionless probabilities are converted to return periods using time-scaling factors, determined by analysis of, and related to the persistence of extreme events [5].

The principal advantages of the joint tide–surge probability approach may be summarised:

- Stable values are obtained from the relatively short periods of data. Even a single year can yield useful results, but a minimum of four years is desirable so as to sample several storms.
- There is no waste of information.
- The probabilities are not based on large extrapolations.
- Estimates of low water level probabilities are also produced.

However, data must be of a good quality, with gauge timing accuracy to better than a few minutes. If there are timing errors (old chart recorders were especially prone to these) tidal variations will appear in the residuals. Recent applications have used the skew surge (Figure 7.4) associated with each high tide level [7]. Joint tide–surge probability estimates of extremes require a high degree of analytical skill, and extra computational effort is involved.

12.2.4 Other methods

Other methods, either similar to or extensions of the annual maxima and joint-probability methods described

briefly above are often applied. One method looks at a fixed number of the maximum extreme levels in a year, typically up to ten, instead of just the single annual maximum value. Sometimes this will mean including some highest levels from one year, which are less than those not included for another year. Care is necessary to make sure that each storm is a separate and independent event. These storm levels are then fitted with an appropriate extreme value distribution

Another method, developed for river hydrology, is to look at the number of times a level exceeds some stated threshold level [4]. Unlike the previous method, this may result in several storms being recorded in one year and few or none in another year. A better approach is to apply this peak over threshold (POT) method to the non-tidal residuals, after removing the tides, and to use the resulting probabilities in a joint-probability calculation.

The reliability of all estimates is limited by the available data and by possible trends and changes in the regional meteorology and oceanography. The possibility of some rare un-sampled event, such as a tsunami, cannot be ignored, nor is it easily incorporated into the estimates. In Alaska, and in Japan, tsunamis are recognised as the most important cause of extreme levels (Chapter 8).

Observations of meteorological variables including atmospheric pressure, wind speed and direction, have been continuous at land stations over many years. Because extreme levels are obviously related to extreme weather conditions, one approach to estimating their probability is to apply the extreme winds and pressures estimated from land-based observations to analytical or ideally to numerical models

A modelling approach is particularly useful for concentrated tropical storms, for example, along the Atlantic and Gulf Coast of the United States,

where the distribution of all extreme hurricanes, cyclones or tornadoes may be estimated from the historical record. The most severe storms may then be used to calculate the response of the water around the port or structure being designed. Both the direction and speed of approach of the storm can be varied in the model until critical maximum level conditions are identified.

12.2.5 Adjusting for sea-level rise

It is important to consider how the exceedance curves, for example in [Figure 12.4a](#), must be adjusted for climate change. At its simplest, where a rise in sea level of, say, 0.2 m is expected for some future time, then it is correct to raise the likelihood statistics, and hence the curve, by a 0.2 m to see what the new annual exceedance probability level will become. This is shown as the heavy dashed line in [Figure 12.4b](#). However, this does assume that the statistics of the variability about a [MSL](#) remains unchanged. Several analyses have shown this to be a reasonable assumption in recent years [8] (see [Section 7.3.3](#)). However, projections of future rises of [MSL](#) have their own associated uncertainties (shown as the red dashed lines in [Figure 12.4b](#)), and future [MSLs](#) may be higher or lower than the best estimate. Including these uncertainties in the computations of future flooding risk tends to increase the risk beyond the risk calculated by simply raising the curve, in our example by 0.2 m. The reason for this is the finite chance that the [MSL](#) will be higher than projected. If the uncertainty in the estimates of future [MSLs](#) can be expressed as a normal (Gaussian) distribution, the curve is uplifted by $\frac{s^2}{2\lambda}$ with s , the standard deviation about the best estimate, λ . This vertical adjustment ensures that the present likelihood (or frequency) of flooding is maintained into the future, under sea-level rise. It depends regionally on the projected sea-level rise, its uncertainty, and the Gumbel scale parameter [9]. Combining present distributions of extremes with uncertainties in future [MSLs](#) is effectively a joint-probability convolution (see [Section 12.2.3](#)).

The aggregated probability of flooding over the lifetime of a fixed asset can be evaluated. If allowances are made for [MSL](#) rise, the greatest likelihood of exceedance occurs in the final years of the design life [10]. When allowing for long-term storm statistics and [MSL](#) changes, pragmatically it might be best to compute numerically the aggregated risks over some defined period of years, allowing to change for future years in the period.

In practice, evaluations of future risks, flooding likelihoods and asset values are inevitably speculative. The uncertainty in the [MSL](#) projections, s , will increase as they extend into the future. It is also possible that the present-day conditions and statistics of extremes will change, with more storms and greater intensity. The s^2 dependence indicates that planning too far ahead for uncertain sea-level rise is difficult. How decisions on investments and protection levels should be made is not definite: future values of assets are unknown (see [Section 12.8](#)), and deferring expenditure now until later makes economic sense. Defence structures should be planned strategically, with options for enhancement; if possible the full defences needed towards the end of a structure's lifetime should be added as appropriate when more distant rises of sea level can be predicted with greater confidence.

12.2.6 Extreme currents

Extreme currents are far more difficult to estimate than extreme levels. The first difficulty is to obtain a sufficiently long series of observations; there are few series extending over more than a year because of the expense and the technical difficulties. Further complications arise because currents are variable with depth at each location, and because they change over short distances, particularly near the shore and around shallow sand banks, as discussed in [Chapter 6](#).

A very basic approach for extreme tidal currents is to determine the tidal current ellipses from charts, observations or numerical models and then to scale these upwards according to the similarity measures found to be appropriate for levels at a nearby port ([Chapter 4](#)). It may be sufficient to scale only the major axis of the mean spring current ellipse. Tidal currents may also be scaled up according to the relationship between spring and highest astronomical tidal levels at a nearby and appropriate port (see [Section 4.4](#)). The presence of inertial currents can make the use of a similarity measure determined for levels invalid for currents because inertial currents do not affect sea levels.

Extreme currents may also be estimated by separation of the observed current vectors into tidal and surge components, as for levels. Two-dimensional frequency distributions are obtained for each component, but in the simplest case of the currents being rectilinear or if only speeds are considered, the problem may be treated in exactly the same way as for estimating extreme levels. An appropriate class interval is 0.1 m/s. For rectilinear currents, where the flow is

restricted to be backwards and forwards along a particular line, one direction must be arbitrarily defined as positive. Where the flow is not rectilinear, the flows in two orthogonal directions are treated separately. North–south and east–west components are usually chosen, but the directions of the major and minor axes of the current ellipses are also suitable. The maximum components in each of the four directions may be then estimated from probability plots produced by combining the probability distributions of the separate tidal and surge components [11].

It is important to make a clear distinction between the maximum current to be expected in a particular direction, and the maximum expected *component* of current resolved along that direction, as determined above. For example, a truly rectilinear flow confined along a single axis would have a theoretical zero probability of flow along any other axis, but the component would have finite values in all directions, except the direction at right angles to the flow axis.

Where there are insufficient observations to make statistical estimates of extreme currents from the observations, the most powerful approach is to use the results of numerical models, ideally three-dimensional models that give current variations with depth. An alternative is to use the results of two-dimensional depth-integrated models, as described earlier, and to adjust for near-surface and near-bottom effects using assumed distributions and empirically determined constants.

Adding extreme tidal currents to extreme surge currents will give extreme total currents higher than are probable in practice. For calculations of extreme levels and extreme currents, it is wise to make conservative estimates and to apply these with caution; however, for currents, because the uncertainties are greater, extra caution is necessary in the interpretation of the estimated extremes.

12.3 Coastal defences

Land reclamation and sea defence schemes have been developed over thousands of years, often in conjunction [12]. The eighteenth-century Acadian dykes of Nova Scotia, Canada (Figure 12.7a), and the Gwent Levels, 111 km² of reclaimed estuarine alluvium fringing the northern side of the Severn Estuary, southwest England, are recent examples. Even more recent are the reclamations of Chongming Island in the Yangtse estuary [13]. These fertile protected lands lie below very high tide levels. The reliability and costs of



Figure 12.7 (a) Old sea defences fronting prime agricultural land at Wolfville, Nova Scotia. Photograph by David Pugh. (b) The Maaslantkering storm surge barrier in the Nieuwe Waterweg, Netherlands, which closes automatically when needed. Photograph from the Rijkswaterstaat, Dutch Ministry of Infrastructure and the Environment.

maintaining protective walls is increasingly controversial, especially as sea levels rise. In practice, total protection would be prohibitively expensive, so only selected projects that protect highly populated areas around estuaries, or vulnerable installations such as nuclear power stations, are justified. Strict economic cost-benefit analyses may be applied (see Section 12.7), but additional, political, arguments are usually involved in the final decisions.

Protection against the sea-level changes that occur over periods of thousands of years is impossible and the ultimate response must be one of slow economic adjustment, for example the gradual migration of residential and industrial areas to higher land. In 2002, a small area of agricultural land at Tollesbury on the UK East Anglia coast of the North Sea was reopened to

flooding from the sea to create new salt marshes, as part of a local managed retreat strategy. The need for this kind of gradual adjustment was recognised in the United States by establishing the National Flood Insurance Program by Federal legislation in 1968; incentives are given to local communities to prohibit new construction within defined flood zones. As of April 2010, the Program insured about 5.5 million homes, the majority of which were in Texas and Florida.

Extensive flooding results when the still water level exceeds the top of the defence structure, but before this level is reached there may be considerable flooding from overtopping by waves. The statistical relationships between extreme levels and extreme waves are critical, and waves can vary over short distances [14, 15].

Several different designs of wall, called *hard engineering solutions*, have been built, each intended to minimise wave overtopping. The modern trend is for gradually sloping defences that progressively remove the energy of the incoming waves. The cost of a defence wall grows rapidly with increases of design height; the width of the footings must also be increased in proportion to the height, so that in terms of material alone the increase is more closely proportional to the square of the height. Waves can also be attenuated by encouraging the development of coastal marshes, or mangroves, for example, called *soft engineering solutions*.

The effectiveness of a sea defence wall against floods can be judged in terms of the maximum or the mean overtopping discharge. These depend on the still water extreme, the wave heights and the wind, as well as the wall design itself. The overtopping discharge for all possible combinations of these parameters must be determined either by experiment or by calculation. Where the wall design incorporates features such as a wave return wall, which tends to throw water into the air, overtopping discharge rates are much greater when the wind blows onshore. Although characteristics of different wall designs can be adequately defined by laboratory tests, the major environmental problem is obtaining a reliable estimate of the probability of occurrence of all possible combinations of water level, wind and wave conditions. Permanent defences need mechanisms for drainage of fresh water. This is done by sluices, movable gates allowing water to flow out under at low tide, which often operate automatically.

The use made by the design engineer of these various statistics in deciding a suitable protection level is not the same in every case. As an example of the balance of

factors, consider the design level for the 1982 Thames Barrier, which was finally set at 7.11 m (23.33 feet) above Ordnance Datum Newlyn (ODN). This figure was taken as a compromise between an inadequate short-term solution and a very high standard that would be effective until the end of the twenty-first century [16]. A further 1.50 m (4.93 feet) was added (on a 1000-year return flood level at Southend) to allow for MSL increases to 2030, and for the combined effects of wind and wave freeboard, and for level increases up the River Thames due to local winds and river discharge.

The Netherlands coastal management schemes are the most ambitious yet built. The early twentieth-century Zuiderzee Works, a system of dams, land reclamation and water drainage works, involved the damming of the Zuiderzee, a large, shallow inlet of the North Sea, reclaimed an area of some 1500 km² of land, and protected existing areas. More recently the Delta Works, triggered by the disastrous 1953 flooding, were finished in 1997. The Maaslantkering storm surge barrier in the Nieuwe Waterweg located between the towns of Hoek van Holland and Maassluis automatically closes when needed (Figure 12.7b). The barrier is connected to a self-operating computer system, which is linked to weather and sea-level data. Normally a 360 m wide gap in the waterway gives ships enough space to pass to Rotterdam, Europe's biggest port, without any inconvenience. The Maaslantkering is expected to be closed once every 10 years due to a storm surge. However, as sea levels rise, the storm surge barrier will need to close more frequently.

Saint Petersburg, Russia, is protected from Baltic Sea surges by a 25 km complex of dams. Historically, the storm surges from the Gulf of Finland had caused over 300 historically recorded floods, several of which had a massive devastating effect. The dam, inaugurated in 2011, has the capability to protect the city from water rising up to 5 m. The scheme includes an economically important road crossing. A scheme (MOSE) to protect Venice, where floods occur many times a year in Piazza San Marco, has a system of 78 mobile barriers across the three entrances to the Venetian Lagoon. When completed, by 2014, barriers will be operated on exceptionally high tides.

All major coastal developments are disruptive, and even life changing for some people, for example the Zuiderzee fishermen. Their planning and building is often as much a social issue as a direct engineering or even economic one. The new European Floods

Directive (2007/60/EC) provides a legal framework, requiring European Union Member States to take into consideration long-term developments, including climate change, as well as sustainable land use practices in their flood risk management. Where coastal habitats may be lost as sea levels rise, the Directive requires compensation habitats to be developed elsewhere, as for example at Tollesbury.

12.4 Lagoons and channels

Around the world many coasts have bays, estuaries or lagoons connected to the ocean. Often this connection is through a narrow inlet channel: the tides inside the bay are controlled by the tidal rise and fall of the level in the ocean and by the geometry of the inlet. Because of the importance of these inlets for water exchange and for navigation, coastal engineers have studied their development and stability in detail. Figure 12.8a summarises the essential parameters of a lagoon–inlet system. The volume of water exchanged between the sea and the lagoon during a tidal cycle is called the *tidal prism*.

The flow through the inlet is controlled by its cross-section and by the resistance of bed friction. It takes a finite amount of time for the water to flow from the ocean to the lagoon, which means that slack water (zero tidal currents) in the inlet occurs typically two or three hours after high or low water in the ocean. This is shown in Figure 12.8b, where the lagoon tide has a smaller amplitude and lags the ocean tide by about three hours. The flow through the inlet is driven by the balance of bottom friction, and by the sea-level difference between the two ends. This is the same as in Section 6.4.2 and Figure 6.8 for East River, New York, although for lagoons the tidal variations at either end of the channel are hydrodynamically dependent.

Slack water occurs in the inlet when the sea levels are the same in the ocean and the lagoon, usually around the same time as high or low water level in the lagoon. This time lag is sometimes called the slack water phase lag or tidal current phase lag for the inlet. Peak flood flow from the sea into the lagoon occurs very close to the time of ocean high water.

Engineers have sometimes investigated entrance designs using solutions to the hydrodynamic equations analogous to those for electrical circuits [17, 18].

Consider the lagoon to have a water level ζ_L and an area A_L , connected by a single channel of length l , depth h , and width w , to the sea, where the level is ζ_0 . In the channel the balance between sea-level difference

pressures, acceleration and bottom friction (F) is given by a slight rearrangement of Equation 6.2:

$$\frac{\partial \zeta}{\partial x} = -\frac{1}{g} \frac{\partial u}{\partial t} + \frac{F}{g\rho h} \quad (12.5)$$

where positive flow is along the axis into the lagoon. Tidal-level changes are assumed small compared with the mean water depth h . Suppose that friction is approximated by a linear relationship:

$$F = -K\rho u$$

where K is a linear bottom frictional co-efficient with units of m/s. From continuity we have:

$$A_L \frac{\partial \zeta_L}{\partial t} = whu$$

Equation 12.5 becomes:

$$\frac{\partial \zeta}{\partial x} = -\frac{1}{g} \frac{A_L}{wh} \frac{\partial^2 \zeta_L}{\partial t^2} - \frac{KA_L}{gwh^2} \frac{\partial \zeta}{\partial t}$$

and by integrating along the channel:

$$g\zeta_0 = g\zeta_L + \frac{KA_L}{wh^2} \frac{\partial \zeta_L}{\partial t} + \frac{A_L}{wh} \frac{\partial^2 \zeta_L}{\partial t^2} \quad (12.6)$$

There is an analogy with electrical circuits and their theory: the surface elevation may be related to voltage, fluid flow to the electric current, bed friction to resistance, the surface area to capacitance and the inertial term to inductance [19]. Suppose the lagoon levels are driven by a sea tide:

$$\zeta_0 = H \cos \sigma t$$

then the solution to Equation 12.6 is:

$$\zeta_L = \alpha H \cos(\sigma t - \theta)$$

where

$$\alpha = \sqrt{(\phi^2 + \psi^2)} \theta = \arctan(\psi/\phi)$$

and

$$\phi = \left(1 - \frac{A_L l \sigma^2}{whg}\right) \psi = \frac{KA_L l \sigma}{wh^2 g}$$

The solution is a damped oscillation with a phase lag. Here, ϕ and ψ are known as the inertial and stress terms. This formalism has been applied for shelf coastal lagoons [19], and for open ocean coral lagoons [20]. By analysing Equation 12.6 it is possible to determine how the phase and amplitude of the surface

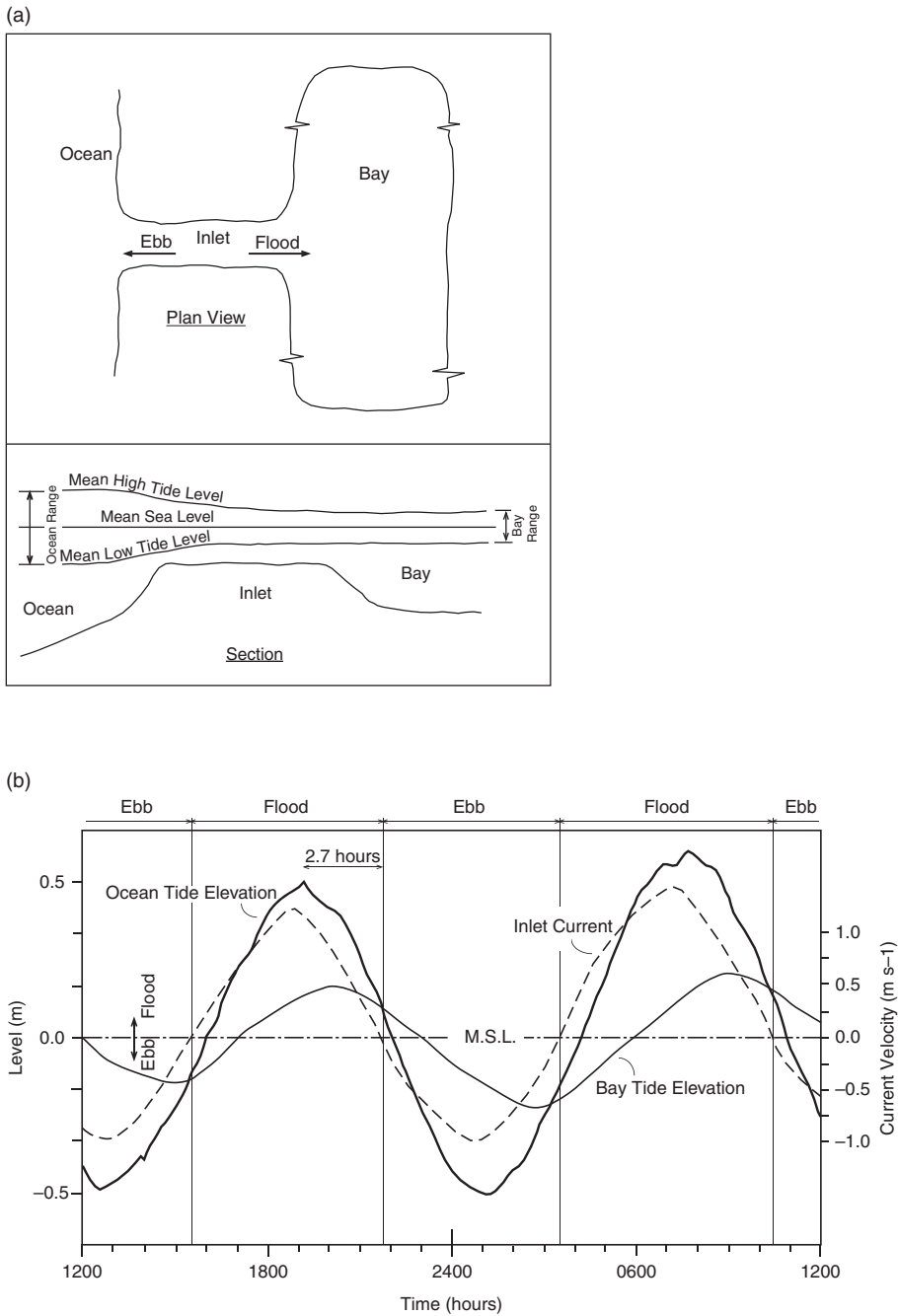


Figure 12.8 (a) Summary of the geographic and tidal conditions for a bay connected to the sea through a narrow entrance. (b) The corresponding ocean and bay tidal levels for St. Lucie Inlet, Florida. Bay levels lag ocean levels by more than an hour and the slack water (currents are shown by the dashed line) occurs nearly 3 hours after high tide in the ocean. Figure provided by Dr Lee Harris, Florida Institute of Technology.

elevation changes with changes to the lagoon area, inlet dimensions and bottom friction.

In this theoretical case, the ebb flow is a maximum close to low tide at the ocean end of the inlet when the

inlet water depth is lowest. This means that the cross-sectional area of the inlet will be smaller during ebb flow than flood flow so that for shallow inlets, for the same quantity of water to leave the inlet as enters during a tidal

cycle, the maximum ebb flow is greater than the maximum flood flow. During ebb flow the outgoing water in the inlet meets the incoming waves; this together with the greater outflow velocity and the shallowness at the entrance combine to create the most hazardous conditions during the tidal cycle for inlet navigation.

There is a close empirical relationship between the volume of water exchanged, the tidal prism, and the minimum inlet cross-section, which holds well for a wide range of coasts and bays worldwide. Figure 12.9 shows this relationship between the tidal prism and the cross-sectional area of the entrance channel at its narrowest point for bays along the Pacific coast of the United States. Along this coast the tides are mixed, and so the tidal prism has been calculated as the volume exchanged between Mean Higher High Water and Mean Lower Low Water.

$$\begin{aligned} \text{Minimum cross-sectional area} \times 10^3 \\ = 0.0656 \times \text{tidal prism} \end{aligned} \quad (12.7)$$

where the cross-section is measured in square metres, and the volume of the tidal prism is measured in cubic metres.

This statistical relationship, which holds well for a wide range of coasts and bays worldwide, can be used to predict some of the effects of artificially widening or deepening an entrance channel, or the effects of recovering low-lying tidal flats within a bay. It implies that if land is reclaimed then there will be a reduction in the entrance area because of a smaller tidal prism.

In extreme cases a smaller volume of water exchanged through the channel, for example on neap tides, can lead to it becoming blocked by sediment. A

good example of this is the Batticaloa Lagoon on the east coast of Sri Lanka, where access to the sea from the lagoon and fish-processing facilities is periodically interrupted by the closure of the lagoon entrance during small neap tides; when this closure occurs, boats can go fishing only after the access channel is reopened. There are many examples worldwide of these Intermittently Closed and Open Lakes and Lagoons (ICOLLs) [21]; they are generally found in temperate regions where tidal ranges are small. It has been estimated that along the New South Wales coast of Australia, 70 of the 90 coastal lakes and lagoons are ICOLLs, connected to the sea only when a sand barrier is broken to release high rainfalls.

Engineers have refined Equation 12.7 to improve its prediction skill by taking into account local sediment supply, river inputs and bay and inlet geometry [22].

12.5 Power generation

Tidal energy manifests itself either as the kinetic energy in tidal currents or as the potential energy of the water head difference between high and low tide levels. The rise and fall of the tide has been exploited for hundreds if not thousands of years [23]. In the eighteenth century there were at least half-a-dozen tide mills grinding corn on the south coast of England. The mill at Woodbridge, Suffolk, can be dated to 1170; the Eling Mill near Southampton is still working today [24]. Tide mills were also common on the Atlantic coast of the United States [25] (Figure 12.10) and Brooklyn, New York, had a mill in 1636. The essential feature was a 'mill-pond' connected to the sea by a small entrance. As the tide rose, the mill-pond filled

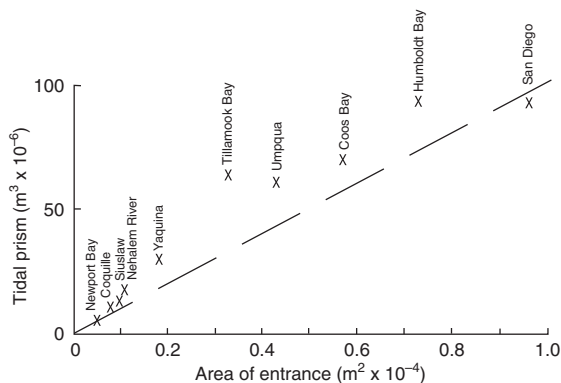


Figure 12.9 The relationship between the cross-sectional area of a lagoon entrance and the volume of water exchanged (the tidal prism) in each tidal cycle for a series of bays on the west coast of the United States. The dashed line shows the relationship if the tidal prism is 10^4 times the area entrance, both in metric units.



Figure 12.10 The Perkins Tide Mill, located in Kennebunkport, Maine, United States, photographed in 1965. The tide mill was built in 1749. A Wikimedia Commons image obtained from Library of Congress, Prints and Photographs Division.

Table 12.2 A comparison of estimated tidal energy fluxes with other sources and sinks of energy

Energy source/sink	Megawatts
Solar radiation incident on the Earth	1.7×10^{11}
Geothermal energy	4.5×10^7
Tidal energy dissipation	3.5×10^6
Global energy loss from earthquakes	3.0×10^5
<i>Capacities</i>	
Three Gorges hydroelectric scheme, China	22500
Kashiwazaki-Kariwa nuclear station, Japan	8200
Bełchatów coal-fired power station, Poland	5000
Aswan Dam hydroelectric scheme, Egypt	2100
La Rance tidal power scheme, France	240
Early tide mills	0.1
Total global generation capacity (2007)	4.5×10^6
Total United States capacity (2010)	1.1×10^6

with water: once the basin was full and the tide began to fall, the return flow was constrained to pass through a sluice equipped with a water wheel.

In more recent times, tidal power is increasingly considered a viable and significant source of electric power. Table 12.2 shows how the 3.5 TW of energy dissipated globally by the tides compares with other energy sources and sinks. As a national example of increasing power demand, the peak for France in 1978 was 38,000 MW, but in 2012 the peak was 100,000 MW. Global demand may double by 2050. The possibility of the tides meeting even a small part of these demands is environmentally attractive. However, traditionally, progress in constructing tidal power stations has been slow, largely because of the relatively high initial capital cost compared to other forms of energy and because of concerns over the environmental impact.¹ Like wind power, tides offer potentially

secure local energy supplies unaffected by the global fluctuations in supply, and steady rise in the price of hydrocarbon-based electricity.

The most accessible technology for tidal power is the same as that used for the old tide mills. It fills a reservoir at high tide and the trapped *potential energy* at low tide is used to drive turbines. The potential energy, relative to low tide level, contained in a basin of area S , filled at high tide, and discharging into the open sea at low tide is:

$$S\rho g \int_0^{2H} z dz = 2S\rho g H^2 \quad (12.8)$$

where H is the tidal amplitude, ρ is the water density and g is gravitational acceleration.

The process could be repeated by filling the basin again from the low water level at the time of high water in the open sea. The total energy theoretically available in each tidal cycle is:

$$4S\rho g H^2$$

and the mean rate of power generation is:

$$2S\rho g H^2 / (\text{tidal period})$$

The energy actually extracted by a scheme depends on several other design factors [26]. The ideal site for tidal power generation is a basin of large area, where tidal ranges are large. The large tidal range is most important because of the square-law dependency. The power available from semidiurnal tidal regimes is twice that available from diurnal tides. In addition to these power requirements there are obvious construction cost savings if the basin has a relatively narrow and shallow entrance.

The French tidal power plant operated at La Rance near St Malo in Brittany, since 1966, was the first modern large-scale scheme to harness tidal energy. In addition to La Rance, smaller schemes have operated in the White Sea near Murmansk in Russia, Kiansghsia in China and at Annapolis, Nova Scotia, Canada. Sihwa Lake station (Figure 12.11) in South Korea, completed in 2011, is currently the largest tidal power installation in the world. Table 12.3 summarises the mean tidal ranges and basin surface areas for five major schemes. Potentially the schemes considered for the Minas Basin and the Severn Estuary could produce many times the energy of La Rance. The Minas Basin scheme has the disadvantage of being

¹ The financial arguments are beginning to change. Some governments provide economic incentives, driven by global-warming commitments, to boost the fraction of national power generation that comes from renewable (non-carbon) sources.

Table 12.3 Characteristics of some areas suitable for tidal power generation

	Inception year	Mean tidal amplitude, H (m)	Basin area, A (km ²)	Theoretical mean power output (MW)
La Rance, France	1966	4.0	22	240
Annapolis, Nova Scotia, Canada	1984	3.2	6	20
Sihwa Lake, South Korea	2011	5.6	30	254
Incheon, South Korea	2017	5.3	106	1320
Severn Estuary, UK		4.0	420	6100
Bay of Fundy, Canada/ United States		5.5	240	6500

**Figure 12.11** The Sihwa tidal power station in South Korea has a production capacity of 254 MW (see Table 12.3). Photograph provided by Dr Sang-Kyung Byun, Korea Ocean Research and Development Institute with acknowledgement to K-Water, Korea.

distant from major areas of power demand. In the Severn Estuary, although the major cities of Cardiff and Bristol are close by, they are also major ports whose commercial interests would be affected if access for shipping were restricted. Schemes that include locks to allow ship passage and use only a part of the tidal range, so that some of the estuary remains for birds to access and feed, may be compromises in any future construction.

Energy is also generated by using submerged rotors, the marine equivalent of windmills, converting the *kinetic energy* of tidal streams [27]. For a turbine of cross-section A resisting a flow of water speed u and density ρ , the available power is:

$$P = \frac{1}{2} C \rho A u^3 \quad (12.9)$$

where C is a dimensionless turbine coefficient. Maximum efficiency occurs (the Lanchester–Betz law) when the speed downstream of the turbine is one-third of the incident water speed u ; obviously there must be a finite downstream speed to remove the water after passing through the turbine. For this optimum condition the maximum value of C is 16/27, or 59 per cent [26]. Fitting the approach to the turbine with a duct that channels water from a wider effective cross-section can increase the efficiency. Practical anchored systems with an array of turbines can produce up to 10 MW in 60 m water depth. Tidal stream systems are much more compact than equivalent wind turbines, because of the high water/air density ratio, and rotation rates are much slower.

Tidal stream power generators can be operated either as single turbine systems or as part of a tidal



Figure 12.12 The 1.2 MW tidal stream generator at the entrance to Strangford Lough, Northern Ireland. Photograph supplied by Marine Current Turbines Ltd, a Siemens business.

fence or farm. Hence, tidal stream devices have an economic advantage because they can be installed and extended incrementally so the initial capital outlay is reduced. Also their environmental impact on coastal communities can be less. At present, interest in the technology is increasing rapidly with schemes installed or planned for Strangford Lough, Northern Ireland (2008, 1.2 MW; see [Figure 12.12](#)), the East River, New York (2015, 1 MW), and the Sound of Islay off the west coast of Scotland (2013, 10MW). On a much more ambitious scale there are proposals for a 400 MW scheme in the Pentland Firth, north of Scotland by 2020. Some 190 possible tidal stream power sites have been identified off Canada's coasts, with a total estimated capacity of 42 GW, or more than 63 per cent of the country's annual total consumption. In the Bay of Fundy three turbines generating 5 MW total power are envisaged [28]. Similar schemes are proposed for Cook Strait in New Zealand [29], and many other locations where large tidal currents are found [30].

[Figure D.4](#) of [Appendix D](#) shows how the tidal phase lines tend to focus on headlands giving an enhanced difference of timing on either side. On a larger conceptual scale, artificial 'headlands' or dams extending out to sea for tens of kilometres, perpendicular to the coast, would create water-level differences on opposite sides of the barrier to drive a series of

bi-directional turbines installed in the dam. There are some natural examples where a narrow isthmus has large tidal differences on opposite sides, and where connecting pipes and turbines could in theory produce power; Peninsula Valdes in Argentinian Patagonia [23] is a site for possible exploitation, but it is remote from major cities, and locally power is available from hydroelectric schemes in the Andes.

Tidal barrier and tidal stream power generation will usually peak twice a day, with the daily peak times varying over a fortnight as the tide goes through its spring-neap cycle. A more regular supply can be achieved by using both ebb and flood flows, and also, if a number of separate barrages are located, where the phase of the tide is different [31]. In addition, two or more 'tidal reservoirs' (secondary water impoundment areas) can be used to smooth the overall supply. Energy delivered to a national grid can be further smoothed out over the tidal cycle when an ancillary energy storage scheme, such as hydroelectric storage, is employed. Careful programming, perhaps a mix of barrage and tidal stream systems, can fit the periodic generation of tidal energy into the overall availability of energy from other sources, such as nuclear and coal-fired stations. Tidal power has a major advantage over other forms of renewable energy in being fully predictable. Also, it provides a more continuous supply throughout the year than winds or waves, for example, which produce their maximum power in the winter months.

However, there are other considerations. Any scheme that removes energy from the tides must also have an effect on their behaviour [27]. Since the most favourable sites for power generation are those where large tidal amplitudes are generated by local dynamic resonances, they are particularly vulnerable to imposed changes. The only satisfactory way to predict the effects of a proposed scheme on the local tides is to apply a numerical model with its outer boundaries well removed from the area of the scheme [32]. Models that take the western edge of the European continental shelf and beyond as their boundary have predicted the effects of several different schemes proposed for the Bristol Channel. These schemes were all shown to have a tendency to reduce the tidal ranges by 10 per cent or more in the vicinity of the barrage. However, at the entrance to the Bristol Channel the effects on the tides were limited to an amplitude reduction of 1 per cent or less, and an advance in the tidal phase by a few minutes.

The addition of a tidal power scheme to a natural tidal system oscillating near resonance need not automatically reduce the tidal range. Tidal resonance occurs when a basin has a length that is a quarter of a semidiurnal tidal wavelength (Section 5.2.2). If the natural length is slightly longer than this critical length, then it is quite probable that the introduction of a barrier near the head may tune the estuary closer to the resonant condition. It has been suggested that both Cook Inlet in Alaska and the Gulf of Maine, Bay of Fundy systems' tidal amplitudes could be increased in this way [33, 34].

Potential disadvantages include the loss of intertidal mudflats, salt marshes and other habitats important for some species of birds. Changes in tidal currents and also wave climate may modify benthic habitats. The turbines of the barrage may impede migratory fish and marine mammals; upstream, where estuaries provide nurseries for breeding fish, these may no longer be accessible. Sediment transport patterns will be interrupted [35]. Any local environmental impacts have to be considered against the benefit to the global environment due to the reduction of carbon emissions [36].

The economics of tidal power schemes are critical for their successful deployment. It took almost 20 years, but once the La Rance initial development investments were recovered, electricity production costs are now claimed to be lower than for nuclear power (€18 per MWh). As discussed, other factors that can make any prospective tidal power site more or less suitable are the distance to the area where power is needed, the existing uses of the basin for navigation or recreation, and the local price of competing power sources such as coal, gas and hydroelectric stations. Strict cost comparisons are always difficult because the future costs of alternative power sources and the operational life of a tidal power scheme are both uncertain.

12.6 Emersion–submersion probabilities

The foreshore between high and low water levels is a zone of intense sedimentary and biological activity. Within this zone the various foreshore levels have different times of exposure to the air and submersion by the sea, depending on the tidal regime and the heights of foreshore. The importance of tidal patterns for beach development, and for plants and animals

that have adapted to live on the sea shore between high and low water levels, is described in more detail elsewhere [22, 37, 38]. See also Section 13.2.

Figure 12.13 shows the frequency distribution of tidal levels for a year at Newlyn, United Kingdom, and at San Francisco and the overall percentage of time for which each level is exposed to the air. These frequency distributions define the levels at which disturbances and stress due to wave activity are most likely to concentrate. The percentage exposure plots are called *exposure* or *emersion curves*; it is easy to present the same statistics in the form of these curves. For intertidal plants and animals these simple curves define their survival environment: harsh and veering from one extreme to another. In preserving the ecology of these complex environments, for example, when minimising the impacts of engineering developments in the coastal zone, other factors matter. These include times and duration of exposure. The most regular cycle of emersion and submersion is found at the MSL, but where there is a mixed tidal regime, the patterns can change substantially over a month, a year, or indeed over a nodal tidal cycle. The time of day at emersion is another critical factor. The dangers of desiccation for a marine plant or animal exposed to the air are obviously much greater if the exposure takes place during the maximum heat of the day. Night-time exposures to winter frosts can also inflict serious stress on plants and animals whose normal preferred habitat is within the more stable temperatures of coastal waters. Coral reefs exposed to cold or rainy weather may suffer extensive damage and subsequent decay of cell tissue. For a semidiurnal tide, the time of day at which extreme low water levels occur is related to the phase of the S_2 constituent. Expressed in local time, if the S_2 low water is near local noon and midnight, the lowest extreme levels will be, on average, also at these times. The S_2 phase is a convenient way of first looking at the vulnerability of a coral reef to solar heating [39].

As a specific example of the importance of emersion and submersion on coastal life, consider the landing and feeding areas for a bird feeding in an estuary. A *bird's eye view* of the issue might be expressed: *I want to know, for arrival in an intertidal area at a random time, what area will be uncovered by water.* This can be expressed as a probability function. For example, what area will be uncovered 70 per cent of the time? These probabilities depend on a sea-level pdf, as in Figure 12.5, and on a second frequency graph, relating

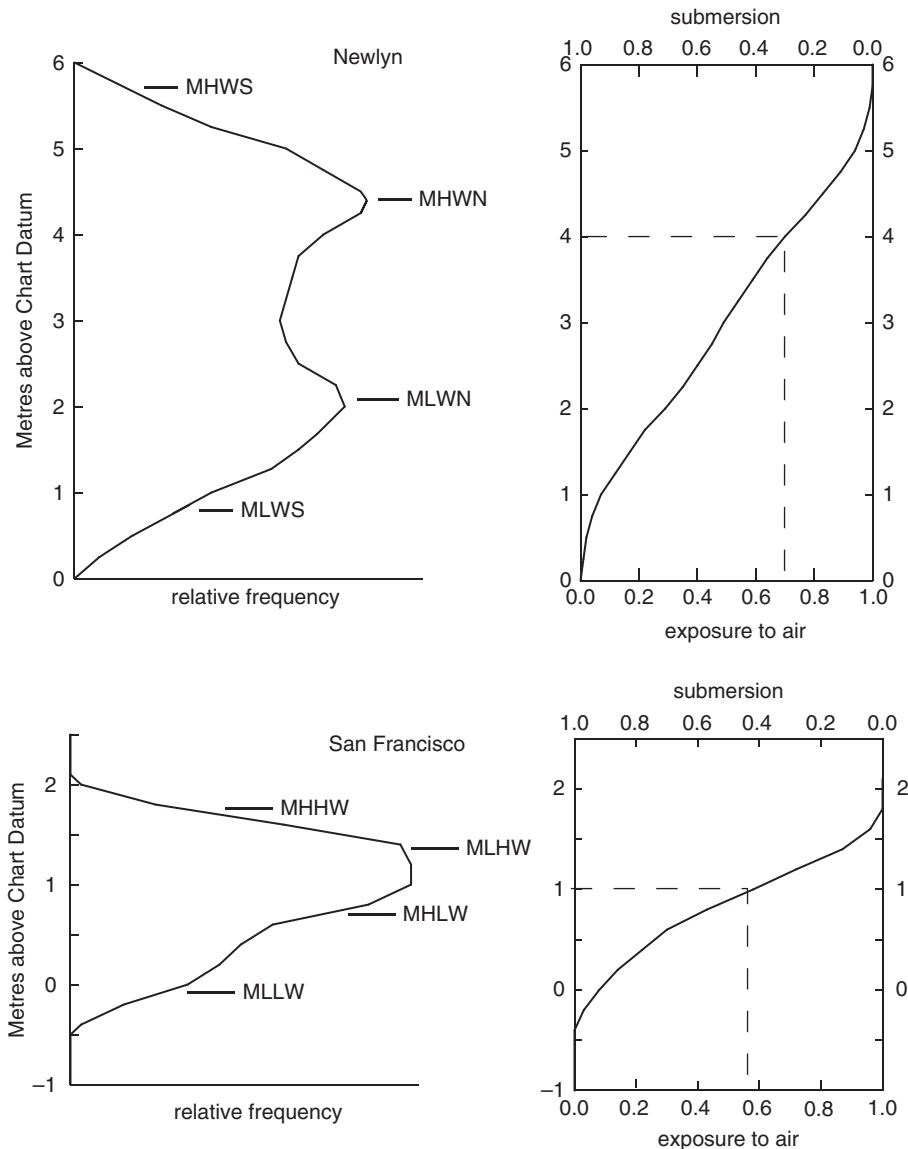


Figure 12.13 The frequency of various tidal levels at Newlyn (semidiurnal tides) and San Francisco (mixed tides) for a year of data. The Newlyn frequencies are shown in more detail in Figure 12.5. The right-hand curves show the fraction of time each level is exposed to air or submerged. At Newlyn the dashed line shows that a level of 4 m above Chart Datum is exposed to the air for 70 per cent of the time. At San Francisco a level of 1 m above Chart Datum is exposed to the air for 55 per cent of the time.

the heights of the foreshore to the same datum. This is illustrated for the Severn Estuary in Figure 12.14a. Graphically the aim is to produce a curve, as in Figure 12.14b, of probabilities and exposure areas.

The procedure for computing the exposure probabilities from the sea-level and littoral-level cumulative curves is as follows.

- From a cumulative sea-level curve like Figure 12.13, calculate the 0.1 to 1.0 probability exposure levels.

- Project these levels onto the cumulative area curve as in Figure 12.14a, to give the area exposed for 0.1 to 1.0 of the time.
- Plot the area exposure against probabilities to get curves like 12.14b.

This approach can be extended to see how, for example, these probabilities change if sea levels rise. The lower curve in Figure 12.14b is for a sea-level rise of 1.0 m. Other refinements, which may be appropriate

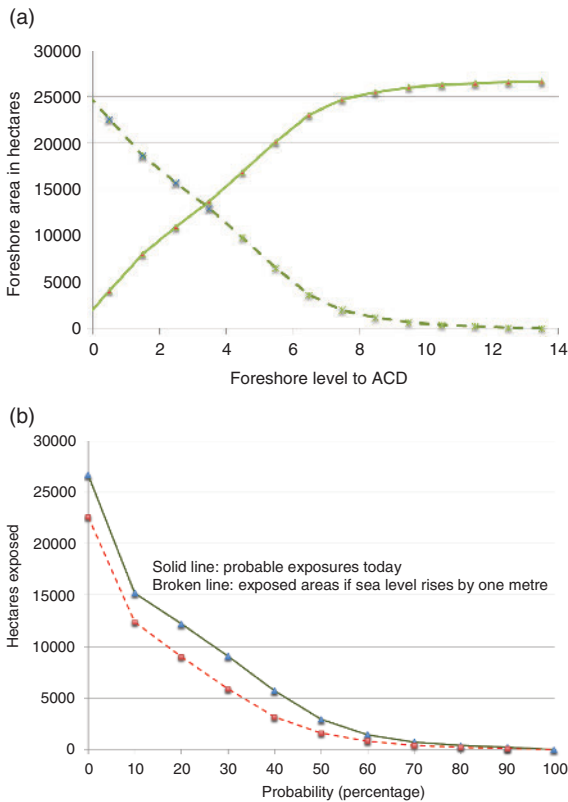


Figure 12.14 (a) Relationships between foreshore areas levels and heights relative to Chart Datum for the Severn Estuary, southwest England, based on large-scale local charts. (b) The probability curve for today's tidal conditions and foreshore levels in the Severn Estuary. The green solid line is the computed curve for the upper estuary curve. For example, in this case, for 70 per cent of the time, there will be at least 732 hectares for the bird to land. The red dashed line is the equivalent curve for a sea level raised by 1.0 m. The difference in the area under the two curves is an indication of the lost landing areas in the higher sea-level scenario.

for different species, could be seasonal curves, or day-night plots.

Figure 12.14a shows that for the Severn Estuary most of the intertidal level is nearer to low water. In this case there are no extensive areas just below Highest Astronomical Tide, presumably because these were recovered and settled in previous centuries as part of the building of surrounding defence walls. In modern terms, this area already has advanced 'coastal squeeze'. Other less protected foreshores will have different level profiles.

12.7 Flood warning systems

The sea can be a source of economic and recreational benefit, but it can also cause major disasters. Loss of



Figure 12.15 Children returning from school through floodwaters during a tidal surge in Chittagong, Bangladesh. Photograph from Jashim Salam/Marine Photobank.

life from shipwrecks is much reduced by better charting, weather forecasting and more powerful ships. However, our vulnerability to natural disasters increases as more and more people choose to live in the low-lying coastal zone, and as our civilisation constructs more elaborate systems of transport and services to support it.

Coastal flooding by the sea from time to time is inevitable. Suitable high walls may protect some coasts, but these are expensive to build, and only justified where large populations are at risk. An alternative is to give warnings of impending flooding sufficiently early for people, their animals, and other valuables to move to higher levels, or plan in other ways (Figure 12.15).

Table 12.4 summarises the causes and characteristics of coastal flooding events. These and other ocean hazards, including coral bleaching, ocean acidification and harmful algal blooms, are collectively the concern of international organisations such as the Intergovernmental Oceanographic Commission of UNESCO (IOC), the World Meteorological Organization (WMO) and the United Nations Environment Program (UNEP). Long-term responses, for example to sea-level rise, include mitigation and adjustment; more immediate flooding hazards, such as surges and tsunamis, require reliable timely warnings.

Table 12.5 gives some of the major historical and more recent flooding disasters. Flood defences and warning systems have been set up by national and international bodies to allow preventative measures, especially for cities and other extensive low-lying areas at risk of flooding. All warning systems have

Table 12.4 Sources and representative characteristics of coastal flooding events (see also Figure 1.7 and individual chapter discussions)

Driver		Space scale	Timescale	Amplitude	Warning time
Tropical cyclone	Storm surges	10–100 km	2–24 hours	2–10 m	3–5 days
Extra-tropical storm	Storm surges	100–1000 m	12–48 hours	Up to 3 m	5 days
Earthquake, meteorite, submarine slides	Tsunamis	Ocean	1–6 hours	10 m plus	20 mins–48 hours
Global warming	Sea level rise	Global	Decades	Decimetres per century	Long term
Climate change	Increased flood risk	Global	Decades		

Table 12.5 Estimated size and impacts of some historical and some recent flooding events. For tsunamis the extreme heights are local to the earthquake epicentre.

Date	Region	Event	Maximum extra flood level	Lives lost
November 1218	Zuider Zee	Extra-tropical surge	Unknown	100,000
January 1362	Germany	Extra-tropical surge		100,000
1607	Bristol Channel	Extra-tropical surge	2 m	3,000
1864, 1876	Bangladesh	Cyclone surge	Unknown	250,000
September 1900	Galveston, Texas	Hurricane surge	4 m	8,000
January–February 1953	Southern North Sea	Extra-tropical surge	3 m	2,100
May 1960	Pacific Ocean	Tsunami	25 m	6,000
March 1962	Atlantic coast, United States	Extra-tropical surge	2 m	32
November 1970	Bangladesh	Cyclone surge	9 m	500,000
April 1991	Bangladesh	Cyclone surge	6 m	140,000
December 2004	Indian Ocean	Tsunami	30 m	250,000
August 2005	Louisiana	Hurricane surge	8 m	1,800
November 2007	Bangladesh	Cyclone surge	3 m	4,500
May 2008	Myanmar	Cyclone surge	6 m	138,000
March 2011	Japan	Tsunami	7 m	16,000
November 2013	Philippines	Cyclone surge	4 m	2,000
unknown	unknown			

common elements: a triggering condition; a monitoring and potential disaster confirmation; and an alert dissemination mechanism [40].

12.7.1 Tropical floods

Exact forecasting of flooding due to hurricanes is not possible because knowing the precise track of the hurricane is vital, and this is very challenging given the nature of the storm dynamics. The landfall position of a hurricane is critical, as winds may be onshore on one side of the track, and offshore only a few tens of kilometres away on the opposite side. The hurricane speed over the ground is around 20 km/hr, but the wind speeds around the low-pressure centre, and the internal energy, are much greater.

The hurricane season in the Atlantic runs from June to November. Along the east coast of the United States, the National Hurricane Center (NHC) forecasts storm surges using the SLOSH model [41] (Sea, Lake and Overland Surges from Hurricanes). The NHC is part of the National Weather Service (NWS), part of the National Ocean and Atmospheric Administration (NOAA). Combining forecast models, with increased understanding of the forces that act on tropical cyclones, and a wealth of data from Earth-orbiting satellites and other sensors, scientists have increased the accuracy of track forecasts over recent decades; forecasts are possible for more than five days in advance, with increasing accuracy as the time ahead reduces. However, exact local details are not so readily forecast, and need regular updating by observations; key forecasting parameters include the central pressure of a cyclone, the storm size, the cyclone's forward motion, its track, and the maximum sustained winds. Topographic features are taken into account in defined grids referred to as SLOSH basins. Overlapping SLOSH basins cover the southern and eastern coastline of the continental United States. The SLOSH model does not model waves, river flow or rain flooding, nor does it include the astronomical tide. Future advancements in the SLOSH model will remove some of these limitations.

To allow for forecast uncertainties of a storm, several model runs with varying input parameters are generated to create a map of maximum levels. A similar multi-run approach allows risk planning for future hurricanes evacuation; these are based on modelling a family of storms (maybe 1000 different speeds, directions and intensities; this is called an *ensemble*) to

produce worst-case water heights for any tropical cyclone occurrence. Several products are prepared for disaster planning. The Maximum of Maximum (MOM; see Figure 12.16) is an ensemble product of maximum storm surge heights for all hurricanes of a given category regardless of forward speed, storm trajectory and the landfall location. MOMs represent the worst case scenario for a given category of storm under 'perfect' storm conditions. The MOMs provide useful information aiding in hurricane evacuation planning and are also used to develop the evacuation zones. Vulnerable barrier islands, with limited bridge access to the mainland, have compulsory evacuation plans, which are prepared and imposed at a local county level.

A similar forecast system for the central Pacific operates from Hawaii. In Bangladesh, a text message service warns local people of impending floods and cyclones. Elevated refuges have been built so fatalities are now dramatically reduced, though flooding is still unavoidable (see Chapter 13).

12.7.2 Extra-tropical surges

Extra-tropical surges are more extensive, and their movements more predictable. Also, the surges they generate are more widespread and it is easier to resolve their physics in models. The Maaslantkering barrier (Figure 12.7b), protecting parts of the Netherlands, operates automatically when computer models warn of flooding, at present roughly every 10 years.

The North Sea surge season runs from August to May. Operation of the Thames barrier, designed to withstand the 1 in 1000 years severe weather event, to protect London is more frequent. A Thames Barrier flood defence closure is triggered by the Environment Agency when a combination of high tides forecast in the North Sea and high river flows indicate that water levels would exceed 4.87 metres in central London. Forecast sea levels at the mouth of the Thames Estuary are generated by Meteorological Office computers and also by models run on the Thames Barrier's own forecasting and telemetry computer systems. About 9 hours before the high tide reaches the barrier a flood defence closure begins with messages to stop river traffic, close subsidiary gates and alert other river users. In the 1980s there were 4 operational closures, 35 closures in the 1990s, and 75 closures in the first decade of this century. More generally the UK Coastal Monitoring and Forecasting (UKCMF) consortium receives 5-day general warnings and more exact

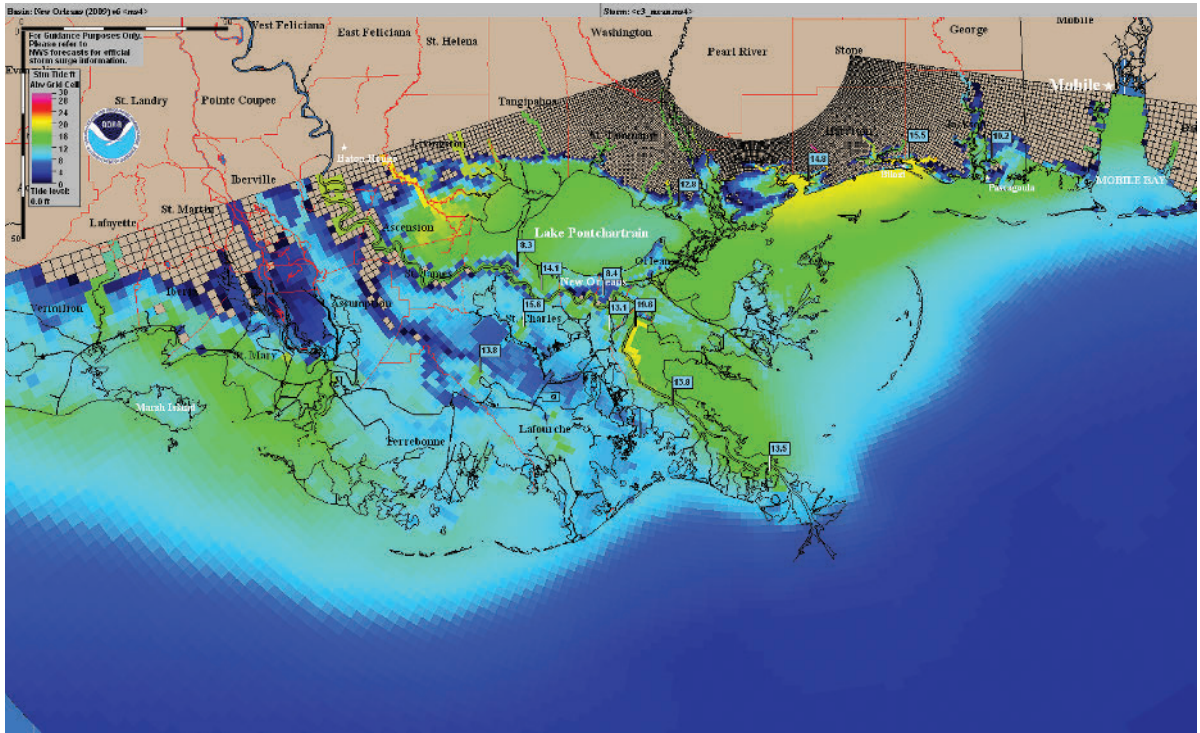


Figure 12.16 The computed Maximum of Maximum (MOM) hurricane levels, for the New Orleans SLOSH Basin (NOAA).

2-day sea-level forecasts, updated every 6 hours from the Met Office. Planning for sea-level rise to 2100, and the uncertainties, has led to the development of new risk assessments, based primarily on regional MSL rise predictions, and possibilities of enhanced extreme river flows.

For London, several hours' advance warnings are possible because of the way in which surges travel as Kelvin waves along the coast of eastern Britain from north to south, and are then reflected northwards along the coast of mainland Europe in the same sense and at the same speed as a tidal Kelvin wave (see Figure 5.11). In a similar way, externally generated surges for Buenos Aires can be anticipated as they track the left-hand Argentinian coast from the south [42].

12.7.3 Tsunamis

As for other flood warning systems, tsunami warning systems need means of detection (see Section 8.6); propagation modelling and flood level and times warnings, and, most important, an effective dissemination system to a public that understands and is able to respond [43]. As discussed in Chapter 8, forecasting

tsunamis is only possible after a seismic or other triggering event. The earthquakes that trigger tsunamis can happen at any time and are not predictable. However, the travel times of known tsunamis and measurements from networks of sea-level gauges (in the deep ocean tsunamis travel at roughly the same speed as an intercontinental jet) can be used to give valuable flood warnings several hours ahead of tsunami arrival in many cases. Major tsunamis occur about once per decade. Based on historical data (see Figure 8.3), about 59 per cent of the world's tsunamis have occurred in the Pacific Ocean, 25 per cent in the Mediterranean Sea, 12 per cent in the Atlantic Ocean, and 4 per cent in the Indian Ocean [44].

The Pacific is the most tsunami-vulnerable ocean. The first tsunami warning system was established in the Pacific Ocean, following the 1960 Chilean earthquake and the ensuing tsunami disasters. The Pacific Tsunami Warning Center (PTWC) of NOAA is based in Hawaii. When an earthquake is detected on an international seismograph network, the tide gauges in the region are monitored. As explained in Chapter 8, only earthquakes that produce vertical movements of the seabed cause tsunamis. If a tsunami

is detected, all other countries in the system are given immediate warning; estimated times of arrival can be given for each location in the Pacific. If no tsunami is observed the warning alert is cancelled. The United States west coast and Alaska are served by a local warning service, set up after the large Alaskan earthquake in March 1964.

The Japan Meteorological Agency (JMA) also has a well-developed tsunami warning system with multiple warning centres. The earthquake epicentre of the March 2011 tsunami (Figure 8.13) that hit northern Japan was only 130 km offshore, so the wave took only about 10 minutes to reach the coast. This shows the inherent difficulties in warning of tsunamis generated by local earthquakes.

Coordination and development of tsunami warning systems is a challenging technical and political intergovernmental activity, under the auspices of the Intergovernmental Oceanographic Commission (IOC) of UNESCO. The IOC, based in Paris, is also the parent body for the Global Sea Level Observing System,GLOSS (Section 2.6), and there are many common features of the GLOSS and tsunami warning systems and their gauges, as discussed in Chapters 2 and 8. Following the 2004 Indian Ocean tsunami, Governments decided to work towards an Indian Ocean tsunami system immediately, but also began planning systems, now operational, for the northeast Atlantic, the Mediterranean, and the Caribbean. Initially, the JMA and the PTWC jointly provided interim warning systems. For the now mature Indian Ocean system (IOTWS), Regional Tsunami Service Providers (RTSPs) in India, Indonesia and Australia are the primary source of tsunami warnings for countries surrounding the Indian Ocean.

The accelerated development of tsunami warning systems by the IOC, after the 2004 Indian Ocean tsunami, was a response to a clear societal and governmental demand. However, although there are good examples of local surge warning coordination, similar coordination of global or at least regional storm surge monitoring, a natural follow on, has not generally become standard for regular international cooperation. Governments have not yet perceived of cooperation, as a priority, although it could be an early target for future regional coastal management, planning and disaster mitigation schemes.

Between the rare tsunami events, operational centres and the IOC place great emphasis on educating the public so that they take tsunami warnings seriously

and act accordingly. For example, tsunami arrival is often preceded by a temporary spectacular withdrawal of the sea (Chapter 8); people on the beach responding to this withdrawal signal by fleeing to high ground has saved many lives.

To summarise, the essential components of all these flood warning systems are:

- a means of detecting and predicting potential flooding,
- a reliable procedure for transmitting these warnings to the public in the areas at risk,
- an educated and responsive public,
- evacuation plans and routes well known.

To gain public respect, it is important that flooding warnings are only issued for serious events. Too many near misses and cancelled warnings reduce public confidence with the result that genuine warnings may be ignored. However, the obvious consequences of delaying before issuing a warning are far more severe. Reliable observations and proven models are necessary to avoid both of these difficulties.

12.8 Economics of coastal defences

The economics of justifying and operating engineered systems is important and complicated. In Section 12.5 we considered investment controls on tidal power generation. One other major economic concern is the cost of building and maintaining sea defences, especially as sea levels rise. Is it worth paying for protection? Usually, yes; but not inevitably. Here we look in a general way at what is involved.

It has been estimated that 23 per cent of the world's population lives within 100 km of the coast, and population densities in coastal regions are about three times higher than the global average. The attractiveness of the coast has resulted in disproportionately rapid expansion of economic activity, settlements, urban centres and tourist resorts. Sixty per cent of the world's 39 megacities with a population of over 5 million each are located within 100 km of the coast, including 12 of the world's 16 cities with populations greater than 10 million [45]. Small island states are particularly vulnerable to climate change impacts. Estimating the economic costs of potential damage, and even of protective measures, is exceedingly difficult because there are so many uncertainties involved. When choosing among strategies for defence, planners balance the risks, the value of amenities, ecosystem services (Chapter 13), and the cost of protection.

The value of coastal amenities is very high, as approximate global estimates published by the inter-governmental Organisation for Economic Cooperation and Development illustrate. A sea-level rise of 1 m by 2100 (at the high end of the IPCC forecast range) would cost \$970 billion worldwide if fully protected against. For the United States alone, estimates suggest a loss of 1500 homes per year, and a projected cumulative impact on coastal property by 2100 ranging between \$20 and \$150 billion. However, the cost will be substantially more than this if coastal resources are either over-or under-protected. Over-protection means that too much money will be spent on defences; under-protection means that the value of the coastal amenity will be lost. In each local area at risk, appropriate cost-benefit analysis is necessary.

The problem of responding to projected sea-level rises has global, regional and local implications. At one extreme vast resources might be expended on protecting the present coastal position and facilities. Unless protective measures are designed with full understanding of the implications, they could result in negative impacts such as increased erosion elsewhere. A complete defence solution would be very difficult to apply for areas such as the Ganges and Nile deltas, and for low-lying coral islands such as the Maldives, in the Indian Ocean, and many others in the Pacific. For the first metre or so of *MSL* rise, defences are probably quite feasible and cost-effective for many of the tidal cities of developed countries, for example, London and Rotterdam.

At the other extreme, a minimum response would be to plan an ordered withdrawal over decades to higher land. The gradual adjustment of low-lying land prices to reflect their finite availability will be the financial response over many decades, similar to the present purchase of leasehold property for a fixed period. For these kinds of economic adjustments to work effectively the markets will need good estimates of the changing risks, and probably incentives to stimulate action.

Cost-benefit analyses are the basis of these assessments. The *costs* of defence will include capital for building a barrier or other form of protection to reduce flooding risk, payment of interest on the capital, and any subsequent maintenance costs. Indirect costs following construction may include loss of some amenities and disruption of natural ecosystem services (see [Chapter 13](#)). The *benefits* will include continuing use of some existing amenities and the generation of

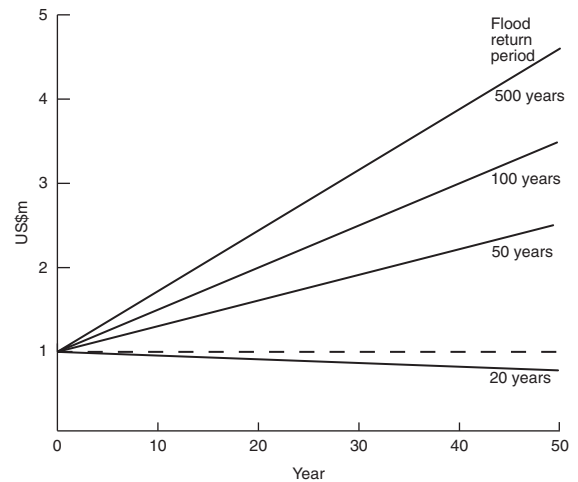


Figure 12.17 The statistical return from a US\$1 million coastal asset, assuming a US\$500,000 protection investment in year zero, repaid over 50 years.

profits from their use, protection of the original value of the assets, and perhaps reduced compensation payment for public liabilities. The future values of all of these factors are much more uncertain even than the effects of climate change. So inevitably are the calculated cost-benefit assessments. The tidal power station at La Rance has now repaid its capital investment costs, and so, as discussed, the ongoing electricity produced is very cost competitive.

[Figure 12.17](#) shows, as an example, the accumulated value of a defended coastal asset for different risks, annual profitability and interest rates. It shows the accumulated value of a US\$1m coastal asset, assuming US\$0.5m invested in protection in year zero, and repaid over 50 years. Value increase is 10 per cent of the asset per annum, and there are interest repayments at 5 per cent of the outstanding loan. Income is not reinvested and there is no allowance for inflation. A flood event is assumed to cause total loss of the asset. Protection only for a 20-year return event is a poor investment as the asset and its value will probably be lost, but investment for higher levels of protection are worth considering. These calculations also show that the uncertainties in non-environmental economic factors, such as interest rates, profitability, and future values, are at least as important as the changing risks of flooding in controlling the likely return on the investment.

If the future economic conditions such as interest rates and profits are uncertain, then why bother with

estimating risks of flooding? Most analyses show that over a long period risk reduction by investing now in defence systems can usually be justified. In the long term, coastal land values have traditionally increased in real terms as population pressures grow, and will probably do so in the future. However, for some low amenity land, the most cost-effective option may be a managed retreat, despite local community protests.

Nevertheless, public opinion should not be ignored, whatever the results of cost-benefit analyses. Financial planning is only a part of the overall political and social decision-making process, and all of these factors will influence the final decision. Estimating cash values is particularly difficult for environmental amenities, which have traditionally not been given an economic value in a strict market sense. What value do present generations place on the environmental capital of recreational beaches, everglades and wetlands? And how can we take into account their value for future generations?

References

- Woodworth, P. L., Pugh, D. T. and Bingley, R. M. 2010. Long term and recent changes in sea level in the Falkland Islands. *Journal of Geophysical Research*, **115**, C09025, doi:10.1029/2010JC006113.
- International Standards. 2009. *Risk Management: Principles and Guidelines*. IOS3100.
- Kotz, S. and Nadarajah, S. 2000. *Extreme Value Distributions: Theory and Practice*. London: Imperial College Press.
- Coles, S. 2001. *An Introduction to Statistical Modelling of Extreme Values*. Berlin: Springer-Verlag.
- Dixon, M. J. and Tawn, J. A. 1992. Trends in U.K. extreme sea levels: a spatial approach. *Geophysical Journal International*, **111**, 607–616, doi:10.1111/j.1365-246X.1992.tb02115.x.
- Hunter, J. 2012. A simple technique for estimating an allowance for uncertain sea-level rise. *Climatic Change*, **113**, 239–252, doi:10.1007/s10584-011-0332-1.
- <http://publications.environment-agency.gov.uk/PDF/SCHO0111BTKI-E-E.pdf>.
- Menéndez, M. and Woodworth, P. L. 2010. Changes in extreme high water levels based on a quasi-global tide-gauge data set. *Journal of Geophysical Research*, **115**, C10011, doi:10.1029/2009JC005997.
- Hunter, J. R., Church, J. A., White, N. J. and Zhang, X. 2013. Towards a global regionally-varying allowance for sea-level rise. *Ocean Engineering*, doi:10.1016/j.oceaneng.2012.12.041.
- Hunter, J. 2010. Estimating sea-level extremes under conditions of uncertain sea-level rise. *Climatic Change*, **99**, 331–350, doi:10.1007/s10584-009-9671-6.
- Pugh, D. T. 1982. Estimating extreme currents by combining tidal and surge probabilities. *Ocean Engineering*, **9**, 361–372.
- Jecock, M. 2011. *Roman and Medieval Sea and River Defences*. English Heritage.
- Zhao, B., Kreuter, U., Li, B. et al. 2004. An ecosystem service value assessment of land-use change on Chongming Island, China. *Land Use Policy*, **21**(2), 139–148. doi:10.1016/j.landusepol.2003.10.003.
- U.S. Army Corps of Engineers. 2012. *Coastal Engineering Manual*. Available from <http://chl.erdc.usace.army.mil/chl.aspx?p=s&a=ARTICLES;101>.
- <http://www.kennisbank-waterbouw.nl/DesignCodes/rockmanual/>
- Horner, R. W. and Clerk, D. 1985. The Thames Barrier. *Proceedings of the Institution of Civil Engineers*, **78**(1), 15–25, doi:10.1680/iicep.1985.1017.
- Miles, J. W. 1971. Resonant response of harbours: an equivalent-circuit analysis. *Journal of Fluid Mechanics*, **46**, 241–265, doi:10.1017/S002211207100051X.
- Wong, K.-C. 1986. Sea-level fluctuations in a coastal lagoon. *Estuarine, Coastal and Shelf Science*, **22**, 739–752, doi:10.1016/0272-7714(86)90096-X.
- Araújo, I. B., Dias, J. M. and Pugh, D. T. 2008. Model simulations of tidal changes in a coastal lagoon, the Ria de Aveiro (Portugal). *Continental Shelf Research*, **28**, 1010–1025, doi:10.1016/j.csr.2008.02.001.
- Pugh, D. T. 1979. Sea levels at Aldabra Atoll, Mombasa and Mahé, western equatorial Indian Ocean, related to tides, meteorology and ocean circulation. *Deep-Sea Research, A*, **26**, 237–258, doi:10.1016/0198-0149(79)90022-0.
- <http://www.dpi.nsw.gov.au/fisheries/habitat/aquatic-habitats/wetland/coastal-wetlands/management-of-coastal-lakes-and-lagoons-in-nsw>. Gale, E., Pattiaratchi, C. and Ranasingh, B. 2006. Vertical mixing processes in intermittently closed and open lakes and lagoons, and the dissolved oxygen response. *Estuarine, Coastal and Shelf Science*, **69**, 205–216. doi:10.1016/j.ecss.2006.04.013
- Dean, R. G. and Dalrymple, R. A. 2002. *Coastal Processes with Engineering Applications*. Cambridge: Cambridge University Press.
- Charlier, R. H. and Finkl, C. W. 2009. *Ocean Energy: Tide and Tidal Power*. Berlin, Heidelberg: Springer.
- King, R. D. 1997. Bishopstone tidemills: an historical perspective on the use of tidal power. *Ocean Challenge*, **7**, 9–11.

25. Redfield, A. C. 1980. *The Tides of the Waters of New England and New York*. Woods Hole, MA: Woods Hole Oceanographic Institution.
26. Garrett, C. and Cummins, P. 2007. The efficiency of a turbine in a tidal channel. *Journal of Fluid Mechanics*, **588**, 243–251, doi:10.1017/S0022112007007781.
27. Hardisty, J. 2009. *The Analysis of Tidal Stream Power*. London: Wiley.
28. <http://www.fundyforce.ca/>
29. Stevens, C. L., Smith, M. J., Grant, B., Stewart, C. L. and Divett, T. 2012. Tidal energy resource complexity in a large strait: The Karori Rip, Cook Strait. *Continental Shelf Research*, **33**, 100–109, doi:10.1016/j.csr.2011.11.012.
30. http://en.wikipedia.org/wiki/Tidal_stream_generatorial_Potentials
31. Yates, N., Walkington, I., Burrows, R. and Wolf, J. 2013 Appraising the extractable tidal energy resource of the UK's western coastal waters. *Philosophical Transactions of the Royal Society, A*, **371**, doi:10.1098/rsta.2012.0181.
32. (1)Shapiro, G. I. 2011. Effect of tidal stream power generation on the region-wide circulation in a shallow sea. *Ocean Science*, **7**, 165–174, doi:10.5194/os-7-165-2011. (2) Hasegawa, D., Sheng, J., Greenberg, D. A. and Thompson, K. R. 2012. Far-field effects of tidal energy extraction in the Minas Passage on tidal circulation in the Bay of Fundy and Gulf of Maine using a nested-grid coastal circulation model. *Ocean Dynamics*, **61**, 1845–1868, doi:10.1007/s10236-011-0481-9.
33. Greenberg, D. 1987. Modelling tidal power. *Scientific American*, **257**, 106–113.
34. Sucusy, P. V., Pearce, B. R. and Panchang, V. G. 1993. Comparison of two-and three-dimensional model simulation of the effect of a tidal barrier on the Gulf of Maine tides. *Journal of Physical Oceanography*, **23**, 1231–1248, doi:10.1175/1520-0485(1993)023<1231:COTATD>2.0.CO;2.
35. Neill, S. P., Litt, E. J., Couch, S. J. and Davies, A. G. 2009. The impact of tidal stream turbines on large-scale sediment dynamics. *Renewable Energy*, **34**, 2803–2812, doi:10.1016/j.renene.2009.06.015.
36. Kirby, R. and Retière, C. 2009. Comparing environmental effects of Rance and Severn barrages. *Proceedings of the Institution of Civil Engineers, Maritime Engineering*, **162**, 11–26, doi:10.1680/maen.2009.162.1.11.
37. Ricketts, E. F., Calvin, J. and Hedgpeth, J. W. (Revised by D.W. Phillips) 1992. *Between Pacific Tides* (5th edition. Original version 1939). Stanford, CA: Stanford University Press.
38. Pugh, D. T. 1996. *Tides, Surges and Mean Sea-Level*. Chichester: John Wiley (Chapters 10 and 11).
39. Pugh, D. T. and Rayner, R. F. 1974. The tidal regimes of three Indian Ocean atolls and some ecological implications. *Estuarine, Coastal and Shelf Science*, **13**, 389–407, doi:10.1016/S0302-3524(81)80036-9.
40. Flather, R. A. 2000. Existing operational oceanography. *Coastal Engineering*, **41**, 13–40, doi:10.1016/S0378-3839(00)00025-9.
41. http://www.nhc.noaa.gov/ssurge/ssurge_slosh.shtml
42. Santoro, P. E., Fossati, M., Piedra-Cueva, I. 2013. Study of the meteorological tides of the Rio de la Plata. *Continental Shelf Research*, **60**, 51–63.
43. Veitch, N. and Jaffray, G. (eds.) 2010. *Tsunamis: Causes, Characteristics, Warnings and Protection*. Hauppauge, NY: Nova Science Publishers.
44. <http://ptwc.weather.gov/faq.php#8>
45. Nicholls, R. J., Wong, P. P., Burkett, V. R. et al. 2007. Coastal systems and low-lying areas. In *Climate Change 2007: Impacts, Adaptation and Vulnerability. Contribution of Working Group II to the Fourth Assessment Report of the Intergovernmental Panel on Climate Change* (eds. M. L. Parry, O. F. Canziani, J. P. Palutikof, P. J. van der Linden and C. E. Hanson), pp. 315–356. Cambridge: Cambridge University Press.

Most of the time I understated what I saw because I couldn't find words powerful enough, but that's the nature of marine life and the inland bays I grew up on. You'd have to be a scientist, a poet and a comedian to hope to describe it all accurately, and even then you'd fall short.

Jim Lynch, The Highest Tide

13.1 Introduction

This chapter contains our personal selection of topics on how the tides and sea-level changes have played important roles in the development of life, and in human history. The populations of coastal zones are increasing dramatically, and tides, storm surges and long-term sea-level changes will continue to play important roles in our lives. Impacts of sea-level change will take place alongside those due to many other climate and environmental stresses.

It is our belief that, if these impacts are to be avoided, or managed, as far as possible, then we have to learn more about the space and time scales of sea-level change and the various reasons for them. Also we have to communicate a greater appreciation of how tides and sea levels have contributed to the coastal environment in general, providing many communities with food sources and places to live and thrive, contributions that continue in many and varied ways today.

13.2 The Moon and us

It is highly likely that we would not be here without the Moon and the tide. The origin of life is a long-standing and controversial subject concerned with how the first known single-cell organisms called prokaryotes originated in the Archean period (3.5 billion years ago) [1]. One candidate mechanism involves lightning in the early atmosphere and the consequent production of amino acids that, when combined in long chains, provided the basic constituents of life. A second mechanism concerns chemical processes at submarine volcanic vents. Such vents, similar to the 'black smokers'

of today [2], are thought to have been common in the Archean, and life at those depths would have been shielded from the ultraviolet radiation that existed at that time due to the absence of an ozone layer. A third mechanism has life originating from the carbon and hydrocarbons in comets and meteorites as they burned in the atmosphere. However, the process that mostly concerns us is the possibility that life originated in intertidal pools that were repeatedly flooded and dried out under the Sun, a process for which the geological record provides evidence [1]. Pre-cellular systems called liposomes have been identified in which the encapsulation of DNA has been achieved using dehydration-hydration cycles similar to those that may have occurred in an intertidal setting on the early Earth [3]. Once self-replication of life was established, then evolution to more complicated forms of life could have taken place by Darwinian selection [4].¹

The Moon played an important role in the origin and maintenance of life on the early Earth, not only by causing the large tides and thereby the intertidal pools, but also by imposing a stabilisation of the Earth's obliquity (the angle of the planet's spin axis with respect to the perpendicular to the orbital plane). Changes in the Earth's orbit and orientation are known to be closely related to large fluctuations in climate, including the ice ages [6]. Consequently, the stabilisation of the Earth's obliquity must have contributed to the maintenance of a more stable climate, and the evolution of life on land, than would otherwise

¹ The ocean could have played further roles in human development, for example via the Aquatic Ape hypothesis, although that particular theory is not widely accepted [1].

have been the case. The Moon may have influenced the Earth's history in several other ways, including the evolution of its atmosphere and magnetic field, the absence of a similar large satellite having contributed to a different history for Venus and Mars [4].

13.3 Intertidal life

The intertidal zone may have been important for the origin of life, but its management today is proving difficult. Not only are there many competing interests, but there are also problems of assessing the value of the resources to be found there. Economists can readily identify immediate cash-yielding assets such as fisheries, wood or agricultural grazing. They also acknowledge, but cannot quantify, the value of ecosystem services such as nurseries, water purification, coastal protection from storms and waves, and even carbon sequestration, which involve no financial transactions but are important for the health of coastal populations, the ocean and, ultimately, Planet Earth.² The intertidal ecosystems are in decline in many regions. For example, mangroves covered some 200,000 km² or 75 per cent of the world's coastlines in the 1970s, but since then 35 per cent has been lost due to coastal developments [7].

In this section, we look first at the importance of tidal patterns for plants and animals in the intertidal zone of the present day, and the zonation of life that results, for different types of coast [8, 9]. The subject has spawned many classic accounts [10, 11, 12, 13]. We then refer to examples of behaviour adaptation to the tide which is to be found in many species.

13.3.1 Zonation of coastal plants and animals

Plants and animals have certain essential requirements if they are to survive and prosper. Each organism has developed special characteristics to enable it to compete successfully in its particular environment. At the extremes, conditions on land and in water, and the

species that live there, are very different. At the coast, certain species and ecosystems have developed to thrive in an environment that changes between these two extremes in a pattern defined by the rise and fall of the tide. This habitat is also often subjected to wave action and to strong currents.

For survival in this highly variable region, species must be able to cope with the relatively uniform conditions of submersion: even temperatures, a plentiful supply of dissolved oxygen, abundant nutrients and organic debris and micro-organisms that can be extracted relatively easily as food. They must also survive varying periods of exposure to air: extremes of temperature, salinity and desiccation. Between high and low tide they may also experience large pressure changes. As a result of these varying environments for adaptation, patterns of species zonation can be observed from the bottom to the top of the tidal range [14].

Marine biologists have looked for relationships between the local tidal régime and the biological zonation in terms of Critical Tidal Levels (CTLs). There are many different ways of doing this from the basic tidal constituents and tidal predictions. We discussed tidal levels and exposure briefly in [Section 12.6](#). See also [Section 6.5](#).

Both waves and surges blur the boundaries of CTLs where these are identified, and this shading of boundaries makes it unproductive to speculate on the influences of a fine structure within the theoretical statistics of CTLs. The boundaries found in the vertical zonation of species must be accentuated by competitive mechanisms within the ecosystems themselves.

A more complete picture of the emersion pattern at any particular level is given by calculating how long a level is exposed. The most regular cycle of emersion and submersion is found at the mean sea level (MSL). The exposure patterns for mixed tidal régimes are much more complex than for diurnal or semidiurnal-dominant régimes. A plant or animal at a 4.4 m level above Chart Datum at Newlyn (a semidiurnal régime, see [Figure 12.13](#)) is normally exposed for periods between 8 and 12 hours, but on 13 occasions in any one year it could be exposed for periods greater than 30 hours. The longest period of exposure would be about 112 hours. For San Francisco there are many more periods of exposure of a day or longer because of the greater diurnal inequality.

Time of day at emersion is also critical. The dangers of desiccation for a marine plant or animal

² Ecosystem services are defined colloquially as 'the benefits of nature to households, communities and economies'. The term has gained currency because it conveys an important idea: that ecosystems are socially valuable in many ways. This idea has great potential to unite the fields of ecology and economics, form the basis of a unified approach to environmental performance measurement, and foster clear public communication on environmental issues. However, the term lacks clear definition.

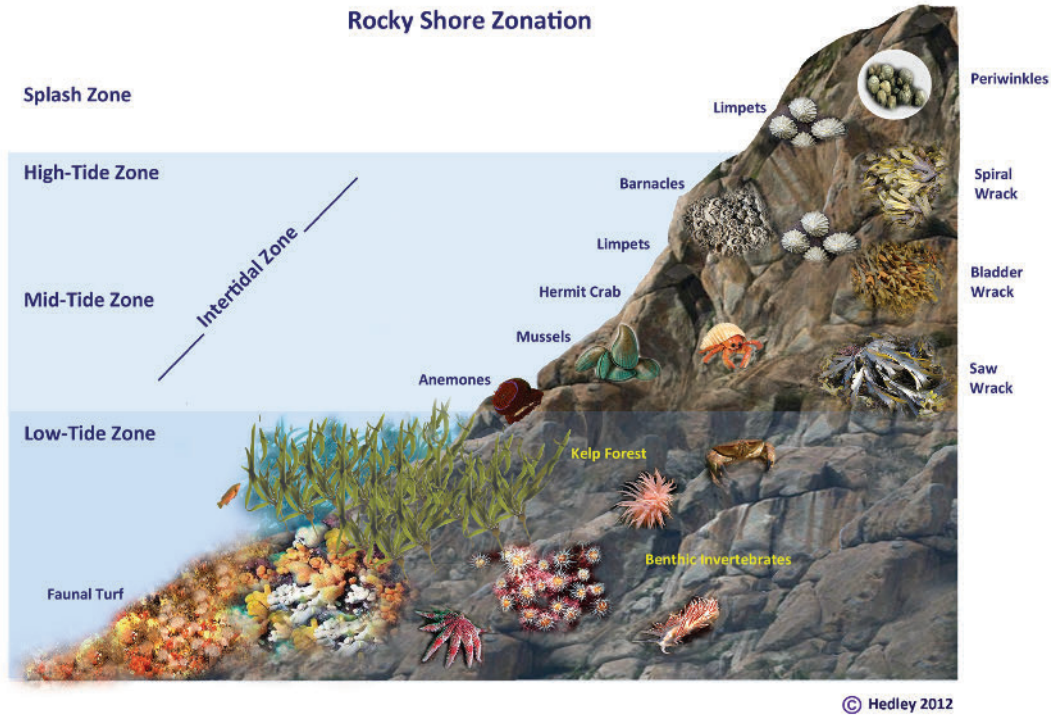


Figure 13.1 The strong horizontal bands or zonation to be found on many rocky shores. Image drawn and supplied by Claire Hedley of the Berwickshire and North Northumberland Coast European Marine Site.

exposed to the air are obviously much greater if the exposure takes place during the maximum heat of the day. Night-time exposures to winter frosts can also inflict serious stress on plants and animals whose normal preferred habitat is within the more stable temperatures of coastal waters.³

13.3.2 Rocky shores

The intertidal area between highest and lowest water levels generally shows high biological productivity and contains a very rich and diverse range of species. The many reasons for this high level of productivity include the regular availability of nutrients during each tidal cycle in water that is shallow enough for photosynthesis. But, as already emphasised, it is also a region of great environmental stress. The potential for high productivity can only be realised by those species that have highly adapted survival mechanisms. Different coastal conditions require different mechanisms.

The three main non-biological factors that determine the distribution of shore species are: the patterns of tidal emersion; the degree of exposure to waves; and the nature of the bottom material or substratum.

There are many adaptation differences between the intertidal zones of sands and muddy shores and those of rocky shores. For example, species on sands and muddy shores can burrow to avoid desiccation, whereas on rocky shores species must develop more robust defences.

Rocky shores are both exposed and accessible; plants and animals live on the rocks and have no place to hide. Because they are so accessible, more is known about their complex biology and ecology than about any other marine habitat [16, 17]. There are strong horizontal bands or zonation (Figure 13.1). The highest levels on rocky shores are almost always exposed to air. Here, encrusting black lichens and blue-green algae exist with periwinkles and some primitive insects. At lower levels there is a succession of zoned periwinkles, barnacles and mussels. These intertidal species often develop in intense clusters to create microhabitats in which more moisture is

³ This topic is discussed at greater length in Reference 15.

retained during exposure. Seaweeds develop at the lower levels. Zonation is caused by a variety of tidal and biological interactions. The upper level of a zone is often determined by physical factors; the lower limit is usually determined by biological factors.

There is a general enhancement of growth in rocky channels through which tidal currents flood and ebb. This is due to the continuous stream of nutrients and essential foods, and because the water is usually clear of sediments, which encourages photosynthesis; the relative absence of settling sediments in the water reduces the risk of clogging of the filter-feeding mechanisms of organisms.

Rock pools in the intertidal regions also provide special biological niches (cf. [Section 13.2](#)). Individual species have different physical and physiological mechanisms for coping with changes of exposure, temperature, higher light intensity, salinity and other variables such as pH and the partial pressures of oxygen and carbon dioxide. Many species shelter in small shallow intertidal rock pools during periods of low tide, preferring the possible extremes of salinity, temperature and of oxygen depletion to total exposure to the air.

13.3.3 Sedimentary shores

Sedimentary shores, coasts formed by gravels, sand and mud deposits, are in a state of continuous erosion and deposition, and their structure is strongly influenced by tides and waves. In many cases the biological flora and fauna are important agents in the dynamics of coastal stability and change. Zonation is less obvious on sedimentary shores than on rocky shores because most of the species there survive by burying themselves from extremes of emersion, temperature and salinity.

Sedimentary shores that support life vary from very sheltered bays, where fine mud accretes, to exposed beaches that are reworked by waves during each storm and, indeed, on every tide [18]. There is a strong relationship between the steepness of the beach and the number of species found. Gently sloping beaches have many more species than steeper beaches where the wave energy is concentrated and destructive.

Within the sediments, large populations of superficially invisible individual species can thrive. When the tide is out the sediments retain a high proportion of water, so that animals burrowing in the trapped water avoid exposure to low salinities. In addition, the sands filter the water during each tidal cycle and concentrate the particulate matter to the advantage of

burrowing animals. Many birds feed in the intertidal zone ([Section 12.6](#)). Such birds are often seen feeding at the water's edge as the advancing and retreating tide reworks the sediments and exposes food. Shingle beaches, consisting of gravels and pebbles, are generally too mobile to allow organisms to establish themselves.

13.3.4 Salt marshes and mangroves

Common features may be identified between the mangrove coasts, which were so extensive just a few decades ago, and the salt marshes that we discussed in the context of MSL change in [Chapter 10](#).

Although the salt marshes found at mid-latitudes ([Figure 13.2](#)) and the mangrove swamps in the tropics ([Figure 13.3](#)) appear very different, they are both colonised by salt-tolerant plants. Both have been established by these plants slowing the water movements, so that suspended sands and muds settle out and are not subsequently eroded. As a result, there is a progressive increase in the levels of both salt marshes and mangrove swamps over a period of years. Detailed analysis of these layers can be very valuable in understanding past sea-level changes, as discussed in [Section 10.9.1](#). A sandy or muddy intertidal area is first colonised by the species that are most tolerant of salt and submersion, and once established, the whole process of salt marsh formation begins. On many sandy beaches *Spartina* grasses are the first to become established at the upper tidal levels. As the sediments accumulate, other less tolerant but more competitive species begin to dominate as the shore levels continue to rise. A network of creeks develops for tidal inflow and outflow.

Mangrove swamps support rich ecosystems, which contain terrestrial species in the branches of the mangroves and marine species within the underlying roots and sediments. Mobile animals such as crabs are particularly well adapted. At low tide, tree-living snakes and monkeys are able to feed on the crabs. In addition to mobile organisms, there is also a rich surface-living epifauna attached to tree trunks and branches.⁴ This includes many species such as barnacles, which are also characteristic of rocky coasts, and there is a similar strong vertical zonation of species.

⁴ Epifauna are animals that live on the surface of a substrate such as rocks.



Figure 13.2 The Jadrtovac salt marsh has an area of 4 km² and is located in Morinje Bay, north of Split, Croatia. The bay connects to the Adriatic Sea through a narrow channel. The marsh is approximately 130 m wide and has distinct zones of vegetation in its upper- and lower-marsh zones. Photograph by Tim Shaw, University of Liverpool.



Figure 13.3 Mangrove swamps at Gazi on the Indian Ocean coast of Kenya. Photograph by David Pugh.

13.3.5 Coral reefs

Coral reefs exposed to cold or rainy weather may suffer extensive damage and subsequent decay of cell tissue. At a location with a semidiurnal tide, the time of day at which extreme low water levels occur will be

related to the phase of the S_2 constituent; at a coral island this is an important factor in assessing the vulnerability of a reef to solar heating [19, 20].

Active coral reefs are automatically associated with sea level because of the light they need for



Figure 13.4 Plankton are carried by tidal currents. In channels they provide abundant feeding for fish and coral. This photograph is from Sinai, Egypt, in the Red Sea. © Alexander Mustard.

photosynthesis (Figure 13.4) [21, 22]. Without enough light, because sea level rises too fast for their growth to keep up, then their productive ecosystems will stop growing [23]. Corals are already under stress worldwide due to the bleaching events that accompany higher temperatures and because of ocean acidification, and at least 70 per cent of reefs are projected to suffer from degradation by 2030 [24]. (There is some debate whether such islands are already eroding [25].) Where the phase of S_2 is such that low spring tides occur around midday, corals will be subjected to a larger diurnal cycle of heating than elsewhere, and will have a greater susceptibility to bleaching [19].⁵

13.3.6 Examples of behaviour adaptation to the tide

The fiddler crab, or Atlantic marsh fiddler (*Uca pugnax*), is found along the east coast of the United States from Massachusetts to Florida (Figure 13.5a). It provides an interesting example of complicated ecosystem interactions and of species adaptation mechanisms.

⁵ For an Earth without a Moon, and so with only solar tides, there would be greater spatial zonation of reef vulnerability; fortunately, over a fortnight the lunar tides moderate the potential effects of solar tides and heating.

They forage the scum of nutrients left by the retreating tide, so helping to recycle minerals and organic matter; as the tide rises they are able to seal their burrows against flooding. Their reproductive cycle is linked to the tides: the mating takes place during spring tides, and the female remains in the burrow for the two-week mating period, before the eggs are released and swept to sea on the next spring tide [26].

The mummichog, an estuarine species of fish found along the east coast of North America from Florida to the Gulf of St Lawrence, has a spawning pattern related to tides. The eggs are laid at levels reached only on spring tides, hidden in leaves or empty mussel shells. Hatching takes place after two weeks when the eggs are again reached by the tides.

On the Californian coast the grunion, a small fish (Figure 13.5b), comes out of the water to lay eggs a few centimetres deep in the wet beach sand, for three or four nights after the spring tides. Spawning occurs primarily at night from March through to August. Eggs hatch after about 10 days, when they are released from the sand by the working of the next series of high spring tides. The baby grunion hatch 2–3 minutes later and are then washed out to sea.

The movements of plaice, which spawn in the Southern Bight of the North Sea, are adapted to the patterns of tidal currents [27, 28, 29]. In the late

(a)



(b)



Figure 13.5 (a) The Fiddler Crab (*Uca pugnax*, or Atlantic marsh fiddler). A Wikimedia Commons image. (b) Grunion spawning at a high tide on a Californian beach. Photograph from the Birch Aquarium at Scripps Institution of Oceanography, San Diego.

autumn, maturing fish migrating from more northerly feeding grounds into the Southern Bight are caught most frequently by mid-water trawls on the south-going tidal currents. In winter, spent females returning to the north are caught more often in midwater on the north-going tidal currents than on the south-going tidal currents. Clearly, travelling in midwater when the tidal currents are in the direction of intended migration allows a fish to make the maximum movement over the ground for the minimum expenditure of energy. This so-called selective tidal stream transport has also been found to occur for sole, cod, dogfish and silver eels. The mechanism is thought to be significant to the movement and distribution of many species of fish on the continental shelves where tidal currents are strong [30, 31, 32].

13.4 Human development

13.4.1 Migration and civilisation

Homo sapiens is thought to have evolved in eastern Africa approximately 200,000 years ago [33]. The period since then has seen two interglacials, the Eemian at about 120,000 years ago and the present one following the Last Glacial Maximum (LGM) (Figure 10.15). In the intervening period, sea levels were much lower than now, enabling human migration from Africa to the Middle East, throughout Southeast Asia and Indonesia to New Guinea and Australia, and during the LGM to North America [34, 35]. Similarly, lower sea levels will have aided the migration of humans and earlier hominids from Africa to Europe [36]. During these glaciated periods, the continental shelves of mid- and low-latitude coasts would have provided extensive and fertile land areas supporting wildlife and suitable for early agriculture.

Climate and sea level stabilised around 6000 years ago, and civilisations developed. The urban civilisations of the Bronze Age (roughly 3000–1000 BC) in the Indus valley, Mesopotamia and Ancient Egypt date from this time, based primarily on major rivers and estuaries with access to the coast. Another example is Pavlopetri in Greece, the ‘oldest submerged city’, which is now under water due to tectonic events [37] (Figure 13.6).⁶ However, some authors have speculated that many other organised communities started earlier than previously thought, being located along the now-flooded continental shelves [38].

Coastal civilisations benefited not only from expanses of generally flat and fertile land for agriculture, especially near to river estuaries, but also from access to the intertidal zone and to fishing in coastal waters. A variety of techniques for fishing included seine netting and fish traps (Figure 13.7) [39].⁷

⁶ Pavlopetri was discovered in 1967 by Nic Flemming. The site is submerged in 3–4 metres of water and covers an area of 500 m². There are 15 buildings, each with three or four rooms. Most of the ruins are dated to 1600–1100 BC and it is believed that they were submerged shortly afterwards following several earthquakes.

⁷ There is also evidence for much older (early Bronze Age) remains. Fish traps can be found at several locations around the United Kingdom. A recently discovered example is located to the west of the Poppit Sands in Cardigan Bay in Pembrokeshire, Wales, not far from St Dogmael’s Abbey. This 280 m long, circular stone wall trap is about 1000 years old but is now completely under water due to a rise in sea level. Other examples in other countries may be found in Reference 39 and http://en.wikipedia.org/wiki/Fishing_weir.

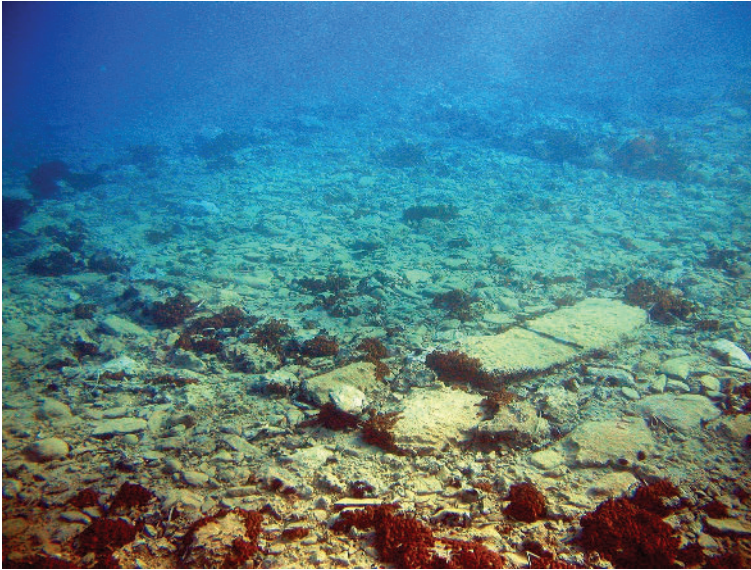


Figure 13.6 A room of the underwater town of Pavlopetri off the coast of southern Laconia in the Peloponnese, Greece. Photograph provided by Dr Nic Flemming, National Oceanography Centre.

As sea levels rose over the continental shelves (Figure 11.17), fronts in the shelf waters developed which are highly productive biologically [40]. These areas are nowadays known to fishermen as ‘hot spot’ locations, where mixing at depth by the ocean tides modifies nutrient fluxes [41].

Coastal communities learned to take advantage of productivity by land and sea, while living in areas prone to inundation by the sea or rivers. One example is given by the societies in the coastal Netherlands, Germany and Denmark who built the artificial hills (terpen) as flood refuge areas (Figure 13.8). On another continent, the indigenous Manhouaht People of Vancouver Island, Canada, developed a strong interest in the tide for access to food along the shore; food from the very low tidal levels was said to be *kwisaap’alhshiti*, ‘food that because it is only occasionally eaten, tastes especially good’ [42]. Chapter 12 has described how societies learned to develop technologies based on exploiting the tide.⁸

13.4.2 Sea level and our history

Sea level has featured prominently in the history and legends of many civilisations, Noah’s Flood and Atlantis being just two examples.⁹ Insight into tides

and sea-level changes is an important factor in the interpretation of many events, especially in European history. Examples include the Greek siege of Troy around 1250 BC [45], the Battle of Thermopylae in 480 BC between the Greek and Persian armies [46], Julius Caesar’s invasions of Britain in 55 and 54 BC [47], the Battle of Maldon in southeast England between Anglo-Saxons and Vikings in 991 [48], and the loss of King John’s crown jewels in The Wash in eastern England in 1216 [49]. Another example from England concerns King Canute, famous for his (probably apocryphal) attempts to command the tide or, more probably, to prove to his courtiers that he could not [50]. Devastating storm surges have impacted many regions around the world at different times. These have often had major consequences for their coastal populations [43, 51] and have sometimes had immediate political consequences.

The role of the tide has been central in many amphibious military campaigns in recent history including the D-Day landings in World War II when tidal predictions were computed accurately [51], and the disastrous landings at Tarawa in the Pacific when they were not [52]. Many other examples of the importance of the tide in major events can be found in the history of tidal science by David Cartwright [53].

⁸ Aspects of the role of sea level in human societies around the world can be found in Reference 43.

⁹ The association of the flooding of the Euxine Lake (Black Sea) around 5600 BC with the story of Noah’s Flood, and similar

accounts in other cultures, was first suggested by Ryan and Pitman [44].

(a)



(b)



Figure 13.7 (a) The remains of several stone tidal fish traps in the Menai Strait in North Wales, photograph taken from Church Island looking towards Anglesey. A Wikimedia Commons image. (b) A photograph showing the size of some of the traps from Dr Cecil Jones, University of Bangor.



Figure 13.8 An artificial hill (terp) at Hooze in Germany, an example of many known to have been constructed in the coastal Netherlands, Germany and Denmark in approximately AD 0–1000. The terpen were mounds constructed to provide refuge during flooding. Photograph by Sandra Buhmann, a Wikimedia Commons image.43.

13.4.3 Myths and traditions

Humans have developed some strange beliefs about the influences of tides on their lives and behaviour patterns [54].

In [Chapter 1](#) we mentioned the legend that no animal can die unless the tide is ebbing. This tradition is mentioned in Charles Dickens' *David Copperfield*, where for the ailing Mr Barkis 'And, it being low water, he went out with the tide'. But the tradition is also mentioned by Aristotle, and it was a native belief on the Queen Charlotte Islands (Haida Gwaii) of Canada, and in Chiloe Island, Chile. Less dramatically, Breton peasants believed that the best butter is made when the tide has just turned and is beginning to flow.

In Japan, tide jewels were magical gems that the Sea God used to control the tides: there were separate ebb and tidal flow jewels. Throwing the 'pearl of ebb' into the sea caused the tides to dry up.

On the Pacific island of Fiji, the term *matiruku* means both 'low tide in the morning' and someone who is periodically insane, but the reason for the link to local tidal conditions is not known. *Matiruku* corresponds to the mood changes of hypomania,¹⁰ which may have special features in Fiji: short duration, frequent recurrence and an intensification of symptoms in the morning [55].

The Bible contains several references to storms at sea, including Jonah's swallowing by a large fish or

whale (Book of Jonah), the calming of the storm in the Sea of Galilee (Mark 4), and notably the parting of the Red Sea (Exodus 14), which it has been suggested was due to a negative storm surge [56]. Easter time varies from year to year, but early or late, Easter weekend is always a good time to see a tidal bore. Spring tides occur when the Earth, Moon and Sun are in line, which is at new and full Moon. Very high spring tides follow when the Moon and Sun are overhead at the equator, near to the 21 March and 23 September equinoxes. The high spring tides of Easter weekend are inevitable because Easter Day is defined in terms of the lunar cycle and the date of the spring equinox. Easter Day is fixed as the first Sunday after the full Moon that happens on, or next after the 21 March spring equinox. It may fall on any one of the 35 days from 22 March to 25 April ([Section 6.6.2](#)).¹¹

13.5 The sea-level present

Millions of people now live along the coastal strips of the continents, benefitting from rich agricultural land, easy transport connections for industry, fishing and relatively new activities such as tourism. Many more live on ocean islands that are only a few metres above sea level. It is thought that nowadays more than 200 million people live in coastal areas that are vulnerable to flooding by extreme sea-level events [57].

¹⁰ Hypomania is closely related to bipolar disorder. See <http://en.wikipedia.org/wiki/Hypomania>.

¹¹ These dates refer to the Easter of Western Christianity, which uses the Gregorian calendar. The Easter of Eastern Christianity, based on the Julian calendar, can be later. See <http://en.wikipedia.org/wiki/Easter>.

These coastal societies have needed information on sea-level variations for many reasons, as earlier chapters in this book have shown. Tidal knowledge has been needed for port operations, efficient dispersal of pollutants, safe navigation and for the efficient exploitation of the power of the tide for energy generation (Chapter 12). Detailed knowledge of non-tidal variability has also been required in order to guard against the risk of flooding due to extreme events such as storm surges or tsunamis (Chapters 7, 8 and 12).

This sort of knowledge remains important, but there is now an additional imperative to understand much better the reasons for long-term changes in mean and extreme sea levels. From the information discussed in Chapter 10, we have learned that sea level changes on many different space and time scales. Therefore, to understand such complexity even more, it is clear that many more sets of measurements and modelling of sea (and land) levels are needed [58]. These research activities span a range of scientific disciplines, as Chapters 9–11 have demonstrated, and many groups around the world are now collaborating in actively studying the historical sea-level record and trying to understand the reasons for the observed changes [59].

As we become more aware of the potential dangers of climate change, including sea-level change, then the various climatic and geophysical reasons for long-term sea-level change need to be even better understood in order to have a better chance of estimating those of the future, and thereby to plan for future coastal protection (Chapter 12). There are many topics for scientists to address but, in our opinion, two stand out:

- Various types of modelling can provide projections of future global-average sea-level rise (Chapter 10). These estimates have large uncertainties, but the uncertainties for specific regions around the world are even larger. Coastal planners need such regional information for their work and there have been attempts to provide it [60]. However, there has to be much better insight into the spatial patterns of sea-level change [61].
- Coastal dwellers are less interested in future change in MSL than in the magnitude and frequency of extreme events (primarily from storm surges, Chapter 7) [62]. If extreme levels increase in line with MSL change, then it is possible to plan for how much to raise coastal defences, taking into consideration the uncertainties in sea-level projections (Section 12.2.5) [63]. However, questions remain as to whether extreme levels will

indeed rise with MSL in this way, and whether the frequency of surge events will change in a warmer world. Coastal planners need answers to these questions.

13.6 The sea-level future

Even though the pace of coastal development has accelerated in recent decades, with many developments worth billions of dollars, these investments have been made largely without consideration of a future sea-level rise, or of other aspects of sea-level science. The developments can be expected to continue, with the 200 million people in flood-prone areas reported above growing to 800 million by the 2080s due to rising populations and coastward migration [57]. A rise in sea level can be expected to result in greater impacts on coastal populations and their expensive infrastructure during major storms, as demonstrated graphically by Hurricane Katrina in New Orleans in 2005, Hurricane Sandy in New York in 2012, and Typhoon Haiyan in the Philippines in 2013.

The sets of predictions of global sea-level rise during the twenty-first century provided by recent Intergovernmental Panel on Climate Change (IPCC) reports (Chapter 10) are considerably lower than some that were published and widely publicised some years ago [64]. Nevertheless, a rise of the order of 0.5–1.0 m can be expected to have major consequences for the many large cities located on the coast and, in particular, for populations in river deltas (Figure 13.9) and



Figure 13.9 Bangladeshi villagers rebuild an embankment at Protap Nagar in Shatkhira, about 176 km southwest of Dhaka, Bangladesh, on Sunday, 31 May 2009. Hundreds of thousands of people in eastern India and Bangladesh were flooded out of their homes by Cyclone Aila, with many crowded into government shelters. Photograph from Press Association/Pavel Rahman.



Figure 13.10 The aftermath of a large surge and wave event at the southwest Pacific coral atoll of Takuu (Marqueen Islands), Papua New Guinea in December 2008. The islands of the atoll have an elevation of about one metre. This flooding event is discussed in Reference 83. Photograph by Dr John Hunter, University of Tasmania.



Figure 13.11 Lemon sharks swimming over a grassy area next to a road after a flooding event during spring tides in March 2012 at the coral island of Diego Garcia in the Chagos Archipelago in the southwest Tropical Indian Ocean. Photograph by Professor Charles Shepard, University of Warwick.

on coral islands (Figure 13.10). Parts of low-lying islands are already occasionally under water (Figure 13.11) [21, 57].

The main impacts of a rise in sea level are qualitatively well known [57, 65, 66, 67]. The increased flood risk implies greater costs for enhanced protection of coastal homes and industry (Chapter 12). For many coastal cities already submerging for either natural or anthropogenic reasons (e.g. groundwater withdrawal), then a sea-level rise will compound existing problems.

Water tables may rise, necessitating expensive pumping strategies, while saltwater intrusion may pollute aquifers used for drinking water. Agricultural land not lost to flooding may also suffer from saltwater intrusion.

As regards the natural world, impacts include the change from fresh-water to more saline coastal ecosystems. Soft cliffs will experience enhanced erosion as deeper waters allow waves to break closer to the coast. Sandy beaches are of great importance to tourism in

many countries and are believed to be already eroding [68]. The Brunn Rule (Section 11.7) may aid in forecasting future changes in sandy beaches, or more probabilistic models of coastal recession that elaborate on Brunn may be used [69]. However, at some locations ‘coastal squeeze’ will occur, where the coastline is unable to migrate inland because of either natural or man-made obstacles (e.g. cliffs or sea-front buildings respectively). As a result, a new coastal equilibrium may not be reached [57]. A form of coastal squeeze also applies to small coral islands with high populations, such as Malé in the Maldives, where migration will not be possible. The potential impacts on coral reefs (Figure 13.4) have been mentioned above.

Studies can be found in the literature concerned with the potential impacts on coastal lowlands in general [70], while others have focused on specific locations such as the coasts of the Netherlands [71] or California [72], or coastal cities including Venice [73], London [74], Shanghai [75] and those of the United States [76, 77], and Alaska where flooding problems are exacerbated by sea ice loss [78]. There are particular implications for developing countries, many of which have cyclone-vulnerable coastal cities [79]. However, a comprehensive assessment of how important sea-level rise impacts might be has been hampered by our inability to predict sufficiently accurately the magnitude of any rise, and to attach reliable costs to them [80, 81]. The full impacts and costs of sea-level rise are still to be fully appreciated by scientists, politicians and the public; it has been argued that the scientific community suffers from a reticence in informing the public of the true scale of future risk [82].

Climate change mitigation measures, if successful, may delay many coastal impacts until later in the twenty-first century and beyond. However, some sea-level rise is bound to occur in this century because of the climate changes that are already inevitable. It will be necessary to plan for them, and for those in the longer term [35]. Adaptation measures will range from the building of barriers to protect major cities such as London (Figure 7.1), the construction of shelters in areas prone to tropical cyclones such as Bangladesh,¹² the strengthening of existing coastal defences, and the planned ‘managed retreat’ from less economically

valuable coastal lands. All of these schemes will require detailed engineering studies of the sort described in Chapter 12. They will all be expensive, but in general the costs should be less than those that would be otherwise incurred during the major storms of the future.

It is vital that all nations have access to the best possible advice on the science, impacts and adaptation to climate and sea-level change, so that they can plan effectively and act on the evidence. The three working groups of the IPCC provide an international lead on these topics, with assessments undertaken every few years.¹³ However, it is essential that complementary studies are undertaken also at regional and national level, as there are so many detailed local factors concerned in the construction of practical adaptation plans. Tides and sea-level changes have played fundamental roles in human history, and they will undoubtedly continue to do so in the future.

References

1. Dostal, J., Murphy, J. B. and Nance, R. D. 2009. *History of the Earth. Volume 2 of Earth System: History and Natural Variability, Encyclopedia of Life Support Systems*. Developed under the auspices of the United Nations Educational, Scientific and Cultural Organization. Oxford, UK: Eolss Publishers (www.eolss.net).
2. Rona, P. A., Klinkhammer, G., Nelsen, T. A., Trefry, J. H. and Elderfield, H. 1986. Black smokers, massive sulphides and vent biota at the Mid-Atlantic Ridge. *Nature*, **321**, 33–37, doi:10.1038/321033a0.
3. Oró, J., Miller, S. L. and Lazcano, A. 1990. The origin and early evolution of life on Earth. *Annual Review of Earth and Planetary Sciences*, **18**, 317–356, doi:10.1146/annurev.earth.18.050190.001533.
4. Benn, C. R. 2001. The Moon and the origin of life. *Earth, Moon and Planets*, 85–86, 61–66, doi:10.1023/A:1017082925182.
5. Hoare, P. 2013. *The Sea Inside*. London: Fourth Estate.
6. See http://en.wikipedia.org/wiki/Milankovitch_cycles.
7. Barbier, E. B., Hacker, S. D., Kennedy, C. *et al.* 2011. The value of estuarine and coastal ecosystem services. *Ecological Monographs*, **81**, 169–193, doi:10.1890/10-1510.1.

¹² Over 2500 cyclone shelters have been built in Bangladesh although many more are needed. Many do double-duty by functioning as school buildings or community centres during normal weather.

¹³ The IPCC scientific assessments are conducted by three working groups: (1) The Physical Science Basis; (2) Impacts, Adaptation and Vulnerability; and (3) Mitigation of Climate Change. See www.ipcc.ch.

8. Raffaelli, D. and Hawkins, S. 1999. *Intertidal Ecology* (2nd edition). Dordrecht: Kluwer.
9. Barnes, R. S. K. and Hughes, R. N. 1999. *An Introduction to Marine Ecology* (3rd edition). Oxford: Wiley-Blackwell.
10. Carson, R. L. 1955. *The Edge of the Sea*. New York: Houghton Mifflin and Oxford: Oxford University Press.
11. Ricketts, E. F., Calvin, J. and Hedgpeth, J. W. 1939. *Between Pacific Tides*. This classic account revised by D. W. Phillips 1992. Stanford, CA: Stanford University Press.
12. Stephenson, T. A. and Stephenson, A. 1972. *Life Between the Tide Marks on Rocky Shores*. First published 1949. San Francisco, CA: Freeman.
13. Lewis, J. R. 1964. *The Ecology of Rocky Shores*. London: English Universities Press.
14. Raffaelli, D. and Hawkins, S. 1999. *Intertidal Ecology*. Dordrecht: Kluwer Academic Publishers.
15. Pugh, D. T. 2004. Changing sea levels. *Effects of Tides, Weather and Climate*. Cambridge: Cambridge University Press.
16. Denny, M. W. and Gaines, S. D. 2007. *Encyclopaedia of Tide Pools and Rocky Shores (Encyclopaedia Of The Natural World)*. Berkeley, CA: University of California Press.
17. Little, C., Williams, G. A. and Trowbridge, C. D. 2009. *The Biology of Rocky Shores (Biology of Habitats)*. Oxford: Oxford University Press.
18. McLachlan, A. and Brown, A. C. 2010. *Ecology of Sandy Shores*. Amsterdam: Academic Press.
19. Pugh, D. T. and Rayner, R. F. 1974. The tidal regimes of three Indian Ocean atolls and some ecological implications. *Estuarine, Coastal and Shelf Science*, **13**, 389–407, doi:10.1016/S0302-3524(81)80036-9.
20. Brown, B. E., Dunne, R. P., Scoffin, T. P. and Le Tissier, M. D. A. 1994. Solar damage in intertidal corals. *Marine Ecology Progress Series*, **105**, 219–230.
21. Sale, P. F. 1991. *The Ecology of Fishes on Coral Reefs*. San Diego, CA: Academic Press.
22. Hopley, D. 2011. *Encyclopedia of Modern Coral Reefs*. Dordrecht: Springer.
23. Nybakken, J. W. and Bertness, M. D. 2004. *Marine Biology: An Ecological Approach* (6th edition). San Francisco, CA: Benjamin Cummings.
24. Frieler, K., Meinshausen, M., Golly, A. *et al.* 2012. Limiting global warming to 2°C is unlikely to save most coral reefs. *Nature Climate Change*, **3**, 165–170, doi:10.1038/nclimate1674.
25. Webb, A. P. and Kench, P. S. 2010. The dynamic response of reef islands to sea-level rise: evidence from multi-decadal analysis of island change in the Central Pacific. *Global and Planetary Change*, **72**, 234–246, doi:10.1016/j.gloplacha.2010.05.003.
26. Robertson, D. R., Petersen, C. W. and Brawn, J. D. 1990. Lunar reproductive cycles of benthic-brooding reef fishes: reflections of larval biology or adult biology? *Ecological Monographs*, **60**, 311–329.
27. Greer Walker, M., Harden Jones, F. R. and Arnold, G. P. 1978. The movements of plaice (*Pleuronectes platessa* L.) tracked in the open sea. *Journal du Conseil International pour l'Exploration de la Mer*, **38**, 58–86.
28. Metcalfe, J. D., Arnold, G. P. and Webb, P. W. 1990. The energetics of migration by selective tidal stream transport: an analysis for plaice tracked in the southern North Sea. *Journal of the Marine Biological Association of the United Kingdom*, **70**, 149–162, doi:10.1017/S0025315400034275.
29. Hunter, E., Cotton, R. J., Metcalfe, J. D. *et al.* 2009. Large scale seasonal swimming patterns of plaice in the North Sea. *Marine Ecology Progress Series*, **392**, 167–178.
30. Gibson, R. N. 2003. Go with the flow: tidal migration of marine animals. *Hydrobiologica*, **503**, 153–161.
31. Forward, R. B. Jr, and Tankersley, R. A. 2001. Selective tidal stream transport of marine animals. *Oceanography and Marine Biology: An Annual Review*, **39**, 305–353.
32. Cohen, J. H. and Forward, R. B. Jr. 2009. Zooplankton diel vertical migration: a review of proximate control. *Oceanography and Marine Biology: An Annual Review*, **47**, 77–109.
33. McDougall, I., Brown, F. H. and Fleagle, J. G. 2005. Stratigraphic placement and age of modern humans from Kibish, Ethiopia. *Nature*, **433**, 733–736, doi:10.1038/nature03258.
34. (1) Lambeck, K. 1996. Shoreline reconstructions for the Persian Gulf since the last glacial maximum. *Earth and Planetary Science Letters*, **142**, 43–57, doi:10.1016/0012-821X(96)00069-6. (2) Lambeck, K., Purcell, A., Flemming, N. C. *et al.* 2011. Sea level and shoreline reconstructions for the Red Sea: isostatic and tectonic considerations and implications for hominid migration out of Africa. *Quaternary Science Reviews*, **30**, 3542–3574, doi:10.1016/j.quascirev.2011.08.008.
35. Church, J. A., Aarup, T., Woodworth, P. L. *et al.* 2010. Sea-level rise and variability: synthesis and outlook for the future. In *Understanding Sea-Level Rise and Variability* (eds. J. A. Church, P. L. Woodworth, T. Aarup and W. S. Wilson), pp. 402–419. London: Wiley-Blackwell.
36. Flemming, N. C., Bailey, G. N., Courtillot, V. *et al.* 2003. Coastal and marine palaeo-environments and human

- dispersal points across the Africa-Eurasia boundary. In *Maritime Heritage* (eds. C. A. Brebbia and T. Gambin), pp. 61–74. Southampton: Wessex Institute of Technology and Malta: University of Malta.
37. (1) Harding, A., Cadogan, G. and Howell, R. 1969. Pavlopetri, an underwater Bronze Age town in Laconia. *Annual of the British School at Athens*, **64**, 113–142. (2) Smith, K. 2009. Mapping the world's oldest submerged town. *Nature News*, doi:10.1038/news.2009.484. (3) <http://en.wikipedia.org/wiki/Pavlopetri>.
 38. Hancock, G. 2003. *Underworld, Flooded Kingdoms of the Ice Age*. London: Penguin Books.
 39. Bannermann, N. and Jones, C. 1999. Fish-trap types: a component of the maritime cultural landscape. *The Journal of Nautical Archaeology*, **28**, 70–84, doi:10.1111/j.1095-9270.1999.tb00823.x.
 40. Simpson, J. H. and Hunter, J. R. 1974. Fronts in the Irish Sea. *Nature*, **250**, 404–406, doi:10.1038/250404a0.
 41. Scott, B. E., Sharples, J., Ross, O. N. *et al.* 2010. Sub-surface hotspots in shallow seas: fine-scale limited locations of top predator foraging habitat indicated by tidal mixing and sub-surface chlorophyll. *Marine Ecology Progress Series*, **408**, 207–226, doi:10.3354/meps08552.
 42. Ellis, D. W. and Swan, L. 1981. *Teachings of the Tides*. Nanaimo, British Columbia: Theytus Books.
 43. Fagan, B. 2013. *The Attacking Ocean: The Past, Present, and Future of Rising Sea Levels*. London: Bloomsbury Publishing.
 44. Ryan, W. and Pitman, W. 1998. *Noah's Flood: The New Scientific Discoveries About the Event that Changed History*. New York: Simon and Schuster.
 45. Kraft, J. C., Rapp, G., Kayan, I. and Luce, J. V. 2003. Harbor areas at ancient Troy: sedimentology and geomorphology complement Homer's Iliad. *Geology*, **31**, 163–166, doi:10.1130/0091-7613(2003)031<0163:HAAATS>2.0.CO;2.
 46. Kraft, J. C., Rapp, G., Szemler, G. J., Tziavos, C. and Kase, E. W. 1987. The pass at Thermopylae, Greece. *Journal of Field Archaeology*, **14**, 181–198, doi:10.1179/009346987792208448.
 47. See http://en.wikipedia.org/wiki/Caesar%27s_invasions_of_Britain
 48. Cartwright, D. and Conway, C. A. 1991. Maldon and the tides. *The Cambridge Review*, **112**, 180–183.
 49. Waters, R. 2006. *The Lost Treasure of King John: The Fenland's Greatest Mystery*. Lincoln: Tucann Design and Print.
 50. See <http://en.wikipedia.org/wiki/Canute>
 51. Parker, B. 2011. The tide predictions for D-Day. *Physics Today*, **64**(9), 35–40, doi:10.1063/PT.3.1257.
 52. Zetler, B. D. 1991. Military tide predictions in World War II. In *Tidal Hydrodynamics* (ed. B. B. Parker), pp. 791–797. New York: John Wiley and Sons.
 53. Cartwright, D. E. 1999. *Tides: A Scientific History*. Cambridge: Cambridge University Press.
 54. Radford, E. and Radford, M. A. 1949. *Encyclopaedia of Superstitions*. Kessinger Publishing, reprinted in 2010 by The Philosophical Library, New York.
 55. Price, J. and Karim, I. 1978. Matiruku, a Fijian madness: an initial assessment. *British Journal of Psychiatry*, **133**, 228–30.
 56. Drews, C. and Han, W. 2010. Dynamics of wind setbackdown at Suez and the eastern Nile Delta. *PLoS ONE*, **5**(8), e12481, doi:10.1371/journal.pone.0012481.
 57. Nicholls, R. J. 2010. Impacts of and responses to sea-level rise. In *Understanding Sea-Level Rise and Variability* (eds. J. A. Church, P. L. Woodworth, T. Aarup and S. Wilson), pp. 17–51. London: Wiley-Blackwell.
 58. Wilson, W. S., Abdalati, W., Alsdorf, D. *et al.* 2010. Observing systems needed to address sea-level rise and variability. *Understanding Sea-Level Rise and Variability* (eds. J. A. Church, P. L. Woodworth, T. Aarup and W. S. Wilson), pp. 376–401. London: Wiley-Blackwell.
 59. Church, J. A., Woodworth, P. L., Aarup, T. and Wilson, W. S. 2010. *Understanding Sea-Level Rise and Variability*. London: Wiley-Blackwell.
 60. For example, Slangen, A. B. A., Katsman, C. A., van de Wal, R. S. W., Vermeersen, L. L. A. and Riva, R. E. M. 2012. Towards regional projections of twenty-first century sea-level change based on IPCC SRES scenarios. *Climate Dynamics*, **38**, 1191–1209, doi:10.1007/s00382-011-1057-6.
 61. Stammer, D. and Gregory, J. 2011. Understanding processes contributing to regional sea level change. *Eos, Transactions American Geophysical Union*, **92**(39), 328, doi:10.1029/2011EO390004.
 62. IPCC, 2012. Summary for Policymakers. In *Managing the Risks of Extreme Events and Disasters to Advance Climate Change Adaptation* (eds. C. B. Field, V. Barros, T. F. Stocker *et al.*). A Special Report of Working Groups I and II of the Intergovernmental Panel on Climate Change. Cambridge: Cambridge University Press.
 63. Hunter, J. 2012. A simple technique for estimating an allowance for uncertain sea-level rise. *Climatic Change*, **113**, 239–252, doi:10.1007/s10584-011-0332-1.
 64. Barth, M. C. and Titus, J. G. 1984. *Greenhouse Effect and Sea Level Rise: A Challenge for this Generation*. New York: Van Nostrand Reinhold. Available from http://papers.risingsea.net/Challenge_for_this_Generation.html.

65. Chen, C.-C., McCarl, B. and Chang, C.-C. 2011. Climate change, sea level rise and rice: global market implications. *Climatic Change*, **110**(3), 543–560, doi:10.1007/s10584-011-0074-0.
66. The range of impacts of future climate change, including sea level change, is reviewed regularly in detail by the IPCC Working Group II (www.ipcc.ch).
67. Khan, A. E., Ireson, A., Kovats, S. *et al.* 2011. Drinking water salinity and maternal health in coastal Bangladesh: implications of climate change. *Environmental Health Perspectives*, **119**, 1328–1332, doi:10.1289/ehp.1002804.
68. (1) Bird, E. C. F. 1993. *Submerging Coasts: The Effects of a Rising Sea Level on Coastal Environments*. Chichester: Wiley. (2) Nicholls, R. J., Wong, P. P., Burkett, V. R. *et al.* 2007. Coastal systems and low-lying areas. In *Climate Change 2007: Impacts, Adaptation and Vulnerability. Contribution of Working Group II to the Fourth Assessment Report of the Intergovernmental Panel on Climate Change* (eds. M. L. Parry, O. F. Canziani, J. P. Palutikof *et al.*). Cambridge: Cambridge University Press.
69. Ranasinghe, R., Callaghan, D., and Stive, M. J. F. 2012. Estimating coastal recession due to sea level rise: beyond the Brunn rule. *Climatic Change*, **110**, 561–574, doi:10.1007/s10584-011-0107-8.
70. McGranahan, G., Balk, D. and Anderson, B. 2007. The rising tide: assessing the risks of climate change and human settlements in low elevation coastal zones. *Environment and Urbanization*, **19**, 17–37, doi:10.1177/0956247807076960.
71. Katsman, C. A., Sterl, A., Beersma, J. J. *et al.* 2011. Exploring high-end scenarios for local sea level rise to develop flood protection strategies for a low-lying delta: the Netherlands as an example. *Climatic Change*, **109**, 617–645, doi:10.1007/s10584-011-0037-5.
72. Heberger, M., Cooley, H., Herrera, P., Gleick, P. H. and Moore, E. 2011. Potential impacts of increased coastal flooding in California due to sea-level rise. *Climatic Change*, **109** (Supplement 1), S229–S249, doi:10.1007/s10584-011-0308-1.
73. Plag, H.-P., Tsimplis, M. N., Hammond, W. and Pugh, D. 2006. *Appraisal of the Relative Sea Level Rise Scenario for Venice*. Final Project Report, Nevada Bureau of Mines and Geology, University of Nevada, Reno, Report NBMG-RP-VEN3.
74. Lavery, S. and Donovan, B. 2005. Flood risk management in the Thames Estuary looking ahead 100 years. *Philosophical Transactions of the Royal Society A*, **363**, 1455–1474, doi:10.1098/rsta.2005.1579.
75. Wang, J., Gao, W., Xu, S. and Yu, L. 2012. Evaluation of the combined risk of sea level rise, land subsidence, and storm surges on the coastal areas of Shanghai, China. *Climatic Change*, **115**, 537–558, doi:10.1007/s10584-012-0468-7.
76. Weiss, J. L., Overpeck, J. T. and Strauss, B. 2011. Implications of recent sea level rise science for low-elevation areas in coastal cities of the conterminous U.S.A. *Climatic Change*, **105**, 635–645, doi:10.1007/s10584-011-0024-x.
77. Strauss, B. H., Ziemiński, R., Weiss, J. L. and Overpeck, J. T. 2012. Tidally-adjusted estimates of topographic vulnerability to sea level rise and flooding for the contiguous United States. *Environmental Research Letters*, **7**, 014033, doi:10.1088/1748-9326/7/1/014033.
78. Lynch, A. H. and Brunner, R. D. 2007. Context and climate change: an integrated assessment for Barrow, Alaska. *Climatic Change*, **82**, 93–111, doi:10.1007/s10584-006-9165-8.
79. Brecht, H., Dasgupta, S., Laplante, B., Murray, S. and Wheeler, D. 2013. Sea-level rise and storm surges: high stakes for a small number of developing countries. *The Journal of Environment and Development*, **21**, 120–138, doi:10.1177/1070496511433601.
80. See the review by Sir Nicholas Stern of the Economics of Climate Change. 2006. http://webarchive.nationalarchives.gov.uk/+http://www.hm-treasury.gov.uk/stern_review_climate_change.htm
81. Blankespoor, B., Susmita, D. and Laplante, B. 2012. *Sea-Level Rise and Coastal Wetlands: Impacts and Costs*. World Bank Policy Research working paper No. WPS 6277. Available from <http://www-wds.worldbank.org>.
82. Hansen, J. E. 2007. Scientific reticence and sea level rise. *Environmental Research Letters*, **2**, 024002, doi:10.1088/1748-9326/2/2/024002.
83. Hoeke, R. K., McInnes, K. L., Kruger, J. *et al.* 2013. Widespread inundation of Pacific islands by distant-source wind-waves. *Global and Planetary Change* (in press).

Appendix A Basic hydrostatic and hydrodynamic equations

This appendix contains the basis equations used in some of the developments in the main chapters. These equations were developed from first principles in the First Edition [1], and similar developments are readily available in standard oceanographic textbooks [2, 3]. For brevity, they are restated here to define the nomenclature and sign conventions.

A.1 The hydrostatic equation

In our coordinate system (see Figure A.1) the hydrostatic pressure P_z at a point, depth z below the water surface, due to the combination of the atmospheric pressure P_A acting on the water surface and the weight of water above the point is:

$$P_z = P_A - \rho g(z - \zeta) \quad (\text{A.1})$$

where ρ is the water density, assumed constant, and ζ is the displacement of the water level from the mean. The negative sign appears because z increases upwards; as z is negative below the mean water surface the formula correctly represents the increase of pressure with depth. This hydrostatic formula has already been used in a simple form in Equation 2.1 to convert bottom pressures, measured using the equipment described in Section 2.3.3, into changes in sea level.

A.2 Conservation of mass

We make the assumption that the density of the water is constant, which means that the mass and the volume of the water are equivalent parameters. In the usual case where the water depth D is large compared with the displacement of the level from the mean, the conservation of mass is expressed by:

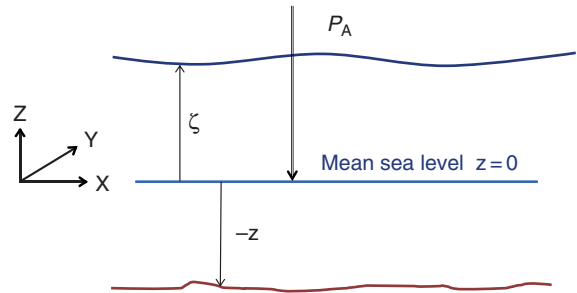


Figure A.1 The basic system of coordinates used for the hydrodynamic equations.

$$\frac{\partial \zeta}{\partial t} + \frac{\partial}{\partial x}(Du) + \frac{\partial}{\partial y}(Dv) = 0 \quad (\text{A.2})$$

where u and v are the horizontal depth-averaged currents in the X and Y directions.

Where the seabed is flat so that the water depth is also constant, the final simplification gives:

$$\frac{\partial \zeta}{\partial t} + D \left(\frac{\partial u}{\partial x} + \frac{\partial v}{\partial y} \right) = 0 \quad (\text{A.3})$$

These mass conservation equations are also called continuity equations. They formally represent the basic fact that a net flux of water into or out of an area must be balanced by a corresponding change in the water level.

A.3 The horizontal momentum equations

By combining the total accelerations and the forces acting on the particle (see Figure A.2), we arrive at the two basic horizontal momentum equations:

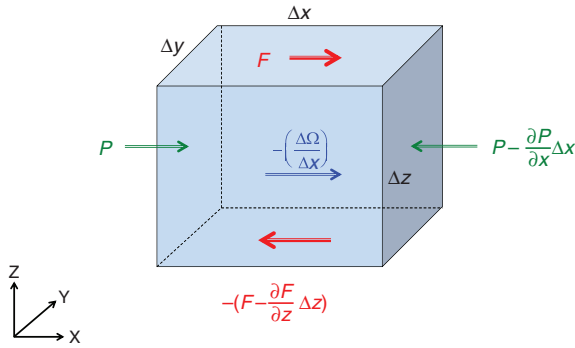


Figure A.2 The forces action on a finite element of water.

$$\begin{aligned} \frac{\partial u}{\partial t} + u \frac{\partial u}{\partial x} + v \frac{\partial u}{\partial y} - f v &= -\frac{\partial \Omega}{\partial x} - \frac{1}{\rho} \left(\frac{\partial P}{\partial x} - \frac{\partial F}{\partial z} \right) \\ \frac{\partial v}{\partial t} + u \frac{\partial v}{\partial x} + v \frac{\partial v}{\partial y} + f u &= -\frac{\partial \Omega}{\partial y} - \frac{1}{\rho} \left(\frac{\partial P}{\partial y} - \frac{\partial G}{\partial z} \right) \end{aligned} \quad (\text{A.4 and A.5})$$

time + advective + Coriolis = tidal + pressure + shear
acceleration = force/mass

We consider the forces acting on a Cartesian element of water with dimensions Δx Δy Δz . The element is located at a fixed place on the surface of the rotating Earth. By restricting our interest to horizontal forces and accelerations, we need only consider the balance in the X and in the Y directions. Each yields a separate equation. A rigorous mathematical development of these is beyond the scope of this account.

The forces and accelerations along the X axis are shown in **Figure A.2**. Three separate forces can be distinguished, the direct tidal forces $-(\Delta\Omega/\Delta x)$ (see **Section 3.2.2**), the pressure forces P , and the shear forces F acting on the upper and lower surfaces. Combining these three forces we have the total force.

Our fixed Eulerian frame requires additional terms $\left(v \frac{\partial u}{\partial y} \text{ and } u \frac{\partial v}{\partial x} \right)$ to allow for the acceleration necessary to give the water, within our fixed element at an instant of time, the appropriate velocity for a subsequent time and position to which it has been advected.

Also, because Newton's second law applies for motions in an absolute un-accelerating coordinate system, when the law is applied to motion in a rotating Earth-bound coordinate system an additional acceleration term $-fv$, the Coriolis term, is required.

Any particle initially projected in a particular direction in the northern hemisphere moves along a path over the Earth's surface that curves to the right. In the southern hemisphere the curvature of the path is to the left. For tidal currents, which persist for times that are significant fractions of a day, the curvature cannot be neglected. The effect is represented in the force equations as an acceleration at right angles to the motion. This acceleration is proportional to the particle speed, and increases from zero at the equator to a maximum at the poles. This would be apparent to an observer in the northern hemisphere as a eastward acceleration. Note that because there is no acceleration along the direction of motion of the particle, there is no net gain of particle energy.

These two equations, (A.4) and (A.5), together with the continuity equation (A.1) and the hydrostatic equation (A.2) are used in the main chapters to describe the physical response of the oceans to the tidal and meteorological forces.

References

1. <http://eprints.soton.ac.uk/19157/1/sea-level.pdf>.
2. Lamb, H. 1932. *Hydrodynamics* (6th edition). Cambridge: Cambridge University Press.
3. Gill, A. E. 1982. *Atmosphere-Ocean Dynamics*. New York: Academic Press.

Appendix B Currents

Although this book is about sea levels, it is fitting that we include here some information on analyses of currents, especially tidal currents, and on the generation of currents, where these are related to sea-level changes.

B.1 Analyses of currents

B.1.1 Current ellipse parameters from component amplitudes and phases

Consider a harmonic constituent whose east-going and north-going components are given by:

$$\begin{aligned} U \cos(\omega t - g_u) \\ V \cos(\omega t - g_v) \end{aligned}$$

(Speeds and phase angles are in radians.)

Then in the usual Cartesian convention (see [Figure B.1](#)) the direction of flow and the current speed are:

$$\theta = \arctan \frac{V \cos(\omega t - g_v)}{U \cos(\omega t - g_u)} \quad (\text{B.1})$$

$$q = [U^2 \cos^2(\omega t - g_u) + V^2 \cos^2(\omega t - g_v)]^{\frac{1}{2}} \quad (\text{B.2})$$

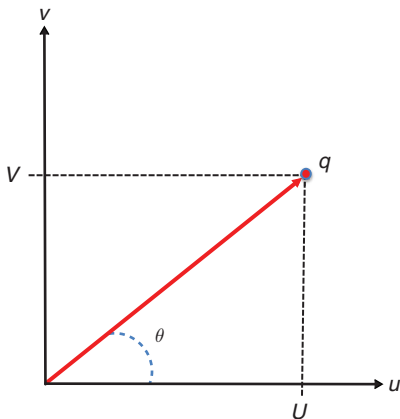


Figure B.1 Resolving currents into Cartesian components.

Semi-major and semi-minor axes of ellipse

From (B.2), using the identity:

$$2 \cos^2 \beta = (1 + \cos 2\beta)$$

the speed becomes:

$$\begin{aligned} q^2 = U^2 \left[\frac{1}{2} + \frac{1}{2} \cos 2(\omega t - g_u) \right] \\ + V^2 \left[\frac{1}{2} + \frac{1}{2} \cos 2(\omega t - g_u) + (g_u - g_v) \right] \end{aligned}$$

or

$$\begin{aligned} q^2 = \frac{1}{2} [U^2 + V^2] \\ + \frac{1}{2} [(U^2 + V^2 \cos 2(g_u - g_v))] \cos 2(\omega t - g_u) \\ - \frac{1}{2} [V^2 \sin 2(g_u - g_v)] \sin 2(\omega t - g_u) \end{aligned}$$

This may be written in the form:

$$q^2 = \frac{1}{2} [U^2 + V^2] + \frac{1}{2} \alpha^2 \cos 2(\omega t - g_u + \delta) \quad (\text{B.3a})$$

or

$$q^2 = \frac{1}{2} [U^2 + V^2 - \alpha^2] + \alpha^2 \cos^2(\omega t - g_u + \delta) \quad (\text{B.3b})$$

where:

$$2\delta = \arctan \frac{V^2 \sin 2(g_u - g_v)}{(U^2 + V^2 \cos 2(g_u - g_v))} \quad (\text{B.4a})$$

$$\begin{aligned} \alpha^2 = & \left[(U^2 + V^2 \cos 2(g_u - g_v))^2 \right. \\ & \left. + (V^2 \sin 2(g_u - g_v))^2 \right]^{\frac{1}{2}} \quad (\text{B.4b}) \\ = & [U^4 + V^4 + 2U^2V^2 \cos 2(g_u - g_v)]^{\frac{1}{2}} \end{aligned}$$

The maximum value of current speed is determined from [Equation B.3b](#) as:

$$q_{\max} = \left[\frac{U^2 + V^2 + \alpha^2}{2} \right]^{\frac{1}{2}} \text{ semi-major axis} \quad (\text{B.5a})$$

and the minimum value as:

$$q_{\min} = \left[\frac{U^2 + V^2 + \alpha^2}{2} \right]^{\frac{1}{2}} \text{ semi-minor axis} \quad (\text{B.5b})$$

The **eccentricity** e of the ellipse is defined as:

$$e^2 = \frac{q_{\max}^2 - q_{\min}^2}{q_{\max}^2}$$

For rectilinear currents the eccentricity is unity; for a circular current ellipse, the eccentricity is zero.

There is zero eccentricity, a constant current speed, so that the vector tip follows a circle ($\alpha = 0$) if:

$$(g_u - g_v) = \frac{\pi}{2}, -\frac{\pi}{2} \quad \text{and} \quad U = V$$

To show this substitute into [Equation B.4b](#):

$$\alpha^2 = [U^4 + V^4 + 2U^2V^2 \cos(\frac{\pi}{\pi})]^{\frac{1}{2}} = [U^2 - V^2] = 0$$

In this case:

$$q_{\max} = q_{\min} = \left[\frac{U^2 + V^2}{2} \right]^{\frac{1}{2}} = U$$

Time of maximum current speeds

The times are calculated from [Equation B.3b](#). The maximum values of q are obtained when:

$$\omega t - (g_u - \delta) = 0, 2\pi, \dots, 2m\pi$$

or

$$\omega t - (g_u - \delta) = \pi, 3\pi, \dots, (2m + 1)\pi \quad (\text{B.6})$$

More generally if the Equilibrium phase at a specified zero hour is $(V_0 + u)$:

$$(V_0 + u) + \omega t = m\pi + (g_u - \delta)$$

and hence the times of maximum currents are:

$$t_{\max} = \frac{1}{\omega} [m\pi - (V_0 + u) + (g_u - \delta)] \quad (\text{B.7})$$

There will be two occasions during each cycle when the value of t_{\max} is reached; these are in the positive and in the negative directions along the direction of the major axis of the current ellipse.

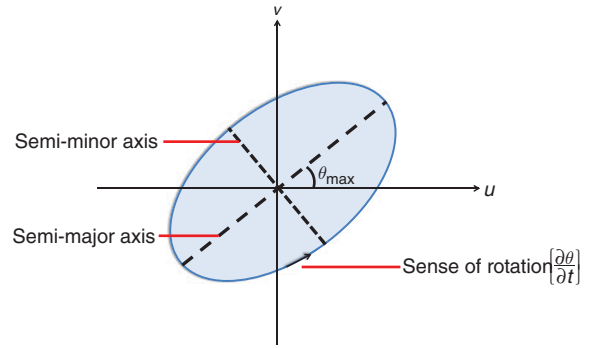


Figure B.2 Definitions of a current ellipse.

Direction of maximum current speed

See [Figure B.2](#). Substituting from [Equation B.6](#) into [Equation B.1](#) we have for the direction of the semi-major axis:

$$\theta_{\max} = \arctan \frac{V \cos((g_u - g_v) - \delta)}{U \cos \delta} \quad (\text{B.8})$$

Sense of the ellipse vector rotation

Rewriting [Equation B.1](#) as:

$$\theta = \arctan \kappa$$

and differentiating with respect to time:

$$\begin{aligned} \frac{\partial \theta}{\partial t} &= \frac{\partial \theta}{\partial \kappa} \frac{\partial \kappa}{\partial t} = \frac{1}{1 + \kappa^2} \frac{\omega UV}{U^2 \cos^2(\omega t - g_u)} \sin(g_v - g_u) \\ &= \frac{\omega UV}{q^2} \sin(g_v - g_u) \end{aligned} \quad (\text{B.9})$$

All terms in this expression are always positive except for the factor $\sin(g_v - g_u)$. Hence:

$$\begin{aligned} 0 < (g_v - g_u) < \pi, & \quad \frac{\partial \theta}{\partial t} \text{ positive; anticlockwise} \\ & \quad \text{vector rotation} \\ \pi < (g_v - g_u) < 2\pi, & \quad \frac{\partial \theta}{\partial t} \text{ negative; clockwise} \\ & \quad \text{vector rotation} \\ (g_v - g_u) = 0, \pi & \quad \frac{\partial \theta}{\partial t} \text{ zero; rectilinear flow} \end{aligned}$$

B.1.2 Rotary current components

The ellipse characteristics of a tidal current constituent can be calculated more readily from a slightly different

parameterisation in terms of two polar vectors, each of constant amplitude, which rotate at the angular speed of the constituent, but in opposite directions. When these vectors are aligned the currents have their maximum speed. A quarter of a revolution later they oppose each other and the current speeds have their minimum value. After a further quarter of a cycle they are again aligned, this time in the opposite direction along the major axis, and the maximum current speeds are again obtained.

If the amplitudes and phases of the clockwise and anticlockwise rotating vectors are (Q_C, g_C) and (Q_{AC}, g_{AC}) their values may be calculated from the (U, g_U) and (V, g_V) component parameters:

$$\begin{aligned} Q_C &= \frac{1}{2}[U^2 + V^2 - 2UV \sin(g_V - g_U)]^{\frac{1}{2}} \\ Q_{AC} &= \frac{1}{2}[U^2 + V^2 + 2UV \sin(g_V - g_U)]^{\frac{1}{2}} \\ g_C &= \arctan \left[\frac{U \sin g_U + V \cos g_V}{U \cos g_U - V \sin g_V} \right] \\ g_{AC} &= \arctan \left[\frac{-U \sin g_U + V \cos g_V}{U \cos g_U + V \sin g_V} \right] \end{aligned} \quad (\text{B.10})$$

These parameters may be obtained directly from the observed currents by an analysis process of complex demodulation:

$$\begin{aligned} &Q_C \exp(jg_C) \exp(-j\omega t) \\ &Q_{AC} \exp(jg_{AC}) \exp(j\omega t) \quad \text{where } j = \sqrt{-1} \end{aligned}$$

In terms of these rotation vector parameters:

$$\begin{aligned} \text{semi-major axis} &= Q_C + Q_{AC} \\ \text{semi-minor axis} &= |Q_C - Q_{AC}| \\ \text{phase of semi-major axis} &= -\frac{1}{2}(g_{AC} - g_C) \\ \text{direction of the semi-major axis} &= \frac{1}{2}(g_{AC} + g_C) \\ &(\text{positive anticlockwise from east}) \\ &= \frac{\pi}{2} - \frac{1}{2}(g_{AC} + g_C) \\ &(\text{clockwise from north}) \end{aligned}$$

The total current vector rotates

anticlockwise if $Q_{AC} > Q_C$

clockwise if $Q_C > Q_{AC}$

From Equation B.10, $Q_{AC} > Q_C$ if $\sin(g_V - g_U) > 0$, i.e. $0 < (g_V - g_U) < \pi$, as above.

B.2 Current dynamics

B.2.1 Ekman transport

The Norwegian scientist and explorer Fridtjof Nansen observed during the 1893–6 polar-ice drift of the *Fram*

that the ice moved in a direction to the right of the wind and not in the direction of the wind itself. Ekman explained this in 1902 in terms of the hydrodynamic equations. Suppose that the wind is blowing over water well away from the coast, which is deep enough for the influence of bottom friction to be negligible. Also suppose that the water density is constant with depth and that the wind/water system has reached its steady-state condition. Finally, suppose that there are no horizontal pressure gradients due, for example, to sea surface gradients. In this limiting case, Equations A.4 and A.5, applied for a wind and wind stress acting along the positive X direction, reduce to:

$$-fv = -\frac{1}{\rho} \frac{\partial F}{\partial z} \quad fu = -\frac{1}{\rho} \frac{\partial G}{\partial z} \quad (\text{B.11})$$

If we integrate these equations through from the bottom of the wind-driven layer to the surface, recognising that the stress at the bottom of this layer will be zero:

$$-f\bar{V} = F_S/\rho \quad f\bar{U} = 0 \quad (\text{B.12})$$

where F_S is the surface wind stress and \bar{U} and \bar{V} are the volume transports per unit length along the X and Y axes, with units of m^2s^{-1} . These equations have the solution:

$$\bar{U} = 0 \quad \bar{V} = -F_S/f\rho \quad (\text{B.13})$$

The net transport is along the negative Y direction, i.e. to the right of the wind stress in the northern hemisphere (where f is positive), and to the left in the southern hemisphere. This is called the Ekman volume transport per metre of section, and is a function of the wind stress and the latitude. Near the equator the corresponding transports are greater as f decreases, but the theory breaks down at the equator itself where infinite volume transports are predicted.

The depth-averaged transport calculated from Equation B.13 tells us nothing about the details of the variation of current directions with depth. More detailed mathematical solutions indicate a surface flow at 45° to the direction of the wind stress; this surface flow in turn drives the lower layers in a direction that is further rotated, and at slower speeds. This progressive rotation and reduction of speed with depth is called the *Ekman spiral*, the net effect of which, over the whole depth, is a transport of water at right angles to the wind stress.

Although Ekman's theory has allowed powerful insight into the relationships between global wind

fields and ocean circulation, the simplifying assumptions are so limiting that the full ideal Ekman spiral is unlikely to be observed in practice. The time needed to establish a dynamic equilibrium may be several days, whereas the wind is likely to change over several hours. Vertical and horizontal density gradients will give further distortions. For continental shelf seas, the important assumptions about no coastal interference or bottom friction influence are seldom valid.

Consider here the depths to which a wind-driven Ekman layer might penetrate. This is defined as the depth D_E at which the progressive rotation results in flow in the opposite direction to the surface wind stress:

$$D_E = \pi \left(\frac{2A_z}{\rho f} \right)^{\frac{1}{2}} \quad (\text{B.14})$$

where f is the Coriolis parameter, ρ is the water density, and A_z is a quantity called the vertical eddy coefficient of viscosity, which represents the efficiency with which the water exchanges momentum vertically through turbulence, from layer to layer: the 'stickiness'. It has units of $\text{kg m}^{-1} \text{s}^{-1}$. A_z/ρ is called the kinematic eddy viscosity.

A_z varies rapidly with depth near the surface and bottom boundary layers and near vertical density gradients.

In our theoretical discussion of Ekman dynamics, Equation B.14 is applied for a value of A_z that is constant at all depths. For average winds and tidal conditions (tidal currents enhance the turbulence which transfers the momentum) a typical value of A_z might be $40 \text{ kg m}^{-1} \text{s}^{-1}$, whereas for stronger winds of 20 m/s or more the value might be as high as $400 \text{ kg m}^{-1} \text{s}^{-1}$. At a latitude of 45° the corresponding values of D_E from Equation B.14 are 87 m and 270 m; thus, for strong winds the depth of the Ekman layer is comparable to the depth of the continental shelves.

If the water is too shallow for the full Ekman spiral to develop, the net transport due to the wind will be at an angle of less than 90° to the wind direction. Another significant factor in shallow water is the turbulence due to bottom friction, which will increase A_z , and hence reduce the angle between the wind and the net transport.

B.2.2 Alongshore winds

When a component of the wind stress acts parallel to a coastline the onset of Ekman transport is followed by the development of water-level differences that have their own influence on the water movements, so distorting the simple Ekman transport dynamics.

Suppose that a semi-infinite sea of depth D exists for all values of y greater than zero (Figure B.3), and

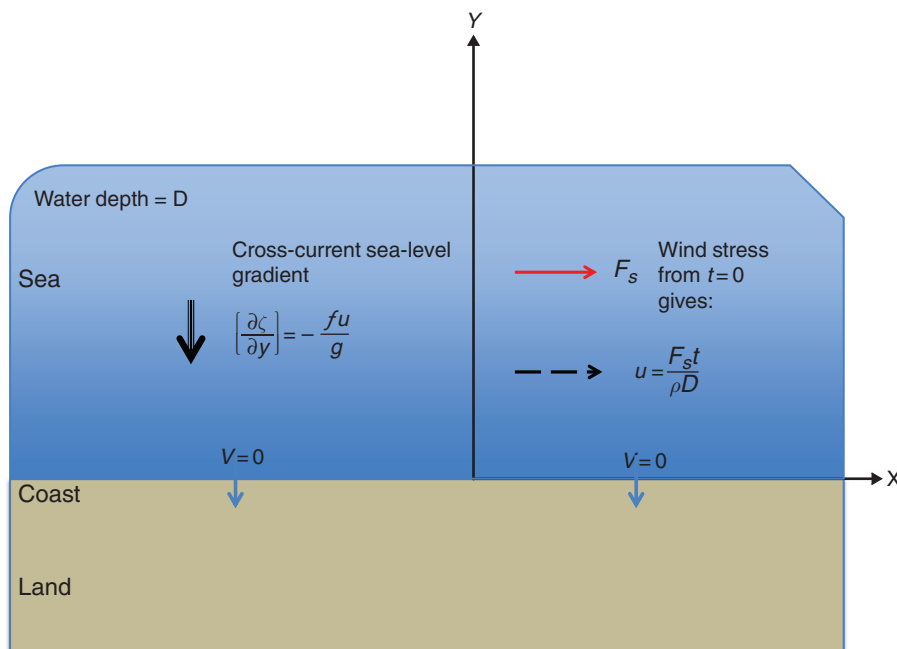


Figure B.3 Coordinates used to develop formulae for the response of a coastal sea to an along-shore wind stress.

that a uniform wind stress F_z is applied to the surface of this sea from time $t = 0$. In the absence of any changes with x , and in the vicinity of the coast where the condition of no cross-boundary flow ($v = 0$) applies, Equations A.4 and A.5 become:

$$\frac{\partial u}{\partial t} = \left(\frac{1}{\rho}\right) \left(\frac{\partial F}{\partial z}\right) \quad \frac{f}{u} = -\left(\frac{1}{\rho}\right) \left(\frac{\partial P}{\partial y}\right) \quad (\text{B.15})$$

Integrating these from $-D$ to the surface, assuming u is constant with depth, and substituting from Equation A.1 for $\left(\frac{\partial P}{\partial y}\right)$:

$$D \left(\frac{\partial u}{\partial t}\right) = \frac{F_z}{\rho} \quad fu = -g \left(\frac{\partial \zeta}{\partial y}\right)$$

which leads directly to:

$$u = \frac{F_z t}{\rho D} \quad (\text{B.16})$$

$$\left(\frac{\partial \zeta}{\partial y}\right) = -\frac{fu}{g} \quad (\text{B.17})$$

The first of these relationships shows the current parallel to the shore increasing steadily with time at a rate inversely proportional to the depth of water to be moved, as would also be the case in the absence of the Earth's rotation; in practice this current will eventually be limited by bottom friction. The second equation shows a sea-level gradient normal to the coast that is in geostrophic equilibrium with the current u , at all times; corresponding to this equilibrium is a linear increase of coastal sea levels with time. Both current flows and sea-level changes are greatest when the water is shallow.

The net result of the applied wind stress is a flow of water in the direction of the wind, but we can now appreciate that this apparently simple intuitive direct relationship is really more complicated: it results from the condition of no Ekman transport across the coastline. The conservation of mass requires a steady increase of coastal levels in response to Ekman transport and this increase develops in geostrophic equilibrium with the long-shore current.

This local sea-level change, due to a dynamic balance of pressure gradients and wind stress, is called the *locally generated surge*, to distinguish it from surges propagating freely as progressive waves that have travelled from external areas of generation.

B.2.3 Inertial currents

The full solution for water movements in response to an imposed wind stress shows that the current u and

the sea surface gradient decrease exponentially away from the coast:

$$u = \frac{F_z t}{\rho D} \exp(-y/R) \quad (\text{B.18})$$

where R is the Rossby radius, defined as:

$$R = \sqrt{g/D}/f \quad (\text{B.19})$$

At 45° latitude in water of 50 m depth, this scale length is 215 km.

Well away from the coast the full solution contains an important oscillatory part, which has a period not far removed from that of the tides. To illustrate this type of motion, suppose that previous driving forces have now stopped and that the water remains in motion after this. Because of the absence of a coast there are no pressure gradients. The Equations A.4 and A.5, and A.2, become:

$$\begin{aligned} \frac{\partial u}{\partial t} - fv &= 0 \\ \frac{\partial v}{\partial t} + fu &= 0 \\ D \left(\frac{\partial u}{\partial x} + \frac{\partial v}{\partial y}\right) &= 0 \end{aligned}$$

and these have the solution:

$$\begin{aligned} u &= q \cos ft \\ v &= -q \sin ft \end{aligned} \quad (\text{B.20})$$

where the coordinate axes are chosen to give the maximum current q along the X axis at $t = 0$. The water masses perform circular motions with a period $2\pi/f$. This is 17 hours at 45° latitude, and 14.6 hours at 55° latitude. Near 30° and 70° latitude, the inertial motions fall within the diurnal and semidiurnal tidal species. The radius of the circular motions, which depends on the water speed, is q/f . For a speed of 0.2 m s^{-1} , typical of inertial motions on a continental shelf, the radius at 55° N is 1.7 km. Inertial currents are most effectively produced by an impulse of winds blowing for not more than half of an inertial period, acting on a relatively thin surface layer above a sharp thermocline, so that the masses of water to be accelerated and the dissipating forces are small. In these circumstances inertial oscillations may persist for several days after their generation and may be advected to other regions.

Gradually, as they decay, the speeds and radius of the motions in the inertial currents diminish. The method of rotary analysis of currents described in Section B.1.2 is particularly effective for identifying inertial currents. See also Section 5.6 on internal tides and critical latitudes.

Appendix C High and low water times and heights from harmonic constituents

Here we derive simple expressions for high and low water times and heights based on constituents from harmonic analyses. These are useful for understanding the tidal characteristics at a site, without needing to reconstitute the time series of observations. There are also legal applications, as discussed in [Appendix E](#). Here it is assumed that the tides are dominated by a single constituent, M_2 , and the formulae are confined to turning points in the combined sea levels [1, 2, 3].

Consider a combination of M_2 and one other constituent:

$$T(t) = H_{M_2} \cos \omega t + A \cos nt + B \sin nt$$

where the time origin $t = 0$ is at the time of maximum M_2 , and the added constituent is:

$$R \cos (nt - \theta) \text{ with an amplitude} \\ R = \sqrt{A^2 + B^2} \text{ and } \tan \theta = B/A$$

A and B represent the in-phase and quadrature parts of the added constituent for this one particular tidal cycle for which maximum M_2 happens to be at $t = 0$.

For any maximum value:

$$\frac{\partial T(t)}{\partial t} = -H_{M_2} \sin \omega t - A \sin nt + B \cos nt = 0$$

When M_2 dominates, then the time of overall high water will have a very small value of t , and if $(R/H_{M_2}) \ll 1$, so that $\cos \omega t \approx \cos nt \approx 1$ and $\sin \omega t \approx \omega t$ and $\sin nt \approx nt$, then:

$$t_{\max} = \frac{Bn}{\omega^2 H_{M_2}}$$

Approximating $\cos \omega t \approx 1 - \frac{1}{2}(\omega t)^2$, the combined high water level at this time is:

$$H_{\max} = H_{M_2} + A + \frac{1}{2} \left[\frac{n}{\omega} \right]^2 \frac{B^2}{H_{M_2}}$$

A similar calculation, defining $t = 0$ at the time of maximum M_2 , gives:

$$t_{\min} = -\frac{Bn}{\omega^2 H_{M_2}}$$

for the combined low water level:

$$H_{\min} = -H_{M_2} + A - \frac{1}{2} \left[\frac{n}{\omega} \right]^2 \frac{B^2}{H_{M_2}}$$

Over many high (or low) tides, each with a different phase of the added constituent with respect to the $t = 0$ of each particular M_2 maximum (or minimum), A and B will vary harmonically each with amplitude R , and so the time average of A will be zero, while the time average of B^2 will be $(R^2/2)$. Therefore the Mean High Water (MHW), Mean Low Water (MLW), Mean Tide Level (MTL) and Mean Tidal Range (MTR) will be as follows:

$$\begin{aligned} \text{MHW} &= \overline{H_{\max}} = H_{M_2} + \frac{1}{4} \left[\frac{n}{\omega} \right]^2 \frac{R^2}{H_{M_2}} \\ \text{MLW} &= \overline{H_{\min}} = H_{M_2} - \frac{1}{4} \left[\frac{n}{\omega} \right]^2 \frac{R^2}{H_{M_2}} \\ \text{MTL} &= 0 \\ \text{MTR} &= \overline{H_{\max}} - \overline{H_{\min}} = 2H_{M_2} + \frac{1}{2} \left[\frac{n}{\omega} \right]^2 \frac{R^2}{H_{M_2}} \end{aligned} \quad (\text{C.1})$$

Mean Sea Level (MSL) is the same as MTL.

Note that the MTR is always slightly more than twice the M_2 amplitude, which might not be expected intuitively. In practice it is necessary to sum the additional terms independently over all constituents other than M_2 and constituents that are multiples of the M_2

angular frequency, which need special treatment as shown below. Obviously, the ratio of speeds (n/ω) in the above expressions means that higher harmonics are more effective in altering the high and low water times and heights. Also, the R^2 term means that only a very few additional constituents matter. For a semi-diurnal regime where Equilibrium ratios apply, S_2 increases the M_2 Mean Tidal Range by 6 per cent and N_2 , by a further 1 per cent. Ratios based on local constituent ratios would give a more accurate result.

For those tidal constituents with angular frequencies that are the multiples of M_2 (also the sub-harmonic M_1 , which is very small and not relevant here), factor A will not average to zero over several tidal cycles, because the contribution is phase locked. Consider the effect on the dominant M_2 constituent of a smaller M_4 constituent where $H_{M_4} \cos(2\omega t - g_{M_4} + V_{M_4})$ and $V_{M_4} = 2V_{M_2}$.

In a similar way to above one may write (neglecting the V terms):

$$T(t) = H_{M_2} \cos(\omega t - g_{M_2}) + H_{M_4} \cos(2\omega t - g_{M_4})$$

which may be differentiated and solved for $\frac{\partial T(t)}{\partial t} = 0$ (and noting that for the M_2 high water, $\omega t = g_{M_2}$), to show that including M_4 shifts the overall high water time by Δt :

$$\Delta t = -\frac{r \sin \theta}{\omega}$$

One then has for M_4 :

$$\begin{aligned} \text{MHW} &= Z_0 + H_{M_2} + H_{M_4} \cos(-2r \sin \theta + \theta) \\ \text{MLW} &= Z_0 - H_{M_2} + H_{M_4} \cos(2r \sin \theta + \theta) \\ \text{MTL} &= Z_0 + H_{M_4} \cos(2r \sin \theta) \cos \theta \\ \text{MTR} &= 2H_{M_2} + 2H_{M_4} \sin(2r \sin \theta) \sin \theta \end{aligned} \quad (\text{C.2})$$

where $\theta = (2g_{M_2} - g_{M_4})$ and $r = \frac{2H_{M_4}}{H_{M_2}}$.
 Z_0 is MSL.

For M_6 , similar calculations give:

$$\begin{aligned} \text{MHW} &= Z_0 + H_{M_2} + H_{M_6} \cos(-3r \sin \theta + \theta) \\ \text{MLW} &= Z_0 - H_{M_2} - H_{M_6} \cos(3r \sin \theta + \theta) \\ \text{MTL} &= Z_0 + H_{M_6} \sin(3r \sin \theta) \sin \theta \\ \text{MTR} &= 2H_{M_2} + 2H_{M_6} \cos(3r \sin \theta) \cos \theta \end{aligned} \quad (\text{C.3})$$

where this time $\vartheta = (3g_{M_2} - g_{M_6})$ and $r = 3\frac{H_{M_6}}{H_{M_2}}$.

The ratio r is very small, and so for M_4 it can be seen that the influence on MTL is potentially significant because of the cosine term; conversely, because of the corresponding sine term, M_6 does not contribute significantly to MTL. In principle, a similar expression for M_8 would have a cosine, and M_{10} a sine; but these and higher terms are usually neglected.

To obtain the overall MHW and other terms, one can use what is called the 'principle of superposition of small independent quantities' to add the terms in expressions C.1, C.2 and C.3 together for M_4 and M_6 , and also the frequencies that are not multiples of M_2 .

In a similar exercise, one can also consider mean values of the times of high and low waters relative to passage of the Moon at Greenwich or mean values of the time between high waters and low waters or between low waters and high waters. These quantities are called *Intervals*. From similar calculations, using Δt as derived above, and confining ourselves to consideration of M_4 :

$$\begin{aligned} \text{Mean High Water Interval (MHWI)} \\ &= \frac{g_{M_2}}{29.98} + \frac{4B_{M_4}}{H_{M_2}} \end{aligned} \quad (\text{C.5})$$

$$\begin{aligned} \text{Mean Low Water Interval (MLWI)} \\ &= 6.21 + \frac{g_{M_2}}{29.98} - \frac{4B_{M_4}}{H_{M_2}} \end{aligned} \quad (\text{C.6})$$

where in this case g_{M_2} , the M_2 phase lag, is expressed in degrees and $B_{M_4} = -H_{M_4} \sin \theta_{M_4}$. Then:

$$\text{Mean HW to LW interval} = 6.21 - \left[\frac{8B_{M_4}}{H_{M_2}} \right] \quad (\text{C.7})$$

$$\text{Mean LW to HW interval} = 6.21 + \left[\frac{8B_{M_4}}{H_{M_2}} \right] \quad (\text{C.8})$$

References

1. Doodson, A. T. and Warburg, H. D. 1941. *Admiralty Manual of Tides*. London: HMSO.
2. Woodworth, P. L., Shaw, S. M. and Blackman, D. B. 1991. Secular trends in mean tidal range around the British Isles and along the adjacent European coastline. *Geophysical Journal International*, **104**, 593–610, doi:10.1111/j.1365-246X.1991.tb05704.x.
3. U.S. Coast and Geodetic Survey, 1952. *Manual of Harmonic Constant Reductions*, Special Publication 260, U.S. Department of Commerce. Available at docs.lib.noaa.gov/rescue/cgs_specpubs/QB275U35 no2601952.pdf.

Appendix D Theoretical tidal dynamics

Fuller accounts of tidal dynamics are found in specialised accounts [1, 2, 3, 4]. Here we present some basic equations to guide the general reader.

D.1 Long progressive waves, no rotation

In Section 5.2 it was shown that a wave of small amplitude in shallow water travels at a speed:

$$c = \sqrt{gD} \quad (\text{D.1})$$

where D is the undisturbed water depth. The associated currents are:

$$u = \zeta \sqrt{g/D} \quad (\text{D.2})$$

so that the maximum currents in the direction of propagation occur at the same time as local high water. Currents at low water are directed in the opposite direction to that of wave propagation.

The total horizontal displacement of a particle during a tidal cycle, T , of a progressive wave, when water is flowing in the same direction is:

$$\zeta \sqrt{g/D} \int_0^{\pi} \cos \omega t dt = \zeta \sqrt{g/D} \frac{2}{\omega} = \zeta \sqrt{g/D} \frac{T}{\pi} \quad (\text{D.3})$$

Some examples are given in Section 5.4.3.

Energetics

Consider the energy associated with the wave (which need not be a simple harmonic) shown in Figure D.1 The potential energy of a vertical column with unit cross-sectional length along the wave front, and an incremental width dx is:

$$\rho g (\zeta + D) \frac{1}{2} (\zeta + D) dx = \frac{1}{2} \rho g (\zeta + D)^2 dx$$

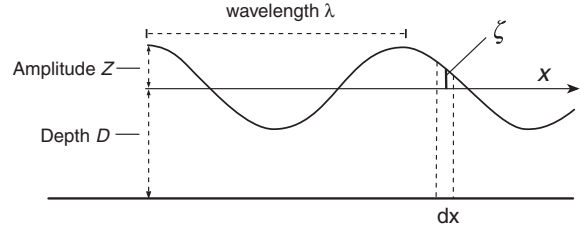


Figure D.1 Basic wave propagation parameters.

Over a complete wavelength the potential energy is:

$$\frac{1}{2} \rho g \int_0^{\lambda} (\zeta + D)^2 dx$$

If there is no wave present, the potential energy of the water of uniform depth D is:

$$\frac{1}{2} \rho g D^2 \lambda$$

The difference is the potential energy due to the wave:

$$\frac{1}{2} \rho g \int_0^{\lambda} \zeta^2 dx + \rho g D \int_0^{\lambda} \zeta dx$$

and since the second term is zero when integrated over a complete wavelength, this potential energy becomes:

$$\frac{1}{2} \rho g \int_0^{\lambda} \zeta^2 dx \quad (\text{D.4a})$$

Similarly, we may calculate the kinetic energy per unit cross-sectional length on the long wave assumption that vertical velocities are small compared with horizontal velocities and $\zeta \ll D$. For the vertical column this is:

$$\frac{1}{2} \rho D u^2 dx = \frac{1}{2} \rho D \zeta^2 (g/D) dx$$

The kinetic energy integrated over a wavelength is:

$$\frac{1}{2} \rho g \int_0^{\lambda} \zeta^2 dx \quad (\text{D.4b})$$

which is the same as the potential energy. The total energy per wavelength is the sum of the potential and kinetic energies:

$$\rho g \int_0^{\lambda} \zeta^2 dx$$

If the surface disturbance takes the form of a harmonic wave $H_0 \cos kx$ (where k is the wave number $2\pi/\lambda$), and λ is the wavelength, this total energy is:

$$\frac{1}{2} \rho g H_0^2 \lambda$$

and the total energy per unit area of surface is:

$$\frac{1}{2} \rho g H_0^2 \quad (\text{D.5a})$$

Energy is transmitted by the wave at the group velocity, which for long waves is the speed $c = \sqrt{gD}$, so that the energy flux per unit width of wave front is:

$$\frac{1}{2} \rho g H_0^2 \sqrt{gD} \quad (\text{D.5b})$$

If the energy flux is to remain constant as the water depth decreases, the wave amplitude must increase so that the factor $H_0^2 \sqrt{D}$ remains constant.

These energy properties have been calculated above for a purely progressive wave. However, the energy fluxes through a section may be considered in a more general way [5]. The energy flux across a section of channel consists of the work done by the water, which crosses the section, plus the potential and kinetic energies, which it transfers. Using the hydrostatic approximation (Equation A.1), the average water head pressure in water of depth D is $\frac{1}{2} \rho g (D + \zeta)$. The entering water does work against the pressure at a rate $\frac{1}{2} \rho g (D + \zeta)^2$ per unit width of wave front. The entering water also brings its own potential and kinetic energy. If we now measure the potential energy of the water column relative to a zero defined as the local mean sea level, the total potential energy per unit area is:

$$\frac{1}{2} \rho g (\zeta^2 - D^2)$$

so the flow of potential energy per unit width of wave front is:

$$\frac{1}{2} \rho g (\zeta^2 - D^2) u$$

The kinetic energy flux per unit width is:

$$\frac{1}{2} \rho (D - \zeta) u^2 \cdot u$$

The total influx of energy per unit width of channel, due to all three sources is:

$$\begin{aligned} & \frac{1}{2} \rho g \{ (D + \zeta)^2 + \zeta^2 - D^2 \} u + \frac{1}{2} \rho (D + \zeta) u^3 \\ & = \rho g (D\zeta + \zeta^2) u + \frac{1}{2} \rho (D + \zeta) u^3 \end{aligned} \quad (\text{D.6})$$

Normally $\zeta \ll D$, and since $u^2 = \zeta^2 (g/D)$ eliminating all terms in ζ^2 gives an energy flux of:

$$\rho g D \zeta u \quad (\text{D.7})$$

If the propagating disturbance consists of a tidal harmonic $H_0 \cos(\omega t - g_{\zeta_0})$ at the flux boundary, with currents that also vary harmonically but lag the elevations $U_0 \cos(\omega t - g_{U_0})$, the average energy flux per unit width over a tidal cycle is:

$$\begin{aligned} & \rho g D H_0 U_0 \int_0^{\frac{2\pi}{\omega}} \cos(\omega t - g_{\zeta_0}) \cos(\omega t - g_{U_0}) dt \\ & = \rho g D H_0 U_0 \cos(g_{\zeta_0} - g_{U_0}) \end{aligned} \quad (\text{D.8})$$

In the case of a progressive wave, where the currents are a maximum in the positive direction at the same time as high water, there is no phase lag and so the energy flow has a maximum value. This formula for energy flux may be compared with the formula for power transmission in an electrical alternating current circuit.

Equation D.7 gives the average energy flux through each unit width of channel for a single harmonic tidal constituent. By writing the elevations and currents in Equation D.7 as the sum of two or more harmonics of different frequencies, it is possible to show that, averaged over a sufficiently long period, the total energy flux due to all the harmonics is equal to the sum of the fluxes in the individual harmonics computed using Equation D.8. This is analogous to the summation properties for the spectral decomposition of variance, and is obviously a very useful way of computing total fluxes from harmonic analyses of elevations and currents.

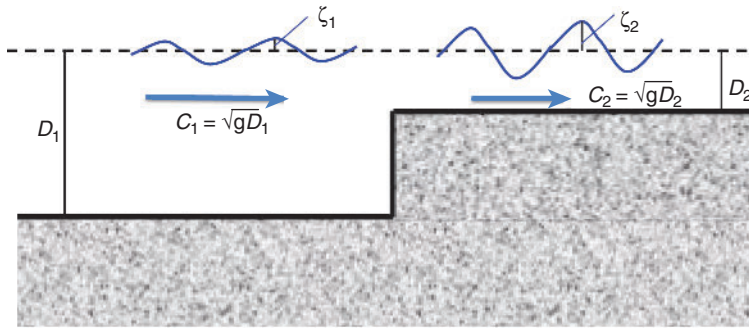


Figure D.2 Wave parameters at a depth discontinuity.

Reflection and transmission of waves at a depth discontinuity

Consider a plane wave of amplitude H_1 propagating along a channel in water depth D_1 , which encounters a step discontinuity in depth (Figure D.2). Beyond the step the depth is D_2 . The wavelength in the shallower water is reduced but the frequency remains the same. H'_1 is the amplitude of the reflected wave and H'_2 that of the transmitted wave.

Matching elevations at $x = 0$ gives:

$$H_1 + H'_1 = H'_2 \quad (\text{D.9})$$

Similarly for the water fluxes the (current \times depth) must be constant:

$$\begin{aligned} D_1 \sqrt{g/D_1} (H_1 - H'_1) &= D_2 \sqrt{g/D_2} H_1 - H'_2 \\ \text{or } c_1 (H_1 - H'_1) &= c_2 H'_2 \end{aligned} \quad (\text{D.10})$$

where c_1 and c_2 are the wave velocities from (D.1).

From (D.9) and (D.10):

$$\begin{aligned} \frac{H'_1}{H_1} &= \frac{\text{reflected wave amplitude}}{\text{incident wave amplitude}} = \frac{c_1 - c_2}{c_1 + c_2} \\ \frac{H'_2}{H_1} &= \frac{\text{transmitted wave amplitude}}{\text{incident wave amplitude}} = \frac{2c_{11}}{c_1 + c_2} \end{aligned} \quad (\text{D.11})$$

Note that these satisfy the condition that if there is no discontinuity ($D_1 = D_2$ and so $c_1 = c_2$) there is no reflected wave and the transmitted wave passes unaltered. It is easy to show by applying Equation D.5b that the total energy of the incident wave is conserved in the reflected and transmitted waves. For typical ocean and shelf depths of 4000 m and 200 m, respectively, the reflected and transmitted waves have amplitudes of 0.64 and 1.64 times the amplitude of the incident wave. These values are only indicative of the behaviour

of long tidal waves incident on a continental slope because the detailed bathymetry of the slope can only be approximately represented by a step change of depth.

D.2 Standing waves

From the progressive wave Equation 5.4 we may write the following expression for two progressive waves travelling in opposite directions as illustrated in Figure 5.3:

$$\begin{aligned} H_0 \cos(kx - \omega t) + H_0 \cos(-kx - \omega t) \\ = 2H_0 \cos \omega t \cos kx \end{aligned}$$

This represents a wave motion called a standing wave, whose amplitude varies harmonically as a function of the distance x , with wavelength $2\pi/K = \lambda$. In each wavelength there are two nodes where $\cos kx = 0$, at which the oscillations have zero amplitude. These are located at $x = \frac{1}{4}(n+1)\lambda$ ($n = 0, 2, \dots$) from the reflecting barrier. There are intermediate antinodes, where the oscillations have maximum amplitude at $x = \frac{1}{2}n\lambda$.

The currents are given (Equation D.2) by:

$$\begin{aligned} H_0 \sqrt{g/D} \cos(kx - \omega t) + H_0 \sqrt{g/D} \cos(-kx - \omega t) \\ = 2H_0 \sqrt{g/D} \cos \omega t \cos kx \end{aligned} \quad (\text{D.13})$$

Maximum currents occur where $\sin kx = 1$, i.e. $x = \frac{1}{4}(n+1)\lambda$ and zero currents occur where $\sin kx = 0$, i.e. $x = \frac{1}{2}n\lambda$ (again $n = 0, 2, \dots$), so there can be vertical walls in these positions. Maximum currents coincide with zero amplitude whereas zero currents occur where the elevation changes are a maximum. This behaviour of standing waves is as shown for oscillation in a box (!) in Figure 5.4.

When a tidal wave is reflected at the head of a basin, the reflected wave will be weaker than the incident wave. The sum of these two can be written:

$$\begin{aligned}
 H_I \cos(kx - \omega t) + H_R \cos(-kx - \omega t) \\
 &= H_R \cos(kx - \omega t) + H_R \cos(-kx - \omega t) \\
 &\quad + (H_I - H_R) \cos(kx - \omega t) \\
 &= 2H_R \cos \omega t \cos kx + (H_I - H_R) \cos(kx - \omega t)
 \end{aligned} \tag{D.14}$$

The result is equivalent to a standing wave of amplitude $2H_R$ and a progressive wave of amplitude $(H_I - H_R)$, which propagates energy towards the head of the basin where it is dissipated by imperfect reflection.

D.3 Long waves on a rotating Earth

The momentum equations in the absence of advective accelerations and friction become (Equations A1.4, A1.5):

$$\begin{aligned}
 \frac{\partial u}{\partial t} - fv &= -g \frac{\partial \zeta}{\partial x} \\
 \frac{\partial v}{\partial t} + fv &= -g \frac{\partial \zeta}{\partial y}
 \end{aligned}$$

The general solutions to these equations are called Poincaré waves, though for describing real ocean tides, a more limited solution, called Kelvin waves, is especially useful.

For depth independent currents, using the hydrostatic equation, the continuity equation is:

$$\frac{\partial \zeta}{\partial t} + D \left(\frac{\partial u}{\partial x} + \frac{\partial v}{\partial y} \right) = 0$$

Consider a solution that has the special property of no flow along the Y axis ($v = 0$). This would apply for wave propagation along a straight boundary at $y = 0$, such as would be presented for a wave travelling along a coastline. In this case the three equations reduce to:

$$\begin{aligned}
 \frac{\partial u}{\partial t} &= -g \frac{\partial \zeta}{\partial x} \\
 fu &= -g \frac{\partial \zeta}{\partial y} \\
 \frac{\partial \zeta}{\partial t} + D \frac{\partial u}{\partial x} &= 0
 \end{aligned}$$

We seek a solution of the form:

$$\begin{aligned}
 \zeta &= \zeta(y) \cos(kx - \omega t) \\
 u &= u(y) \cos(kx - \omega t)
 \end{aligned}$$

where the amplitudes of the harmonic variations are functions only of the distance for the boundary at

$y = 0$. Substituting these into the three simplified hydrodynamic equations yields:

$$\begin{aligned}
 \omega u(y) \sin(kx - \omega t) &= gk \zeta(y) \sin(kx - \omega t) \\
 fu(y) \cos(kx - \omega t) &= -g \frac{\partial \zeta(y)}{\partial y} \cos(kx - \omega t) \\
 \omega \zeta(y) \sin(kx - \omega t) - Dku(y) \sin(kx - \omega t) &= 0
 \end{aligned}$$

from which:

$$\begin{aligned}
 \omega u(y) &= gk \zeta(y) \\
 fu(y) &= -g \frac{\partial \zeta(y)}{\partial y} \\
 Dku(y) &= \omega \zeta(y)
 \end{aligned}$$

Dividing the first and third of these:

$$\frac{\omega}{Dk} = g \frac{k}{\omega}$$

or

$$\frac{\omega^2}{k^2} = gD$$

But ω/k is the speed of propagation of the wave, c , from which we deduce that $c = \sqrt{g/D}$ in this solution. This is the same as for a wave in a non-rotating system, as is the relationship between currents and elevations (Equation D.2 and Equation D.1). The second equation can be rearranged:

$$\frac{\partial \zeta(y)}{\partial y} = -\frac{f}{g} u(y) = -\frac{f}{c} \zeta(y)$$

therefore:

$$\zeta(y) = H_0 \exp(-fy/c) \quad \text{and} \quad u(y) = \sqrt{g/D} \zeta(y) \tag{D.15}$$

where H_0 is the amplitude at $y = 0$.

These solutions to the hydrodynamic equations on a rotating Earth are called **Kelvin waves**, and they provide a good description of many observed tidal characteristics. The effect of the rotation appears only in the factor $\exp(-fy/c)$, which gives a decay of wave amplitude away from the boundary with a length scale $c/f = \frac{\sqrt{g/D}}{f}$, which depends on the latitude and the water depth. This scale is called the Rossby radius of deformation. At a distance $y = cf$ from the boundary the amplitude has fallen to $0.37 H_0$. At 45° N in water of 4000 m depth the Rossby radius is 1900 km, but in water 50 m deep this is reduced to 215 km.

Kelvin waves are not the only solution to the hydrodynamic equations on a rotating Earth. A

special solution when $\omega = f$ gives inertial currents (Section 4.4.3). The more general solution, called Poincaré waves, allows finite values of the v current in the presence of a coast. The amplitude varies sinusoidally rather than exponentially in the direction transverse to the direction of wave propagation. The transverse velocity component also varies sinusoidally, which allows Poincaré waves to be realistic solutions provided that coastlines are located along one of the lines of zero transverse velocity.

Away from the coast another form of solution, sometimes called Sverdrup waves, allows both u and v to have finite values, with wave amplitudes independent of y . The literature is varied [6] in its terminology: modern usage [4] calls the general solutions Poincaré waves; Sverdrup's name is usually related to friction-modified, long gravity waves. Poincaré (and Sverdrup) waves have phase speeds that exceed those of Kelvin waves, but the energy, which is transmitted at the group velocity, has a maximum speed of transmission of $\sqrt{g/D}$. Other solutions, while of great interest in mathematical studies of tidal behaviour, are beyond the scope of this account.

In the case of a wave reflected at the head of a channel in a non-rotating system, there is a series of nodes, each with zero surface level changes, at distances $x = \frac{1}{4}(n+1)\lambda$ from the reflecting boundary at $x = 0$ (see Figure 5.3). The node extends as a line across the channel. In a rotating system the nodal line is reduced to a nodal point, called the amphidromic point, at the same distance from the reflecting boundary. The position of this nodal point depends on the relative amplitudes of the ingoing and reflected Kelvin waves. By adding two Kelvin waves travelling in opposite directions it is possible to show that the y displacement of the amphidrome from the centre of the channel ($y = 0$) is:

$$y = -\frac{\sqrt{g/D} \ln \alpha}{2f} \quad (\text{D.16})$$

Because the reflected wave is smaller than the incident wave, the ratio between reflected and ingoing wave amplitudes will be less than 1, and so $\ln \alpha$ is negative. Hence the amphidrome displacement y is to the left of the direction of the incoming wave in the northern hemisphere. Only if the incident and reflected waves have equal amplitude is the nodal point or amphidrome in the middle of the channel. Figure D.3 shows how the location of the cancelling point moves as the amplitude of the reflected wave is reduced. If the reflected wave is sufficiently weakened,

the point at which the cancelling takes place does not have a real existence, but is apparently located outside the channel in which the waves propagate. In this case the amphidrome is said to be degenerate.

D.4 Co-tidal and co-amplitude lines

The preparation of co-tidal and co-amplitude charts from observations of sea levels and bottom pressures alone is quite straightforward, but the accuracy with which the lines can be traced offshore is usually limited by the scarcity of available data. These data can be supplemented by knowledge of the harmonic constituents of the depth-averaged currents, which are dynamically related to changes in elevations by the momentum and continuity equations. Solving the equations for an individual harmonic constituent at an offshore station:

$$H_{\zeta} = \cos(\omega t - g_{\zeta})$$

gives H_{ζ} and g_{ζ} . The amplitudes and phases of two components of currents give four extra parameters, the directions of the co-tidal and co-amplitude lines and the gradients on the co-tidal and co-amplitude surfaces [3, 7].

To avoid laborious algebra the direction of the X axis is taken along the direction of the major axis of the current ellipse. In the usual Cartesian convention of angles being measured positive anticlockwise from this direction, the directions of the co-tidal and co-amplitude lines are given by:

$$\tan \psi = -\frac{\omega U + fV}{\omega V + fU} \cot(g_{\zeta} - g_u) \quad (\text{D.17})$$

$$\tan \psi' = \frac{\omega U + fV}{\omega V + fU} \tan(g_{\zeta} - g_u) \quad (\text{D.18})$$

where ψ is the direction of the co-tidal line, ψ' is the direction of the co-amplitude line, ω is the constituent

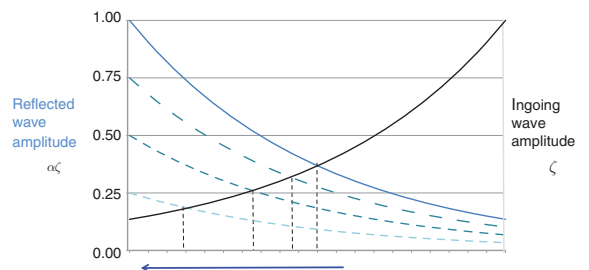


Figure D.3 Showing the cancelling points of incident and reflected Kelvin waves.

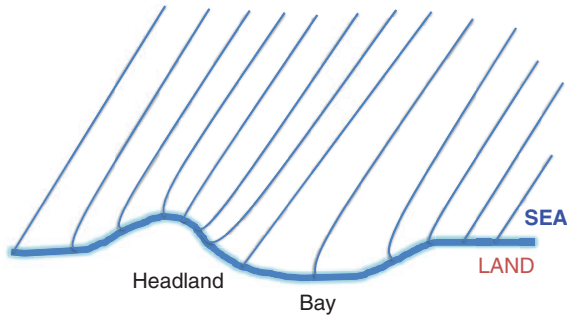


Figure D.4 Co-tidal lines converge on headlands and diverge in bays.

speed, U and V are the semi-major and semi-minor axes of the current ellipse, and g_u is the current phase relative to the Equilibrium Tide. The full analysis includes the harmonic constituents of the frictional term, which can be evaluated by harmonic analysis of a time series of friction generated by Equation 6.3 from the full time series of tidal currents. The non-linear form of this relationship between friction and currents means that much of the friction variance appears at higher harmonics. For example, M_2 produces large frictional terms at M_4 . At the Inner Dowsing tower (Figures 1.3 and 4.6.) with strong currents in 20 m depth, including friction changes the values of ψ and ψ' by 9° and 24° respectively.

Equations D.17 and D.18 show that, in the absence of friction, the co-tidal and co-amplitude lines are always at right angles to each other:

$$\psi' = \psi + \frac{\pi}{2}$$

For a progressive wave, high water and flow along the major axis are simultaneous. From Equation D.17 $\tan \Psi = -\infty$, $\Psi = \pi/2$, and from Equation D.18 $\tan \Psi' = \tan 0$, and so $\Psi' = 0$. The co-tidal lines are parallel to the crest of the wave, and the co-amplitude lines are perpendicular to this direction. This is the relationship that applies for a Kelvin wave. For a standing wave, flow along the major axis is zero at high water, and $(g_\zeta - g_u) = \pi/2$. Hence from Equation D.17 $\tan \Psi = 0$, $\Psi = 0$ and from Equation D.18 $\tan \Psi' = \infty$, $\Psi' = \pi/2$.

The co-tidal lines are parallel to the major axis and the co-amplitude lines are perpendicular.

In the case of a tidal wave near a coastline the flow will be parallel to the coast and so the semi-minor axis will be very small by comparison with the semi-major axis. The angles become:

$$\tan \psi = -(\omega/f) \cot(g_\zeta - g_u)$$

$$\tan \psi' = -(\omega/f) \tan(g_\zeta - g_u)$$

The lines have constant angles with the direction of the coast. Over an area sufficiently small for $(g_\zeta - g_u)$ to be constant the effect of this is to concentrate co-tidal lines onto headlands or capes and to make them more diffuse in bays, as shown in Figure D.4. This effect also causes the range of the tide to change more rapidly near headlands.

References

1. Lamb, H. (1994). *Hydrodynamics* (6th edition). Cambridge: Cambridge University Press. Originally published in 1879, the 6th extended edition appeared first in 1932.
2. Proudman, J. 1953. *Dynamical Oceanography*. London: Methuen and Co.
3. Defant, A. 1961. *Physical Oceanography: Volume II*. Oxford: Pergamon Press.
4. Gill, A. E. 1982. *Atmosphere-Ocean Dynamics*. London: Academic Press.
5. Taylor, G. I. 1920. Tidal friction in the Irish Sea. *Philosophical Transactions of the Royal Society of London, A*, **220**, 1–33, doi:10.1098/rsta.1920.0001.
6. Platzman, G. W. 1971. Ocean tides and related waves. In *Mathematical Problems in the Geophysical Sciences: Volume 2* (ed. W. H. Reid) pp. 239–291. Providence, Rhode Island: American Mathematical Society.
7. Proudman, J. and Doodson, A. T. 1924. The principal constituents of the tides of the North Sea. *Philosophical Transactions of the Royal Society of London, A*, **224**, 185–219.

Appendix E Legal definitions in the coastal zone

In [Chapter 2](#) we looked at different tidal levels and their use as zero or Datum Levels [1]. Tidal datums are also used to define shorelines, adopted as the state, national and international boundaries shown on maps. Generally the important levels are some form of High Tide, and some form of Low Tide, depending on locally adopted definitions. The determination of these levels, and their projection to mapped shorelines may require long records of sea-level measurements, often a complete nodal cycle of 18.61 years. Inevitably, knowledge of tidal principles has an important role to play in the development and interpretation of legal rules, but the technical aspects of defining tidal boundaries have sometimes been underemphasised [2].

The three components of a robust boundary definition are:

- clear and measurable tidal level parameters,
- a means of converting these levels into map coordinates,
- a legal system for interpreting and enforcing the boundaries.

To these we might add a process for adjusting to tidal and coastal changes over the long-term.

The area of coast covered and uncovered as the tide rises and falls ([Figure E.1](#)) is variously called the intertidal zone, the littoral zone, the tidelands or the foreshore. There have been several legal commentaries on the definition and significance of this intermediate territory [3, 4]. The upper and lower limits may be defined in many ways in terms of the local tidal regime. Legal rights within this zone and within the subtidal zone have been interpreted in different ways at different times in different countries. Although the intertidal areas were originally of little economic value, ownership issues have become increasingly important as valuable mineral rights are contested.

For international boundaries, the United Nations Convention on the Law of the Sea (UNCLOS), which came into force in 1994, requires countries to define a

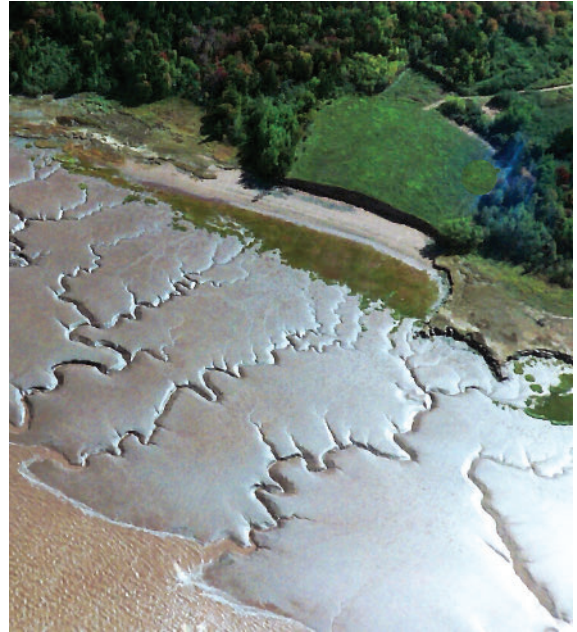


Figure E.1 Defining boundaries in the muddy and inaccessible coastal zone is sometimes best done from the air, but accuracy is limited. Photograph from the Minas Basin, Canada, supplied by David Pugh.

Territorial Sea Baseline. Territorial Seas are measured outwards from this line, usually for 12 nautical miles. UNCLOS (Article 5) defines the baseline as ‘the low-water line along the coast as marked on large scale charts officially recognised by the coastal State’. Exactly what is meant by ‘low-water’ is not more clearly defined, and many countries have elected to use Lowest Astronomical Tide, the datum recommended by the International Hydrographic Organization for use on navigation charts. Obviously this maximises the offshore area covered. Under certain circumstances UNCLOS allows the baseline to jump across bays and rivers and between islands, as well as along heavily indented areas of coastline. At the other tidal extreme,

UNCLOS defines islands as land features that are 'above water at high tide', but there is no definition, nor a mention of a high tide datum as used on nautical charts; countries that adopt lower high tide datums will obviously define more features as islands, and hence optimise extension of their claim over sea areas. Countries are free to decide how they define these tidal terms.

Defining ownership of **the foreshore in national legislation** has a long and interesting history, beginning in Europe. The English legal expert Lord Hale (1609–76) wrote a treatise, establishing as settled law in England the principle that the Crown has ownership of the foreshore, which extends landwards as far as it is covered by 'the ordinary flux of the sea'. The common-law term 'ordinary high water mark' has been generally used to describe the boundary between the Crown's foreshore and the adjoining privately owned lands, but this term has also been subjected to several interpretations. The United Kingdom foreshore boundaries are shown on large-scale maps published by the Ordnance Survey. In 1854 the Lord Chancellor, in giving judgement on the limits of foreshore boundaries around England and Wales, defined these boundaries as following the High and Low Water Marks of a medium or average tide. In Scottish law [5], there has been no legal definition of foreshore boundaries but ancient custom has decreed that the extent of the foreshore shall be limited by mean spring tides.

Procedures and terms have changed over the years. The UK Ordnance Survey mapped the High and Low Water Marks of a mean or average tide in England and Wales and of an average spring tide in Scotland. Before August 1935 the lines surveyed in England and Wales were called *High and Low Water Marks of Ordinary Tides*. Since 1935 the term 'Medium' was adopted in place of 'Ordinary'. In Scotland the lines were called 'High and Low Water Mark Ordinary Spring Tides'. Since March 1965 the descriptions in England and Wales are Mean High (or Low) Water, abbreviated to MH(or L) W; and in Scotland Mean High (or Low) Water Springs abbreviated to MH (or L) WS. Tidal lines are surveyed by either air or ground survey methods depending upon the type of foreshore [6]. When conditions favour ground survey, direct measurements from foreshore detail are used; but where ground conditions are difficult, air photographs are taken on infrared film. These show the water's edge distinctly and are used for making a survey. The ground survey or the aerial photography is carried

out at a time when a High (or Low) Water is expected to reach a level equal to that of Mean High (or Low) Water or Mean High (or Low) Water Springs. As high water generally leaves a clear mark, until the next high water there is not much difficulty in surveying this line. Low water, however, often presents considerably greater difficulty and its definition is less accurate.

Although the foreshore is generally owned by the Crown, and administered through The Crown Estate, the public are entitled by common law to exercise certain rights over the seashore, including navigation and fishery. However, there is no right to go on the foreshore to take seaweed without appropriate permission, nor does the public have the right to dig for bait on the foreshore. Permits are required to use metal detectors. The legal position is very complicated and subject to increasing scrutiny as the demands for the exploitation of the coastal zone become more extensive. The Ordnance Survey does not re-define its tidal boundaries at set intervals of time. Changes in tidal boundaries due to changes in coastal geomorphology and in mean sea level (MSL) are incorporated as new surveys are undertaken.

The law relating to ownership of the **tidelands in the United States** varies from state to state. It stems from two separate European systems, Roman law which is followed on the continent of Europe, and common law which evolved in England, and has been generally adopted by the 13 original states and most of the later-admitted states. After the Revolution, the former British colonies succeeded to the rights of the Crown in respect of their tidelands. Absolute title to all tidelands passed to the original states, in trust, except where they had previously been granted into private ownership. Each state is free to adopt its own rules of real property, and questions of ownership are determined under state constitution, statutes and case law.

Most American coastal states have adhered to the basic English common-law rule that the ordinary high water mark (now interpreted as the line of mean high water) constitutes the legal boundary between privately owned uplands and state-owned tidelands (see Figure E.2). As a generalisation, sixteen coastal states deem the mean high water line to be the private/state boundary. However, six Atlantic Coast states, Delaware, Massachusetts, Maine, New Hampshire, Pennsylvania and Virginia, use the mean low water line as the boundary. In Louisiana the boundary is the line of the highest winter tide. In Texas, if the source of upland title is a Spanish or Mexican grant predating

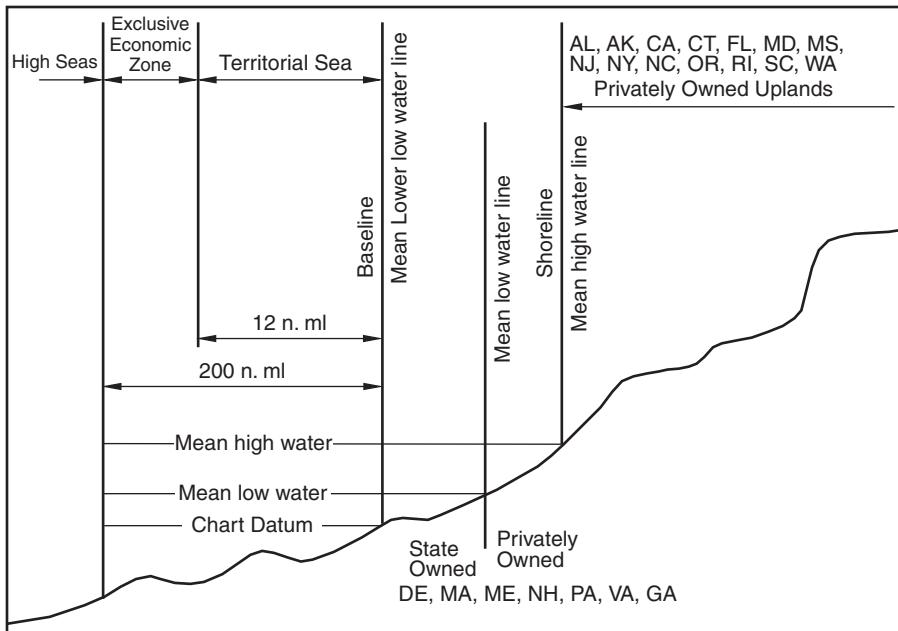


Figure E.2 Some tidally defined boundaries for different states in the United States. The drawing is not to scale. If the privately owned boundary is near the low water line then beaches are seldom available for public access. Based on information provided by NOS/NOAA.

Texas' independence, the line of mean higher high water is the legal boundary. Hawaii adheres to its aboriginal, customary concept whereby the private/public boundary is marked by the upper reaches of the wash of the waves.

In general, 'gradual, imperceptible' physical changes in the location on the ground of the boundary, natural or artificial, result in a shift of the legal boundary. The National Ocean Service (NOAA) charts are the official charts of the United States; they automatically become legal documents in regard to the portrayal of maritime boundaries and tidal datums. Datums are commonly calculated from observations for each National Tidal Datum Epoch; the Epoch is a 19-year period (the Nodal Cycle), which is reviewed annually for possible revision, and must be actively considered for revision every 25 years. The current *Epoch 1983–2001*, was introduced in 2003. This gradual adjustment allows boundaries to change progressively, for example if there are climate-related [MSL](#) or tidal changes.

The United States Submerged Lands Act of 1953 defined the Federal State boundary as three nautical miles beyond the line of 'ordinary low water', except for coasts bounding the Gulf of Mexico where the extent is nine nautical miles.

NOAA calculates four datums from observations, for each National Tidal Datum Epoch [1]:

Mean Higher High Water (MHHW)

The average of the higher high water heights of each tidal day. The corresponding line is the property boundary between privately owned uplands and state owned tidelands for the State of Texas when the upland parcel's original source of title is a pre-1840 grant by Spain, Mexico or the Republic of Texas. Prior to 28 November 1980 the Mean Higher High Water line was delineated on nautical charts as the shoreline in areas of predominately diurnal tides.

Mean High Water (MHW)

The average of all the high water heights. This is used to define the line of the property boundary between privately owned uplands and state owned tidelands for most maritime states. Since 1980 the Mean High Water line is delineated on nautical charts as the shoreline.

Mean Low Water (MLW)

The average of all the low water heights. Mean Low Water is the level used to define the boundary between private and state property in six east coast states. Along the east coast of the United States, the Mean Low Water line is the boundary between inland waters and the territorial sea. Mean Low Water has been used as the elevation for Chart Datum for NOS nautical charts

along the east coast of the United States, but will eventually be replaced by MLLW.

Mean Lower Low Water (MLLW)

The average of the lower low water in each tidal day. Along the west and Gulf coasts the Mean Lower Low Water line is the boundary between inland waters and territorial seas. It is used as Chart Datum for hydrographic surveying along the west and Gulf coasts of the United States. With the adoption of the National Tidal Datum Convention of 1980, it is also authorised for use as Chart Datum for the east coast, and will eventually replace MLW to give a uniform system for defining Chart Datum for the United States.

Detailed legislation varies considerably within the general legal concept or the land between high and low tide being in public ownership. In Argentina a law from 1869 places the boundary between public and private land at the High Astronomical Tide mark, with an extension inland, generally 50 m, for Federal Coastguard jurisdiction; there are some variations of this inland extension for provincial or municipal jurisdiction.

Australia also has this general concept of foreshore, with state variations. An interesting technological development combines tidal modelling and lidar beach-level mapping to define boundaries [7]; in one application sea level and seabed levels are measured simultaneously by aircraft fitted with infrared and green lasers.

References

1. U.S. Department of Commerce. 2001. *Tidal Datums and Their Applications*. NOAA Special Publication NOS CO-OPS 1. Washington, D.C.: U.S. Department of Commerce, National Oceanic and Atmospheric Administration, National Ocean Service. Available from http://tidesandcurrents.noaa.gov/publications/tidal_datums_and_their_applications.pdf.
2. Graber, P. H. F. 2005. Coastal boundaries. In *Encyclopaedia of Coastal Science* (ed. M. L. Schwartz), pp. 246–251. Dordrecht, Netherlands: Springer.
3. Shalowitz, A. L. 1962 and 1964. *Shore and Sea Boundaries: Volumes 1 and 2*. Washington, D.C.: U.S. Department of Commerce, Coast and Geodetic Survey.
4. Moore, S. A. 1888. *A History of the Foreshore and the Law Relating Thereto*. London: Stevens and Haynes. Available online at <http://archive.org/details/ahistoryforesho00hallgoog>.
5. Scottish Law Commission. 2003. *Report on the Law of the Foreshore and Sea Bed*. Scottish Law Commission No. 190. Available from www.scotlawcom.gov.uk/download_file/view/245/141/.
6. Baily, B. 2011. Tidal line surveying and Ordnance Survey mapping for coastal geomorphological research. *Survey Review*, **43**, 252–268.
7. Collier, P. and Quadros, N. D. 2006. Resolving spatial uncertainty in the tidal interface. In *Administering Marine Spaces: International Issues*, pp. 36–51. The International Federation of Surveyors, Special Publication 36.

Glossary

- AGE OF THE TIDE:** old term for the lag between the time of new or full Moon (SYZYGY) and the time of maximum spring tidal range. It can be estimated as $(g_{S_2} - g_{M_2})^0$, in hours.
- AMPHIDROME:** a point in the sea where there is zero tidal amplitude due to cancelling of tidal waves. CO-TIDAL LINES radiate from an amphidromic point and CO-RANGE LINES encircle it.
- ANNULAR MODES:** patterns of variability in the atmospheric circulation corresponding to changes in the zonally averaged mid-latitude westerlies. The Northern Annular Mode is associated with the NORTH ATLANTIC OSCILLATION, while the Southern Annular Mode plays an important role in driving the Antarctic Circumpolar Current.
- APHELION:** furthest point from the Sun in the Earth's orbit; at present in early July.
- APOGEAN TIDE:** tide of reduced range when the Moon is near apogee, its furthest point from the Earth in its elliptical orbit.
- ATLANTIC MERIDIONAL OVERTURNING CIRCULATION:** the warm northward, near-surface flow in the Atlantic Ocean that is compensated by a colder return flow at depth. The AMOC is part of the global thermohaline circulation.
- ATLANTIC MULTIDECADAL OSCILLATION:** a mode of variability in the North Atlantic observed in sea surface temperatures with warm phases roughly every 70 years.
- BAROTROPIC CHANGES:** changes in sea level that can be described by considering depth-averaged motions in the ocean. BAROCLINIC CHANGES refer to those that require knowledge of motions throughout the water column. (Different definitions are used in the oceanographic literature.)
- BENCH MARK:** see TIDE GAUGE BENCH MARK.
- BORE:** a tidal wave, which propagates as a solitary wave with a steep leading edge up certain rivers. Formation is favoured in wedge-shaped shoaling estuaries at times of SPRING TIDE. Other local names include eagre (River Trent, England), pororoca (Amazon, Brazil), and mascaret (Seine, France).
- BOTTOM PRESSURE:** pressure on the seabed measured by a bottom pressure recorder. BPRs have been operated at depths of 4000 m or more and record the changes in pressure due to variability in the mass of water and atmosphere above them.
- BRUUN RULE:** a method of relating changes in beach profile to changes in MEAN SEA LEVEL assuming a closed sediment system.
- CHART DATUM:** the datum to which levels on a nautical chart and tidal predictions are referred; usually defined in terms of a low water tidal level, which means that Chart Datum is not a horizontal surface, but it may be considered so over a limited local area.
- CLIMATE CHANGE:** a modification in the Earth's climate that persists for an extended period. Climate change may be due to natural internal processes in the climate system, external natural forcings such as solar activity, or anthropogenic changes including increasing greenhouse gases.
- CO-RANGE LINES:** lines on a tidal chart joining places that have the same TIDAL RANGE or amplitude; also called *co-amplitude lines*. Usually drawn for a particular TIDAL CONSTITUENT or tidal condition (for example, mean spring tides).
- CO-TIDAL LINES:** lines on a tidal chart joining places where the tide has the same phase; for example, where high waters occur at the same time. Usually drawn for a particular TIDAL CONSTITUENT or tidal condition.
- CRITICAL TIDAL LEVEL:** a level on the shore where the emersion/submersion tidal characteristics change sharply. Some biologists have suggested that zonation of plants and animals is controlled by a series of such levels, but detailed analysis of tidal statistics shows that the tidal transitions are seldom as sharply defined as the biological boundaries.

- CURRENT PROFILE:** the detailed variation of current speed and direction between the seabed and the sea surface.
- DATA REDUCTION:** the process of checking, calibration and preparation necessary to convert raw measurements into a form suitable for analysis and application.
- DATUM:** a reference level or surface to which levels on land or in the ocean may be referred. See also **CHART DATUM**.
- DECLINATION:** the angular distance of an astronomical body north or south of the celestial equator, taken as positive when north and negative when south of the equator. The Sun moves through a declinational cycle once a year, and the Moon moves through a cycle in 27.21 mean solar days. The solar declination varies between 23.5° N and 23.5° S. The cycles of the lunar declination vary in amplitude over an 18.61-year period from 28.5° to 18.5°.
- DEGENERATE AMPHIDROME:** a terrestrial point on a tidal chart towards which **CO-TIDAL LINES** appear to converge. ‘An imaginary point where nothing happens.’
- DISPERSIVE WAVES:** waves that have a phase velocity that depends on either frequency or amplitude are said to be dispersive. The shape of the overall packet of dispersive waves changes as it progresses.
- DIURNAL TIDE:** once-daily tidal variations in sea level, which increase with lunar or solar **DECLINATION** north and south of the equator. When added to **SEMIDIURNAL TIDES** they can cause a diurnal inequality, a difference between the heights of the two high waters and of the two low waters of a lunar day.
- DOUBLE TIDE:** a double-headed tide with a high water consisting of two maxima of similar height separated by a small depression (double high water), or a low water consisting of two minima separated by a small elevation (double low water). Also known as an agger or gulder. Examples occur at Southampton, UK; along the coast of the Netherlands; and off Cape Cod, United States.
- DRIFT:** the speed of the water; sometimes qualified to mean just **TIDAL CURRENTS**. Sometimes also the distance a craft is moved by currents and winds.
- DYNAMIC HEIGHT:** the height of the sea surface relative to a reference pressure level in the ocean (e.g. 1500 dbar, which is approximately 1500 m depth) which can be assumed to be a ‘level of no motion’. Changes in sea level and dynamic height should have similarities but the latter is a measure of the upper-ocean baroclinic structure only.
- EARTH TIDE:** tidal movements of the solid Earth, due to direct gravitational forcing and loading of the adjacent seabed by marine tides.
- EBB CURRENT:** the movement of a **TIDAL CURRENT** away from the shore or down a tidal river or estuary.
- EKMAN PUMPING:** a vertical circulation in the ocean arising from frictional stress between winds and the ocean surface (as in **EKMAN TRANSPORT**). Cyclonic winds induce an upwelling called *Ekman pumping*, and anticyclonic winds a downwelling called *Ekman suction*.
- EKMAN TRANSPORT:** the ocean transport resulting from a balance between the Coriolis force and the frictional stress due to the action of the wind on the ocean surface.
- EL-NIÑO–SOUTHERN OSCILLATION:** a coupled atmosphere–ocean phenomenon every 3 to 7 years that consists of a weakening of the trade winds, modifications to tropical air pressure patterns (the Southern Oscillation), warming of the tropical eastern Pacific, and an exchange of many decimetres of sea level from the western to the eastern Pacific by equatorial **KELVIN WAVES**. In between El Niño events, La Niña conditions can take place with lower than normal temperatures in the eastern tropical Pacific.
- EMISSION SCENARIO:** an estimate of the future emissions of greenhouse gases and aerosols as used in projections of future climate by study groups such as the IPCC. See also **REPRESENTATIVE CONCENTRATION PATHWAY**.
- EMPIRICAL ORTHOGONAL FUNCTION:** In sea-level studies, Empirical Orthogonal Function (or Principal Component) analysis is a statistical technique for decomposing the spatial and temporal variability of sea level in terms of a set of independent basis functions, each of which is associated with a time series and spatial pattern. Most of the variance in a data set will usually be accounted for by a small number of the most important EOFs.
- ENTRAINMENT:** stimulation of an organism by local environmental factors, to adopt a new phase in its cycle of behaviour. For example, a short cold treatment in the laboratory can initiate new tidal rhythms in crabs that have become inactive.

- EQUATION OF TIME:** the difference between apparent and mean solar time at the same longitude due to the Earth's elliptical orbit around the Sun; mean time now being the standard form of time for civil use.
- EQUILIBRIUM TIDE:** the hypothetical tide that would be produced by the lunar and solar tidal forces in the absence of ocean constraints and dynamics.
- EQUINOXES:** the two points in the celestial sphere where the celestial equator intersects the ecliptic; also the times when the Sun crosses the equator at these points. The vernal equinox is the point where the Sun crosses the equator from south to north and it occurs about 21 March. Celestial longitude is reckoned eastwards from the vernal equinox, which is also known as the *First Point of Aries*. The autumnal equinox occurs about 23 September. The larger solar contribution to the SEMIDIURNAL TIDES leads to large tides at these times, known as *equinoctial tides*.
- EULERIAN CURRENT:** flow past a fixed point as measured, for example, by a moored current meter.
- EUSTATIC SEA-LEVEL CHANGES:** either (1) the global-average change in sea level, or (2) that part of sea-level change due to changes in ocean mass (e.g. from ice sheet melting). It has been suggested that, because of the different definitions, this expression be no longer used.
- EVECTION:** the effect of the Sun's gravity on the ellipticity of the Moon's orbit.
- FINGERPRINT:** the spatial pattern in sea-level variability that can be identified with either a geophysical process (e.g. response of the solid Earth due to removal of ice loads) or a mode of ocean circulation variability.
- FIRST POINT OF ARIES:** see EQUINOXES.
- FLOOD CURRENT:** the movement of a TIDAL CURRENT towards the shore or up a tidal river or estuary.
- GEOCENTRIC SEA LEVEL:** sea level measured by a satellite altimeter with respect to the centre of the Earth, or more often with respect to an Earth-centred standard ellipsoid. These measurements are usually referred to as *geocentric sea surface heights*.
- GEOID:** an equipotential surface of the gravity field that would be equivalent to (or closely parallel to) the sea surface that would exist if there were no oceanographic contributions to the MEAN SEA SURFACE. The potential of this surface is denoted by geodesists as W_0 . It varies above and below the geometrical ellipsoid of revolution by as much as 100 m due to the uneven distribution of mass within the Earth. The mean sea-level surface varies about the geoid by typically decimetres, but in some cases by more than a metre.
- GEOMETRICAL SPREADING:** the reduction in amplitude of a tsunami wave due to its progressive expansion from its source.
- GEOSTROPHY:** the balance on a rotating Earth between the Coriolis force due a current (or wind) and the cross-current horizontal pressure gradient. The speed of the current is proportional to the gradient.
- GLACIAL ISOSTATIC ADJUSTMENT:** the deformation of the solid Earth accompanying the response of the Earth–ocean system to the removal (or addition) of ice loads. GIA affects sea and land levels around the world. It was formerly referred to as *post-glacial rebound*, an expression which gave the false impression that GIA is confined to the previously loaded areas.
- GLOSS:** the Global Sea Level Observing System network of sea-level gauges coordinated by the Intergovernmental Oceanographic Commission. One purpose of GLOSS is to monitor long-term variations in the global level of the sea surface, by reporting sea-level observations to the PERMANENT SERVICE FOR MEAN SEA LEVEL and other agencies.
- GNSS:** a satellite-based Global Navigation Satellite System capable of accurately locating points in a three-dimensional geometric framework. The most developed GNSS is the US military Global Positioning System (GPS).
- GRADIOMETRY:** the technique of using pairs of accelerometers on satellites such as GOCE to measure gradients of the gravity field.
- GRAVITATION, NEWTON'S LAW OF:** states that all particles in the universe are attracted to other particles with a force that is proportional to the product of their masses and inversely proportional to their distance apart squared.
- GREENHOUSE EFFECT:** the effect, analogous to that which operates in a greenhouse, whereby because of atmospheric effects the Earth's surface is maintained at a much higher temperature than that appropriate to balance the incident solar radiation. Solar radiation penetrates the atmosphere, but some of the longer-wavelength return radiation is

- absorbed by the water vapour, carbon dioxide, ozone, trace gases and aerosols in the atmosphere. Observed increases in the concentrations of atmospheric carbon dioxide due to the burning of fossil fuels, and of other components, could lead to a steady increase of global temperatures: the resulting thermal expansion of the oceans and the melting of ice caps would increase sea levels. Concern about possible coastal flooding due to this increase has stimulated recent research into climate dynamics.
- GREENWICH MEAN TIME:** time expressed with respect to the Greenwich meridian (zero degrees longitude), often used as a standard for comparisons of global geophysical phenomena, including tidal constituents. More correctly called *Universal Time (UT)*.
- HARBOUR OSCILLATIONS:** see SEICHE and TSUNAMI.
- HARMONIC ANALYSIS:** the representation of tidal variations as the sum of several harmonics, each of different period, amplitude and phase. The periods fall into three *tidal species*: long period, diurnal and semidiurnal. Each tidal species contains *groups* of harmonics, which can be separated by analysis of a month of observations. In turn, each group contains *constituents*, which can be separated by analysis of a year of observations. In shallow water, harmonics are also generated in the third-diurnal, fourth-diurnal and higher species. These constituents can be used for harmonic prediction of tides.
- HEAD:** the difference in water level at either end of a strait, channel, inlet, etc.
- HEAD OF TIDE:** the upstream or inland extreme of tidal influence; sometimes called *fall line*.
- HIGH WATER:** the maximum water level reached in a tidal cycle.
- HIGHER HIGH WATER (HHW):** the highest of the high waters (or single high water) of any specified tidal day due to the enhanced diurnal declinational effects of the Moon and Sun.
- HIGHER LOW WATER (HLW):** the highest of the low waters of any specified tidal day due to the reducing declinational effects of the Moon and Sun.
- HIGHEST ASTRONOMICAL TIDE:** the highest tidal level that can be predicted to occur under any combination of astronomical conditions.
- HYDRAULIC CURRENT:** a current in a channel caused by a difference (sometimes called *head*) in the surface elevation at the two ends. Such a current may be expected in a strait connecting two bodies of water in which the tides differ in time or range. The current in the East River, New York, connecting Long Island Sound and New York Harbour, is an example.
- HYDRODYNAMIC LEVELLING:** the transfer of SURVEY DATUM levels by comparing MEAN SEA LEVEL at two sites, and adjusting them to allow for gradients on the sea surface due to currents, water density, winds and atmospheric pressures.
- INDIAN OCEAN DIPOLE:** Interannual variability in east–west gradients of sea surface temperature in the tropical Indian Ocean.
- INDIAN SPRING LOW WATER:** a tidal low water datum, designed for regions of mixed tides, which is depressed below MEAN SEA LEVEL by the sum of the amplitudes of the principal semidiurnal lunar and solar tides and the principal diurnal tides ($M_2 + S_2 + K_1 + O_1$); originally developed for parts of the Indian Ocean.
- INTERGLACIAL:** the warm period between ice age glaciations when sea level was close to that at present. The last interglacial (the Eemian) occurred between about 130,000 and 114,000 years BP. The present interglacial is called the Holocene and started about 12,000 BP although sea levels did not become close to those of today until about 7000 BP.
- INTERNAL TIDE:** tidal waves that propagate at density differences within the ocean. They travel slowly compared with surface gravity waves and have wavelengths of only a few tens of kilometres, but they can have amplitudes of tens of metres. The associated internal currents are baroclinic motions.
- ISOSTATIC:** an adjective referring to an equilibrium between two loads, such as between atmosphere and ocean in the LOCAL INVERSE BAROMETER, or in the asymptotic response of the solid Earth to changes in loads in GLACIAL ISOSTATIC ADJUSTMENT.
- KELVIN WAVE:** a long wave in the oceans whose characteristics are altered by the rotation of the Earth, and constrained by a lateral boundary. Tidal progression is mainly by Kelvin waves. In the northern hemisphere the amplitude of the wave decreases from right to left along the crest, viewed in the direction of wave travel.
- LAGRANGIAN CURRENT:** the movement through space of a particle of water as measured by drogues or drifting buoys.

LOCAL ESTABLISHMENT or LUNITIDAL

INTERVAL: an old term for the interval of time, at a particular location, between the transit (upper or lower) of the Moon and the next semidiurnal high water. This varies slightly during a spring–neap tidal cycle. The interval at the times of full and new Moon is called *high water full and change*. See also NON-HARMONIC TIDAL ANALYSIS.

LOCAL INVERSE BAROMETER

RELATIONSHIP: a description of an increase of air pressure of 1 mbar resulting in an approximately 1 cm fall in sea level, such that there is no change in sub-surface pressure.

LONG WAVE: a wave whose wavelength from crest to crest is long compared with the water depth.

Tides propagate as long waves. The speed of travel is given by the square root of (water depth \times gravitational acceleration) ($c = \sqrt{gD}$).

LOW WATER: the minimum water level reached in a tidal cycle.

LOWER HIGH WATER (LHW): the lowest of the high waters of any specified tidal day due to the reducing declinational effects of the Moon and the Sun.

LOWER LOW WATER (LLW): the lowest of the low waters (or single low water) of any specified tidal day due to the enhancing declinational effects of the Moon and the Sun.

LOWEST ASTRONOMICAL TIDE: the lowest level that can be predicted to occur under average meteorological conditions and under any combination of astronomical conditions; often used to define CHART DATUM.

LUNAR DAY: the time of the rotation of the Earth with respect to the Moon. The mean lunar day is approximately 1.035 times the mean solar day.

LUNAR TRANSIT: passage of the Moon over the local meridian; when it passes through the observer's meridian it is called the *upper transit*, and when it passes through the same meridian but 180 degrees from the observer's position it is called the *lower transit*.

MAELSTROM: a tidal whirlpool found between the islands of Moskenesy and Mosken in the Lofoten Islands of northern Norway. The term is generally applied to other tidal whirlpools.

MEAN DYNAMIC TOPOGRAPHY: the difference between the MEAN SEA SURFACE and the GEOID. The MDT has values of order ± 1 m throughout the ocean.

MEAN HIGH WATER: the average of high water values over a specified period.

MEAN HIGH WATER SPRINGS: average SPRING TIDE high water level, averaged over a sufficiently long period.

MEAN HIGHER HIGH WATER: a tidal datum; the average of the higher high water height of each tidal day, averaged over the United States NATIONAL TIDAL DATUM EPOCH.

MEAN LOW WATER SPRINGS: a tidal datum, the average SPRING TIDE low water level averaged over a sufficiently long period.

MEAN LOWER LOW WATER: a tidal datum, the average of the lower low water height of each tidal day observed over the United States NATIONAL TIDAL DATUM EPOCH.

MEAN SEA LEVEL: sea level measured continuously by a tide gauge with respect to the height of a TIDE GAUGE BENCH MARK and averaged over a specified period such as a month or year. MSL measured over an extended period such as 19 years has often been used as a national SURVEY DATUM to which heights in a country are referred.

MEAN SEA LEVEL TRENDS: changes of mean sea level at a site over long periods of time, typically decades, also called *secular changes*.

MEAN SEA SURFACE: A map of the average height of the surface of the ocean obtained by altimetry, averaged over a stated period and expressed relative to the STANDARD ELLIPSOID.

MEAN TIDE LEVEL: the arithmetic average of MEAN HIGH WATER and MEAN LOW WATER. This level is not identical with MEAN SEA LEVEL because of higher harmonics in the tidal constituents.

MESOSCALE VARIABILITY: the variations in sea level throughout the ocean on timescales of 10–100 days and space scales of 50–500 km associated with eddies, meanders of ocean currents and instabilities of frontal systems.

METEOTSUNAMI: a tsunami-like LONG WAVE caused by a meteorological disturbance that propagates to a coastline where it may be amplified by local resonances and result in coastal flooding.

METEOROLOGICAL TIDE: see RADIATIONAL TIDE.

MIXED TIDE: a tidal regime where both the diurnal and semidiurnal components are significant.

MONSOON SEASONAL REVERSING: seasonal reversing of tropical and sub-tropical winds and

- associated changes in precipitation and ocean circulation. Monsoons are caused by differential heating between the continents and ocean and are observed primarily in Africa, Indian Ocean, Asia and Australia.
- NATIONAL TIDAL DATUM EPOCH:** the specific 19-year period adopted by the National Ocean Service (United States) as the official time segment over which sea-level observations are taken and reduced to obtain mean values for datum definition. The present Epoch is 1983 through 2001. It is reviewed annually for revision and must be actively considered for revision every 25 years.
- NEAP TIDE:** tide of small range, which occurs twice a month when the Moon is in QUADRATURE.
- NODAL FACTORS:** small adjustments to the amplitudes and phases of harmonic tidal constituents to allow for modulations over the 18.61-year, the period of a nodal tidal cycle.
- NODAL TIDE:** a long period astronomical tide with a period of 18.61 years.
- NON-HARMONIC TIDAL ANALYSIS:** analysis and prediction using traditional methods such as the LOCAL ESTABLISHMENT.
- NON-TIDAL RESIDUAL (or simply RESIDUAL):** that part of the observed sea level due to weather and other non-tidal effects. Sometimes assumed to be the same as SURGE, but could include other effects such as SEICHES and TSUNAMIS.
- NORTH ATLANTIC OSCILLATION:** variations in air pressure difference between Iceland and the Azores and the associated fluctuations in the strength of westerly winds across the Atlantic.
- NUMERICAL MODELLING:** numerical simulation of the changes in the oceans or climate system by means of solution of sets of equations that contain the physical laws that govern motions and fluxes.
- ORTHOMETRIC HEIGHT:** height above the GEOID (or sometimes used for height above a national height system).
- PERIGEAN TIDE:** tide of increased range when the Moon is near perigee, its nearest approach to the Earth in its elliptical orbit. The effect is particularly evident in the tides along the east coast of Canada and the United States.
- PERIHELION:** the nearest approach to the Sun in the Earth's orbit; at present near 4 January.
- PERMANENT SERVICE FOR MEAN SEA LEVEL:** the organisation responsible for collection, analysis, interpretation and publication of mean sea-level data from a global network of gauges. PSMSL is a member of the World Data System of the International Council for Science.
- POLE TIDE:** small variations in sea level due to the Chandler Wobble of the axis of rotation of the Earth. This has a period close to 436 days and maximum amplitudes of several millimetres at 45° N/S. (The pole tide is not an astronomical tide.) Anomalous larger amplitudes are observed in the North and Baltic Seas.
- POINCARÉ WAVE:** general solutions to gravity wave dynamics in the ocean on a rotating Earth. Within a channel in a rotating system, a Poincaré wave has sinusoidally varying cross-channel velocity with an integral or half-integral number of cross-channel waves spanning the channel.
- PRESSURE TIDE GAUGES:** instruments that measure the pressure below the sea surface; this pressure may be converted to sea levels if the air pressure, the gravitational acceleration and the water density are known.
- PROCESS-BASED MODEL:** a numerical model that simulates the global climate system based on a set of functional components and their interactions with each other. Also called an *Atmosphere Ocean General Circulation Model*.
- PROGRESSIVE WAVE:** a wave whose travel can be followed by monitoring the movement of the crest. Energy is transmitted but the water particles perform oscillatory motions. See also KELVIN WAVE.
- QUADRATURE OF MOON:** position of the Moon when its longitude differs by 90° from the longitude of the Sun. The corresponding phases are known as first quarter and last quarter.
- RADIATIONAL TIDE:** tide generated by regular periodic meteorological forcing. These are principally at annual, daily and twice-daily periods.
- RANGE:** the difference between high and low water in a tidal cycle. Ranges greater than 4 m are sometimes termed *macrotidal* and those less than 2 m are termed *microtidal*. Intermediate ranges are termed *mesotidal*.
- RECTILINEAR CURRENT:** see REVERSING CURRENT.
- RELATIVE SEA LEVEL:** sea level measured by a TIDE GAUGE relative to a local TIDE GAUGE BENCH MARK on the nearby land. Changes include both local vertical land movements, and local sea-level changes.

REPRESENTATIVE CONCENTRATION

PATHWAY: A scenario of a time line of emissions of greenhouse gases, aerosols and chemically active gases, as well as changes in land use, as used by the IPCC to make projections of climate change.

RESONANCE: the phenomenon of the large amplitudes that occur when a physical system is forced at its natural period of oscillation. Tidal resonance occurs when the natural period of an ocean or sea is close to the period of the tidal forcing.

RESPONSE ANALYSIS: the representation of observed tidal variations in terms of the frequency-dependent amplitude and phase responses to input or forcing functions, usually the gravitational potential due to the Moon and Sun, and the radiational meteorological forcing.

RETURN PERIOD: the average time between events such as the flooding of a particular level. This information may also be expressed as the level that has a particular return period of flooding, for example, 100 years. The inverse of the return period is the statistical probability of an event occurring in any individual year.

REVERSING CURRENT: a TIDAL CURRENT that flows alternately in approximately opposite directions with a slack water at each reversal of direction. Also known as a *rectilinear current*.

REVISED LOCAL REFERENCE: the subset of the PERMANENT SERVICE FOR MEAN SEA LEVEL data set in which the time series of MEAN SEA LEVEL at each station is expressed relative to a consistent datum for that station.

ROTARY CURRENT: a TIDAL STREAM that flows continuously with the direction of flow changing through all points of the compass during a tidal cycle. Found away from coastal or shallow water flow restrictions, where REVERSING CURRENTS are more probable.

RUNUP: the maximum height above MEAN SEA LEVEL that a TSUNAMI floods the land. The phase of runup starts when the wave shoals and breaks and ends when the water has reached its highest level.

SATELLITE ALTIMETRY: a space method for measuring the vertical range between a satellite and the sea (or land, lake or ice) surface using radar or laser techniques. If the height of the satellite is known with respect to the centre of the Earth, then the range measurement provides GEOCENTRIC SEA LEVEL.

SEA LEVEL: the level of the sea after averaging out the short-term variations due to wind waves. Also called *water level* in the United States.

SEA-LEVEL COMMITMENT: the ongoing rise of sea level that would occur for many hundreds of years due to the thermal inertia of the ocean and slow processes in the cryosphere, even if greenhouse gas emissions are stabilised at some point.

SEA-LEVEL RECONSTRUCTION: an attempt to estimate a long time series of regional or global-average sea level based on a inhomogeneous sea-level data set.

SEA-LEVEL MEASUREMENTS: may be made in many ways. In all cases some means of averaging out the effects of waves is necessary. For the reading of tide poles the averaging is by eye; in STILLING WELLS the waves are damped out by a narrow constriction; acoustic, fixed radar and PRESSURE GAUGES may apply electronic averaging to rapid samples; SATELLITE ALTIMETRY is corrected for general wave conditions within the footprint of the transmission.

SEA-LEVEL RISE: long-term increases of MEAN SEA LEVEL. The expression is popularly applied to anticipated increases in sea level due to the GREENHOUSE EFFECT and associated global warming.

SEA SURFACE HEIGHT: the term often used for sea levels measured by SATELLITE ALTIMETRY.

SEDIMENT TRANSPORT: the total sediment transported by a current is the sum of the *bed load*, material partly supported by the bed as it rolls or bounces along, and the *suspended load* in the water.

SEICHE: the oscillation of a body of water at its natural period set in motion by a meteorological or other disturbance. Coastal measurements of sea level often show seiches with amplitudes of a few centimetres and periods of a few minutes due to oscillations of the local harbour, estuary or bay, superimposed on the normal tidal changes.

SEMIDIURNAL TIDE: tidal change of level twice in a lunar day. Worldwide, semidiurnal tides are the most important because the global ocean is near to resonance at the period of semidiurnal gravitational forcing.

SEMI-EMPIRICAL MODEL: a parameterisation of historical sea-level change, primarily in terms of global or regional temperature change, with the aim of estimating future sea-level change from predicted temperatures.

- SET:** the direction to which a current flows.
- SHOALING:** the amplification of a TSUNAMI wave from the time when it enters depths of 100 m or so, typical of a continental shelf, up until the time that it impacts a shoreline. The velocities and wavelengths of shoaling waves reduce as their amplitudes increase.
- SIDEREAL DAY:** the period of rotation of the Earth with respect to the vernal equinox (approximately 0.99727 of a mean solar day).
- SKREW SURGE:** The difference between the maximum sea level recorded by a tide gauge during a STORM SURGE event around the time of tidal high water and the predicted high water level from the astronomical tide during the same event (the two maxima not necessarily coinciding exactly in time).
- SLACK WATER:** the state of a tidal current when its speed is near zero, especially the moment when a reversing (rectilinear) current changes direction and its speed is zero. For a theoretical standing tidal wave, slack water occurs at the times of high and of low water, while for a theoretical progressive tidal wave, slack water occurs midway between high and low water.
- SOURCE FUNCTION:** a map of sea-floor displacements arising from a submarine earthquake.
- SPACE GRAVITY:** a general term for space techniques for measuring the gravity field at the altitude of a satellite and thereby inferring the gravity field at sea level. Higher-flying but longer duration missions such as GRACE provide information on the changes from month to month in the distribution of mass in the ocean, as well as in the cryosphere and hydrosphere, and changes in the gravity field due to processes in the solid Earth. Lower-flying but shorter duration missions such as GOCE provide high spatial resolution ‘snapshots’ of the gravity field.
- SPRING TIDE:** SEMIDIURNAL TIDE of large range, which occurs twice a month when the Moon is new or full.
- STANDARD ELLIPSOID:** first-order description of the shape of the Earth expressed in terms of an equatorial radius and flattening coefficient.
- STANDING WAVE:** wave motion in an enclosed or semi-enclosed sea, where the incident and reflected progressive waves combine to give a node of zero tidal amplitude. Maximum tidal amplitudes are found at the head of the basin where reflection occurs. No energy is transmitted in a standing wave, nor is there any progression of the wave pattern.
- STERIC SEA-LEVEL CHANGES:** changes in sea level resulting from changes in water density. Those caused by temperature changes only are called *thermosteric* changes, while those caused by changes in salinity are called *halosteric* changes.
- STILL WATER LEVEL:** the total observed sea level from all processes (tide, surge, MSL etc.) but not including wind waves.
- STILLING-WELL GAUGES:** instrument system for measuring sea levels; tidal changes of levels are detected by the movement of a float in a well, which is connected to the open sea by a restricted hole or narrow pipe. Wind waves are eliminated by the constriction of the connection.
- STOLEN TIDE:** a tide that approaches by stealth; particularly a local term for the high tides that creep up the gullies and marshes of coastal Lincolnshire, England.
- STORM TIDE:** the sum of a STORM SURGE and astronomical tide.
- SUB-SURFACE PRESSURE:** the pressure that would be measured by a pressure sensor at a fixed point just below low tide.
- SURGE or STORM SURGE:** the changes of sea level in coastal waters caused by winds and air pressures acting on the sea surface. A positive surge refers to an increased sea level. A storm surge event or storm tide event is an occasion with a particularly large positive storm surge.
- SURVEY DATUM:** the datum to which levels on land surveys are related; often defined in terms of a MEAN SEA LEVEL. Survey datum is a horizontal surface to within the accuracy of the survey methods.
- SYZYGY:** astronomical condition of alignment of the Earth, Moon and Sun at new and full Moon, the time of maximum spring tidal forcing. Also useful for crossword puzzles.
- TERRESTRIAL REFERENCE SYSTEM:** a set of definitions and mathematical models that allow geodetic measurements to be related to each other in a systematic fashion. A terrestrial reference frame is the practical realisation of a system in terms of coordinates and motions of networks of Reference Stations.
- TIDAL CURRENT:** periodic tidal water movement. See also TIDAL STREAM.
- TIDAL CONSTITUENT:** see HARMONIC ANALYSIS.

- TIDAL EXCURSION:** the Lagrangian movement of a water particle during a tidal cycle.
- TIDAL PRISM:** the volume of water exchanged between a lagoon or estuary and the open sea in the course of a complete tidal cycle.
- TIDAL PUMPING:**
- The net flux of some property, heat, salinity, sediment for example, over several tidal cycles, due to the concentrations being different in the ebb and flow parts of the cycle.
 - Spring tidal pumping is the increase in mean water level of a tidal basin in response to the larger tidal forcing of the **SPRING TIDE**.
- TIDAL RANGE:** the difference between low and high water tidal levels, equal to twice the tidal amplitude.
- TIDAL STREAM:** horizontal water movements due to tidal forcing. Also known as **TIDAL CURRENT**.
- TIDE GAUGE:** a device for measuring sea level with respect to a **TIDE GAUGE BENCH MARK** on the nearby land. Tide gauges are available based on float, pressure, acoustic, radar and other technologies, with different techniques appropriate to different applications.
- TIDE GAUGE BENCH MARK:** a stable benchmark near a gauge, to which *tide gauge datum* is referred. It is connected to local auxiliary benchmarks to check local stability and to guard against accidental damage. Tide gauge datum is a horizontal plane defined at a fixed arbitrary level below a Tide Gauge Bench Mark.
- TIDES:** periodic movements that have a coherent amplitude and phase relationship to some periodic geophysical force.
- TIDEWATER:** water affected by tidal influences, especially in coastal and estuarine regions.
- TRAVEL-TIME CHART:** a map showing the time of the leading wave and height of a **TSUNAMI** at points in the ocean.
- TSUNAMETER:** a bottom pressure recording system installed on the seabed and connected via an acoustic link to a surface buoy with a satellite transmitter that enables real-time values of bottom pressure to be sent to tsunami warning centres.
- TSUNAMI:** a series of long waves propagating across the ocean as a consequence of the displacement of large volumes of water due to submarine Earthquakes, landslides or volcanoes.
- VANISHING TIDE:** period when the local semidiurnal and diurnal tidal constituents conspire to give several hours of relatively constant sea level.
- VERNAL EQUINOX:** see **EQUINOXES**.
- WATER LEVEL:** a term used synonymously with **SEA LEVEL**, especially in the United States.
- WENTWORTH SCALE:** used to classify sediments in terms of their particle sizes.
- WIND STRESS:** the shear force exerted by the wind on the ocean surface.
- WIND STRESS CURL:** a measure of the angular momentum of the wind field that relates to the 'spinning up' of the ocean circulation.
- ZONATION:** the pattern of colonisation of the sea shore, whereby individual species flourish in bands associated with particular tidal levels.
- Where applied, the exact legal tidal definitions vary from country to country. More extensive lists are found in the following publications:
- Hicks S. D. 1999. *Tide and Current Glossary*. Washington, D.C.: U.S. National Oceanic and Atmospheric Administration.
- International Hydrographic Organization. 1994. *Hydrographic Dictionary*. Special Publication No. 32, 5th edition. Monaco: International Hydrographic Organization.

Index

- abiki waves, 171
Absolute Gravity, 299
Absolute Gravity meter, 300
acoustic tide gauges, 27
adaptation of species, 350
ADCs, 212
Admiralty, 92, 94, 141
Adriatic Sea, 170, 304
aerial photography, 377
age of the tide, 9, 61, 76, 97, 152
Agung volcanic eruption, 277
Aila, Cyclone, 355
Alaska, 196, 357, *see also* Cook Inlet
Alaska earthquake, 196
Aldabra Island, 168
Aleutian Islands, 190
altimeter missions, 230
altimetry
 corrections, 229
 dry, 226
 ionospheric, 226
 mapping functions, 226
 sea state bias, 229
 total electron content, 226
 wet, 226
 data assimilation, 77
 for MSL, 254
 for surge monitoring, 161
 for tsunami detection, 212
 MSL trends, 275
 orbit accuracy, 228
 orbit repeat periods, 229
Amazon river, 146, 147, 278
amphidromes, 105, 120, 151
analysis
 altimeter data, 77
 currents, 82, 363
 economics, 346
 harmonic, 62, 77, 139
 higher harmonics, 136
 non-harmonic, 61
 response, 78, 139
 rotary currents, 86, 364
 tidal comparisons, 81
 tidal errors, 88
Andaman fault, 194
Andaman Sea, 167
Andes chain, 306
angular speeds, 64
Annapolis power station, 332
annular sea-level variability, 178
Antarctic Circumpolar Current, 30, 97,
 178, 240, 254, 266
Antarctica, 178, 266, 277, 282, 310
Antarctica, ice storage, 279, 301, 308
anti-amphidrome, 108
antinodes, 372
apogee, 45, 52
Aquatic Ape hypothesis, 345
Arabian Sea, 258
archaeological MSL surveys, 304
Archaen period, 345
Arctic Ocean, 110, 111, 178,
 240, 309
Arctic Oscillation, 178, 264
Argentina, 119, 334, 379
Argentine Basin, 180
Argo floats, 279, 280, 281
Argos data transmission, 279
Ascension Island, 122, 123
astronomical
 basic periods and frequencies, 49
 constants, 37
 energy sources, 151
asymmetry, 39
 statistical skewness, 144
 tidal
 ebb and flow, 142, 143
 level pdfs, 143
 St Lawrence river, 145
Atlantic Meridional Overturning
 Circulation, 266, 275, 309
Atlantic Ocean perigean tides, 52, 109
Atlantis, 352
atmospheric pressure, 7, 155, 262, *see*
 also inverted barometer
atmospheric tide, 80
Average Recurrence Interval (ARI), 320
Aysén fjord, Chile, 197

B Gauge datum control, 27
Balearic islands, 169
Baltic Sea, 170, 258, 260, 262, 304, 328,
 385
Bangkok, 296
Bangladesh, 165, 337, 339, 355, 357
baroclinic tides, 124
barotropic hot spots, 175
barotropic models, 155, 159
barystatic mass change, 279
bathymetry, 111, 120, 161, 175, 200,
 202, 243, 264, 312, 372
Batticaloa Lagoon, 331
Battle of Maldon, 352
Bay of Bengal, 108, 157, 210, 252, 257,
 307
Bay of Fundy, *see* Fundy, Bay of
Beaufort Scale, 157
Bede, 94, 99
benthic boundary layer, 139
Bermuda, 3, 51, 124, 267
Bernoulli, Daniel, 2, 61
bird feeding patterns, 333, 335, 348
black box analysis, 78
Black Sea, 110, 258, 352
bleaching of coral reefs, 350
body tide, 127
bolides, 197
bore, tidal, 94, 147, 148, 354
Boston, United States, 261
bottom friction, 134, 149, 151,
 156, 329
bottom pressure from GRACE, 278
Boussinesq models, 205
Bragg reflection, 212
Brazil, 108, 119
Brazil–Malvinas Confluence, 254
Brest, 129, 273
Bristol Channel
 large tidal range, 3
 modelling, 160
 power schemes, 334
 resonance, 114
Broadband Global Area Network, 209
Bronze Age, 351
Bruun, Per
 coastal MSL changes, 313
 Rule, 313, 357
buddy checking, 32
Buenos Aires, 167, 340
Bureau Gravimétrique International,
 235
Burma, 7, 157

California, 357
Californian coast, 112, 125, 233, 258
Cape Hatteras, 115
carbon sequestration, 346
Caribbean, *see* Gulf of Mexico
Carpentaria, Gulf of, 5, 98, 118

- Cartwright, David, 63, 261, 352
 Chagos Islands, 266
 CHAMP, 236
 Chandler Wobble, 260, 261
 Chart Datum, 21, 57, 76, 89
 Chicxulub, Mexico, 197
 Chile, 201
 climate change, 276, 280, 324, 326, 341, 345, 357
 predictions, 283
 projections, 283
 CNES, 227
 co-amplitude lines, 98, 99, 105, 138, 374
 coastal
 defences, 327
 dynamics, 310
 flooding, 311, 319, 338
 MSL, 272
 ownership, 377
 squeeze, 337
 tides, 133
 Cocos Islands, 258
 colatitude, 238
 Colombo, Sri Lanka, 208
 Common Law, 377
 COMPASS, 212, 224
 compensation habitats, 329
 Concepción, Chile, 305
 conservation of mass, 156, 361
 constituent, tidal, 64, 100
 Cook Inlet, Alaska, 119, 335
 Coordinated Universal Time, 86, *see also* [Greenwich Mean Time](#)
 coral reefs, 335, 349
 Corinth landslide, 195
 Coriolis acceleration, 99, 105, 156, 175, 256, 362
 cost-benefit analyses, 342
 co-tidal lines, 98, 99, 105, 138, 374
 Courtown, 6, 51, 71, 77, 138, 151
 credo of smoothness, 78
 Critical Tidal Levels, 346
 currents
 analysis, 82, 363
 bottom friction, 139
 Brazil–Malvinas Confluence, 175
 coastal, 22
 coastal curvature, 135
 data processing, 31
 depth mean, 120
 direction convention, 31, 83, 120
 eddies, 242
 ellipse rotation, 120
 ellipses, 86, 363
 Eulerian, 141
 extreme, 326
 flood and the ebb, 135
 in channels, 140, 141, 348
 internal tides, 125
 Lagrangian, 141
 power generation, 333
 profile, 139
 radar measurements, 212
 shelf tides, 112, 119
 tidal
 residual, 141
 streams, 6, 119
 variability, 88
 daily tidal harmonics, 138
 damped oscillation, 329
 DART buoys, 206, 210, 212
 Darwin, Charles, 305
 Darwin, George, 63
 data
 archaeology, 34, 275
 assimilation, 161
 reduction, 31
 datum
 categories, 20
 definitions, 20
 legal definitions, 376
 David Copperfield, 354
 D-Day landings, 352
 Delta Works, Netherlands, 328
 Den Helder, 273
 design encounter probability, 322
 design guidelines, 319
 Dessiou, Joseph, 61
 Dickens, Charles, 354
 Diego Garcia, Chagos Archipelago, 356
 digital filters, 252
 diminishing factor, 256, 261
 diurnal tidal species, 44
 Doodson, Arthur, 33, 63, 68
 Doppler current measurements, 82
 DORIS, 223, 227, 228, 300
 Double Differencing, 226
 double high and low waters, 6, 133, 138
 drag coefficient, 134
 Drake Passage, 97, 180, 201, 202, 229
 drift of a ship, 83
 dynamic height, 240
 Earth
 altimetry tide correction, 232
 elastic response, 127
 geocentric coordinates, 126
 geodesy, 223
 gravity field, 234
 internal density structure, 129
 MSL responses, 301
 orbit changes, 345
 permanent tidal deformation, 232
 rotation, 36, 48, 62, 98, 103, 107, 112, 140, 362, 373
 slowing rotation, 151
 surface heat flux, 152
 tectonic MSL changes, 303
 tides, 7, 73, 78, 99, 107, 126, 151
 vertical crustal movement, 297
 earthquake
 2010, Chile, 307
 magnitude, 189, 195
 submarine, 193
 Easter tides, 147, 354
 eccentricity of current ellipses, 364
 eccentricity of orbits, 46
 ECDIS, 94
 eclipses, 152
 ecliptic reference system, 44
 economic analyses, 337, 341
 ecosystem services, 346
 eddy kinetic energy, 256
 eddy viscosity, 107
 edge waves, 112, 167, 173
 Eemian interglacial epoch, 268, 280
 Ekman
 dynamics, 140, 366
 layer, 366
 pumping, 175, 263
 spiral, 365, 366
 transport, 175, 365
 El Chichón volcanic eruption, 277
 El Niño, *see* [ENSO](#)
 electrical circuit analogy, 329
 electromagnetic reflection gauges, 28
 Electronic Chart Display, 94
 elliptic reference system, 45
 ellipsoid of revolution, 21
 ellipsoid, standard, 226, 227
 ellipsoidal heights, 226
 Eltanin asteroid impact, 198
 emersion curves, 335
 emersion–submersion, 335
 empirical orthogonal functions, 272
 energy
 flux comparisons, 332
 tidal dissipation, 124
 tidal fluxes, 149
 English Channel, 2, 6, 113, 120, 124, 136, 138, 139, 142
 ENSO, 162, 252, 264, 265, 275, 276
 environmental services, 318
 epifauna, 348
 Equation of Time, 46, 47
 equatorial
 atmospheric tide, 123
 baroclinic wave, 181
 Kelvin waves, 264
 plane, 39, 62
 radius, 226
 reference system, 44
 solar orbit, 52
 tides, 50
 Equilibrium Tide, 43, 48, 56, 60, 62, 73, 78, 79, 82, 97, 109, 123, 127, 152, 256, 260, 261
 extremes, 54

- equinoctial tides, 53, 69
 equipotential surface, 233
 ERS/Envisat, 77, 78, 212, 232, 301
 Esperance, Australia, 169
 Eulerian
 currents, 141
 reference frame, 362
 Europa, 40
 European Floods Directive, 328
 eustatic
 ambiguity, 382
 IPCC meaning, 279
 evection, 64
 explosion, tsunami generation, 198
 exposure curves, 335
 Extended Doodson Number, 65, 68
 extra-tropical surges, 157, 339
 extreme
 currents, 326
 repeat coincidence tides, 56
 sea levels, 7, 162, 286, 319
 tidal distortions, 133
 tidal forces, 53

 Falkland Islands, 143, 167, 168, 205, 206, 263, 274
 seiches, 167
 fiddler crab, 350, 351
 Fiji, 354
 fingerprinting, 275, 283, 308
 finite-difference modelling, 161
 finite-element modelling, 161
 First Point of Aires, 44, 45, 71
 fish traps, 351
 five-day waves, 179
 Flamsteed, John, 94
 Flanders Marine Institute, 209
 flooding, 1, 7, 22, 53, 94, 129, 157, 158, 197, 311, 319, 326, 337, 338, 352, 354, 355, 356
 Florida, 172
 footprint of altimeter, 227
 foreshore, 335, 337, 376, 377
 form factors for tides, 77
 Fourier analysis, 12
 Fourier transform, 79
 Froude number, 148
 Fundy, Bay of, 3, 97, 117, 122, 334, 335, *see also* Minas Basin

 GALILEO, 212, 224
 Galveston, 7, 308
 gas emission scenarios, 283
 gas hydrates, 195
 Gauss
 distribution, 164, 326
 filter, 178, 279
 law of gravitation, 37
 Gazi, Kenya, 349
 Geirangerfjord, Norway, 197

 general circulation model, 266, 267
 Generalised Extreme Value (GEV)
 distribution, 322
 geocentric datum, 22, 126, 223, 232, 254
 geoid, 20, 21, 22, 233, 234, 236, 239, 240, 242, 244, 245, 246, 248
 geometrical wave spreading, 199
 GEOSAT, 212
 Gerstenkorn Event, 47
 GGOS, 224
 Gissler, Nils, 262
 Glacial Isostatic Adjustment, 127, 225, 243, 271, 278, 296, 297, 301, 312
 Glacial Maximum, 268, 301, 311, 351
 Global Geodetic Observing System, 224
 Global Navigation Satellite System, 212, 237
 Global Telecommunications System, 19, 209
 global tidal energy, 151
 Global Vertical Datum, 248
 GLONASS, 212, 224
 GLOSS, 17, 31, 33, 34, 192, 296
 GNSS, 298
 GOCE, 215, 236, 237, 239, 243
 GPS, 25, 31, 195, 210, 223, 225, 236, 242, 254, 296
 corrections, 226
 GPS-buoy system, 213
 GRACE, 30, 111, 178, 214, 236, 237, 239, 278, 279, 309, 311
 GRAIL, 237
 Grand Banks tsunami, 189, 195
 Grand Banks wave resonance, 171
 gravimeters, 299
 gravity
 annual cycle, 258
 anomalies, 240, 242, 278
 Earth tides, 7
 gradiometer, 237, 238
 inverse square attraction, 36
 measurement locations, 235
 normal force, 43
 potential, 40
 satellite orbits, 235
 tides, 9
 Green
 estuary wave amplitudes, 145, 203
 functions, 78, 127, 128, 129, 301
 Greenland, 273, 277, 279, 282, 285, 308, 310
 Greenwich Mean Time, 49, 86, *see also* Coordinated Universal Time
 Greenwich meridian, 56, 62, 73, 225
 groundwater extraction, 307
 group, tidal, 64
 grunion, 350, 351
 Gulf of Alaska, 206, 207
 Gulf of Bohai, 257
 Gulf of Cambay, 3

 Gulf of Mexico, 258, 298, 308
 Gulf of St Lawrence, 116, 117, 120
 Gulf of St Malo, 3
 Gulf Stream, 14, 240, 242, 248, 254, 273
 Gumbel cumulative distribution, 322
 Gumbel scale parameter, 326

 Halifax, Nova Scotia, 198
 Halley, Edmond, 2, 26
 halosteric MSL changes, 276
 Hamburg, 7
 hard engineering solutions, 328
 harmonic analysis, 68
 harmonic constituents
 major, 64
 shallow-water, 75
 stability, 82
 tabulation, 65
 Harris, Rollin A., 107
 Harvest platform, 233
 Hawaiian Islands, 108, 125, 190
 Hikkaduwa, Sri Lanka, 190
 Holden family, 2, 61, 94
Homo Sapiens, 351
 Honolulu, 12, 64, 68, 79, 108
 horizontal eddy viscosity, 156
 horizontal tractive forces, 41
 hour angle, 48
 Hudson Bay, 116, 151, 242, 278, 301, 304, 305
 hurricane flooding, 339
 hurricanes, 266, 320, 326
 Hutchinson, William, 61
 hydrodynamic equations, 361
 hydrostatic equation, 361
 hypomania, 354

 ICOLLS, 331
 IERS, 225, 233
 Inchon, 3
 Indian Ocean, 108, 151
 seiches, 169
 tides, 76
 tsunami, 341
 Tsunami Warning System (IOTWS), 211
 Indian Ocean Dipole, 264, 266
 Indonesia, 118, 120, 140
 Indus valley, 351
 inertial currents, 86, 367
 infragravity waves, 173
 inlet, lagoon, 329
 InSAR, 300
 interannual MSL variability, 264
 interglacial epochs, 268, 280
 Intergovernmental Oceanographic Commission, 17, 34, 209, 337, 341
 Intergovernmental Panel on Climate Change, *see* IPCC

- internal tides, 89, 107, 124, 125, 126
 internal waves, 124, 156
 International Association of Geodesy, 224, 234
 International Council for Science, 253
 International Gravity Field Service, 234
 International Hydrographic Organization, 376
 International Terrestrial Reference Frame, 223
 intertidal
 biological species, 335, 347
 bird landings, 335
 level pdfs, 337
 mangroves, 348
 pools, 345, 348
 salt marshes, 269
 zone, 346, 376
 inverse barometer, 123, 155, 174, 206, 229, 258, 259, 262, 263
 Io, tides, 40
 IPCC, 253, 276, 277, 279, 283, 284, 312, 355, 357
 Irish Sea, 114, 120, 151
 isostatic adjustment, 262
 ITRF2008, 223, 224

 Japan, 8, 171
 Japan Meteorological Agency, 195, 341
 Jason satellite missions, 77, 178, 212, 228, 232, 233, 254, 255, 275, 281
 joint tide–surge
 modelling, 156
 probability, 324
 Julian century, 68
 Julius Caesar, 352
 Jupiter, 40

 Kappa notation, 73, 87
 Karumba, 10, 11, 50, 77, 144
 sea level pdf, 319
 Katrina, Hurricane, 7, 8, 157, 162, 286, 355
 Kaula, Rule, 239
 Kelvin
 equatorial waves, 264
 Lord, 2, 63
 predicting machine, 92, 94
 wave, 99, 103, 104, 107, 120, 151, 340, 373
 Kepler, Johannes, 2
 laws of planetary motion, 45
 Kerguelen Plateau, 175
 King Canute, 352
 King John's crown jewels, 352
 Krakatoa, 189, 197, 277
 Kuril Islands, 199, 201
 Kuroshio current, 240, 254

 La Rance power station, 332, 335, 342
 Lac aux Feuilles, 122, *see* Leaf Bay
 LAGEOS geodetic satellites, 234, 235
 lagging of spring tidal amplitudes, 51
 lagoon tides, 329
 Lagrangian currents, 141
 Lagrangian filter, 32
 Lake Geneva, 165
 Lanchester–Betz law, 333
 landslides, 195
 Laplace, Marquis de, 2, 63, 106
 leading of spring tidal amplitudes, 51
 Leaf Bay, 116, 122
 least-squares fitting, 73
 Leeuwin current, 258
 legal definitions, 376
 Legendre polynomials, 41, 238
 LIB, *see* inverse barometer
 Lisbon earthquake, 8, 189, 200
 lithosphere, 301
 Lituya Bay, Alaska
 landslide, 196
 Liverpool, 23, 61, 82, 93, 94, 146, 263, 273
 load tide, 127
 local tsunamis, 192
 locally generated surge, 367
 location parameter, 323
 Loch Ness, 129
 London, 357
 Long Island Sound, 102, 115, 116, 141
 long wave
 dynamics, 99
 energy flux, 370
 non-dispersive, 193
 progression, 370
 reflection, 372
 refraction, 200
 long-period tidal species, 44
 Los Angeles, 301, 302
 Love numbers, 99, 127, 232, 256, 261
 lowest astronomical tide, 21
 Lubbock, John, 61
 lunar evection, 57
 lunar laser ranging, 152

 Maaslantkering barrier, 327, 328, 339
 macrotidal range, 77
 Madden–Julian waves, 179, 181
 Maelstrom, 141
 Maine, Gulf of, 117
 Makran subduction zone, 210
 Malacca Strait, 120
 Maldiv Islands, 203, 357
 Malta, 170
 Malvinas, *see* Falkland Islands
 managed retreat, 328
 mangroves, 346, 348, 349
 Manhousaht People, 352
 Mascarene Plateau, 125

 Massachusetts Institute of Technology, 266
 matiruku, hypomania, 354
 Mauritius, 168
 Maximum Of Maximum floods, 339
 Mean Dynamic Topography, 234, 240
 Mean High Water, 263
 Mean Sea Level, 76, 252, 326
 acceleration, 271, 273
 future commitment, 285
 future projections, 280, 284, 356
 global average reconstructions, 271
 integrated monitoring system, 279
 interannual correlation, 266
 modelling future levels, 283
 relative changes, 298
 secular trends, 271
 mean sea surface, 223, 229, 240, 241
 Mean Tidal Range, 368
 Mean Tide Level, 10, 76, 253, 368
 medieval fish ponds, 269
 Mediterranean
 seasonal MSL cycle, 258
 seiches, 169
 tides, 109, 125
 tsunamis, 189, 192, 340
 Menorca, 171
 Merian's Formula, 101, 102, 107, 166, 167
 Mesopotamia, 351
 mesoscale variability, 254
 mesotidal range, 77
 meteorological residual, 9, 157, 164, 324
 statistics, 164
 meteorological tides, 69
 meteotsunamis, 170, 171, 193
 Metonic cycle, 57, 92
 microseisms, 296
 microtidal range, 77
 Milankovich orbital effects, 57
 milghuba, 170
 Minas Basin, 93, 122, 376
 potential power scheme, 332
 Minoan civilisation, 189
 mixing fronts, tidal, 150
 Mombasa, 3, 4, 12, 51, 77, 168
 Monterey Bay, 125
 Mozambique Channel, 108
 Mount Pinatubo, 277
 Mount Tambora, 197
 mummichog, 350
 Munk, Walter, 173
 Murray Mouth, 143

 Nagasaki Bay, 171
 Nansen, Fridjof, 365
 Nargis cyclone, 157, 286
 national datums and MSL, 21
 National Flood Insurance Program, 328

- National Oceanography Centre (UK), 30, 31
- National Tidal Datum Epoch (USA), 21, 378
- Navier–Stokes equations, 205, 361
- Netherlands, 357
- New York, 13
- flooding, 7
 - harbour freezing, 318
 - hurricane Sandy, 7, 355
 - tidal currents, 141, 329
 - tidal power, 334
 - tide mill, 331
 - tides, 64, 68, 116
 - tsunami risk, 197
- New Zealand, 108, 334
- Newfoundland, 171
- Newlyn, 10, 139, 143, 322
- diurnal tides, 13
 - emersion statistics, 335, 346
 - extreme levels, 321
 - nodal tides, 70, 87
 - Ordnance Datum, 244
 - residuals, 165
 - sea level pdf, 319, 336
 - tidal stability, 88
 - tide predictions, 11, 89, 90
- Newton, Isaac, 2
- law of gravitational attraction, 36, 97
 - laws of motion, 36, 362
 - polar flattening, 226
 - Principia*, 2
- Nezugaseki, Japan, 296, 297
- Nice airport slide, 196
- Nilometers, 94
- Nivellement Général de la France, 246
- NOAA, 21, 24, 92, 141, 211, 339, 340, 378
- Noah's Flood, 352
- nodal
- modulations, 71
 - MSL changes, 244, 261
 - tidal changes, 70, 376
 - tides, 53, 261
- non-dispersive propagation, 100
- non-divergent shelf waves, 113
- non-harmonic equivalent terms, 75
- Normaal Amsterdams Peil, 244
- North American Vertical Datums, 246
- North Atlantic gyre, 278
- North Atlantic Oscillation, 162, 261, 264
- North Sea, 6, 81, 114, 120, 129, 150, 312, 339
- currents, 84
 - flooding, 7, 157, 158
 - pole tide, 260
 - seasonal tide, 159
 - selective tidal stream transport, 350
 - tides, 113
- Nova Scotia, 327
- N-waves, 203, 205
- Nyquist criterion, 75
- obliquity of the ecliptic, 45
- OECD, 342
- open-sea gauges, 30
- orbit of satellite
- prograde, 228
 - retrograde, 228
 - sun-synchronous, 229
- orbital elements, 45, 68
- Ordnance Datum Liverpool, 244
- Ordnance Datum Newlyn, 21, 244
- Ordnance Datums, 244
- Ordnance Survey (UK), 377
- origin of life, 345
- Orissa, 7
- orthometric heights, 242
- Osaka, 308
- overtopping, 328
- Pacific Decadal Oscillation, 264
- Pacific Ocean, 107, 125, 151, 340
- tsunamis, 190
- palaeo-tides, 47
- Panama Canal, 242
- Papua New Guinea, 305, 356
- Patagonian Shelf, 151
- Pavlopetri, Greece, 351, 352
- peak over threshold, 325
- pearl of ebb tradition, Japan, 354
- Peninsula Valdes, Argentina, 334
- Pentland Firth, 120, 334
- perigean spring tides, 52
- perigee, 45, 52
- perihelion, 46, 56, 261
- Perkins Tide Mill, 331
- permanent tide, 232
- Persian Gulf, 118, 120
- photosynthesis, 347
- plaice, 350
- pneumatic pressure gauges, 26
- Poincaré waves, 111, 112, 373
- Poisson distribution, 322
- polar drift, 260
- polar ice sheets, 268
- polar motion, 223, 260
- pole tide, 260
- poles, tide, 22
- Port Arthur, Tasmania, 274
- Port Leopold, Canada, 263
- Port Louis, Falkland Islands, 274
- Port Stanley, Falkland Islands, 167
- Portland Bill, 136, 142
- power generation, 331, 333
- Precise Point Positioning, 226
- predictions of tides, 89
- priming of tides, 51, 146
- probability density functions, 11
- progressive wave, 100, 107, 120, 150, *see also long wave*
- Proudman resonance, 171
- Proudman, Joseph, 171
- PSMSL, 33, 252, 253, 256, 265, 267, 271, 273, 305, 307
- PTWC, 192
- public opinion, 343
- Puerto Gallegos, Argentina, 3
- Qiantang river, 147
- bore, 147, 149
- Québec City, 145, *see also St Lawrence River*
- Québec MSL for datums, 246, *see also St Lawrence river*
- Rada Covadonga, 180
- radar gauges, 28, 209
- radiation stress, 172
- radiational tides, 9, 80, 122
- Rayleigh
- criterion, 69, 74
 - seismic pulse, 206
- Red Sea, 109, 110, 258, 268
- reference ellipsoid, 226
- refraction of tsunamis, 200
- refuge mounds, 354
- related tidal constituents, 74
- relative MSL, 254, 296, 301
- Representative Concentration
- Pathways, 284
- residual currents, 142
- resonance, 48, 97, 100, 102, 103, 107, 113, 129, 171, 334, 386
- response analysis, 78, 80
- response weights, 79
- return period, 320
- Revised Local Reference datum, 33, 254
- Richter scale, 189
- ridge waveguides for tsunamis, 200
- Right Ascension, 44, 46, 47, 49, 64
- Ring of Fire, 190
- risk, 319, 342
- rissaga, 169, 172
- River Dee, 146
- rivers
- level stands, 146
 - runoff, 242
 - spring–neap effects, 145
 - tides, 144
- rocky shores, 347
- Rodrigues Island, 169, 170
- Roman law, 377
- Ross, James Clark, 2, 262, 263, 274
- Rossby
- Haurwitz oscillation, 179
 - radius, 104, 105, 107, 112, 113, 118
 - radius defined, 367
- rotary current components, 86

- runup, 195, 203
runup factor, 205
- St Albans Abbey tide table, 94
St Helena, 29, 129
St Lawrence River, 116, 145, 257
St Lucie Inlet, 330
St Petersburg, 328
salt marsh records of sea level, 269
salt marshes, 271, 328, 348, 349
Samoa tsunami, 199
San Francisco
 age of tides, 76
 currents, 92
 emersion statistics, 335, 336, 346
 MSL, 265
 non-tidal statistics, 164
 Standard Port, 93
 tidal form factor, 77
 tidal predictions, 93
 tides, 4, 5, 64, 68
Sanborn Cove, Maine, 269
Saros period, 57
satellite
 altimetry, 126
 data transmission, 19
 low Earth orbit, 212
 navigation systems, 224
Satellite Laser Ranging, 223, 235
scale parameter, 323
Scandinavia, 301
Schureman, Paul, 68
Scottish Law, 377
sea defence walls, 328
sea floor earthquake, 000, *see also*
 tsunamis
sea-level budget enigma, 277
sea-level slopes, 248
Sea Palling, England, 158
Sea Surface Height, 227
Seasat, 254
seasonal cycle of MSL, 256
Secondary Stations, 92
secular MSL changes, 269
secular tidal changes, 129
sediment transport, 143
sedimentary shores, 348
seiches, 8, 101, 125, 207
 periods, 165
 uninodal, 101
selective tidal stream transport, 351
semi-diurnal tidal species, 44
semi-empirical models of MSL rise, 283
set-down, 172, 173
Severn Estuary, 327, 337
 power generation, 333
Seychelles, 168
Seymour Narrows, 198
shallow-water
 constituents, 72
 dynamics, 156
 response analysis, 80
 tides, 71, 76, 133
Shanghai, China, 115, 308, 357
Sheerness, 158, 159, 165, 166, *see also*
 Thames Estuary
shelf resonances, 171
Shetland Islands, 167, 195, 196
shoaling of tsunamis, 203
SI units, 18
sidereal period, 37
significant wave height, 227
skew-surge, 159, 160, 161
slack water, 329
sloping beaches, 348
SLOSH, 339
sluices, 328
Snell's law, 200
Socorro Island, 301
soft engineering solutions, 328
solstitial tides, 51
SONEL, 298
source function, tsunami, 195
Southampton
 double tides, 6
 shallow-water tides, 133
 tide mill, 331
 tides, 134
Southern Annular Mode,
 178, 266
Southern Ocean, 175, 309, *see also*
 Antarctic Circumpolar Current
Southern Oscillation Index, 264
Spartina grasses, 348
species, tidal, 64, 68
spectral analysis, 13
Split, Croatia, 349
Sputniks, 234
Sri Lanka, 167
Standard Port, 83, 84
Standard Stations, 89
standing waves, 100, 101, 115, 120,
 150, 372
Starlette, 234
still water level, 8, 254
stilling well, 24, 78
Stockholm, 296, 297
Storegga slide, 189, 195, 196
storm surge, 156, 157
straining, tidal, 111
Strait of Gibraltar, 125
Strait of Messina, 125, 140, 141
Strangford Lough, 334
submarine cables, 210
Submerged Lands Act, 378
submerged rotors, 333
Sukuiso, Japan, 190
Sumatra
 2004 earthquake, 189
 earthquake, 209, 307
 tsunami, 194, 201, 202
sundial time, 46, *see also* Equation of
 Time
sun-synchronous orbits, 77
surf beat, 173
Sverdrup volume transport, 175
Sverdrup waves, 374
SWOT, 162
synodic period, 51
synthetic aperture radar, 125
Synthetic Aperture Radar
 Interferometry, 301
syzygy, 3, 53
- Tafjorden, Norway, 197
Takoradi, Ghana, 273
Tasmania, Australia, 298
terpen refuge areas, 352
Territorial Seas, 376
Thames Barrier, 158, 328, 339
Thames Estuary, 2, 23, 129, 158,
 159, 164
thermotic MSL changes, 275
tidal constants, 60
tidal prism, 329, 331
Tide Gauge Bench Mark, 21, 33, 225,
 297
tide tables, 2, 89, 92, 319
tide+surge models, 156
tidelands, 377
tide-surge interaction, 157
TIGA, 298
time zone conversion, 86
Tōhoku
 2011 earthquake, 189, 201
 tsunami, 195, 204
TOPEX/Poseidon, 77, 212, 228, 229,
 232, 233, 254, 260, 275
Toyoy, 308
transoceanic tsunamis, 192
travel-time chart for tsunamis, 202
trends in tides, 129
Trieste, 308
Trincomalee Bay, Sri Lanka, 169
Tropic of Cancer, 46, 50
Tropic of Capricorn, 46, 50
tropic tides, 50
tropical storms, 157, 161, 323
troposphere altimeter corrections, 226
tsunamis, 189
 amplitude dispersion, 193, 199, 203
 asteroid and comet impacts, 197, 198
 bottom pressure detection, 206
 catalogues, 189, 191
 Chile, 307
 deaths, 191
 distance of dispersive destruction, 199
 distance of non-linear destruction,
 203
 frequency dispersion, 193

- Indian Ocean, 8
- infrasound detection, 214
- local, 195
- man-made explosions, 198
- modelling, 200
- MOST, 200
- ocean ridge wave guide, 200
- progressive wave, 200
- propagation, 199
- source function, 194
- submarine earthquake, 193
- submarine landslides, 196
- terrestrial landslides, 196
- travel-time chart, 202
- tsunameters, 194, 208
- volcanic eruptions, 197
- warning, 340
- watch alert, 209
- Tuamotu Archipelago, 125
- Tunguska air burst, 198

- UNCLOS, 376
- undersea earthquakes, 189
- Ungava Bay, 3, 116, 122

- United Nations Environment Program, 337
- universal gravitational constant, 39
- University of Hawaii Sea Level Center, 33, 164, 254

- Valdivia earthquake, 190
- Van Allen radiation, 228
- Van de Castelee test, 22
- Vancouver Island, 196, 352
- variance, 13
- Venice, 8, 110, 170, 308, 328, 357
- Venus, 40, 346
- vertical tidal forces, 41
- Very Long Baseline Interferometry, 223
- Vieux-Québec, 145
- viscosity, 366
- volcanic eruptions, 197, 274
- Von Humboldt, Alexander, 3
- vorticity, 142

- Walker circulation, 264
- wave set-up, 172, 256
- wave speed, 135

- weather effects, 7, 155
- West Antarctic Ice Sheet, 278, 281
- wet correction, 226
- Whewell, William, 108, 109
- wind stress, 155, 263
- withdrawal preceding tsunami arrival, 203
- World Data Service for Geophysics, 192
- World Geodetic System, 226
- World Meteorological Organization, 337

- X₀ filter, 33, 252

- Yellow Sea, 114, 115, 151
- young flood stand, 133
- Young, Thomas, 2
- Yucatan peninsula asteroid, 197

- Zapiola Rise, 175
- zonation of plants and animals, 346, 347, 350
- zone, intertidal, 346
- Zuiderzee Works, 328

